CONTENTS

Marine Information Science

Research Note

Perspective

A numerical simulation of the generation and evolution of nonlinear internal waves across the Kara Strait

Qun Li[1]*, Huiding Wu[1], Hongwei Yang[2], Zhanhai Zhang[1]

[1] Polar Research Institute of China, Ministry of Natural Resources, Shanghai 200136, China

[2] College of Mathematics and Systems Science, Shandong University of Science and Technology, Qingdao 266590, China

Abstract

Nonlinear internal waves (NIWs) are ubiquitous around the Kara Sea, a part of the Arctic Ocean that is north of Siberia. Three hot spot sources for internal waves, one of which is the Kara Strait, have been identified based on Envisat ASAR. The generation and evolution of the NIWs through the interactions of the tide and topography across the strait is studied based on a nonhydrostatic numerical model. The model captures most wave characteristics shown by satellite data. A typical inter-packets distance on the Barents Sea side is about 25 km in summer, with a phase speed about 0.65 m/s. A northward background current may intensify the accumulation of energy during generation, but it has little influence on the other properties of the generated waves. The single internal solitary wave (ISW) structure is a special phenomenon that follows major wave trains, with a distance about 5–8 km. This wave is generated with the leading wave packets during the same tidal period. When a steady current toward the Kara Sea is included, the basic generation process is similar, but the waves toward the Kara Sea weaken and display an internal bore-like structure with smaller amplitude than in the control experiment. In winter, due to the growth of sea ice, stratification across the Kara Strait is mainly determined by the salinity, with an almost uniform temperature close to freezing. A pycnocline deepens near the middle of the water depth (Barents Sea side), and the NIWs process is not as important as the NIWs process in summer. There is no fission process during the simulation.

Key words: nonlinear internal wave, nonhydrostatic numerical model, Kara Sea, synthetic aperture radar

1 Introduction

The life cycle of nonlinear internal waves (NIWs) continues to be an active research area (Lee and Beardsley, 1974; da Silva et al., 2015; Zhao et al., 2016; Xu et al., 2016). A common generation mechanism involves stratified tidal flows over large-amplitude topography, such as sills, continental shelf-slope regions (Vlasenko et al., 2014), and submarine ridges (Buijsman et al., 2010; Wang et al., 2010; Xu et al., 2014).

Research focusing on the dynamics of the NIWs at high latitudes is sparse compared with studies at lower latitudes. Tides appear to be the main energy source supporting enhanced vertical mixing in the marginal seas of the Arctic Ocean and these may generate vertical heat fluxes greater than 50 W/m^2 (Rippeth et al., 2015). Internal gravity waves generated by tide-topography interactions and their ultimate breakup are a major mechanism for enhanced vertical mixing and dissipation rate over rough topography. The NIWs are ubiquitous around the Kara Sea, a sea on the margin of the Arctic Ocean (Kozlov et al., 2015; Morozov et al., 2008). Three hot spot sources for the internal waves, one of which is the Kara Strait, have been identified based on Envisat ASAR. The Kara Strait (with its center approximately 70.5°N, 58°E) is about 4° below the critical latitude of the semidiurnal internal tide. It is in northeastern Europe, between the Barents Sea and Kara Sea. Many field experiments have been conducted around the Kara Strait. Morozov et al. (2003) reported mooring records deployed inside the strait. Temperature fluctuations indicated an internal tide with M_2 frequency. Further observations were made about 10 a later (Morozov et al., 2008), using towed CTD measurements across the section from the Kara Sea to the Barents Sea. This section provided a snapshot of the vertical displacement of temperature, and indicated an internal bore structure toward the Barents Sea and a hydraulic jump just downstream (from south to north) of the sill. A radar image analysis shows short-period internal wave (IW) trains following the internal bore. Morozov et al. (2008) presented a 2-D nonhydrostatic numerical model for the observed phenomenon and this was consistent with the experimental results. However, they did not provide an analysis of the generation and evolution of the internal tide.

A linear theory predicts that the internal tide activity is suppressed close to or above the critical latitude, which is 74.5°E for M_2 frequency (Vlasenko et al., 2003). Vlasenko et al. (2003) noted that when nonlinearity of the generated waves was sufficiently strong, topography-scale short IWs were produced with characteristics similar to those of unsteady lee waves. Kurkina and Talipova (2011) modeled the generation and evolution process of

*Corresponding author, E-mail: liqun@pric.org.cn

large amplitude NIWs around Spitsbergen Island. They suggested that the strong nonlinear unsteady lee internal waves were generated by the barotropic tide in the Barents Sea above the critical latitude.

We studied the dynamic process of the NIWs across the Kara Strait using a 2-D nonhydrostatic numerical model. In this report, Section 2 presents observational evidence and background conditions. Numerical model configuration details are given in Section 3, and the model results are discussed in Section 4. A summary and discussion are presented in Section 5.

2 Background

2.1 *Observational evidence*

Severe weather and ice conditions limit the *in situ* observation of internal wave processes around the Kara Sea. Mooring and hydrographic section investigation across the Kara Strait in the summer of 1997 provided the first evidence of large-amplitude internal waves (≈10–20 m at 80 m water depth, with an upper layer approximately 25–30 m), and identified tide-sill interaction as the main mechanism.

In contrast to the *in situ* measurements, remote sensing is often used to capture the NIWs in the ocean, especially SAR imagery. Kozlov et al. (2015) made IW observations from July to October 2007 around the Kara Sea using satellite ENVISAT ASAR data. They presented spatial statistics of IW signatures and their properties in the Kara Sea. Three hot spot sources, one of which is the Kara Strait, were identified. Basic wave characteristics were consistent with previous *in situ* data. A group of typical ASAR images is shown in Fig. 1. At the initial time, the waves generated on both sides are nearly symmetric, with 2-D characteristics (Fig. 1a, BA wave towards the Barents Sea and KA wave toward the Kara Sea). After exiting the source region, the wave showed different characteristics that resembled wave trains on the Barents Sea side (Figs 1b and c, BA wave in two adjacent tidal periods) and the 3-D features were pronounced. A typical feature in Fig. 1b is two adjacent single-wave structures near the source region, separated by a distance of approximately 6 km (BA and BC waves). These features were verified in the modeling results.

2.2 *Bathymetry and stratification across the Kara Strait*

Bathymetry across the Kara Strait is asymmetric, with a depth of approximately 80 m in the Barents Sea and a depth of approximately 200 m in the Kara Sea (Fig. 2a). The length scale of the sill is approximately 20 km, with the shallowest depth of approximately 50 m (Fig. 2b). The slope is steeper on the Barents Sea side
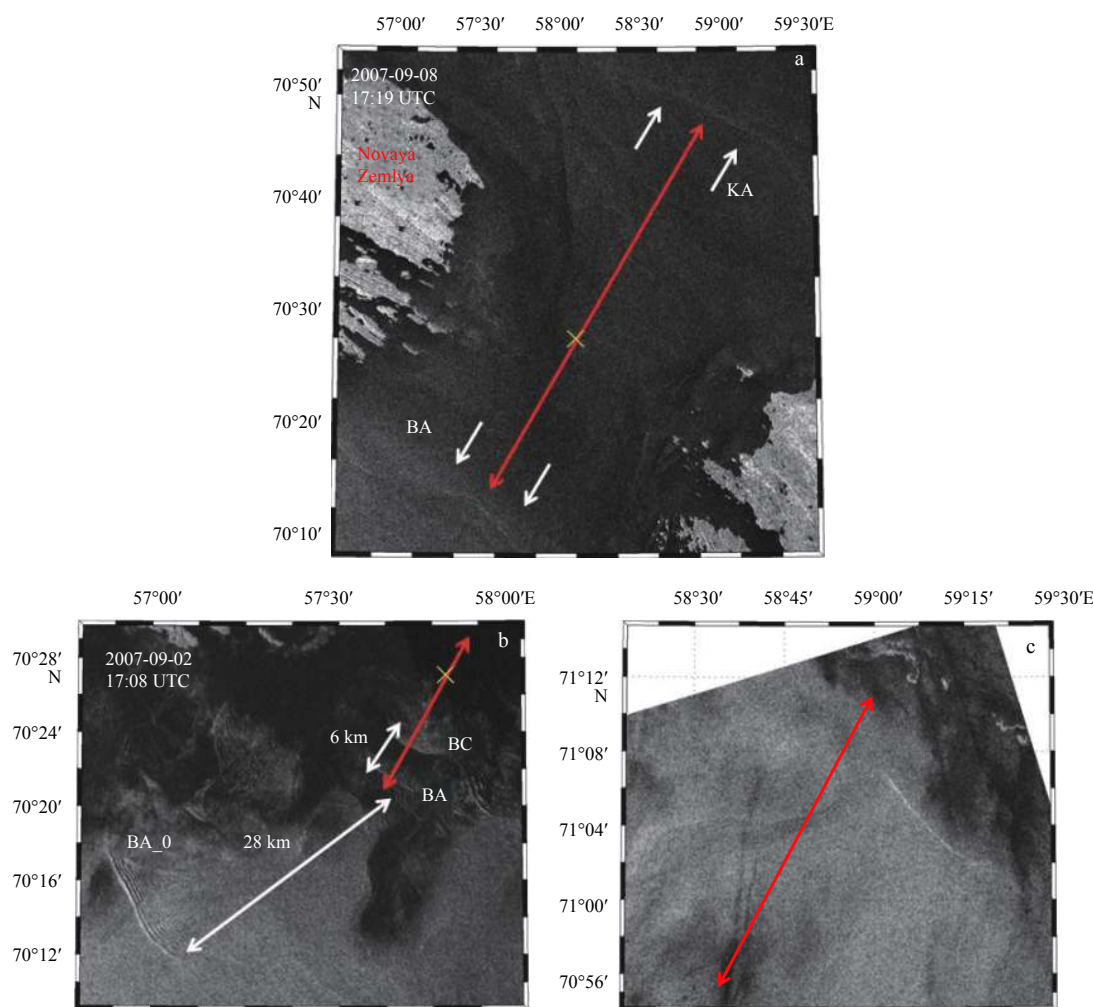

Fig. 1. ENVISAT ASAR images of internal waves (bore/packets) around the Kara Strait. The red line indicates topography section used in the model. The white line with double arrow indicates inter-packets distance. The white line with single arrow indicates particular wave. The "×" indicates the summit of the sill and the name of the wave is consistent with the name in the model results.

than on the Kara Sea side. The difference of the topography features between the sides may result in different properties of tide-induced IWs towards the opposite direction.

Stratification around the Kara Strait shows seasonal differences (Fig. 3). In summer, the upper layer has low salinity owing to the melting of sea ice, and its temperature increases through solar radiation absorption (Fig. 3a). This produces a strong gradient of temperature, salinity and density at the approximately 30 m depth (Fig. 3b, solid line). Below the pycnocline, stratification is weak. In winter, the sea ice cover may reach this region, producing a mixed layer of approximately 20 m of nearly freezing water and the salinity reaching approximately 32.5 (Fig. 3a, dashed line). Stratification in winter is mainly determined by the salinity because the temperature difference over the entire depth is small and the pycnocline is greater than 40 m (Fig. 3b, solid line).

2.3 *Tide and background current*

A tide analysis shows that the major axis of the tidal current is consistent with the cross-section of the strait, and the amplitude of the tide was approximately 0.2 m/s. There was a background current with amplitude of approximately 0.12 m/s from the Barents to the Kara Seas. Recent *in situ* measurements have verified the existence of tide-induced, large-amplitude IWs (Morozov et al., 2008).

Internal tides may be generated under the conditions of efficient tidal forcing and dramatically varying bathymetry combined with suitable stratification. Combining the bathymetry and stratification allows the calculation of a forcing term to quantify internal tide generation. This is

$$F(z) = 2\pi N^2(z)\, U H_x / (H\omega_f), \tag{1}$$

where U is the barotropic tidal current; H is water depth and ω_f is the forcing frequency (Pichon et al., 2013). Vertical integration $\int_0^H F(z)\,\mathrm{d}z$ of the forcing term provides evidence of a dominant region of the internal tide generation across the strait (Fig. 2b). The integrated forcing displays several IT excitation regions. The strongest of these occurs around the shallowest sill, and the
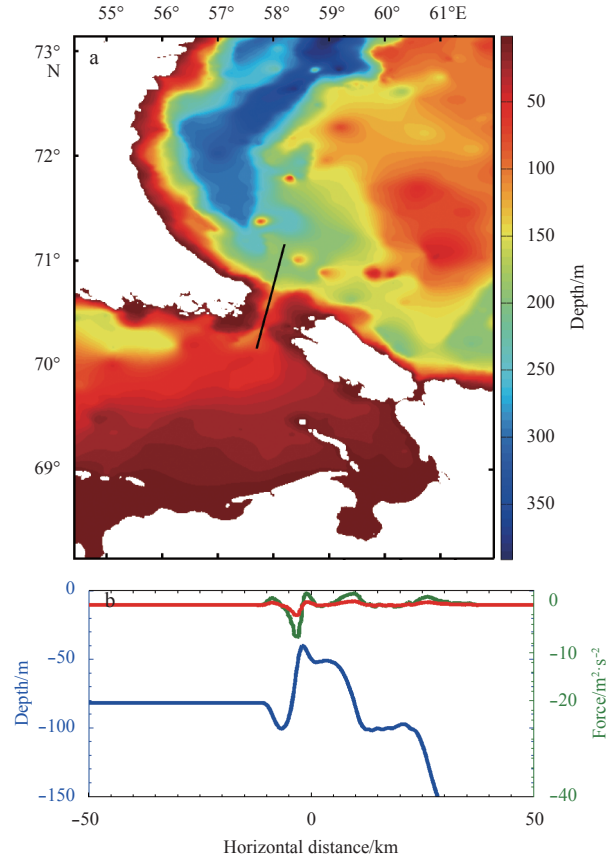
Fig. 2. Topography around Kara Strait and 2-D bathymetry section across the strait (black line) used in the model (bathymetry data from GEBCO1 min, (IOC, IHO, and BODC, 2003)) (a) and the vertical integrated forcing calculated with Eq. (1) (b). The green is summer stratification and the red is winter stratification.

second is downstream at a distance of approximately 10 km. These multiple structures increase the pattern complexity of generated IWs. Furthermore, forcing in summer was more than three
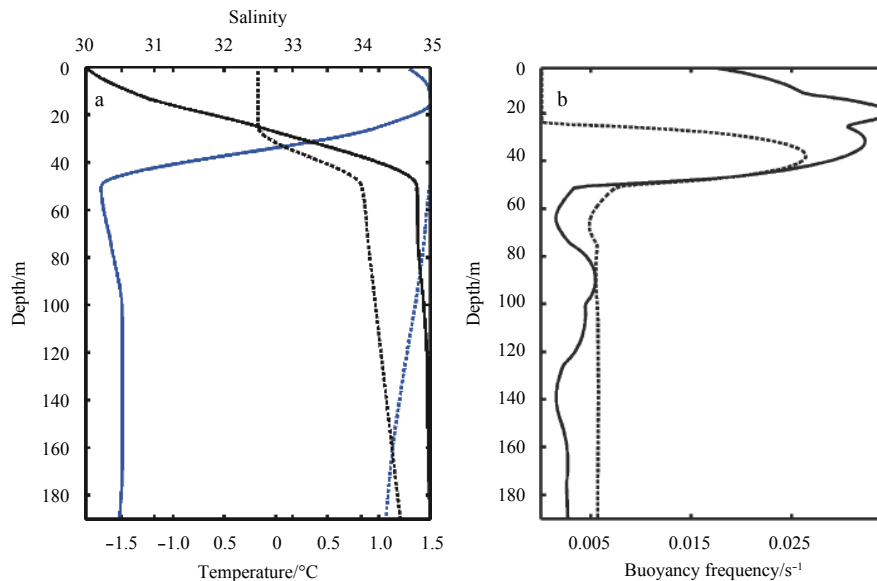
Fig. 3. Temperature (blue) and salinity (black) profiles from observations (Harms and Karcher, 1999) in summer (solid) and winter (dashed) (a) and corresponding buoyancy frequencies (solid black represents summer and dashed black winter) (b).

times greater than that in winter, because of the weaker and thinner pycnocline during winter (Fig. 2b).

3 Model configuration

The background conditions support the existence of tide-induced IWs, as verified by the *in situ* observations and ASAR data. Another effective method to investigate the dynamic processes is based on numerical modeling. We used the Massachusetts Institute of Technology general circulation model (MITgcm) for all of the numerical experiments (Marshall et al., 1997). The MITgcm integrates the incompressible Boussinesq equations, assuming a linear equation of state:

$$\frac{\partial}{\partial t}\,\vec{u} + \vec{u}\cdot\nabla\,\vec{u} + f\,\vec{k}\times\vec{u} = -\nabla p + b\,\vec{k} +$$
$$\nu_{h}\left(\frac{\partial^2}{\partial x^2} + \frac{\partial^2}{\partial y^2}\right)\vec{u} + \nu_{v}\frac{\partial^2}{\partial z^2}\,\vec{u}, \tag{2}$$

$$\nabla\cdot\vec{u} = 0, \tag{3}$$

$$\frac{\partial}{\partial t}\,b + \vec{u}\cdot\nabla b = k\nabla^2 b, \tag{4}$$

where $\vec{u} = (u, v, w)$ is the velocity vector; p is density-scaled pressure; t, x, y and z are time and space coordinates; b is buoyancy; ν_h and ν_v are horizontal and vertical viscosity constants; k is tracer diffusivity; f is the Coriolis parameter; and $\vec{k}$ is the unit vector in the vertical direction (see http://mitgcm.org, for more details).

In contrast with common large-scale processes in the ocean, the ISWs represent a balance of nonlinearity and dispersion, with the latter derived from a nonhydrostatic pressure. Therefore, we turned on the nonhydrostatic capability of the MITgcm in all of the experiments, allowing an explicit simulation of the dynamic properties of ISWs. A sufficiently high grid resolution was used to resolve mixing processes due to instability, and no sophisticated subgrid-scale mixing scheme was used. As in Vlasenko et al. (2014), the Richardson number-dependent parameterization for turbulent closure of the vertical viscosity v and the diffusivity k (Pacanowski and Philander, 1981) was used:

$$\nu = \frac{\nu_0}{(1 + \alpha Ri)^n} + \nu_b,$$
$$k = \frac{\nu}{(1 + \alpha Ri)} + k_b, \tag{5}$$

where $Ri = N^2(z)/(u_z^2 + v_z^2)$ is the Richardson number; u and v are the components of horizontal velocity; $\nu_b = 10^{-5}$ m²/s and $k_b = 10^{-5}$ m²/s are the background viscosity and diffusivity, respectively; $\nu_0 = 1.5\times10^{-2}$ m²/s; $\alpha = 5$ and $n = 1$ are adjustable parameters. Such a parameterization increases v and k in areas where Ri is small. The horizontal viscosity and diffusivity were set to a constant 0.5 m²/s.

The horizontal computation domain had a length of 300 km and was comprised of 6 000 grid cells, with the sill summit at the center. The horizontal grid resolution around the focusing region was $\Delta x = 20$ m, which is adequate to resolve most relevant processes in the model. These included the disintegration of the internal tides or lee waves and the subsequent generation of internal solitary wave trains. This resolution was increased to several hundreds of meters toward the open boundary. The choice of a horizontal grid is consistent with the resolution requirement in nonhydrostatic IW modeling (Vitousek and Fringer, 2011).

There were 200 layers in the vertical dimension, with the deepest region of approximately 190 m on the Kara Sea side. The vertical grid resolution was $\Delta z = 0.95$ m, and the time step $\Delta t = 5$ s was used to keep the model stable.

The tide and the background current were applied on the open boundaries to keep the barotropic flow in phase on the south and north sides. By doing so, depth-integrated horizontal flow (volume flux) was independent of the horizontal coordinate (da Silva et al., 2015).

4 Results

4.1 Results of linear theory

With linear approximation and variable separation technologies, an eigenequation for the vertical mode structure (Cushman-Roisin and Beckers, 2011) can be derived:

$$\frac{d^2}{dz^2}\,W + k_h^2\,\frac{N^2(z) - \omega^2}{\omega^2 - f^2}\,W = 0, \tag{6}$$

with boundary conditions $W = 0$ at $z = 0$ and $z = -H$, corresponding to a rigid lid at the top and flat bottom. As an eigenvalue problem, there is an entire series of special (ω, k_h) values for which $W(z)$ may be nonzero. These are called eigenvalues, and corresponding $W(z)$ solutions are called eigenfunctions or, more specifically in this configuration, vertical modes. The normalized $W(z)$ has a vertical structure of a different mode with (ω, k_h). The pair of (ω, k_h) represents the dispersion relation of the stratified ocean, from which we can examine basic wave properties under different stratifications. With the frequency of the M_2 tide, the first two modes with stratification used here were calculated and are presented in Fig. 4 for waves on the Barents Sea side. The maximum amplitude of the Mode 1 wave was around the pycnocline, while Mode 2 with two extremes was on both sides of the

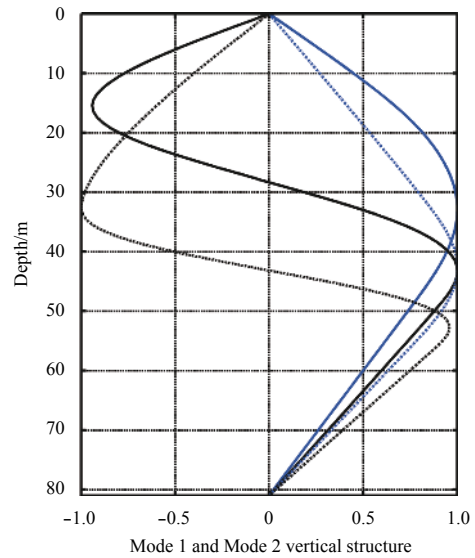**Fig. 4.** Mode 1 and Mode 2 vertical structure function (from iwave, a Matlab program for the calculation of Eq. (4.1) (Cushman-Roisin and Beckers, 2011)) on the Barents Sea side (the solid blue line is Mode 1 with summer stratification and the solid black line is Mode 2 with summer stratification; the dashed blue is Mode 1 with winter stratification and the dashed black is Mode 2 with winter stratification).

pycnocline. In the winter case, the Mode 1 structure was almost symmetric, which may induce weak nonlinearity according to a KdV theory (Grimshaw et al., 2010).

We let $k_h \in [2\pi/(50 \text{ km}), 2\pi/(5 \text{ km})]$ be within the range of typical observation, and a series of corresponding frequency ω was calculated. Figure 5 shows this relation under the winter (dashed blue) and summer (solid blue) stratifications on the Barents Sea (at 81 m depth) side, along with the M_2 tide frequency (dashed red), $f = 1.37 \times 10^{-4} \text{s}^{-1}$ was used in the calculation (corresponding to latitude 70.5°N). The frequency and the wavelength have an inverse relation, i.e., lower-frequency waves are typically longer. At the frequency of the semidiurnal tides, we found the typical wavelength in the winter case to be 15 km, and in the summer case it was 23 km.
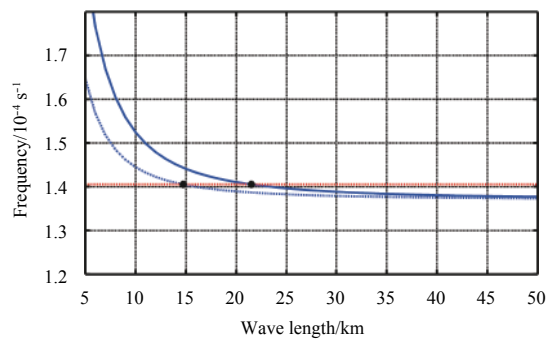

Fig. 5. Dispersion relation based on summer (solid blue curve) and winter (dot-dash blue line) stratification on Barents Sea (depth 81 m) side. The dot-dash red line shows M_2 tide frequency.

The basic parameter classifying the generation mechanism is the Froude number (Vlasenko et al., 2005), which is defined as the ratio of forcing current to phase speed of the generated baroclinic waves. Table 1 shows linear phase velocity results calculated using the mode equation, and they are used as a reference in the following analysis.

Table 1. Linear phase speed (m/s) for first two modes for two different local water depths, with summer and winter stratifications

	Speed			
	Summer		Winter	
	80 m	45 m	80 m	45 m
Mode 1	0.67	0.45	0.45	0.23
Mode 2	0.28	0.21	0.14	0.10

Note: Eighty meters was water depth on the Barents Sea side and 45 m was water depth at the sill crest.

4.2 *Model results*

Using the theoretical analysis, we investigated the details of the dynamic process of IW generation and evolution. We conducted three experiments, among which the reference experiment included only tide forcing (Table 2) and used the summer T/S profile shown in Fig. 3a. We also studied the sensitivity of model results via the other two experiments. One experiment had an additional steady current tuned to simulate the observed background current across the strait (northward) as forcing, and the other with the winter stratification.

4.2.1 *Generation and evolution of NIWs in reference experiments*

Figure 6 presents a Hovmöller diagram of displaced isopycnal at a depth of 25 m. A Phase speed is estimated from the

Table 2. Experiments configuration

Exp. ID	Forcing	Stratification	Forcing amplitude/m·s⁻¹
1	only semi-diurnal tide	summer	0.2 (U_{ti})
2	tides plus northward steady current	summer	0.2 (U_{ti}) + 0.12 (U_0)
3	only semi-diurnal tide	winter	0.2 (U_{ti})

Note: U_{ti} is the tide speed.
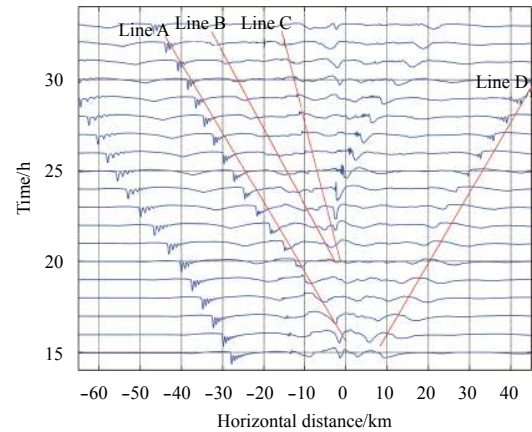
Fig. 6. Hovmöller diagram presenting displaced isopycnal at 25 m depth along the model transect, with time increasing vertically upward (1 h step). The red line A to C indicates the evolution of various wave trains generated during the same tidal period. Line D shows one ISWs toward the Kara Sea.

slope of Line A, Line B is approximately 0.69 m/s, and Line C is approximately 0.30 m/s, which is similar to the estimation based on the linear theory (Table 1). The spatial structure of the modeled mode-1 IW compared well with that captured by the ASAR image (Fig. 1) and *in situ* observations. The inter-ISW distance of O (0.5–1 km) after two tidal periods with leading wave amplitude approximately 15 m were similar to previous reports (Kozlov et al., 2015; Morozov et al., 2008). The distance between two main consecutive ISW packets was approximately 25 km on the Barents side, and a slightly larger distance on the Kara Sea side, from which we estimated a phase speed of approximately 0.72 m/s. This is consistent with the linear theory and estimation based on the slope of a single wave train in the Hovmöller diagram. Within one wave packet, nonlinear characteristics were clear when compared with the inter-ISW distance of the following two wave packets. For example, at $t = 25$ h in Fig. 6, inter-ISW distance increased from that at $x = -27$ km to the one at $x = -55$ km. If we follow the evolution of the isopycnal in Fig. 6 from $t = 15$ h, an isopycnal disturbance around the summit of the sill began splitting into two parts, one toward the Barents Sea and the other toward the Kara Sea. After about 6 h evolution ($t = 21$ h), nonlinear effects steepened the front of the initial disturbance and disintegration into a solitary structure began. Meanwhile, just behind this leading wave at a distance of approximately 5 km, a dome structure gradually split into two parts. One propagated along line B, with a phase speed similar to the leading wave train, and the other had a slower phase speed of approximately 0.30 m/s, which is consistent with the Mode 2 phase speed (Table 1). The wave indicated by Line B exhibited internal bore properties. Its speed was slower than the leading wave as seen in the first tidal period, when the distance of this structure from the leading wave front reached approximately 15 km. This process is clarified in

Fig. 7 because the evolution of one single isopycnal is insufficient to illustrate the multimodal structure.

The superposition of the baroclinic horizontal speed and isopycnal gives more detail on the IW generation process during tide-topography interaction. In Fig. 7, we present this superposition for one tidal period (t = 15–25 h). The horizontal baroclinic speed was calculated by the modeled horizontal speed minus the vertically integrated horizontal speed. This means that the integrated baroclinic horizontal speed was 0. Figure 7 shows this process from t = 15 h as in Fig. 6, i.e., the onset of generation of the southward disturbance during the second tidal period. From t = 15 h (F-1, Fig. 7a), the southward tidal current reached 0.46 m/s, which was close to its maximum. This was comparable with the phase speed of Mode 1 IWs at 45 m depth under the summer stratification (Table 1). Wave KA toward the Kara Sea released from the main sill, and with the increase of flooding current, a trough began to develop downstream of the main sill (Fig. 7b, t = 17 h). As the tidal current speed is still larger than the phase speed of Mode 1, the trough downstream of the sill became clearer (BA), and a Mode 2 convex type wave BB emerged just behind the BA wave. Its phase speed from the linear theory was approximately 0.3 m/s (Table 1), which means that it could be trapped for a longer time during the flooding. After about 1 h, the BA was released and propagated over the sill toward the Barents Sea. Subsequently, at t = 19 h, the trapped Mode 2 wave (BB) was fi-

nally released and passed over the summit of the sill (Fig. 7c). On the basis of snapshot of the vertical structure of the horizontal velocity field, this wave propagated toward the Barents Sea (Fig. 7c, BB wave).

From t = 21 h (Fig. 7d), nonlinear effects became increasingly important on both sides of the leading waves, which became steeper on their front side. Leading wave BA on the Barents Sea side even began to disintegrate. During this process, the Mode 2 type wave following the leading wave gradually decayed, becoming a blur away from the main topography. Wave BC emerged in Fig. 7e. After several hours of evolution (Fig. 7f), that wave evolved into an internal bore structure following the leading BA wave in the same tidal period, with a following distance of approximately 10 km.

A complete view of the baroclinic wave field after two tidal periods is shown in Fig. 8. Two clear ISW trains emerged, with an inter-packet distance of approximately 27 km, a result slightly larger than that from the linear theory. This is partially attributable to the nonlinear properties of the ISW trains. On the basis of the weakly nonlinear KdV theory (Grimshaw et al, 2010; Li and Farmer, 2011; Chen et al., 2014), the nonlinear contribution to the phase speed, $\alpha A/3$; α = 0.041 8, is the nonlinear parameter on the Barents Sea side. With A=15 m, this contribution reached 20%–30%, which could explain the difference from the linear theory. On the Kara Sea side, the ISW trains were weaker than their
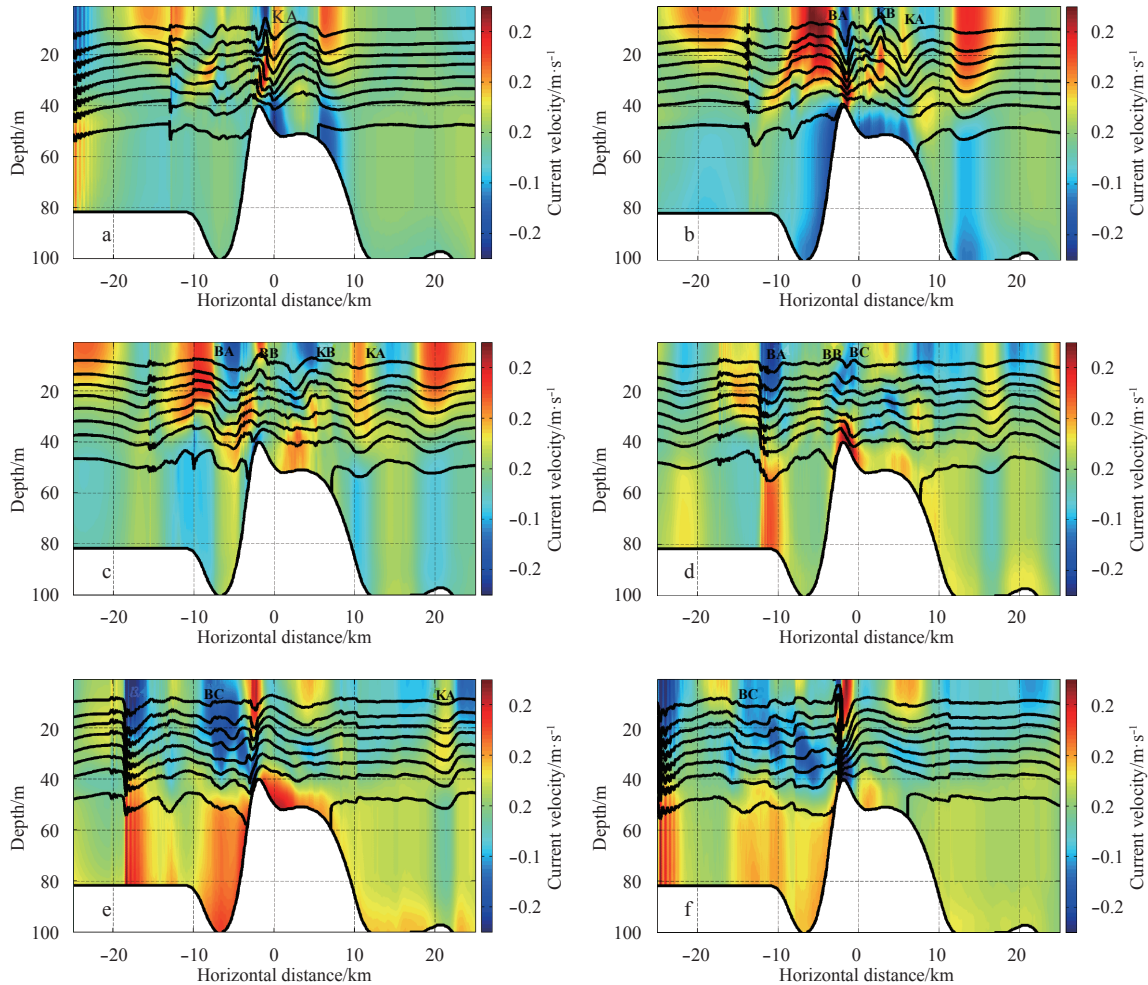

Fig. 7. Superposed baroclinic current together with isopycnal for t = 15–25 h. We defined that for flooding from the Barents to the Kara Sea, the start time was F-1 and every 2 h subsequently.
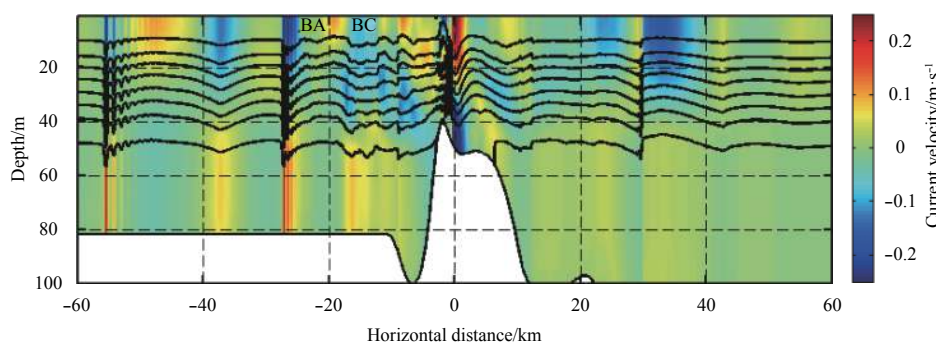
Fig. 8. Superposition of baroclinic current and isopycnal at *t* = 26 h.

counterparts on the Barents Sea, and a clear disintegration emerged at *x* = 30 km. The spatial characteristic of the wave from the previous period (*x* = –55 km), the leading wave train BA, and the following bore-like wave BC were similar to those captured in the ASAR image (Fig. 1c). The waves on both sides (BA and KA) had bore-like structures and little disintegration between –20 and 20 km, similar to those in Figs 1a and b.

4.2.2 *Influence of background current*

In the control experiment, only the tide was considered, and the final IW packets on the Barents Sea side were similar to typical observations. On the opposite side, the IW packets were weak but still clear. However, observations indicate that the wave toward the Kara Sea frequently has a single wave structure. Figure 9 shows a vertical section of the model results from the experiment with the background current (0.12 m/s) added. The generation process was similar to the reference experiment. The wave toward the Barents Sea was slowed by an opposing steady current and the amplitude of the generated wave was slightly stronger than the amplitude in the control experiment. The maximum Froude number in the tide-only experiment was close to 1, and together with the background, the Froude number was slightly larger than the critical value for the generation process of the wave on the Barents Sea side. This process may enhance the accumulation of initial energy and therefore increase the final wave packets. However, it decreases the energy of the waves toward the Kara Sea. Figure 9 shows that the disturbance on the Kara Sea side had a smaller vertical displacement and propagated with an internal bore structure (*x* = 43 km). No ISW trains emerged compared with the control experiment. Compared with the wave in the first tidal period at *x* = 68 km, the displacement was difficult to identify, meaning that dissipation of the internal bore structure was substantial compared with the solitary wave. The lead-

ing ISW in the first tidal period could drain energy from the initial disturbance to ultimately evolve into an isolated single wave. The amplitude of the wave train in the first tidal period was larger than that in the second tidal period, which had just begun the disintegration process.

4.2.3 *Influence of stratification*

The model results after two tidal periods in winter are presented in Fig. 10. The oscillations are more regular than the summer case. Owing to weak nonlinear characteristics of the winter stratification, there was no substantial disintegration, even though the wave amplitude was comparable to summer levels. Mode 1 phase speed in the winter case was 0.23 m/s at a depth of 45 m and 0.28 m/s at a depth of 55 m (Table 1). Thus, the energy accumulation time was longer during generation (longer trapped time). The phase speed of the Mode 2 wave was only 0.1 m/s, which means that it was nearly trapped around the topography during the entire tidal period, and the signal of the Mode 2 type wave was not as clear as in the summer case away from the topography. The wavelength of the internal tide (labeled in Fig. 10 between the vertical red lines) was approximately 16 km (Fig. 10), which is consistent with the linear theory. The trough around *x* = –22 km is similar to the internal bore structure in the summer case, and was generated in the same tidal period by a bulge of the topography at around *x* = 5 km. The lengths of the two troughs were consistent with the distance of the two sources. The difference is that the second wave in the winter case was stronger and comparable to the main wave (generated by the interaction of the tide and the sill centered around *x* = –4 km). This may have obscured the wave structure in a snapshot of the wave field (Fig. 10). Since the basic generation process is similar to that of the summer case, the full cycle is not shown here.

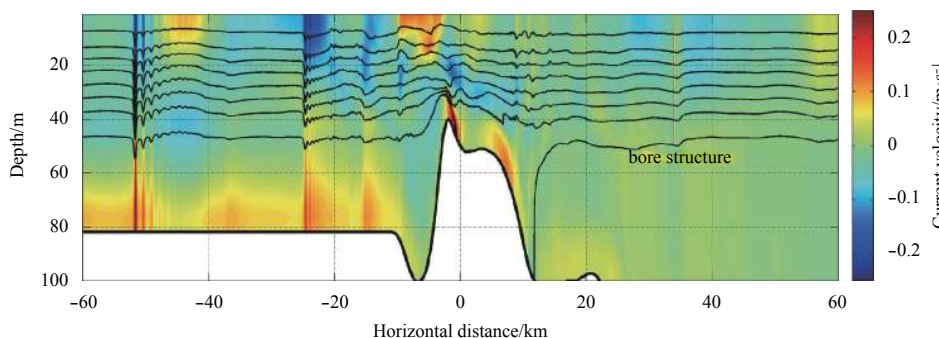The effect of a steady current on the IT generation could be

Fig. 9. Superposition of baroclinic current and isopycnal for *t* = 26 h with a background steady current.
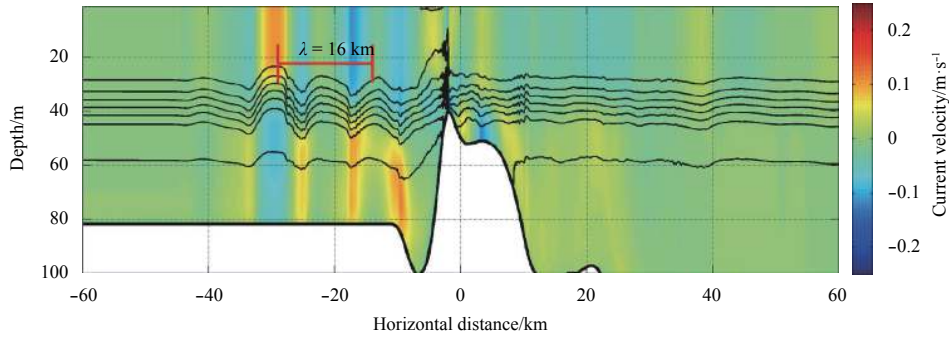
Fig. 10. Superposition of baroclinic current and isopycnal for t = 26 h under winter stratification.

explained by the Doppler effect (Li and Farmer, 2011), The Doppler shift induced by the superimposed flow changes the equivalent Froude number Fr_{Doppler}:

$$Fr_{\mathrm{Doppler}} = \frac{U_{ti}}{c \mp U_0}. \tag{7}$$

And so, the northward current increases the amplitude of internal tides propagating against the steady current (toward Barents Sea) but reduces the amplitude of the internal tide propagating with the current. Further analysis on the evolution of IT in Li and Farmer (2011) for the Luzon area employed a two-layer approximation. It revealed that the IT is expected to steepen because of nonlinearity, with rotation inhibiting but not preventing this. The parameters are the Ursell number U_r and nonhydrostatic dispersion, and the Ostrovsky number Q_s, which are ratios of nonlinearity to nonhydrostatic dispersion, and nonlinearity to rotation effect, respectively. For the two-layer system these are given by

$$U_r = \frac{AL^2\,(h_1 - h_2)}{h_1^2 h_2^2}, \tag{8}$$

$$Q_s = 12\pi^2\,\frac{\alpha A}{\gamma L^2} = \frac{36\pi^2 A g'\,(h_1 - h_2)}{f^2 \lambda^2\,(h_1 + h_2)}, \tag{9}$$

where A and L are respectively the amplitude and length scale of the initial disturbance; h_1 and h_2 are the upper and lower layer depth; and g' is the reduced gravity. In the definition of Ostrovsky number, λ is wavelength of a simple harmonic wave. In the summer case, h_1 = 30 m and h_2 = 160 m, with typical amplitudes of 10 m for the initial disturbance and the length scale of the initial disturbance about 2–3 km (Fig. 6), the Ursell number is about 200, which means that nonhydrostatic effect plays a role at the initial time. Furthermore, the Ostrovsky number Q_s greater than 2 in the summer case, which means that the nonlinearity dominates and rotation plays a minor role. This process is clearly displayed in Fig. 6, where it can be seen that the disintegration process started just after the initial disturbance propagated over the sill. In the winter case, the Ostrovsky number is very small due to the small difference of a layer thickness, and thus the fission process is not important as in the summer case, as shown by the model results.

5 Summary

Remote sensing and *in situ* data revealed the widespread existence of the NIWs around the Kara Strait, which is an import-
ant channel for the northward transport of relatively warm Barents Sea water into the Arctic Ocean. Tidal properties, typical stratification in summer, and topography across the Kara Strait provide favorable conditions for the internal tide generation. The calculation of the phase speed based on the stratification shows that the flow is marginally critical. This claim is verified by the numerical simulations of the nonhydrostatic MITgcm, which was applied to a realistic 2-D bathymetry across the Kara Strait and driven by the barotropic tidal and the typical background current. In this study, a 2-D nonhydrostatic numerical simulation was employed to examine the generation and propagation properties of the ISWs. The model captured the basic wave characteristics shown by the satellite data. A typical wavelength on the Barents Sea side is about 25 km in summer, with a phase speed about 0.65 m/s. In the control experiment, the model successfully reproduced the single internal solitary wave (ISW) structure following the major wave trains, with a distance about 5–8 km (Fig. 1b), which was generated with the leading wave packets in the same tidal period. Meanwhile, the ISWs trains towards the Kara Sea were also obvious. When a steady current toward the Kara Sea is included, the basic generation process is similar, but the northward current increases the amplitude of the internal tides propagating against the steady current but reduces the amplitude of the internal tide propagating with the current, explained as Doppler effect during the internal tide generation (Li and Farmer, 2011). In this case, the waves toward the Kara Sea weakened and displayed an internal bore-like structure with smaller amplitude than in the control experiment, this was consistent with that in Figs 1a and c. With the winter stratification, the pycnocline weakened and deepens near the middle of the water depth (Barents Sea side), and thus the NIWs process is not as important as its counterpart in summer and there was no fission process during the simulation.

The ISWs are not restricted to the Kara Strait region. Two other hotspots are the southeastern part of the Novaya Zemlya Trough and the vicinity of Cape Zhelaniya (Kozlov et al., 2015). These may also be related to the tide and the typical topographic structure. Our calculations have captured the basic properties of the internal tide, but other characteristics have not been adequately explained. For example, after exiting from the main source region, 3-D characteristics weakened, and their evolution in most cases was no longer along the main axis of the cross-strait direction because of the topography and rotation effects. As a typical dynamic process in a stratified ocean, the generation and evolution of the NIWs at the study latitude were similar to other hotspots in the global ocean, but with a smaller wavelength because of proximity to the critical latitude. The Kara Strait plays a role in water exchange between the warm Barents Sea and cold

Kara Sea. Future work will focus on the role of the NIW in vertical mixing of the various water masses and its influence on the exchange processes across the Kara Strait.

References

Buijsman M C, Kanarska Y, McWilliams J C. 2010. On the generation and evolution of nonlinear internal waves in the South China Sea. Journal of Geophysical Research, 115(C2): C02012, doi: 10.1029/2009JC005275

Chen Zhiwu, Xie Jieshuo, Wang Dongxiao, et al. 2014. Density stratification influences on generation of different modes internal solitary waves. Journal of Geophysical Research, 119(10): 7029–7046, doi: 10.1002/2014JC010069

Cushman-Roisin B, Beckers J M. 2011. Introduction to Geophysical Fluid Dynamics, Volume 101, Second Edition: Physical and Numerical Aspects. Englewood Clifts, NJ: Prentice Hall, 320

da Silva J C B, Buijsman M C, Magalhaes J M. 2015. Internal waves on the upstream side of a large sill of the Mascarene Ridge: a comprehensive view of their generation mechanisms and evolution. Deep-Sea Research: Part I. Oceanographic Research Papers, 99: 87–104, doi: 10.1016/j.dsr.2015.01.002

Grimshaw R, Pelinovsky E, Talipova T, et al. 2010. Internal solitary waves: propagation, deformation and disintegration. Nonlinear Processes in Geophysics, 17(6): 633–649, doi: 10.5194/npg-17-633-2010

Harms I H, Karcher M J. 1999. Modeling the seasonal variability of hydrography and circulation in the Kara Sea. Journal of Geophysical Research, 104(C6): 13431–13448, doi: 10.1029/1999JC900048

IOC, IHO and BODC. 2003. Centenary Edition of the GEBCO Digital Atlas, published on CD-ROM on behalf of the Intergovernmental Oceanographic Commission and the International Hydrographic Organization as part of the General Bathymetric Chart of the Oceans. Liverpool, UK: British Oceanographic Data Centre

Kozlov I E, Kudryavtsev V N, Zubkova E V, et al. 2015. Characteristics of short-period internal waves in the Kara Sea inferred from satellite SAR data. Izvestiya, Atmospheric and Oceanic Physics, 51(9): 1073–1087, doi: 10.1134/S0001433815090121

Kurkina O E, Talipova T G. 2011. Huge internal waves in the vicinity of the Spitsbergen Island (Barents Sea). Natural Hazards and Earth System Science, 11(3): 981–986, doi: 10.5194/nhess-11-981-2011

Lee C Y, Beardsley R C. 1974. The generation of long nonlinear internal waves in a weakly stratified shear flow. Journal of Geophysical Research, 79(3): 453–462, doi: 10.1029/JC079i003p00453

Li Qiang, Farmer D M. 2011. The generation and evolution of nonlinear internal waves in the deep basin of the South China Sea. Journal of Physical Oceanography, 41(7): 1345–1363, doi: 10.1175/2011JPO4587.1

Marshall J, Adcroft A, Hill C, et al. 1997. A finite-volume, incompressible Navier-Stokes model for studies of the ocean on parallel computers. Journal of Geophysical Research, 102(C3): 5753–5766, doi: 10.1029/96JC02775

Morozov E G, Paka V T, Bakhanov V V. 2008. Strong internal tides in the Kara Gates Strait. Geophysical Research Letters, 35(16): L16603, doi: 10.1029/2008GL033804

Morozov E G, Parrilla-Barrera G, Velarde M G, et al. 2003. The Straits of Gibraltar and Kara Gates: a comparison of internal tides. Oceanologica Acta, 26(3): 231–241, doi: 10.1016/S0399-1784(03)00023-9

Pacanowski R C, Philander S G H. 1981. Parameterization of vertical mixing in numerical models of tropical oceans. Journal of Physical Oceanography, 11(11): 1443–1451, doi: 10.1175/1520-0485(1981)011<1443:POVMIN>2.0.CO;2

Pichon A, Morel Y, Baraille R, et al. 2013. Internal tide interactions in the Bay of Biscay: observations and modelling. Journal of Marine Systems, 109–110: S26–S44, doi: 10.1016/j.jmarsys.2011.07.003

Rippeth T P, Lincoln B J, Yueng-Djern Lenn, et al. 2015. Tide-mediated warming of Arctic halocline by Atlantic heat fluxes over rough topography. Nature Geoscience, 8(3): 191–194, doi: 10.1038/NGEO2350

Vitousek S, Fringer O B. 2011. Physical vs. numerical dispersion in nonhydrostatic ocean modeling. Ocean Modelling, 40(1): 72–86, doi: 10.1016/j.ocemod.2011.07.002

Vlasenko V, Stashchuk N, Hutter K. 2005. Baroclinic Tides: Theoretical Modeling and Observational Evidence. Cambridge: Cambridge University Press, 372

Vlasenko V, Stashchuk N, Hutter K, et al. 2003. Nonlinear internal waves forced by tides near the critical latitude. Deep-Sea Research: Part I. Oceanographic Research Papers, 50(3): 317–338, doi: 10.1016/S0967-0637(03)00018-9

Vlasenko V, Stashchuk N, Inall M E, et al. 2014. Tidal energy conversion in a global hot spot: On the 3-D dynamics of baroclinic tides at the Celtic Sea shelf break. Journal of Geophysical Research, 119(6): 3249–3265, doi: 10.1002/2013JC009708

Wang Gang, Qiao Fangli, Dai Dejun. 2010. A 2D-numerical modeling of the generation and propagation of internal solitary waves in the Luzon Strait. Acta Oceanologica Sinica, 29(6): 1–11, doi: 10.1007/s13131-010-0071-6

Xu Zhenhua, Liu Kun, Yin Baoshu, et al. 2016. Long-range propagation and associated variability of internal tides in the South China Sea. Journal of Geophysical Research, 121(11): 8268–8286, doi: 10.1002/2016JC012105

Xu Zhenhua, Yin Baoshu, Hou Yijun, et al. 2014. Seasonal variability and north-south asymmetry of internal tides in the deep basin west of the Luzon Strait. Journal of Marine Systems, 134: 101–112, doi: 10.1016/j.jmarsys.2014.03.002

Zhao Zhongxiang, Alford M H, Girton J B, et al. 2016. Global observations of open-ocean mode-1 M_2 internal tides. Journal of Physical Oceanography, 46(6): 1657–1684, doi: 10.1175/JPO-D-15-0105.1

Analytical study of the effect of the geometrical parameters during the interaction of regular wave-horizontal plate-current

Smail Naasse[1], Meriem Errifaiy[1]*, Chakib Chahine[1]

[1] Laboratory Physics of Polymers and Critical Phenomena, Hassan Ⅱ University Casablanca, Casablanca P B 7955,
  Morocco

Abstract

The present work is an analytical study of the influence of geometrical parameters, such as length, thickness and immersion of the plate, on the reflection coefficient of a regular wave for an immersed horizontal plate in the presence of a uniform current with the same direction as the propagation of the incident regular wave. This study was performed using the linearized potential theory with the evanescent modes while searching for complex roots to the dispersion equation that are neither pure real nor pure imaginary. The results show that the effects of the immersion and the relative length on the reflection coefficient of the plate are accentuated by the presence of the current, whereas the plate thickness practically does not have an effect if it is relatively small.

Key words: current, regular wave, evanescent modes, reflection, dispersion equation, complex roots, geometrical parameters

1 Introduction

A submerged horizontal plate may serve as breakwater to protect harbors, inlets and beaches from wave action. As with all submerged structures, the horizontal plate does not obstruct the ocean view, which is critical for recreational and residential shore development. Moreover, the horizontal plate enables the circulation of water above and beneath it; hence, its environmental impact is minimal.

With the plate being a more or less thick rectangular structure, the parameters that come into play when interacting with regular waves are the characteristics of the incident wave, the geometry of the plate (length, thickness), its nature (porosity, elasticity), its disposition (vertical, inclined or horizontal) and its immersion. Several researchers are particularly interested in the effect of the geometrical parameters during the interaction of regular waves with a submerged plate. Patarapanich (add the reference) showed analytically, using the wave plane model, that the reflection coefficient depends on the relative depth of the incident wave, the immersion ratio of the plate and the length of the plate relatively to the wavelength of the wave that propagates above the plate (Patarapanich, 1984) and compared experimental results with the solution obtained numerically by the finite-element method (Patarapanich and Cheong, 1989). The interaction of a rectangular structure with a regular wave was studied analytically by Zheng et al. (2007a, b), notably focusing on the effect of the thickness, the immersion and the length of the structure on the reflection coefficient, the hydrodynamic coefficients and the forces exerted by the regular waves on the structure. The interaction of regular waves with a thick plate in the presence of a permeable breakwater was numerically investigated by Hsu and Wu (1998) and Rao et al. (2009), they experimentally studied the effect of the relative depth. The case of a porous plate was investig-

ated numerically (BEM) by Yueh and Chuang (2009). In 2014, Behera and Sahoo (2015) investigated the interaction of a gravity wave with a flexible porous plate. An experimental study on the attenuation of regular waves by an inclined plate was presented by Acanal et al. (2013). In 2014, Ning et al. (2014) presented a numerical study on the higher harmonics during the interaction of a nonlinear wave with a horizontal cylinder in the presence of a current. In 2017, Bai et al. (2017) investigated the forces exerted on a horizontal cylinder during the passage of a regular wave in the presence of a sheared current. However, in these studies, the effects of geometrical parameters on wave reflection by a submerged plate in the presence of a current were not investigated.

In this work, we are interested in the effects of the geometrical parameters of a rigid and impermeable horizontal plate on the reflection coefficient of regular waves propagating in the presence of a uniform current having the same direction as the incident wave. This study was conducted as part of the linear potential theory using the model of evanescent modes. The roots of the dispersion equation are searched as complex numbers to obtain solutions with real nonzero and imaginary nonzero parts (Errifaiy et al., 2016).

First, we present the formulation of the problem of the interaction of a regular wave with a horizontal plate in the presence of a current. The velocity potential sought is in the form of a superposition of the potential corresponding to the current and that corresponding to a regular wave. The velocity potential in the subdomains upstream and above the plate is the sum of the uniform current, two modes propagating in opposite directions and a series of evanescent modes. In the subdomain downstream of the plate, the velocity potential is the sum of the uniform current, a mode propagating downstream and a series of evanescent modes. In the subdomain below the plate, the velocity potential

*Corresponding author, E-mail: errifaiy.m@gmail.com

is the sum of the uniform current, an oscillating horizontal current and a series of evanescent modes. By means of the matching conditions between the subdomains that express the continuity of the velocity potential and of the horizontal velocity at the attack and trailing edges of the plate, one obtains a linear algebraic system whose unknowns are the constants involved in the writing of the potential. The resolution of this system allows us to determine the reflection coefficient.

Second, we studied the effect of the geometric parameters on the reflection of a regular wave by a submerged horizontal plate in the absence of a current: the results concerning the effect of the immersion ratio and the plate length during the interaction of wave-thin plate are compared of those of Patarapanich and Cheong (1989) and of those of Brossard et al. (2009). The results concerning reflection by a thick plate are compared with those of Liu and Iskandarani (1991).

Afterward, we studied the effect of geometric parameters on the reflection of a regular wave by a submerged horizontal plate in the presence of a current: the results are compared with those of Rey and Touboul (2011) and with those of Lin et al. (2014). In these two cases, the reflection coefficient is calculated using the present model in two ways: first by supposing that the plate thickness is zero and second by taking into account the real plate thickness.

Finally, the model is used to predict the effects of the relative plate thickness, the immersion ratio and the relative plate length on the reflection coefficient. Notably, we investigated the effect on the maximum of the reflection coefficient and on the reflection bandwidth. The reflection band is defined by adopting the criterion used in electronics to define the pass band. With this definition, the width of the reflection band is the width of the interval $[k_1 H, k_2 H]$ so that the value of the reflection coefficient corresponding to $k_1 H$ and $k_2 H$ is equal to $R_{\max}/\sqrt{2}$, where $R_{\max}$ denotes the maximum of the reflection coefficient.

2 Interaction of wave-current-plate

In this part, we present the calculation of the reflection coefficient of a regular wave in the presence of a uniform current interacting with a fixed horizontal plate completely immersed in a channel. This study was conducted as part of the linearized potential theory using the evanescent modes model. The studied regular wave is of low wave steepness, and the surface tension is negligible. A monochromatic wave is emitted upstream; downstream, the wave does not undergo any reflection.

2.1 *Velocity potential*

The horizontal plate is totally immersed in a channel. The plate is e in thickness and $2l$ in length, covering the entire width of the channel. The domain of study is reported as a Cartesian coordinate system (O, x, y), in which the axis (Oy) is directed vertically upward, the axis (Ox) coincides with the position of the free surface at rest, and origin O coincides with the center of the plate orthogonal projection on the axis (Ox). The geometry of the domain of study leads us to define four subdomains, as shown in Fig. 1.

Seeking the potential in the form of a superposition of the potentials associated with the current $\phi_c(x, y, t) = Ux$ and with a monochromatic regular wave $\phi_h(x, y, t) = \varphi(x, y)\,\mathrm{e}^{i\omega t}$, (Rey et al., 2003; Errifaiy et al., 2016) obtained the total potential as follows:

In subdomains D_p, $1 \leqslant p \leqslant 3$:

$$\phi_p(x, y, t) = Ux + \Big[A_p \mathrm{e}^{ik_p^- x}\cosh\big(k_p^-\,(y+$$
$$H_p)\big) + B_p \mathrm{e}^{ik_p^+ x}\cosh\big(k_p^+\,(y + H_p)\big) +$$
$$\sum_{n=1}^{N} A_{pn}\mathrm{e}^{k_{pn}x}\cos\big(k_{pn}\,(y + H_p)\big) +$$
$$B_{pn}\mathrm{e}^{-k_{pn}x}\cos\big(k_{pn}\,(y + H_p)\big) \Big]\mathrm{e}^{i\omega t}. \tag{1}$$

In this equation, H_1 and H_2 are both equal to the water depth in the channel ($H_1 = H_2 = H$), H_3 is equal to the plate immersion ($H_3 = h$), ω is the wave pulsation, N denotes the number of evanescent modes, A_{1n} and B_{2n} are all zero, A_1 is given by $A_1 = ga_i \dfrac{1}{\big(\omega - Uk_1^-\big)\cosh\big(k_1^- H\big)}$ (where a_i is the amplitude of the wave that propagates at the free surface and g is the acceleration of gravity), and the constants $k_p^{\pm}$ and k_{pn} are the roots of the following equations:

$$\big(\omega \pm U\big(k_p^{\pm}\big)\big)^2 = g\big(k_p^{\pm}\big) \times \tanh\big(\big(k_p^{\pm}\big)H_p\big), \tag{2}$$

$$(i\omega + U(k_{pn}))^2 = g(k_{pn}) \times \tan\big((k_{pn})H_p\big). \tag{3}$$

In subdomain D_4:

$$\phi_4(x, y, t) = Ux + \Big[\Big(A_4 + B_4 x + \sum_{n=1}^{N}\big(A_{4n}\mathrm{e}^{-(\mu_n x)} +$$
$$B_{4n}\mathrm{e}^{(\mu_n x)}\big)\cos\big(\mu_n\,(y + H)\big)\Big)\Big]\mathrm{e}^{i\omega t}. \tag{4}$$

direction of propagation

current

D_1 e h D_3 H D_2
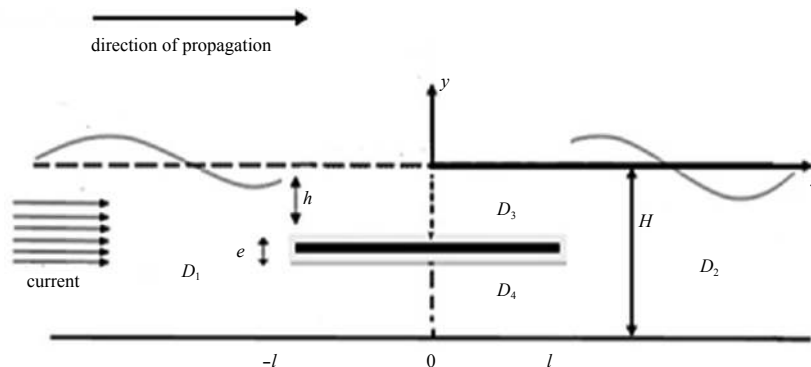
D_4

$-l$ 0 l

Fig. 1. Descriptive schemas of the wave propagation with a submerged plate in the presence of a current.

$$\mu_n = \frac{n\pi}{H - h - e}, \tag{5}$$

where e is the plate thickness.

All constants $\{B_1, B_{1n}, A_3, B_3, A_{3n}, B_{3n}, A_4, B_4, A_{4n}, B_{4n}, A_2$ and A_{2n} for $1 \leqslant n \leqslant N\}$ that are present in Eqs (1) and (4) are unknown.

The roots of Eq. (2) are the wavenumbers of the propagating modes. The roots of Eq. (3) correspond to evanescent modes. In the absence of a current (U=0), these roots are pure real. However, in the presence of a current, it is easy to verify, first, that this equation has no pure real roots and, second, that the pure imaginary roots are those corresponding to Eq. (2). Therefore, to establish this model, it is necessary to search for roots (k_{pn}) with a nonzero real part and a nonzero imaginary part as well.

Equation (1) shows that the velocity potential corresponding to subdomains D_1 and D_3 is the sum of the uniform current, two modes propagating in opposite directions and a series of evanescent modes. In subdomain D_2, the velocity potential is the sum of the uniform current, a mode propagating downstream and a series of evanescent modes. Equation 4 shows that the velocity potential corresponding to subdomain D_4 is the sum of the uniform current, an oscillatory current and a series of evanescent modes.

2.2 *Reflection coefficient calculation*

The reflection coefficient of the regular wave that propagates at the free surface is given by

$$R = \frac{(\omega + Uk_1^+)}{(\omega - Uk_1^-)} \times \frac{\cosh(k_1^+ H)}{\cosh(k_1^- H)} \times \frac{B_1}{A_1}. \tag{6}$$

To determine the reflection coefficient R, we must resolve a linear algebraic system of (6N+6) equations and (6N+6) unknowns, which are the constants $\{B_1, B_{1n}, A_3, B_3, A_{3n}, B_{3n}, A_4, B_4, A_{4n}, B_{4n}, A_2$ and A_{2n} for $1 \leqslant n \leqslant N\}$ that are present in Eqs (A1) and (A4) (see Appendix).

This system is obtained by means of the matching conditions between the subdomains that express the continuity of the velocity potential and of the horizontal velocity at the attack and trailing edges of the plate (x=−l and x=l, respectively).

The elements of the matrix corresponding to this system depend on the following: the relative depth kH (which expresses the ratio of the water depth in the channel to the wavelength of the incident wave in the absence of a current), the Froud number

$U/\sqrt{gH}$ and the geometrical parameters, namely, the plate immersion ratio (h/H), the relative plate length ($2l/h$) and the relative plate thickness (e/h) (see Appendix). Accordingly, the reflection coefficient depends on the same parameters.

3 Effects of the geometrical parametrical parameters in the absence of a current

3.1 *Immersion ratio and relative plate length effect*

During the interaction of a regular wave with a horizontal plate immersed in the absence of a current, the effects of immersion and plate length were experimentally and numerically (finite element method) studied by Patarapanich and Cheong (1989) and experimentally studied by Brossard et al. (2009). We compared the values of the reflection coefficient calculated using the present model with the results of Patarapanich (Fig. 2) and with those of Brossard et al. (2009) (Fig. 3). In these figures, the coefficient of reflection is represented as a function of the ratio of the plate length (2l) to the wavelength (L) of the wave propagating above the plate.

The results of the model fit well with the results calculated via the finite element method by Patarapanich (Fig. 2) and are close to the experimental results of Patarapanich (Fig. 2) and those of Brossard (Fig. 3).

The curves in Figs 2 and 3 show the following:

(1) The reflection coefficient increases as the immersion ratio decreases.

(2) At a constant immersion ratio, the reflection coefficient increases to the maximum and then decreases.

3.2 *Plate thickness effect*

In the available literature, most studies assumed the plate thickness to be zero for simplicity. The plate thickness was considered only in a few studies.

Liu and Iskandarani (1991) studied the interaction of a linear and nonlinear wave with a thick plate.

Liu et al. (2009) by studying the reflection coefficient evolution as function of the plate length to wavelength ratio during the interaction of water waves with twin plates, showed that the reflection coefficient decreases with increasing plate thickness.

Zheng et al., (2007b) studied the interaction between water waves and a rectangular structure for an oblique incidence. In their study, the representation of the reflection coefficient as a function of kH showed that the reflection coefficient increases with the increase of the structure thickness.
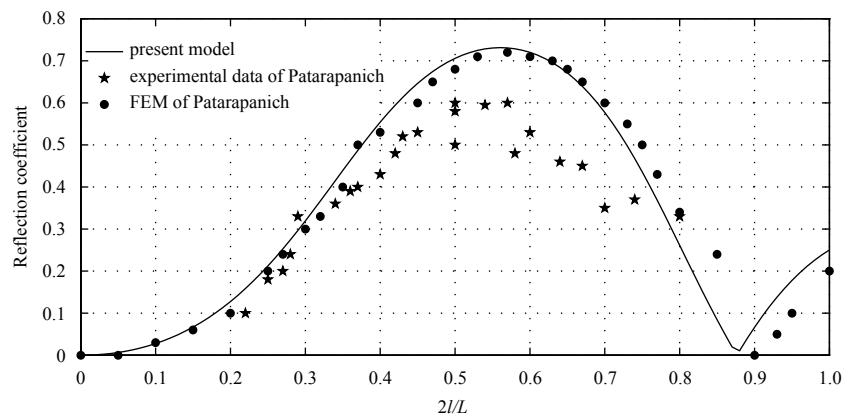

Fig. 2. Reflection coefficient as a function of 2l/L for a relative depth kH=1.256 and a plate immersion ratio h/H=0.3.
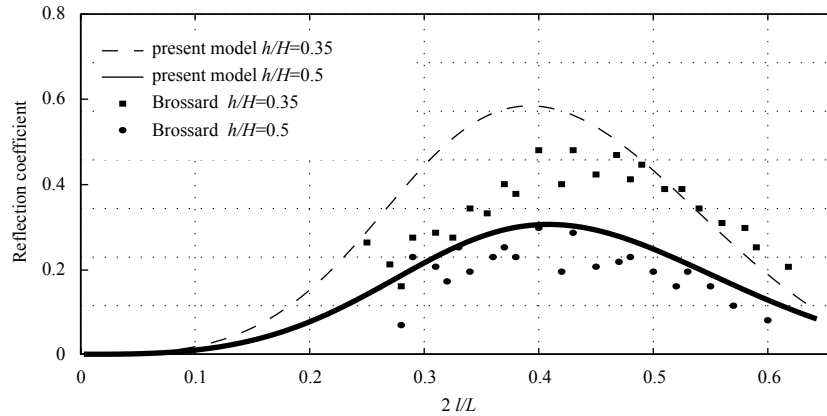
Fig. 3. Reflection coefficient as a function of $2l/L$ for a plate length $2l$=25 cm and two values of the plate immersion ratio h/H=0.5, 0.35.

To study the effect of the plate thickness on the reflection coefficient during the interaction of a regular wave with a thick plate, we first compared the results calculated using this model with those of Liu and Iskandarani (1991). The results presented in Fig. 4 are in good agreement with those of Philip L-F Liu and Iskandarani (1991). Second, we calculated the reflection coefficient of a regular wave, in normal incidence, during its interaction with a rectangular structure. In keeping the settings of the configuration taken by Zheng et al. (2007b) (except for the incidence angle), we represent the reflection coefficient versus kH in Fig. 5. The curves obtained are similar to those of Zheng et al. (2007b).

4 Effect of the geometrical parameters in the presence of a current

As shown above, during the regular wave–current–plate interaction, in addition to the current velocity, the reflection coefficient of a regular wave also depends on the geometrical parameters of the examined problem. These geometrical parameters are the relative depth of water in the channel, the relative thickness of the plate, its immersion ratio and its relative length. The present model is used to study the effect of each of these parameters on the reflection coefficient. This study was conducted as part of the linearized potential flow theory using the evanescent modes model. To take account of the evanescent modes in the presence of a current, the dispersion equation was solved by seeking complex roots that are neither pure real nor pure imaginary. In this model, the number of evanescent modes taken into account is N=30 (Errifaiy et al., 2016).
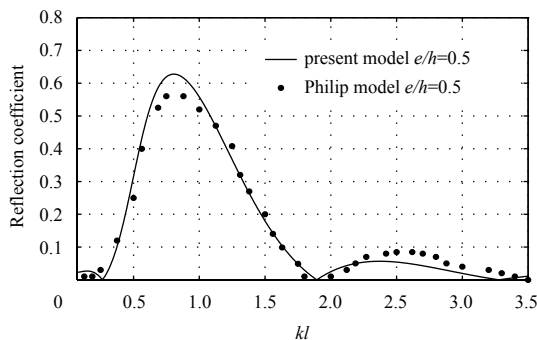
Fig. 4. Reflection coefficient as a function of kl for l/h=2, relative plate thickness e/h=0.5 and a plate immersion ratio h/H=0.25.
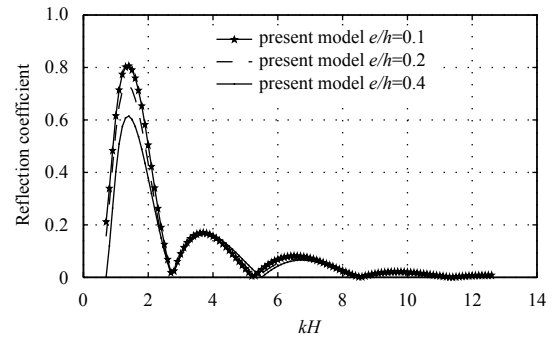
Fig. 5. Reflection coefficient as a function of kH for a plate immersion ratio h/H=0.2, a relative plate length $2l/h = 6$, and different values of the relative plate thickness e/h=0.1, 0.2, 0.4.

4.1 *Plate thickness effect*

To study the effect of the plate thickness, the reflection coefficient is calculated using this model with a thin plate and a thick plate in the presence of a current. First, the results were compared with those obtained experimentally by Rey and Touboul (2011) and with the numerical results of Lin et al. (2014). Afterward, the model was used to predict the effect of the relative plate thickness (e/h) on the reflection coefficient for different values of the plate immersion ratio (h/H).

4.1.1 *Comparison with the data of Rey and Touboul (2011)*

Rey and Touboul (2011) experimentally investigated the reflection of a regular wave in the presence of a current of velocity (U=0.3 m/s), interacting with a plate of thickness e=0.1 m immersed in a flat horizontal channel with a water depth H=3 m. The plate is immersed at depth h=0.5 m below the level of the free surface.

We compare our results with those of Rey and Touboul (2011) in Fig. 6. The calculations of the reflection coefficient by the present model were performed, first, by keeping the value of the thickness taken by these authors and, second, by supposing that the plate is without thickness.

In Fig. 6, we represent the dependence on the period of the values of the reflection coefficient measured experimentally by Rey and Touboul (2011) and calculated analytically by the present model. The analytical calculations were made in the presence of a current velocity (U=0.3 m/s), for a thin plate (e=0 m) and a plate of thickness (e=0.1 m).

Fig. 6. Reflection coefficient as a function of the period for plate thicknesses *e*=0.1 m and *e*=0 m, plate length 2*l*=1.53 m, plate immersion *h*=0.5 m, water depth *H*=3 m and current velocity *U*=0.3 m/s.

The curves in Fig. 6 show the following:

(1) The difference between the analytical results calculated by the present model for *e*=0 m and *e*=0.1 m is weak.

(2) There is good agreement between the results of Rey and those of the model, especially for the long periods (the long waves). The shift in the range of the short periods (short wavelengths) may be explained by the fact that the analytical model does not take into account the vortex emission by the plate (Lebon et al., 2016) or the surface tension, whose effect increases when the wavelength decreases.

4.1.2 *Comparison with the computation of Lin et al. (2014)*

Lin et al. (2014) performed a numerical study (BEM) of the same problem with a plate of thickness *e*=0.01 m immersed at *h*=0.1 m and *h*=0.07 m with a water depth *H*=0.2 m for U/C_{g0} =0.12 (ratio of the current velocity relative to the C_{g0} group velocity calculated in the absence of a current).

We compare our results with those of Lin et al. (2014) in Fig. 7. The calculations of the reflection coefficient by the present model were first performed by keeping the value of the thickness taken by these authors and then by supposing that the plate is without thickness.

In Fig. 7, we represent the dependence on the period of the values of the reflection coefficient for $U/C_{g0} = 0.12$ (ratio of the current velocity relative to the C_{g0} group velocity calculated in the absence of a current). The results calculated by this model with a thin plate (*e*=0 m) and a thick plate (*e*=0.01 m) are compared with those calculated numerically by Lin et al. (2014).

The curves in Fig. 7 show that there is good agreement between the result calculated by this model with plate thicknesses *e*=0 m and *e*=0.01 m and those calculated numerically by Lin et al. (2014).

4.1.3 *Model prediction*

The results in Figs 6 and 7 show the following:

(1) The results calculated by the present model are in agreement with the experimental values of Rey and Touboul (2011) (Fig. 6) and the values of Lin et al. (2014) (Fig. 7).

(2) The difference between the results calculated by this model with a plate without thickness and those calculated taking into account the thickness of the plate is weak.

In the following, we used the model to study the variation of the reflection coefficient for different thicknesses of the plate at different immersions.

Figures 8a–d represent the values of the reflection coefficient as a function of *kH* (relative depth of the incident wave in the absence of a current) for different values of the relative plate thickness (*e*/*h*), different values of the plate immersion ratio (*h*/*H*) and Froud number $U/\sqrt{gH} = 0.045$. It shows that reflection coefficient decreases when the relative plate thickness (*e*/*h*) increases.

In Table 1, we present the relative difference in the maximum of the reflection coefficient $(M–M_0)/M_0$, where M_0 is the reflection coefficient maximum for the plate without thickness (*e*=0 m).

Fig. 7. Reflection coefficient as a function of period for a plate length 2*l*=0.25 m, water depth *H*=0.2 m, relative current velocity $U/C_{g0} = 0.12$ (C_{g0} is the group velocity at *T*=0.75 s) and plate thicknesses *e*=0 m and *e*=0.01 m. In Fig. 7a, the plate immersion *h*= 0.1 m, and in Fig. 7b, *h*=0.07 m.
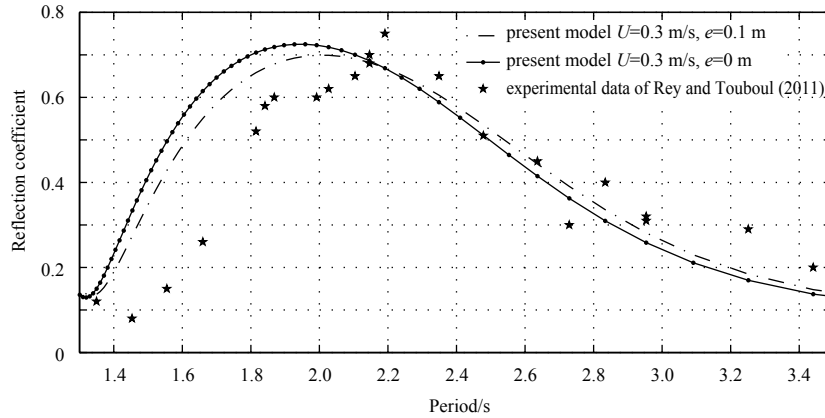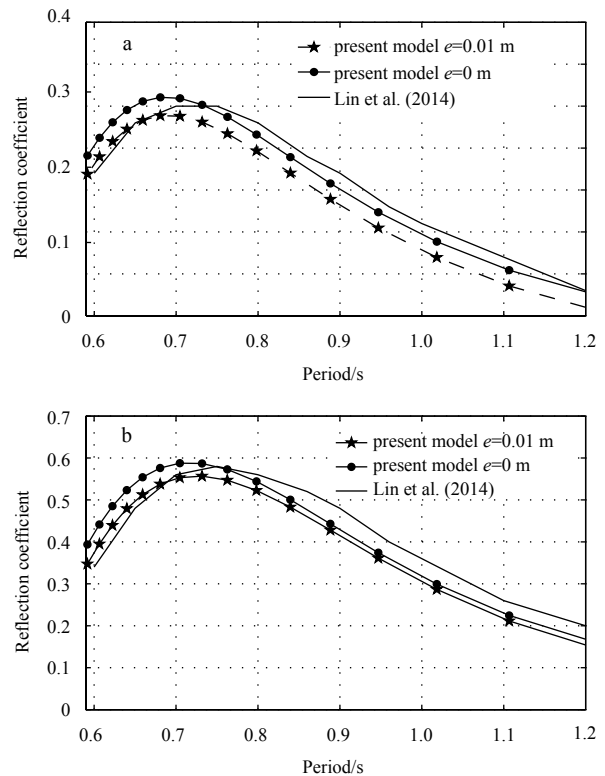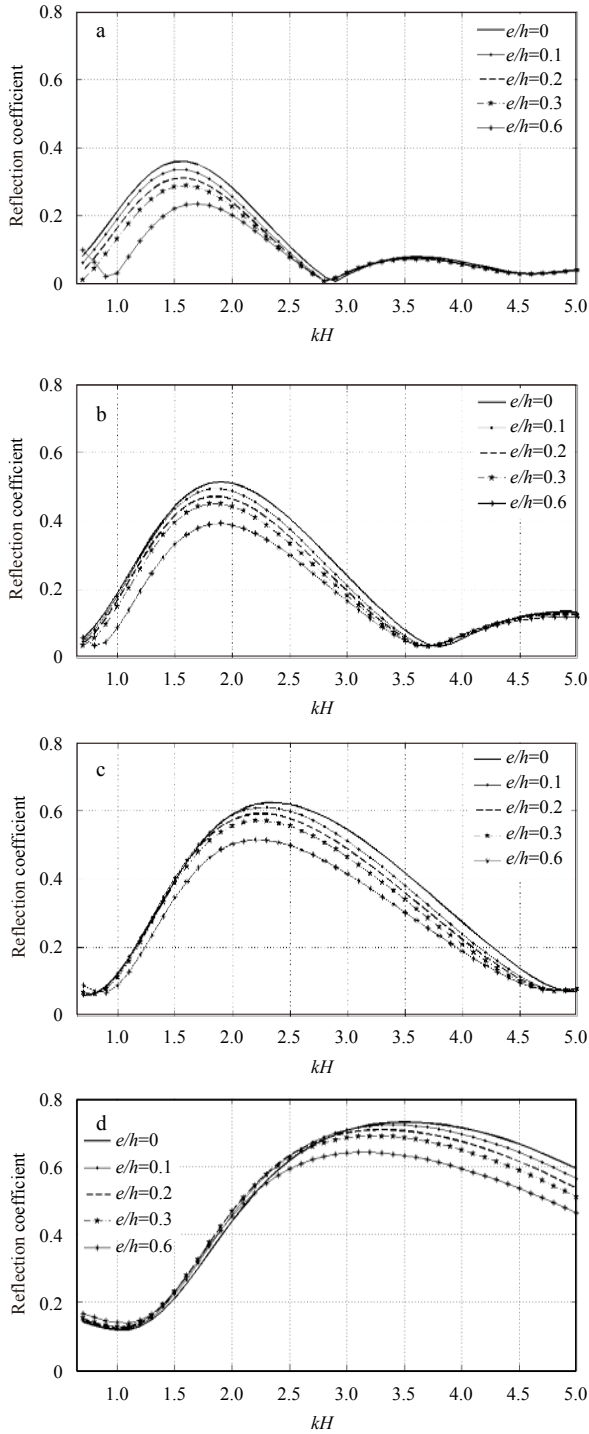
Fig. 8. Reflection coefficient as a function of *kH* for a relative plate length 2*l*/*h*=3, Froud number $U/\sqrt{gH}$ =0.045, and different values of relative plate thickness *e*/*h*=0, 0.1, 0.2, 0.3 and 0.6. *a*. Immersion ratio *h*/*H*=0.5, b. *h*/*H*=0.35, *c*. *h*/*H*=0.25, and d. *h*/*H*=0.15.

At the same immersion, the relative difference in the maximum of the reflection coefficient $(M–M_0)/M_0$ increases when the relative thickness increases. For the same relative thickness, the relative difference in the maximum of the reflection coefficient $(M–M_0)/M_0$ decreases when the immersion ratio decreases. For relative thickness (e/h) =0.1, the relative difference in the maximum of the reflection coefficient $(M–M_0)/M_0$ is approximately 7%

for immersion 0.5 and does not exceed 3% for other immersions.

Consequently, we can conclude that the relative plate thickness effect on the reflection coefficient decreases when the immersion ratio decreases.

4.2 *Effect of plate immersion*

In this section, we study the effect of the plate immersion ratio on the reflection coefficient during the regular wave–current–thin plate interaction. For this study, the reflection coefficient calculated by the present model is represented as a function of *kH* (relative depth of the incident wave in the absence of a current) for different values of the plate immersion and different values of the Froude number.

We study the effect on the maximum of the reflection coefficient and on the reflection bandwidth. The reflection band is defined by adopting the criterion used in electronics to define the pass band. With this definition, the width of the reflection band is the width of the interval $[k_1H, k_2H]$ so that the value of the reflection coefficient corresponding to k_1H and k_2H is equal to $R_{\max}/\sqrt{2}$, where $R_{\max}$ denotes the maximum of the reflection coefficient.

To study the effect of the plate immersion ratio, we represent the variations of the reflection coefficient as a function of the relative depth *kH* for different immersion ratios (*h*/*H*=0.25, *h*/*H*=0.50, *h*/*H*=0.75) (Fig. 9). The analytical calculations were performed using this theoretical model for a relative plate length (2*l*/*h*)=3. Three cases are considered: in the absence of a current (Fig. 9a) and for two values of the Froud number $U/\sqrt{gH}$ =0.045 (Fig. 9b) and $U/\sqrt{gH}$ =0.061 (Fig. 9c). In Table 2, we presented the reflection bandwidth and the relative difference of the maximum of the reflection coefficient $(M–M_0)/M_0$, where M_0 is the reflection coefficient maximum in the absence of a current.

The curves in Figs 9a–c and the results presented in Table 2 show that:

(1) The reflection coefficient maximum and the width of the reflection band decrease with the increase of the plate immersion ratio.

(2) When the plate immersion ratio increases, the width of the reflection band is shifted to higher values of *kH* (short wavelength).

(3) When the Froud number increases, the reflection coefficient maximum also increases, the reflection band is not shifted and its width is practically unchanged.

Thus, we can conclude that the nearer the plate is to the free surface (low immersion), the more important is the effect of current and the shift of the efficiency of the plate toward the large values of *kH*.

4.3 *Effect of the relative plate length*

To consider the impact of the length of the plate on the reflection coefficient in the presence of a current, we represent the variations of the reflection coefficient as a function of *kH* (relative depth of the incident wave in the absence of a current) for different values of the relative length of the plate (2*l*/*h*=3, 3.5 and 4) and for different values of the Froud number. The three cases considered are $U/\sqrt{gH} = 0$ (in the absence of a current) (Fig. 10a), $U/\sqrt{gH} = 0.045$ (Fig. 10b) and $U/\sqrt{gH} = 0.061$ (Fig. 10c). In Table 3, we present the reflection bandwidth and the relative difference of the maximum reflection coefficient $(M–M_0)/M_0$, where M_0 is the reflection coefficient maximum in the absence of a current.

The curves in Figs 10a–c and the results presented in Table 3

Table 1. Relative difference in the maximum value of the reflection coefficient for Froud number $U/\sqrt{gH} = 0.045$

e/h	$h/H=0.5$				$h/H=0.35$				$h/H=0.25$				$h/H=0.15$			
	0.1	0.2	0.3	0.6	0.1	0.2	0.3	0.6	0.1	0.2	0.3	0.6	0.1	0.2	0.3	0.6
$\dfrac{M-M_0}{M_0}$	0.07	0.14	0.20	0.35	0.03	0.08	0.12	0.23	0.02	0.05	0.08	0.17	0.01	0.03	0.06	0.12
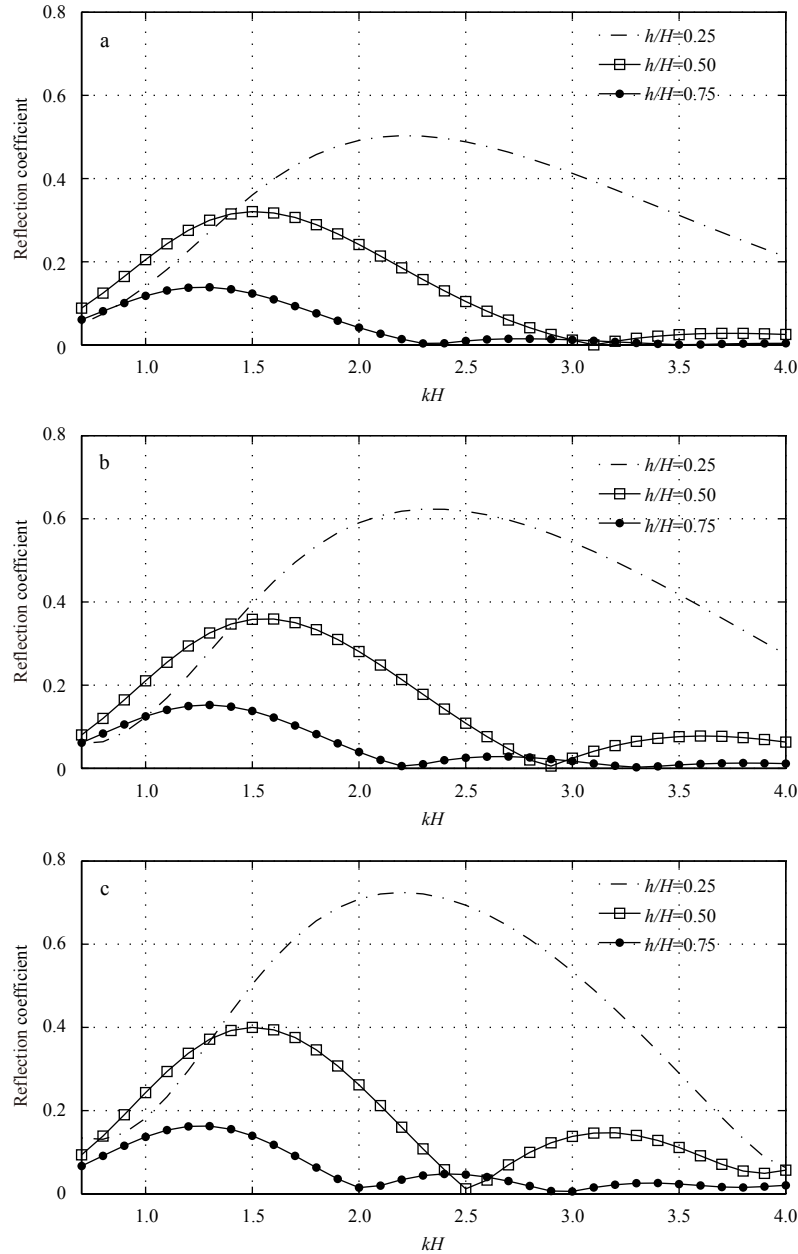
Fig. 9. Reflection coefficient as a function of kH for a thin plate (e=0 m), a relative plate length $2l/h$=3, and different values of the plate immersion ratio (h/H=0.25, 0.50 and 0.75). a. Froud number $U/\sqrt{gH}$ = 0, b. $U/\sqrt{gH}$ = 0.045, and c. $U/\sqrt{gH}$ = 0.061.

show that:

(1) The reflection coefficient maximum increases very slightly with the increase of the relative plate length.

(2) When the relative plate length increases, the reflection band is shifted to low values of kH (high wavelength) and the width of this band decreases.

(3) When the Froud number increases, the reflection coefficient maximum increases and the reflection band is not shifted and is of practically unchanged width.

We concluded that the effect of the relative length of the plate on the reflection coefficient is accentuated by the current velocity and that this accentuation decreases with the increase of the relative plate length.

5 Conclusions

In this paper, we studied the influence of the geometrical parameters of a plate during the regular wave–current–plate interaction. These parameters are the relative depth of water in the

Table 2. Relative difference in the maximum value of the reflection coefficient and the reflection bandwidth for different values of the immersion ratio (h/H=0.25, 0.50 and 0.75) and different values of the Froud number ($U/\sqrt{gH}$=0, 0.045 and 0.061)

h/H	$\dfrac{U}{\sqrt{gH}} = 0$			$\dfrac{U}{\sqrt{gH}} = 0.045$			$\dfrac{U}{\sqrt{gH}} = 0.061$		
	0.25	0.50	0.75	0.25	0.50	0.75	0.25	0.50	0.75
$\left\|\dfrac{M - M_0}{M_0}\right\|$				23.7%	12%	10%	43.5%	24.8%	17.5%
$\|k_2H - k_1H\|$	1.80	1.05	0.85	1.80	1.00	0.80	1.60	0.85	0.70

Fig. 10. Reflection coefficient as a function of kH for a thin plate, plate immersion ratio h/H=0.50 and different values of the relative plate length $2l/h$=3.0, 3.5 and 4.0. a. Froud number $U/\sqrt{gH} = 0$, b. $U/\sqrt{gH} = 0.045$, and c. $U/\sqrt{gH}$=0.061.

channel, the relative thickness of the plate, its immersion ratio and its relative length. We studied the effect on the maximum values of the reflection coefficient and the reflection band.

This study was conducted as part of the linearized potential flow theory using the evanescent modes model. To take account of the evanescent modes in the presence of a current, the disper-sion equation was solved by seeking complex solutions that are neither pure real nor pure imaginary. The number of evanescent modes taken into account was N=30. This investigation revealed that:

(1) Plate thickness influence. The relative plate thickness ef-fect on the reflection coefficient decreases when the immersion

Table 3. Relative difference in the maximum value of the reflection coefficient and reflection bandwidth for different values of the relative plate length ($2l/h$=3, 3.5 and 4) and different values of the Froud number ($U/\sqrt{gH}$=0; 0.045 and 0.061)

$2l/h$	$\dfrac{U}{\sqrt{gH}}=0$			$\dfrac{U}{\sqrt{gH}}=0.045$			$\dfrac{U}{\sqrt{gH}}=0.061$		
	3.0	3.5	4.0	3.0	3.5	4.0	3.0	3.5	4.0
$\left\|\dfrac{M-M_0}{M_0}\right\|$				12%	10.3%	7.8%	24.8%	19.3%	15.7%
$\|k_2H - k_1H\|$	1.02	0.82	0.7	1.00	0.80	0.75	0.85	0.80	0.70

ratio decreases.

(2) Immersion ratio influence. The reflection coefficient maximum and the width of the reflection band decrease with the increase of the plate immersion ratio. When the plate immersion ratio increases, the width of the reflection band is shifted to higher values of kH (short wavelength). When the Froud number increases, the reflection coefficient maximum also increases, and the reflection band is not shifted and is of practically unchanged width.
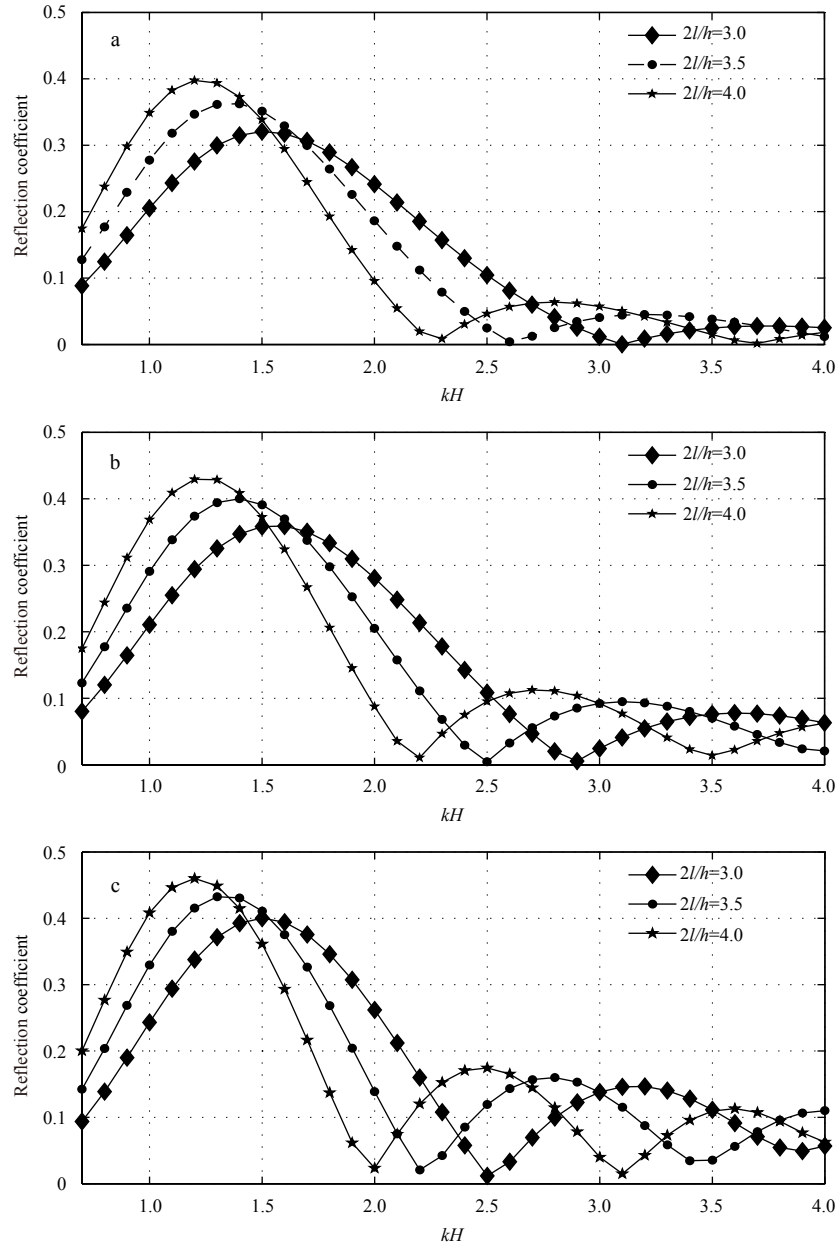
(3) Plate length influence. The reflection coefficient maximum increases very slightly with the increase of the relative plate length. When the relative plate length increases, the reflection band is shifted to low values of kH (high wavelength), and the width of this band decreases. When the Froud number increases, the reflection coefficient maximum increases as well, and the reflection band is not shifted and is of practically unchanged width.

References

Acanal L, Loukogeorgaki E, Yagci O, et al. 2013. Performance of an inclined thin plate in wave attenuation. Journal of Coastal Research, 1(65): 141–146

Bai Junli, Ma Ning, Gu Xiechong. 2017. Study of interaction between wave-current and the horizontal cylinder located near the free surface. Applied Ocean Research, 67: 44–58, doi: 10.1016/j.apor.2017.06.004

Behera H, Sahoo T. 2015. Hydroelastic analysis of gravity wave interaction with submerged horizontal flexible porous plate. Journal of Fluids and Structures, 54: 643–660, doi: 10.1016/j.jfluidstructs.2015.01.005

Brossard J, Perret G, Blonce L, et al. 2009. Higher harmonics induced by a submerged horizontal plate and a submerged rectangular step in a wave flume. Coastal Engineering, 56(1): 11–22, doi: 10.1016/j.coastaleng.2008.06.002

Errifaiy M, Naasse S, Chahine C. 2016. Analytical determination of the reflection coefficient by the evanescent modes model during the wave-current-horizontal plate interaction. Comptes Rendus Mécanique, 344(7): 479–486, doi: 10.1016/j.crme.2016.03.004

Hsu H H, Wu Y C. 1998. Scattering of water wave by a submerged horizontal plate and a submerged permeable breakwater. Ocean Engineering, 26(4): 325–341, doi: 10.1016/S0029-8018(97)10032-4

Lebon B, Perret G, Coëtmellec S, et al. 2016. A digital holography set-up for 3D vortex flow dynamics. Experiments in Fluids, 57(6): 103, doi: 10.1007/s00348-016-2187-8

Lin Hongxing, Ning Dezhi, Zou Qingping, et al. 2014. Current effects on nonlinear wave scattering by a submerged plate. Journal of Waterway, Port, Coastal, and Ocean Engineering, 140(5): 04014016, doi: 10.1061/(ASCE)WW.1943-5460.0000256

Liu Yong, Li Yucheng, Teng Bin. 2009. Wave motion over two submerged layers of horizontal thick plates. Journal of Hydrodynamics, 21(4): 453–462, doi: 10.1016/S1001-6058(08)60171-7

Liu P L F, Iskandarani M. 1991. Scattering of short-wave groups by submerged horizontal plate. Journal of Waterway, Port, Coastal, and Ocean Engineering, 117(3): 235–246, doi: 10.1061/(ASCE)0733-950X(1991)117:3(235)

Ning Dezhi, Lin Hongxing, Teng Bin, et al. 2014. Higher harmonics induced by waves propagating over a submerged obstacle in the presence of uniform current. China Ocean Engineering, 28(6): 725–738, doi: 10.1007/s13344-014-0057-9

Patarapanich M. 1984. Maximum and zero Reflection from submerged plate. Journal of waterway, Port, Coastal, and Ocean Engineering, 110(2): 171–181, doi: 10.1061/(ASCE)0733-950X(1984)110:2(171)

Patarapanich M, Cheong H F. 1989. Reflection and transmission characteristics of regular and random waves from a submerged horizontal plate. Coastal Engineering, 13(2): 161–182, doi: 10.1016/0378-3839(89)90022-7

Rao S, Shirlal K G, Varghese R V, et al. 2009. Experimental investigation of hydraulic performance of a horizontal plate breakwater. International Journal of Earth Sciences and Engineering, 2: 424–432

Rey V, Capobianco R, Dulou C. 2003. Réflexion de la houle par une plaque immergée en présence d'un courant. Revue de Mécanique Appliquée et Théorique, 1(4): 207–218

Rey V, Touboul J. 2011. Forces and moment on a horizontal plate due to regular and irregular waves in the presence of current. Applied Ocean Research, 33(2): 88–99, doi: 10.1016/j.apor.2011.02.002

Yueh C Y, Chuang S H. 2009. Wave scattering by a submerged porous plate wave absorber. In: Proceedings of the 19th International Offshore and Polar Engineering Conference. Osaka, Japan: International Society of Offshore and Polar Engineers, 1167–1173

Zheng Y H, Liu P F, Shen Y M, et al. 2007b. On the radiation and diffraction of linear water waves by an infinitely long rectangular structure submerged in oblique seas. Ocean Engineering, 34(3–4): 436–450

Zheng Y H, Shen Y M, Tang J. 2007a. Radiation and diffraction of linear water waves by an infinitely long submerged rectangular structure parallel to a vertical wall. Ocean Engineering, 34(1): 69–82, doi: 10.1016/j.oceaneng.2005.12.004

Appendix:

The continuity of the velocity potential at the edge of attack ($x=-l$):

$$\phi_1\left(-l,y\right)=\phi_3\left(-l,y\right)\quad -h\leqslant y\leqslant 0,\ \phi_1\left(-l,y\right)=\phi_4\left(-l,y\right)\quad -H\leqslant y\leqslant -h. \tag{A1}$$

Multiplying these two equations respectively by $\cos\left(k_{3n}\left(y+h\right)\right)$ and $\cos\left(\mu_n\left(y+H\right)\right)$ and then integrating, we obtain:

$$\int\limits_{-h}^{0}\phi_1\left(-l,y\right)\cos\left(k_{3n}\left(y+h\right)\right)\mathrm{d}y=\int\limits_{-h}^{0}\phi_3\left(-l,y\right)\cos\left(k_{3n}\left(y+h\right)\right)\mathrm{d}y\qquad\left(1\leqslant n\leqslant N\right),$$

$$\int\limits_{-H}^{-h}\phi_1\left(-l,y\right)\cos\left(\mu_n\left(y+H\right)\right)\mathrm{d}y=\int\limits_{-H}^{-h}\phi_4\left(-l,y\right)\cos\left(\mu_n\left(y+H\right)\right)\mathrm{d}y\qquad\left(1\leqslant n\leqslant N\right). \tag{A2}$$

This gives 2N equations (2 equations for each value of n). Two other equations are obtained by replacing $\cos\left(k_{3n}\left(y+h\right)\right)$ by $\cosh\left(k_3\left(y+h\right)\right)$ and $\cos\left(\mu_n\left(y+H\right)\right)$ by 1 (one) in the previous process. Hence, the number of equations is 2N+2.

The continuity of the horizontal velocity at the edge of attack ($x=-l$):

$$\frac{\partial\phi_1\left(-l,y\right)}{\partial x}=\frac{\partial\phi_3\left(-l,y\right)}{\partial x}\quad -h\leqslant y\leqslant 0,\quad \frac{\partial\phi_1\left(-l,y\right)}{\partial x}=\frac{\partial\phi_4\left(-l,y\right)}{\partial x}\quad -H\leqslant y\leqslant -h. \tag{A3}$$

By multiplying these two equations by $\cos\left(k_{1n}\left(y+H\right)\right)$ and then integrating and summing, we obtain:

$$\int\limits_{-H}^{0}\frac{\partial\phi_1\left(-l,y\right)}{\partial x}\cos\left(k_{1n}\left(y+H\right)\right)\mathrm{d}y=\int\limits_{-h}^{0}\frac{\partial\phi_3\left(-l,y\right)}{\partial x}\cos\left(k_{1n}\left(y+H\right)\right)\mathrm{d}y+$$

$$\int\limits_{-H}^{-h}\frac{\partial\phi_4\left(-l,y\right)}{\partial x}\cos\left(k_{1n}\left(y+H\right)\right)\mathrm{d}y\qquad\left(1\leqslant n\leqslant N\right). \tag{A4}$$

Replacing $\cos\left(k_{1n}\left(y+H\right)\right)$ by $\cosh\left(k_1^+\left(y+H\right)\right)$ in the previous process, we obtain another equation. In addition, by using the matching conditions between the subdomains at the edge of attack, we obtain 3N+3 equations.

Using a similar process at the edge of trailing ($x=l$), by replacing ϕ_1 by ϕ_2, k_1^+ by k_1^-, $-k_{1n}$ by $-k_{1n}$, k_3^- by k_3^+ and k_{3n} by $-k_{3n}$, we obtain 3N+3 other equations.

Therefore, using the continuity of the velocity potential and of the horizontal velocity at the attack and trailing edges of the plate, we obtain the following system (Eqs (A5)–(A16)):

$$\int\limits_{-h}^{0}\phi_1\left(-l,y\right)\cos\left(k_{3n}\left(y+h\right)\right)\mathrm{d}y=\int\limits_{-h}^{0}\phi_3\left(-l,y\right)\cos\left(k_{3n}\left(y+h\right)\right)\mathrm{d}y\qquad\left(1\leqslant n\leqslant N\right), \tag{A5}$$

$$\int\limits_{-h}^{0}\phi_1\left(-l,y\right)\cosh\left(k_3^-\left(y+h\right)\right)\mathrm{d}y=\int\limits_{-h}^{0}\phi_3\left(-l,y\right)\cosh\left(k_3^-\left(y+h\right)\right)\mathrm{d}y, \tag{A6}$$

$$\int\limits_{-H}^{-h}\phi_1\left(-l,y\right)\cos\left(\mu_n\left(y+H\right)\right)\mathrm{d}y=\int\limits_{-H}^{-h}\phi_4\left(-l,y\right)\cos\left(\mu_n\left(y+H\right)\right)\mathrm{d}y\qquad\left(1\leqslant n\leqslant N\right), \tag{A7}$$

$$\int\limits_{-H}^{-h}\phi_1\left(-l,y\right)\mathrm{d}y=\int\limits_{-H}^{-h}\phi_4\left(-l,y\right)\mathrm{d}y, \tag{A8}$$

$$\int\limits_{-H}^{0}\frac{\partial\phi_1\left(-l,y\right)}{\partial x}\cos\left(k_{1n}\left(y+H\right)\right)\mathrm{d}y=\int\limits_{-h}^{0}\frac{\partial\phi_3\left(-l,y\right)}{\partial x}\cos\left(k_{1n}\left(y+H\right)\right)\mathrm{d}y+$$

$$\int\limits_{-H}^{-h}\frac{\partial\phi_4\left(-l,y\right)}{\partial x}\cos\left(k_{1n}\left(y+H\right)\right)\mathrm{d}y\qquad\left(1\leqslant n\leqslant N\right), \tag{A9}$$

$$\int_{-H}^{0} \frac{\partial \phi_1(-l,y)}{\partial x} \cosh\left(k_1^+(y+H)\right) \mathrm{d}y = \int_{-h}^{0} \frac{\partial \phi_3(-l,y)}{\partial x} \cosh\left(k_1^+(y+H)\right) \mathrm{d}y +$$
$$\int_{-H}^{-h} \frac{\partial \phi_4(-l,y)}{\partial x} \cosh\left(k_1^+(y+H)\right) \mathrm{d}y, \tag{A10}$$

$$\int_{-h}^{0} \phi_2(l,y) \cos\left(k_{3n}(y+h)\right) \mathrm{d}y = \int_{-h}^{0} \phi_3(l,y) \cos\left(k_{3n}(y+h)\right) \mathrm{d}y \qquad (1 \leqslant n \leqslant N), \tag{A11}$$

$$\int_{-h}^{0} \phi_2(l,y) \cosh\left(k_3^+(y+h)\right) \mathrm{d}y = \int_{-h}^{0} \phi_3(l,y) \cosh\left(k_3^+(y+h)\right) \mathrm{d}y, \tag{A12}$$

$$\int_{-H}^{-h} \phi_2(l,y) \cos\left(\mu_n(y+H)\right) \mathrm{d}y = \int_{-H}^{-h} \phi_4(l,y) \cos\left(\mu_n(y+H)\right) \mathrm{d}y \qquad (1 \leqslant n \leqslant N), \tag{A13}$$

$$\int_{-H}^{-h} \phi_2(l,y) \mathrm{d}y = \int_{-H}^{-h} \phi_4(l,y) \mathrm{d}y, \tag{A14}$$

$$\int_{-H}^{0} \frac{\partial \phi_2(l,y)}{\partial x} \cos\left(k_{1n}(y+H)\right) \mathrm{d}y = \int_{-h}^{0} \frac{\partial \phi_3(l,y)}{\partial x} \cos\left(k_{1n}(y+H)\right) \mathrm{d}y +$$
$$\int_{-H}^{-h} \frac{\partial \phi_4(l,y)}{\partial x} \cos\left(k_{1n}(y+H)\right) \mathrm{d}y \qquad (1 \leqslant n \leqslant N), \tag{A15}$$

$$\int_{-H}^{0} \frac{\partial \phi_2(l,y)}{\partial x} \cosh\left(k_1^-(y+H)\right) \mathrm{d}y = \int_{-h}^{0} \frac{\partial \phi_3(l,y)}{\partial x} \cosh\left(k_1^-(y+H)\right) \mathrm{d}y +$$
$$\int_{-H}^{-h} \frac{\partial \phi_4(l,y)}{\partial x} \cosh\left(k_1^-(y+H)\right) \mathrm{d}y. \tag{A16}$$

The expressions of potentials Eq. (A1) and Eq. (A4) show that the functions ϕ_p are linear with respect to the constants $\{B_1, B_{1n}, A_3, B_3, A_{3n}, B_{3n}, A_4, B_4, A_{4n}, B_{4n}, A_2$ and A_{2n} for $1 \leqslant n \leqslant N\}$. After integration, Eqs (A5) to (A16) depend on the following constants: the geometrical parameters h/H, $2l/h$ and e/h; the relative depth kH (where k is the wavenumber of the incident wave in the absence of a current); and the Froud number $U/\sqrt{gH}$. As a result, Eqs (A5)–(A16) are also linear with respect to the constants $\{B_1, B_{1n}, A_3, B_3, A_{3n}, B_{3n}, A_4, B_4, A_{4n}, B_{4n}, A_2$ and A_{2n} for $1 \leqslant n \leqslant N\}$. These equations therefore constitute a linear algebraic system of $6N+6$ equations and $6N+6$ unknowns, which are the constants $\{B_1, B_{1n}, A_3, B_3, A_{3n}, B_{3n}, A_4, B_4, A_{4n}, B_{4n}, A_2$ and A_{2n} for $1 \leqslant n \leqslant N\}$. The linearity of this system results from the linearity of the velocity potential. The elements of the matrix corresponding to this system depend on the following: geometrical parameters h/H, $2l/h$ and e/h; the relative depth kH (where k is the wavenumber of the incident wave in the absence of a current); and the Froud number $U/\sqrt{gH}$.

Wave parameters retrieval for dual-polarization C-band synthetic aperture radar using a theoretical-based algorithm under cyclonic conditions

Yingying Ding[1], Juncheng Zuo[1], Weizeng Shao[1]*, Jian Shi[2], Xinzhe Yuan[3], Jian Sun[4], Jiachen Hu[1], Xiaofeng Li[5]

[1] Marine Science and Technology College, Zhejiang Ocean University, Zhoushan 316000, China

[2] College of Meteorology and Oceanography, National University of Defense Technology, Nanjing 210007, China

[3] National Satellite Ocean Application Service, Ministry of Natural Resources, Beijing 100081, China

[4] Physical Oceanography Laboratory, Ocean University of China, Qingdao 266100, China

[5] Global Science and Technology, National Oceanic and Atmospheric Administration (NOAA) National Environmental Satellite, Data, and Information Service (NESDIS), College Park, MD 20740, USA

Abstract

Theoretical-based ocean wave retrieval algorithms are applied by inverting a synthetic aperture radar (SAR) intensity spectrum into a wave spectrum, that has been developed based on a SAR wave mapping mechanism. In our previous studies, it was shown that the wave retrieval algorithm, named the parameterized first-guess spectrum method (PFSM), works for C-band and X-band SAR at low to moderate sea states. In this work, we investigate the performance of the PFSM algorithm when it is applied for dual-polarization c-band sentinel-1 (S-1) SAR acquired in extra wide-swath (EW) and interferometric wide-swath (IW) mode under cyclonic conditions. Strong winds are retrieved from six vertical-horizontal (VH) polarization S-1 SAR images using the c-band cross-polarization coupled-parameters ocean (C-3PO) model and then wave parameters are obtained from the image at the vertical-vertical (VV) polarization channel. significant wave height (SWH) and mean wave period (MWP) are compared with simulations from the WAVEWATCH-III (WW3) model. The validation shows a 0.69 m root mean square error (RMSE) of SWH with a –0.01 m bias and a 0.62 s RMSE of MWP with a –0.17 s bias. Although the PFSM algorithm relies on a good quality SAR spectrum, this study confirms the applicability for wave retrieval from an S-1 SAR image. Moreover, it is found that the retrieved results have less accuracy on the right sector of cyclone eyes where swell directly affects strong wind-sea, while the PFSM algorithm works well on the left and rear sectors of cyclone eyes where the interaction of wind-sea and swell is relatively poor.

Key words: wave parameters, synthetic aperture radar, cyclonic condition

1 Introduction

Ocean waves are the main feature of the upper ocean dynamic processes and play an important role in atmosphere-ocean interactions. Moreover, an extreme wave is also a natural hazard in coastal waters. Therefore, waves are a crucial factor in oceanography and offshore engineering. At present, waves are derived from operational wave models and are usually forced by forecast winds. However, forecast waves have less accuracy when using less accurate values for winds. Satellites carrying an altimeter sensor are a remote-sensing technique for wave monitoring over global seas. For instance, open-access wave data derived from such satellites as Topex/Poseidon, Jason-2 and HY-2, have been popularly used by investigators world-wide. The spatial coverage of an altimeter wave is relatively small (~10 km) with a revisit frequency of 10–15 d and the available wave data from an altimeter only covers the track footprints of a satellite orbit. This kind of limitation does not satisfy the requirements of marine research, especially when researching cyclonic conditions. Synthetic aperture radar (SAR) has the capability of monitoring the sea surface with a large swath coverage (up to 600 km) and fine spatial resolution (up to 1 m). SAR-derived waves can improve wave forecasts and make up the gaps in remotely sensed measurements at coastal waters.

Traditionally, the methodology of a wave retrieval algorithm was exploited for deriving a wave spectrum from a SAR intensity spectrum based on the SAR wave mapping mechanism, e.g., tilt modulation, hydrodynamic modulation (Alpers et al., 1981), and non-linear velocity bunching (Alpers and Bruening, 1986). To date, these algorithms have included the "max-planck institute" (MPI) algorithm (Hasselmann and Hasselmann, 1991), the semi

*Corresponding author, E-mail: shaoweizeng@zjou.edu.cn

parametric retrieval algorithm (SPRA) (Mastenbroek and de Valk, 2000), the partition rescaling and shift algorithm (PARSA) (Schulz-Stellenfleth et al., 2005), and the parameterized first-guess spectrum method (PFSM) (He, 1999; Sun and Guan, 2006). In particular, it has been shown that the PFSM algorithm works for C-band (Lin et al., 2017) and X-band (Shao et al., 2015) SAR at low to moderate sea states. It is necessary to understand that prior information on wind is needed in order to produce a first-guess wave spectrum when applying the theoretical-based algorithms that are used to deal with the modulation transfer function (MTF) of non-linear velocity bunching. Moreover, the MTF of velocity bunching was theoretically derived at low to moderate sea state (Hasselmann and Hasselmann, 1991), therefore, the applicability MTF of velocity bunching at high seta needs to be studied. In practice, wind can be directly retrieved from a SAR image.

The geophysical model function (GMF) is commonly applied for wind retrieval from a SAR image. It describes the empirical relationship between a SAR-measured backscattering signal in co-polarization (vertical-vertical (VV) and horizontal-horizontal (HH)), called the normalized radar cross section (NRCS), and a wind vector at 10 m height above the sea surface (Masuko et al., 1986). C-band GMFs include CMOD4 (Stoffelen and Anderson, 1997), CMOD-IFR2 developed at the Institut Francais de Recherche pour Exploitation de la MER (IFREMER) (Quilfen et al., 1998), CMOD5N for neutral wind (Hersbach, 2010), C-SARMOD (Mouche and Chapron, 2015), CMOD7 (Stoffelen et al., 2017) and C-SARMOD2 (Lu et al., 2018). The CMOD family has been well studied over the last few decades and has been implemented for various C-band SAR data, e.g., ENVISAT-ASAR (Yang et al., 2011a), RADARSAT-1/2 (R-1/2) (Yang et al., 2011b; Shao et al., 2014) and Sentinel-1A/1B (S-1) (Monaldo et al., 2016) and Gaofen-3 (GF-3) (Shao et al., 2017a, 2019). However, the backscattering signal encounters a saturation problem at strong winds (probably at wind speeds greater than 25 m/s) (Hwang et al., 2010; Voronovich and Zavorotny, 2014; Shao et al., 2017b), indicating these GMFs do not work under these conditions. Under these circumstances, the PFSM algorithm is not applicable for typhoon and hurricane wave retrieval from SAR images.

Several empirical models, e.g., CWAVE_ERS for ERS-1/2 (Schulz-Stellenfleth et al., 2007), CWAVE_ENVI for ENVISAT-ASAR (Li et al., 2011), CWAVE_S1 for S-1 (Stopa and Mouche, 2007) and CSAR_WAVE for GF-3 (Sheng et al., 2018), have also been developed, and are aimed at directly retrieving the wave parameters from SAR images without having to calculate the complex MTF of each modulation. These models work at low to moderate sea states, because data collection taken at high sea states is unavailable in the tuning process. Although two empirical models are preliminarily exploited for wave retrieval in hurricanes and typhoons (Romeiser et al., 2015; Shao et al., 2018a), these have only been tuned through a few images and simulations from a numerical wave model and they need to be refitted for different SAR bands and imaging modes.

Several recent works are devoted to study the characteristic of typhoon/hurricane generated waves on SAR (Mouche et al., 2017; Hwang and Walsh, 2016; Zhang et al., 2018), however, typhoon and hurricane wave monitoring is still a challenge for the SAR research community. Interestingly, strong winds (up to 55 m/s) can be retrieved from cross-polarization (basically vertical-horizontal, VH) NRCS, because cross-polarization NRCS does not saturate as easily as the co-polarization backscattering signal (Hwang and Fois, 2015; Shao et al., 2017a). Recently, a methodo-

logy for strong wind retrieval using C-band cross-polarization NRCS was developed for R-2 SAR (Zhang and Perrie, 2012; Shen et al., 2014; Zhang et al., 2017) and GF-3 SAR (Shao et al., 2018c). This issue presents an interesting question and that is whether the MTF of velocity bunching and PFSM algorithm is suitable for wave retrieval at the VV-polarization channel as using a SAR-derived strong wind from an image at the VH-polarization channel under cyclonic conditions.

We organize this paper as follows: S-1 SAR images and other auxiliary data are introduced in Section 2. Section 3 shows the methodologies of cross-polarization strong wind retrieval algorithms, scheme of co-polarization wave retrieval algorithm PFSM and the setup of WW3 model. The validation is presented in Section 4 when comparing the retrieval results with measurements from the simulations of the numeric wave model WAVE-WATCH-III (WW3). The discussion is included in Section 5 and the conclusion and summary are given in Section 6.

2 Description of dataset

In total, six S-1 images with visible cyclone eyes acquired in dual-polarization (VV and VH) during the period of August 27 to September 23, 2016 were made available for this study. These images were acquired in extra wide-swath (EW) and interferometric wide-swath (IW) mode with a pixel size of 40 m and 10 m respectively at both azimuth and range directions. The quick-look images of Typhoon Lionrock, Hurricane Lester, Hurricane Gaston, Hurricane Hermine, and Hurricane Karl overlaying the tracks of cyclones are shown in Fig. 1, in which the maximum wind speeds are up to 60 m/s at the several SAR imaging moments.

Although measurements from a satellite altimeter, e.g., Jason-2, are useful for wave analysis (Liu et al., 2016), wave measurements from altimeter Jason-2 passing the six S-1 SAR images were unavailable. Therefore, the WW3 model (the latest version 5.16) in the spirit of the previous WAM model, which was developed by the National Centers for Environmental Prediction (NCEP) of the National Oceanic and Atmospheric Administration (NOAA), was employed to simulate the wave fields during the period of the five cyclones. Since 1979, the European Centre for Medium-Range Weather Forecasts (ECMWF) has released a daily global reanalysis dataset at intervals of six hours, e.g., sea surface wind and wave parameters, which has a fine spatial resolution. We employed ECMWF winds at 0.125° grids as the forcing fields and water depth information is derived from 30 arc-second topography data consisting of the General Bathymetric Chart of the Oceans (GEBCO) from the British Oceanographic Data Centre (BODC). The WW3 model performs simulations of wave fields well (Bi et al., 2015; Zheng et al., 2016; Liu et al., 2017) and the validation of WW3-simulated hurricane waves against National Data Buoy Center (NDBC) buoys of the NOAA was used in our recent study (see Fig. 8 in Shao et al., 2018c). WW3-simulated wave parameters, e.g., significant wave height (SWH) and mean wave period (MWP), are used to study the accuracy of SAR-derived waves under cyclonic conditions.

In this study, we also use independent sources, e.g., polarimetric radiometer WindSAT, in order to validate the SAR-derived wind speed from VH-polarization S-1 SAR images by using a cross-polarization wind retrieval algorithm. WindSAT is a space borne satellite for measuring sea surface winds using a polarimetric radiometer with a swath coverage of more than 350 km following the orbit, and the standard deviation (STD) of wind speed is about 1.4 m/s as validated against the measurements of aircraft (Meissner and Wentz, 2012). Therefore, WindSAT wind
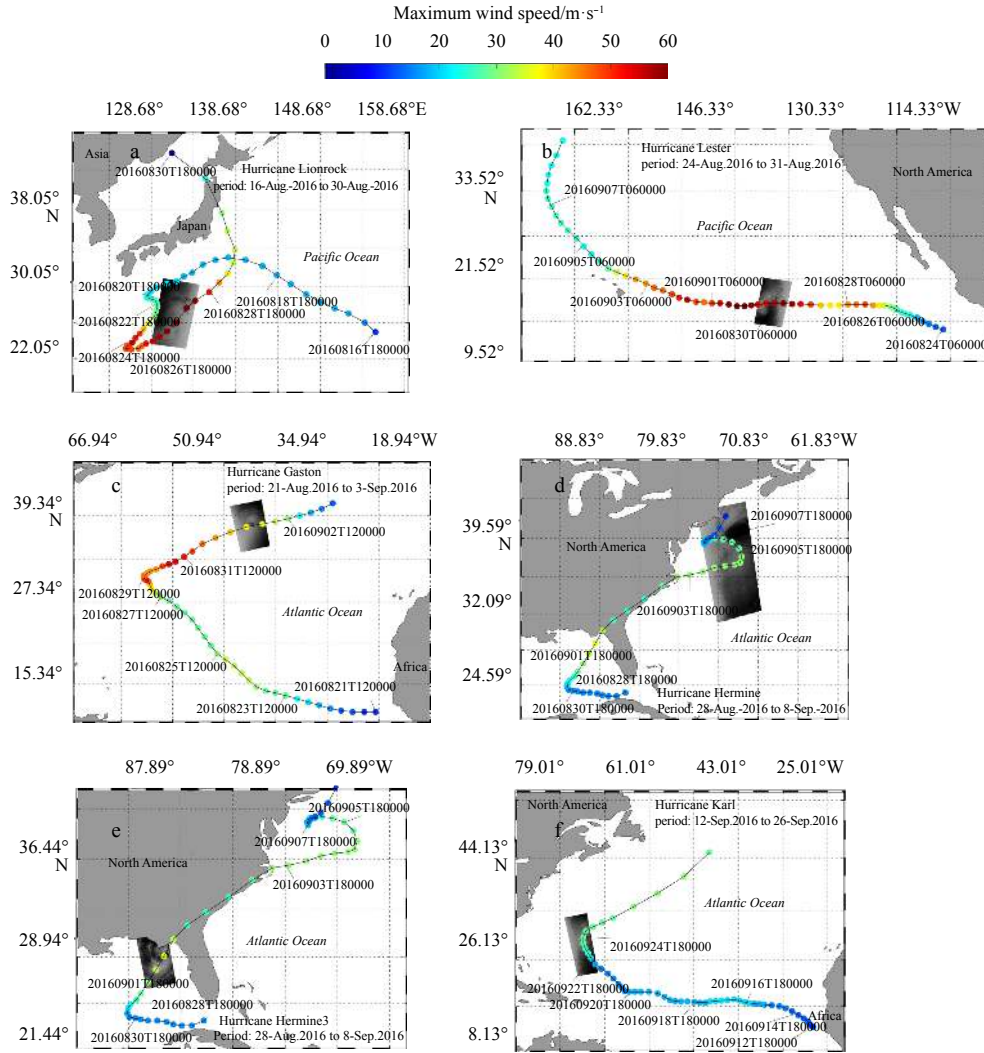
Fig. 1. The quick-look images of six Sentinel-1 (S-1) SAR images in VV-polarization overlaying the tracks of cyclones. a. The image for Typhoon Lionrock acquired in extra wide-swath (EW) mode on August 27, 2016 at 20:53 Universal Time Coordinated (UTC); b. the image for Hurricane Lester acquired in EW mode on August 30, 2016 at 14:46 UTC; c. the image for Hurricane Gaston acquired in EW mode on September 1, 2016 at 20:30 UTC; d. the image for Hurricane Hermine acquired in EW mode on September 4, 2016 at 22:32 UTC; e. the image for Hurricane Hermine acquired in interferometric wide-swath (IW) mode on September 1, 2016 at 23:44 UTC; and f. the image for Hurricane Karl acquired in EW mode on September 23, 2016 at 22:23 UTC.

products satisfy the requirements of global wind monitoring, especially in typhoon and hurricane conditions. It is proved that overall root mean square error (RMSE) difference of the retrieved wind speeds from WindSAT with respect to the H* wind analysis data developed by the Hurricane Research Division (HRD) is 2.75 m/s in hurricanes (Zhang et al., 2016). The Wind-SAT products with wind speed smaller than 30 m/s are used in this study, due to we think the WindSAT winds are most reliable at such wind condition.

3 Methodology

When applying the PFSM wave retrieval algorithm to retrieve waves, prior information on wind speed is necessary. Therefore, we first present the methodology of the cross-polarization coupled-parameters ocean (C-3PO) model, which was developed for retrieving hurricane winds using cross-polarized SAR NRCS at C-band. Then the theoretically based PFSM wave retrieval algorithm scheme is briefly introduced.

3.1 *C-3PO model*

It was initially revealed in a study by Vachon and Wolfe (2011) that cross-polarization NRCS has a strong linear relationship with wind speed and a quadratic linear model was developed to retrieved wind speed at low to moderate winds (up to 25 m/s). Later, a C-band cross-polarized ocean surface strong wind retrieval model for dual-polarization SAR, named C-2POD, was developed based on a collocated dataset, including R-2 VH-polarized NRCS, measurements from a stepped-frequency microwave radiometer (SFMR) and wind speeds from the NOAA H* wind model (Zhang and Perrie, 2012). In fact, VH-polarized NRCS has also been related to radar incidence angle based on a statistical analysis (Hwang et al., 2015). However, C-2POD models only include the term of wind speed, taking the following function,

$$\sigma_0 = p_1 + p_2 \times U_{10}, \tag{1}$$

where σ_0 is the cross-polarized NRCS united in dB and coeffi-

cients p_1 and p_2 are the tuned constants, U_{10} is the wind speed at 10 m above sea surface united in m/s.

As proposed in Zhang et al. (2017), an advanced C-3PO model considers the terms of wind speed and radar incidence angle through theoretical analysis by using a hybrid backscattering model. The C-3PO model is stated as follows:

$$\sigma_0 = A\,(U_{10}) \times [1 + B\,(\theta)]\,, \tag{2a}$$

$$A\,(U_{10}) = a_1 \times U_{10}^2 + a_2 \times U_{10} + a_3, \tag{2b}$$

$$B\,(\theta) = b_1 \times \frac{\theta - 34.5}{34.5}\,, \tag{2c}$$

where σ_0 is the cross-polarized NRCS united in dB, θ is the radar incidence angle united in degree and matrix a and coefficient b_1 are the tuned constants. The C-3PO model has a better performance than the C-2POD model, because a 2.81 m/s RMSE of wind speed is achieved when using the C-3PO model at wind speeds ranging from 9 to 40 m/s, which is less than a 2.90 m/s RMSE using the C-2POD model (Zhang et al., 2017).

3.2 *The PFSM algorithm*

The advantage of the PFSM algorithm is that a SAR-derived wave spectrum is composed of two portions, including wind-sea and swell spectrum, which are retrieved from two corresponding portions separated from a prior SAR spectrum. The separation wave number k_s is calculated using the following equation,

$$k_s = \left(\frac{2.87gV^2}{R^2 U_{10}^4 \cos^2\varphi \left(\sin^2\varphi \sin^2\theta + \cos^2\varphi \right)} \right)^{0.33}, \tag{3}$$

where g is the gravity acceleration, V is the satellite flight velocity, R is the satellite slant range, U_{10} is the SAR-derived wind speed, θ is the radar incidence angle and φ is the angle of wave propagation direction relative to radar look direction. The portion of the SAR spectrum at wave numbers greater than the separation wave number k_s is non-linearly mapped by the wind-sea and the left portion is linearly mapped by the swell.

For wind-sea retrieval, a "first-guess" spectrum is produced using the widely-used parametric JONSWAP model (see Appendix) after searching for several best-fit parameters of the model, including the sea surface wind speed at 10 m height U_{10}, wave propagation velocity at peak c_p and wave propagation direction at peak φ, which are prior obtained from a SAR image, similar to the SPRA scheme. Following this, the MPI scheme is employed to retrieve the wind-sea spectrum by minimizing a cost function (Hasselmann and Hasselmann, 1991). In the meantime, the swell spectrum is directly obtained by inverting the linear-mapping SAR spectrum, which considers the tilt modulation and hydrodynamic modulation (Alpers et al., 1981) without the velocity bunching (Hasselmann and Hasselmann, 1991). The detailed flowchart of retrieval process has been exhibited as Fig. 2 in our previous study (Shao et al., 2015).

According to traditional wave theory, SWH H_s and MWP T_0 is calculated using Eqs (4) and (5) from a retrieved one-dimensional wave number spectrum W_k,

$$H_s = 4 \times \sqrt{\int W_k \mathrm{d}k}, \tag{4}$$

$$T_0 = \frac{\displaystyle\int W_k \mathrm{d}k}{\displaystyle\int k^2 W_k \mathrm{d}k}\,. \tag{5}$$

3.3 *WW3 model setup*

As mentioned in Section 2, ECMWF winds at 0.125° grids are the forcing field for the wave simulation. It should be noted that ECMWF winds have a coarser spatial resolution than water depth data from 30 arc-second GEBCO. Therefore, ECMWF winds and GEBCO bathymetric data are both bi-linearly interpolated to be 0.1° in order to obtain reasonable simulations. The simulated two-dimensional wave spectrum is default resolved into 24 regular azimuthal directions at an interval of 15° and the frequency bins f are logarithmically ranged from 0.041 18 to 0.718 6 at an interval of $\Delta f/f$=0.1. The time step of spatial propagation is set to 300 s in both the longitude and latitude directions. In particular, the package of the non-linear term for four wave-wave interactions (quadruplets), named Generalized Multiple Discrete Interaction Approximation (DIA), was implemented for the WW3 model, because it showed a good performance for simulation of typhoon waves according to our recent study (Shao et al., 2018b).

The global simulations from the WW3 model with 0.5° grids are treated as the open boundary. The ultimate WW3-simulated wave fields at 0.2° grids, including the spatial coverages of typhoon and hurricanes, are stored at an interval of 30 min, indicating that the time difference between SAR acquisition time and WW3-simulated results is within 15 min.

4 Validation

In this section, we first present the validation of SAR-derived wind speed against measurements from WindSAT. Then a comparison between the inverted wave parameters and WW3-simulated results is shown.

4.1 *Wind speed*

Figure 2 shows the SAR-derived wind maps corresponding to the six S-1 SAR images acquired in VH-polarization, in which the cyclone eyes are clearly observed. Although the retrieved wind speed is up to 40 m/s, the saturation problem is not found which encounters as applying the C-band co-polarization GMFs. However, discontinuities exist in the retrieved wind maps, indicated by more obvious changes of wind speed at the edge of each radar beam than in other regions. This is caused by the instrumental noise of the radar beam, because the S-1 SAR image acquired in EW and IW mode is comprised of several radar beams. In fact, R-2 (Shen et al., 2014) and GF-3 (Shao et al., 2018c) SAR acquired in dual-polarization also suffer from this problem. For this reason, the European Space Agency (ESA) is privately working on reducing the influence of instrumental noise by means of re-calibrating the S-1 SAR image.

The sub-scenes of S-1 SAR images covering the WindSAT grids are used here. Moreover, the time difference between collected sub-scenes and WindSAT winds is less than 1 h. In total, in this study, around 1 000 matchups are available. Figure 3 gives a visual comparison, showing the SAR-derived wind speeds when using the empirical C-3PO model and WindSAT winds for 2 m/s of wind speed bin, in which the error bars represent the standard deviation of each bin. It is found that the RMSE of wind speed is 2.9 m/s with a 1.1 m/s bias and there is a trend of underestimation at wind speeds greater than 10 m/s. It is not surprising that this performance is worse than the standard error 2 m/s of SAR-derived wind speed for co-polarization, because the in-
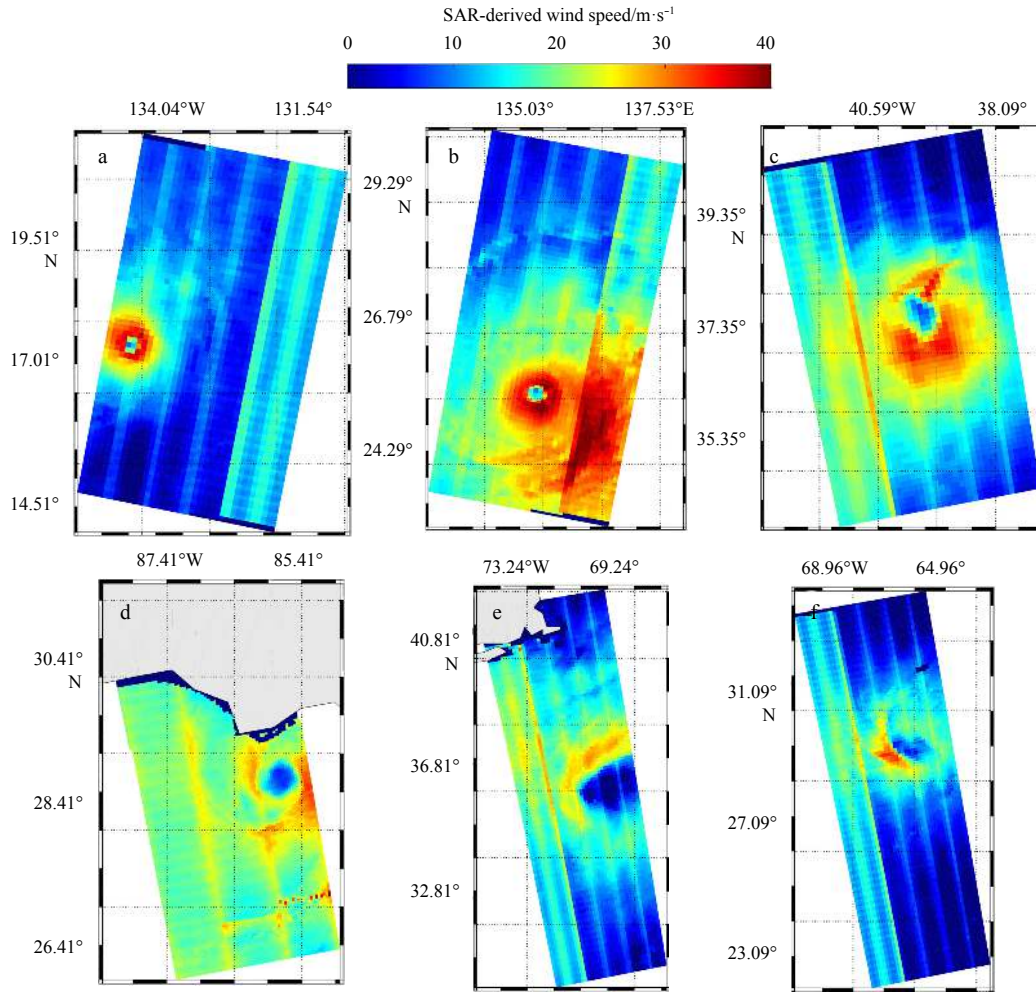
Fig. 2. The SAR-derived wind maps of six S-1 SAR images acquired in VH-polarization. a. The wind map for Typhoon Lionrock on August 27, 2016 at 20:53 UTC; b. the wind map for Hurricane Lester acquired on August 30, 2016 at 14:46 UTC; c. the wind map for Hurricane Gaston on September 1, 2016 at 20:30 UTC; d. the wind map for Hurricane Hermine on September 1, 2016 at 23:44 UTC; e. the wind map for Hurricane Hermine on September 4, 2016 at 22:32 UTC; and f. the wind map for Hurricane Karl on September 23, 2016 at 22:23 UTC.
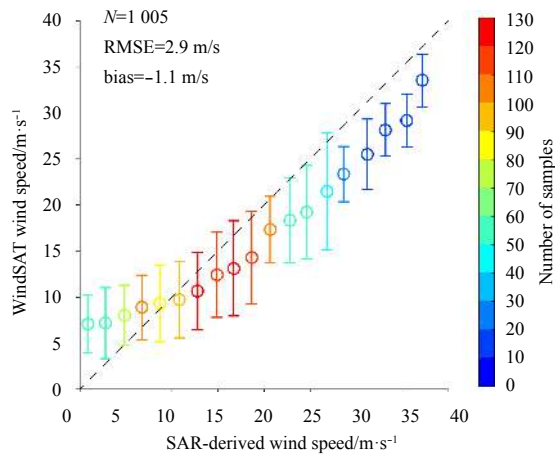

Fig. 3. Comparison between SAR-derived wind speeds using the C-3PO empirical algorithm and WindSAT winds for 2 m/s of wind speed bin, in which the error bars represent the standard deviation of each bin.

strumental noise of the radar beam from S-1 is different from that of the R-2, and the C-3PO model should be adapted for S-1 SAR. However, winds retrieved from VH-polarization SAR images do not encounter the saturation problem. In this situation, we think the retrieved wind is useful for wave retrieval from VV-polarization S-1 SAR images.

4.2 *Wave parameters*

In the wave retrieval process, the whole S-1 SAR image is divided into a number of sub-scenes with 128×128 pixels, which have a spatial coverage of 1×1 km² and 4×4 km² for EW and IW mode, respectively. It is well known that the non-linear effect due to velocity bunching is more pronounced in extreme weather conditions, causing the short waves to be undetectable. Additionally, precipitation also contaminates the SAR backscattering signature of cyclones. In this circumstance, the inhomogeneous sub-scene with poor-quality SAR intensity spectra, where the ratio of image variance and squared image mean is greater than 1.05 (Li et al., 2011), are excluded here. Out of those sub-scenes, φ is extracted from the SAR intensity spectrum, which is an indispensable variable when employing the PFSM algorithm.

As an example, we present the sub-scene extracted from the

S-1 SAR image taken on September 1, 2016 at 23:44 UTC in Hurricane Hermine, as shown in Fig. 4a. Figure 4b shows the two-dimensional SAR spectrum of the corresponding sub-scene in polar coordinates. The retrieved one-dimensional wave spectrum is shown in Fig. 4c. The SAR-derived SWH is 1.8 m and MWP is 5.4 s, while SWH is 2.4 m and MWP is 5.2 s from the WW3 model.

In order to systematically evaluate the retrieval accuracy of SWH and MWP, we compare the retrieval results with simulations from the WW3 model at strong winds. Figure 5 shows that the RMSE of SWH is 0.69 m with a –0.01 m bias and the RMSE of MWP is 0.62 s with a –0.17 s bias when using the PFSM algorithm. It is found that there is larger deviation at low sea state. We think this is caused by inaccurate wind speeds retrieved from VH-polarization S-1 SAR images at low winds smaller than 5 m/s. The accuracy of wave parameters retrieval is anticipated to be improved using more accurate wind speeds from co-polarization S-1 SAR images at low winds or re-calibrating images with low instrumental noise at the edge of radar beams. The pixel size of collected S-1 SAR images are 40 m and 10 m for azimuth and range directions, respectively, indicating that ocean wave with wave length less than 50 m (approximately a 5 s MWP) cannot been measured due to the coarse spatial resolution of collected SAR images. This is the probable explanation that the minimum MWP of retrieved waves is about 5 s in Fig. 5.
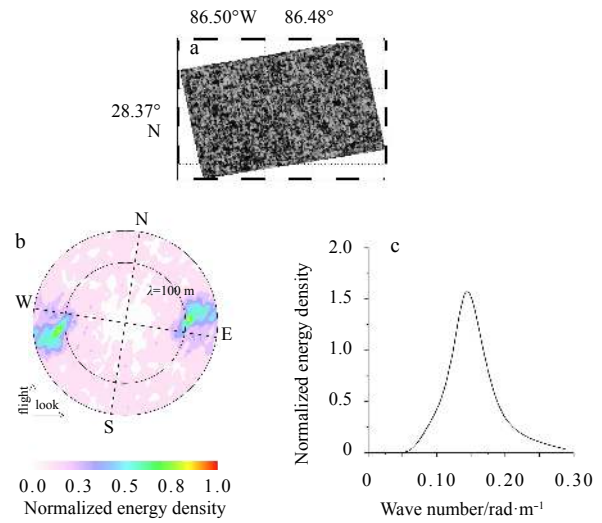

Fig. 4. The retrieval result for a case study. a. The sub-scene extracted from the S-1 SAR image taken on September 1, 2016 at 23:44 UTC in Hurricane Hermine; b. the two-dimensional SAR spectrum, corresponding to Fig. a; and c. one-dimensional wave spectra retrieved using the PFSM algorithm.
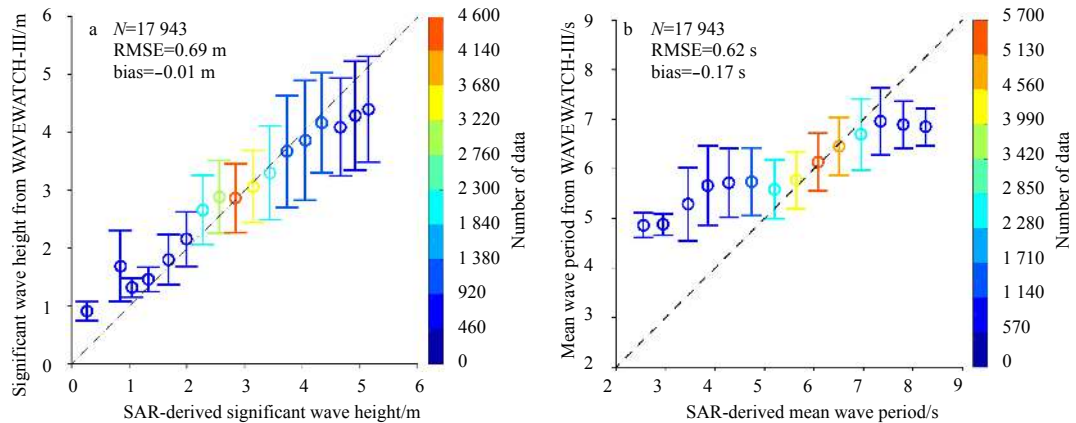

Fig. 5. Comparison between SAR-derived wave parameters using the PFSM algorithm and simulations from WAVEWATCH-III model, in which the error bars represent the standard deviation of each bin. a. Significant wave height for a 0.5 m bin, and b. mean wave period for a 0.5 s bin.

Fig. 6. Comparison between SAR-derived significant wave height using the PFSM algorithm and simulations from WAVEWATCH-III model, in which the error bars represent the standard deviation of each bin. a. Wind-sea for a 0.3 m bin, and b. swell for a 0.3 m bin.

We also compare the SAR-derived SWHs of wind-sea and swell with simulations from WW3 model, as shown in Fig. 6. It is not surprising that a 0.52 RMSE of linear-inverted swell SWH is achieved, which is better than a 0.66 RMSE of nonlinear-inverted wind-sea SWH. In general, the above validation indicates, that the PFSM algorithm can be applied for wave retrieval from a S-1 SAR image under cyclonic conditions, which is similar to wave retrieval from C-band SAR at low to moderate sea states.

5 Discussion

As pointed in our previous study (Shao et al., 2017a), wave characteristics under extreme weather conditions are complicated (Hwang, 2016; Hwang and Fan, 2017; Hwang and Walsh, 2016; Young, 2017), e.g., wind-sea dominates at the right side of a cyclone movement, wind-sea and cross swell mix at the left side of a cyclone movement and opposing swell dominates at the rear side. The wave system in Hurricane Gaston moving north-eastern in the Northern Hemisphere is illustrated in Fig. 7 (reproduce the Fig. 8 in Shao et al., 2017a). Therefore, we have undertaken further study around the accuracy of SWH and MWP at different parts of cyclone eyes.

Figure 8 shows cases at the right side of a cyclone eye, where wind-sea dominates in typical conditions of strong winds on the right-hand sector. Wind-sea and swell propagate in the same direction, causing the interaction of swell and strong wind-sea energy. This leads to a situation whereby the inverted waves using the PFSM algorithm show a large deviation from the WW3-simulated results (a 0.74 m RMSE of SWH and a 0.71 s RMSE of MWP) especially at SWH greater than 3 m. In contrast, wind-sea and swell orthogonally propagate at the left side of the cyclone eye, where the wind-sea energy is independent of swell energy. Retrieval results show a 0.59 m RMSE of SWH and a 0.52 s RMSE of MWP, as shown in Fig. 9, indicating a good agreement with simulations from the WW3 mode. As for wave retrieval at the rear of the cyclone where wind-sea and swell propagate in opposite directions, Fig. 10 shows that the RMSE of SWH is 0.60 m and RMSE of MWP is 0.42 s.

6 Conclusion and summary

In our previous studies, it was shown that the theoretically-based PFSM wave retrieval algorithm worked for C- and X-band SAR at low to moderate conditions. From August to September 2016, several cyclones, e.g., Typhoon Lionrock, Hurricane Lester,

Hurricane Gaston, Hurricane Hermine, and Hurricane Karl, were captured by S-1. Therefore, it poses an interesting question as to whether wave can be retrieved from an S-1 SAR image acquired in dual-polarization under cyclonic conditions.

Because the co-polarization backscattering signal encounters saturation problems at strong winds, the winds were retrieved from a VH-polarization S-1 SAR image using the C-3PO model. The RMSE of wind speed is 2.9 m/s with a 1.1 m/s bias as compared with a retrieved wind speed of up to 40 m/s using measurements from WindSAT, although the instrumental noise of S-1 SAR results in obvious changes of wind speed around the edge of radar beams. Together with SAR-derived winds, we demonstrate the applicability of the PFSM algorithm at high sea state. Validation against the simulations from the WW3 model shows a 0.69 m RMSE of SWH with a –0.01 m bias and a 0.62 s RMSE of MWP with a –0.17 s bias. We further investigate the performance at dif-

Fig. 7. The wave system in Hurricane Gaston moving north-eastern in the Northern Hemisphere.

Fig. 8. Comparison between SAR-derived wave parameters using the PFSM algorithm and simulations from WAVEWATCH-III model for cases at the rear of a cyclone eye, in which the error bars represent the standard deviation of each bin. a. Significant wave height for a 0.5 m bin, and b. mean wave period for a 0.5 s bin.
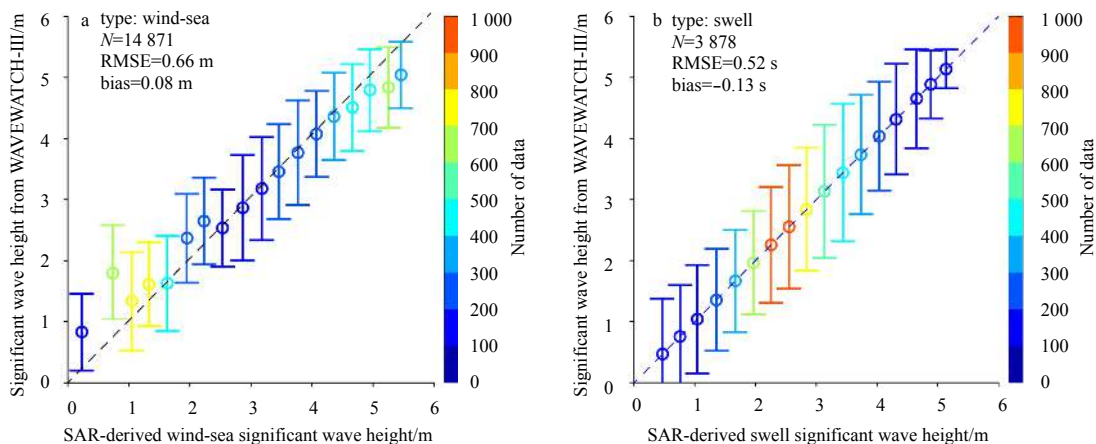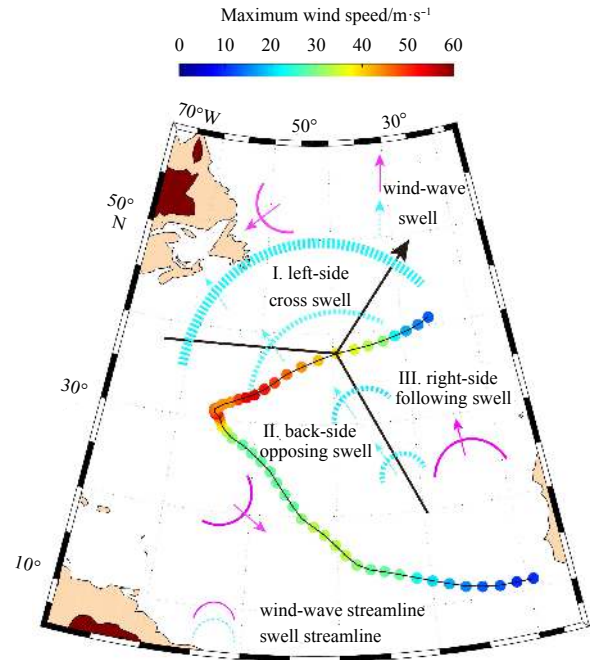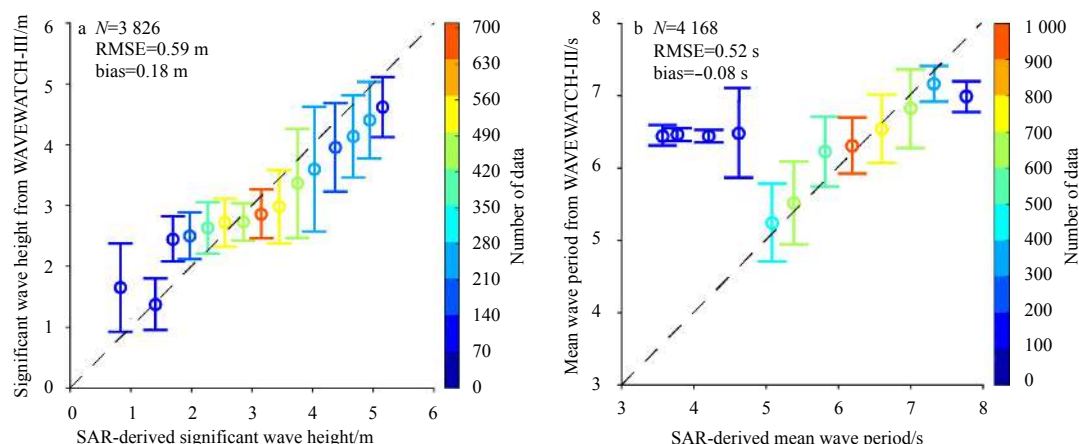
Fig. 9. Comparison between SAR-derived wave parameters using the PFSM algorithm and simulations from WAVEWATCH-III model for cases at the right of a cyclone eye, in which the error bars represent the standard deviation of each bin. a. Significant wave height for a 0.5 m bin and b. mean wave period for a 0.5 s bin.
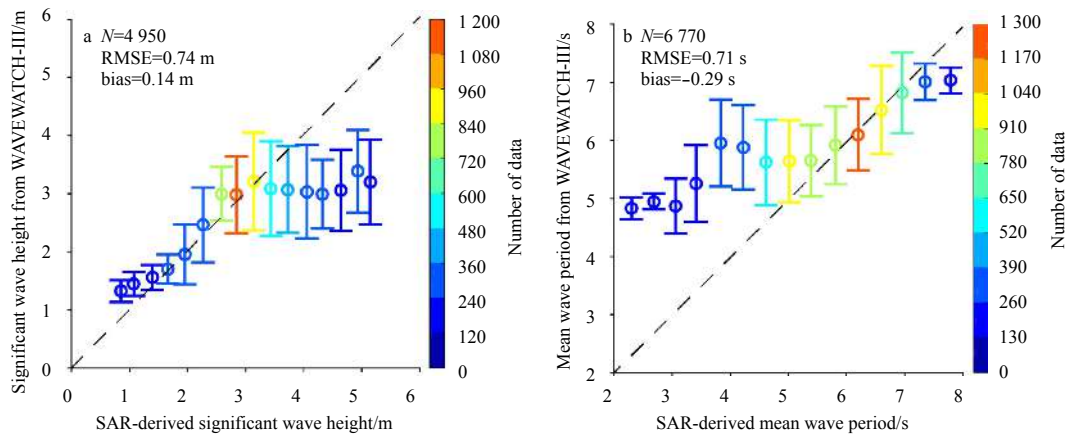

Fig. 10. Comparison between SAR-derived wave parameters using the PFSM algorithm and simulations from WAVEWATCH-III model for cases at the rear of a cyclone eye, in which the error bars represent the standard deviation of each bin. a. Significant wave height for a 0.5 m bin, and b. mean wave period for a 0.5 s bin.
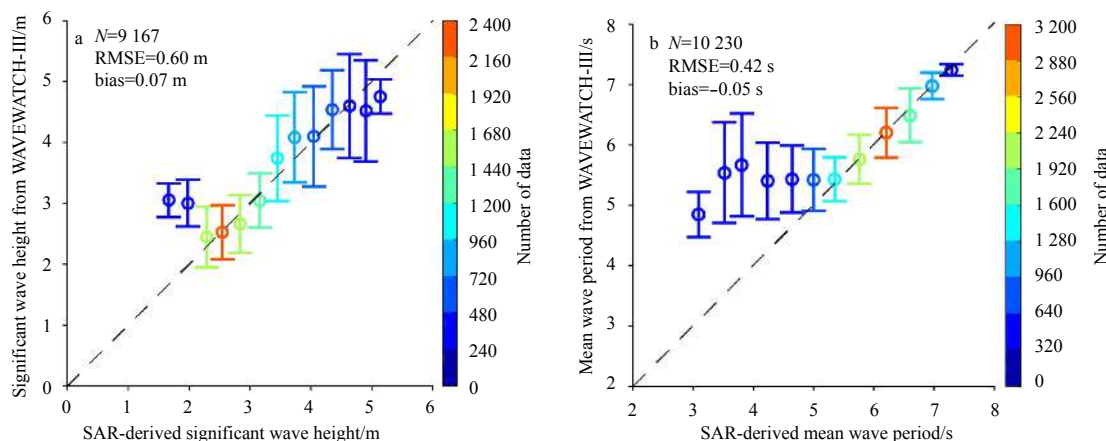
ferent parts of cyclone eyes. The interaction between swell energy and strong wind-sea energy to the right of a cyclone eye leads to less accurate retrieval results than that at left and rear of a cyclone eye, where this type of interaction is relatively poor.

It is concluded that the PFSM algorithm is suitable for estimating wave parameters from a C-band S-1 SAR image under cyclonic conditions, although the PFSM algorithm does rely on a good quality of SAR spectrum. The adaptability of the PFSM algorithm in details will be further studied through more images the improvement of MTF at high winds, e.g., the change of sea water dielectric coefficient and feature of azimuthal cut-off of velocity bunching.

References

Alpers W R, Bruening C. 1986. On the relative importance of motion-related contributions to the SAR imaging mechanism of ocean surface waves. IEEE Transactions on Geoscience and Remote Sensing, GE-24(6): 873–885, doi: 10.1109/TGRS.1986.289702

Alpers W, Ross D B, Rufenach C L. 1981. On the detectability of ocean surface waves by real and synthetic aperture radar. Journal of Geophysical Research, 86 (C7): 6481–6498

Bi Fan, Song Jinbao, Wu Kejian, et al. 2015. Evaluation of the simula-

tion capability of the Wavewatch III model for Pacific Ocean wave. Acta Oceanologica Sinica, 34(9): 43–57, doi: 10.1007/s13131-015-0737-1

Hasselmann K, Hasselmann S. 1991. On the nonlinear mapping of an ocean wave spectrum into a synthetic aperture radar image spectrum and its inversion. Journal of Geophysical Research: Oceans, 96(C6): 10713–10729, doi: 10.1029/91JC00302

He Yijun. 1999. A parametric method of retrieving ocean wave spectra from synthetic aperture radar images. Chinese Sciences Bulletin, 44(13): 1218–1224, doi: 10.1007/BF02885970

Hersbach H. 2010. Comparison of C-band scatterometer CMOD5.N equivalent neutral winds with ECMWF. Journal of Atmospheric and Oceanic Technology, 27(4): 721–736, doi: 10.1175/2009JTECHO698.1

Hwang P A. 2016. Fetch- and duration-limited nature of surface wave growth inside tropical cyclones: With applications to air–sea exchange and remote sensing. Journal of Physical Oceanography, 46(1): 41–56, doi: 10.1175/JPO-D-15-0173.1

Hwang P A, Fan Yalin. 2017. Effective fetch and duration of tropical cyclone wind fields estimated from simultaneous wind and wave measurements: Surface wave and air–sea exchange computation. Journal of Physical Oceanography, 47(2): 447–470, doi: 10.1175/JPO-D-16-0180.1

Hwang P A, Stoffelen A, van Zadelhoff G J, et al. 2015. Cross-polarization geophysical model function for C-band radar backscattering from the ocean surface and wind speed retrieval. Journal of Geophysical Research: Oceans, 120(2): 893–909 doi: 10.1002/2014JC010439

Hwang P A, Walsh E J. 2016. Azimuthal and radial variation of wind-generated surface waves inside tropical cyclones. Journal of Physical Oceanography, 46(9): 2605–2621, doi: 10.1175/JPO-D-16-0051.1

Hwang P A, Zhang Biao, Toporkov J V, et al. 2010. Comparison of composite Bragg theory and quad-polarization radar backscatter from RADARSAT-2: With applications to wave breaking and high wind retrieval. Journal of Geophysical Research: Oceans, 115(C8): C08019

Li Xiaoming, Lehner S, Bruns T. 2011. Ocean wave integral parameter measurements using Envisat ASAR wave mode data. IEEE Transactions on Geoscience and Remote Sensing, 49(1): 155–174, doi: 10.1109/TGRS.2010.2052364

Lin Bo, Shao Weizeng, Li Xiaofeng, et al. 2017. Development and validation of an ocean wave retrieval algorithm for VV-polarization Sentinel-1 SAR data. Acta Oceanologica Sinica, 36(7): 95–101, doi: 10.1007/s13131-017-1089-9

Liu Qingxiang, Babanin A, Fan Yalin, et al. 2017. Numerical simulations of ocean surface waves under hurricane conditions: assessment of existing model performance. Ocean Modelling, 118: 73–93, doi: 10.1016/j.ocemod.2017.08.005

Liu Qingxiang, Babanin A V, Zieger S, et al. 2016. Wind and wave climate in the Arctic Ocean as observed by altimeters. Journal of Climate, 29(22): 7957–7975, doi: 10.1175/JCLI-D-16-0219.1

Lu Yiru, Zhang Biao, Perrie W, et al. 2018. A C-band geophysical model function for determining coastal wind speed using synthetic aperture radar. IEEE Journal of Selected Topics in Applied Earth Observations and Remote Sensing, 11(7): 2417–2428, doi: 10.1109/JSTARS.2018.2836661

Mastenbroek C, de Valk C F. 2000. A semiparametric algorithm to retrieve ocean wave spectra from synthetic aperture radar. Journal of Geophysical Research: Oceans, 105(C2): 3497–3516, doi: 10.1029/1999JC900282

Masuko H, Okamoto K, Shimada M, et al. 1986. Measurement of microwave backscattering signatures of the ocean surface using X band and K_a band airborne scatterometers. Journal of Geophysical Research: Oceans, 91(C11): 13065–13083, doi: 10.1029/JC091iC11p13065

Meissner T, Wentz F J. 2012. The emissivity of the ocean surface between 6 and 90 GHz over a large range of wind speeds and earth incidence angles. IEEE Transactions on Geoscience and Remote Sensing, 50(8): 3004–3026, doi: 10.1109/TGRS.2011.2179662

Monaldo F, Jackson C, Li Xiaofeng, et al. 2016. Preliminary evaluation of Sentinel-1A wind speed retrievals. IEEE Journal of Selected Topics in Applied Earth Observations and Remote Sensing, 9(6): 2638–2642, doi: 10.1109/JSTARS.2015.2504324

Mouche A, Chapron B. 2015. Global C-band Envisat, RADARSAT-2 and Sentinel-1 SAR measurements in copolarization and cross-polarization. Journal of Geophysical Research: Oceans, 120(11): 7195–7207, doi: 10.1002/2015JC011149

Mouche A A, Chapron B, Zhang Biao, et al. 2017. Combined co- and cross-polarized SAR measurements under extreme wind conditions. IEEE Transactions on Geoscience and Remote Sensing, 55(12): 6746–6755, doi: 10.1109/TGRS.2017.2732508

Quilfen Y, Chapron B, Elfouhaily T, et al. 1998. Observation of tropical cyclones by high-resolution scatterometry. Journal of Geophysical Research: Oceans, 103(C4): 7767–7786, doi: 10.1029/97JC01911

Romeiser R, Graber H C, Caruso M J, et al. 2015. A new approach to ocean wave parameter estimates from C-band ScanSAR images. IEEE Transactions on Geoscience and Remote Sensing, 53(3): 1320–1345, doi: 10.1109/TGRS.2014.2337663

Schulz-Stellenfleth J, König T, Lehner S. 2007. An empirical approach for the retrieval of integral ocean wave parameters from synthetic aperture radar data. Journal of Geophysical Research: Oceans, 112(C3): C03019

Schulz-Stellenfleth J, Lehner S, Hoja D. 2005. A parametric scheme for the retrieval of two-dimensional ocean wave spectra from synthetic aperture radar look cross spectra. Journal of Geophysical Research: Oceans, 101(C5): C05004

Shao Weizeng, Hu Yuyi, Yang Jingsong, et al. 2018a. An empirical algorithm to retrieve significant wave height from Sentinel-1 synthetic aperture radar imagery collected under cyclonic conditions. Remote Sensing, 10(9): 1367, doi: 10.3390/rs10091367

Shao Weizeng, Li Xiaofeng, Hwang P, et al. 2017a. Bridging the gap between cyclone wind and wave by C-band SAR measurements. Journal of Geophysical Research: Oceans, 122(8): 6714–6724, doi: 10.1002/2017JC012908

Shao Weizeng, Li Xiaofeng, Sun Jian. 2015. Ocean wave parameters retrieval from TerraSAR-X images validated against buoy measurements and model results. Remote Sensing, 7(10): 12815–12828

Shao Weizeng, Sheng Yexin, Li Huan, et al. 2018b. Analysis of wave distribution simulated by WAVEWATCH-III model in typhoons passing Beibu Gulf, China. Atmosphere, 9(7): 265, doi: 10.3390/atmos9070265

Shao Weizeng, Sheng Yexin, Sun Jian. 2017b. Preliminary assessment of wind and wave Retrieval from Chinese Gaofen-3 SAR imagery. Sensors, 17(8): 1705, doi: 10.3390/s17081705

Shao Weizeng, Sun Jian, Guan Changlong, et al. 2014. A method for sea surface wind field retrieval from SAR image mode data. Journal of Ocean University of China, 13(2): 198–204, doi: 10.1007/s11802-014-1999-5

Shao Weizeng, Yuan Xinzhe, Sheng Yexin, et al. 2018c. Development of wind speed retrieval from cross-polarization Chinese Gaofen-3 synthetic aperture radar in typhoons. Sensors, 18(2): 412, doi: 10.3390/s18020412

Shao Weizeng, Zhu Shuai, Sun Jian, et al. 2019. Evaluation of wind retrieval from co-polarization Gaofen-3 SAR imagery around China Seas. Journal of Ocean University of China, 18(1): 80–92, doi: 10.1007/s11802-019-3779-8

Shen Hui, Perrie W, He Yijun, et al. 2014. Wind speed retrieval from VH dual-polarization RADARSAT-2 SAR images. IEEE Transactions on Geoscience and Remote Sensing, 52(9): 5820–5826, doi: 10.1109/TGRS.2013.2293143

Sheng Yexin, Shao Weizeng, Zhu Shuai, et al. 2018. Validation of significant wave height retrieval from co-polarization Chinese Gaofen-3 SAR imagery using an improved algorithm. Acta Oceanologica Sinica, 37(6): 1–10, doi: 10.1007/s13131-018-1217-1

Stoffelen A, Anderson D. 1997. Scatterometer data interpretation: Estimation and validation of the transfer function CMOD4. Journal of Geophysical Research: Oceans, 102(C3): 5767–5780, doi:

10.1029/96JC02860

Stoffelen A, Verspeek J A, Vogelzang J, et al. 2017. The CMOD7 geophysical model function for ASCAT and ERS wind retrievals. IEEE Journal of Selected Topics in Applied Earth Observations and Remote Sensing, 10(5): 2123–2134, doi: 10.1109/JSTARS. 2017.2681806

Stopa J E, Mouche A. 2017. Significant wave heights from Sentinel–1 SAR: validation and applications. Journal of Geophysical Research: Oceans, 122(3): 1827–1848, doi: 10.1002/2016JC012364

Sun Jian, Guan Changlong. 2006. Parameterized first-guess spectrum method for retrieving directional spectrum of swell-dominated waves and huge waves from SAR images. Chinese Journal of Oceanology and Limnology, 24(1): 12–20, doi: 10.1007/ BF02842769

Vachon P W, Wolfe J. 2011. C-Band cross-polarization wind speed retrieval. IEEE Geoscience and Remote Sensing Letters, 8(3): 456–459, doi: 10.1109/LGRS.2010.2085417

Voronovich A G, Zavorotny V U. 2014. Full-polarization modeling of monostatic and bistatic radar scattering from a rough sea surface. IEEE Transactions on Antennas and Propagation, 62(3): 1362–1371, doi: 10.1109/TAP.2013.2295235

Yang Xiaofeng, Li Xiaofeng, Pichel W G, et al. 2011a. Comparison of ocean surface winds from ENVISAT ASAR, MetOp ASCAT scatterometer, buoy measurements, and NOGAPS model. IEEE Transactions on Geoscience and Remote Sensing, 49(12): 4743–4750, doi: 10.1109/TGRS.2011.2159802

Yang Xiaofeng, Li Xiaofeng, Zheng Quanan, et al. 2011b. Comparison of ocean-surface winds retrieved from QuikSCAT scatterometer and Radarsat-1 SAR in offshore waters of the U.S. west coast. IEEE Geoscience and Remote Sensing Letters, 8(1): 163–167, doi: 10.1109/LGRS.2010.2053345

Young I R. 2017. A review of parametric descriptions of tropical cyclone wind-wave generation. Atmosphere, 8(10): 194

Zhang Guosheng, Li Xiaofeng, Perrie W, et al. 2017. A hurricane wind speed retrieval model for C-band RADARSAT-2 cross-polarization ScanSAR images. IEEE Transactions on Geoscience and Remote Sensing, 55(8): 4766–4774, doi: 10.1109/TGRS.2017. 2699622

Zhang Lei, Liu Guoqiang, Perrie W, et al. 2018. Typhoon/Hurricanegenerated wind waves inferred from SAR imagery. Remote Sensing, 10(10): 1605, doi: 10.3390/rs10101605

Zhang Biao, Perrie W. 2012. Cross-polarized synthetic aperture radar: a new potential measurement technique for hurricanes. Bulletin of the American Meteorological Society, 93(4): 531–541, doi: 10.1175/BAMS-D-11-00001.1

Zhang Lei, Yin Xiaobin, Shi Hanqing, et al. 2016. Hurricane wind speed estimation using WindSat 6 and 10 GHz brightness temperatures. Remote Sensing, 8(9): 721, doi: 10.3390/rs8090721

Zheng Kaiwen, Sun Jian, Guan Changlong, et al. 2016. Analysis of the global swell and wind sea energy distribution using WAVEWATCH III. Advances in Meteorology, 2016: 8419580

Appendix:

The two-dimensional wave spectrum $W_{k,\phi}$ in terms of wave number k and propagation direction ϕ has a relationship with the two-dimensional wave spectrum in terms of wave frequency ω and ϕ,

$$W_{k,\phi} = W_{\omega} \times G_{\phi} \times \frac{\mathrm{d}\omega}{\mathrm{d}k}, \tag{A1}$$

in which G_{ϕ} is the directional function and W_{ω} is the one-dimensional JONSWAP spectrum taking the following function.

$$W_{\omega} = \alpha \times \frac{g^2}{\omega^2} \times \exp\left[-1.25 \times \left(\frac{\omega_0}{\omega}\right)^4\right] \times \Gamma, \tag{A2}$$

where

$$\Gamma = \gamma^{\exp\left[-\frac{(\omega-\omega_p)^2}{2\sigma^2\omega^2}\right]}, \tag{A3}$$

$$\alpha = 0.006 \times \left(\frac{U_{10}}{c_\mathrm{p}}\right)^{0.55}, \tag{A4}$$

$$\omega^2 = g \times k \times \tanh kd, \tag{A5}$$

$$\omega_\mathrm{p} = \frac{g}{c_\mathrm{p}}, \tag{A6}$$

$$\sigma = \begin{cases} 0.07 & \omega \leqslant \omega_\mathrm{p}, \\ 0.09 & \omega > \omega_\mathrm{p}. \end{cases} \tag{A7}$$

where g is the gravity acceleration, γ is the peak-enhancement constant assumed to be 3.3, σ is a peak-width parameter, U_{10} is the sea surface wind speed at 10 m height, d is the water depth and c_p is wave propagation velocity at peak.

G_{ϕ} is defined as the normalized distribution of wave energy density at all propagation directions, which is stated as follows:

$$G_{\phi} = 0.5 \times \beta \times \mathrm{sech}^2[\beta \times (\phi - \phi_\mathrm{p})], \tag{A8}$$

where

$$\beta = \begin{cases} 2.61 \times \left(\frac{\omega_\mathrm{p}}{\omega}\right)^{1.3} & 0.56 \leqslant \frac{\omega_\mathrm{p}}{\omega} \leqslant 0.95, \\ 2.28 \times \left(\frac{\omega_\mathrm{p}}{\omega}\right)^{1.3} & 0.95 < \frac{\omega_\mathrm{p}}{\omega} \leqslant 1.6, \\ 1.24 & \text{others} \end{cases} \tag{A9}$$

where ϕ_p is the wave propagation direction at peak.

The one-dimensional spectrum W_k is obtained after integrating $W_{k,\phi}$ over all directions,

$$W_k = \int W_{k,\phi} \mathrm{d}\phi. \tag{A10}$$

Upper ocean high resolution regional modeling of the Arabian Sea and Bay of Bengal

Dwivedi Suneet[1]*, Mishra Alok Kumar[1], Srivastava Atul[1]

[1] K Banerjee Centre of Atmospheric and Ocean Studies and M N Saha Centre of Space Studies, University of Allahabad, Allahabad UP 211002, India

Abstract

In this paper, effort is made to demonstrate the quality of high-resolution regional ocean circulation model in realistically simulating the circulation and variability properties of the northern Indian Ocean (10°S–25°N, 45°–100°E) covering the Arabian Sea (AS) and Bay of Bengal (BoB). The model run using the open boundary conditions is carried out at 10 km horizontal resolution and highest vertical resolution of 2 m in the upper ocean. The surface and sub-surface structure of hydrographic variables (temperature and salinity) and currents is compared against the observations during 1998–2014 (17 years). In particular, the seasonal variability of the sea surface temperature, sea surface salinity, and surface currents over the model domain is studied. The high-resolution model's ability in correct estimation of the spatio-temporal mixed layer depth (MLD) variability of the AS and BoB is also shown. The lowest MLD values are observed during spring (March-April-May) and highest during winter (December-January-February) seasons. The maximum MLD in the AS (BoB) during December to February reaches 150 m (67 m). On the other hand, the minimum MLD in these regions during March-April-May becomes as low as 11–12 m. The influence of wind stress, net heat flux and freshwater flux on the seasonal variability of the MLD is discussed. The physical processes controlling the seasonal cycle of sea surface temperature are investigated by carrying out mixed layer heat budget analysis. It is found that air-sea fluxes play a dominant role in the seasonal evolution of sea surface temperature of the northern Indian Ocean and the contribution of horizontal advection, vertical entrainment and diffusion processes is small. The upper ocean zonal and meridional volume transport across different sections in the AS and BoB is also computed. The seasonal variability of the transports is studied in the context of monsoonal currents.

Key words: Indian Ocean modeling, Arabian Sea and Bay of Bengal, mixed layer depth, transport

---

1 Introduction

Understanding the Arabian Sea (AS) and Bay of Bengal (BoB) circulation and the variability of the Indian Ocean exhibits on different time scales (seasonal, interannual, decadal and longer) is very important for the Indian subcontinent. The better understanding of the AS and BoB circulation and variability of the surface and sub-surface variables shall not only help in the improvement of forecasting of the Indian summer monsoon rainfall and tropical cyclones (Dube et al., 1990; Achuthavarier et al., 2012; Subrahmanyam et al., 2005; Ali et al., 2015; Vinayachandran et al., 2015) but it will also have a potential positive impact on the economy of the regions surrounding the ocean. Moreover, the variability in the hydrography and circulation of the AS and BoB also influences and gets influenced by the tropical Pacific interannual variability (Gutzler and Harrison, 1987; Annamalai et al., 2005; Schott et al., 2009 and references therein), and the monsoons over East Africa, and Australia (Annamalai and Murtugudde, 2004; Vecchi and Harrison, 2004; Song et al., 2007).

The Indian Ocean circulation is greatly influenced by the near surface air-sea forcings (Schott and McCreary, 2001; Callaghan et al., 2014; Vinayachandran et al., 2015). The circulation is generally considered to be wind and buoyancy driven (Liu and Alexander, 2007). The air-sea interaction processes (including Indian

summer monsoon rainfall), wind stress, heat and freshwater flux strongly impact AS and BoB circulation. The AS and BoB circulation, on the other hand, influences the Indian summer monsoon rainfall (Roxy et al., 2015; Krishnamurthy and Kirtman, 2003; Wu and Kirtman, 2004 and references therein). It is, therfore, important to understand the impact of air-sea forcings on the quality of the ocean circulation model output. Several researchers have carried out sensitivity studies for this purpose in the AS and BoB using different air-sea forcing products (Wajsowicz, 2002; Prasad, 2004; Agarwal et al., 2007; Sharma et al., 2007; Chakraborty et al., 2014). However, none of these studies have focused on understanding the relative roles of wind and buoyancy forcings on the mixed layer depth variability of the region using 3-D high-resolution model output. One of the aims of this study is, therefore, to decipher the relative roles of interannually varying winds, heat and freshwater flux forcings in influencing the AS and BoB mixed layer depth variability at eddy-resolving scales. Moreover, the spatio-temporal mixed layer heat budget (Huang et al., 2010, 2012; Foltz et al., 2003) analysis of the northern Indian Ocean using long term high-resolution model output is also not available even though it is important for investigating the processes that control the seasonal cycle of seasurface temperature in the northern Indian Ocean (Thangaprakash et al., 2016 and refer-

*Corresponding author, E-mail: suneetdwivedi@gmail.com

ences therein). In the present manuscript, we, therefore, also make an attempt to quantify the mixed layer heat budget using our model output and estimate the relative contributions coming from surface fluxes, advection, diffusion, and entrainment terms.

Various observational and ocean circulation modeling studies have been performed in the recent past in the region surrounding the AS and BoB. Sharma et al. (2007, 2010, 2012) studied the sea surface salinity (SSS) variability in the tropical Indian Ocean using an ocean general circulation model (OGCM). Kantha et al. (2008) simulated the North Indian Ocean circulation and variability for the period 1993–2004. Rao and Sivakumar (2003) used observations to explain the seasonal variability of SSS and mixed layer salt budget in the AS and BoB. Thadathil et al. (2002) studied various aspects of the surface layer temperature inversion in the BoB. Vinayachandran and Kurian (2007) investigated the low salinity regimes during the summer monsoon in the western BoB. Schott and McCreary (2001) presented an in-depth review on the monsoon circulation of the Indian Ocean. Prasanna Kumar and Narvekar (2005) studied mixed layer depth seasonal variability and its implication to nutrients and primary productivity in the central AS. The mixed layer depth variability in the central BoB and associated changes in nutrients and chlorophyll was examined by Narvekar and Prasanna Kumar (2006). Shenoi et al. (1999) and Shankar et al. (2002) explained tropical Indian Ocean surface circulation using long-term ocean observations. Thompson et al. (2006, 2008) used ocean model to understand the variability of the Indian Ocean circulation and salinity. Han et al. (2001) examined how salinity distributions in the BoB affect dynamics, thermodynamics, and mixed layer physics in the upper Indian Ocean. Durand et al. (2007) investigated the effect of salinity on the formation of the barrier layer in the southeastern Arabian Sea (SEAS). Durand et al. (2011) used an ocean model to study the impact of monthly Ganges-Brahmaputra river discharge variations on the BoB salinity and temperature. Similarly, de Boyer Montégut et al. (2014) examined the role of salinity fronts on the spatio-temporal structure of the AS barrier layers during summer monsoon season. Akhil et al. (2014) studied the processes responsible for strong SSS seasonal cycle in the BoB.

One of the main reasons behind the incomplete understanding of the AS and BoB circulation and variability is the limited availability of the high-resolution (surface and subsurface) data of the oceanographic variables (of hydrography and velocity) in space and time. The availability of such data is also important in realistic estimation of the ocean heat content, mixed layer depth, and volume transport. The correct knowledge of these on the other hand is very important from the point of view of biological production and source-sink of carbon containing gases (Bates 2006a, b). The satellite dataset is limited to surface variables only and the *in situ* (depth dependent) observations are a few. The recourse is taken in this case by running high-resolution OGCMs in a limited area (AS and BoB of the Indian Ocean, for example) and validating the model results against the available observations. The OGCMs offer themselves as a powerful tool for this purpose and help in generating 3-dimensional time varying oceanic fields at desired resolutions. However, examples of such studies which have focused on understanding the Indian Ocean variability at eddy-resolving scales of O (10 km) are a few. Wu et al. (2007) have used an eddy-resolving OGCM to investigate the evolution of freshwater plumes and salinity fronts in the northern BoB. Using the altimetry data and an eddy-resolving ocean model Cheng et al. (2013) examined the intraseasonal variability of sea surface height over the BoB. Diansky et al. (2006) studied the monsoon

circulation in the Indian Ocean using a high-resolution σ-coordinate ocean model. Huang et al. (2015) used a (1/8)° coupled biochemical-physical Indian Ocean Regional Model to provide an estimate of the oceanic physical state along with the biochemical processes in the Indian Ocean. Masumoto et al. (2008) and George et al. (2010) demonstrated the advantage of using eddy-permitting ocean model for the Indian Ocean towards the simulation of major surface and subsurface variables. Momin et al. (2014) have also argued for higher horizontal resolution in their Indian Ocean intercomparison study, though their model resolution was still too coarse. Similarly, Vinayachandran et al. (1996) also showed the usefulness of ocean models with higher horizontal resolution in better simulation of the BoB circulation. Benshila et al. (2014) demonstrated the advantage of high-resolution modeling studies in investigating the seasonal structure of sea surface salinity of the BoB.

However, none of these high-resolution studies have focused on the evolution of surface and subsurface hydrography (temperature, and salinity), and circulation (velocity) of AS and BoB together over a longer duration of time (which also takes into account concomitant effect of climate change in recent decades, for example). In addition to this, seasonal variability of the mixed layer depth of the AS and BoB and its relation to monsoonal currents has not been studied in detail using high-resolution model data. Moreover, reliable estimates of the transport of water mass from AS to BoB and vice versa and the associated changes during summer and winter monsoon seasons are also not present due to lack to quality-controlled high resolution dataset. Another major objective of this study is, therefore, to perform high-resolution (10 km) ocean circulation modeling in the Indian Ocean surrounding the AS and BoB regions during 1998–2014. The model results are compared and contrasted against the available ocean observations. The reliable estimates of hydrography, circulation, mixed layer depth, and volume transport (zonal and meridional) are obtained.

The paper is organized as follows. Section 2 gives a brief account of the ocean circulation model configuration. The results and discussion are given in Section 3. The quality of the model output, the spatio-temporal variability of the mixed layer depth, the mixed layer heat budget analysis, and the quantification of volume transports are given in this section. Conclusions are in Section 4.

2 Model configuration

The ocean circulation model MITgcm (Marshall et al., 1997) is configured to run at a horizontal resolution of 10 km around the region (10°S–25°N, 45°–100°E) in the northern Indian Ocean. The MITgcm is a z-coordinate model and solves the incompressible Navier-Stokes equation. The Boussinesq and hydrostatic approximations are used here. We use 36 levels in the vertical (Table 1) with highest resolution of 2 m near the surface and then slowing telescoping out at depth. To represent the sub-grid scale mixing in vertical, we use K-profile parameterization (KPP) scheme (Large et al., 1994). The bathymetry of the model (Fig. 1) is derived from the high-resolution (1′) topography data of Smith and Sandwell (1997). The eddy (harmonic) viscosity and diffusivity are chosen in horizontal and vertical. The model uses no-slip condition on sides as well as bottom. The bottom frictional drag coefficient is taken as 0.001. A third order direct space-time advection scheme is employed for temperature and salinity. The nonlinear equation of state is used following Jackett and McDougall (1995). The model is forced by the 6-hourly NCEP/NCAR reanalysis (Kalnay et al., 1996) air temperature, relative humidity,

Table 1. Depth of vertical levels in the model

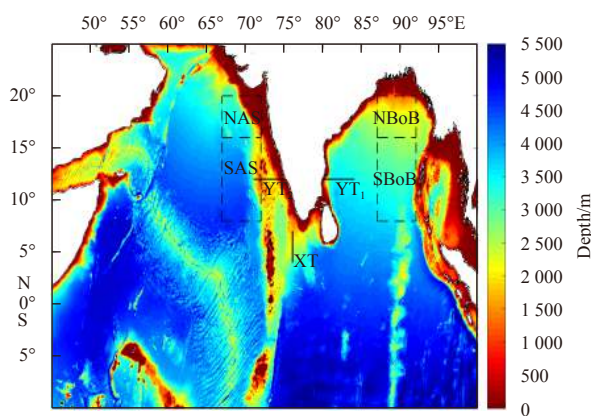| Level	Depth/m
1	2
2	2
3	2
4	2
5	2
6	3
7	3
8	3
9	3
10	3
11	4
12	4
13	4
14	5
15	5
16	6
17	8
18	10
19	13
20	17
21	22
22	28
23	35
24	45
25	55
26	70
27	90
28	130
29	190
30	250
31	350
32	450
33	500
34	500
35	600
36	600

Fig. 1. Bathymetry of the northern Indian Ocean around (10°S–25°N, 45°–100°E). The horizontal lines in the Arabian Sea and Bay of Bengal represent sections along which meridional volume transport is computed. The vertical line at the interface of Arabian Sea and Bay of Bengal represents section along which zonal volume transport is computed.

downward long-wave and short-wave radiation, precipitation, runoff, zonal and meridional wind data. The model calculates the air-sea fluxes, namely, ocean surface wind stress, and heat flux from these prescribed atmospheric states (interpolated to model grid) using the bulk formulae (Large and Pond, 1982). The fresh-water flux is computed as evaporation minus precipitation minus runoff. The model uses the open boundary conditions on all the sides. The values of temperature, salinity, zonal and meridional velocity prescribed at each boundary are extracted from the ocean reanalysis system 4 (ORAS4) (Balmaseda et al., 2013). The boundary values are updated at an interval of 30 d. The model computes net flow across the boundaries and adjusts all normal velocities on boundaries to obtain zero net inflow. The model's surface salinity is relaxed towards monthly climatology with a time scale of 30 d (Li et al., 2015). The model is spun-up for five years (from 1 January 1993 to 31 December 1997) with the initial temperature and salinity values derived from the World Ocean Atlas 2013 (WOA13). The output of the model is stored on a daily basis. The various datasets described in this section are also summarized in Table 2.

3 Results and discussion

3.1 *Quality of the model output*

The MITgcm is customized to run over the Arabian Sea and Bay of Bengal regions of the northern Indian Ocean for 17 a from 1 January 1998 to 31 December 2014 using the setup described in Section 2. The model uses the initial temperature, salinity, sea level elevation, zonal and meridional velocity from the spin-up run. We show in Fig. 2 (upper panel) the climatological sea surface temperature (SST) from model over the region of study. The corresponding SST values from the TRMM Microwave Imager (TMI) (Wentz et al., 2015) are also shown in the figure. It is clear from the figure that the model is able to reasonably capture the mean state of the SST. The lowest SST values are observed in the western AS. The spatial correlation coefficient of the temporally averaged model SST with the corresponding TMI values is 0.91 (at 99.9% significance level). The SST bias (TMI-model) is also shown in the figure. We see from the figure that the bias is very small in most parts of the domain. The bias seen along the coasts, however, may be ignored since TMI has known problems along the coasts (Wang et al., 2011). The SST root mean square error (RMSE) between the annually averaged model and TMI is 0.35 °C which is much smaller than the standard deviation of 0.92 °C of the annually averaged TMI SST, thus confirming the quality of model output.

The climatological sea surface salinity (SSS) results are also shown in Fig. 2 (lower panel). The comparison of model SSS is made against the NIO Climatological Atlas (NIOA) (Chatterjee et al., 2012). The model realistically simulates high surface salinity values in the AS and low values in the BoB. The spatial correlation coefficient between the temporally averaged model SSS and the corresponding NIOA SSS is 0.95, with a significance level of 99.9%. The model shows small SSS bias with respect to NIOA in nearly all the regions except in the northern BoB. The RMSE between the annually averaged model and NIOA SSS is 0.36 which is much smaller than the standard deviation of 1.28 of the annually averaged NIOA SSS.

To make an assessment of the model's ability in capturing the spatio-temporal variability of the SST and SSS in the region of study, we compute their monthly and daily standard deviation from the model's data during 1 January 1998 to 31 December 2014 (Figs 3a and b, respectively). The corresponding monthly

Table 2. Dataset used in the model

| Type	Data
Bathymetry	Smith and Sandwell (1997)
Initial condition	temperature and salinity from World Ocean Atlas 2013 (WOA13)
External forcing	6-hourly varying NCEP/NCAR reanalysis (Kalnay et al., 1996) air temperature, relative humidity, downward long-wave and short-wave radiation, precipitation, runoff, zonal and meridional wind data
Relaxation	SSS from the Ocean Reanalysis System 4 (ORAS4) (Balmaseda et al., 2013)
Open boundary Conditions	temperature, salinity, zonal and meridional velocity from the Ocean Reanalysis System 4 (ORAS4) (Balmaseda et al., 2013)
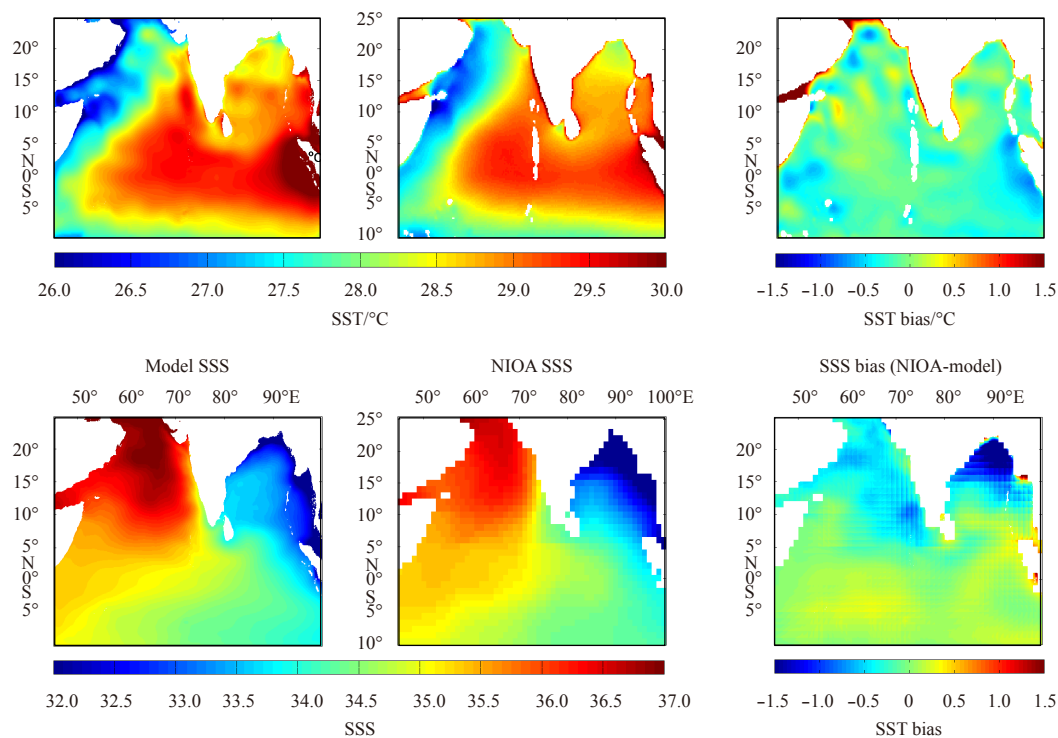
Fig. 2. Comparison of the climatological SST between model and TMI dataset during 1998–2014 (left upper panel); SST bias between Model and TMI SST (right upper panel); comparison of the climatological SSS between Model and NIOA dataset during 1998–2014 (left lower panel); and SSS bias between Model and NIOA SSS (right lower panel).

SST and SSS standard deviation values from the TMI and NIOA are shown in Fig. 3a, whereas, daily SST and SSS standard deviation values from the TMI and Aquarius (https://podaac.jpl.nasa.gov/aquarius; weekly values interpolated to daily values during 2012–2014) are shown in Fig. 3b. It is clear from the figures that barring a few places, the model is able to distinguish the region of high and low SST and SSS monthly and daily variability over the northern Indian Ocean domain covering the AS and BoB. Further, the daily variability of SST and SSS is always higher as compared to its monthly variability. The SST of the northern part of the domain is more variable as compared to the southern part. We also see from the figure that except western part of the model domain, the SST variability in general monotonically decreases from north to south. The northern BoB and AS show higher SST variablity compared to the southern portion. The SSS variability on the other hand, is higher in the southern AS as compared to northern AS. In the BoB, however, the northern region shows higher SSS variability. Nevertheless, except northern BoB and southern AS, all the other regions of the model domain exhibit very low SSS variability.

The surface and sub-surface variables in the AS and BoB ex-

hibit significantly interesting changes at a seasonal scale (Rao and Sivakumar, 2003; de Boyer Montégut et al., 2007; Schott et al., 2009). Thus, the correct simulation of the seasonal variability of SST and SSS is very important. The cyclogenesis, and near-surface mixing properties in the AS and BoB are largely understood in terms of the seasonal variability of surface temperature and salinity (Neetu et al., 2012). We show in Fig. 4 the seasonal variability of the SST and compare it with the TMI SST and NIOA SST data. The seasonal averages are obtained for December-January-February, March-April-May, June-July-August, and September-October-November. We observe that the SST seasonal variability is very well capured by the model. The highest SST is obtained during spring months of March-April-May and lowest during the winter months of December-January-February, as expected. The northern BoB exhibits high SST values during June-July-August and September-October-November. This may happen primarily due to moderately high shortwave radiation compounded with shallow mixed layer depth as a result of increased freshwater flux and precipitation (see Section 3.2 below). Moreover, the creation of a barrier layer in the Bay of Bengal blocks heat transfer from surface to deep ocean. We also find that western and south-west-
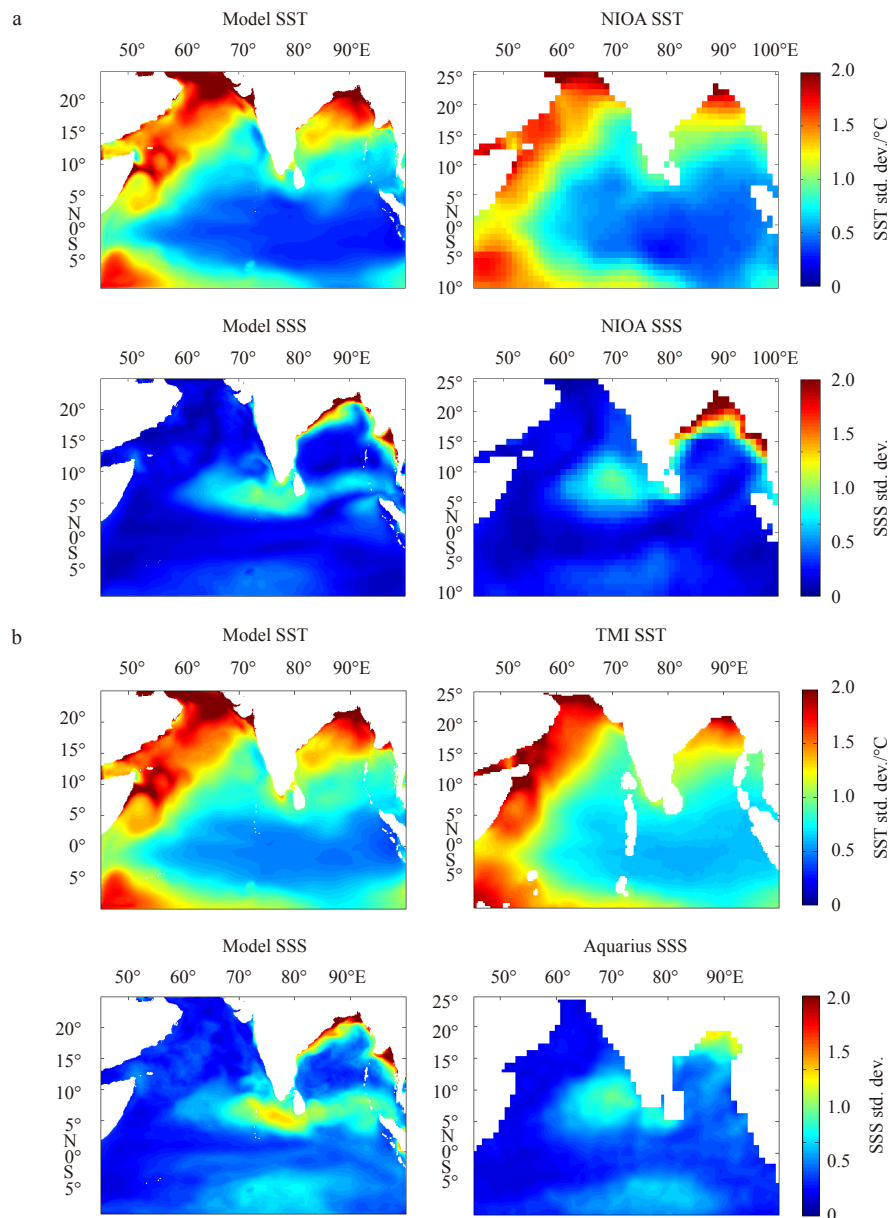
Fig. 3. Standard deviation (std. dev.) of the monthly SST from model and TMI (a, upper panel); standard deviation of the monthly SSS from model and NIOA (a, lower panel); standard deviation of the daily SST from model and TMI (b, upper panel); standard deviation of the daily SSS from model and Aquarius (b, lower panel).

ern part of the domain shows particularly low SST values during June-July-August months.

The seasonal variability of the SSS is shown in Fig. 5. It is clearly evident from the figure that the model very well simulates the SSS seasonal variability. We notice that the AS has higher SSS than BoB in general. The northern BoB has particularly low SSS values during June-July-August (monsoon) and September-October-November (post-monsoon season) as a result of increased freshwater transport from major adjoining rivers (Ganga, Brahmaputra and Irrawaddy) (Sengupta et al., 2006). The southern BoB has higher SSS than northern BoB in all the seasons. We see, however, an exactly opposite nature in the AS. In the southern AS, we find lowest SSS during December-January-February which may be due to coastal runoff, and also due to movement of less saline BoB water towards AS and its mixing with the saltier

AS water.

To guage the quality of the model output in simulating the temporal evolution of the SST and SSS, we make an index of these variables in the upper and lower BoB and AS region. The monthly SST and SSS values during 1998–2014 (17 a) are area averaged over the region (7°–11°N, 67°–72°E) in the southern AS (SAS), (16°–20°N, 67°–72°E) in the northern AS (NAS), (87°–92°E, 7°–11°N) in the southern BoB (SBoB), and (16°–20°N, 87°–92°E) in the northern BoB (NBoB). We show in Fig. 6a, the time series of the SST indices for the model as well as TMI. The model and TMI SST time series are highly correlated at values 0.93 and 0.90 in the SAS and NAS, respectively. Similarly, the correlation of 0.94 and 0.96 exists between the model and TMI SST time series in the SBoB and NBoB, respectively. These correlations are significant at 99.9% level. The RMSE between the model and TMI SST time
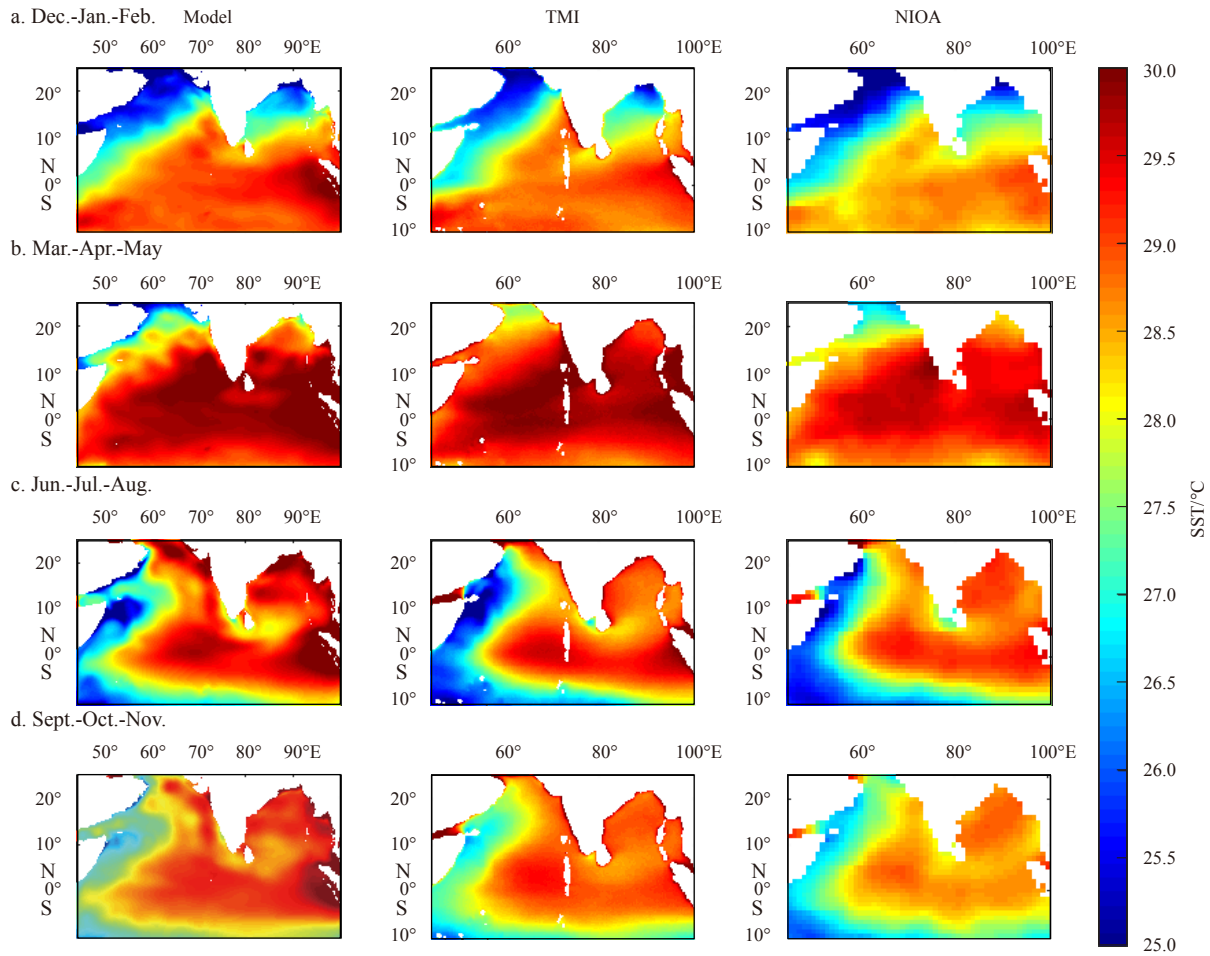
Fig. 4. Seasonal SST map from the model output for December-January-February, March-April-May, June-July-August, and September-October-November during 1998–2014 (first column, top to bottom); seasonal SST map from the corresponding TMI dataset (second column, top to bottom); and seasonal SST map from the corresponding NIOA dataset (third column, top to bottom).

series is 0.33°C (0.55°C) and 0.31°C (0.47°C) in the SAS (NAS) and SBoB (NBoB), respectively. These values are much smaller than the standard deviation of 0.82°C (1.21°C) and 0.87°C (1.51°C) of the TMI SST time series over these regions. The SST time series shows near-periodic (12 months) interannual fluctuations but the trend is nearby absent in all the selected regions over this time period. It is interesting to note that the SST variations in the NAS and NBoB are almost identical to each other, though magnitude is little higher in the BoB. We notice that the range of SST variability is higher in the northern domain (i.e., NAS and NBoB) as compared to southern domain. In the northern domain, the SST peaks during the month of May with a smaller peak occuring in the month of October also. Similarly, the minimum SST is obtained during January–February with another minima occuring during August. In the SAS and SBoB, the SST values are highest during May and lowest during January–February. In the bottom panel of Fig. 6a, we show the SST bias map between the model and TMI values. It may be seen from the figure that the biases are of the same order in all the regions. Morever, barring few exceptions, the biases are generally low. In the years of 2013 and 2014, the March–April SST bias in the NBoB and SBoB, respectively are relatively higher and the model is found to underestimate the SST values. On the other hand, the model overestimates August

SST values of 2007 and 2009 in the SAS and NAS regions, respectively.

The monthly time series of the SSS indices in the SAS, NAS, SBoB and NBoB is shown in Fig. 6b for the model and ORAS4 data. The model and ORAS4 monthly SSS time series are significantly correlated with each other in all the regions (Table 3). The RMSE between the two time series is also smaller than the corresponding standard deviations (Table 3). It is seen from the figure that the SSS of the AS is much higher than BoB. The SSS in the SAS remains high with lowest values (~35) observed during March–April. The NAS, on the other hand shows very high SSS values (>36) throughout the year with very small monthly variations. The SBoB SSS values also show small monthly fluctuations around 33. The SSS in the NBoB, however, shows highest monthly variability and ranges between 30 and 34. The lowest SSS values in the NBoB are obtained during the month of October. The model-data bias between the monthly SSS time series of model and ORAS4 is shown in the bottom panel of Fig. 6b. It may be seen from the figure that the SSS bias is very small in all the regions, except in the NBoB. In other words, the model underperforms in the NBoB region, whereas, it performs very well in all other regions in terms of monthly SSS simulation. This may be due to incorrect vertical parametrization and boundary condi-
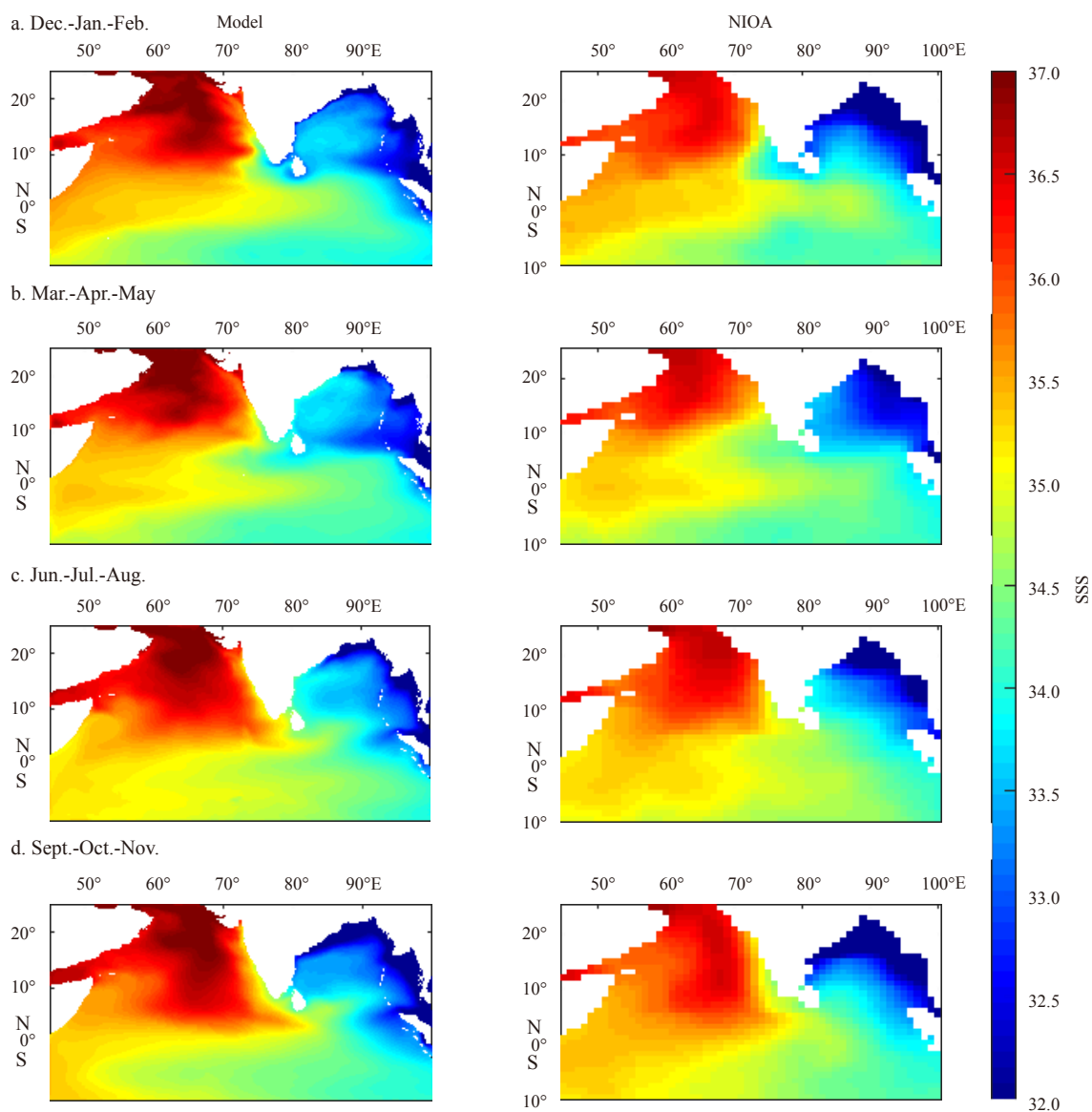
Fig. 5. Seasonal SSS map from the model output for December-January-February, March-April-May, June-July-August, and September-October-November during 1998–2014 (first column, top to bottom); and seasonal SSS map from the corresponding NIOA dataset (second column, top to bottom).

tions in the NBoB. The underperformance of the model's SST and SSS during monsoon (and to some extent post-monsoon) season may also be due to use of very coarse river runoff and precipitation data from the NCEP during these seasons.

It has been argued in recent researches that understanding the intraseaonal variability of the ocean surface variables (more importantly SST) and how it interacts with the atmospheric intraseasonal oscillations is critical for the correct prediction of Indian monsoon rainfall (Schiller and Godfrey, 2003; Li et al., 2015 and references therein; Keerthi et al., 2016). Thus, it will be worthwhile to also study the intraseasonal variability of the SST and SSS over the model domain. For this purpose, we extract the 20–60 d intraseasonal mode from the daily data of model SST area averaged over the NAS, SAS, NBoB and SBoB regions for each season (Fig. 7). The corresponding intraseasonal modes from the TMI observations are also extracted to quantify the model's performance at intraseaonal scale. Table 4 summarizes

the correlation and RMSE between the intraseasonal modes of observation and model. The mean and standard deviation of intraseasonal TMI values are also given in Table 4. The model's ability in simulating the SST variability at intraseasonal scale is clearly evident from Fig. 7 and Table 4. It is clear from the Table that correlation between the model and observation is significantly high and RMSE between the model and observation is less than the standard deviation of observation in all the regions and for the intraseaonal modes of all the seasons. This confirms the realistic simulation of model simulated intreaseaonal modes. Table 4 also shows that the intraseasonal SST of the southern part of AS and BoB (i.e., SAS and SBoB) is in general cooler and more variable as compared to the respective northern parts (i.e., NAS and NBoB). The highest intraseasonal SST variability is seen in the spring season of March-April-May in the SAS (0.64°C) and SBoB (0.61°C). On the other hand, the lowest intraseasonal SST variability is obtained in winter months of December-January-
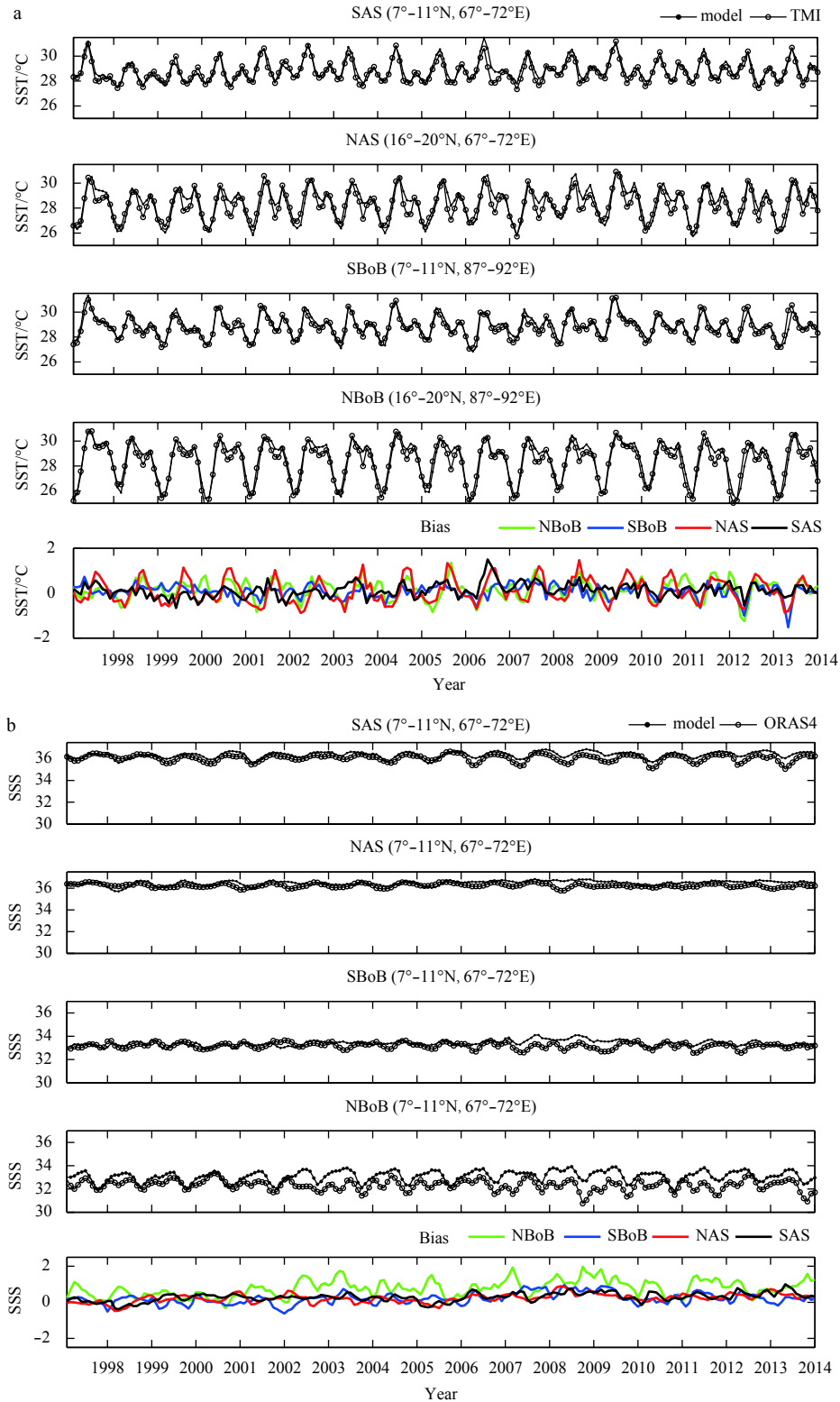
Fig. 6. Quality of model's SST and SSS in northern and southern part of AS and BoB. a. Monthly time series of the SST from model and TMI dataset during 1998–2014. The SST from the model and TMI is shown by dot and circle, respectively. The model-observation bias is shown in fifth row. b. Monthly time series of the SSS from model and ORAS4 dataset during 1998–2014. The SSS from the model and ORAS4 is shown by dot and circle, respectively. The model-observation bias is shown in fifth row.

February in the NAS (0.30°C) and NBoB (0.28°C) regions. The intraseasonal variability of the SSS over the model domain is not given since the continuous daily SSS observations for the period

of simulation are not available.

To demonstrate the quality of model simulation in representing the sub-surface characteristics of temperature and salinity,

Table 3. SST and SSS monthly variability over the NAS, SAS, NBoB and SBoB regions of model domain

Variable	Regions											
	NAS			SAS			NBoB			SBoB		
	RMSE	$\mu \pm \sigma$	r	RMSE	$\mu \pm \sigma$	r	RMSE	$\mu \pm \sigma$	r	RMSE	$\mu \pm \sigma$	r
SST	0.55	28.3 ± 1.21	0.90	0.33	28.7 ± 0.82	0.93	0.47	28.3 ± 1.51	0.96	0.31	28.8 ± 0.87	0.94
SSS	0.12	36.25 ± 0.18	0.64	0.24	36.0 ± 0.33	0.81	0.39	32.3 ± 0.46	0.72	0.17	33.19 ± 0.25	0.60

Note: RMSE is the root mean square error between model and observation, μ and σ are mean and standard deviation of observation, respectively, and r represents correlation coefficient between model and observation.
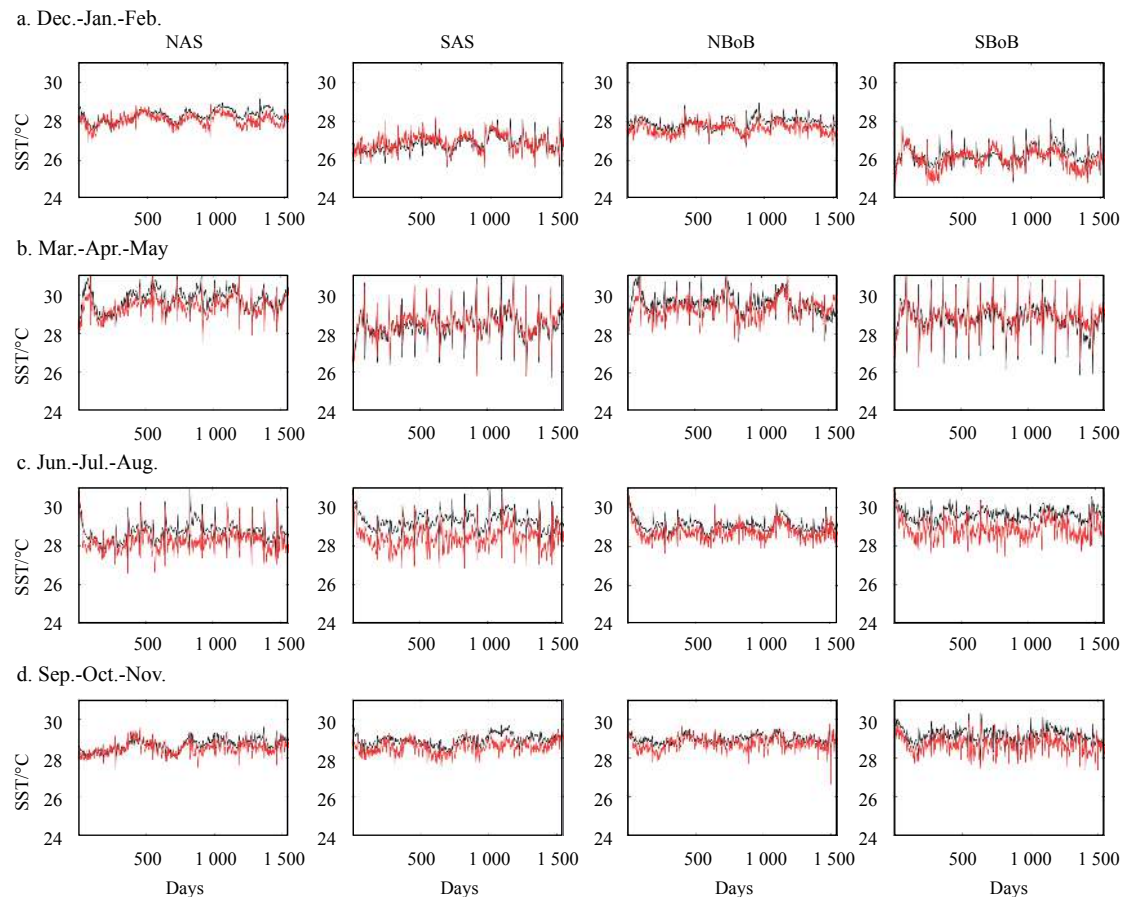
Fig. 7. 20–60 d intraseasonal SST time series from model (black) and TMI dataset (red) during 1998–2014 area averaged over the NAS, SAS, NBoB and SBoB regions.

Table 4. The 20–60 d intraseasonal SST variability over the NAS, SAS, NBoB and SBoB regions of model domain

Seasons	Regions											
	NAS			SAS			NBoB			SBoB		
	RMSE	$\mu \pm \sigma$	r	RMSE	$\mu \pm \sigma$	r	RMSE	$\mu \pm \sigma$	r	RMSE	$\mu \pm \sigma$	r
Dec.-Jan.-Feb.	0.22	28.0 ± 0.30	0.78	0.28	26.9 ± 0.40	0.78	0.24	27.6 ± 0.28	0.66	0.29	26.0 ± 0.47	0.74
Mar.-Apr.-May	0.38	29.4 ± 0.48	0.82	0.31	28.5 ± 0.64	0.91	0.36	29.3 ± 0.49	0.72	0.36	28.8 ± 0.61	0.88
Jun.-Jul.-Aug.	0.46	28.2 ± 0.51	0.81	0.50	28.4 ± 0.56	0.86	0.30	28.7 ± 0.38	0.83	0.40	28.9 ± 0.48	0.82
Sep.-Oct.-Nov.	0.18	28.5 ± 0.32	0.71	0.26	28.6 ± 0.32	0.64	0.23	28.7 ± 0.32	0.68	0.35	28.7 ± 0.41	0.73

Note: RMSE is the root mean square error between model and TMI observation, μ and σ are mean and standard deviation of observation, respectively and r represents correlation coefficient between model and TMI observation.

we show in Fig. 8, the latitude-depth maps of temperature and salinity at 70°E in the AS and 90°E in the BoB. The model capu-tures the layered structured of the upper ocean with correct mag-nitude very well. One of the possible regions for the small discre-

pencies, if any, in the mixed layer depth and thermocline ob-served between model and NIOA may be their different horizon-al and vertical resolutions. The sub-surface temperature and sa-linity structures are very different in the AS and BoB. The latit-
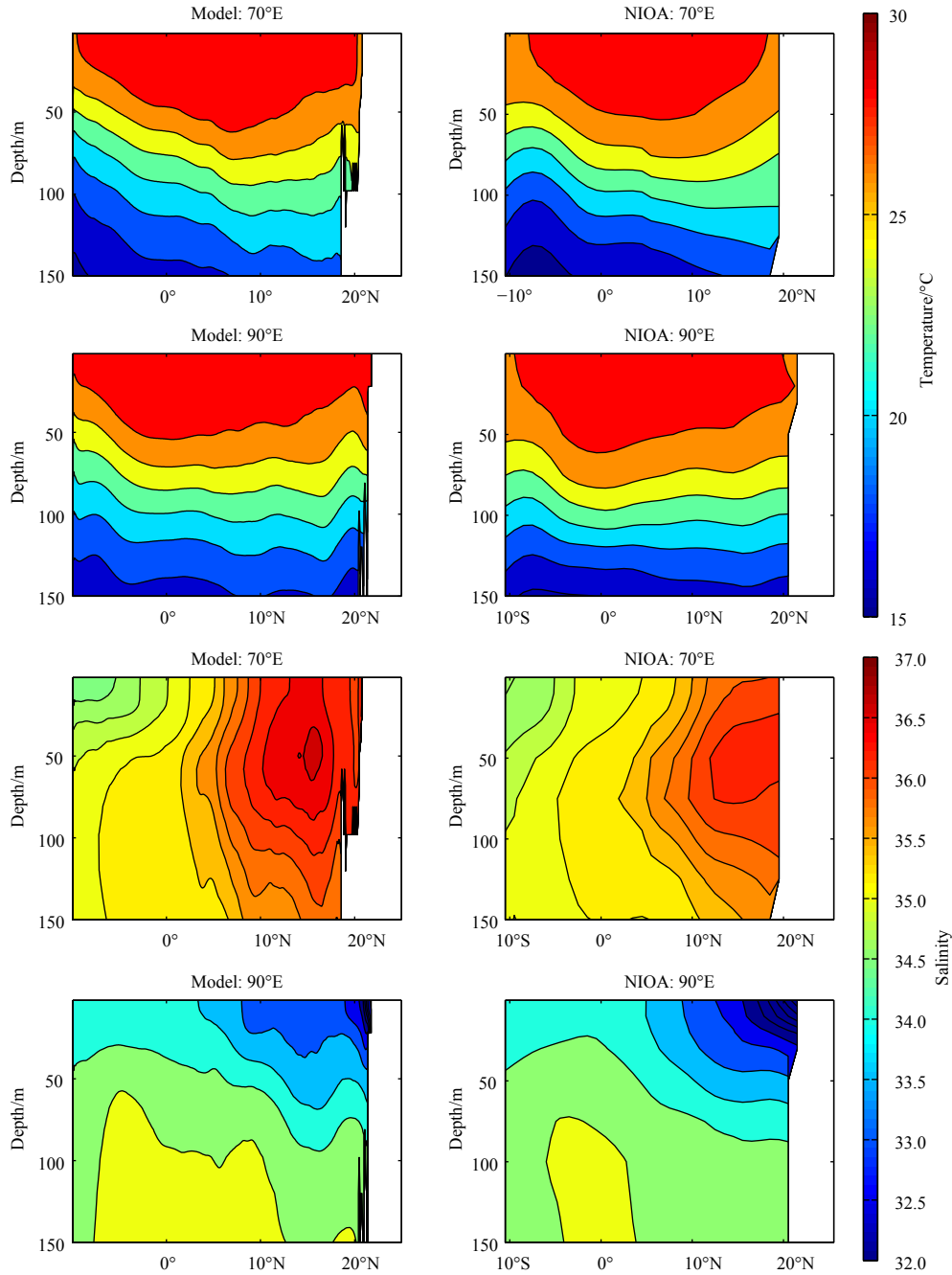
Fig. 8. Latitude-depth map of temperature and salinity. The model temperature and salinity values shown in the first column are compared with the corresponding NIOA values shown in the second column.

ude-depth map of the temperature shows that the thermocline in the AS has a tilted structure with values increasing from south to north. The BoB, however, shows no such nature and thermocline is nearly flat. The salinity diagram shows that the values are nearly opposite in the AS and BoB at higher latitudes. For example, in the region 15°–22°N, where the highest salinity values are observed in the AS, the BoB region shows the lowest salinity. The low salinity of the BoB in this region is mainly attributed to freshening of water as a result of river runoff from major adjoining rivers of the region. On the other hand, higher evaporation than precipitation in the northern AS is the principal reason of high salinity in that region. The presence of salty outflow from the Red Sea and Persian Gulf is also the reason for high salinity of

the region.

3.2 *Mixed layer depth*

The estimation of mixed layer depth (MLD) is very important for oceanic investigations including upper ocean productivity, air-sea exchange processes, and long-term climate change (Thomson and Fine, 2003, Keerthi et al., 2013). We compute the MLD of the model domain using Lorbacher et al. (2006) criterion, which is based on the shallowest extreme curvature of near surface density profiles. We show in Fig. 9 (upper panel) the spatial maps of the seasonal variation of the MLD over our region of study. The corresponding MLD maps from ARGO (Holte et al., 2016) are also shown in Fig. 9 (lower panel) for comparison.
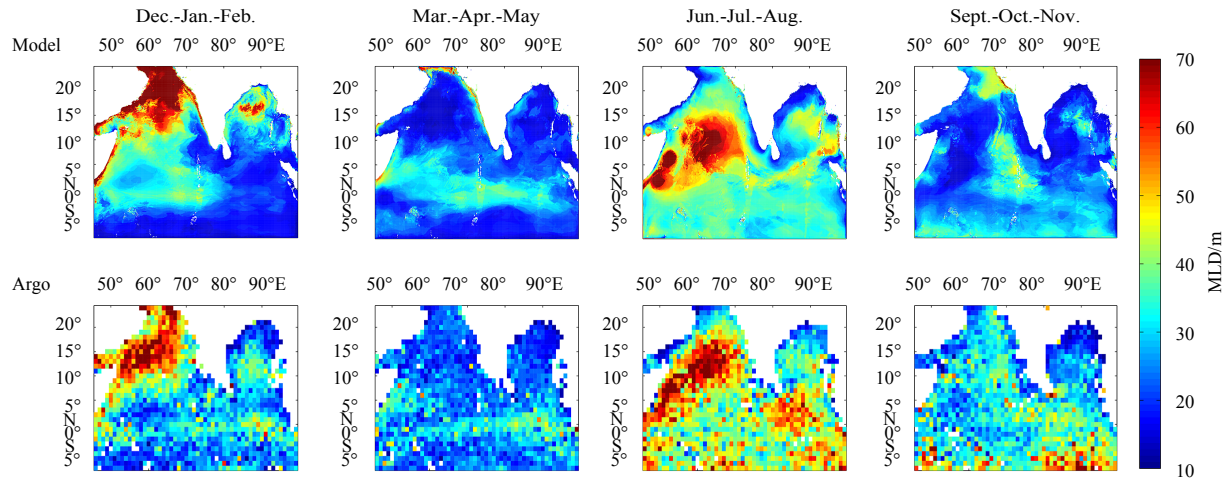
Fig. 9. Seasonal mixed layer depth (MLD) variability from model (upper panel); and from Argo (lower panel).

Holte et al. (2016) computed MLD using more than 1 250 000 Argo profiles (collected between January 2000 and May 2016) and a hybrid algorithm (Holte and Talley, 2009).

Figure 9 clearly demonstrates the model's ability in correct estimation of the MLD seasonal variations (both spatially as well as temporally). The model MLD values are close to the ARGO MLD estimates in all the seasons. Moreover, our results also suggest that the MLD is deeper in the AS as compared to the BoB (de Boyer Montégut et al., 2007, Keerthi et al., 2013). The MLD remains low in the upper northern BoB in all the seasons. The lowest MLD values are observed in the months of March-April-May and highest during December-January-February. The mean MLD in the AS region during December-January-February, March-April-May, June-July-August and September-October-November is 50, 22, 44, 27 m, respectively. On the other hand, the mean MLD in the BoB region during the same season is 31, 18, 32, 23 m, respectively. Thus, the mean MLD of the AS remains higher as compared to the BoB during all the seasons. The mean MLD during March-April-May is very shallow in the AS as well as BoB. We, however, observe intermediate MLD values during monsoon season of June-July-August. Interestingly, in the post-monsoon months of September-October-November, the mean MLD of the AS and BoB remain very close to each other. The maximum MLD is obtained during winter (December-January-February) with AS and BoB having MLD values of 150 m and 67 m, respectively. The minimum MLD in the AS and BoB (nearly 11–12 m) is, however, obtained during the spring (March-April-May). It is also interesting to note that the AS and BoB MLD during December-January-February and June-July-August exhibits dipole like structure with opposite signs during these seasons. For example, during the December-January-February, the northern and central AS and BoB show high MLD whereas southern part of domain shows low MLD values. Contrary to this, we observe higher values of MLD in southern domain as compared to northern and central AS and BoB during June-July-August.

Figure 9 shows that the season-to-season variability of the MLD is quite significant. In general, the air-sea fluxes are considered as drivers of the MLD variability. It is, therefore, important to illustrate and understand the seasonal MLD variability vis-à-vis seasonal changes in the air-sea fluxes. For this purpose, we show in Fig. 10a the seasonal map of air-sea fluxes, namely, wind stress, net heat flux, and net freshwater flux (buoyancy flux). It is clear from the 1st column of Fig. 10a that the negative buoyancy

flux brought by the excess of evaporation over precipitation largely explains the relatively deep MLDs in December-January-February season (de Boyer Montégut et al., 2007) seen in Fig. 9 (the 1st column). In addition to this, low shortwave radiation flux and high negative latent heat flux and sensible heat flux (Fig. 10b, the 1st column) (resulting in negative net heat flux) is also responsible for deep MLDs during December-January-February. Whereas, the main reason behind very low MLD values in the AS and BoB during March-April-May are very weak easterlies (weak wind stress, the 2nd column of Fig. 10a) over the region of interest. Very high shortwave radiation flux (Fig. 10b, the 2nd column) (resulting in positive net heat flux) also contributes to MLD shallowing during March-April-May. During the monsoon (June-July-August) season (Fig. 10a, the 3rd column), high wind stress and low shortwave radiation as well as high negative latent heat flux (Fig. 10b, the 3rd column) (resulting in negative net heat flux) are responsible for high MLD values in the southern AS. On the other hand, due to high freshwater flux (precipitation-evaporation) in the northern BoB, the MLD remain shallower. In the post-monsoon months of September-October-November, the MLDs, along coastal and adjoining areas in the BoB have low (to very low) values, whereas other regions of the domain also have low to intermediate values. This happens as a result of low wind stress in the region of interest (Fig. 10a, the 4th column) and increased freshwater flux (runoff from rivers) in the BoB. The net heat flux in most parts of the AS and BoB remains very small due to cancelling effect of its component fluxes (Fig. 10b; the 4th column).

3.3 *Mixed layer heat budget*

In order to understand the seasonal variability of the mixed layer temperature in general, and SST in particular, the estimation of mixed layer heat budget is important. Even though it is largely believed that the major contribution in the SST variability comes from seasonally varying air-sea fluxes, however, the horizontal and vertical temperature advections also play a major role at some locations. It will be, therefore, useful to explicitly compute all possible contributions to the mixed layer heat budget. This will help us understand and quantify importance of each individual term in the spatio-temporal variability of SST.

Following Stevenson and Niiler (1983), Moisan and Niiler (1998), and Huang et al. (2010), we compute the mixed layer heat
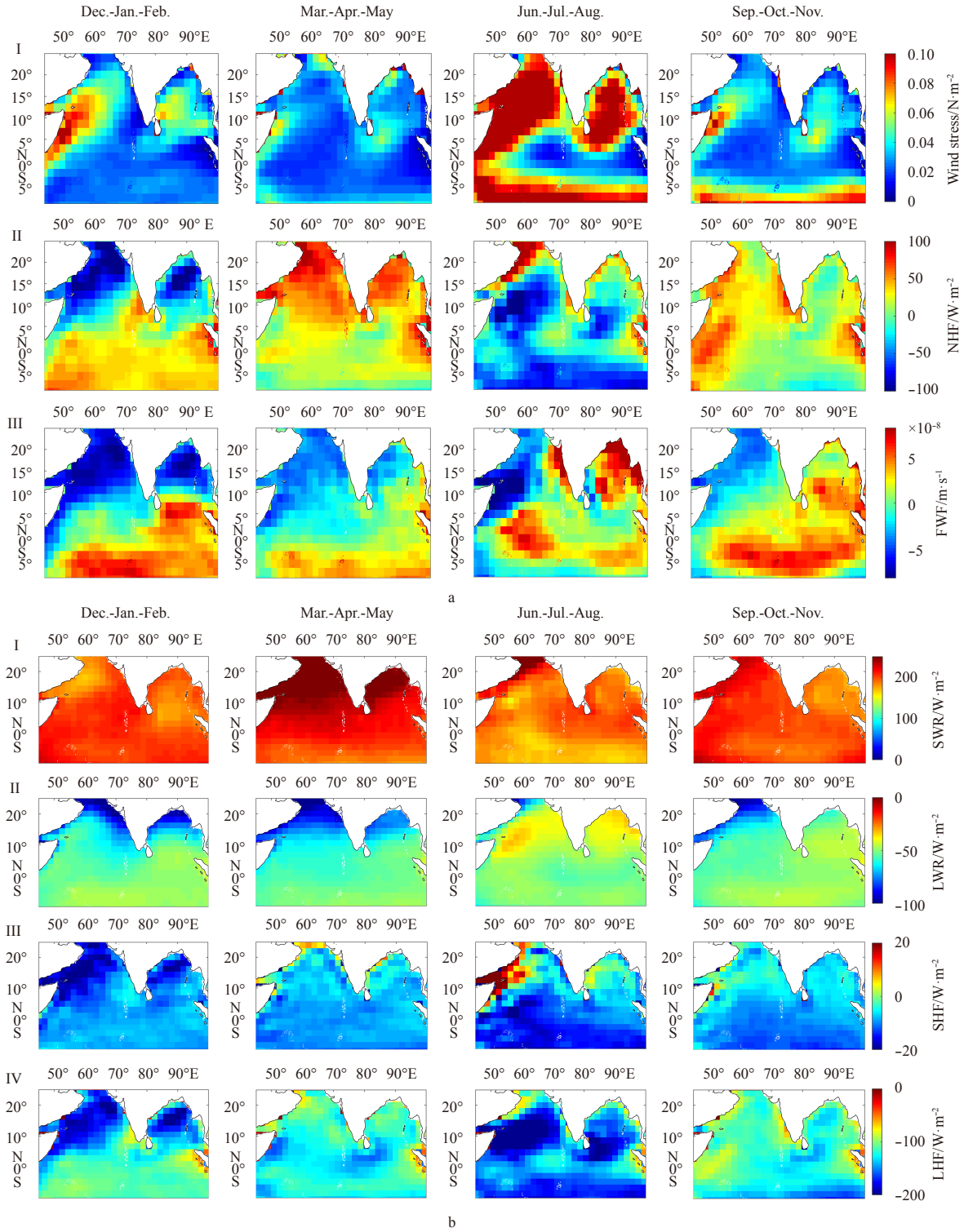
Fig. 10. Seasonal map of wind stress, net heat flux (NHF) and net freshwater flux (FWF) (a); and seasonal map of shortwave radiation flux (SWR), downward longwave radiation flux (LWR), sensible heat flux (SHF) and latent heat flux (LHF) (b).

budget as

$$T_t = F, \tag{1}$$

where $T_t \left(= \dfrac{\partial T}{\partial t} \right)$ is the mixed layer temperature tendency and F is the forcing. The forcing is sum of zonal advection (Q_u), meridi-

onal advection (Q_v), vertical entrainment (Q_w), net surface heat flux (Q_q), and vertical diffusion (Q_{zz}). In other words, F is expressed as

$$F = Q_u + Q_v + Q_w + Q_q + Q_{zz}. \tag{2}$$

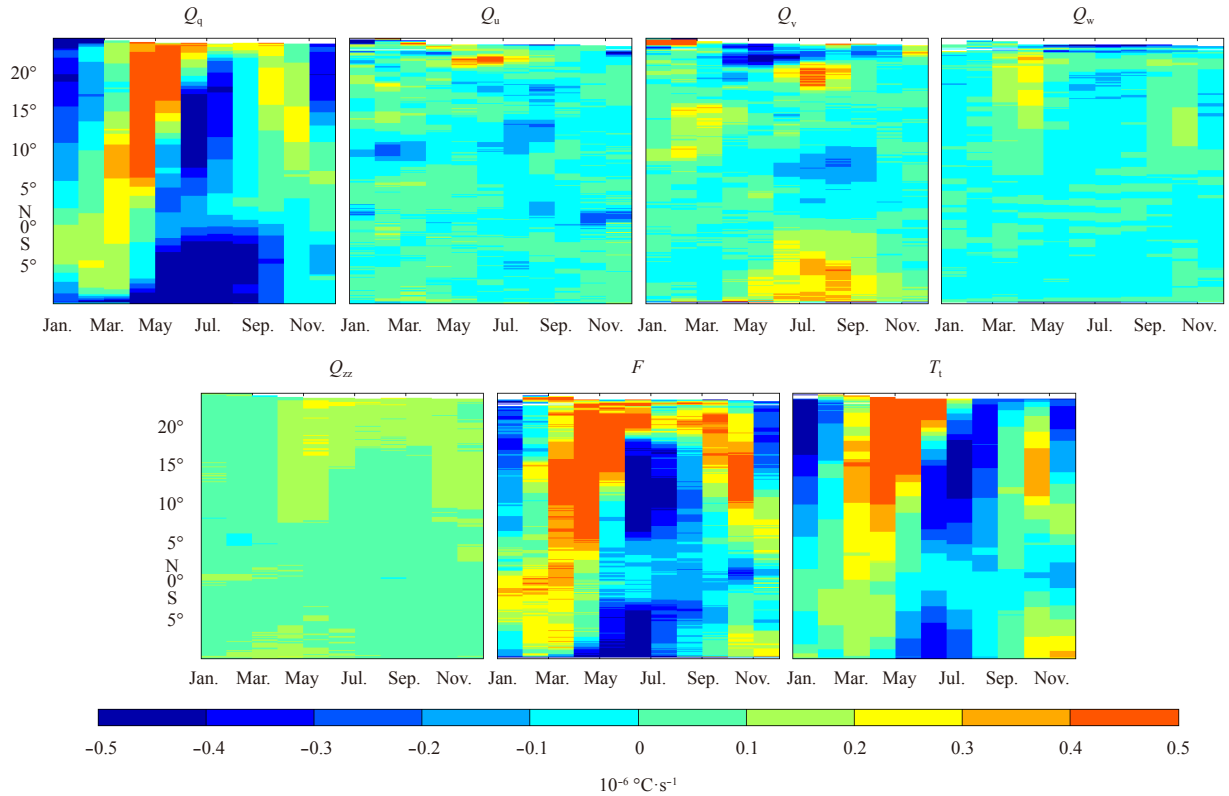The consistency between T_t and F is used to check the clos-

Fig. 11. Time-latitude map of mixed layer heat budget at 67°E.

ure of the temperature equation. For further computational details on each of these terms please refer to Appendix A of Huang et al. (2010).

The time-latitude map of different terms of mixed layer heat budget at 67°E is shown in Fig. 11. We see from figure that even though T_t and F are very close to each other (thus giving good closure of temperature tendency), however, they are not exactly the same. The difference between them may be due to missing contributions from (weak horizontal) diffusion term. The differences could also be due to numerical errors. It is clear from the figure that out of all forcing terms, Q_q is most dominant term. The contribution from zonal advection Q_u is generally insignificant except few places. The meridional advection Q_v on the other hand helps in increasing the mixed layer heat budget (and SST) of southern part of domain (south of 5°S) during July to September. The Q_v reduces mixed layer heat budget between 5° and 10°N during June to October and north of 21°N during April to November. The vertical entrainment Q_w remains very low in the AS except during April. The diffusion term Q_{zz} although remains low, but helps in increasing the mixed layer heat budget north of 15°N during April to November. The contributions from Q_q (and therefore forcing F) suggest that in the Arabian Sea at 67°E (north of 5°N), we get low SST in December–February, high SST in March–May, low SST again in June–August, and intermediate SST values in September–November months. This is consistent with the SST variability (at 67°E) shown in Fig. 4. The F and Q_q values of Fig. 11 also suggest that the SST of the southern part of domain remains low during May–September months of the year.

The time-latitude map of mixed layer heat budget at 90°E is shown in Fig. 12. In this case also, we clearly notice that the largest contribution to the mixed layer heat budget is coming from air-sea fluxes Q_q. While the effect of vertical entrainment Q_w

is smaller in this case compared to at 67°E, however, the spatio-temporal contributions from zonal advection Q_u are larger here especially during summer monsoon months (June–September) between 5°–10°N. The meridional advection Q_v plays a similar role in this case as seen at 67°E. In the southern part of domain it tends to increase the SST during May–September. On the other hand, negative Q_v values in northern part of domain (between 0–10°N) during Jun–October helps in maintaining intermediate SST values in these regions during these months. The vertical entrainment and diffusion terms give only small positive contribution (north of 15°N) in F at 90°E. The Q_q (and F) map clearly suggests that at 90°E in the Bay of Bengal (north of 5°N), the SST tendency should remain low during December–January and high during March–April. The SST tendency also remains low at 90°E between 5°–12°N and south of 5°S during May–September. These observations are also consistent with the SST variability shown in Fig. 4 thus demonstrating the robustness of mixed layer heat budget calculations.

For correctly capturing the mechanisms responsible for mixed layer temperature (or SST) variability using mixed layer heat budget analysis, it is important to see if a reasonable closure of heat budget exists using the model output. To demonstrate the closure, we show the seasonal variability of forcing F and mixed layer temperature tendency T_t in Fig. 13. The bias map (bottom panel of Fig. 13) suggests that the mixed layer temperature budgets have a good closure, indicating that the results regarding the mechanisms controlling the mixed layer temperature (or SST) evolution are quite robust. The differences between them point towards the role of missing term of horizontal diffusion processes and numerical errors in our calculations. Nevertheless, the variation of seasonal variability of F and T_t is largely coherent with the seasonal evolution of SST seen in Fig. 4.
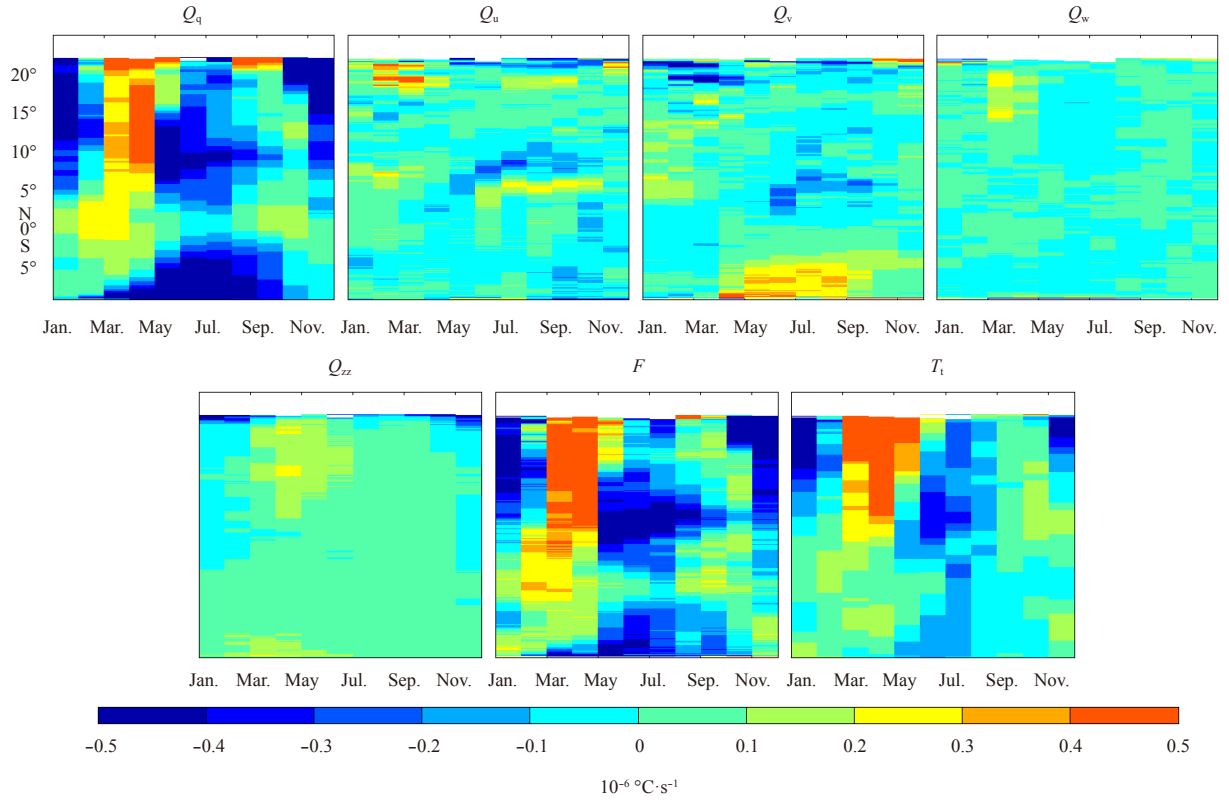
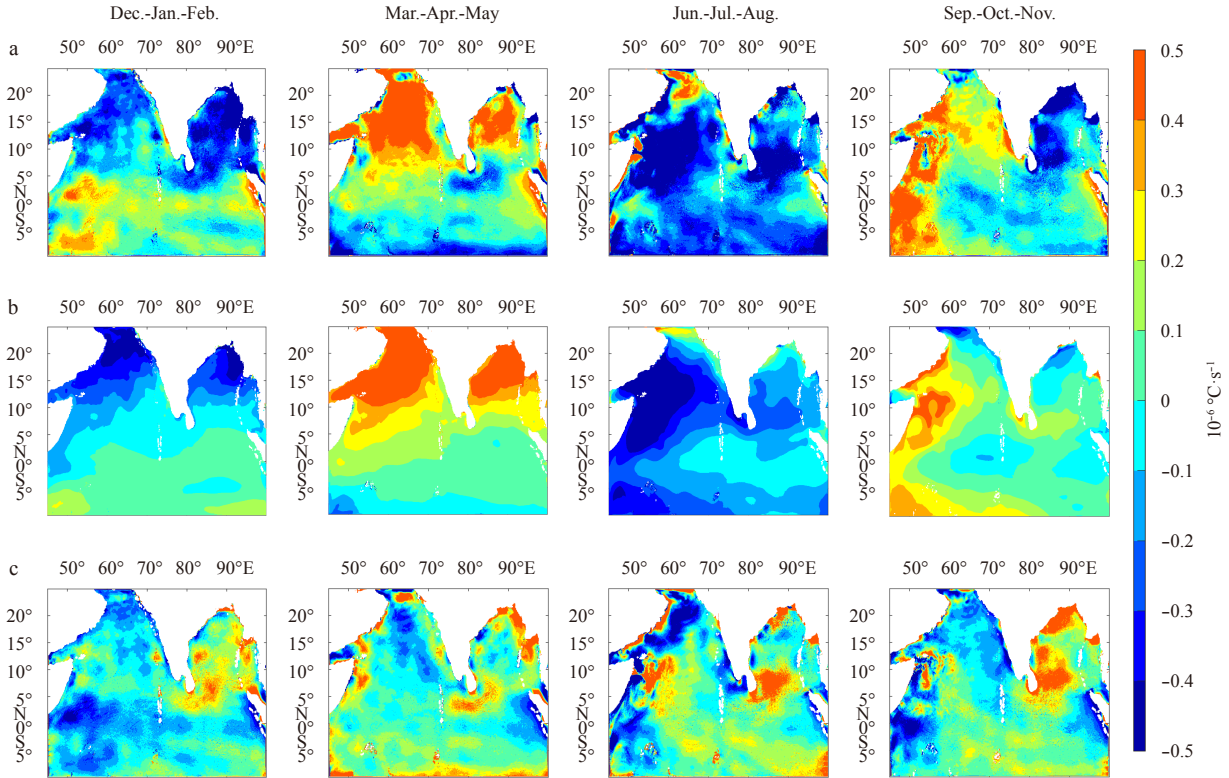**Fig. 12.** Time-latitude map of mixed layer heat budget at 90°E.

Fig. 13. Seasonal variability of forcing F (a); mixed layer temperature tendency T_t (b). c shows the bias map between F and T_t.

The monthly mixed layer heat budget area-averaged over the SAS, NAS, SBoB and NBoB region is shown in Fig. 14. In the SAS region, the highest positive (negative) heat budget is obtained during April (June). We notice that F and T_t values are close to each other. Apart from Q_q, the contribution from all other terms is small. In the NAS region, the highest positive (negative) heat
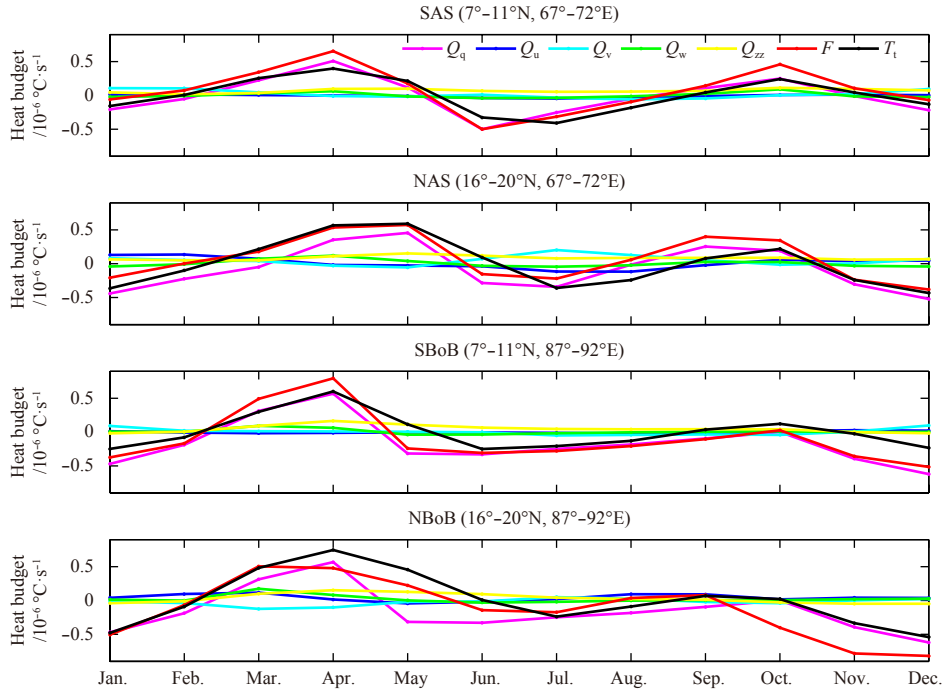
Fig. 14. Monthly mixed layer heat budget averaged over the SAS, NAS, SBoB and NBoB regions.

budget is obtained during May (July). We notice that F and T_t values are close to each other except during June–September. In addition to Q_q, the contribution from vertical advection Q_v and diffusion Q_{zz} also becomes important in these months. These terms try to increase the mixed layer heat so that good closure between F and T_t may be obtained. In the SBoB, the highest positive (negative) heat budget is obtained during April (December–January). We see a good closure between F and T_t except during May and November–December. The maximum (minimum) contribution to the mixed layer heat budget comes from air-sea fluxes (horizontal entrainment). In the NBoB, the highest positive (negative) heat budget is obtained during April (November–December). The F and T_t are close to each other in all the months, except during October-December. In the NBoB, we see significant contribution in the mixed layer heat budget coming from Q_v and Q_{zz}, although with opposite signs (especially during February–June) with maximum contribution still coming from Q_q. While the meridional advection reduces the mixed layer heat budget of the region, the vertical diffusion tends to increase it. It is clear from the Figure, that the net air-sea heat flux plays most important role in controlling the mixed layer temperature variability of the northern Indian Ocean.

3.4 *Surface currents and volume transport*

In an effort to demonstrate the quality of model solutions in simulating the surface circulation, we show in Fig. 15 the seasonally varying surface currents of the region during the period of simulation. The model results are compared with the OSCAR surface current (Bonjean and Lagerloef, 2002) data, which is a combination of *in situ* and satellite altimeter derived current products. We find that the model surface currents match very well with OSCAR. We notice from Fig. 15 that during December-January-February (winter monsoon season), the southeasterly currents flow northwards in the southern AS and BoB. In the AS, the flow is dominantly meridional (south-north), whereas upper BoB shows a weak anti-cyclonic behavior. During March-April-May strong anticyclonic motion is observed in the BoB covering

the northern and parts of central bay. The poleward East Indian coastal current (EICC) (Schott and McCreary, 2001) is also seen in the upper bay. The currents, on the other hand, are found to be weak in the AS. In the summer monsoon season of June-July-August, the BoB currents are dominantly (zonal) eastwards, except in the northernmost bay, where we notice a feeble cyclonic circulation. The model perfectly reproduces the direction of the observed currents although with somewhat greater magnitudes (Fig. 15; the 3rd column). In the AS, we notice northwesterly currents (including West Indian coastal current, WICC) flowing southwards which are almost opposite in direction to December-January-February currents. During September-October-November, we observe cyclonic circulation in the northern bay. Both the EICC and WICC flow equatorwards. The zonal summer monsoon current (SMC) flowing from southern AS towards southern BoB during June-July-August and winter monsoon current (WMC) flowing in exactly opposite direction during December-January-February are also well reproduced by the model. The discrepancies in modeled and observed (OSCAR) surface current data seen in the 3rd column of Fig. 15 may be mainly due to their very different horizontal and temporal resolutions. For example, the OSCAR data is available at 1/3-degree horizontal resolution and 5 d of temporal resolution. On the other hand, our model output uses daily data at a horizontal resolution of 0.09 degree.

We also compute zonal and meridional volume transport across different sections (shown in Fig. 1 by vertical and horizontal lines, respectively) in the AS and BoB using Eq. (3) as below:

$$\text{zonal volume transport} = \int_0^{L_y} \int_{-h}^0 u(x, y, z, t)\, \mathrm{d}z\mathrm{d}y, \quad (3\text{a})$$

$$\text{meridional volume transport} = \int_0^{L_x} \int_{-h}^0 v(x, y, z, t)\, \mathrm{d}z\mathrm{d}x, \quad (3\text{b})$$
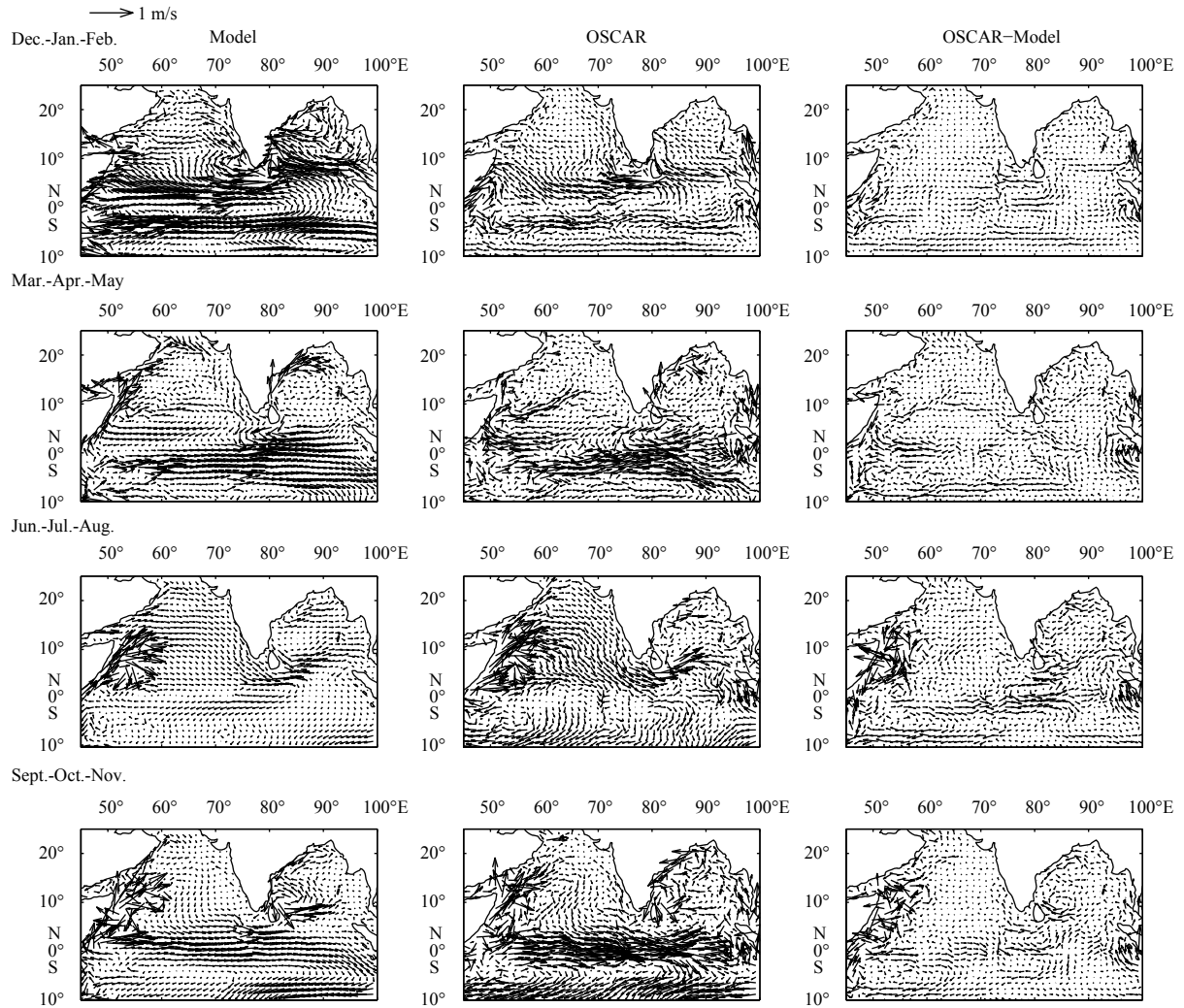
Fig. 15. Seasonal variability of surface currents during 1998–2014 from model data, OSCAR observations and difference between OSCAR and model data.

where h is the ocean depth at position (x, y), u is the zonal velocity, v is the meridional velocity, Ly and Lx are the widths of the meridional and zonal transects, respectively. The meridional volume transport for the upper 100 m is computed along the section (12°N, 71°–75°E) in the Arabian sea and (12°N, 80°–84°E) in the Bay of Bengal. The zonal transport for the upper 100 m is computed along the section (4°–7°N, 76°E) at the interface of AS and BoB. These sections are so chosen that by studying the transport of water mass across them (which includes surface as well as intermediate and deep ocean), we can infer the variability of the monsoonal currents, namely, WICC in AS, EICC in the BoB, and SMC (WMC) at the interface of AS and BoB on seasonal and interannual time scales. Moreover, this will also help us quantify seasonal transport of water mass from the BoB to AS and vice versa during summer and winter monsoon seasons. In Fig. 16, we show the monthly climatology of the volume transport across these sections and compare the results with the corresponding values from the ECCO state estimates. Figure 16 (upper panel) shows that in the AS section, the peak north to south meridional transport (–2.4×10⁶ m³/s) is found during July (monsoon season), whereas peak south to north transport (+3.7×10⁶ m³/s) is obtained during November-December (post-monsoon season).

However, the annually averaged volume transport across this section is very small ((0.1± 1.06)×10⁶ m³/s). Similarly, in the BoB (Fig. 16, middle panel) the mean meridional transport across the chosen section is nearly zero (–0.02±2.2)×10⁶ m³/s, i.e., almost equal amount of water flows through these section in the north to south and south to north directions. The peak north-to-south meridional volume transport (–2.6×10⁶ m³/s) across the BoB section is seen during February-March, whereas highest south to north transport is obtained during monsoon season of October-November (+2.7×10⁶ m³/s). Thus, the signs of meridional volume transport in the AS and BoB are almost opposite to each other (r = –0.75) during different months of the year. However, the difference between the AS and the BoB meridional volume transport should not be simply looked as opposite in phase, because the transport of EICC has a semiannual component, whereas the WICC has a single peak and trough over a year. The correlation between volume transport time series obtained from the model and ECCO state estimate is 0.81 and 0.85 in the AS and BoB, respectively. Even though these correlations are highly significant, however, phase differences between the model and ECCO values are seen in the BoB during some months. The zonal volume transport across a section at the interface of AS and BoB is shown
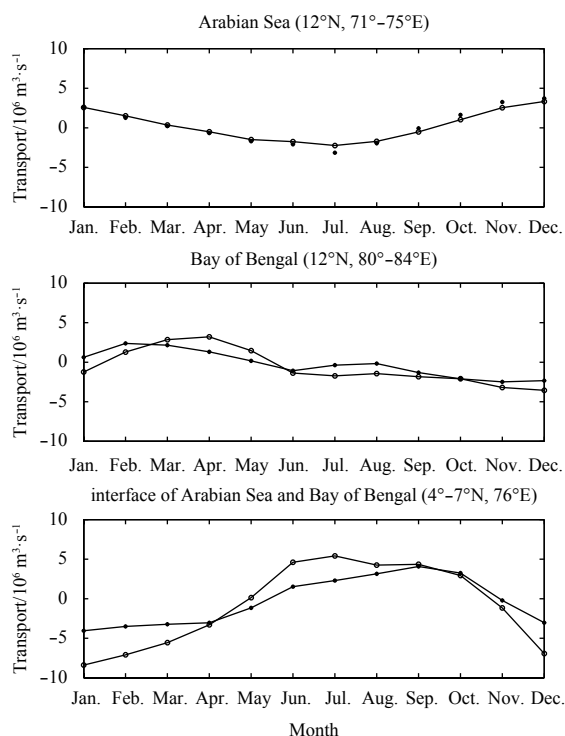
Fig. 16. Seasonal variability of the meridional volume transport computed across the section (12°N, 71°–75°E) in the Arabian Sea (upper panel); meridional volume transport computed across the section (12°N, 80°–84°E) in the Bay of Bengal (middle panel); and zonal volume transport computed across the section (4°–7°N, 76°E) at the interface of Arabian Sea and Bay of Bengal (lower panel). The values from the model and ECCO2 are shown by star and circle, respectively.

in Fig. 16 (lower panel). It is clear from the Figure that the peak east-west transport (-4.1×10^6 m³/s) is obtained during January (winter season), whereas the peak zonal transport ($+4.5 \times 10^6$ m³/s) in opposite direction i.e., west-east direction is observed during August–September (summer monsoon) months. The correlation between model and ECCO derived zonal transport time series is 0.95. The mean zonal flow across this section is from east to west (i.e., from BoB to AS) with transport in the range of ($-0.6 \pm 2.2) \times 10^6$ m³/s.

4 Conclusions

An ocean circulation model, MITgcm is configured to run at a horizontal resolution of 10 km in the northern Indian Ocean around (10°S–25°N, 45°–100°E) covering both the Arabian Sea as well as Bay of Bengal. It is shown that the regional high-resolution ocean circulation model realistically simulates the circulation and hydrography of the Arabian Sea and Bay of Bengal during 1998–2014. For example, the seasonal variability of the surface as well as sub-surface temperature and salinity compares well with the best available observations. The temporal evolution of the SST and SSS is studied in terms area-averaged indices of these variables in the upper and lower BoB and AS regions. The mixed layer depth of the region is computed and its spatio-temporal variability is studied for the period of simulation. The lowest MLD values are observed during spring (March-April-May) months and highest during winter (December-January-February). We use surface air-sea fluxes to explain seasonal mixed lay-

er depth variability. The mixed layer heat budget analysis is carried out to understand factors responsible for the seasonal evolution of mixed layer temperature (SST). The contributions from seasonally varying air-sea fluxes, horizontal temperature advection, vertical entrainment and diffusion are taken into account for this purpose. The results show that surface fluxes play a dominant role on the SST variability. The zonal and meridional volume transport across different sections in the Arabian Sea and Bay of Bengal are also computed and characteristics of monsoonal currents are examined in the light of these. The signs of meridional volume transport in the Arabian Sea and Bay of Bengal are almost opposite to each other. In the present study we are able to demonstrate the quality of our high-resolution hydrography, mixed layer depth, and velocity estimates over the northern Indian Ocean. Our future work will focus on reducing the model-observation misfits using data assimilation.

References

Achuthavarier D, Krishnamurthy V, Kirtman B P, et al. 2012. Role of the Indian Ocean in the ENSO-Indian summer monsoon teleconnection in the NCEP climate forecast system. Journal of Climate, 25(7): 2490–2508, doi: 10.1175/JCLI-D-11-00111.1

Agarwal N, Sharma R, Basu S K, et al. 2007. Evaluation of relative performance of QuikSCAT and NCEP re-analysis winds through simulations by an OGCM. Deep Sea Research Part I: Oceanographic Research Papers, 54(8): 1311–1328, doi: 10.1016/j.dsr.2007.04.006

Akhil V P, Durand F, Lengaigne M, et al. 2014. A modeling study of the processes of surface salinity seasonal cycle in the Bay of Bengal. Journal of Geophysical Research: Oceans, 119(6): 3926–3947, doi: 10.1002/2013JC009632

Ali M M, Nagamani P V, Sharma N, et al. 2015. Relationship between ocean mean temperatures and Indian summer monsoon rainfall. Atmospheric Science Letters, 16(3): 408–413, doi: 10.1002/asl2.576

Annamalai H, Murtugudde R. 2004. Role of the Indian Ocean in regional climate variability. In: Wang C, Xie S P, CartonJ A, eds. Earth's Climate: The Ocean-Atmosphere Interaction. Washington, DC: AGU, 213-246

Annamalai H, Xie S P, McCreary J P, et al. 2005. Impact of Indian Ocean sea surface temperature on developing El Niño. Journal of Climate, 18(2): 302–319, doi: 10.1175/JCLI-3268.1

Balmaseda M A, Mogensen K, Weaver A T. 2013. Evaluation of the ECMWF ocean reanalysis system ORAS4. Quarterly Journal of the Royal Meteorological Society, 139(674): 1132–1161, doi: 10.1002/qj.v139.674

Bates N R, Pequignet A C, Sabine C L. 2006a. Ocean carbon cycling in the Indian Ocean: 1. Spatiotemporal variability of inorganic carbon and air-sea CO_2 gas exchange. Global Biogeochemical Cycles, 20(3): GB3020, doi: 10.1029/2005GB002491

Bates N R, Pequignet A C, Sabine C L. 2006b. Ocean carbon cycling in the Indian Ocean: 2. Estimates of net community production. Global Biogeochemical Cycles, 20(3): GB3021, doi: 10.1029/2005GB002492

Benshila R, Durand F, Masson S, et al. 2014. The upper Bay of Bengal salinity structure in a high-resolution model. Ocean Modelling, 74: 36–52, doi: 10.1016/j.ocemod.2013.12.001

Bonjean F, Lagerloef G S E. 2002. Diagnostic model and analysis of the surface currents in the tropical Pacific Ocean. Journal of Physical Oceanography, 32(10): 2938–2954, doi: 10.1175/1520-0485(2002)032<2938:DMAAOT>2.0.CO;2

Callaghan A H, Ward B, Vialard J. 2014. Influence of surface forcing on near-surface and mixing layer turbulence in the tropical Indian Ocean. Deep Sea Research Part I: Oceanographic Research Papers, 94: 107–123, doi: 10.1016/j.dsr.2014.08.009

Chakraborty A, Sharma R, Kumar R, et al. 2014. An OGCM assessment of blended OSCAT winds. Journal of Geophysical Research: Oceans, 119(1): 173–186, doi: 10.1002/2013JC009406

Chatterjee A, Shankar D, Shenoi S S C, et al. 2012. A new atlas of temperature and salinity for the North Indian Ocean. Journal of Earth System Science, 121(3): 559–593, doi: 10.1007/s12040-012-0191-9

Cheng Xuhua, Xie Shangping, McCreary J P, et al. 2013. Intraseasonal variability of sea surface height in the Bay of Bengal. Journal of Geophysical Research: Oceans, 118(2): 816–830, doi: 10.1002/jgrc.20075

Diansky N A, Zalesny V B, Moshonkin S N, et al. 2006. High resolution modeling of the monsoon circulation in the Indian Ocean. Oceanology, 46(5): 608–628, doi: 10.1134/S000143700605002X

de Boyer Montégut C, Durand F, Bourdallé-Badie R, et al. 2014. Role of fronts in the formation of Arabian Sea barrier layers during summer monsoon. Ocean Dynamics, 64(6): 809–822, doi: 10.1007/s10236-014-0716-7

de Boyer Montégut C, Vialard J, Shenoi S S C, et al. 2007. Simulated seasonal and interannual variability of the mixed layer heat budget in the northern Indian Ocean. Journal of Climate, 20(13): 3249–3268, doi: 10.1175/JCLI4148.1

Dube S K, Luther M E, O'Brien J J. 1990. Relationships between interannual variability in the Arabian Sea and Indian summer monsoon rainfall. Meteorology and Atmospheric Physics, 44(1–4): 153–165, doi: 10.1007/BF01026816

Durand F, Papa F, Rahman A, et al. 2011. Impact of Ganges-Brahmaputra interannual discharge variations on bay of Bengal salinity and temperature during 1992–1999 period. Journal of Earth System Science, 120(5): 859–872, doi: 10.1007/s12040-011-0118-x

Durand F, Shankar D, de Boyer Montégut C, et al. 2007. Modeling the barrier-layer formation in the Southeastern Arabian Sea. Journal of Climate, 20(10): 2109–2120, doi: 10.1175/JCLI4112.1

Foltz G R, Grodsky S A, Carton J A, et al. 2003. Seasonal mixed layer heat budget of the tropical Atlantic Ocean. Journal of Geophysical Research, 108(C5): 3146, doi: 10.1029/2002JC001584

George M S, Bertino L, Johannessen O M, et al. 2010. Validation of a hybrid coordinate ocean model for the Indian Ocean. Journal of Operational Oceanography, 3(5): 25–38

Gutzler D S, Harrison D E. 1987. The structure and evolution of seasonal wind anomalies over the near-equatorial eastern Indian and western Pacific Oceans. Monthly Weather Review, 115(1): 169–192, doi: 10.1175/1520-0493(1987)115<0169:TSAEOS>2.0.CO;2

Han Weiqing, McCreary Jr J P, Kohler K E. 2001. Influence of precipitation minus evaporation and bay of Bengal rivers on dynamics, thermodynamics, and mixed layer physics in the upper Indian Ocean. Journal of Geophysical Research: Oceans, 106(C4): 6895–6916, doi: 10.1029/2000JC000403

Holte J, Gilson J, Talley L D, et al. 2016. Argo mixed layers. San Diego: Scripps Institution of Oceanography/UCSD, http://mixedlayer.ucsd.edu [2016-11-27]

Holte J, Talley L. 2009. A new algorithm for finding mixed layer depths with applications to Argo data and Subantarctic Mode Water formation. Journal of Atmospheric and Oceanic Technology, 26(9):1920-1939, doi: 10.1175/2009JTECHO543.1

Huang Boyin, Xue Yan, Wang Hui, et al. 2012. Mixed layer heat budget of the El Niño in NCEP climate forecast system. Climate Dynamics, 39(1–2): 365–381, doi: 10.1007/s00382-011-1111-4

Huang Boyin, Xue Yan, Zhang Dongxiao, et al. 2010. The NCEP GODAS ocean analysis of the tropical pacific mixed layer heat budget on seasonal to interannual time scales. Journal of Climate, 23(18): 4901–4925, doi: 10.1175/2010JCLI3373.1

Huang Ke, Derada S, Xue Huijie, et al. 2015. A 1/8° coupled biochemical-physical Indian Ocean regional model: physical results and validation. Ocean Dynamics, 65(8): 1121–1142, doi: 10.1007/s10236-015-0860-8

Jackett D R, McDougall T J. 1995. Minimal adjustment of hydrographic profiles to achieve static stability. Journal of Atmospheric and Oceanic Technology, 12(2): 381–389, doi: 10.1175/1520-0426(1995)012<0381:MAOHPT>2.0.CO;2

Kalnay E, Kanamitsu M, Kistler R, et al. 1996. The NCEP/NCAR 40-year reanalysis project. Bulletin of the American Meteorological Society, 77: 437–471, doi: 10.1175/1520-0477(1996)077<0437:TNYRP>2.0.CO;2

Kantha L, Rojsiraphisal T, Lopez J. 2008. The North Indian Ocean circulation and its variability as seen in a numerical hindcast of the years 1993-2004. Progress in Oceanography, 76(1): 111–147, doi: 10.1016/j.pocean.2007.05.006

Keerthi M G, Lengaigne M, Drushka K, et al. 2016. Intraseasonal variability of mixed layer depth in the tropical Indian Ocean. Climate Dynamics, 46(7–8): 2633–2655, doi: 10.1007/s00382-015-2721-z

Keerthi M G, Lengaigne M, Vialard J, et al. 2013. Interannual variability of the tropical Indian Ocean mixed layer depth. Climate Dynamics, 40(3–4): 743–759, doi: 10.1007/s00382-012-1295-2

Krishnamurthy V, Kirtman B P. 2003. Variability of the Indian Ocean: relation to monsoon and ENSO. Quarterly Journal of the Royal Meteorological Society, 129(590): 1623–1646, doi: 10.1256/qj.01.166

Large W G, McWilliams J C, Doney S C. 1994. Oceanic vertical mixing: a review and a model with a nonlocal boundary layer parameterization. Reviews of Geophysics, 32(4): 363–403, doi: 10.1029/94RG01872

Large W G, Pond S. 1982. Sensible and latent heat flux measurements over the ocean. Journal of Physical Oceanography, 12(5): 464–482, doi: 10.1175/1520-0485(1982)012<0464:SALHFM>2.0.CO;2

Li Yuanlong, Han Weiqing, Lee T. 2015. Intraseasonal sea surface salinity variability in the equatorial Indo-Pacific Ocean induced by Madden-Julian oscillations. Journal of Geophysical Research: Oceans, 120(3): 2233–2258, doi: 10.1002/2014JC010647

Liu Zhengyu, Alexander M. 2007. Atmospheric bridge, oceanic tunnel, and global climatic teleconnections. Reviews of Geophysics, 45(2): RG2005, doi: 10.1029/2005RG000172

Lorbacher K, Dommenget D, Niiler P P, et al. 2006. Ocean mixed layer depth: a subsurface proxy of ocean-atmosphere variability. Journal of Geophysical Research: Oceans, 111(C7): C07010, doi: 10.1029/2003JC002157

Marshall J, Adcroft A, Hill C, et al. 1997. A finite-volume, incompressible Navier Stokes model for studies of the ocean on parallel computers. Journal of Geophysical Research: Oceans, 102(C3): 5753–5766, doi: 10.1029/96JC02775

Masumoto Y, Morioka Y, Sasaki H. 2008. High-resolution Indian Ocean simulations-Recent Advances and Issues from OFES. In: Hecht M W, Hasumi H, eds. Ocean Modeling in an Eddying Regime. Washington DC: American Geophysical Union, doi: 10.1029/177GM14

Moisan J R, Niiler P P. 1998. The seasonal heat budget of the North Pacific: net heat flux and heat storage rates (1950–1990). Journal of Physical Oceanography, 28(3): 401–421, doi: 10.1175/1520-0485(1998)028<0401:TSHBOT>2.0.CO;2

Momin I M, Mitra A K, Mahapatra D K, et al. 2014. Impact of model resolutions on Indian Ocean simulations from Global NEMO Ocean Model. Indian Journal of Geo-Marine Science, 43(9): 1667–1674

Narvekar J, Prasanna Kumar S. 2006. Seasonal variability of the mixed layer in the central Bay of Bengal and associated changes in nutrients and chlorophyll. Deep Sea Research Part I: Oceanographic Research Papers, 53(5): 820–835, doi: 10.1016/j.dsr.2006.01.012

Neetu S, Lengaigne M, Vincent E M, et al. 2012. Influence of upper-ocean stratification on tropical cyclone-induced surface cool-

ing in the Bay of Bengal. Journal of Geophysical Research: Oceans, 117(C12): C12020, doi: 10.1029/2012JC008433

Prasad T G. 2004. A comparison of mixed-layer dynamics between the Arabian Sea and Bay of Bengal: one-dimensional model results. Journal of Geophysical Research: Oceans, 109(C3): C03035, doi: 10.1029/2003JC002000

Prasanna Kumar S, Narvekar J. 2005. Seasonal variability of the mixed layer in the central Arabian Sea and its implication on nutrients and primary productivity. Deep Sea Research Part II: Topical Studies in Oceanography, 52(14–15): 1848–1861, doi: 10.1016/j.dsr2.2005.06.002

Rao R R, Sivakumar R. 2003. Seasonal variability of sea surface salinity and salt budget of the mixed layer of the North Indian Ocean. Journal of Geophysical Research: Oceans, 108(C1): 9-1–9-14, doi: 10.1029/2001JC000907

Roxy M K, Ritika K, Terray P, et al. 2015. Drying of Indian subcontinent by rapid Indian Ocean warming and a weakening land-sea thermal gradient. Nature Communications, 6: 7423, doi: 10.1038/ncomms8423

Schiller A, Godfrey J S. 2003. Indian Ocean intraseasonal variability in an ocean general circulation model. Journal of Climate, 16(1): 21–39, doi: 10.1175/1520-0442(2003)016<0021:IOIVIA>2.0.CO;2

Schott F A, McCreary Jr J P. 2001. The monsoon circulation of the Indian Ocean. Progress in Oceanography, 51(1): 1–123, doi: 10.1016/S0079-6611(01)00083-0

Schott F A, Xie Shangping, McCreary Jr J P. 2009. Indian Ocean circulation and climate variability. Reviews of Geophysics, 47(1): RG1002, doi: 10.1029/2007RG000245

Sengupta D, Bharath Raj G N, Shenoi S S C. 2006. Surface freshwater from Bay of Bengal runoff and Indonesian throughflow in the tropical Indian Ocean. Geophysical Research Letters, 33(22): L22609, doi: 10.1029/2006GL027573

Shankar D, Vinayachandran P N, Unnikrishnan A S. 2002. The monsoon currents in the north Indian Ocean. Progress in Oceanography, 52(1): 63–120, doi: 10.1016/S0079-6611(02)00024-1

Sharma R, Agarwal N, Basu S, et al. 2007. Impact of satellite-derived forcings on numerical ocean model simulations and study of sea surface salinity variations in the Indian Ocean. Journal of Climate, 20(5): 871–890, doi: 10.1175/JCLI4032.1

Sharma R, Agarwal N, Momin I M, et al. 2010. Simulated sea surface salinity variability in the tropical Indian Ocean. Journal of Climate, 23(24): 6542–6554, doi: 10.1175/2010JCLI3721.1

Sharma R, Mankad B, Agarwal N, et al. 2012. An assessment of two different satellite-derived precipitation products in relation to simulation of sea surface salinity in the tropical Indian Ocean. Journal of Geophysical Research, 117(C7): C07001, doi: 10.1029/2012JC008078

Shenoi S S C, Saji P K, Almeida A M. 1999. Near-surface circulation and kinetic energy in the tropical Indian Ocean derived from Lagrangian drifters. Journal of Marine Research, 57(6): 885–907, doi: 10.1357/002224099321514088

Smith W H F, Sandwell D T. 1997. Global sea floor topography from satellite altimetry and ship depth soundings. Science, 277(5334): 1956–1962, doi: 10.1126/science.277.5334.1956

Song Qian, Vecchi G A, Rosati A J. 2007. Indian Ocean variability in the GFDL coupled climate model. Journal of Climate, 20(13): 2895–2916, doi: 10.1175/JCLI4159.1

Stevenson J W, Niiler P P. 1983. Upper ocean heat budget during the Hawaii-to-Tahiti shuttle experiment. Journal of Physical Oceanography, 13(10): 1894–1907, doi: 10.1175/1520-0485(1983)013<1894:UOHBDT>2.0.CO;2

Subrahmanyam B, Murty V S N, Sharp R J, et al. 2005. Air-sea coupling during the tropical cyclones in the Indian Ocean: a case study using satellite observations. Pure and Applied Geophysics, 162(8–9): 1643–1672, doi: 10.1007/s00024-005-2687-6

Thadathil P, Gopalakrishna V V, Muraleedharan P M, et al. 2002. Surface layer temperature inversion in the Bay of Bengal. Deep Sea Research Part I: Oceanographic Research Papers, 49(10): 1801–1818, doi: 10.1016/S0967-0637(02)00044-4

Thangaprakash V P, Suprit K, Kumar N S, et al. 2016. What controls seasonal evolution of sea surface temperature in the Bay of Bengal? Mixed layer heat budget analysis using moored buoy observations along 90°E. Oceanography, 29(2): 202–213, doi: 10.5670/oceanog

Thompson B, Gnanaseelan C, Parekh A, et al. 2008. North Indian Ocean warming and sea level rise in an OGCM. Journal of Earth System Science, 117(2): 169–178, doi: 10.1007/s12040-008-0007-0

Thompson B, Gnanaseelan C, Salvekar P S. 2006. Variability in the Indian Ocean circulation and salinity and its impact on SST anomalies during dipole events. Journal of Marine Research, 64(6): 853–880, doi: 10.1357/002224006779698350

Thomson R E, Fine I V. 2003. Estimating mixed layer depth from oceanic profile data. Journal of Atmospheric and Oceanic Technology, 20(2): 319–329, doi: 10.1175/1520-0426(2003)020<0319:EMLDFO>2.0.CO;2

Vecchi G A, Harrison D E. 2004. Interannual Indian rainfall variability and Indian Ocean sea surface temperature anomalies. In: Wang C, Xie S P, Carton J A, eds. Earth's Climate: The Ocean-Atmosphere Interaction. Washington, DC: AGU, 247–260

Vinayachandran P N, Jahfer S, Nanjundiah R S. 2015. Impact of river runoff into the ocean on Indian summer monsoon. Environmental Research Letters, 10(5): 054008, doi: 10.1088/1748-9326/10/5/054008

Vinayachandran P N, Kurian J. 2007. Hydrographic observations and model simulation of the Bay of Bengal freshwater plume. Deep Sea Research Part I: Oceanographic Research Papers, 54(4): 471–486, doi: 10.1016/j.dsr.2007.01.007

Vinayachandran P N, Shetye S R, Sengupta D, et al. 1996. Forcing mechanisms of the Bay of Bengal circulations. Current Science, 71: 753–763

Wajsowicz R. 2002. Air-sea interaction over the Indian Ocean due to variations in the Indonesian throughflow. Climate Dynamics, 18(5): 437–453, doi: 10.1007/s00382-001-0187-7

Wang Yu, Liu Peng, Li Tianyi, et al. 2011. Climatologic comparison of HadISST1 and TMI sea surface temperature datasets. Science China Earth Sciences, 54(8): 1238–1247, doi: 10.1007/s11430-011-4214-1

Wentz F J, Gentemann C, Hilburn K A. 2015. Remote sensing systems TRMM TMI[indicate whether you used Daily, 3-Day, Weekly, or Monthly] Environmental Suite on 0.25 deg grid. Santa Rosa, CA: Remote Sensing Systems, www.remss.com/missions/tmi

Wu Renguang, Kirtman B P. 2004. Impacts of the Indian Ocean on the Indian summer monsoon-ENSO relationship. Journal of Climate, 17(15): 3037–3054, doi: 10.1175/1520-0442(2004)017<3037:IOTIOO>2.0.CO;2

Wu Lingjuan, Wang Fan, Yuan Dongliang, et al. 2007. Evolution of freshwater plumes and salinity fronts in the northern Bay of Bengal. Journal of Geophysical Research: Oceans, 112(C8): C08017, doi: 10.1029/2005JC003308

Spatial and temporal evolution of landfast ice near Zhongshan Station, East Antarctica, over an annual cycle in 2011/2012

Jiechen Zhao[1, 2, 3], Qinghua Yang[4, 5]*, Bin Cheng[6], Matti Leppäranta[7], Fengming Hui[8]*, Surui Xie[9], Meng Chen[10], Yining Yu[8], Zhongxiang Tian[2], Ming Li[2], Lin Zhang[2]

[1] College of Oceanic and Atmospheric Sciences, Ocean University of China, Qingdao 266100, China

[2] National Marine Environmental Forecasting Center, Beijing 100081, China

[3] First Institute of Oceanography, Ministry of Natural Resources, Qingdao 266061, China

[4] Guangdong Province Key Laboratory for Climate Change and Natural Disaster Studies, School of Atmospheric Sciences, Sun Yat-sen University, Zhuhai 519082, China

[5] Southern Marine Science and Engineering Guangdong Laboratory (Zhuhai), Zhuhai 519082, China

[6] Finnish Meteorological Institute, Helsinki 00101, Finland

[7] Institute of Atmospheric and Earth Sciences, University of Helsinki, Helsinki 00014, Finland

[8] College of Global Change and Earth System Sciences (GCESS), Beijing Normal University, Beijing 100875, China

[9] School of Geosciences, University of South Florida, Tampa 33620, USA

[10] Meteorological Service of Youyang Tujia and Miao Autonomous County, Chongqing 409800, China

Abstract

Annual observations of first-year ice (FYI) and second-year ice (SYI) near Zhongshan Station, East Antarctica, were conducted for the first time from December 2011 to December 2012. Melt ponds appeared from early December 2011. Landfast ice partly broke in late January, 2012 after a strong cyclone. Open water was refrozen to form new ice cover in mid-February, and then FYI and SYI co-existed in March with a growth rate of 0.8 cm/d for FYI and a melting rate of 2.7 cm/d for SYI. This difference was due to the oceanic heat flux and the thickness of ice, with weaker heat flux through thicker ice. From May onward, FYI and SYI showed a similar growth by 0.5 cm/d. Their maximum thickness reached 160.5 cm and 167.0 cm, respectively, in late October. Drillings showed variations of FYI thickness to be generally less than 1.0 cm, but variations were up to 33.0 cm for SYI in March, suggesting that the SYI bottom was particularly uneven. Snow distribution was strongly affected by wind and surface roughness, leading to large thickness differences in the different sites. Snow and ice thickness in Nella Fjord had a similar "east thicker, west thinner" spatial distribution. Easterly prevailing wind and local topography led to this snow pattern. Superimposed ice induced by snow cover melting in summer thickened multi-year ice, causing it to be thicker than the snow-free SYI. The estimated monthly oceanic heat flux was ~30.0 W/m² in March–May, reducing to ~10.0 W/m² during July–October, and increasing to ~15.0 W/m² in November. The seasonal change and mean value of 15.6 W/m² was similar to the findings of previous research. The results can be used to further our understanding of landfast ice for climate change study and Chinese Antarctic Expedition services.

Key words: landfast ice, thickness, oceanic heat flux, Prydz Bay, East Antarctica

1 Introduction

In contrast to the rapid decline of sea ice extent and volume in the Arctic, the total Antarctic sea ice area has increased by about 0.4×10^6 km² since the late 1970s (Liu et al., 2010; Parkinson and Cavalieri, 2012). Sea ice observations from space-borne sensors and *in situ* surveys have played a major role in understanding the variability of Antarctic sea ice. Ice thickness is a key sea ice property, however, remote sensing of large-scale sea ice thickness from space remains a major challenge (Kwok and Sulsky, 2010; Worby et al., 2008; Lu et al., 2014). Field observations are the traditional approach to map Antarctic landfast ice thickness.

Landfast ice forms along the Antarctic coastline and shelf edges, typically in narrow bands with a varying width up to 150 km from the continent (IPCC, 2013). It generally comprises between 5% (winter) and 35% (summer) of the Antarctic sea ice area (Fraser et al., 2012), and a greater fraction of ice volume in East Antarctica (Giles et al., 2008); therefore, landfast ice is an import-

ant factor in understanding Antarctic sea ice cover changes. Furthermore, near-shore landfast ice can be feasibly used to examine the variations of Antarctic sea ice thickness with repeat access for sea ice measurements (Heil et al., 2011).

The Antarctic Fast-Ice Network (AFIN) has been established to coordinate landfast ice observations from scientific stations operated by international contributors (Heil et al., 2011). Research focusing on landfast sea ice in Lützow-Holm Bay found that deep snow cover on multi-year ice (MYI) led to large thickness growth during summer due to snow-ice formation at the top of the ice, but only minor growth during winter (Kawamura et al., 1997). Gough et al. (2013) investigated evolution of multi-year snow-ice in McMurdo Sound and found that ice temperature remaining around –2.5°C until the first week of March, and ~200 cm thick ice showed bottom melting at a constant rate of 0.2 cm/d from mid-March to the end of April. In the Atka Bay, landfast ice observations suggested that super-cooled water including platelet ice contributes strongly to sea-ice formation, snow cover was very heterogeneous throughout the entire bay and strong easterly winds lead to thicker sea ice and snow cover in the west (Hoppmann et al., 2012). Long-term field observations in the Davis Station, Prydz Bay, showed that the maximum ice thickness had inter-annual variation with a decadal increase from 130 cm to 180 cm (Heil et al, 1996, 2006).

At the Zhongshan Station (ZS), field work conducted in winter 1992 focused on first-year ice (FYI) and found that it was mainly composed of congelation ice (He et al., 1998). Investigation of landfast ice in Nella Fjord in summer 2003 showed that snow and

ice thickness both increased along the prevailing wind direction, and average ice thickness was 170.0 cm, which may be a sign of MYI (Tang et al, 2006). Annual mass balance and heat flux were observed and estimated from mid-February to late November of 2006, providing important material comparison with the current study, but MYI observations were not included at this time (Lei et al., 2010).

In this paper, spatial and temporal evolution of landfast ice near ZS was analyzed based on the field observations from December 2011 to December 2012. Landfast ice breakup and refreezing were virtually recorded from the shore. Second-year ice (SYI) observations were carried out for the first time, accompanied by FYI observations near ZS. Snow thickness was recorded by a sonar and stainless-steel ruler, while ice thickness was observed manually by borehole measurements from March to December. The winter spatial distribution of snow and ice thickness inside Nella Fjord was assessed for the first time. The oceanic heat flux was estimated by the residual method. Through analysis of these observations, the primary conditions of the annual FYI and SYI cycle, were provided for scientific goals and expedition services.

2 Observations and methods

2.1 *Meteorology*

The ZS (69°22′S, 76°22′W) is located in the Larseman Hill of East Antarctica, close to the Australian Davis Station and Russian Progress Station (Fig. 1). All these stations are operated year-
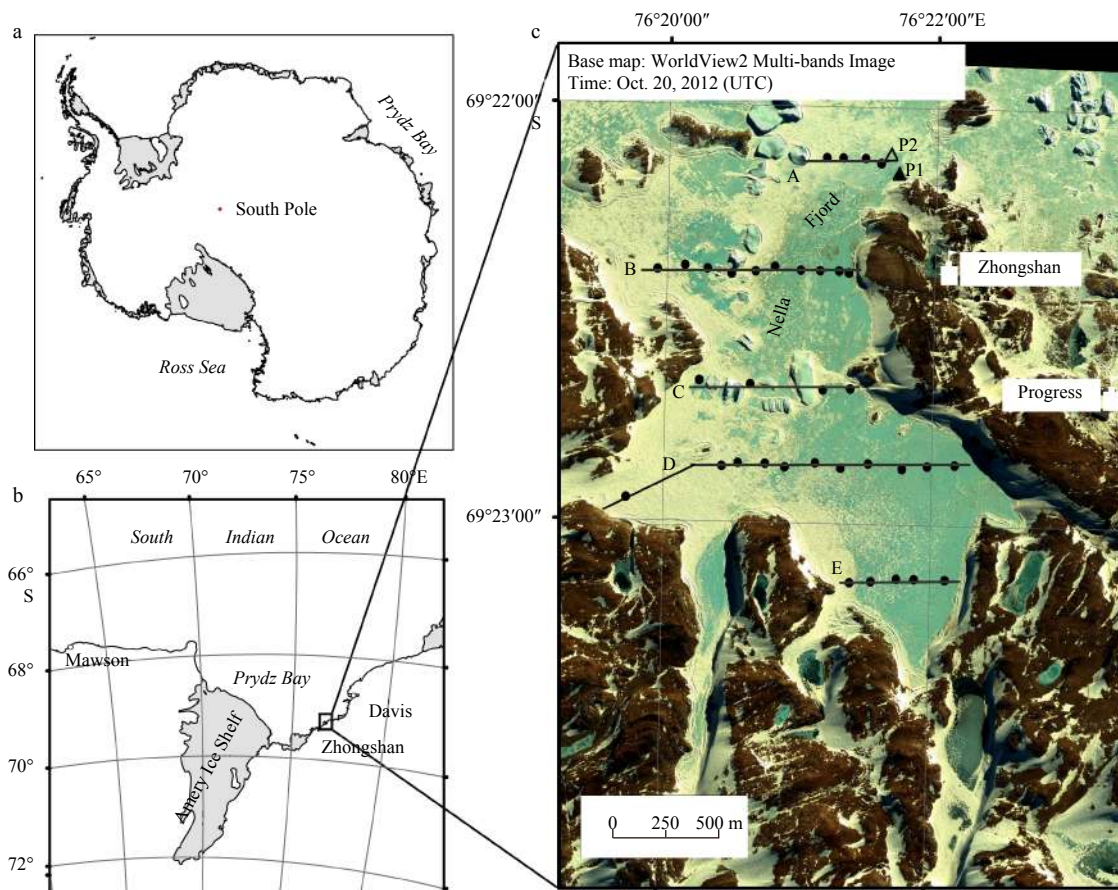

Fig. 1. Location of the Prydz Bay (a) and Zhongshan Station (b); observation field in the Nella Fjord: fixed Sites P1 (solid triangle) and P2 (open triangle), and Sections A, B, C, D and E with measurement sites (black dots) (c).

round. In the operational year 2011/2012, annual observations at ZS started in December 2011 after R/V *Xuelong*, Chinese polar icebreaker, arrived with observation devices and continued until December 2012 when snow and ice melted heavily.

Meteorological parameters including surface pressure, air temperature, wind speed and direction, and humidity were measured by the ZS automatic weather station (WMO No. 89573) at an elevation of 15 m (Fig. 2a). Cloudiness and visibility were recorded manually by a meteorologist at UTC 00:00, 06:00, 12:00 and 18:00 every day. Air temperature on the ice was recorded every minute by a sensor T109 (Campbell Scientific, Inc., Logan, UT, USA) deployed on a tripod (Figs 2b and c) near the ice observation Site P1 (Fig. 1c) from March 25 to November 30, 2012. The altitude of the sensor T109 was 2 m.

2.2 *Snow and ice*

2.2.1 *Fixed sites observations*

The evolution of landfast ice, including breakage and refreezing, was monitored manually in the sound of Nella Fjord by a digital camera mounted on the shore. Photographs were taken every 5 d from December 2011 to March 2012. The photographs covered the area of Sites P1 and P2 (Fig. 1c). Part of the nearshore landfast ice could survive to next winter and become SYI. Those photographs offered a good material to detect the boundary between FYI and SYI (Fig. 2b).

Manual snow and ice thickness measurements were carried out at P1 and P2, about 100 m and 200 m off the shore, respectively (Fig. 1c). The measurements started from March 10, 2012 and the frequency was 2–5 d, but paused during the two months of polar night (end of May to end of July) and recovered after then. Snow thickness was measured by a stainless-steel ruler, which was pushed into the snow down to the ice surface to obtain the thickness (Fig. 2d). The accuracy was 0.1 cm. Ice thickness was measured by a gage with the accuracy of 0.1 cm in boreholes drilled by a Kovacs ice auger (5 cm in diameter) (Figs 2e and f). At every observation, boreholes were drilled carefully to avoid repeating the previous ones. Usually one borehole was

drilled at P1 for each observation day, but occasionally three boreholes were drilled to assess the variations of thickness from different boreholes. However, more than three boreholes were drilled for every observation day at P2, because considerable large variations in ice thickness among different boreholes were found there in the initial measurements.

A tripod was deployed near P1 (Fig. 2b) and a sonar sensor SR50A (Campbell Scientific, Inc., Logan, UT, USA) was mounted to it to automatically record the snow thickness (Fig. 2c). An infrared sensor SI-111 (Campbell Scientific, Inc., Logan, UT, USA) was also mounted to it to record the snow/ice surface temperature. The sampling frequency of both sensors was 1 min, and the observation period was from March 25 to November 30, 2012.

2.2.2 *Section observations*

Five sections were positioned to survey snow and ice thickness inside the Nella Fjord from September 29 to October 2, 2012. This was the first time that winter spatial observations had been carried out in this area, including 34 measurement sites along five sections (Fig. 1c). The snow and ice thickness measurements were made manually and in the same way as for the fixed sites. The location of each site was recorded with a handheld GPS receiver. Spatial distributions in the whole fjord were obtained using a Kriging interpolation method.

3 Results

3.1 *Meteorological conditions*

In the annual cycle of December 2011 to December 2012, the mean air temperature was –10.4°C (Fig. 3b). The highest monthly mean air temperature occurred in January 2012 (–0.6°C) and the lowest was in July 2012 (–19.6°C). The warmest and coldest daily mean air temperatures were 6.1°C and –34.5°C, observed on January 18 and May 24, respectively. The mean relative humidity was 54% (Fig. 3c). The mean wind speed was 7.1 m/s, and the highest hourly mean wind speed was 32.8 m/s recorded on June 29 (Fig. 3e). Precipitation was not observed at ZS, but it was available from Progress Station. Large accumulated precipitation oc-
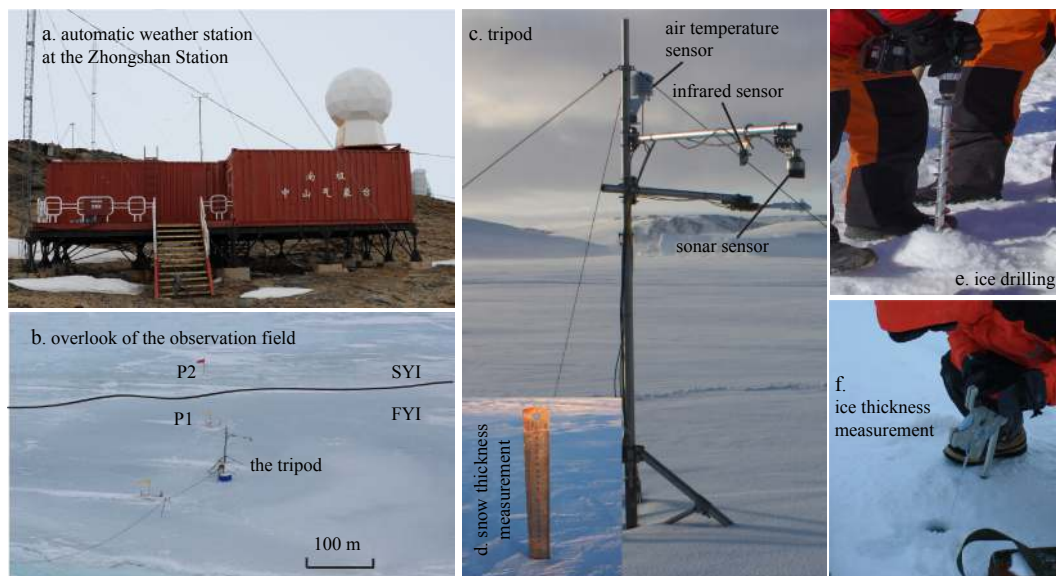
Fig. 2. Automatic weather station at Zhongshan Station (a); overlook of the observation field, the black line represents the boundary of FYI and SYI (b); photograph of the tripod (c); the stainless-steel ruler for snow thickness measurement (d); ice drilling by a Kovacs ice auger (e); and ice thickness measurement by a gage (f).
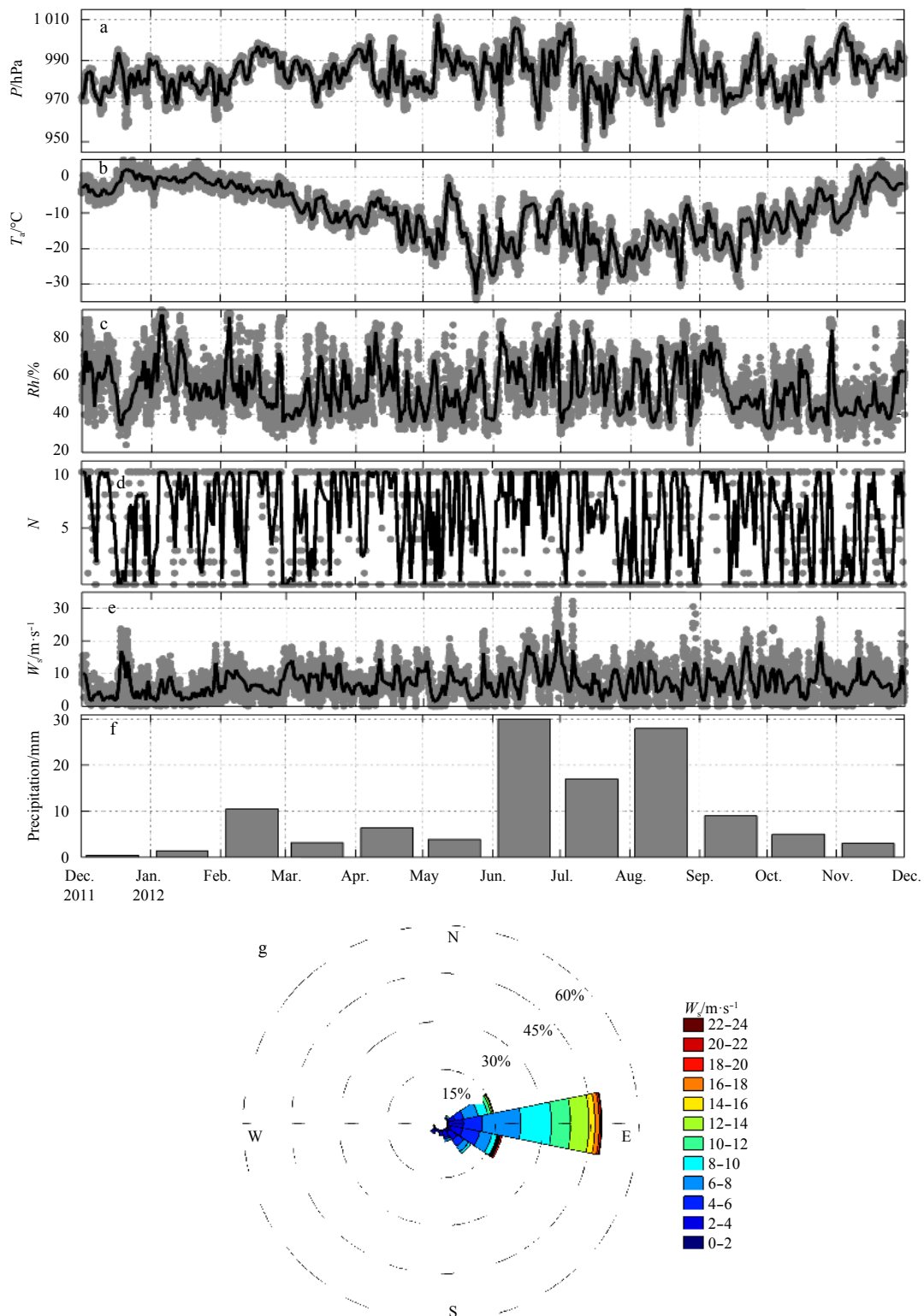
Fig. 3. The time series of surface air pressure (a), surface air temperature (b), surface relative humidity of air (c), cloudiness (d), surface wind speed (e), precipitation (f), and wind rose diagram (g). Gray dots represent hourly data in a, b, c and e, but 6-hourly data in d. Black lines represent the daily mean values. The gray bar in f is the monthly accumulated precipitation at Progress Station.

curred during June–August was 18–30 mm per month, while other months were less than 10 mm per month (Fig. 3f). The prevailing wind came from the east, accounting for 48% of the annual cycle period (Fig. 3g). Snowfall induced by the Prydz Bay cyc-

lones in Larseman Hill was frequent and snow was blown away by the strong winds, which redistributed the snow spatial pattern. Therefore, the measured snow accumulation was not sufficiently accurate to represent the real snowfall amount.

Compared with the climatology from Year 1989 to 2014, the annual mean air temperature was 0.6°C lower, relative humidity was 4% lower, and wind speed was 0.1 m/s larger.

3.2 *Ice breakup and refreezing*

The landfast ice characteristics shown in Fig. 4 were charted by photographs taken along the coast, field records, and high-resolution satellite images. Ice floes of different sizes transported by strong prevailing easterly winds were accumulated in the northeast of ZS and usually survived over the summer to become MYI (Area I in Fig. 4a). The landfast ice at the sound of Nella Fjord started to melt at the end of October and melt ponds were apparent from early December, 2011 (Fig. 4b). Ice was partly broken up from January 23, 2012 after one strong cyclone visit (Area II in Fig. 4a). Then, open water was present for about 20 d, until mid-February, when the day-night melting-freezing cycles commenced. Ice was formed again at the end of February to start a new FYI. Melt ponds were common over Area III, but surrounding islands and small icebergs kept the ice unbroken. Area IV was covered by thick snow and melting was common in the snow surface, but the ice beneath the snow survived to the next winter. Therefore, ice in Areas III and IV was MYI. According to field records, ice at P2 was SYI, which had different evolution compared with MYI inside the fjord.

The ice breakup and refreezing time in late January and mid-February were similar to observations near ZS in 2006 (Lei et al., 2010) and at Davis Station since 2000 (Heil et al., 2006). The breakup date and extent of breakage are strongly dependent on the cyclone strengths and timing. The landfast ice could survive to the next winter, indicating that ice in the Nella Fjord does not disappear by melting, but by dynamic processes (Yang et al., 2015a). The same phenomena was also observed on the Arctic Siberian coast (Yang et al., 2015b).

3.3 *Snow thickness*

Snow thickness observed automatically at the sonar site and manually at P1, P2, and the tripod are illustrated in Fig. 5. There was a close relationship between the automatic and manual observations at the tripod site, with Pearson's correlation coefficient of 0.71. This implies that the sonar sensor could record the changes of snow thickness with high reliability. Between July and August all measurement sites showed large snow accumulation, but the values were considerably different. Considering the close locations, this phenomenon suggested that snow accumulation was strongly affected by the ice surface roughness and had large spatial variations. Snowfall near ZS was caused by the moisture transport induced by strong cyclones, and strong wind coming along usually redistributed the snow cover quickly. Five major snowfall events occurred and were recorded by the sonar after June. Half of the accumulated snow was blown away by a strong wind within 24 h after the snowfall events S1 and S2. In S5, snow thickness reduced from 31.0 cm to 15.0 cm in 72 h because of the strong wind.

Before June, ice surface was almost snow-free. The maximum thickness record by ruler at the tripod site was 26.0 cm on October 29, but 31.0 cm measured by sonar on October 31 during the snowfall event S5. Manual observations missed this important largest value and date, but sonar captured it.

3.4 *Ice thickness*

The evolution of FYI at P1 and SYI at P2 is illustrated in Fig. 6. The first field measurement was carried out on March 10 at P2 and the ice thickness was 116.0 cm. The first measurement at P1 was conducted one day later on March 11 and the ice thickness was 22.0 cm, about 100 cm less than SYI at P2 (Fig. 6a). The FYI grew continuously from March to October. From March to May, the mean growth rate was 0.7 cm/d (Fig. 7), and between August and October ice growth slowed down to the mean rate of 0.4 cm/d. The maximum growth rates were around 1.0 cm/d, similar to the observations of the landfast ice off ZS in 2006 (Lei et al., 2010). The maximum thickness of FYI was 160.5 cm observed on Octo-
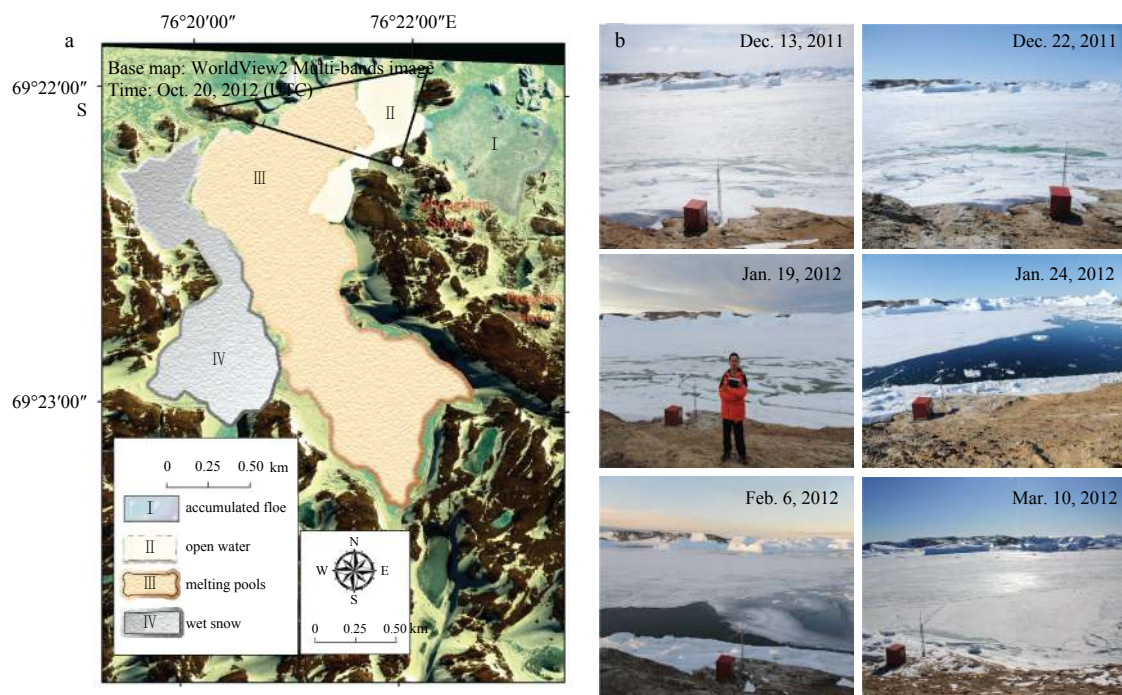

Fig. 4. Landfast ice characteristics in the Nella Fjord during January 2012 (a) and ice evolution in the sound of the Nella Fjord (b). In Fig. 4a, the white circle represents the location of the camera and the black triangle shows the area of the coverage of the photographs.
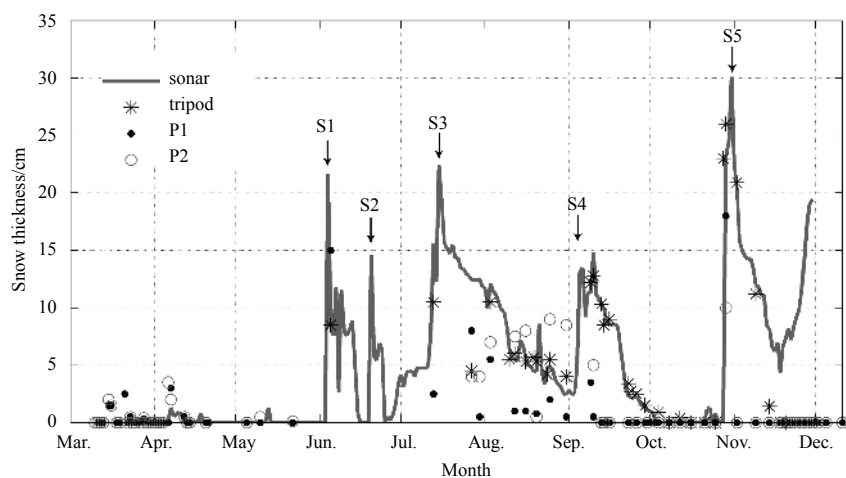
Fig. 5. Observed snow thickness at P1, P2, the tripod, and by the sonar sensor. Five major snowfall events are marked by S1, S2, S3, S4 and S5.
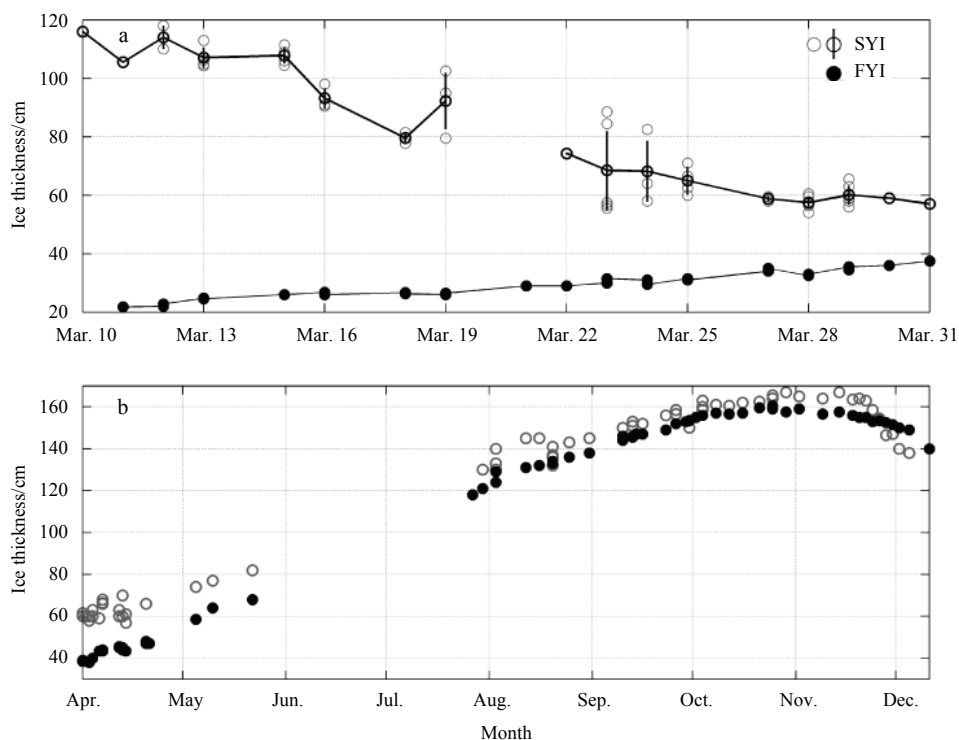

Fig. 6. Ice thickness of FYI and SYI in March (a) and April–December 2012 (b). Grey circles represent each drilling result, black circles represent averaged values and bars are standard deviation. Black dots represent each drilling result for FYI.

ber 25, 2012. This was less than 174.0 cm in 2006 (Lei et al., 2010), 176.0 cm in 2010, and 186.0 cm in 2011 observed by ZS wintering personnel. Bottom melting started from the end of October, with a rate of 0.4 cm/d. Melting became a little weaker in November, 0.3 cm/d, and in December it increased to 1.0 cm/d. During the no-data period in the polar night, mean growth rate was estimated as 0.8 cm/d.

The SYI showed a quite different curve in March, 2012, melting with a monthly mean rate of 2.7 cm/d (Fig. 6a), leading to ice thickness reduction from 116.0 cm (March 10) to 57.0 cm (March 31). On March 10 and 11, an easy-drill-through layer was observed at 60.0–80.0 cm depth below the ice surface. In the first two weeks of April, SYI thickness changed slightly with a stable value of about 60.0 cm. From April 15, SYI began to grow quickly. The growing trend was similar to FYI, but SYI was generally 10.0 cm– 20.0 cm thicker than FYI. SYI growth slowed down in August and began melting at the end of October. The maximum thickness of SYI was 167.0 cm on October 29. Monthly mean melting rate in November was 0.6 cm/d, twice that of FYI, but in December it was only 0.5 cm/d, half of the FYI melt rate. The larger value of SYI in Fig. 7 during November and December suggested that SYI began to show larger spatial variation during the melting season.

The FYI growth and simultaneous SYI ablation in March have previously been studied in detail and SYI ablation was attributed to nonlinear temperature profile and internal melting (Zhao et al., 2017).
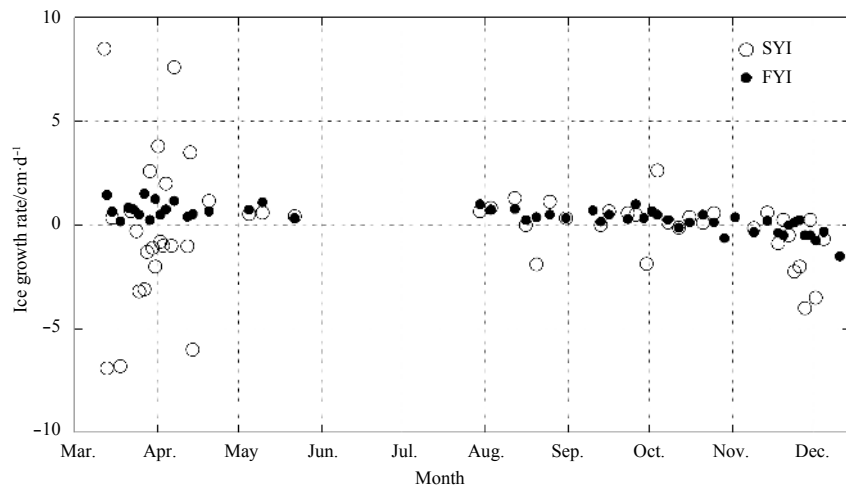
Fig. 7. Ice growth rate of FYI and SYI from March to December 2012.

3.5 *Observations variation*

At P1, ice thickness variations between different boreholes for each observation day were smaller than 1.0 cm. Considering the flat surface, this indicated that the FYI grew synchronously and the bottom was fairly smooth.

The ice thickness variation at P2 is shown in Table 1. A total of 17 visits were made to P2 in March, and in each visit, at least three drillings were performed. On March 23, six boreholes were drilled, the maximum number in this month. The measured ice thickness varied from 55.5 cm to 88.5 cm, leading to the largest thickness difference among the borehole sets (33.0 cm). The mean ice thickness was 81.4 cm in March. The data presented in Table 1 suggest that SYI thickness had a large spatial deviation in a small spatial scale (~10 m) and the largest variation reduced over time, likely because thinner ice grows more rapidly. The recorded ice surface unevenness was around 5.0–10.0 cm during the winter, which implies that 30% of the variations came from an uneven surface and 70% came from an uneven bottom.

Table 1. Statistics of SYI thickness variation at P2 in the different months

	Mar.	Apr.	Aug.	Sep.	Oct.
Number of measurements	17	10	6	7	7
Max drillings in single measurement	6	4	5	3	3
Mean ice thickness/cm	81.4	61.8	141.5	153.0	162.6
Largest variation/cm	33.0	10.0	10.0	7.0	4.5

3.6 *Regional distribution*

The spatial mean snow thickness was 11.3 cm inside the Nella Fjord. Snow cover was thin in the eastern part and thick in the western part of the fjord. The thickest snow was recorded in the eastern end of Section D, exceeding the range of the 100-cm ruler. Small icebergs influenced the snow distribution, and snow around them was 5.0 cm–10.0 cm thicker than in other areas (Fig. 8a). The overall distribution of snow in this fjord was determined by the surface wind direction and topography. The prevailing strong easterly winds blew the snow westward, and the north-south oriented hills in the eastern side blocked the snow drift, forcing the snow to accumulate there, leading to a "west thicker, east thinner" pattern, as shown in Fig. 8b.

Similar to the snow thickness distribution, the ice thickness in the east was generally larger than in the west, and the spatial correlation coefficient between snow and ice thickness was 0.52. Ice in 55% of the 34 sites was thicker than 200.0 cm, and the maximum ice thickness was 307.0 cm in Section D. The spatial mean ice thickness was 202.7 cm. A similar "west thicker, east thinner" pattern and maximum ice thickness of 201.0 cm was observed in January 2003 in the Nella Fjord (Tang et al., 2007).

3.7 *Oceanic heat flux estimations*

In the classic Stefan's Law, ice surface temperature is used to estimate ice thickness in the growth season. This law has been used inversely for oceanic heat flux estimation; however, ice surface temperature is rarely available, and therefore it is usually replaced by surface air temperature. In this study, we were able to obtain snow/ice surface temperature (T_o), field surface air temperature (T_a), and surface air temperature at ZS (T_{zs}) at the same time. The daily mean values in Fig. 9 show that T_o was (1.3 ± 1.5)°C lower than T_a. The cases $T_o < T_a$ accounted for 83% throughout the time series. T_a was (0.1 ± 3.4)°C larger than T_{zs}. The difference between T_a and T_{zs} was generally oscillating within a range of ±5.0°C.

The residual method (Mcphee and Untersteiner, 1982) was used to estimate the oceanic heat flux for FYI at P1 with the three differently measured temperatures described above. This method has been already widely used in previous studies (Perovich and Elder, 2002; Lytle et al., 2000; Purdie et al., 2006; Lei et al., 2010). The residual method was also used with a full numerical model of ice thickness by Yang et al. (2015a).

At the base of the sea ice, assuming a quasi-steady heat flux, the thermal energy balance is simplified by

$$\rho_i L_f dH/dt = k_i \left(T_f - T_o\right)/H - F_w, \qquad (1)$$

where ρ_i is the sea ice density at the basal layer, L_f is the sea ice latent heat of freezing, dH/dt is the ice growth rate, k_i is the thermal conductivity of sea ice, T_f is the sea water freezing point, T_o is the ice surface temperature, H is the ice thickness, and F_w is the oceanic heat flux.

In Eq. (1) the term on the left-hand side represents latent heat flux (F_l), resulting from ice growth, and the first term on the right-hand side represents the conductive heat flux (F_c) at the base ($F_c \geqslant 0$). For simplification, the thermal inertia is ignored in the
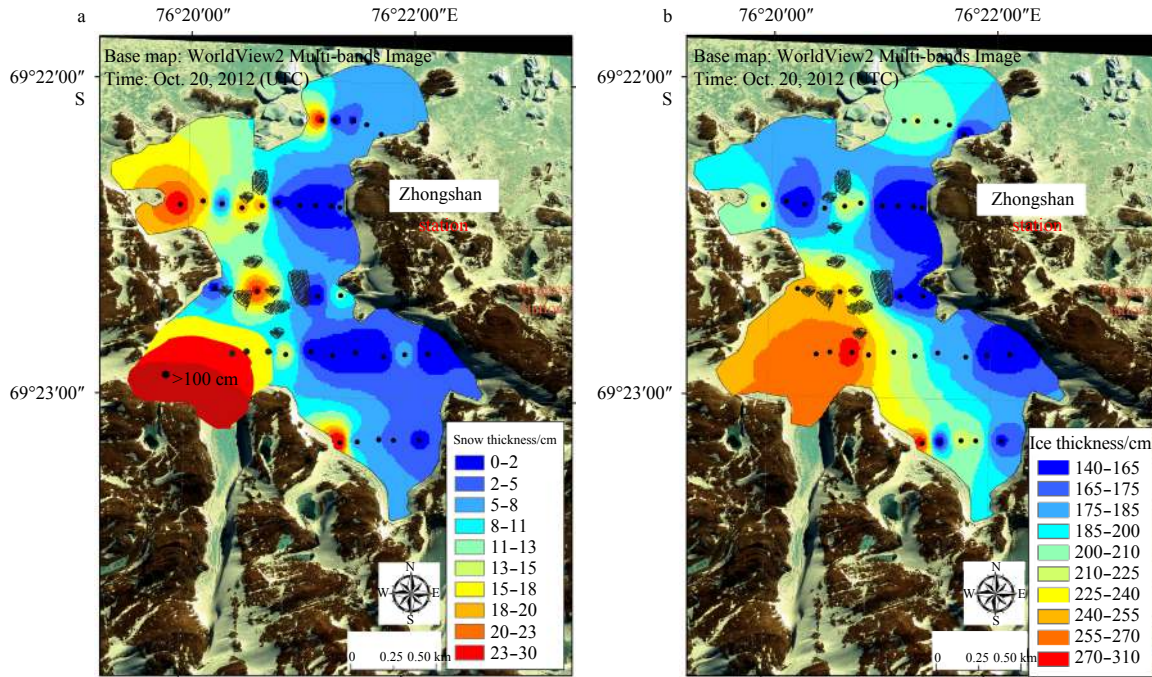
Fig. 8. Snow (a) and ice (b) thickness spatial distribution in the Nella Fjord measured from September 29 to October 2, 2012. The black solid circles represent measurement sites. The black slashes represent the locations and shape of small icebergs.
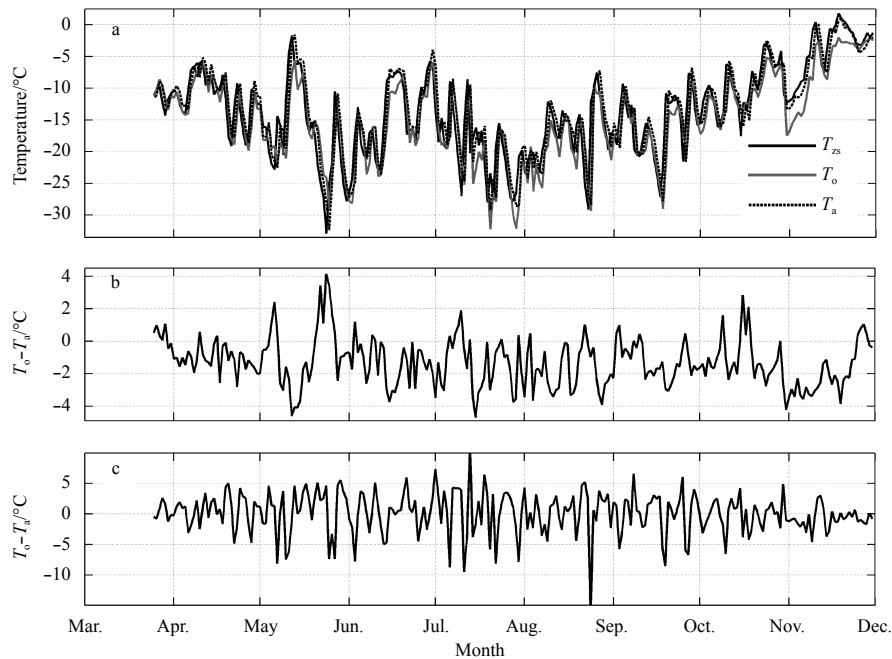
Fig. 9. Time series of daily mean snow/ice surface temperature (T_o), field air temperature (T_a) and surface air temperature at ZS (T_{zs}) (a), $T_o - T_a$ (b) and $T_a - T_{zs}$ (c).

quasi-steady approach.

In the calculations, a three-record moving average was applied to the original observations, and then the observed ice thickness was linearly interpolated into daily values. The growth rate was calculated based on the interpolated daily values. Ice density was set to 910 kg/m³, sea ice latent heat of freezing was set to 333.4 kJ/kg, and thermal conductivity was set to 2.2 W/(m·°C). To examine the sensitivities of F_c to the temperature

from different sources, T_o, T_a and T_{zs} were used separately. F_c calculated with T_o was (2.7 ± 3.9) W/m² larger than that with T_a, and (2.2 ± 9.1) W/m² larger than that with T_{zs}.

The heat fluxes after a 7-d running mean are shown in Fig. 10. From mid-March, F_c decreased with ice thickening and was close to zero in the end of November when the ice surface temperature was around 0°C (Fig. 10a). F_l was stable around –20.0 W/m² until the end of September, after which it decreased and become

Fig. 10. Conductive heat flux at ice base (F_c) (a), latent heat flux (F_l) (b), ocean heat flux (F_w) (c), and monthly mean estimated ocean heat flux of FYI (d). All lines represent a 7-d moving average. Error bars in (d) represent the standard deviation of F_w in every month.
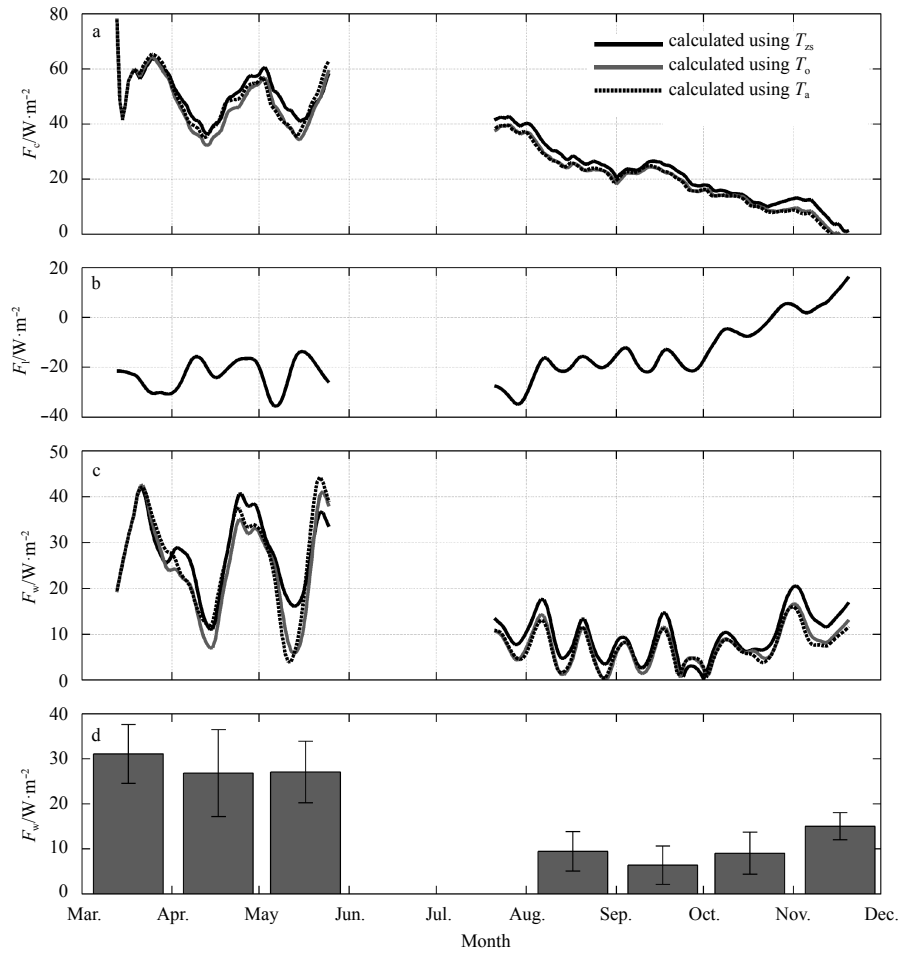
positive at the end of October. This indicated that the onset of the basal melting resulted in a reversed direction of the latent heat flux (Fig. 10b). F_w remained 20.0–40.0 W/m² during the initial ice growth period, with a maximum monthly mean value of (33.8 ± 7.5) W/m² in March. After July, F_w fell to around 10.0 W/m² (Fig. 10c). The minimum monthly mean was (4.7 ± 8.0) W/m² in September.

4 Discussion

Compared with the snow-free area, the thick snow cover on FYI usually slowed down the ice growth in winter, leading to thinner ice. However, for MYI in the Nella Fjord, thick snow cover prevented solar radiation from penetrating into ice in summer, so summer melting was limited to the snow layer (Maykut and Untersteiner, 1971; Yang et al., 2015a). Snow layer melting and re-freezing generated superimposed ice, then contributed to the total ice thickness. These mechanisms explain why the thick MYI was accompanied by deep snow cover. This phenomenon has been previously observed on MYI in McMurdo Sound (Gough et al., 2013).

Field records showed that the surface of SYI was almost level, and therefore the variation occurred in the bottom geometry. According to Archimedes' Principle, the scale of bottom topography variations can be ten times the scale of surface topographical variations when the horizontal scale exceeds the characteristic length of floating ice, which is tens of meters for 1 m ice.

The largest spatial variations of SYI thickness was 33.0 cm, much smaller than MYI in the Arctic (~100 cm; Ackley et al., 1974), and SYI in McMurdo Sound (~ 50 cm; Gough et al., 2013).

In winter, the cold and arid climate may cause substantial sublimation. The sonar sensor recorded a total 1-cm surface sublimation in a no-snow-fall period from March 24 to April 3. The mean sublimation rate was 0.09 cm/d, in accordance with the estimation by Yang et al. (2015a). Sublimation became weaker when the surface became wet and ponds formed in the melting season.

The scaling and heat balance of FYI and MYI annual cycle was examined by a quasi-steady method (Leppäranta, 1993; Yang et al., 2015a). After the open water had refrozen in mid-February, FYI started to grow quickly because of the large temperature difference between ice surface and bottom, but SYI continued to melt until mid-April. The quasi-steady heat balance was the same as Eq. (1). It was clear that, since $F_w>0$, ice grows or melts depending on the thickness. If $T_f-T_o≈10°C$ and $F_w ≈30$ W/m², we have the thickness for equilibrium status (no melting and growing), $H ≈70$ cm. This means ice will melt when thickness is more than 70 cm, which agrees with field observations. The bottom melting of SYI was also observed in McMurdo Sound (Gough et al., 2013), but the melting rate [(0.23 ± 0.02) cm/d] was much smaller than observed in this paper.

Estimating F_w of SYI in March using Eq. (1), the value was

around 100 W/m², which was much larger than the FYI range. In March, a soft layer was observed at 60.0–80.0 cm under the ice surface, which suggests that internal melting occurred. Modeling study by Zhao et al. (2017) showed that SYI in March had a nonlinear temperature profile and was isothermal in the low part. The uniform temperature structure prevented the conductive heat transport, leading to large internal and bottom melting.

5 Conclusions

The spatial and temporal evolution of the landfast ice, including FYI and SYI near the Antarctic ZS during December 2011 to December 2012 was studied using the field observations of the wintering team. The year-long measurements of SYI and winter surveys at several sections across the whole Nella Fjord were conducted for the first time.

The landfast ice in the Nella Fjord showed melt ponds from early December 2011, then ice cover partly broke in late January after a strong cyclone, and open water re-froze in the middle of February 2012 when the air temperature decreased. Other areas of ice surrounded by icebergs and small islands survived until the next winter. This allowed FYI and SYI to be simultaneously observed near ZS for the first time.

In March FYI grew quickly with a mean rate of 0.8 cm/d, but SYI experienced a rapid melting with a mean rate of 2.7 cm/d, which have been related to the nonlinear temperature profile and internal ice melting (Zhao et al., 2017). The SYI started to grow quickly from mid-April and reached the maximum thickness of 167.0 cm, a little larger than FYI maximum thickness of 160.5 cm. The FYI thickness showed minor spatial variations (~1.0 cm), but SYI thickness varied substantially with the largest variation 33.0 cm observed on March 23. This large thickness variation was associated with the particularly uneven SYI bottom.

Snow distribution largely depended on the surface roughness. According to sonar records, large snowfall events rarely occurred before June, which was concordant with observations at the Progress Station. Most snowfall was promptly blown away by the strong wind. The largest snow thickness detected by sonar was 31.0 cm at the end of October. Records at P1, P2, and the tripod did not support the maximum value recorded by sonar, suggesting that manual observations may miss important information because of their low frequency.

Sectional surveys in the Nella Fjord were carried out in winter and the results showed that snow and ice showed a similar pattern of "east thicker, west thinner". The spatial mean snow and ice thickness were 11.3 cm and 202.7 cm, respectively, which was much larger than FYI. The prevailing wind and topography influenced the spatial distribution of snow thickness and then snow melting in summer contributed substantially to MYI thickness as the form of superimposed ice. This mechanism explained the similar snow and ice pattern for MYI in the Nella Fjord.

The estimated oceanic heat flux had a similar annual cycle to that shown by Lei et al. (2010) at ZS and Heil et al. (1996) at Davis, but was different from the two-peak pattern at Mawson (Allison, 1981). The annual average oceanic heat flux of 15.6 W/m², was larger than 5.6 W/m² at ZS in 2006 (Lei et al., 2010), but similar to the findings of Yang et al. (2015a) who estimated the oceanic heat flux of the landfast ice off ZS with a 1-D sea ice thermodynamics model.

It should be noted that the lack of ice core data caused the insufficient analysis of SYI melting and superimposed ice contribution to MYI in this study. Ice temperature/salinity profiles and oceanographic observations beneath the ice should be carried out simultaneously in future to further increase our understanding of the mass balance of FYI and SYI near ZS.

References

Ackley S F, Hibler W D, Kugzruk F K, et al. 1974. Thickness and roughness variations of Arctic multi-year sea ice. Proceedings of Ocean 74-IEEE International Conference Engineering in the Ocean Environment. Halifax, Nova Scotia: 109–117

Allison I. 1981. Antarctic ice growth and oceanic heat flux. Proceedings of the Canberra Symposium, IAHS Publications, 131: 161–170

Fraser A D, Massom R A, Michael K J, et al. 2012. East Antarctic Fast Sea Ice Distribution and Variability, 2000-08. Journal of Climate, 25(4): 1137–1156, doi: 10.1175/JCLI-D-10-05032.1

Giles K A, Laxon S W, Ridout A L. 2008. Circumpolar thinning of Arctic sea ice following the 2007 record ice extent minimum. Geophysical Research Letter, 35: L22502, doi: 10.1029/2008GL035710

Gough A J, Mahoney A R, Langhorne P J, Haskell T G. 2013. Salinity evolution and mechanical properties of snow-loaded multiyear sea ice near an ice shelf. Antarctic Science, (25): 821–831

He J F, Chen B, Wu K. 1998. Developing and structural characteristics of first-year sea ice and with effects on ice algal biomass of zhongshan station, east Antarctica. Journal of Glaciology and Geocryology, 4: 358–367

Heil P, Allison I, and Lytle V I. 1996. Seasonal and interannual variations of the oceanic heat flux under a fast Antarctic ice cover. Journal of Geophysical Research, 101: 25,741–25,752, doi: 10.1029/96JC01921

Heil P. 2006. Atmospheric conditions and fast ice at Davis, East Antarctica: A case study. Journal of Geophysical Research, 111: C05009

Heil P, Gerland S, Granskog M A. 2011. An Antarctic monitoring initiative for fast ice and comparison with the Arctic. The Cryosphere Discussion, 5: 2437–2463, doi: 10.5194/tcd-5-2437-2011

Hoppmann M, Nicolau M. 2012. The influence of platelet ice and Snow on Antarctic Fast Sea Ice. From Knowledge to Action-IPY2012, Montréal, Canada

Kawamura T, Oshima K I, Takizawa T, et al. 1997. Physical, structural and isotopic characteristics and growth processes of fast sea ice in Lützow-Holm Bay, Antarctica. Journal of Geophysical Research, 102: 3345–3355, doi: 10.1029/96JC03206

Kwok R, Sulsky D. 2010. Arctic Ocean Sea ice thickness and kinematics: Satellite retrievals and modeling. Oceanography, 23(4): 134–143, doi: 10.5670/oceanog

Lei Ruibo, Li Zhijun, Cheng Bin, et al. 2010. Annual cycle of fast sea ice in Prydz Bay, east Antarctica. Journal of Geophysical Research, 115: C02006

Leppäranta M. 1993. A review of analytical models of sea-ice growth. Atmosphere-Ocean, 31(1): 123–138, doi: 10.1080/07055900.1993.9649465

Liu Jiping, Curry J A. 2010. Accelerated warming of the Southern Ocean and its impact on the hydrological cycle and sea ice. PNAS, 107(34): 14987–14992, doi: 10.1073/pnas.1003336107

Lu Peng, Li Zhijun. 2014. Uncertainties in retrieved ice thickness from freeboard measurements due to surface melting. Annals of Glaciology, 55(66)

Lytle V I, Massom R, Bindoff N, et al. 2000. Wintertime heat flux to the underside of east Antarctic pack ice. Journal of Geophysical Research, 105(28): 759–769

Maykut G A, Untersteiner N. 1971. Some results from a time dependent thermodynamic model of sea ice. Journal of Geophysical Research, 76: 2–4

McPhee M G, Untersteiner N. 1982. Using sea ice to measure vertical heat flux in the ocean. Journal of Geophysical Research, 87: 2071–2074, doi: 10.1029/JC087iC03p02071

Parkinson C L, Cavalieri D J. 2012. Antarctic sea ice variability and trends, 1979-2010. The Cryosphere, 6(2): 871–880

Perovich D K, Elder B. 2002. Estimates of ocean heat flux at SHEBA. Geophysical Research Letter, 29(9): 1344

Purdie C R, Langhorne P J, Leonard G H, et al. 2006. Growth of first-year fast Antarctic sea ice determined from winter temperature measurements. Annals of Glaciology, 44: 170–176, doi: 10.3189/172756406781811853

Tang Shulin, Qin Dahe, Ren Jiawen. 2006. Sea ice characteristics between Middle Weddell Sea and Prydz Bay, Antarctic during the 2003 Australian summer. Earth Science Frontiers, 13(3): 213–218

Tang Shulin, Qin Dahe, Ren Jiawen, et al. 2007. Structure, salinity and isotopic composition of multi-year fast sea ice in Nella Fjord, Antarctica. Cold Regions Science and Technology, 49: 170–177, doi: 10.1016/j.coldregions.2007.03.005

Worby A P, Geiger C A, Paget M J, et al. 2008. Thickness distribution of Antarctic sea ice. Journal of Geophysical Research, 113: C05S92

Yang Yu, Leppäranta M, Li Zhijun, et al. 2015a. Model simulations of the annual cycle of the fast ice thickness in the East Siberian Sea. Advances in Polar Sciences, 26(2): 168–178

Yang Yu, Li Zhijun, Leppäranta M, et al. 2015b. Modelling the thickness of fast sea ice in Prydz Bay, East Antarctica. Antarctic Science, 28(1): 59–70

Zhao Jiechen, Cheng Bin, Yang Qinghua, et al. 2017. Observations and modelling of first-year ice growth and simultaneous second-year ice ablation in the Prydz Bay, East Antarctica. Annals of Glaciology, 58: 59–67, doi: 10.1017/aog.2017.33

Unusual coastal ocean cooling in the northern South China Sea by a katabatic cold jet associated with Typhoon Mujigea (2015)

Yuxin Shi[1], Lingling Xie[1]*, Quanan Zheng[1, 2], Shuwen Zhang[1], Mingming Li[1], Junyi Li[1]

[1] Guangdong Key Laboratory of Coastal Ocean Variation and Disaster Prediction, Guangdong Ocean University, Zhanjiang 524088, China

[2] Department of Atmospheric and Oceanic Science, University of Maryland, College Park, Maryland 20742, USA

Abstract

This study deals with a unusual cooling event after Typhoon Mujigea passed over the northern South China Sea (SCS) in October 2015. We analyze the satellite sea surface temperature (SST) time series from October 3 to 18, 2015 and find that the cooling process in the coastal ocean had two different stages. The first stage occurred immediately after typhoon passage on October 3, and reached a maximum SST drop of –2°C on October 7 as the usual cold wake after typhoon. The second stage or the unusual extended cooling event occurred after 7 d of the typhoon passage, and lasted for 5 d from October 10 to 15. The maximum SST cooling was –4°C and occurred after 12 d of typhoon passage. The mechanism analysis results indicate that after landing and moving northwestward to the Yunnan-Guizhou Plateau (YGP), Typhoon Mujigea (2015) met the westerly wind front on October 5. The low-pressure and positive-vorticity disturbances to the front triggered meridional air flow and low-pressure trough, thus induced a katabatic cold jet downward from the Qinghai-Tibet Plateau (QTP) passing through the YGP to the northwestern SCS. The second cooling reached the maximum SST drop 4 d later after the maximum air temperature drop of –9°C on October 11. The simultaneous air temperature and SST observations at three coastal stations reveal that it is this katabatic cold jet intrusion to lead the unusual SST cooling event.

Key words: Typhoon Mujigea (2015), second-round cooling, katabatic cold jet, South China Sea, westerly wind front

---

1 Introduction

Typhoon is severe atmospheric vortex movement, occurring frequently in low and middle latitudes. Typhoon landing brings strong winds, rainstorms, and storm surges, which may cause severe disasters and damages to lives and properties in the coastal regions. Sea surface temperature (SST), a basic parameter of the ocean, plays an important role in the strong air-sea interaction during the typhoon process (Cione and Uhlhorn, 2003; Webster et al., 2005; Yang and Hou, 2014; Lin and Chan, 2015; Glenn et al., 2016; Wang et al., 2017). Therefore, SST response to typhoon has attracted much attention of researchers in recent decades (Price, 1981; Wentz et al., 2000; Zheng et al., 2006; Price et al., 2008; Zhang et al., 2014; Allahdadi and Li, 2018).

The typhoon passage usually induces the SST drop in the open ocean (Price, 1981; Walker et al., 2005; D'Asaro et al., 2007; Shan et al., 2014; Zhang et al., 2016). The SST drop ranges from less than –1°C up to –11°C (Lin et al., 2003; Zheng et al., 2010; Chiang et al., 2011). The maximum cooling mostly appears on the right side of the typhoon track (Nelson, 1996; Black and Dickey, 2008). Dare and McBride (2011) analyzed SST response to typhoon in the global oceans from 1981 to 2008. They found

the maximum SST cooling occurred between Day –1 to Day +7 relative to the typhoon passage with the most common occurrence of 1 d after typhoon passage. Xu and Su (2007) analyzed SST response to typhoon in the northwestern Pacific from 2001 to 2005. They found that the maximum SST cooling mostly occurred 2 or 3 d after typhoon passage. It usually takes several days to weeks for recovery, except that accelerated by advection of warm water (Yang et al., 2012b; D'Asaro et al., 2014; Liu et al., 2017). The storm intensity and the translation speed affect the degree of SST response and the recovery time (Price, 1981; Cione and Uhlhorn, 2003; Tsai et al., 2008). In the coastal ocean, the SST drop seems to be less related to the typhoon intensity (Xu and Su, 2007; Xie et al., 2017). The maximum SST drop can also appear on the left side of the typhoon track (Kuo et al., 2014; Lai et al., 2013). The maximum SST drop generally occurs 1 or 2 d after typhoon passage and recovers quickly 3–5 d later (Liang and Ge, 2014), faster than that in the deep ocean (Yang et al., 2012a; D'Asaro et al., 2014). Typhoon not only causes cooling but also warming in the coastal ocean, and the incidence angle of typhoon with respect to the shelf is an important factor affecting SST response as well (Pan and Sun, 2012; Tsai et al., 2012; Xie et al., 2017).

The northern South China Sea (SCS) is an area where the typhoons pass frequently (Wang et al., 2007). The SST drop after typhoon passage has been investigated by previous investigators (Shang et al., 2008; Zheng et al., 2008; Pan and Sun, 2012; Yang et al., 2012a or b?; Zhang et al., 2014; Liu et al., 2014). However, a second-round SST drop after recovery of the first maximum SST drop has seldom reported. Typhoon Mujigea (2015) was a super-typhoon occurred in October 2015. It passed through the northern SCS and landed at Zhanjiang, China on October 3–4, 2015. The coastal ocean SST decreased to a maximum cooling of –2°C on October 7 after 3 d of Mujigea passage (Shi et al., 2017). The SST warmed up on October 8, while a following second-round cooling occurred on October 10 after 7 d of typhoon passage. The maximum cooling reached –4°C and lasted for 5 d, stronger than the first cooling event on October 7. This study reports this unusual second-round cooling event, and aims to reveal the mechanism for the second cooling event further.

This paper is organized as follows: the next section introduces typhoon Mujigea (2015) and datasets used for this study. Section 3 describes the extended cooling event induced by the typhoon. The SST variability at three offshore stations is quantitatively analyzed. Section 4 analyzes the atmospheric and oceanic mechanisms probably affecting the extended SST cooling on the basis of heat budget equation. Section 5 examines the dynamics of interaction of typhoon with the large-scale atmospheric circulation to induce the unusual ocean cooling. Sections 6 and 7 contain the discussion and conclusions, respectively.

2 Data and methodology

2.1 *Data sources*

2.1.1 *Typhoon and wind*
The typhoon data used in this study are downloaded from the Typhoon Database of the Joint Typhoon Warning Center (JTWC), including every 6 h typhoon intensity, center position, center minimum pressure, and maximum wind speed (http://weather.unisys.com/hurricane/w_pacific/2015/index.php/).

The sea surface wind data are ASCAT surface wind data products downloaded from ftp://ftp.ifremer.fr/ifremer/cersat/products/gridded/mwf-ascat/data/daily/Netcdf/2015/. The spatial resolution is 0.25°×0.25°. The temporal resolution is 1 d.

2.1.2 *Air temperature, precipitation and geopotential height*
The air temperature at 2 m and the precipitation data are downloaded from the ERA-Interim provided by European Center for Medium-Range Weather Forecasts (ECMWF) (http://apps.ecmwf.int/datasets/data/interim-full-daily/levtype=sfc/). The spatial resolution is 0.125°×0.125°.The temporal resolution is 6 and 12 h, respectively. The 500 hPa geopotential height data are the NCEP-DOE reanalysis data provided by the Earth System Research Laboratory (ESRL) (http://www.esrl.noaa.gov/psd/data/gridded/data.ncep.reanalysis2.pressure.html). The spatial resolution is 2.5°×2.5°. The temporal resolution is 1 d.

2.1.3 *SST, SSHA and sea surface current*
The SST data are downloaded from the UK Meteorological Office (UKMO) (http://data.nodc.noaa.gov/ghrsst/L4/GLOB/UKMO/OSTIA/2015/). The spatial resolution is 0.125°×0.125°, and the temporal resolution is 1 d.

The sea surface height anomaly (SSHA) data are downloaded from AVISO (http://www.aviso.altimetry.fr/en/data/data-access/gridded-data-extraction-tool.html), which are merged by multiple satellite data. The spatial and temporal resolutions are

0.25°×0.25° and 1 d, respectively.

The sea surface current data are derived from the simple ocean data assimilation (SODA) dataset developed by the University of Maryland, College Park, Maryland, USA (http://www.atmos.umd.edu/~ocean/index_files/soda3.3.1_mn_download.htm). The spatial resolution is 0.25°×0.25°. The temporal resolution is 5 d.

2.1.4 *Surface heat flux*
Surface heat flux data are downloaded from the ERA-Interim provided by European Center for Medium-Range Weather Forecasts (ECMWF) (http://apps.ecmwf.int/datasets/data/interim-full-daily/levtype=sfc/). The data include surface net solar radiation, surface net thermal radiation, surface sensible heat flux and surface latent heat flux. The spatial resolution is 0.125°×0.125°. The temporal resolution is 12 h.

2.2 *Study area and Typhoon Mujigea (2015)*
The study area is the northwestern continental shelf of the SCS ranging from 18° to 23°N and from 109° to 115°E. The Typhoon Mujigea (2015) was generated in the Pacific at 2:00 UTC on October 2, 2015, and moved northwestward. After entering the SCS, its intensity was continuously strengthened. It became a tropical storm at 20:00 on October 2, and entered the study area at 14:00 on October 3. As shown in Fig. 1, Mujigea (2015) developed to be a strong typhoon at 18:00 on October 3, with the maximum wind speed of 48 m/s. The gale circle had a radius of 100 km, covering the northwestern SCS. After stayed in the study area for one day, the typhoon landed at Zhanjiang, China at 14:00 on October 4. The radius of the wind circle reduced, but the maximum wind speed strengthened to 57 m/s. It weakened to a strong tropical storm at 18:00 on October 4, moved northwestward faster to the inland, and continued to weaken to a tropical storm at 15:00 on October 5.

3 Extended impact of Typhoon Mujigea (2015) on SST in the northwestern SCS
Figure 2 shows a time series of the SST anomaly (ΔSST) in the
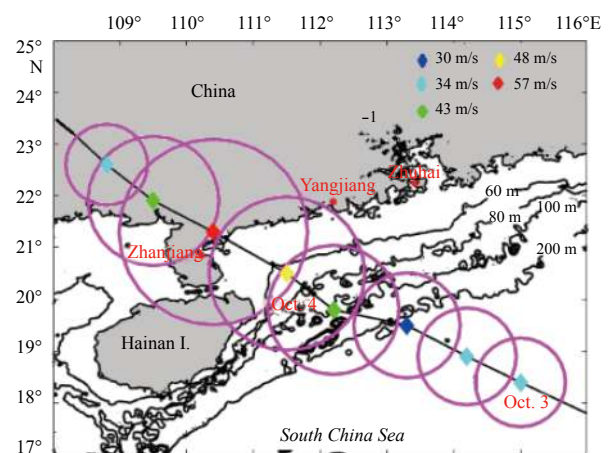
Fig. 1. Track of Typhoon Mujigea (2015) and bottom topography of the northwestern continental shelf of the SCS. Black fold line with magenta circles represents the typhoon track with the range of gale wind. Color diamonds represent the maximum wind speeds. The ocean bottom topographic data are from ETOPO1 (http://maps.ngdc.noaa.gov/viewers/wcs-client/). Isobaths are in m.
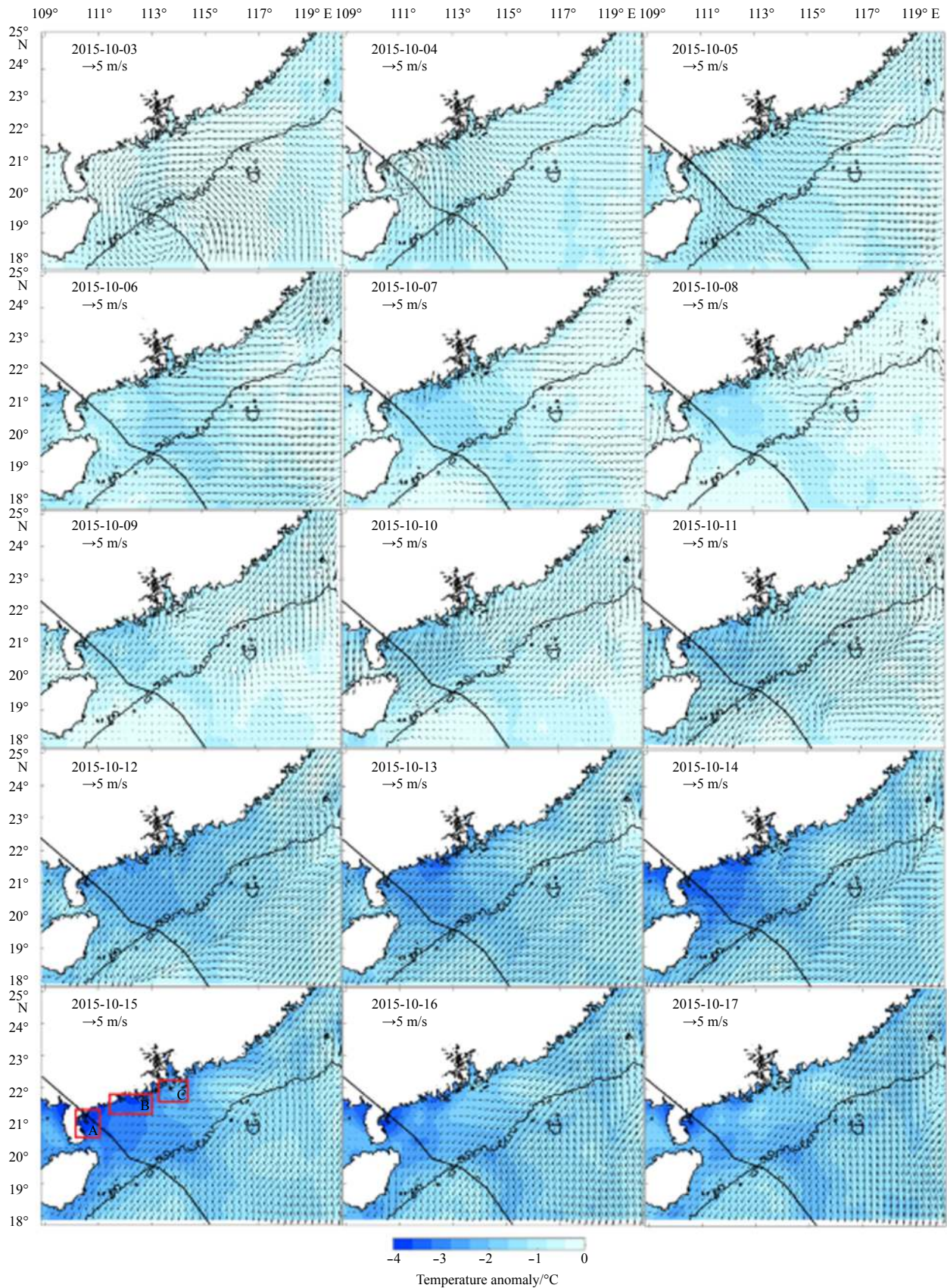
Fig. 2. Time series images of ΔSST and sea surface wind in the northwestern SCS after the Typhoon Mujigea (2015) passage. Black lines represent the typhoon track. Black contours are isobaths of 200 m. Dates of images read year-month-day. Red boxes A, B and C are three offshore test stations near Zhanjiang, Yangjiang and Zhujiang River Estuary, respectively.

northwestern SCS and the corresponding wind field during Typhoon Mujigea (2015) passage. ΔSST is calculated as the daily SST minus the average SST of 7 d from September 26 to October 2 before the typhoon entering the northwestern SCS. One can see that Mujigea entered into the study area on October 3, when its center was located near the 200-m isobath. The SST was cooler in the most area and had a maximum ΔSST of –1°C west of the Zhujiang (Pearl) River Estuary. On October 4, the typhoon center approached the Leizhou Peninsula. ΔSST increased on the right side of typhoon track. On October 5, the northwestern SCS continued to cool down. On October 7, the maximum SST drop reached –2°C. During this period, the sea surface wind changed from the southeasterly wind to the easterly wind, and the wind speeds weakened. The SST began to rebound on October 8. So far, the first cooling stage ended with a maximum ΔSST of –2°C occurred 4 d after typhoon passage. The lag time of the first SST cooling is consistent with previous statistical results (Xu and Su, 2007).

This study focuses on examination of second round of SST drop started on October 10, i.e., the extended cooling event. On the following days, the magnitude and coverage of the negative ΔSST strengthened and spread from the coast to the offshore water. ΔSST reached the maximum value of –4°C near the Leizhou Peninsula on October 15. The study area returned to warming up from October 16 to 17, i.e., the extended cooling lasted for 5 d from October 10 to15.The maximum SST drop was about –4°C on October 15, 12 d after the typhoon passage on October 3. The whole extended cooling process was accompanied by northeasterly wind, which appeared on October 9, reached the maximum wind speed of 15 m/s on October 10–11, and then weakened till October 17.

In order to further understand the extended cooling process, we select three offshore test Stations A–C, where the largest ΔSSTs appeared, for the quantitative analysis. As shown in Fig. 2, Station A is located near Zhanjiang, B near Yangjiang, and C near the Zhujiang River Estuary. The time series of the spatial mean SST anomaly ΔSST$_m$ at the stations are shown in Fig. 3. One can see a similar declined trend at three stations. We further divide the cooling process into two stages. The first stage occurred from October 3 to 7. The second stage, i.e., the extending cooling stage, occurred from October 10 to 15. Between the two cooling stages,

there was a recovery period of about 3 d from October 7 to 10. At the first stage, ΔSST$_m$ declined continuously from –0.2°C to a maximum of –1.5°C at Station A (black line), from –0.5°C to –1.7°C at Station B (blue line), and from –0.5°C to –1.1°C at Station C (red line), respectively. The maximum cooling occurred on October 6 at Station C, one day earlier than that at Stations A and B, and lagged the typhoon passage for 3 d. Then, ΔSST$_m$ at three stations rose on October 8 in the recovery period. The rebound at Station C is the most remarkable with ΔSST$_{mC}$ reached –0.7°C on October 9. However, ΔSST$_m$ declined again on October 10 at the second stage. The maximum ΔSST$_m$ reached –3.6°C, –3.3°C and –2.5°C on October 15 at Stations A, B and C, respectively. The second cooling stage was much stronger than the first stage at all three stations, with the maximum SST drops twice of that at the first stage.

The three-day recovery period between the two cooling stages implies the following possibilities. (1) The first cooling stage and the second one are independent events with different mechanisms. (2) Without the second cooling event, the ocean SST would recover to the normal state after the first cooling event. (3) The second cooling event originates from a remote rather than a local location, so that it needs a couple of days to return to the SCS after the first cooling event.

4 Analysis of causes of extended cooling

The decline of SST results from the ocean heat loss, which can be calculated from the heat budget equation of the ocean surface in the form of (Stewart, 2008)

$$Q_t = Q_{sw} + Q_{lw} + Q_L + Q_s + Q_{adv}, \quad (1)$$

where Q_{sw} is the solar short-wave radiation, Q_{lw} is the net long-wave radiation, Q_L is the latent heat, Q_s is the sensible heat, and Q_{adv} is the ocean advection (Stewart, 2008). Ignoring the radiation variation, the heat loss in the study area may be attributed to the atmospheric processes such as wind, precipitation and cold air, which affect the latent and sensible heat fluxes Q_L and Q_s, and the ocean dynamic processes such as cold flow and cold vortex associated with the advection Q_{adv}. In the case of extended cooling, the effects of these factors will be analyzed as follows.
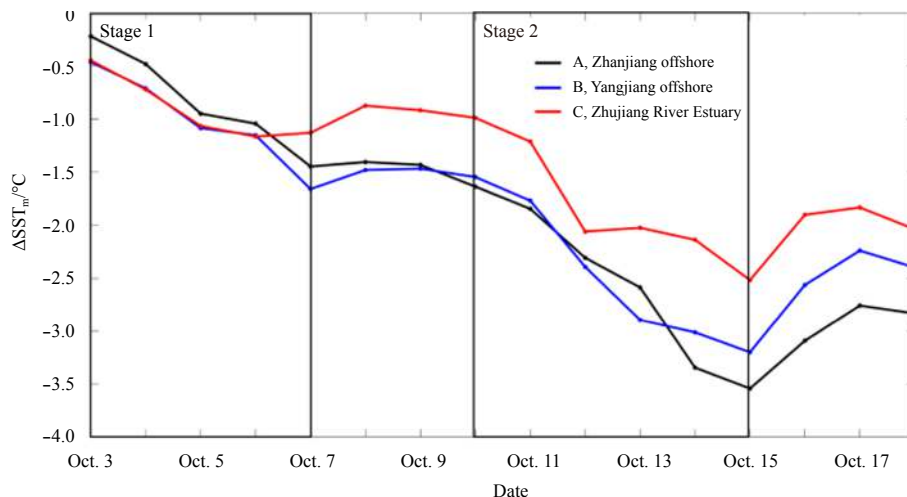

Fig. 3. Variability of the region-averaged ΔSST$_m$ (°C) at Stations A, B and C as shown in Fig. 2. Two black boxes represent the first cooling stage and the extended cooling stage, respectively.
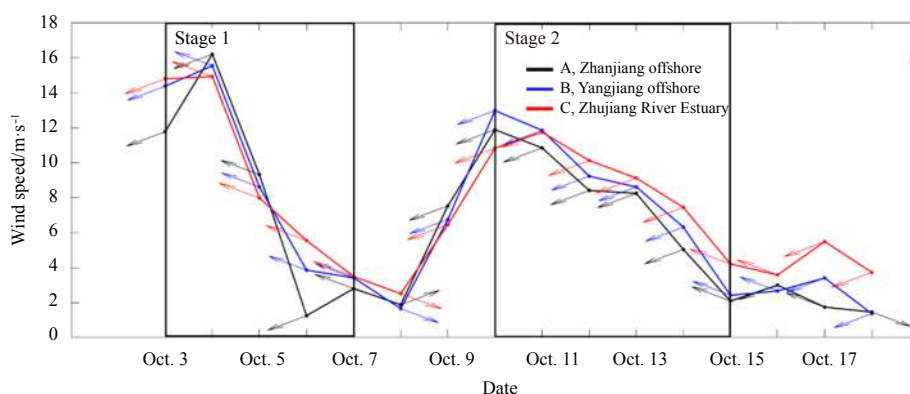
Fig. 4.   Variability of the region-averaged sea surface wind speeds at Stations A, B and C. Arrows represent the wind direction.

4.1   *Sea surface winds*

Figure 4 shows variation of the averaged wind vector at Stations A-C. One can see that the southeasterly winds were prevailed during the first cooling stage from October 3 to 7, consistent with the wind field shown in Fig. 2. The maximum speed was 16 m/s occurred on October 4, when Typhoon Mujiega (2015) landed. The wind speed decreased to about 2 m/s on October 8, and then dramatically increased to 12 m/s on October 11 with the wind direction changing to northeasterly from October 9. At the extended cooling stage from October 10 to 15, northeasterly winds controlled the coastal ocean. However, the wind speeds decreased from a maximum of 13 m/s on October 10 to a minimum of 2 m/s on October 15 at Stations A and B, and one day later at Station C. Comparing the variability of wind speed to that of the SST drop, one can see that the wind speed decreased as ΔSST_m enhanced at the extended cooling stage. The correlation coefficients between the wind speed and the minus values of ΔSST_m are 0.98, 0.92 and 0.84 at Stations A, B and C, respectively.

According to Eq. (1), the sea surface heat loss should be out of phase with the wind speed decrease, i.e., negatively correlated. The above positive correlation coefficients and the northward and seaward spread of the SST cooling shown in Fig. 2 imply that the weakened northeasterly wind should not be related to the extended cooling, but the two accompanied processes are controlled together by large-scale atmospheric circulation system.

4.2   *Precipitation*

Figure 5 shows the precipitation process in the study area after Mujiega (2015) passage. One can see that the precipitation centers were located on the both side of the typhoon track on October 3. The maximum precipitation rate reached 20 mm/d. On October 4, the precipitation center was located on the right side of the typhoon track. The maximum precipitation rate reached 18 mm/d. On October 5, after the typhoon landing, the precipitation decreased and the maximum participation rate of 6 mm/d appeared in the coastal ocean of western Guangdong, China. On October 6, the precipitation centers moved to Hainan Island and the Zhujiang River Estuary with the maximum precipitation rate of 5 mm/d and 6 mm/d, respectively. On October 7, the precipitation continued decreasing with the maximum rate of 4 mm/d. After October 10, a new precipitation process appeared around the Hainan Island but moved southward out of the study area on October 15. On the other hand, the extended cooling area rapidly expanded from the coastal ocean on October 11 to the slope waters near 200 m isobaths on October 15. From the above analysis, we find an important fact, i.e., the development process of pre-

cipitation did not coincide with that of the extended cooling. This means that precipitation is not a decisive factor to form the SST distribution patterns at the extended cooling stage. Therefore, we need to continue the search for other processes, which are significant for the extended cooling.

4.3   *Air temperature*

Besides the wind and precipitation, the air temperature is an important factor directly affecting the sea surface heat flux. Figure 6 shows the time series weather charts of the 2-m temperature anomaly, i.e., ΔT_{2M}, and the potential heights at 500 hPa after Mujiega (2015) passage. ΔT_{2M} is calculated as the daily 2-m air temperature minus that an average value between September 26 and October 2 before Mujiega (2015) entering the northwestern SCS. One can see that the low-pressure center of the typhoon landed over the Leizhou Peninsula on October 4. In the northern coverage of the typhoon, the air temperature dropped with ΔT_{2M} of about –2°C. On October 5, the low center reached the Yunnan-Guizhou Plateau (YGP) and ΔT_{2m} decreased dramatically to –5°C. On October 6, the typhoon center weakened but a meridional low-temperature disturbance band still existed in the zonally-distributed potential height contours. On October 7, a katabatic cold jet from Qinghai-Tibet Plateau (QTP) developed along the trough between the Yunnan Plateau and the Guizhou Plateau. The cold jet intensified and rapidly intruded southwestward to the coastal area near the Beibu Gulf on October 9. On October 10, the cold air expanded both southward and eastward, covered the Beibu Gulf and reached the Guangdong coastal area. The cold air continually intruded southward to cover the northwestern SCS on October 11. The maximum ΔT_{2M} reached –10°C. The cold air over the coastal ocean faded on October 12, and the temperature inland warmed up after October 13.

We further calculate the time series of regional mean of air temperature anomaly, i.e., ΔT_{2Mm}, at Stations A–C. The results are shown in Fig. 7. One can see that the trends of the air temperature variability are very close, i.e., the biggest drop occurred on October 11 at the second cooling stage. The maximum drop of ΔT_{2Mm} was –9°C, –8.5°C and –7.8°C, respectively. Comparing Figs 3 and 7, one can see that variations of air temperature and SST are in good agreement. ΔT_{2Mm} increased on October 8 and 9, and the SST had a corresponding recovery period between the two cooling stages, implying the effect of air temperature on SST variation. ΔT_{2Mm} was the lowest at Station C, and the SST drop was the lowest as well. In addition, ΔT_{2Mm} at the stations simultaneously reached the maximum drop on October 11, while SST simultaneously reaching the maximum drop on October 15, i.e.,

Fig. 5. Time series images of precipitation in the northwestern SCS after the Typhoon Mujigea (2015) passage. Black lines represent the typhoon track. Black contours are isobaths of 200 m. Dates of images read year-month-day.
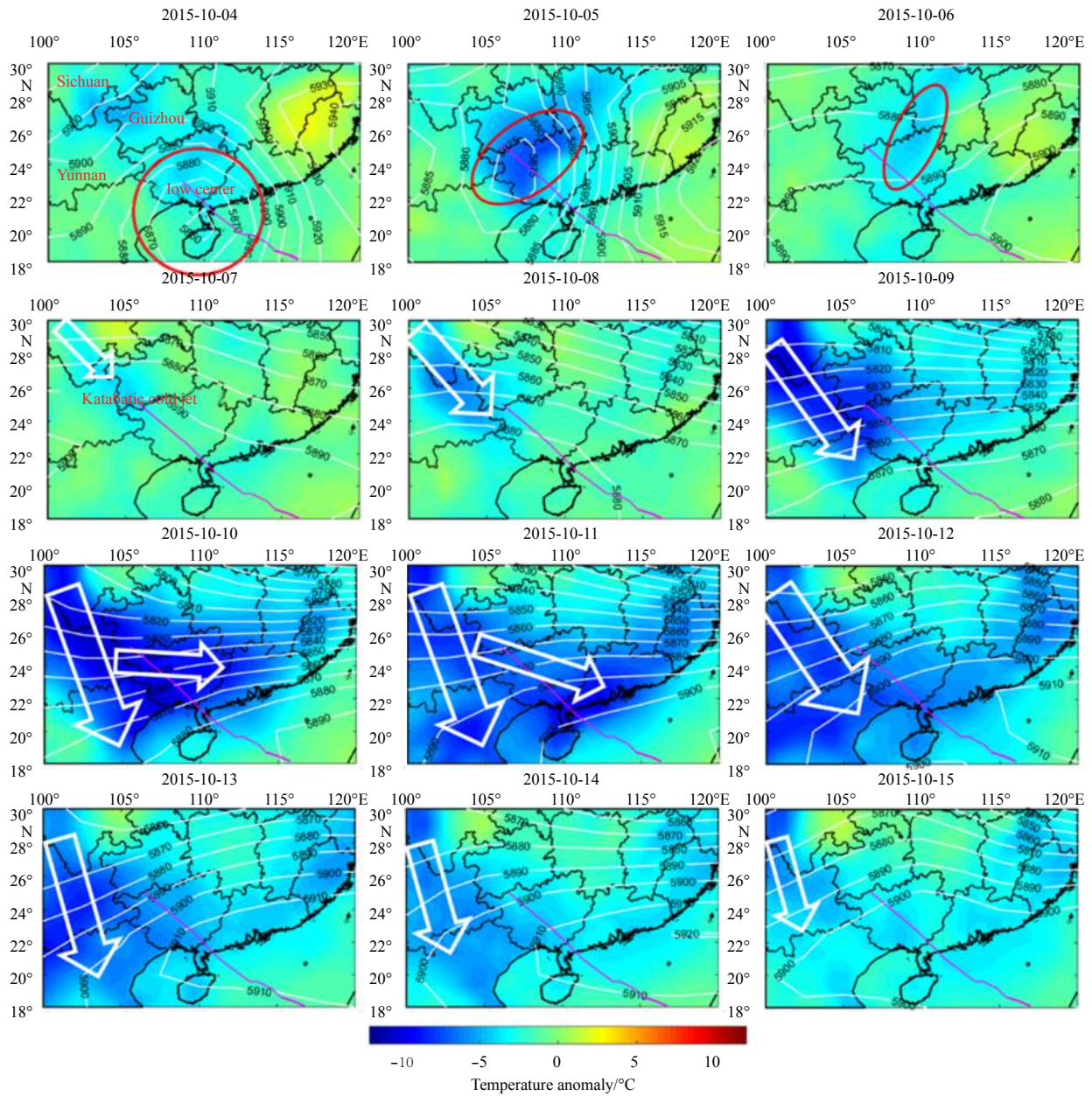
Fig. 6. Time series weather charts of the air temperature anomaly at 2 m (ΔT_{2M}) and the potential height (white contours with numerals in m) at 500 hPa on October 4–15 after Typhoon Mujigea (2015) passage.
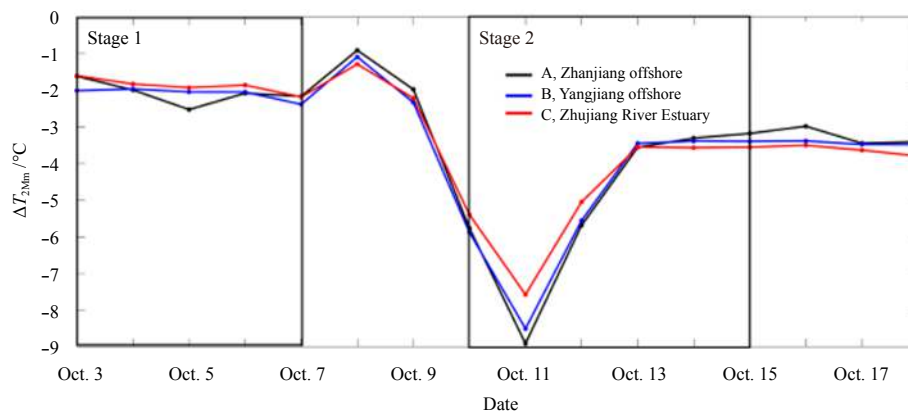
Fig. 7. Variability of the region-averaged sair temperature anomaly at 2 m ΔT2Mm at Stations A, B and C.

lagged behind the air temperature dropping for 4 d.

In order to verify the correlation between the cold air and the extended cooling of SST, we calculate the 4-d lag correlation coefficients between ΔSST_m and ΔT_{2Mm}, since the maximum SST drop occurred 4 d later than the maximum air temperature drop. The results show that ΔSST_m and ΔT_{2Mm} have correlation coefficients of 0.75, 0.82 and 0.75 for Stations A, B and C, respectively, implying that ΔSST_m is highly dependent on ΔT_{2Mm}.

4.4 *SSHA*

Figure 8 shows the SSHA time series images in the study area after Typhoon Mujigea (2015) passage. One can see that there was a negative SSHA center near the coast on the right side of the typhoon track on October 3 and 4, when the typhoon passed over the study area. The negative center moved westward and strengthened on October 5–7, consistent with the SST cooling at the first stage. After October 7, the negative SSHA weakened and disappeared on October 11. From October 12, the SSHA returned back to the climatological features in October, i.e., positive SSHA along the coast with the highest values of about 30 cm near the Zhujiang River Estuary. The SSHA were positive with magnitude increased from about 25 to 35 cm from October 11 to 15, completely unlike the low SSHA from –5 to –40 cm at the first cooling stage, implying that the variation of SSHA did not lead to the extended cooling.

The sea surface current velocity vectors derived from 5-d SODA dataset are also shown in Fig. 8. One can see that there was weak southwestward flow with a magnitude less than 0.1 m/s. The flow directions were consistent with that of the surface wind at the extended cooling stage as shown in Figs 2 and 4. Thus, the water in the northern SCS might be transported southward. However, as shown in Fig. 2, the SST in the northern SCS was unusually higher than that in the study area at the second cooling stage. Thus, the surface current could not bring negative heat flux to contribute to the extended cooling.

In summary, among the atmospheric and oceanic processes, the drop of air temperature is a main mechanism contributing the extended cooling event. Thus, cold air southward intrusion after the disturbance of typhoon will be analyzed in the next section.

5 Typhoon induced cold air southward intrusion

5.1 *Katabatic cold jet*

Typhoon Mujigea (2015) is a super typhoon occurred in local autumn. In this season, cold air develops over the northern Eurasian continent, and the subtropical high (SH) with hot air retreats southward. Between the cold air and the SH, the front of the westerly wind strengthens and favors the cold-air outbreak if meridional flow develops in the zonal wind. The landed typhoon might meet and disturb the westerly wind front, trigger the meridional circulation in the zonal wind, and induce the southward intrusion of cold air (Meng, 1984).

On the large-scale circulation, as shown in the left panels of Fig. 10, the SH (bold-white contour line of 5 880 m) controlled the area south of 30°N before Typhoon Mujigea (2015) landing on October 3, 2015. The front of the westerly wind (dense white contour lines) was zonally distributed at about 30–60°N with its southern edge over the YGP at about 110°E. As the typhoon moved northwestward to the YGP on October 5, it hit the southern edge of the front. Meanwhile, the SH broke into two parts. The low-pressure and positive-vorticity disturbance of typhoon induced the instability of the zonal front. A cyclonic eddy at

about 110°E followed by an anticyclonic meander ridge at 80°E developed in the zonal wind on October 7. The eddy and the meander grew in following days, as well as a meridional trough (black curve) within the eddy. Thus, meridional component of winds was enhanced in the westerly. The eddy moved southeastward with the meridional trough slanted zonally. On October 11, the trough was almost zonally distributed. Then, cold air outbreak swapped the south China as the trough transferred from zonal to meridional orientation.

In local small-scale circulation near the QTP and the YGP as shown in the right panels of Fig. 9, one can see that there was southwesterly wind (black arrow) on October 3–5 when Typhoon Mujigea (2015) approaching. As the eddy and meridional flow developed in the westerly with the typhoon-front interaction, the wind on the QTP and YGP turned to be northwesterly on October 7. Such northwesterly wind favored the cold air on the QTP blowing downward and the katabatic cold jet (blue dash circle) formed at the YGP near the typhoon track (magenta line). The northwesterly wind enhanced on October 9. Thus, the cold jet intensified and intruded southeastward to the Biebu Gulf. On October 11, the cold air extended to the Guangdong coast and the air temperature in the study area dropped most. The cold air intrusion weakened on October 12, when the SH retreated back to the YGP and the wind changed to southwesterly. Then, the SST cooled again with the maximum drop of –4°C occurred 4 d later on October 15.

We further revisit recent studies of typhoons in autumn, and find that typhoons Krosa (2007), Bopha (2012) and Lionrock (2016) attracted cold air intrusion. The SST drop for an extended cooling event is then calculated as the daily SST after typhoon passage minus the average SST of 7 d before typhoon entering the coastal ocean. The results indicate that the maximum SST drop reached –5°C.

5.2 *Net air-sea heat flux*

Figure 10 shows the net air-sea heat flux in the study area during the cold air intrusion. The net heat flux is the sum of the solar short-wave heat flux, the net long-wave heat flux, the latent heat flux and the sensible heat flux, of which the data downloaded from ECMWF. One can see that positive values of $(1–2)\times10^6$ J/m^2 dominated the northern SCS on October 7, indicating the heat absorption from the atmosphere (Fig. 10a). On October 9 (Fig. 10b), the Beibu Gulf changed from absorbing the heat to losing the heat, and the net heat flux reduced to $–1\times10^6$ J/m^2, while other regions still absorbed heat. This is consistent with the time and location of cold air intrusion shown in Fig. 6. On October 11 (Fig. 10c), the whole northern SCS lost heat, and the maximum heat loss exceeded $–6\times10^6$ J/m^2. October 11 was also the day when the air temperature dropped sharply in the northern SCS. On October 16 (Fig. 10d), heat absorption from atmosphere appeared in coastal ocean, consistent with the air temperature and SST recovery after the extending cooling stage shown in Figs 2 and 6.

Time series of the net heat flux during the whole process at Stations A–C were shown in Fig. 10e. One can see that the net heat flux loss from October 8 to 15 was consistent with that of the air temperature anomaly ΔT_{2Mm} shown in Fig. 7, implying the significant contribution of air temperature variation to the sea surface heat flux at the second cooling stage. We calculate the total sea surface heat loss ΔQ by accumulating the net heat flux from October 10 to 15 shown in Fig. 10e. The result is $–8\times10^6$ J/m^2, one to two orders smaller than the previous results of heat loss relatively to depth of the 26°C isotherm (~50–100 m) during typhoon passage (Shay et al., 2000; Sun et al., 2012; Jaimes and Shay, 2015). We believe our result is reasonable if considering the

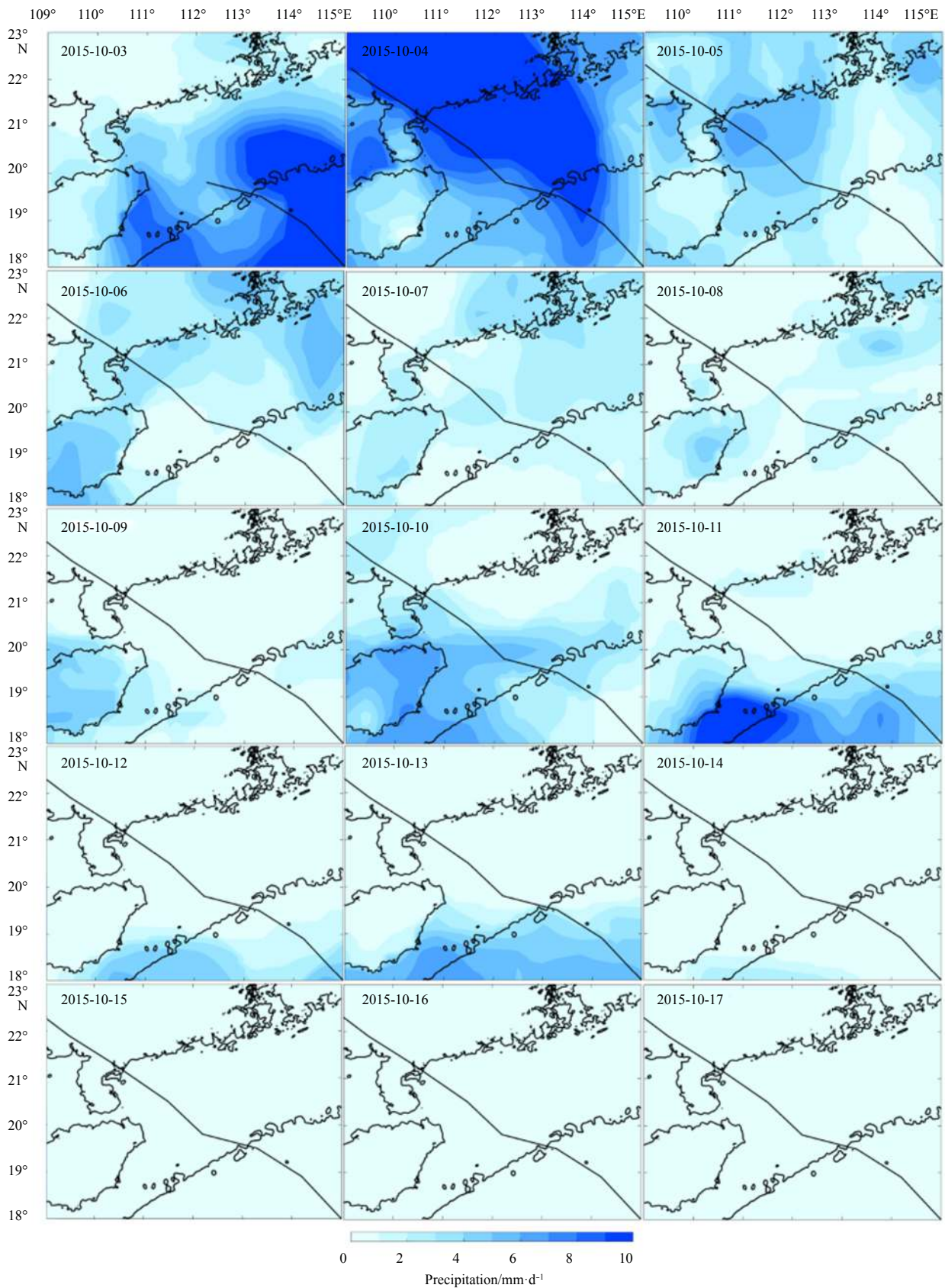**Fig. 8.** Time series images of SSHA in the northwestern SCS after the Typhoon Mujigea (2015) passage. Black lines represent the typhoon track. Black contours are isobaths of 200 m. Dates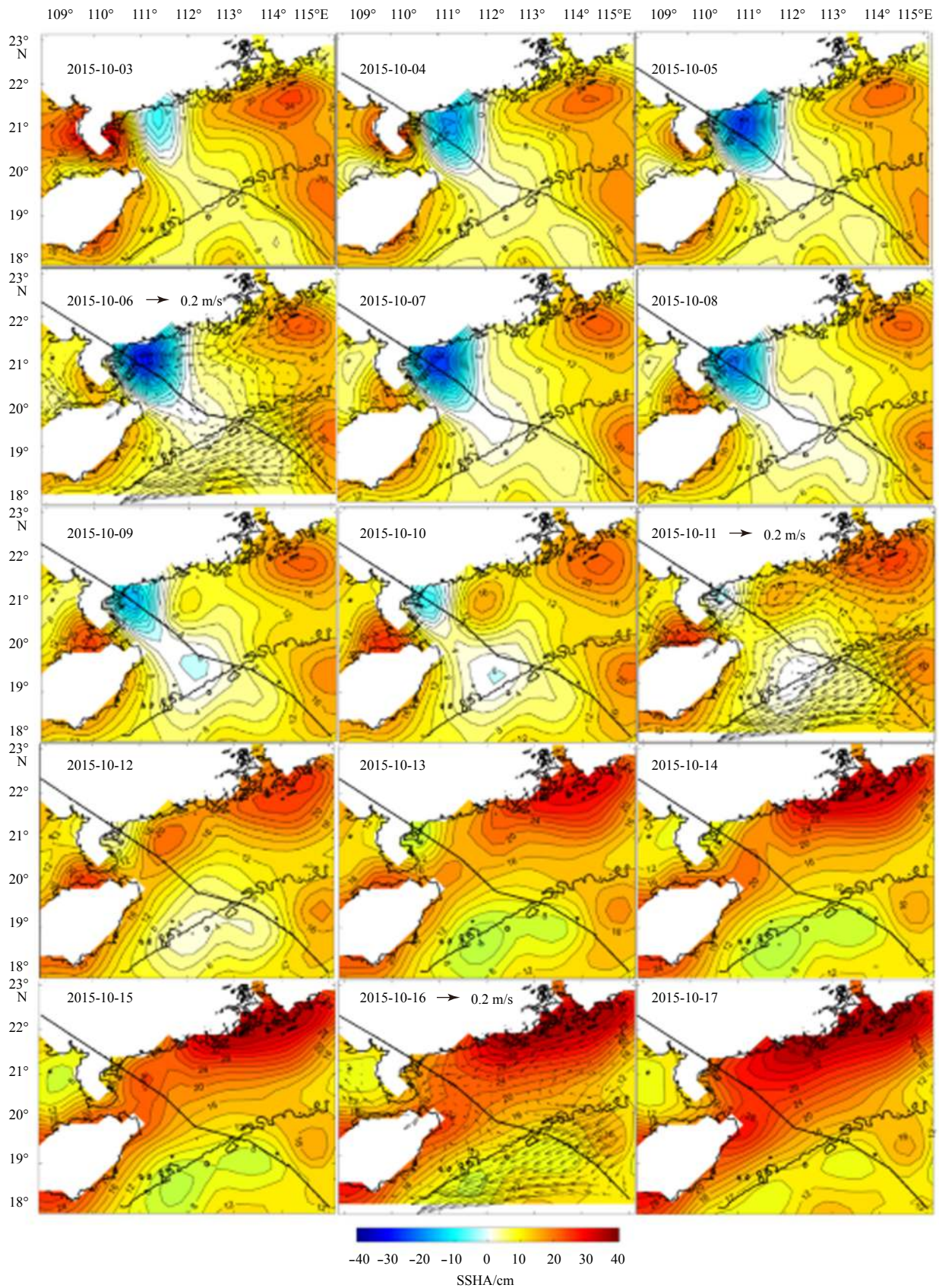 of images read year-month-day. Arrowson October 6,11 and 16 represent the surface current velocity vectors derived from SODA dataset.

different cooling mechanism from the previous investigations. Here, the heat loss was forced by the cold air intrusion and occurred in the near surface layer, while the heat loss during typhoon passage calculated by previous investigators was that in the whole upper layer above 26°C isotherm and supplied the heat to typhoon. In our cases, it is a reasonable estimate that only the top surface 0.5-m water was cooled by the cold air intrusion. According to the Joule's law, the SST cooling ΔSST associated with the heat loss ΔQ is

$$\Delta \mathrm{SST} = \Delta Q / (C_p \times M_a) = \Delta Q / (C_p \times \rho \times h), \qquad (2)$$

where M_a is the water mass per unite area, C_p is the specific heat capacity of the sea water, ρ is the density of the sea surface water, and h is the thickness of the top surface water. Taking $\rho = 1.02 \times 10^3$ kg/m^3, $C_p = 4 \times 10^3$ J/(kg·°C), and $h = 0.5$ m, we have $\Delta SST = -3.9$°C as $\Delta Q = -8 \times 10^6$ J/m^2. This value is almost identical with the maximum SST cooling of -4°C at the second cooling stage given in previous sections, further indicating the significant contribution of the cold air intrusion and the heat loss to the unusual SST cooling event.

Meanwhile, we find there was no remarkable similarity of the heat flux to ΔT_{2Mm} from October 3 to 7, implying the different

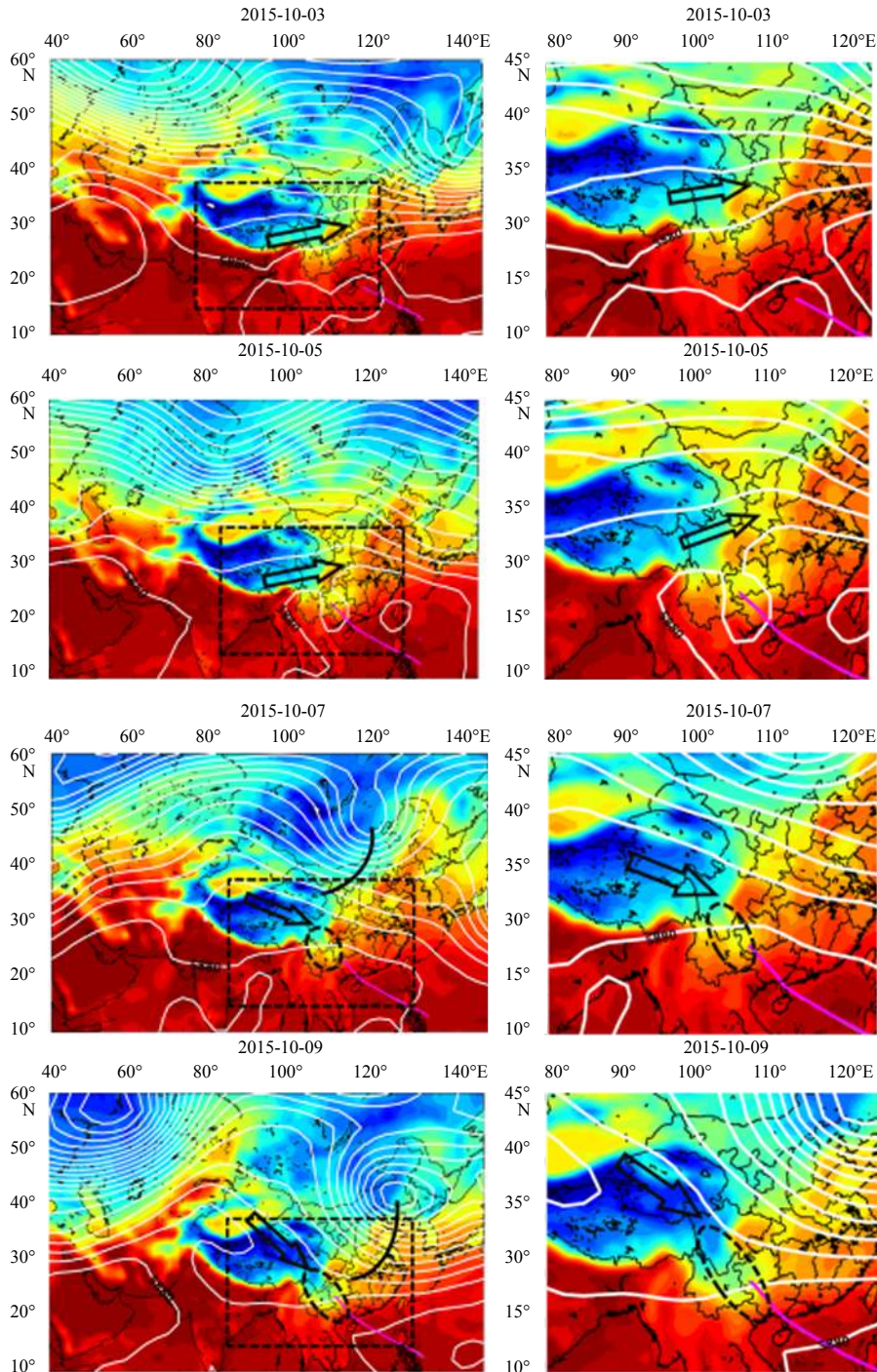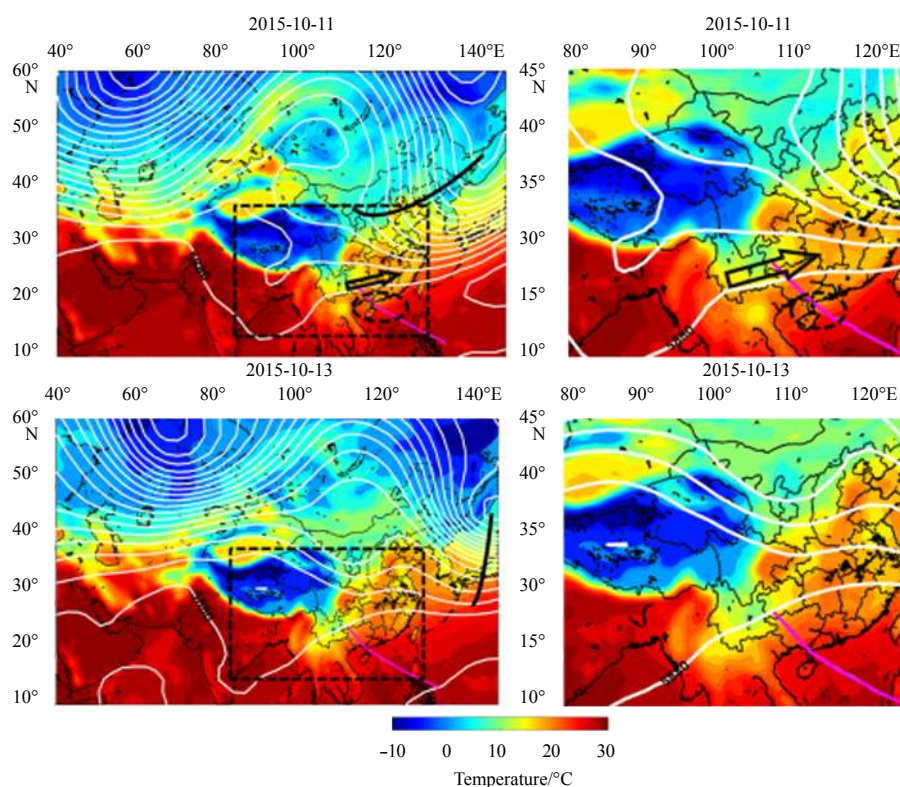**Fig. 9.**

Fig. 9. Variation of the large-scale atmosphere circulation shown by 2-m air temperature and the potential height at 500 hPa (white contours) after Typhoon Mujigea (2015) landed. The bold white contours of 5 880 m represent the subtropical high (SH). The black curve represents the westerly trough. Magenta lines represent the track of Typhoon Mujigea (2015). Dashed black circles represent the cold air intrusion area. Black arrows show the local wind direction.

mechanisms of heat loss at the first stage from the cold air at the second stage. In fact, the SST cooling at the first stage is similar to the typhoon cold wake (D'Asaro et al., 2014). The strong ocean mixing and cold water upwelling directly induced by typhoon play the important roles in the heat loss at the first stage, while the katabatic cold jet induced by landed typhoon dominates the heat loss and SST cooling at the second stage.

6 Discussion

6.1 *Atmospheric or oceanic processes significant for extended cooling event*

The cold wakes after typhoon area generally observed phenomenon in the ocean. The cold anomaly may last for weeks to month before recovery to normal states (D'Asaro et al., 2014). The maximum SST drop of the typhoon wake seldom occurred longer than 7 d after typhoon passage (Dare and McBride, 2011; Yang et al., 2012b). The first cooling event is such a cold wake immediately occurring after typhoon passage and reached a maximum SST drop about 3–4 d later. However, the extend cooling event in the studied case started on the seventh day after typhoon passage, and reached a maximum drop on the twelfth day. The usual extended cooling is different from the cold wake at the first stage, which is attributed to ocean response to typhoon, such as mixing and upwelling (Zhang et al., 2014).

In order to determine the dominant process in the extended cooling event, we analyze both atmospheric and oceanic mechanisms that contribute the ocean surface heat flux in Sections 4 and 5. We find that the atmospheric process of the cold air intru-

sion dominate in the second cooling stage. Here, the temporal-spatial scale analysis provides further evidence to determine the significant oceanic and atmospheric processes. For the time scale, as shown in Fig. 3, there were 7 d from the typhoon passing the northwestern SCS on October 3 to the beginning of the extended SST cooling on October 10, and 12 d to the maximum SST drop on October 15. This is much longer than a 2–3 d time lag of the coastal ocean cooling response to the typhoon passage. On the other hand, the extended SST cooling occurred 4 d after the air temperature drop. This lag time is consistent with that of the ocean response to atmospheric process. For the spatial scale, as shown in Fig. 2, the extended SST cooling spread from the coastal water to the continental shelf area. The coverage of the extended cooling is larger than that covered by the typhoon, and the maximum SST drop is also larger than that at the first stage after typhoon passage. These phenomena imply that there is a large-scale and powerful atmospheric process from the land, rather than the local oceanic processes, having major contribution to the second cooling event. The air temperature drops associated with a katabatic cold jet are thus found to be a dominant mechanism responsible to the extended SST cooling event.

6.2 *Typhoon-westerly interaction and katabatic cold jet formation*

In Section 5, we attribute the cold air intrusion inducing the extended SST cooling event to the interaction of typhoon with the westerly front and the associated katabatic cold jet from the QTP and the YGP.

In fact, previous investigators have analyzed the role of typhoon interacting with the westerly in the cold air outbreaks.
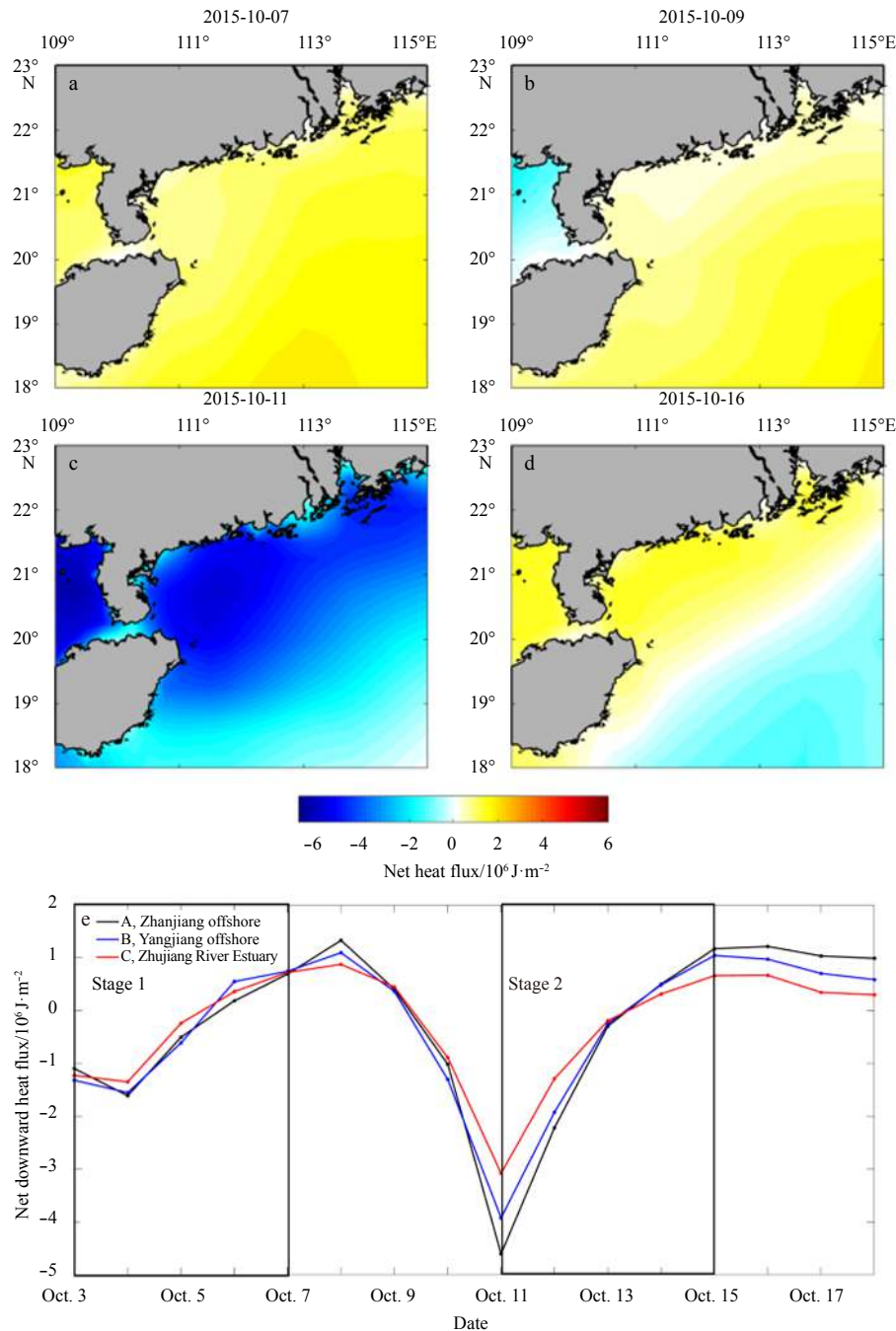
Fig. 10. Time series of net heat flux after the Typhoon Mujigea (2015) passage (a–d), and temporal variability of the regional mean net heat flux at Stations A, B and C (e).

Meng et al. (1983) statistically analyzed the historical typhoons entering Guangxi, China in September and October from 1958 to 1990. They found 16 of total 23 typhoons induced cold dew. Meng (1984) presented that the northwestward typhoon in the SCS in autumn could attract the cold air southward intrusion, when typhoon met the westerly trough. Hu (1989) theoretically analyzed the effects of typhoon on the East Asian circulation in autumn. They suggested that the typhoon is a medium that transfers the energy in the low latitudes to the westerly, reducing the zonal wind in the westerly, enhancing the meridional circulation, and thus inducing southward intrusion of cold air. Zhou and Ren (1992) also found that the enhanced eddy energy by typhoon

helps the cold air accelerating southward. In recent years, researchers investigated the co-effects of autumn typhoon and cold air on precipitation (Chen et al., 2017). The numerical simulation by Wang et al. (2017) showed that the mid-latitude circulation will be more meridional if typhoon strongly interacts with the westerly trough.

In this study, the weather charts clearly show that cyclonic eddy and anticyclonic meander as well as trough and ridge developed in the westerly after Typhoon Mujigea (2015) approaching the southern edge of the westerly front near the YGP. As a consequence, meridional circulation strengthened, and the cold air in the north intruded southward behind the westerly trough.

What is more, the developed northwesterly wind and over the QTP and the YGP led the cold air on the QTP downward as a katabatic cold jet intensively intruding southeastward to the northern SCS. If focusing on the pathway of the cold jet intrusion as shown in Fig. 6, one can see that both the cold jet and the typhoon go through the same air flow corridor approximately along Guangxi, Yunnan, and Guizhou, and the typhoon track is on the right and the cold jet on the left. It seems that this corridor is the pathway for exchange of warm-humidity air from the ocean by the typhoon and the cold-dry air from the QTP by the cold jet. The cold jet seems to be a cold typhoon from the land as the feedback of the atmosphere to the landed typhoon from the ocean, and plays important role in the extended cooling of the coastal ocean. The detailed dynamics of typhoon-westerly interaction and katabatic cold jet worth further pursing in the further research.

7 Conclusions

Using multiple satellite data and weather charts from October 3 to 18, 2015, this study analyzes a new phenomenon of unusual coastal ocean cooling event associated with typhoon Mujigea (2015) passing the northwestern SCS. Mechanisms of the unusual SST cooling event associated with the wind, precipitation, air temperature, surface current, and SSHA are analyzed. The major findings are summarized as follows:

(1) A second coastal cooling event suddenly occurred on October 10 after three-day recovery from the first cooling event starting on October 3, 2015 immediately after typhoon passage. This unique extended cooling event lasted for 5 d, and reached a maximum SST drop of –4°C on October 15, which had been 12 d later since the typhoon passage on October 3, 2015.

(2) The cold air intrusion of a katabatic cold jet lead to the unusual cooling event. The air temperature sharply dropped in advance of the second SST cooling event, and contributed most to the ocean heat loss. The maximum air temperature drop reached –9°C on October 11, 2015, and the maximum SST drop occurred 4 d later. The lagged correlation coefficient of the air temperature drop and the SST drop reached 0.8.

(3) The landed typhoon disturbed the westerly front and triggered meridional air flow and low-pressure trough, so that the katabatic cold jet intruded downward from the QTP, passed through the YGP and moved to the coastal ocean of the northwestern SCS. It is this cold air feedback to typhoon cools the SST again after the first cooling occurring immediately after the typhoon passage.

References

Allahdadi M N, Li Chunyan. 2018. Numerical simulation of Louisiana shelf circulation under hurricane Katrina. Journal of Coastal Research, 34(1): 67–80, doi: 10.2112/JCOASTRES-D-16-00129.1

Black W J, Dickey T D. 2008. Observations and analyses of upper ocean responses to tropical storms and hurricanes in the vicinity of Bermuda. Journal of Geophysical Research, 113(C8): C08009, doi: 10.1029/2007JC004358

Chen Peng, Pang Yue, Zhang Hong, et al. 2017. Analysis of the"9.17" heavy rainfall in Chongqing under the influence of the typhoon and cold air. Torrential Rain and Disasters, 36(3): 227–234

Chiang T L, Wu C R, Oey L Y. 2011. Typhoon Kai-Tak: An ocean' sperfect storm. Journal of Physical Oceanography, 41(1): 221–233, doi: 10.1175/2010JPO4518.1

Cione J J, Uhlhorn E W. 2003. Sea surface temperature variability in hurricanes: Implications with respect to intensity change. Monthly Weather Review, 131(8): 1783–1796, doi: 10.1175//2562.1

D'Asaro E A, Black P G, Centurioni L R, et al. 2014. Impact of typhoons on the ocean in the Pacific. Bulletin of the American Meteorological Society, 95(9): 1405–1418, doi: 10.1175/BAMS-D-12-00104.1

D'Asaro E A, Sanford T B, Niiler P P, et al. 2007. Cold wake of hurricane Frances. Geophysical Research Letters, 34(15): L15609

Dare R A, McBride J L. 2011. Sea surface temperature response to tropical cyclones. Monthly Weather Review, 139(12): 3798–3808, doi: 10.1175/MWR-D-10-05019.1

Glenn S M, Miles T N, Seroka G N, et al. 2016. Stratified coastal ocean interactions with tropical cyclones. Nature Communications, 7: 10887, doi: 10.1038/ncomms10887

Hu Jian. 1989. Effects of recurving typhoon activity on the variations of autumnal circulation over East Asia. Chinese Journal of Atmospheric Sciences, 13(3): 305–312

Jaimes B, Shay L K. 2015. Enhanced wind-driven downwelling flow in warm oceanic eddy features during the intensification of Tropical Cyclone Isaac (2012): Observations and theory. Journal of Physical Oceanography, 45(6): 1667–1689, doi: 10.1175/JPO-D-14-0176.1

Kuo Yichun, Lee Ming'an, Chern C S. 2014. Typhoon-induced ocean responses off the southwest coast of Taiwan. Ocean Dynamics, 64(11): 1569–1581, doi: 10.1007/s10236-014-0776-8

Lai Qiaozhen, Wu Liguang, Shie C L. 2013. Sea surface temperature response to typhoon Morakot (2009) and the influence on its activity. Journal of Tropical Meteorology, 29(2): 221–234

Liang Xiaohong, Ge Lili. 2014. Analysis of impacts of typhoons on sea surface temperature of coastal region of Jiangsu Province. Journal of Aquaculture, 35(10): 37–42

Lin I I, Chan J C L. 2015. Recent decrease in typhoon destructive potential and global warming implications. Nature Communications, 6: 7182, doi: 10.1038/ncomms8182

Lin I I, Liu W T, Wu C C, et al. 2003. New evidence for enhanced ocean primary production triggered by tropical cyclone. Geophysical Research Letters, 30(13): 1718

Liu Shanshan, Sun Liang, Wu Qiaoyan, et al. 2017. The responses of cyclonic and anticyclonic eddies to typhoon forcing: The vertical temperature-salinity structure changes associated with the horizontal convergence/divergence. Journal of Geophysical Research, 122(6): 4974–4989

Liu Zenghong, Xu Jianping, Sun Chaohui, et al. 2014. An upper ocean response to Typhoon Bolaven analyzed with Argo profiling floats. Acta Oceanologica Sinica, 33(11): 90–101, doi: 10.1007/s13131-014-0558-7

Meng Yuanwen. 1984. The effect of typhoon on the southward movement of cold air. Journal of Tropical Meteorology, (1): 84–89

Meng Yuanwen, Wu Rencai, Jiang Boren. 1983. The role of typhoon in the process of cold dew. Journal of Guangxi Meteorology, (4): 1–4

Nelson N B. 1996. Cover the wake of hurricane Felix. International Journal of Remote Sensing, 17(15): 2893–2895, doi: 10.1080/01431169608949116

Pan Jiayi, Sun Yujuan. 2012. Estimate of ocean mixed layer deepening after a typhoon passage over the South China Sea by using satellite data. Journal of Physical Oceanography, 43(3): 498–506

Price J F. 1981. Upper ocean response to a hurricane. Journal of Physical Oceanography, 11(2): 153–175, doi: 10.1175/1520-0485(1981)011<0153:UORTAH>2.0.CO;2

Price J F, Morzel J, Niiler P P. 2008. Warming of SST in the cool wake of a moving hurricane. Journal of Geophysical Research, 113(C7): C07010

Shan Haixia, Guan Yuping, Huang Jianping. 2014. Investigating different bio-responses of the upper ocean to Typhoon Haitang using Argo and satellite data. Chinese Science Bulletin, 59(8): 785–794, doi: 10.1007/s11434-013-0101-9

Shang Shaoling, Li Li, Sun Fengqin, et al. 2008. Changes of temperature and bio-optical properties in the South China Sea in response to Typhoon Lingling, 2001. Geophysical Research Letters, 35(10): L10602

Shay L K, Goni G J, Black P G. 2000. Effects of a warm oceanic feature on Hurricane Opal. Monthly Weather Review, 128(5): 1366–1383, doi: 10.1175/1520-0493(2000)128<1366:

EOAWOF>2.0.CO;2

Shi Yuxin, Xie Lingling, Li Mingming, et al. 2017. Impacts of Typhoon Mujigea on sea surface temperature and chlorophyll-a concentration in the coastal ocean of western Guangdong. Journal of Guangdong Ocean University, 37(3): 49–58

Stewart R H. 2008. Introduction to Physical Oceanography. Texas: Texas A&M University, 51–52

Sun Liang, Yang Juanjian, Xian Tao, et al. 2012. Ocean responses to Typhoon Namtheun explored with Argo floats and multiplatform satellites. Atmosphere Ocean, 50(Sup1): 15–26, doi: 10.1080/07055900.2012.742420

Tsai Y, Chern C S, Wang J. 2008. The upper ocean response to a moving typhoon. Journal of Oceanography, 64(1): 115–130, doi: 10.1007/s10872-008-0009-1

Tsai Y, Chern C S, Wang J. 2012. Numerical study of typhoon-induced ocean thermal content variations on the northern shelf of the South China Sea. Continental Shelf Research, 42: 64–77, doi: 10.1016/j.csr.2012.05.004

Walker N D, Leben R R, Balasubramanian S. 2005. Hurricane-forced upwelling and chlorophyll a enhancement within cold-core cyclones in the Gulf of Mexico. Geophysical Research Letters, 32(18): L18610

Wang Xidong, Liu Hailong, Foltz G R. 2017. Persistent influence of tropical North Atlantic wintertime sea surface temperature on the subsequent Atlantic hurricane season. Geophysical Research Letters, 44(15): 7927–7935, doi: 10.1002/2017GL074801

Wang Guihua, Su Jilan, Ding Yihui, et al. 2007. Tropical cyclone genesis over the South China Sea. Journal of Marine Systems, 68(3–4): 318–326, doi: 10.1016/j.jmarsys.2006.12.002

Webster P J, Hollan G J, Curry J A, et al. 2005. Changes in tropical cyclone number, duration, and intensity in a warming environment. Science, 309(5742): 1844–1846, doi: 10.1126/science.1116448

Wentz F J, Gentemann C, Smith D, et al. 2000. Satellite measurements of sea surface temperature through clouds. Science, 288(4567): 847–850

Xie Lingling, He Chaofeng, Li Mingming, et al. 2017. Response of sea surface temperature to typhoon passages over the upwelling zone east of Hainan Island. Advances in Marine Science, 35(1): 8–19

Xu Wenling, Su Jie. 2007. The impact of typhoons on sea surface temperature in the Western North Pacific Ocean. Periodical of Ocean University of China, 37(S2): 17–22

Yang Bing, Hou Yijun. 2014. Near-inertial waves in the wake of 2011 Typhoon Nesat in the northern South China Sea. Acta Oceanologica Sinica, 33(11): 102–111, doi: 10.1007/s13131-014-0559-6

Yang Jianyuan, Sun Liang, Duan Anmin, et al. 2012a. Impacts of the binary typhoons on upper ocean environments in November 2007. Journal of Applied Remote Sensing, 6(1): 063583

Yang Lei, Wang Dongxiao, Peng Shiqiu. 2012b. Comparison between MM5 simulations and satellite measurements during Typhoon Chanchu (2006) in the South China Sea. Acta Oceanologica Sinica, 31(2): 33–44, doi: 10.1007/s13131-012-0190-3

Zhang Han, Chen Dake, Zhou Lei, et al. 2016. Upper ocean response to typhoon Kalmaegi (2014). Journal of Geophysical Research, 121(8): 6520–6535

Zhang Shuwen, Xie Lingling, Zhao Hui, et al. 2014. Tropical storm-induced turbulent mixing and chlorophyll-*a* enhancement in the continental shelf southeast of Hainan Island. Journal of Marine Systems, 129: 405–414, doi: 10.1016/j.jmarsys.2013.09.002

Zheng Zhewen, Ho C R, Kuo N J. 2008. Importance of pre-existing oceanic conditions to upper ocean response induced by Super Typhoon Hai-Tang. Geophysical Research Letters, 35(20): L20603, doi: 10.1029/2008GL035524

Zheng Zhewen, Ho C R, Zheng Quanan, et al. 2010. Satellite observation and model simulation of upper ocean biophysical response to Super Typhoon Nakri. Continental Shelf Research, 30(13): 1450–1457, doi: 10.1016/j.csr.2010.05.005

Zheng Quanan, Lai R L, Huang N E, et al. 2006. Observation of ocean current response to 1998 Hurricane Georges in the Gulf of Mexico. Acta Oceanologica Sinica, 25(1): 1–14

Zhou Xuequn, Ren Chong. 1992. Effects of autumn recurving typhoon in northwestern Pacific on the cold air over the South China Sea. Marine Forecasts, 9(2): 74–78

Asymmetric response of the eastern tropical Indian SST to climate warming and cooling

Shan Xu[1, 2], Yiyong Luo[2]*, Fukai Liu[1, 2]

[1] College of Oceanic and Atmospheric Sciences, Ocean University of China, Qingdao 266100, China

[2] Physical Oceanography Laboratory, Ocean University of China, Qingdao 266100, China

Abstract

The response of the eastern tropical Indian Ocean (ETIO) to heat fluxes of equal amplitude but opposite sign is investigated using the Community Earth System Model (CESM). A significant positive asymmetry in sea surface temperature (SST) is found over the ETIO—the warming responses to the positive forcing exceeds the cooling to the negative forcing. A mixed layer heat budget analysis is carried out to identify the mechanisms responsible for the SST asymmetry. Results show that it is mainly ascribed to the ocean dynamical processes, including vertical advections and diffusion. The net surface heat flux, on the contrary, works to reduce the asymmetry through its shortwave radiation and latent heat flux components. The former is due to the nonlinear relationship between SST and cloud, while the latter is resulted mainly from Newtonian damping and air-sea stability effects. Changes in the SST skewness are also evaluated, with more enhanced negative SST skewness over the ETIO found for the cooling than heating scenarios due to the asymmetric thermocline-SST feedback.

Key words: tropical Indian Ocean, SST asymmetry, climate warming, climate cooling, negative SST skewness

1 Introduction

The Indian Ocean dipole (IOD) is an intrinsic ocean–atmosphere coupled mode over the tropical Indian Ocean on interannual time scales and is usually phase-locked to austral spring (Saji et al., 1999; Webster et al., 1999). This dipole mode has a positive phase (pIOD) and a negative phase (nIOD). A pIOD (nIOD) event is featured with cold (warm) SST anomalies over the eastern tropical Indian Ocean (ETIO) but warm (cold) SST anomalies over the western tropical Indian Ocean (WTIO), accompanied with easterly (westerly) anomalies of surface winds along the equatorial Indian Ocean. It has great impacts on regional and global climate (Saji and Yamagata, 2003), like droughts in southeast Australia (Cai et al., 2009), rainfall in South America (Chan et al., 2008) and East Africa (Behera et al., 2005) and Indian summer monsoon (Ashok et al., 2004).

Previous studies (Hong et al., 2008, 2010; Cai and Qiu, 2013) found, over the ETIO region, the cold SST anomalies during the pIOD events are able to grow larger than the warm SST anomalies during the nIOD events, and this SST anomaly asymmetry is referred as the negative SST skewness. The formation processes responsible for the negative SST skewness are still a contentious issue. Several possible mechanisms have been proposed, including the nonlinear ocean temperature advection (Hong and Li, 2008; Hong et al., 2010; Cai and Qiu, 2013), the asymmetric thermocline-SST feedback as a part of the Bjerknes loop (Zheng et al., 2010; Ogata et al. 2013; Cai and Qiu, 2013), and the asymmetric SST-cloud-radiation feedback (Hong et al., 2008, 2010). For example, Hong et al. (2008) found that the nonlinear ocean temper-

ature advective process assists to reinforce cold anomalies in the positive events but damp the warm anomalies in the negative events. Zheng et al. (2010) proposed that the asymmetric thermocline-SST feedback is a main driver in generating the negative SST skewness in ETIO: the surface warming induced by subsurface thermocline shoaling is more effective than the cooling resulted from a deepening thermocline, as the mean thermocline in the ETIO is deep. This hypothesis was further verified by Cai and Qiu (2013) and Ng et al. (2014a). Hong and Li (2010) argued that the thermocline feedback itself has little contribution and the skewness comes from a greater damping during nIOD than pIOD due to a breakdown of the SST-cloud-radiation feedback. In more details, during pIOD events the cold SST anomalies in the ETIO decrease cloud cover and atmospheric convection, allowing more incoming shortwave radiation, which in turn dampens the initial cooling. When cold SST anomalies in the ETIO drops to a threshold value, the breakdown occurs, leading to cloud-free conditions. Under this situation, the cold SST anomalies are able to grow freely since the anomalous atmospheric convection and incoming radiation remain constant.

Furthermore, studies have also suggested that the climatological mean state over the tropical Indian Ocean could to some extent alter the IOD frequency as well as the negative SST skewness. Under global warming, for instance, although IOD variance or amplitude has little changes (Zheng et al., 2010), the moderate pIOD events become more extreme (Ng et al., 2014b) and the frequency of extreme pIOD events increases by nearly three times because of the mean state change (Cai et al., 2014). Over the

ETIO, the negative SST skewness weakens by nearly 40% as the shoaling thermocline enhances the thermocline-SST feedback (Zheng et al., 2013). Furthermore, Cowan et al. (2014) found that this negative SST skewness is further enhanced during aerosol forcing than greenhouse gases (GHG) forcing. Therefore, it is important to examine how the mean states over the tropical Indian Ocean will change in response to different external forcings.

Recent studies have found significant changes of the tropical Indian Ocean under both GHG and aerosol forcings, with the former inducing a pIOD-like pattern (Luo et al., 2016) but the latter a nIOD-like pattern (Dong and Zhou, 2014; Cowan et al., 2014). In addition, there exists an asymmetry in the amplitude of SST changes over the ETIO, where the cooling responding to aerosol forcing exceeds the warming to GHG forcing (Li and Luo, 2018). These above conclusions on the tropical Indian Ocean are obtained from simulations with the historical anthropogenic GHG forcing and aerosol single forcing, in which the energy fluxes into the atmosphere-ocean coupled system are opposite in sign but not equal in amplitude, it is still not clear that whether this asymmetry is resulted from the asymmetric amplitude of the energy flux forcing between GHG and aerosols. In response to the uniform heating and cooling of equal amplitude energy heat fluxes, a zonal dipole asymmetric SST pattern is found in the equatorial Pacific Ocean with a positive anomaly in the east but a negative anomaly in the west (Liu et al., 2017). However, the mean climate and its variability are quite different between the tropical Pacific and tropical Indian, such as, the leading interannual mode is ENSO for the former but it is IOD for the latter. In addition, their responses to climate forcings also have significant differences. Under global warming, for example, the tropical Pacific SST is featured with an El Niño-like warming pattern with the ocean dynamics being its leading formation process (e.g., Luo et al., 2015, 2017), while the tropical Indian SST is characterized by a pIOD-like warming pattern with the Bjerknes feedback being its leading formation process (e.g., Zheng et al., 2013; Luo et al., 2016). Given these significant differences between the two basins as described above, it is important to understand the distinct signatures of response over the tropical Indian Ocean under climate warming and cooling. In this study, we employ NCAR's Community Earth System Model (CESM) and impose heat fluxes of equal amplitude but opposite sign into the ocean surface to examine the response of the tropical Indian Ocean to heating and cooling.

As will be shown later, asymmetric changes appears in many of surface and subsurface fields in the tropical Indian Ocean, thus, our main purpose of this study is to investigate the nonlinearity of the tropical Indian Ocean mean state in response to external forcings as well as its maintaining mechanisms. The rest of this paper is organized as follows. Section 2 briefly describes the models and simulations. Section 3 introduces the asymmetric changes over the tropical Indian Ocean under climate warming

and cooling. Section 4 conducts a mixed layer heat budget analysis to examine the relative role of oceanic advection, diffusion, and air-sea heat flux for the SST asymmetry in the tropical Indian Ocean. Section 5 examines the underlying mechanisms that cause the negative SST skewness over the ETIO. Finally, a summary is given in Section 6.

2 Model and experiment design

The model employed by this study is CESM1.1, which is composed of Community Atmospheric Model Version 5 (CAM5), the Community Land Model Version 4 (CLM4) and the Parallel Ocean Program Version 2 (POP2). Three sets of experiments are designed with various degrees of complexity: the fully coupled, the slab ocean, and the partially coupled overriding experiments. For the fully coupled experiments in which all the model components are active, we first integrate an unforced control experiment (CTRL, Table 1) for 250 a. Then, two perturbation experiments, which are labeled HEAT and COOL (Table 1), are integrated for 250 a by adding and subtracting a uniform heat flux of 6 W/m² into the ocean surface, respectively. Results presented below are averaged over the last 100 a, and the sum of the anomalies in the two perturbation runs is used to quantify their asymmetry.

For the slab ocean experiments, we disable the ocean dynamics via employing a motionless slab ocean model (SOM). A control run (CTRL_SOM, Table 1) is integrated for 75 a with ocean heat transport fixed at a repeating annual cycle derived from CTRL. Branching out at the 51th year of the CTRL_SOM, HEAT_SOM and COOL_SOM (Table 1) are then integrated for 25 a with a uniform heat flux of 6 W/m² added into and extracted from the ocean, respectively. Therefore, the relative contribution of ocean dynamical processes can be identified by comparing the slab ocean experiments from the fully coupled experiments.

In order to evaluate the role of shortwave radiation in generating the SST asymmetry in the equatorial Indian Ocean, two partially coupled experiments HEAT_SW and COOL_SW (Table 1), are integrated for 50 a. They are the same as their fully coupled counterparts except that the time series of shortwave radiation is replaced with a seasonally repeating climatological field from CTRL, and thus the shortwave radiation feedback is disabled. By comparing the fully coupled with partially experiments, the role of shortwave radiation for the SST asymmetry can be assessed. Further details of these experiments can be found in Liu et al. (2017).

3 Nonlinear response in spatial structure

In the HEAT experiment, SST is characterized by a pIOD-like pattern over the tropical Indian Ocean, with a larger positive SST anomaly in the WTIO than that in the ETIO (Fig. 1a), an anomalous easterly along the equator (vectors in Fig. 1d) and a shoaling of the thermocline in the ETIO (green lines in Fig. 1g). In the

Table 1. Experiments with CESM1.1

| Experiments	Name	Run/a	Description
Fully coupled experiments	CTRL	250	control run
	HEAT	250	adding uniform 6 W/m² to the ocean
	COOL	250	extracting uniform 6 W/m² from the ocean
Slab ocean experiments	CTRL_SOM	75	slab ocean control run
	HEAT_SOM	25	adding uniform 6 W/m² to the slab ocean
	COOL_SOM	25	extracting uniform 6 W/m² from the slab ocean
Partially coupled experiments	HEAT_SW	50	same as HEAT, but shortwave radiation is specified to climatology
	COOL_SW	50	same as COOL, but shortwave radiation is specified to climatology
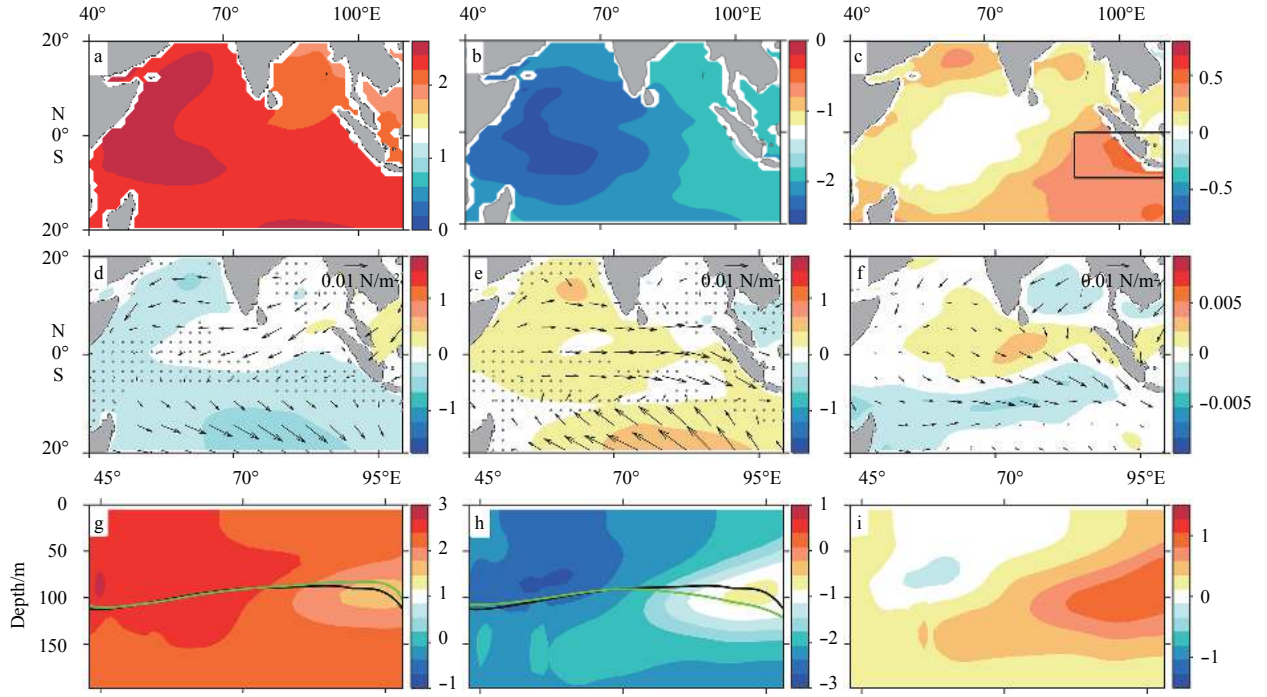
Fig. 1. Changes in SST (shadings; °C) (a–c), surface wind stress (vector; N/m²) and its magnitude wind speed (shadings; m/s) (d–f), and temperature averaged over 5°S–0° (shadings; °C) (g–i) and thermocline depths (black line for CTRL and green line for perturbed run) in HEAT (left), COOL (middle) and their corresponding asymmetry (right). Presented in this and the following figures are results averaged over the last 100 years of model integration if not specified. Black rectangle indicates the ETIO region (10°S–0°, 90°–110°E). The stippling denotes regions where the difference between the CTRL and the perturbation experiments is not statistical significant at the 95% confidence level based on a two-tailed student's *t* test.

COOL experiment, changes in both thermal structure and surface wind are reversed and display a nIOD-like pattern, including a lower negative SST anomaly in the WTIO than that in the ETIO (Fig. 1b), an anomalous westerly along the equator (vectors in Fig. 1e), and a deepening of thermocline over the ETIO (green lines in Fig. 1h). The temperature responses at both surface (Figs 1a and b) and subsurface (Figs 1g and h) are robust (Figs 1g and h) since all the values are significant at 95% confidence level. In addition, the changes in HEAT and COOL are similar to what happens under GHG (Zheng et al., 2010, 2013; Luo et al., 2016) and aerosols (Li and Luo, 2018; Cowan et al., 2014), respectively.

However, the SST changes in HEAT and COOL do not cancel out, especially over the ETIO where there is a positive asymmetry of 0.4°C (Fig. 1c). In addition, the temperature asymmetry appears to be even more significant at the subsurface ocean there, with a maximum of 1.2°C at depth of 100 m (Fig. 1i). This feature is related to the deepening of the thermocline in response to cooling being greater than its shoaling to heating. These above asymmetric responses of temperature in the tropical Indian Ocean are very similar to those between the warm and cold phases of IOD (e.g., Zheng et al., 2010; Cai and Qiu, 2013; Ng et al., 2014a).

4 Mixed layer heat budget analysis

In this section, we examine the mixed layer heat budget to understand the processes that maintain the SST asymmetry over the ETIO. The heat budget analysis is performed for variable mixed layer (Stevenson and Niiler, 1983) following the equation:

$$T_t = Q_n + Q_r + Q_a, \tag{1}$$

where T_t represents the mixed layer temperature tendency; $Q_n = (Q_t - Q_h)/(\rho_0 c_p h)$ is the net surface heat flux into the upper ocean, where Q_t is the total surface heat flux into the ocean, Q_h is the heat penetration at the bottom of the mixed layer, and ρ_0 and c_p are the density and specific heat of sea water; Q_r represents the ocean heat transport by unresolved subgrid-scale processes as well as submonthly oceanic processes, and Q_a is oceanic advection which is comprised of zonal (Q_x), meridional (Q_y), and vertical (Q_z) components. The sum of Q_r and Q_a is the total ocean heat transport effect due to three-dimensional advection and diffusion, which balances the net surface heat flux into the ocean. All the heat budget terms are defined as downward positive and upward negative.

To make a more thorough investigation of the ocean dynamics, the oceanic advection terms are further decomposed into linear and nonlinear parts as follows:

$$\begin{cases} Q_x = -\left(\bar{u}T_x' + u'\bar{T}_x\right) - u'T_x', \\ Q_y = -\left(\bar{v}T_y' + v'\bar{T}_y\right) - v'T_y', \\ Q_z = -\left(\bar{w}T_z' + w'\bar{T}_z\right) - w'T_z', \end{cases} \tag{2}$$

where u, v and w are the zonal, meridional and vertical velocity averaged over the mixed layer, and T_x, T_y and T_z are the mixed layer temperature gradients in zonal, meridional and vertical directions, respectively. The overbar and prime represent the climatological mean and departure from the mean, respectively. The terms within the first bracket on the right hand side represent the two linear dynamic heating (LDH) terms, and the last terms on

the right hand side represent the nonlinear dynamic heating (NDH) terms.

4.1 *Ocean heat transport*

Figure 2 shows the spatial distribution of the total ocean heat transport, oceanic advection, and diffusion in HEAT and COOL, along with their asymmetries over the tropical Indian Ocean. It is clear that the total ocean heat transport, especially its vertical advection and diffusion components, favors the SST asymmetry over the ETIO (contours in the right panels of Fig. 2)

For the HEAT experiment, all of the zonal, meridional, and vertical advections act to cool the ETIO (shadings in Figs 2a, d and g) and the changes in most of the ETIO region are of statistical significance at 95% confidence level. A decomposition of these advections finds that the anomalous cooling in the zonal advection is resulted mainly from anomalous westward surface current (Fig. 3a), the anomalous cooling in the meridional advection is due to a reduction of both southward meridional current and meridional temperature gradient (Fig. 3b), and the anomalous cooling in the vertical advection is a result of both increased stratification and strengthened upwelling (Fig. 3c).

For the COOL experiment, it is not surprising the signs of the anomalous meridional and vertical advections (shadings in Figs 2e and h) are reversed compared to those in the heating experiment. However, these anomalies in COOL appear to be larger than those in HEAT. In addition, zonal advection also exerts a cooling effect in the ETIO in the cooling scenario (Fig. 3a). However, different from the heating scenario, this cooling effect

is primarily due to the change of zonal temperature gradient, including $-\bar{u}T_x^{'}$ and $-u^{'}T_x^{'}$.

According to Fig. 3, the overall positive asymmetry in advection is mainly contributed from its meridional and vertical components. A further decomposition into LDH and NDH terms finds that the LDH terms are decisive in generating the positive SST asymmetry over the ETIO, with a larger contribution from the vertical (0.04°C/month) than the meridional direction (0.02°C/month). In more details, the asymmetric meridional advection (Fig. 3b) is due largely to the linear term $-\bar{v}T_y^{'}$. For the vertical advection (Fig. 3c), while the nonlinear term $-w^{'}T_z^{'}$ plays a damping role, both of its linear terms $-w^{'}\bar{T}_z$ and $-\bar{w}T_z^{'}$ contribute to the positive asymmetry, with the former's contribution being more significant than the latter's.

The diffusion term significantly warms the upper ocean over the ETIO in HEAT (shadings in Fig. 2j) but has a cooling effect in COOL (shadings in Fig. 2k). Their combined effect of HEAT and COOL results in a positive asymmetry over the ETIO and contributes to the SST asymmetry there (shadings in Fig. 2l).

The above analysis indicates the decisive role of ocean dynamical processes in generating the SST asymmetry over the ETIO. To further vindicate this, we perform a set of experiments with a SOM (see Section 2 for details) in which ocean heat transport is prescribed, and thus the ocean dynamical effect can be inferred by comparing its result with that from the fully coupled experiments. As shown in Fig. 4, without the modulation of ocean dynamical effect, the maximum warming (cooling) appears over
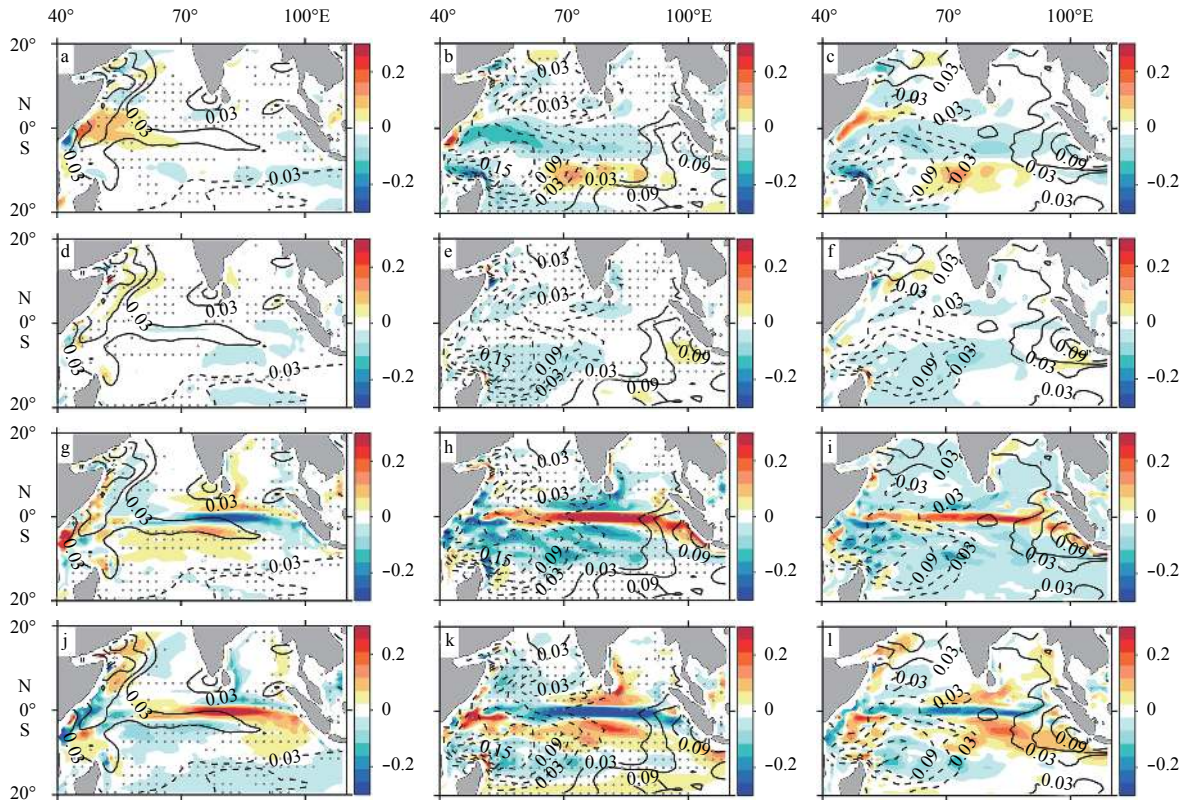
Fig. 2. Changes in the zonal advection (a–c; °C/month), meridional advection (d–f; °C/month), vertical advection (g–i; °C/month), and diffusion (shadings; °C/month) in HEAT (left), COOL (middle) and their asymmetry (right). Superimposed are the changes in the total ocean heat transport (contour interval (CI) = 0.03°C/month), with the solid and dashed contours denoting positive and negative anomalies, respectively. The stippling denotes regions where the difference between the CTRL and the perturbation experiments is not statistical significant at the 95% confidence level based on a two-tailed student's *t* test.

Fig. 3. Decomposition of zonal (a), meridional (b), and vertical advections (°C/month) (c) averaged in the ETIO in HEAT (red bars) and COOL (blue bars) as well as their asymmetry (grey bars).

the southeastern Indian Ocean in HEAT_SOM (COOL_SOM) rather than western Indian Ocean in fully coupled experiment HEAT (COOL). These SST anomalies in the slab ocean experiments resu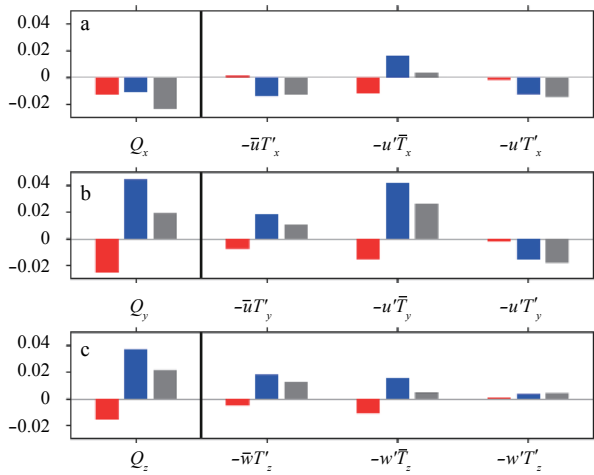lt in a negative SST asymmetry over the ETIO (Fig. 4c), which is in sharp contrast to the positive SST asymmetry there (Fig. 1c) in the fully coupled experiments. Therefore, the slab ocean experiments verify that the ocean dynamic processes are essential for generating the SST asymmetry over the ETIO in the fully coupled experiments.

4.2 *Surface heat flux*

Figure 5 shows the changes in the air-sea surface heat flux (Q_n) and its four components in the HEAT and COOL experiments as well as their asymmetries. The net surface heat flux (contours in Fig. 5) acts to balance the ocean heat transport, implying that the surface heat flux should act to dampen the SST asymmetry over the ETIO.

For the HEAT experiment, the total surface heat flux exerts a warming effect over the ETIO (contours in the left panels of Fig. 5), resulting from a combination of warming in longwave radiation (Fig. 5a) and cooling in both latent heat flux (Fig. 5g) and shortwave radiation (Fig. 5d). By comparison, the effect of sensible heat flux is relatively small. The positive anomaly in longwave radiation is attributed to the enhanced water vapor feedback: an increase of water vapor content in a warmer climate leads to an increase of downward longwave radiation, and thus warm the surface ocean (Du and Xie, 2008).

For the COOL experiment, the ETIO is featured with a pro-

nounced heat loss (contours in the middle panels of Fig. 5). This heat loss is mainly attributed to the cooling effect from the shortwave radiation and longwave radiation (Figs 5b and e). On the contrary, the latent heat flux plays a warming role (Fig. 5h). The cooling effect from the shortwave radiation is related to an increase of total cloud cover over the ETIO region, which hinders shortwave radiation from reaching the surface ocean.

As for their asymmetry, the net surface heat flux acts to dampen the positive SST asymmetry over the ETIO (contours in the right panels of Fig. 5) and the damping effect comes mainly from shortwave radiation and latent heat flux (Figs 5f and i). While the longwave radiation exerts a positive contribution for the SST asymmetry over the ETIO (Fig. 5c), the sensible heat flux has negligible contribution (Fig. 5l).

The above analysis finds that the shortwave radiation is the primary factor in reducing the positive SST asymmetry in the ETIO. In order to further demonstrate this, we apply an overriding technique to the CESM to eliminate the contribution of shortwave radiation (see Section 2). Figure 6 shows the SST changes in the partially coupled experiments. It is found that, without the regulation of shortwave radiation, there appears a nIOD-like SST pattern in the tropical Indian Ocean in both warming and cooling scenarios (Figs 6a and b), resulting in a strong positive SST asymmetry over the ETIO (Fig. 6c). Compared with the fully coupled experiments (Fig. 1c), this SST asymmetry in the partially coupled experiment is much larger in amplitude, indicating the essential role of the shortwave radiation in damping the SST asymmetry over the ETIO.

In addition to the shortwave radiation, the latent heat flux is another damping factor for the positive SST asymmetry over the ETIO. Following Luo et al. (2017), it can be further decomposed into four major terms: Newtonian cooling (Q_{EO}), the effects of wind-evaporation-SST (WES) feedback (Q_{EW}), air-sea surface temperature difference (Q_{EdT}), and relative humidity (Q_{ERH}). As shown in Fig. 7, the negative residual latent heat flux (–2.1 W/m^2) in the ETIO between HEAT and COOL comes from Newtonian cooling Q_{EO}(–3.1 W/m^2) and air-sea surface temperature difference Q_{EdT} (–2.0 W/m^2), while the WES feedback Q_{EW} (1.0 W/m^2) and air-sea surface temperature difference Q_{EdT} (2.0 W/m^2) operate to impede the damping and avail the SST asymmetry formation there. The Q_{EO} asymmetry results from a stronger Q_{EO} induced by a larger SST anomaly in HEAT than COOL. The asymmetric change in Q_{EdT} is associated with the change in air-sea temperature difference. Specifically, the surface ocean gets warmer than its overlying air temperature in HEAT while the air-sea temperature difference barely changes in COOL.

The positive longwave radiation asymmetry in the ETIO results from the nonlinear relationship between saturation vapor pressure and temperature. In the warming climate, the same size of temperature anomalies can cause larger anomalies of satura-
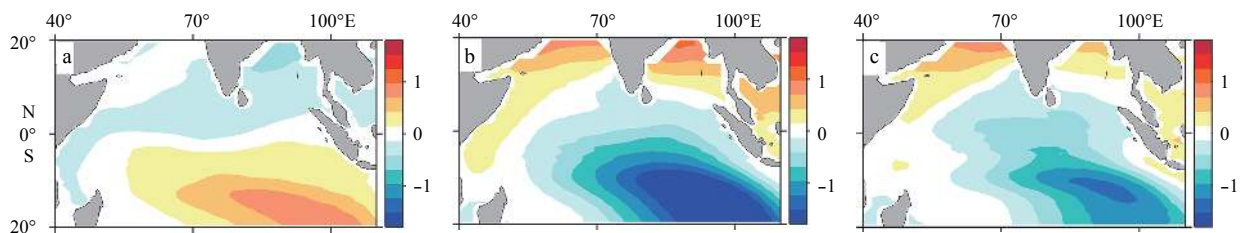

Fig. 4. Changes in SST (°C; mean values removed) in the slab ocean experiments HEAT_SOM (a), COOL_SOM (b), and their asymmetry (c).
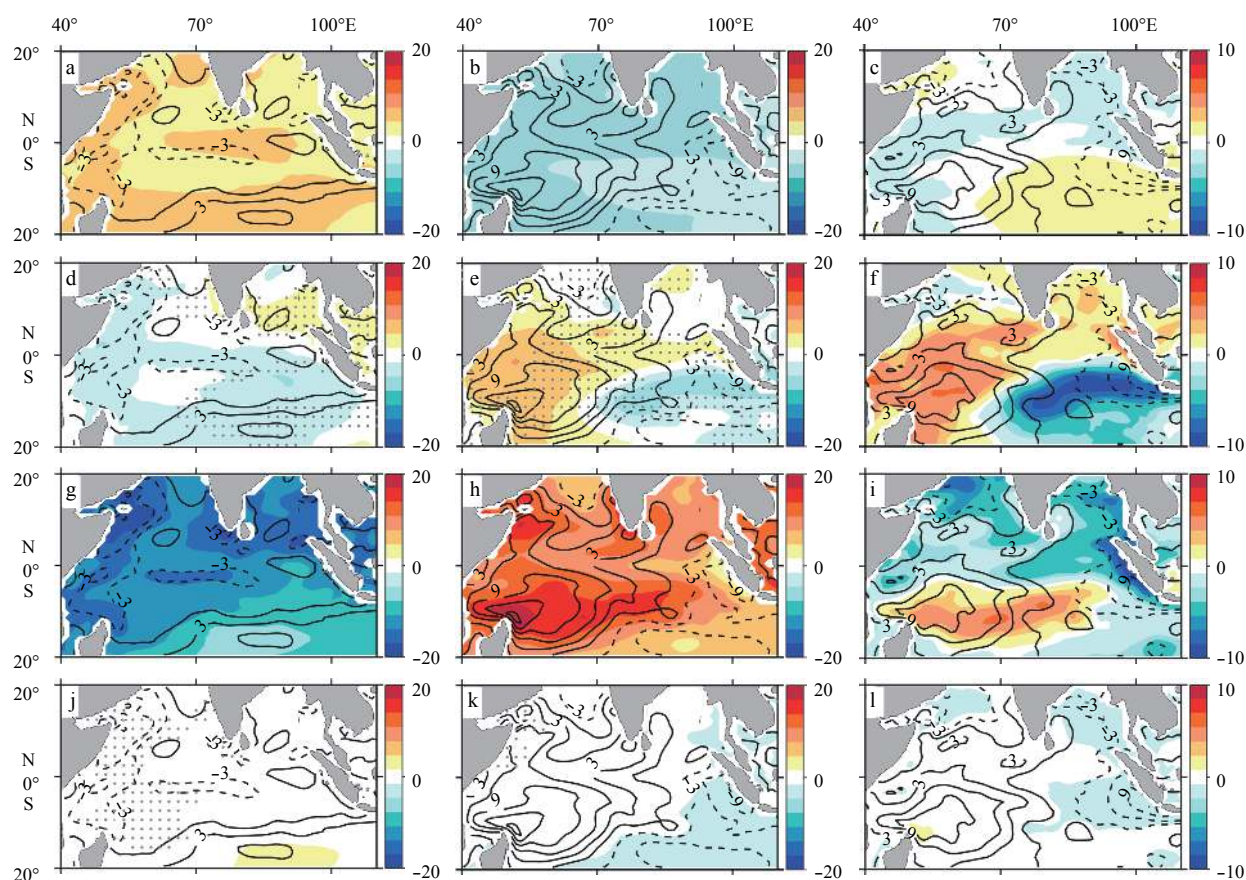
Fig. 5. Changes in longwave radiation (a–c; W/m²), shortwave radiation (d–f; W/m²), latent heat flux (g–i; W/m²) and sensible heat flux (shadings: W/m²) (j–l) in HEAT (left), COOL (middle) and their corresponding asymmetry (right). Superimposed are changes in the net surface heat flux (CI=3 W/m²), with the solid and dashed contours denoting positive and negative anomalies, respectively. The stippling denotes regions where the difference between the CTRL and the perturbation experiments is not statistical significant at the 95% confidence level based on a two-tailed student's *t* test.
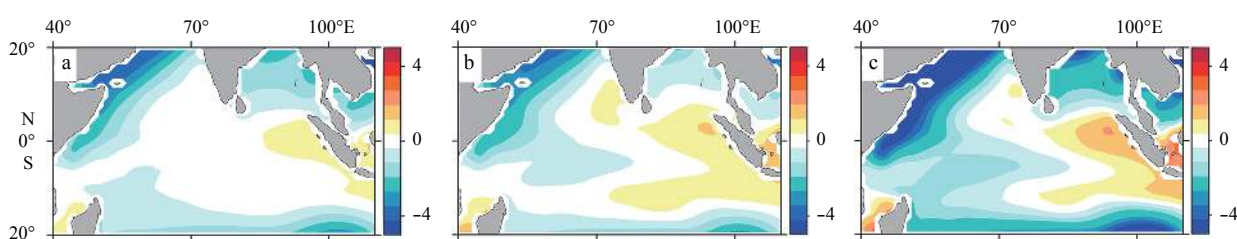

Fig. 6. Changes in SST (°C; mean values removed) in the shortwave overriding experiments HEAT_SW (a), COOL_SW (b), and their asymmetry (c).

tion vapor pressure (Huang et al., 2016). In consequence, climate warming can cause bigger water vapor anomalies in the lower troposphere in contrast to climate cooling. This leads to a positive longwave radiation asymmetry over the ETIO with the magnitude of increase in longwave radiation in HEAT being larger than that of decrease in COOL (Figs 5c, a and b).

5 Response of the SST skewness

Our previous analysis has found that the changes in the TIO under HEAT and COOL are not symmetric, with a positive SST asymmetry over the ETIO. Another important characteristic of the ETIO region is the negative SST skewness during boreal autumn. Skewness is commonly used to measure the asymmetric

statistics of SST anomalies between the interannual pIOD and nIOD events (Hong et al., 2008; Zheng et al., 2010). The skewness is calculated as $m_3/(m_2)^{3/2}$, where $m_k = \sum_{i=1}^{N} \dfrac{\left(x_i - \bar{X}\right)^k}{N}$ is the kth moment and x_i is the ith datum, $\bar{X}$ the climatological mean, and N the length of the data. In this section, we investigate the mechanisms that give rise to the negative SST skewness in ETIO in the control simulation, and then compares the change of SST skewness in the climate warming and cooling conditions.

Figure 8 shows the distribution of SST skewness in CTRL, HEAT and COOL. A significant negative skewness appears over Sumatra-Java coast (Fig. 8a), indicating the amplitude of SST anomalies is larger for cold than warm events in the ETIO. Note that
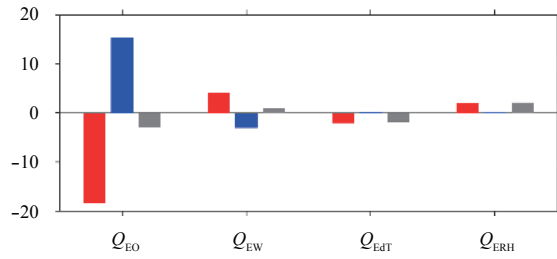
Fig. 7. Changes in latent heat flux components including Newtonian cooling effect Q_{EO}, WES effect Q_{EW}, stability effect Q_{EdT}, and relative humidity effect Q_{ERH} (in W/m²) in HEAT (red bar), COOL (blue bars) and their asymmetry (gray bars) averaged over the ETIO region.

the maximum skewness shows a strong westward bias, which is a common phenomenon in climate models (Cowan et al., 2014). A strong negative SST skewness in the ETIO is also found in both the warming and cooling simulations with a westward bias. While this negative SST skewness over the ETIO region is found to be significantly enhanced in COOL, it does not change much in HEAT.

As discussed in the introduction, previous studies suggested that the negative SST skewness in the ETIO is mainly attributed to

the Bjerknes feedback, nonlinear dynamic heating (NDH) and asymmetric SST-cloud-radiation feedback. Here, we evaluate these feedback processes to reveal the mechanisms that contribute to the negative SST skewness over the ETIO region in our control simulation. To this end, we formulate composites for the positive and negative samples and then calculate the coupling coefficients of the dynamical and thermodynamical feedbacks through linear regression for each sample separately (e.g., Cai and Qiu, 2013; Liu et al., 2014; Cowan et al., 2014). The regression coefficient can be regarded as the strength for each feedback. The calculation is based upon the last 100 a of the model integration during May to November.

The first feedback we focus on is the Bjerknes feedback. It involves the interactions between SST and wind, wind and thermocline, and thermocline and SST. Here, the thermocline depth is defined as the location of the maximum vertical gradient of temperature. The central tropical Indian Ocean (CTIO, 5°S–5°N, 70°–90°E), where the response of wind to SST is the greatest (not shown), is selected to evaluate the wind response (Hong et al., 2008). Figure 9a shows the scatter diagram of averaged wind stress anomalies in the CTIO region versus SST anomalies in the ETIO region. It can be seen that a SST anomaly of the same magnitude over the ETIO induces the size of anomalous easterlies being slightly smaller for negative samples than the size of anomalous westerlies for positive samples, indicating that this response
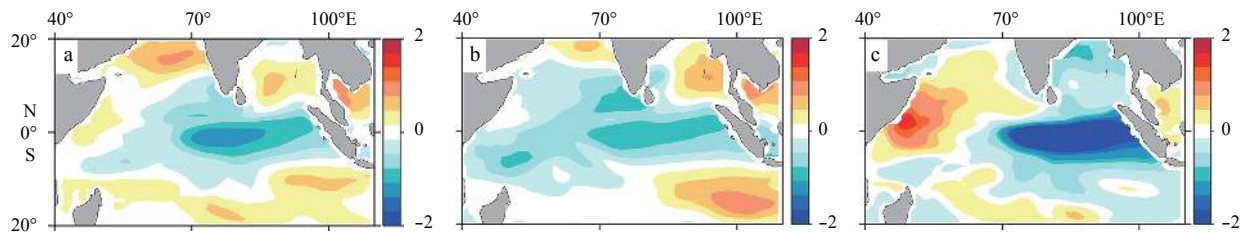
Fig. 8. Distribution of the SST skewness (°C) during September to November in CTRL (a), HEAT (b) and COOL (c).
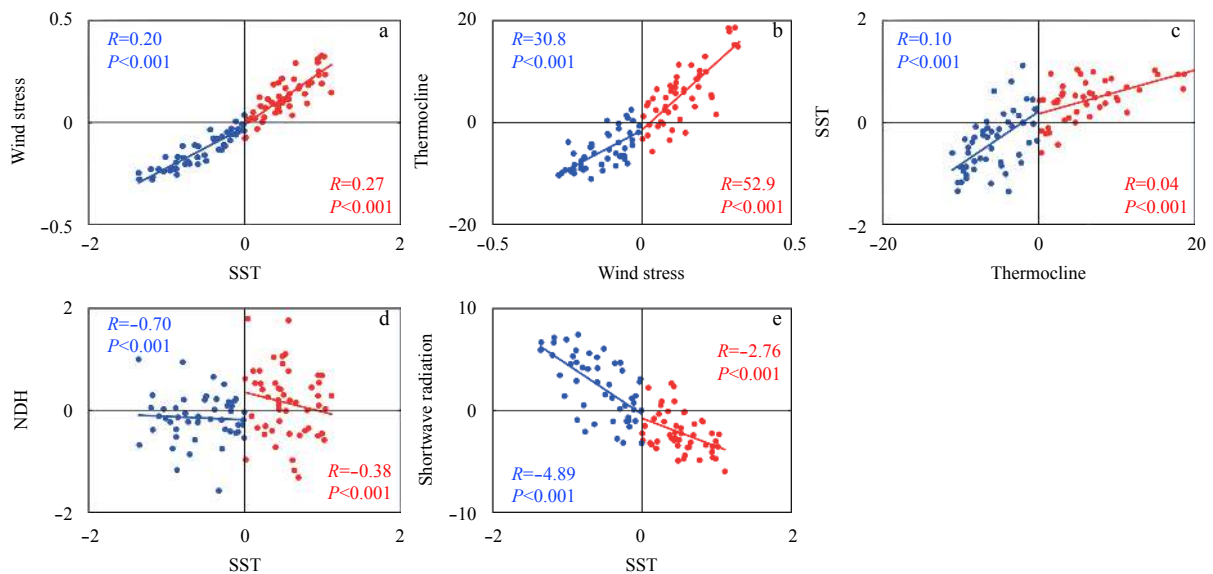
Fig. 9. Scatter diagram of CTIO wind stress (N/m²) to ETIO SST (°C) (a), ETIO thermocline (m) to CTIO wind stress (N/m²) (b), ETIO thermocline (m) to SST (°C) (c), ETIO NDH (10⁵ °C/s) to SST (°C) (d) and ETIO SST (°C) to shortwave radiation (W/m²) (e) for positive (red) and negative (blue) samples from May to November in CTRL simulation. All the results are calculated from the last 100 a. Linear regression using samples with a negative and positive index value are conducted separately with the regression coefficient R and p value indicated.

is unfavorable for negative skewness in our simulation. The response of thermocline to wind (Fig. 9b) is also not favorable for the negative ETIO SST skewness because of a stronger coupling for positive samples than the negative. As for the asymmetric SST response to thermocline anomalies (Fig. 9c), there appears a pronounced asymmetric relationship with the coupling coefficient for cold samples being nearly two times more than warm samples. This indicates that SST is much more sensitive to an anomalous shoaling of thermocline than its deepening since a shallower (deeper) thermocline facilitates a stronger (weaker) SST coupling (Liu et al., 2014), suggesting that the thermocline-SST feedback is favorable for the negative skewness in the ETIO.

The response of NDH to SST is shown in Fig. 9d. The NDH is obtained by adding up the three last terms in Eq. (1) averaged over the ETIO region. In our control simulation, the NDH process acts to damp the warm SST anomalies while reinforce the cold SST anomalies, and thus generates a strong asymmetry between the warm and cold samples and is favorable for the ETIO negative SST skewness.

In terms of the SST-cloud-radiation feedback, it works in the condition that the cold SST anomalies decrease to a certain threshold and a cloud-free condition generates (Hong et al., 2008, 2010). In this way, the damping effect of shortwave to SST cooling will vanish and the feedback breakdowns. However, the existence of cloud-free condition is still under debate. Following Hong and Li (2010), we focus on the relationship between shortwave radiation to SST anomalies. Figure 9e shows that the shortwave radiation generates a greater damping of cool SST anomaly than a warm anomaly. This damping asymmetry suggests that the breakdown of SST-cloud-radiation feedback does not happen in our control simulation and the thermal damping is even much bigger for cold samples. Therefore, the SST-cloud-radiation feedback does not contribute to the ETIO negative SST skewness.

The above analysis suggests that the air-sea feedbacks play a significant role in generating the negative SST skewness over the ETIO region. This negative skewness is mainly attributed to the asymmetric thermocline-SST feedback and the nonlinear dynamic heating. Next, we will investigate whether these above feedbacks can provide an explanation as to why cooling in mean state generates a more significant negative SST skewness compared to warming. Given that the other two feedbacks in the Bjerknes feedback loop and the SST-cloud-radiation are not factors in generating the ETIO SST skewness, we will concentrate

on the changes of thermocline-SST feedback and NDH processes on SST skewness in the warming and cooling scenarios.

Here, we use residual to examine whether the target feedback favors the negative SST skewness over the ETIO region. The residual is defined as the difference of coupling coefficients between the positive and negative samples. For a positive feedback, if the residual is below zero, it means that the target feedback in the negative samples is stronger than that in the positive samples, thus this feedback contributes to the negative SST skewness over the ETIO; and vice versa. A stronger negative residual represents that the target feedback favors the more enhanced negative SST skewness.

Thermocline-SST feedback: Figure 10a shows the coupling coefficients between thermocline to SST over the ETIO region for positive, negative samples and their residuals in HEAT and COOL experiments. Since the residuals in both scenarios are negative, the thermocline-SST feedback contributes to the negative skewness. For the COOL, a further anomalous deepening of thermocline during warm events induces only modest changes in SST while an anomalous shoaling during cold events can cause more pronounced surface cooling, thus significantly enhancing the negative SST skewness over the ETIO; for the HEAT, the responses in the warming and cooling cases tend to be more symmetric. Hence, the negative residual appears to be much stronger in COOL than HEAT (grey bars in Fig. 10a) and this thermocline-SST feedback contributes to the more enhanced negative SST skewness in COOL than HEAT. The thermocline response to the warming and cooling can be seen in Figs 1g and h. The warming (cooling) generates a positive (negative) mean zonal thermocline gradient across the tropical Indian Ocean with a greater shoaling (deepening) in the ETIO region relative to the west (Figs 1g and h). This positive (negative) west-east tilt of mean thermocline in HEAT (COOL) is less (more) strongly associated with ETIO SST skewness. This result is consistent with Cowan et al. (2014). In short, the thermocline-SST feedback is a source of the negative SST skewness change in both HEAT and COOL simulations and favors the more enhanced negative skewness in COOL (Fig. 8b).

Nonlinear dynamic heating: For warm SST anomalies (red bars in Fig. 10b), the NDH damping effect becomes much stronger in COOL than HEAT. For the cold SST anomalies (blue bars in Fig. 10b), the NDH still acts to reinforce the cold SST anomalies in HEAT, it operates on the other way, working to dampen the initial cooling in COOL. Thus, the NDH generates

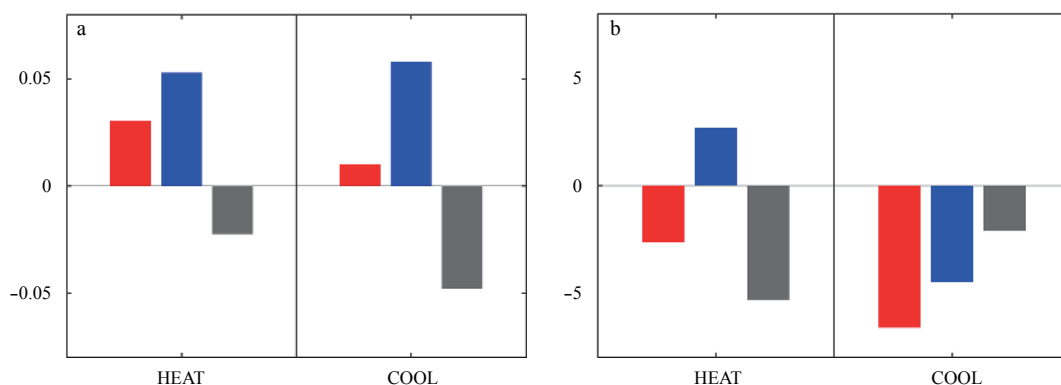**Fig. 10.** Coupling coefficients of thermocline to SST (°C/m) (a), NDH to SST (10^5 s) (b) for positive (red bars) and negative (blue bars) samples from May to November in HEAT and COOL simulations, as well as their residuals (grey bars). Residual is defined as the difference in coupling coefficients between positive and negative samples, calculated from the last 100 years of the model integration.

less residual in COOL than HEAT (grey bars in Fig. 10b). Therefore, although the NDH is a source of the negative SST skewness in ETIO, but it cannot explain the more enhanced negative skewness in COOL than HEAT.

To sum up, the asymmetry in ETIO SST, measured by skewness, will enhance under climate cooling scenarios but has slightly variation under warming. The enhancement in COOL is mainly originated from the thermocline-SST feedback. Other feedbacks, like NDH processes or SST-cloud-radiation feedback, cannot solely explain the response of SST skewness in the heating and cooling scenarios.

6 Summary

In this study, we have investigated the asymmetric response of the tropical Indian SST to energy fluxes of equal amplitude but opposite sign into the ocean surface in CESM climate system. Results show that a warmer climate induces a pIOD-like SST pattern and a cooler one leads to a nIOD-like SST pattern. Although the latter is a reversal of the former, there is a strong positive asymmetry in the SST changes over the ETIO, where warm SST anomalies responding to the positive forcing exceeds cold SST anomalies responding to the negative forcing.

The mixed layer heat budget analysis over the ETIO reveals that it is the oceanic vertical advection that generates the ETIO SST asymmetry, with its linear term making more contribution. In addition, oceanic diffusion also makes a significant contribution to this asymmetry. A comparison of solutions between the slab ocean experiments and the fully coupled experiments further verifies that the ocean dynamical processes play a dominant role in shaping the positive SST asymmetry over the ETIO. In contrast, the surface heat flux works to alleviate the SST asymmetry through its components of shortwave radiation and latent heat flux, with the former being associated with the nonlinear relationship between SST and cloud, and the latter being resulted mainly from Newtonian damping and air-sea temperature difference. The vital role of shortwave radiation in reducing the positive SST asymmetry is further confirmed by a set of partially coupled overriding experiments.

We also find two feedbacks that contribute to the negative SST skewness over the ETIO in CTRL: thermocline-SST feedback and NDH process. The ETIO negative SST skewness has also experienced some changes in the perturbation runs, with being considerably enhanced in COOL than HEAT. This is resulted mainly from the asymmetric thermocline-SST due to asymmetric response of the deep mean thermocline and its gradient between heating and cooling. For the NDH process, it also contributes to the negative SST skewness over the ETIO region through damping the warm SST anomalies while reinforcing the cold SST anomalies. However, it has negligible effects in the enhancement of negative SST skewness in COOL. And the SST-cloud-radiation feedback do not favor the negative SST skewness over the ETIO region and thereby cannot explain their corresponding changes.

References

Ashok K, Guan Zhaoyong, Saji N H, et al. 2004. Individual and combined influences of ENSO and the Indian Ocean dipole on the Indian summer monsoon. Journal of Climate, 17(16): 3141–3155, doi: 10.1175/1520-0442(2004)017<3141:IACIOE> 2.0.CO;2

Behera S K, Luo Jingjia, Masson S, et al. 2005. Paramount impact of the Indian Ocean dipole on the east African short rains: A CGCM study. Journal of Climate, 18(21): 4514–4530, doi: 10.1175/JCLI3541.1

Cai Wenju, Cowan T, Raupach M. 2009. Positive Indian ocean dipole

events precondition southeast Australia bushfires. Geophysical Research Letters, 36(19): L19710, doi: 10.1029/2009GL039902

Cai Wenju, Qiu Yun. 2013. An observation-based assessment of nonlinear feedback processes associated with the Indian Ocean dipole. Journal of Climate, 26(9): 2880–2890, doi: 10.1175/JCLI-D-12-00483.1

Cai Wenju, Santoso A, Wang Guojian, et al. 2014. Increased frequency of extreme Indian Ocean dipole events due to greenhouse warming. Nature, 510(7504): 254–258, doi: 10.1038/nature13327

Chan S C, Behera S K, Yamagata T. 2008. Indian Ocean dipole influence on south American rainfall. Geophysical Research Letters, 35(14): L14S12

Cowan T, Cai Wenju, Ng B, et al. 2014. The response of the Indian Ocean dipole asymmetry to anthropogenic aerosols and greenhouse gases. Journal of Climate, 28(7): 2564–2583

Dong Lu, Zhou Tianjun. 2014. The Indian Ocean sea surface temperature warming simulated by CMIP5 models during the Twentieth Century: competing forcing roles of GHGs and anthropogenic aerosols. Journal of Climate, 27(9): 3348–3362, doi: 10.1175/JCLI-D-13-00396.1

Du, Yan, Xie Shangping. 2008. Role of atmospheric adjustments in the tropical Indian Ocean warming during the 20th century in climate models. Geophysical Research Letters, 35(8): L08712

Hong C C, Li T. 2010. Independence of SST skewness from thermocline feedback in the eastern equatorial Indian Ocean. Geophysical Research Letters, 37(11): L11702

Hong C C, Li T, Ho Lin, et al. 2008. Asymmetry of the Indian Ocean dipole. Part I: Observational analysis. Journal of Climate, 21(18): 4834–4848, doi: 10.1175/2008JCLI2222.1

Hong C C, Li T, Luo Jingjia. 2010. Asymmetry of the Indian Ocean dipole. Part II: Model diagnosis. Journal of Climate, 21(18): 4849–4858

Huang Gang, Hu Kaiming, Qu Xia, et al. 2016. A Review about indian ocean basin mode and its impacts on East Asian summer climate. Chinese Journal of Atmospheric Sciences (in Chinese), 40(1): 121–130

Li Zhi, Luo Yiyong. 2018. Response of the tropical Indian Ocean to greenhouse gases and aerosol forcing in the GFDL CM3 coupled climate model. Atmosphere-Ocean, 56(1): 40–54, doi: 10.1080/07055900.2018.1427040

Liu Lin, Xie Shangping, Zheng Xiaotong, et al. 2014. Indian Ocean variability in the CMIP5 multi-model ensemble: the zonal dipole mode. Climate Dynamics, 43(5–6): 1715–1730

Liu Fukai, Luo Yiyong, Lu Jian, et al. 2017. Asymmetric response of the equatorial Pacific SST to climate warming and cooling. Journal of Climate, 30(18): 7255–7270, doi: 10.1175/JCLI-D-17-0011.1

Luo Yiyong, Lu Jian, Liu Fukai, et al. 2015. Understanding the El Niño-like oceanic response in the tropical Pacific to global warming. Climate Dynamics, 45(7–8): 1945–1964

Luo Yiyong, Lu Jian, Liu Fukai, et al. 2016. The positive Indian ocean dipole–like response in the tropical Indian Ocean to global warming. Advances in Atmospheric Sciences, 33(4): 476–488, doi: 10.1007/s00376-015-5027-5

Luo Yiyong, Lu Jian, Liu Fukai, et al. 2017. The role of ocean dynamical thermostat in delaying the El Nino-like response over the equatorial Pacific to climate warming. Journal of Climate, 30(8): 2811–2827, doi: 10.1175/JCLI-D-16-0454.1

Ng B, Cai Wenju, Walsh K. 2014a. Nonlinear feedbacks associated with the Indian ocean dipole and their response to global warming in the GFDL-ESM2M coupled climate model. Journal of Climate, 27(11): 3904–3919, doi: 10.1175/JCLI-D-13-00527.1

Ng B, Cai Wenju, Walsh K. 2014b. The role of the SST-thermocline relationship in Indian Ocean Dipole skewness and its response to global warming. Scientific Reports, 4: 6034

Ogata T, Xie Shangping, Lan Jian, et al. 2013. Importance of ocean dynamics for the skewness of the Indian Ocean dipole mode. Journal of Climate, 26(7): 2145–2159, doi: 10.1175/JCLI-D-11-00615.1

Saji N H, Goswami B N, Vinayachandran P N, et al. 1999. A dipole

mode in the tropical Indian Ocean. Nature, 401(6751): 360–363

Saji N H, Yamagata T. 2003. Possible impacts of Indian Ocean dipole mode events on global climate. Climate Research, 25(2): 151–169

Stevenson J W, Niiler P P. 1983. Upper Ocean heat budget during the Hawaii-to-Tahiti shuttle experiment. Journal of Physical Oceanography, 13(10): 1894–1907, doi: 10.1175/1520-0485 (1983)013<1894:UOHBDT>2.0.CO;2

Webster P J, Moore A M, Loschnigg J P, et al. 1999. Coupled ocean–atmosphere dynamics in the Indian Ocean during 1997–98.

Nature, 401(6751): 356–360, doi: 10.1038/43848

Zheng Xiaotong, Xie Shangping, Du Yan, et al. 2013. Indian Ocean dipole response to global warming in the CMIP5 multimodel ensemble. Journal of Climate, 26(16): 6067–6080, doi: 10.1175/JCLI-D-12-00638.1

Zheng Xiaotong, Xie Shangping, Vecchi G A, et al. 2010. Indian Ocean dipole response to global warming: Analysis of ocean–atmospheric feedbacks in a coupled model. Journal of Climate, 23(5): 1240–1253, doi: 10.1175/2009JCLI3326.1

High-resolution sequence architecture and depositional evolution of the Quaternary in the northeastern shelf margin of the South China Sea

Hanyao Liu[1], Changsong Lin[1]*, Zhongtao Zhang[2], Bo Zhang[2], Jing Jiang[1], Hongxun Tian[1], Huan Liu[1]

[1] School of Ocean Sciences, China University of Geosciences, Beijing 100083, China

[2] Shenzhen Branch of CNOOC Ltd., Guangzhou 518000, China

Abstract

The northeastern shelf margin of the South China Sea (SCS) is characterized by the development of large scale foresets complexes since Quaternary. Based on integral analysis of the seismic, well logging and paleontological data, successions since ~3.0 Ma can be defined as one composite sequence, consist of a set of regional transgressive to regressive sequences. They can be further divided into six 3rd order sequences (SQ0–SQ5) based on the Exxon sequence stratigraphic model. Since ~1.6 Ma, five sets of deltaic systems characterized by development of wedge-shaped foresets complexes or clinoforms had been identified. High-resolution seismic data and the thick foresets allowed further divided of sub-depositional sequences (4th order) of regression to transgression, which is basically consistent with published stacked benthic foram O-isotope records. Depositional systems identified in the study area include deltaic deposits (inner-shelf deltas and shelf-edge deltas), incised valleys, and slope slumping massive deposits. Since ~1.6 Ma, clinoforms prograded from the southern Panyu Lower Uplift toward the northern Baiyun Depression, shelf slope break migrated seaward, whereas the shelf edge of SQ0 migrated landward. The development of incised valleys in the continental shelf increased upward, especially intensive on the SB3 and SB2. The slumping massive deposits increased abruptly since SB2, which corresponds to the development of incised valleys. The evolution of depositional systems of continental slope mainly controlled by the combined influence of sea level changes, tectonic movements, sediment supply and climate changes. Since ~3.0 Ma, relative sea level of the northern SCS had been experienced transgression (~3.0 Ma BP) to regression (~1.6 Ma BP). The regional regression and maximum transgressions of the composite sequences were apparently enhanced by uplift or subsidence related to tectono-thermal events. In addition, climatic variations including monsoon intensification and the mid-Pleistocene transition may have enhanced sediment supply by increasing erosion rate and have an indispensable influence on the development of the incised valleys and 5 sets of deltaic systems since ~1.6 Ma.

Key words: sequence architecture, depositional systems, continental slope, Quaternary, Zhujiang (Pearl) River Mouth Basin

1 Introduction

The South China Sea (SCS), the largest marginal basin on the continental margin of Southeast Asia, has attracted special attention for Earth scientists world-wide because of its particular location (interactions among three large plates: Indian, Pacific and Eurasian) and its oil and gas potential (Chen et al., 1993; Gong and Li, 2004; Jiang et al., 2017; Lin et al., 2017; Lüdmann and Wong, 1999; Wang and Li, 2009; Wang et al., 2003, 2014). The study area of this paper located around the Panyu Lower Uplift–Baiyun Depression, northern shelf margin of the SCS.

The shelf margins, transitional zone from the continental shelf to the deep sea, are important areas of sedimentary geology and marine sedimentary process studies (Lin et al., 2017). A large quantity of sedimentary studies showing that the development and depositional evolution of shelf margin are not only related to sea level variations, but also basin tectonism, sediment supply and climatic changes (Lin et al., 2001; Alves et al., 2014). Over the past few years, the northern margin of the SCS has been the subject of detailed investigations, many studies have focused on the development and depositional characteristics on Oligocene–Miocene strata, comprising distribution of depositional systems, sequence architecture, depositional evolution, and controlling factors (Dong et al., 2008; Jiang et al., 2017; Wu and Xu, 2010; Liu et al., 2011; Xie et al., 2009; Zhu et al., 2011). However, for the Quaternary strata on the northern margin of the SCS, only few studies related to the high-resolution sequence stratigraphy (Chen et al., 1993; Huang et al., 1995; Ge et al., 2012; Kou, 1990; Kou and Du, 2010; Liu et al., 2011; Lüdmann et al., 2001; Zhuo et al., 2015), particularly their responses to sea level changes, basin tectonism, sediment supply and climate changes.

This paper focus on the continental margin systems, established the sequence architecture and depositional evolution

*Corresponding author, E-mail: lincs58@163.com

model since ~3.0 Ma, further created the high-resolution depositional sequences (4th order) since ~1.6 Ma, aimed to reveal their relationship to the sea level, tectonic setting, sediment supply and climatic changes of the Quaternary in the northern SCS, which has an important Guiding significance for studies in continental margin basins.

2 Geological setting

Located in the northeastern of the SCS, Zhujiang (Pearl) River Mouth Basin (ZRMB) is one of the most important petroliferous basins in China. With a general strike of SW–NE, the ZRMB is about 800 km long and 300 km wide, covering an area of more than 175 000 km² (Chen, 2000). From the north to south, the ZRMB consists of five tectonic units: the Northern Depression Belt, the Central Uplift Belt, the Southern Depression Belt, and the Southern Uplift Belt (Gong and Li, 2004; Wang and Li, 2009). The shelf margin of present day located between the Panyu Lower Uplift and the northwestern of Baiyun Depression (Fig. 1). Panyu Lower Uplift, with an area of ~7 500 km², has a total water depth around 100–200 m, located in the middle of the Central Uplift Belt. The Baiyun Depression, with an area of ~25 500 km², filled with more than 10 000 m deposits.

During the Baiyun event (~23.8 Ma BP), the deep mantle of the Baiyun Depression started rising, resulting intensive thermal subsidence, further causing the shelf slope moved to the location of present day abruptly (Ding et al., 2013; Pang et al., 2009; Sun et al., 2008; Xie et al., 2014). About 6.5 Ma BP, collision between the Luzon Arc and Eurasian Plate resulted the uplift of Taiwan, further causing a series of neotectonic activities in the SCS (Huang et al., 1997) (Fig. 2). In addition, two main collision phases on the northern SCS was identified at 5–3 Ma and 3–0 Ma, respectively, accompanying stress regime transformed from compression into transtension (Lüdmann and Wong, 1999). Regionally, in the ZRMB, the Liuha Movement at the end of the Pliocene–early Pleistocene, was characterized by uplift, faulting, folding and denudation of the Quaternary strata, also related to the arc-continent collision (Wu et al., 2004).

Since ~3.0 Ma, the northern SCS had experienced an extensive transgression. Afterward, ~1.6 Ma, started a regression in general, enhanced the preservation of the Quaternary geological records in the study area (Jiang et al., 2017). In the ZRMB, the thickness of Quaternary strata increased seaward, varies between 100 m and 400 m on the continental shelf, reaching a peak of ~600 m at the distal shelf margin (Jiang et al., 2017; Lüdmann et al., 2001). The age frame of Quaternary was founded using the dating data of shallow boreholes (ZQ1–ZQ4), and the paleontological data from local well loggings (Fig. 2) (Feng et al., 1996; Qin, 1996; Zhuo et al., 2015).

During the Quaternary, as the onsets of the northern hemisphere ice sheet (~3.2–2.5 Ma), climate and the monsoon became intensive variable with glaciation to inter-glaciation cycles (Huang et al., 2005; Wang et al., 2003, 2014). One of the most important events about Quaternary climate is the mid-Pleistocene Transition, which marks the dominant climate periodicity extended from 41 ka to 100 ka (Martin et al., 2008; Prell, 1982) (Fig. 2).

3 Research methods

In recent years, due to petroleum and hydrocarbon exploration activities, also resource investigations of the government, abundant data have been obtained in the SCS. Extensive seismic, well logging, shallow boreholes and paleontological data provided the basis for the comprehensive study of sequence architecture and depositional evolution. Five zero phase 3D seis-

mic volumes involved in this study, 3D seismic volumes A and B cover an area of ~1 200 km² and ~13 000 km², respectively (Fig. 1c), which have a dominant frequency of 30–60 Hz, resulting in a vertical resolution of ~10 m assuming the seismic velocities of 1 600 m/s (Zhou et al., 2015; Zhuo et al., 2015). Numerous 2D seismic lines linking between 3D surveys A and B have a vertical resolution ~20 m (Zhou et al., 2015; Zhuo et al., 2015). Using Geoframe et al. software of seismic interpretation, all of these seismic and well-logging data can be integrated well.

Using the integrated data with seismic and well logging, we firstly established sequence stratigraphic framework in the light of the guideline of sequence stratigraphy (Catuneanu et al., 2009). In seismic profiles, the characteristic of sequence boundaries can be interpreted as unconformities, such as onlap, downlap, toplap, truncation, downcutting and variations of stratigraphic stacking patterns (Jiang et al., 2017; Lin et al., 2001, 2017; Lin, 2009). By analyzing the shapes and combination types of well logging data (lithology; GR: natural gamma ray; DT: acoustic log), internal sequence boundaries and depositional systems tracts can be further determined. The age of major unconformities can be constrained by dating data of published shallow boreholes ZQ3 (Feng et al., 1996) (Fig. 3) and biostratigraphic age data of calcareous nannofossil and foraminifera (Gong and Li, 2004; Qin, 1996) (Fig. 2). The identification of depositional systems mainly based on the analyses of seismic and log-lithology facies (Mitchum et al., 1985; Vail et al., 1977a, b), 3D seismic amplitude slices, and geomorphological structure according to the predecessors' summary (Li et al., 2011; Gong et al., 2013, 2016).

4 High-resolution sequence stratigraphic framework

4.1 *Sequence classification and age constrain*

Depositional sequences are composed of a series of depositional sequences of various orders, which corresponds to the division of the sequence stratigraphic units (Lin, 2009). The division of sequence stratigraphic units of various orders is on the basis of their duration (Mitchum et al., 1985; Vail et al., 1977a, 1991). Major unconformities identified in the study area contain one 2nd order (T0) and six 3rd order sequence boundaries (SB0–SB5), which can divide the Quaternary strata into six 3rd order sequence units (SQ0–SQ5). Within the 3rd sequences, flooding surfaces and internal unconformities (high frequency sequence boundaries) also can be recognized which further divided SQ0–SQ5 into more than 20 high frequency sequences.

In order to determine the chronostratigraphic framework, the age of the major unconformities (T0, SB0–SB6) had been constrained. Previous studies about shallow boreholes ZQ1–ZQ4 provided accurate dating data (Feng et al., 1996). Fortunately, ZQ3 just located in the 3D seismic volume A, which provided the possibility of the accurate well-seismic calibration. The SB3 was identified at a depth of 117 m which almost corresponds to the Brunhese-Matuyama palaeomagnetic reversal boundary (ca. 780 ka) of ZQ3, and the SB2 was identified at a depth of 85 m which could placed between (469.011±23.451) ka to (337.157±16.858) ka BP (Fig. 3). Likewise, SB1 ranges from (235.025±11.751) ka and (48.023±2.401) ka BP, and the SB0 lies from (48.023±2.401) ka BP to present (Fig. 3). The result was comparable to the chronostratigraphic framework of Zhuo et al. (2015). The age of the major unconformities (SB0–SB3) in the main study area (3D seismic volume B) can be further determined by the calibration of 2D seismic profiles linking between 3D surveys A and B (Fig. 4). Although, ZQ3 did not penetrate the early Pleistocene strata, the
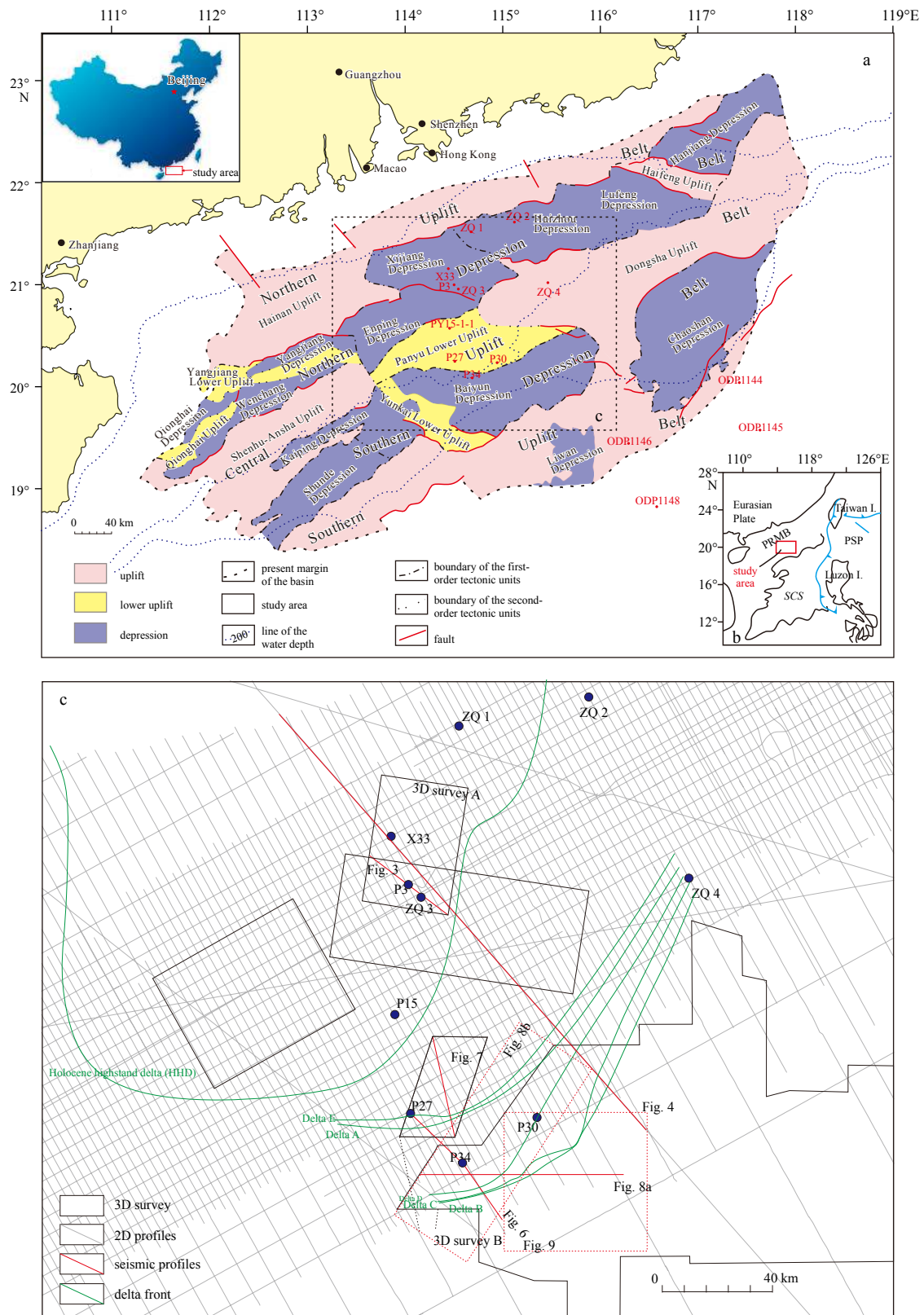
Fig. 1. The location of the South China Sea and distribution and tectonic unit division of the Zhujiang River Mouth Basin (a). The tectonic setting of the South China Sea modified from Lin et al. (2017) is shown in (b). Attached maps (c) showing the location of seismic and borehole data used in the paper, the evolution of the Quaternary paleo-delta front are mapped in Fig. 1c, the position of Holocene highstand delta is according to Pang et al. (2009). SCS: South China Sea; ZRMB: Zhujiang River Mouth Basin; PSP: Philippine Sea Plate.
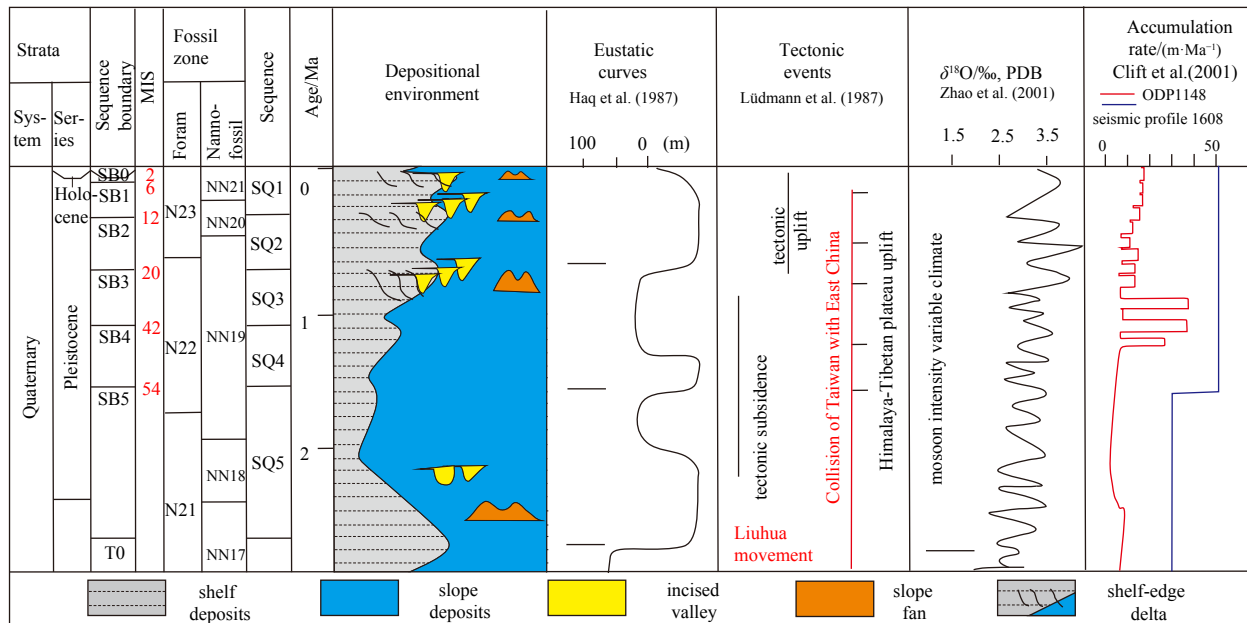
Fig. 2. Summarize of sequence classification, depositional evolution and geological setting of the Quaternary in the Zhujiang River Mouth Basin.
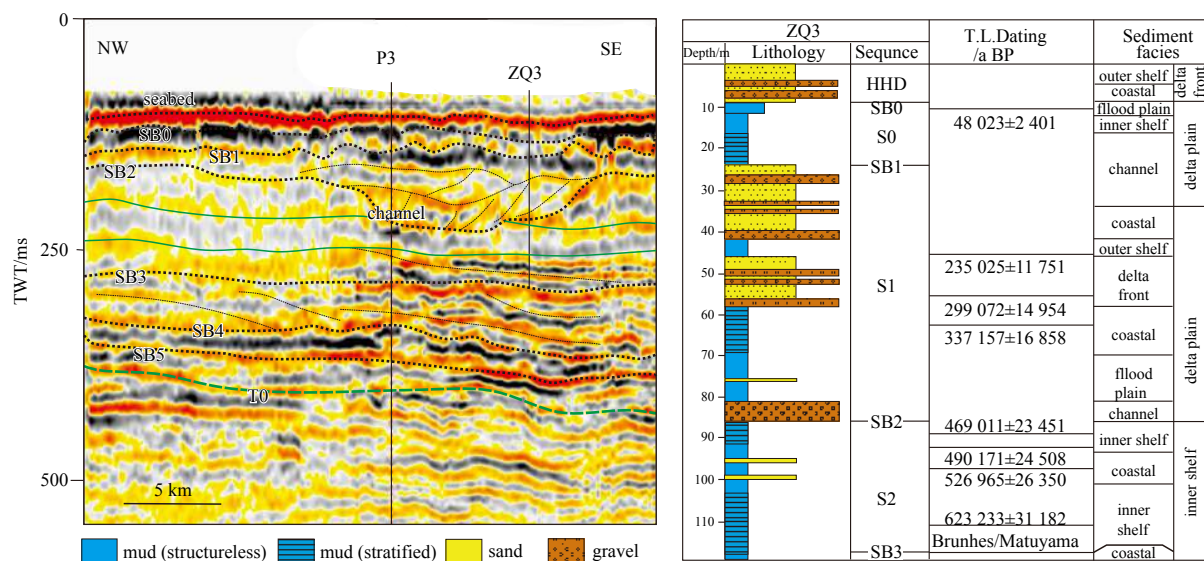
Fig. 3. Dating data and environment of shallow boreholes ZQ3 (after Feng et al. (1996); and Zhuo et al. (2015)) with inner shelf seismic profile, the age framework since mid-Pleistocene of study area are established using the well-seismic calibration. See Fig. 1c for location of seismic profile and well loggings.

age of SB4, SB5 and T0 can be constrained by the biostratigraphic age data in the study area (Fig. 5). According to the paleontological data of P3, P27, P34 from the internal data of the China National Offshore Oil Corporation, T0 was considered as the base of the Quaternary and have an age between 3.0–2.5 Ma, similarly, the age of SB5 and SB4 were identified as ~1.6 and ~1.3 Ma, respectively. As the stacked benthic foram O-isotope records are a good proxy for the amplitude of sea level cycles during the Quaternary, the sequence boundaries can be related to the lowstand of the marine O-isotope stages (Anastasakis and Piper, 2013; Imbrie et al., 1993). Thus, the age of sequence boundaries (including internal high frequency sequence boundaries) can be further assumed corresponding to the O-isotope curve, resulting sequence boundaries SB0 to SB5

quence boundaries SB0 to SB5 are assumed relating to the lowstand of MIS 2, MIS6, MIS12, MIS20, MIS 42, MIS54, respectively (Figs 2 and 6).

The basal boundary T0 characterized by large scale erosion or angular unconformity. In the 3D seismic profiles: T0 extended to the whole study area showing strong amplitude, high frequency and strong continuity parallel reflection features; Around the Dongsha Uplift, the Pliocene strata was mostly eroded and the angular unconformity had been strengthened. In the well logging profiles: Lithology and logging data around T0 shows an abrupt change, GR curve formed funnel-shape (Fig. 5). Depositional sequences since ~3 Ma can be defined as one regional transgressive to regressive sequence. Sequence boundaries SB0 to SB5
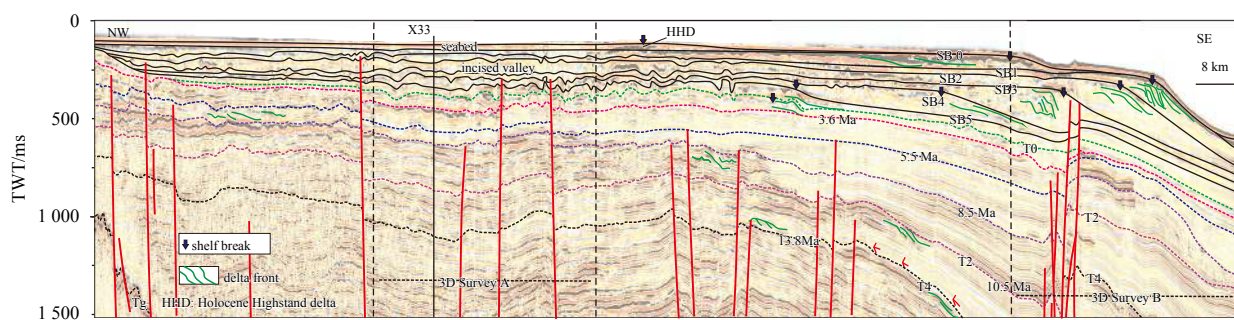
Fig. 4. Illustration of 2D seismic profiles linking between 3D Survey A and B showing the age framework and depositional evolution. See Fig. 1c for location of seismic profile and well loggings.
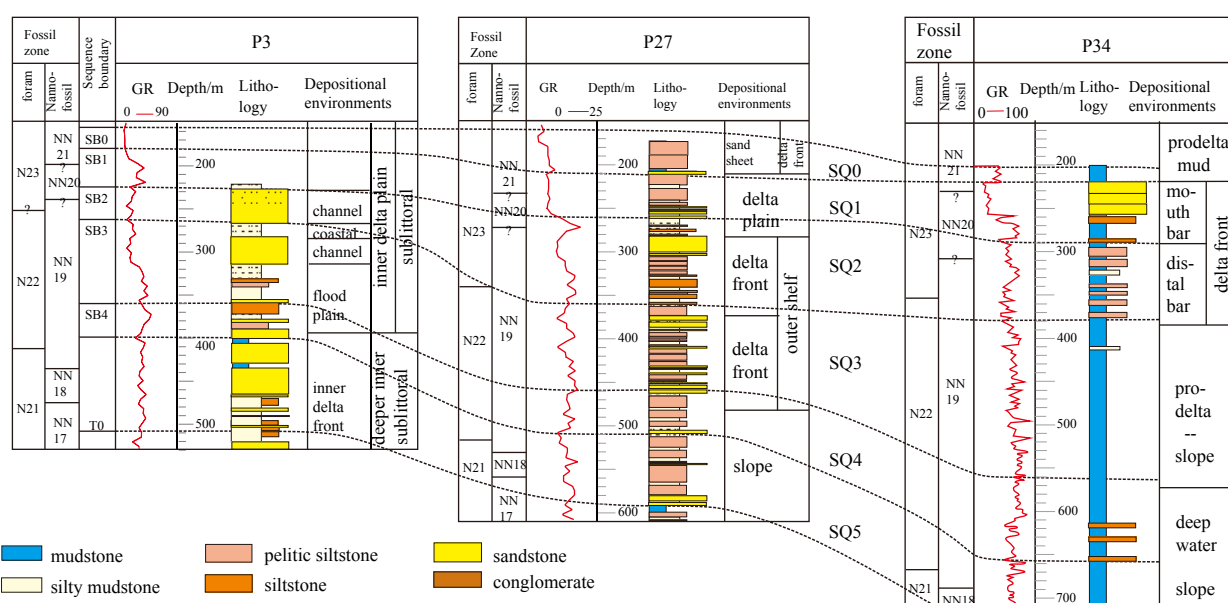

Fig. 5. Sequence classification and depositional environment of well loggings using the biostratigraphic age data and well-seismic calibration (Gong and Li, 2004; Qin, 1996). See Fig. 1c for the location.

extended extensively, which divided Quaternary strata into six 3rd order sequences (SQ5–SQ0) with a cycle ~0.4 Ma (Fig. 6). Since SB5, five sets of high-angle prograding clinoforms (SQ4–SQ0) had been identified. Along the unconformities (SB0–SB5), with the relatively strong amplitudes and subparallel reflections, similar features had been found in the seismic profiles, such as toplap contacts or truncation and downcutting at the top of the clinoforms; downlap contacts at the bottom of the base; and onlap contacts against the slope. In addition, lithology and logging data commonly show an abrupt change along the unconformities in the well logging profiles (Fig. 5). Within SQ5–SQ0, four maximum flooding surfaces (MFS) had been identified through tracing the onlap point. Commonly, the MFS extended extensively and easily merged with the sequence boundaries except in the incised valleys and slope area (Fig. 6). High-resolution seismic data and the thick progradational clinoforms since SB5 (~1.6 Ma) allowed the further divide of sub-depositional sequences of regression to transgression. The 4th order sequences bounded by internal high frequency sequence boundaries, which terminate by minor toplap and downlap against the top and bottom of 3rd sequence boundaries (Fig. 6). Minor onlap contacts also can be identified against the slope (Fig. 6). The internal boundaries can be tracked on a large scale within the 3rd

sequence around southern Panyu Lower Uplift to northern Baiyun Depression (Fig. 6).

4.2 *Sequence architecture (SQ0–SQ5)*

Six 3rd order sequences (SQ5–SQ0) had been identified in the study area since ~3 Ma, which characterized by the development of high-angle clinoforms (Figs 6–8). Within SQ5–SQ0, depositional systems are basically consistent with the Exxon sequence stratigraphic model (Vail, 1987), highstand, transgressive and lowstand systems tracts can be identified. SQ5 mainly feature as high-frequency parallel seismic reflections representing extensive transgressive to highstand systems tracts, which can also be documented by borehole and logging data, while lowstand systems tracts mainly appear within the incised valleys and upper slope as slumping massive deposits (Figs 6–8). SQ4–SQ0 display the similar architectures which mainly characterized by the rapid development of a series of high-angle progradational clinoforms on the continental shelf to shelf edge zone representing the highstand systems tracts and the incised valleys and slumping massive deposits on the upper slope representing lowstand systems tracts. While the transgressive systems tracts usually characterized by thin layers of strong amplitude seismic reflections overlying the highstand systems tracts which indicated the rapid
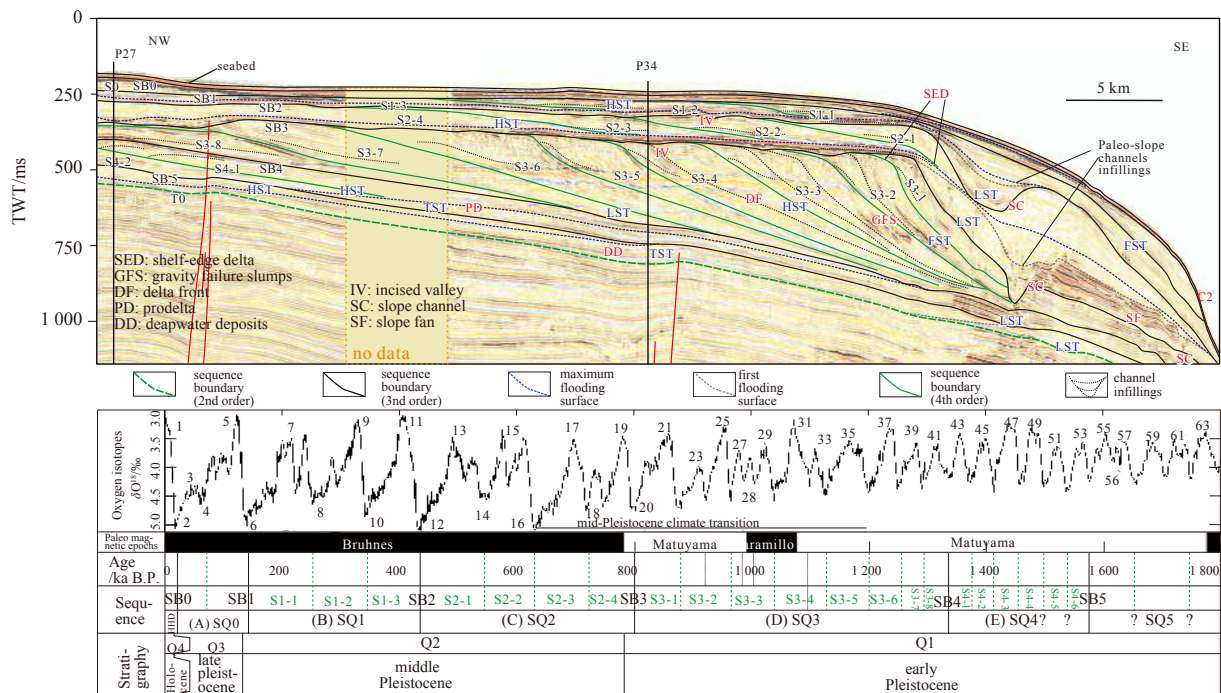
Fig. 6. High-resolution sequence stratigraphic framework of seismic profile in the outer-shelf to shelf margin zone with the constrain of stacked benthic foram O-isotope records (Lisiecki and Raymo, 2005). See Fig. 1c for the location.
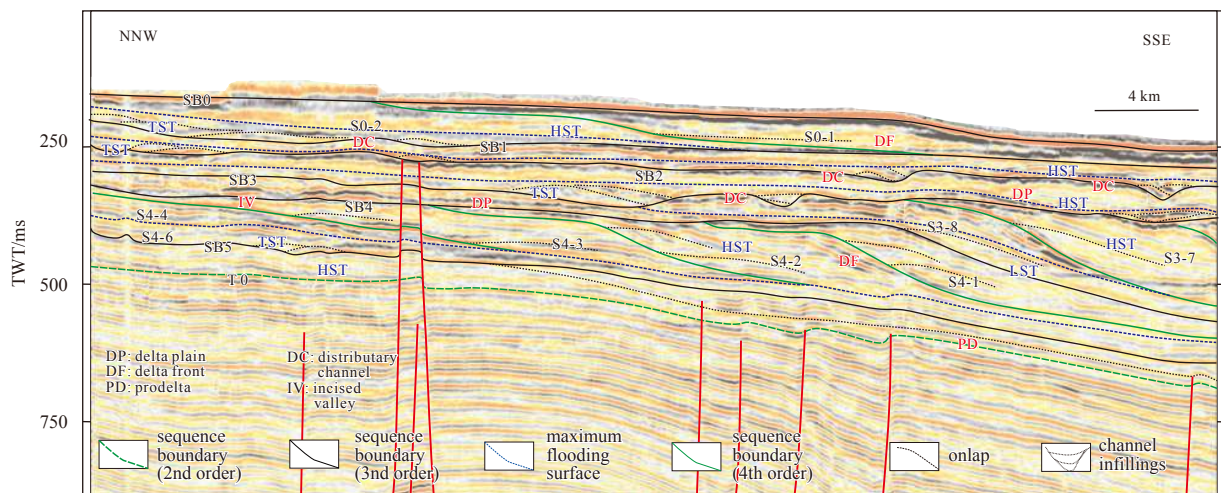

Fig. 7. High-resolution sequence stratigraphic framework of seismic profile in the mid-shelf zone, sequence architecture and depositional evolution are shown in the profile. See Fig. 1c for location of seismic line.

transgression, sometimes they are too thin to identify (Figs 6–8). In addition, forced falling stages can be identified at the end of highstand stages divided by the forced regression surface (Lin, 2009). Since SB5, a total of five sets of high-angle prograding clinoforms (SQ4–SQ0) can be interpreted as five sets of progradational delta to shelf-edge delta systems which feature oblique-tangential seaward-dipping seismic reflections and coarsening-upward well-logging patterns. From inner shelf to the shelf edge, the internal structure of the clinoforms usually characterized by the general increasing of the dipping angle and the thickness of foresets, display a transition from a regular toplap to declining of-flap structures, indicated the general falling of relative sea level and abundant sediment supply.

Within SQ4–SQ0, the thick progradational clinoforms had

been further divided into 23 sub-depositional sequences of regression to transgression, the internal sequences mainly formed by progradational wedges with the average seaward-dipping angle ~1°–3° which indicated the minor regression of sea level, minor transgression also can be identified through the onlap contacts against the slope (Figs 6–8). The stacked benthic foram O-isotope records are a good proxy for the minor sea level fluctuations, which can be a contrast to the internal sequences. In SQ4, however, because of the limit of 3D seismic data, internal sequences cannot be identified completely, only 4–5 minor progradational wedges are visible (Fig. 7), causing the difficulty of comparing with the stacked benthic foram O-isotope records. Fortunately, since SB4, the prograding complexes (SQ3–SQ0) had prograded into southern Panyu Lower Uplift to northern Baiyun
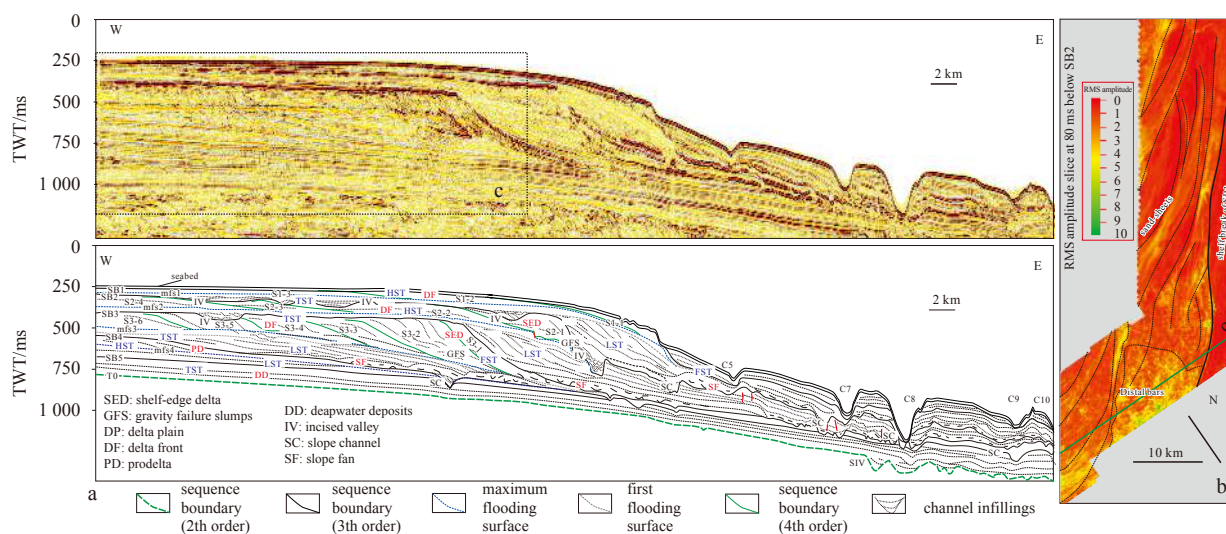
Fig. 8. High-resolution sequence stratigraphic framework of seismic profile in the outer shelf to shelf margin zone. The sequence architecture and depositional evolution consist of deltaic deposits, incised valleys, upper slope gravity failure slumps are shown in (a).TheRMS amplitude slice (b) at 80 ms below SB2 display the delta front of SQ3 consisting of distal bars and sheet-like sand bar deposits. See Fig. 1c for location of the seismic line and RMS slice.

Depression, which just located in the 3D seismic survey B. SQ3 features large scale prograding complexes with ~100–400 m height, which can be divided into 8 internal sequences formed by progradational wedges (S3-8 to S3-1); Comparing with SQ3, SQ2 and SQ1 had prograded slightly basinward, the thickness and seaward-dipping angle of internal progradational foresets reduced relatively, SQ2 with the average height of ~100 m can be divided into 4 progradational wedges (S2-4 to S2-1), SQ1 with the average height of ~60 m can be divided into 3 progradational wedges (S1-3 to S1-1); SQ0 displays single progradational wedge which retrograded landward comparing with SQ1 indicating the transgression right after SB1 (Fig. 6); Holocene deposition barely found in the study area, the Holocene Zhujiang River Delta had been restricted within the inner-shelf (Lüdmann et al., 2001) (Fig. 1c, 4). Since 3rd order sequence boundaries SB0 to SB4 are related to the lowstand of MIS 2, MIS6, MIS12, MIS20, MIS 42, respectively, with comparing to the stacked benthic foram O-isotope records, the amount of 4th order sequence boundaries equals to the amount of the lowstands of the O-isotope stage within the 3rd sequences (SQ3–SQ0) (Fig. 6). As the sequence boundaries can be related to the lowstand of the marine O-isotope stages (Anastasakis and Piper, 2013; Imbrie et al., 1993), all these internal progradational wedges are considered corresponding to the lowstand of the O-isotope stage, which indicate the sea level changes of orbital scale cycles. Within SQ3, the high frequency of internal sequences show a transition from ~41 ka to ~100 ka, within SQ2 to SQ0, the sub-sequences are dominanted by the cycle of ~100 ka (Fig. 6).

5 Depositional systems and Evolution

5.1 *Deltaic deposits*

The Quaternary strata are characterized by the development of a series of progradational clinoforms from outer shelf to shelf margin. Since SB5, five sets of high-angle prograding clinoforms (SQ4–SQ0) had been identified which embody five sets of progradational deltaic systems (E–A) representing delta to shelf-edge delta. Based on the well logging and seismic data, three del-

taic depositional facies have been recognized: (1) delta plain (inter distributary plains and distributary channels); (2) the prograding delta front (proximal river mouth bars, distal bars and sand-sheets); and (3) prodelta muddy deposits. Delta plain deposits display a parallel to sub-parallel and small channel-shaped seismic structure which represent inter-distributary plains and distributary channels (Figs 3, 4 and 7). The well logging usually shows fining-upward cycle, which is dominated by siltstone, while the channels commonly fill with sandstone (Figs 3 and 5). The end of delta plain lobe generally link with mouth bar deposits representing the proximal delta front zone. Delta front deposits display thick imbricate, S-shaped to tangential progradational foresets or clinoforms seismic reflections and coarsening-upward well logging patterns, whose major lithology slightly finer than the delta plain (Figs 5, 6 and 8). Proximal river mouth bars, distal bars and sand-sheets deposits have been identified within the delta front. Proximal river mouth bars deposits are dominated by sandstone with a funnel-box shaped GR curve (Fig. 5); At the end of delta front, distal bars feature coarsening-upward prograding complexes which are dominated by (pelitic) siltstone (Fig. 5); sand-sheets are also identified at the distal front characterized by sheet-liked bars of pelitic siltstone, RMS amplitude slices indicate that the delta front is dominated by a series of lobe-shaped sand-sheets and distal bars (Fig. 8b). Prodelta deposits commonly progradad into the slope zone or bathyal environment with parallel to subparallel and dome-shaped seismic reflections dominated by mudstone with a high GR value (Figs 5, 6 and 8). From inner-shelf to shelf margin, the main environment of Quaternary transform from sublittoral of inner delta plain with channels to slope–deep water of prodelta, lithology became finer overall (Figs 3–5).

The phase of sea level can determine the type and the nature of the delta. The inner-shelf delta, which developed in nearshore environments on the inner-shelf usually formed in the highstand, whereas the shelf-edge delta characterized by thick clinoforms which prograded into the continental margin usually formed in the forced falling to lowstand stage (Carvajal et al., 2009; Dixon et al., 2012; Henriksen et al., 2009; Porębski and Steel, 2001, 2003).

Deltas E and A which corresponds to the sea level fall of MIS 42 and MIS 2, respectively, are assumed to be inner-shelf delta by the interpretation of seismic data. The progradation of deltas E and A are relatively weak cause the main part of them mainly developed on the inner-shelf, the delta front of them are identified on the Panyu Lower Uplift with a height ~60 m and ~80 m which characterized by subparallel to S-shaped seismic reflections (Fig. 7). With abundant sediment supply, Deltas D, C and B are prograded seaward into the shelf margin zone rapidly during the forced falling stage, which can be interpreted as shelf-edge deltas. Shelf-edge deltas and clinoforms generated by shelf margin accretion are quite different, except the two types coincide when deltas reach the shelf edge (Porębski and Steel, 2001, 2003). Delta D feature thick S-shaped to oblique-tangential seaward-dipping seismic reflections and coarsening-upward well-logging patterns forming during the lowstand of MIS 20, the deltaic progradational beds are approximately 200 m thick and can be distinguished from the underlying shelf-edge clinoforms (Figs 6 and 8). Delta C and B showing the similar structure are relatively thin, but their delta fronts display the even more rapid progradation than D, which related to the sea level fall of MIS 12 and MIS 6, respectively (Figs 6 and 8). The sub-sequences within these deltaic foresets are also identified representing the sea level changes of orbital scale cycles (Fig. 6). Based on 3D and 2D seismic data, the position of these five delta front (E–A) have been mapped showing the evolution of the paleo-delta (Fig. 1c), where the delta front E to B prograded from the southern Panyu Lower Uplift toward the northern Baiyun Depression, and shelf slope break migrated seaward, whereas the delta front A return to the inner shelf. Holocene highstand delta is considered as a bay delta, which had been constrained into the inner shelf because of the strong longshore currents and wave action (Lüdmann et al., 2001).

5.2 *Incised valleys and slumping massive deposits*

On the outer shelf, intensive incised valleys developed responding to the 3rd sequence boundary during the lowstand stage. In the seismic profiles, incised valleys commonly feature U-shaped and V-shaped with the depth about tens of meters, and with the width about tens of kilometers (Figs 6 and 8). Internal fillings which can be divided into sub-units usually display a single-story to multistory asymmetric structure and mainly migrated seaward (Figs 6 and 8). In the well-logging profiles, incised valleys commonly show low GR values and sudden changes of lithology (Fig. 5). Since Quaternary, the incised valleys have become more and more intensive upwards, especially on SB3 and SB2 (Fig. 8).

The slumping massive deposits or slope slumps developed on the upper slope during lowstand stage. According to the seismic profiles, the slumping massive deposits migrated basinward in general and increased within SQ3–SQ1 and characterized by strong amplitudes and chaotic reflections with an average thickness of ~30 m (Figs 6 and 8), which are considered to be related with the development of shelf-edge deltas. The RMS amplitude slices at 20 ms upon SB3 and SB2 show that the slumps of shelf-edge delta fronts stepped over the shelf break zone and transport into the slope channels zone, cover an average area of ~500 km² and increased abruptly since SB2, which corresponds to the development of incised valleys (Fig. 9). Small gullies were identified in the head of the slumping massive deposits linking between the shelf-edge delta and the slumping massive deposits, indicated the process of the slumping-gravity flow.

Slumping-gravity flow transport along the front edges which play an important sediment supply for slope fan deposits have been identified in the western part of study area based on the integral analysis of the seismic data. The slumping massive deposits of shelf-edge deltas are considered as the major sediment supply for slope fans, which are caused by the extensive erosion of the shelf area and the gravity imbalance of the rapid progradational shelf-edge deltas during the sea level fall. The progradation of SQ4 and SQ0 are limited, causing the thin strata during these periods in the slope area. SB5 and SB4 usually merge with SB3 and SB0 merge with SB1 in the seismic profiles (Figs 6 and 8).

6 Controls on sequence architecture and depositional evolution

6.1 *Sea level changes and tectonics*

The relative sea level changes are the central cause of the development of depositional cycles and sequence architecture (Lin, 2009). The sea level changes reflected in the seismic structure are almost match with the stacked benthic foram O-isotope records, in particular, the major sequence boundaries are commonly consistent with regression events and correlated with low δ^{18}O values (Fig. 6). The development of T0 was considered to correspond to the declining sea levels caused by the onset of the Arctic ice-sheet development (Wang et al., 2014), an increase by ~1.9‰ of δ^{18}O at the same period is recorded in ODP Site 1 148 (Zhao et al., 2001) (Fig. 2); The development of SB5 and SB3 are consistent with the global sea level falls related to Haq et al. s' (1987) sea level change curve (Fig. 2), which indicates that development can be correlated globally; The development of SB2 and SB0 are assumed corresponding to the ice-sheet expansion of the Mid-Brunhes Event (MBE) and LGM, which both display larger-amplitude changes in δ^{18}O records (Wang et al., 2014) (Figs 6 and 10). The depositional evolution is also consistent with the transgression to regression cycles, deltaic deposits featuring progradational clinoforms are formed during highstand to falling stage, with the sea level continue to fall, resulted the extensive erosion on the shelf area forming incised valleys and slumping massive deposits.

Tectonic subsidence/uplift is believed to be the major control for the development of sequences. The tectonic subsidence may enhance the process of deposits, whereas the uplift could enhance the relative sea level falls and further strengthen the progradation of deposits. Since ~3.0 Ma, the collision between Luzon Arc and east China had been identified (Lüdmann and Wong, 1999), Liuha Movement at the end of the Pliocene–Early Pleistocene is considered to be correlated with the collision of Taiwan with Luzon Arc (Wu et al., 2004). These arc-continent collisions resulted the uplift, faulting, folding and denudation of the Quaternary strata along with T0 in the seismic profiles, especially around the Dongsha Uplift zone. The extensive transgression strata in SQ5 characterized by the shelf-break zone migrated landward intensively which differs with the trend of Haq et al. s' (1987) sea level change curve, are considered as the result of a high rate of regional tectonic subsidence at that time (Li et al., 1999; Jiang et al., 2017).

The relative sea level changes are considered as the sum of the eustatic and tectonic contributions. Since ~1.6 Ma, since 0.10‰–0.11‰ changes in ^{16}O/^{18}O ratio represent approximately 10 m in sea level change (Chiocci et al., 1997), and the relative sea level curve in the study area can be obtained from seismic data based on v=1 500 m/s, thus the tectonic contribution could be computed as a first approximation using the correlation between the present locations of the 5 sets of delta fronts and the stacked
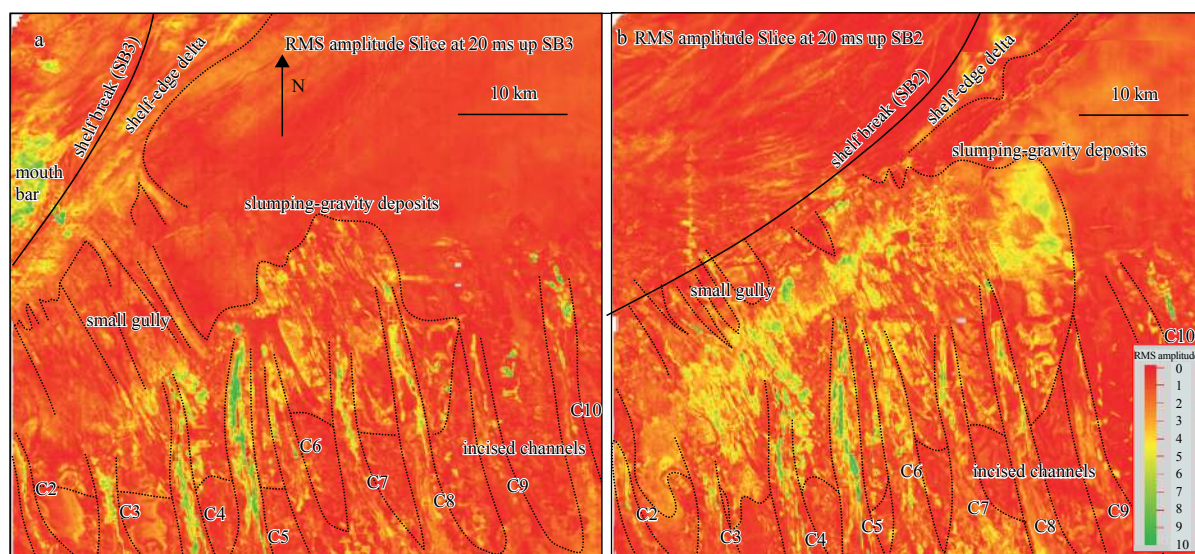
Fig. 9. RMS amplitude slices at 20 ms up SB3 and SB2 showing the evolution of slumping massive deposits from SQ3 to SQ2, note the slumping massive deposits increased abruptly since SB2. See Fig. 1c for the location.

benthic foram O-isotope records without consideration of the influence of sediment loading, compaction and erosion (Lüdmann et al., 2001). The result shows a subsidence rate ~76 m/Ma during the period of SQ3, and then three uplift phases during SQ2–SQ0 (Fig. 10). The tectonic subsidence may enhance the deposits of thick strata of SQ3, whereas the uplift could enhance the relative sea level falling and further strengthen the progradation of clinoforms of SQ2–SQ0.

6.2 *Sediment supply and climate changes*

Sediment supply is critical to the depositional architecture and can determine the patterns of deposits in all sedimentary basins (Catuneanu, 2006). In the study area, Quaternary strata is quite thick (~200–600 m), which is considered to be enhanced by the tectonic subsidence (see Section 6.1) and abundant sediment supply. Based on the previous studies on seismic profiles in the ZRMB and ODP1148, the sedimentation rates peaked during the Pleistocene (reaching 50.7 and 49.01 m/Ma, respectively) (Clift et al., 2002) (Fig. 2), which are consistent with the onset of the progradation of shelf-edge clinoforms. The abundant sediment supply may be correlated with the uplift and denudation of Western Yunnan Plateau during the Quaternary, which could have supplied large amounts of sediments to the South China Sea Basin (Wang et al., 1999). Furthermore, the increases in sedimentation rates were recorded at ~2–4 Ma around the globe, implying increased erosion rates (Nott and Roberts, 1996; Oline et al., 1999; Zheng et al., 2000; Zhang et al., 2001). The extreme climate changes during Quaternary might result in a frequent and abrupt change of temperature, precipitation and vegetation, which prevented fluvial and glacial systems from establishing equilibrium states and caused more incisions and denudations of surfaces, and further provided abundant sediment supply (Zhang et al., 2001).

Pleistocene climate started with the onset of the Arctic ice-sheet development, which differs from a stable and warm-wet climate before Quaternary, characterized by an extreme climate with frequent and high-amplitude cycles of glaciation to inter-glaciation (Huang et al., 2005; Zhang et al., 2001). According to the previous studies in the SCS (Luo and Sun, 2013; Tang et al.,

2004; Zhang et al., 1997; Zhang and Long, 2008), the climate changes are related to glacio-eustatic changes and can further cause the sea level changes, which constrained the depositional cycles and sequence architecture (see Section 6.1). In addition, the extreme climate changes and abundant sediment supply are considered to enhance the progradation of the clinoforms and the development of incised valleys, which further resulted the deposits of slope slumps during Quaternary (Zhang et al., 2001).

6.2.1 *The mid-Pleistocene transition*

The mid-Pleistocene transition (MPT), as a significant climate event in the Quaternary, marks the dominant climate periodicity extended from 41 ka to 100 ka (Martin et al., 2008; Prell, 1982). The SCS probably was more sensitive to the MPT than the open ocean (Wang et al., 2014). It is clear now the MPT covered a long time interval from ~1.2 Ma to ~0.6 Ma and centered on ~0.9 Ma, which can be seen in the stacked oxygen isotope records (Figs 6 and 10) (Lisiecki and Raymo, 2005; Elderfield et al., 2012; Shackleton, 1987). Along with the completion of MPT, the amplitude and duration of eustatic changes increased abruptly (Zhuo et al., 2015), which caused the extensive formation of progradational clinoforms and incised valleys. In the seismic profiles, SB3 are considered to be constrained by the MPT. The depositional architecture before SB3 are relative stable and can be divided into more 4th sub-sequences with 41–100 ka cycles; After SB3, besides the 4th sub-sequences are mainly constrained by 100 ka, the clinoforms prograded farther seaward into the shelf-margin forming shelf-edge deltas, and the incised valleys developed more intensively along the sequence boundaries, further causing the development of slumping massive deposits (Figs 9 and 11).

6.2.2 *The East Asian monsoon*

With the intensive climate variations, the relationship between monsoon of SCS and glaciation to inter-glaciation cycles became closer, and the winter monsoon had been strengthened intensively (Wang et al., 2003), in particular, the East Asian monsoon system had an important influence on climate in the SCS and the surrounding areas (Zhisheng et al., 2001). Besides the boreal ice sheet growth, the East Asian monsoon is linked to the
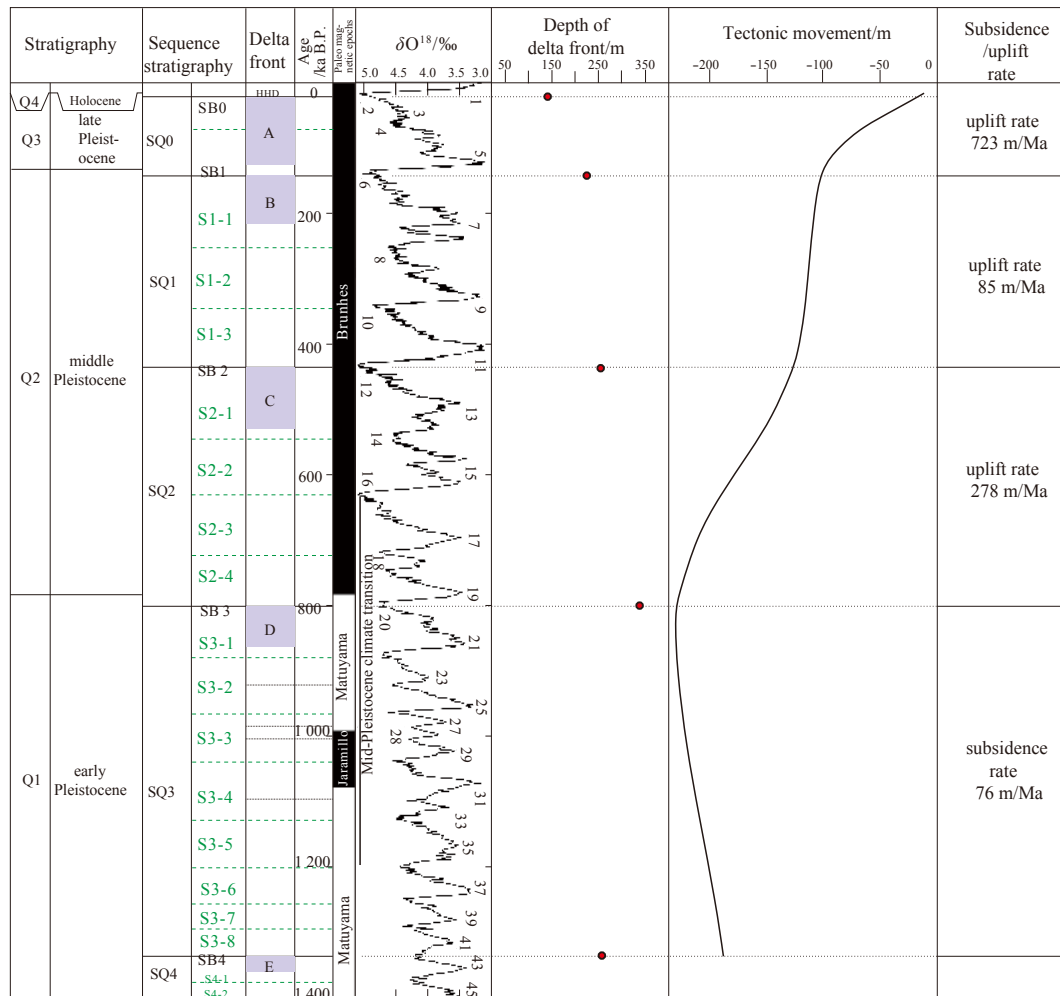
Fig. 10. Tectonic contribution are computed using the correlation between the present locations of the 5 sets of delta fronts and the stacked benthic foram O-isotope records (Lisiecki and Raymo, 2005), the depth of delta front in the study area can be obtained from seismic profile (Fig. 6) based on v=1 500 m/s. Tectonic contribution = Eustatic sea level (derived from O-isotope records) - Relative sea level (the depth of delta front) (Lüdmann et al., 2001).
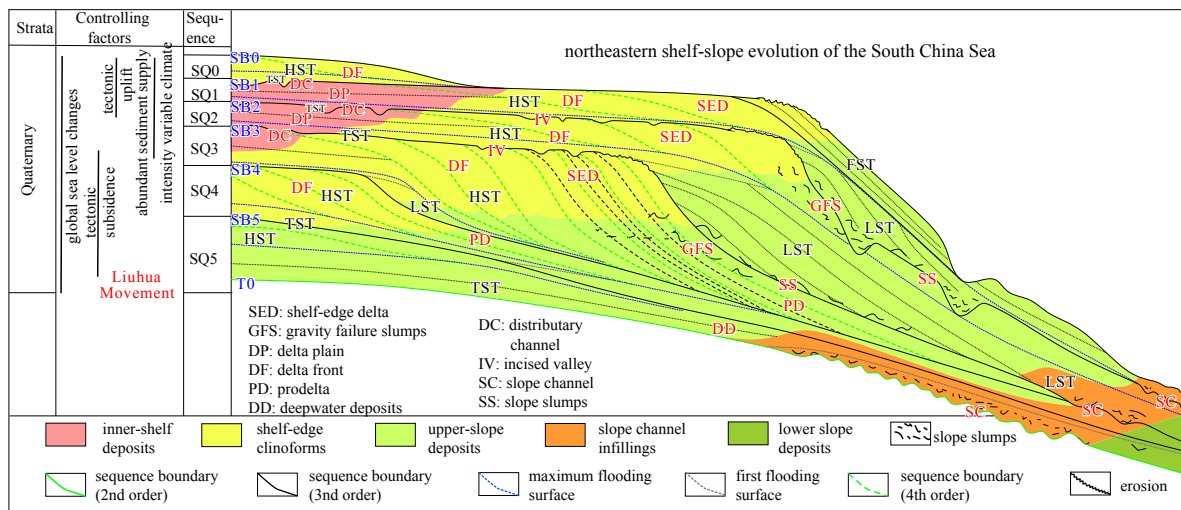
Fig. 11. Schematic map summarizing the sequence classification, depositional evolution and the controlling factors in the Zhujiang River Mouth Basin since Quaternary.

phases of Himalaya-Tibetan plateau uplift (Prell and Kutzbach, 1987), the warm-wet South Asian air mass was considered to be blocked by the plateau uplift and further strengthened the cold-dry climate of East Asian monsoon (Clift et al., 2008; Meng et al., 2011). According to the micropaleontological and palynological studies, the East Asian winter monsoon enhanced in 3.2–2.2 Ma, and strengthened at ~1.7, 1.3, 0.9, 0.45 and 0.15 Ma (Jian et al., 2001; Jian and Huang, 2003), which are almost consistent with the major sequence boundaries in the study area. The East Asian monsoon intensification events are considered to result cooler and drier climate conditions and correlated to the increased magnitude of sea level fall (Zhuo et al., 2015), which further caused the onset of intensive development of the progradational clinoforms and incised valleys (Fig. 11).

7 Conclusions

(1) Regional unconformity T0 and six local unconformities SB5–SB0 characterized by onlap, downlap, toplap, truncation, downcutting, divided the Quaternary strata into six 3rd order sequences (SQ0–SQ5). Twenty-three 4th order sub-sequences can be further divided within the large scale progradational complexes or clinoforms of SQ4–SQ0. The chronostratigraphic framework of 4th sequences is constructed by correlating the unconformities with the lowstand of the stacked benthic foram O-isotope records.

(2) The Quaternary strata are characterized by a series of high-angle foresets complexes or clinoforms. Deltaic deposits, incised valleys, and slope slumping massive deposits are recognized in the Quaternary strata. Deltaic deposits have been interpreted into two types: a. inner shelf deltas which display relatively weak progradation (Deltas E and A); and b. shelf-edge delta which are prograded seaward into the shelf margin zone (Deltas D, C and B). Three deltaic depositional facies have been recognized: a. delta plain (interdistributary plains and distributary channels); b. the prograding delta front (proximal river mouth bars, distal bars and sand-sheets); and c. prodelta muddy deposits. The depositional evolution in the study area has been reconstructed based on the integral analysis of seismic data. Since SQ4–SQ1, Deltas E–B prograded from the southern Panyu Lower Uplift toward the northern Baiyun Depression, shelf slope break migrated seaward, whereas Delta A return to the inner shelf. The development of incised valleys in the continental shelf increased upward, especially intense on the SB3 and SB2. The slumping massive deposits increased abruptly since SB2, which corresponds to the development of incised valleys.

(3) The tectonic curve since SB4 was established by the correlation between the present locations of the 5 sets of delta fronts and the stacked benthic foram O-isotope records. The sequence architecture and depositional evolution in the study area were controlled by the combined influence of sea level changes, tectonism, sediment supply and climate changes. Besides the control of global sea level changes, the tectonic subsidence may enhance the deposits, whereas the uplift could enhance the relative sea level falls and further strengthen the progradation of deposits. Furthermore, the abundant sediment supply and intensive climate changes since Quaternary are considered to enhance the development of 5 sets of progradational clinoforms and incised valleys since SB5, especially SQ3 to SQ1.

References

Alves T M, Bell R E, Jackson A L, et al. 2014. Deep-water continental margins: geological and economic frontiers. Basin Research, 26(1): 3–9, doi: 10.1111/bre.2014.26.issue-1

Anastasakis G, Piper D J W. 2013. The changing architecture of sea-level lowstand deposits across the Mid-Pleistocene Transition: South Evoikos Gulf, Greece. Quaternary Science Reviews, 73: 103–114, doi: 10.1016/j.quascirev.2013.04.018

Carvajal C, Steel R, Petter A. 2009. Sediment supply: The main driver of shelf-margin growth. Earth-Science Reviews, 96(4): 221–248, doi: 10.1016/j.earscirev.2009.06.008

Catuneanu O. 2006. Principles of Sequence Stratigraphy. Canada: Elsevier Science, 1–16

Catuneanu O, Abreu V, Bhattacharya J P, et al. 2009. Towards the standardization of sequence stratigraphy. Earth-Science Reviews, 92(1–2): 1–33

Chen Cangmin. 2000. Petroleum geology and conditions for hydrocarbon accumulation in the eastern Pearl River Mouth Basin. China Offshore Oil and Gas (Geology) (in Chinese), 14(2): 73–83

Chen P P H, Chen Z Y, Zhang Qimin. 1993. Sequence stratigraphy and continental margin development of the northwestern shelf of the South China Sea. AAPG Bulletin, 77(5): 842–862

Chiocci F L, Ercilla G, Torre J. 1997. Stratal architecture of western Mediterranean margins as the result of the stacking of quaternary lowstand deposits below 'glacio-eustatic fluctuation base-level'. Sedimentary Geology, 112(3–4): 195–217

Clift P, Lee J I, Clark M K, et al. 2002. Erosional response of South China to arc rifting and monsoonal strengthening; A record from the South China Sea. Marine Geology, 184(3–4): 207–226

Clift P D, Hodges K V, Heslop D, et al. 2008. Correlation of Himalayan exhumation rates and Asian monsoon intensity. Nature Geoscience, 1(12): 875–880, doi: 10.1038/ngeo351

Ding Weiwei, Li Jiabiao, Li Jing, et al. 2013. Morphotectonics and evolutionary controls on the Pearl River Canyon system, South China Sea. Marine Geophysical Research, 34(3–4): 221–238

Dixon J F, Stee R J, Olariu C. 2012. River-dominated, shelf-edge deltas: delivery of sand across the shelf break in the absence of slope incision. Sedimentology, 59(4): 1133–1157, doi: 10.1111/sed.2012.59.issue-4

Dong Wei, Lin Changsong, Qin Chenggang, et al. 2008. High resolution sequence framework, depositional pattern and litho-stratigraphic traps of Hanjiang formation in Panyu Uplift, Pearl River Mouth Basin. Geoscience (in Chinese), 22(5): 794–802

Elderfield H, Ferretti P, Greaves M, et al. 2012. Evolution of ocean temperature and ice volume through the mid-Pleistocene climate transition. Science, 337(6095): 704–709, doi: 10.1126/science.1221294

Feng Zhiqiang, Feng Wenke, Xue Wanjun, et al. 1996. Evaluation of Marine Geologic Hazards and Engineering Geological Conditions in the Northern South China Sea (in Chinese). Nanjing, China: Hehai University Publishing House, 177–178

Ge Huangmin, Li Qianyu, Zhong Guangfa, et al. 2012. High resolution Quaternary seismic sequence stratigraphy and paleo-environmental evolution in the northern South China Sea. Marine Geology & Quaternary Geology (in Chinese), 32(4): 49–60

Gong Zisheng, Li Sitian. 2004. Dynamic Research of Oil and Gas Accumulation in Northern Marginal Basins of South China Sea (in Chinese). Beijing: Science Press, 1–50

Gong Chenglin, Wang Yingmin, Steel R J, et al. 2016. Flow processes and sedimentation in unidirectionally migrating deep-water channels: From a three-dimensional seismic perspective. Sedimentology, 63(3): 645–661, doi: 10.1111/sed.2016.63.issue-3

Gong Chenglin, Wang Yingmin, Zhu Weilin, et al. 2013. Upper Miocene to Quaternary unidirectionally migrating deep-water channels in the Pearl River Mouth Basin, northern South China Sea. AAPG Bulletin, 97(2): 285–308, doi: 10.1306/07121211159

Haq B L, Hardenbol J, Vail P R. 1987. Chronology of fluctuating sea levels since the Triassic. Science, 235(4793): 1156–1167, doi: 10.1126/science.235.4793.1156

Henriksen S, Hampson G J, Helland-Hansen W, et al. 2009. Shelf edge and shoreline trajectories, a dynamic approach to stratigraphic

analysis. Basin Research, 21(5): 445–453, doi: 10.1111/bre.2009.21.issue-5

Huang Baoqi, Jian Zhimin, Zhao Quanhong, et al. 2005. Variations in deep-water masses from the northern south China Sea since the late Pliocene. Earth Science—Journal of China University of Geosciences (in Chinese), 30(5): 529–533

Huang Chiyue, Wu Weiyu, Chang C P, et al. 1997. Tectonic evolution of accretionary prism in the arc-continent collision terrane of Taiwan. Tectonophysics, 281(1–2): 31–51

Huang Zhenguo, Zhang Weiqiang, Chai Fuxiang. 1995. The submerged Zhujiang delta. Acta Geographica Sinica (in Chinese), 50(3): 206–214

Imbrie J, Berger A, Boyle E A, et al. 1993. On the structure and origin of major glaciation cycles 2. The 100,000-year cycle. Paleoceanography, 8(6): 699–735, doi: 10.1029/93PA02751

Jian Zhimin, Huang Wei. 2003. Rapid climate change and high-resolution deep-sea sedimentary records. Advance in Earth Sciences (in Chinese), 18(5): 673–680

Jian Zhimin, Wang Pinxian, Zhao Quanhong, et al. 2001. Late pliocene enhanced east asian winter monsoon: evidence of isotope and foraminifers from the northern south china sea. Quaternary Sciences (in Chinese), 21(5): 461–469

Jiang Jing, Shi Hesheng, Lin Changsong, et al. 2017. Sequence architecture and depositional evolution of the Late Miocene to quaternary northeastern shelf margin of the South China Sea. Marine and Petroleum Geology, 81: 79–97, doi: 10.1016/j.marpetgeo.2016.12.025

Kou Yangqi. 1990. Ancient River Channels in the northern South China Sea shelf and engineering geologic significance. Marine Geology & Quaternary Geology (in Chinese), 10(1): 37–45

Kou Yangqi, Du Deli. 2010. Sedimentary features of shallow ancient river channels on the northern shelf of the South China Sea. Acta Geologica Sinica (in Chinese), 8(1): 85–98

Lüdmann T, Wong H K. 1999. Neotectonic regime on the passive continental margin of the northern South China Sea. Tectonophysics, 311(1–4): 113–138

Lüdmann T, Wong H K, Wang Pinxian. 2001. Plio-Quaternary sedimentation processes and neotectonics of the northern continental margin of the South China Sea. Marine Geology, 172(3–4): 331–358

Li Fei, Cheng Rihui, Wang Gongsheng, et al. 2011. Application of seismic attribute analysis to study sedimentary systems of the Yingcheng formation, lower cretaceous, Shiwu Oilfield. Journal of Jilin University (Earth Science Edition) (in Chinese), 41(S1): 54–59

Li Sitian, Lin Changsong, Zhang Qiming, et al. 1999. Episodic rifting of continental marginal basins and tectonic events since 10 Ma in the South China Sea. Chinese Science Bulletin, 44(1): 10–23, doi: 10.1007/BF03182877

Lin Changsong. 2009. Sequence and depositional architecture of sedimentary basin and process responses. Acta Sedimentologica Sinica (in Chinese), 27(5): 849–862

Lin Changsong, Eriksson K, Li Sitian, et al. 2001. Sequence architecture, depositional systems, and controls on development of lacustrine *basin* fills in part of the Erlian *basin*, northeast China. AAPG Bulletin, 85(11): 2017–2043

Lin Changsong, Lu Jinyan, Cai Shixiang, et al. 2001. Depositional architecture and developing settings of large-scale incised valley and submarine gravity flow systems in the Yinggehai and Qiongdongnan basins, South China Sea. Chinese Science Bulletin, 46(8): 690–693, doi: 10.1007/BF03182838

Lin Changsong, Jiang Jing, Shi Hesheng, et al. 2017. Sequence architecture and depositional evolution of the northern continental slope of the South China Sea: responses to tectonic processes and changes in sea level. Basin Research, 30(1): 568–595

Lisiecki L E, Raymo M E. 2005. A Pliocene-Pleistocene stack of 57 globally distributed benthic δ^{18}O records. Paleoceanography, 20(1): PA1003

Liu Baojun, Pang Xiong, Yan Chengzhi, et al. 2011. Evolution of the Oligocene-Miocene shelf slope-break zone in the Baiyun deep-water area of the Pearl River Mouth Basin and its significance in oil-gas exploration. Acta Petrolei Sinica (in Chinese), 32(2): 234–242

Luo Yunli, Sun Xiangjun. 2013. Vegetation evolution and its response to climatic change during 3.15–0.67 Ma in deep-sea pollen record from northern South China Sea. Chinese Science Bulletin, 58(3): 364–372, doi: 10.1007/s11434-012-5374-x

Martin J H, Pillans B, Farquhar S A. 2008. The Early-Middle Pleistocene Transition: Characterization and proposed guide for the defining boundary. Episodes, 31(2): 255-259

Meng Xianwei, Xia Peng, Zheng Jun, et al. 2011. Evolution of the East Asian monsoon and its response to uplift of the Tibetan Plateau since 1.8 Ma recorded by major elements in sediments of the South China Sea. Chinese Science Bulletin, 56(6): 547–551, doi: 10.1007/s11434-010-4258-1

Mitchum R M Jr. 1985. Seismic stratigraphic expression of submarine fans. AAPG Special Volumes, 167: 117–136

Nott J, Roberts R G. 1996. Time and process rates over the past 100 m.y.: A case for dramatically increased landscape denudation rates during the late Quaternary in northern Australia. Geology, 24(10): 883–887, doi: 10.1130/0091-7613(1996)024<0883:TAPROT>2.3.CO;2

Oline H B, Eldholm O, Skogseid J. 1999. Cenozoic evolution of the northern Vøring margin. Geological Society of America Bulletin, 111(12): 1792–1807, doi: 10.1130/0016-7606(1999)111<1792:CEOTNV>2.3.CO;2

Pang Xiong, Chen Changmin, Zhu Ming, et al. 2009. Baiyun movement: a significant tectonic event on Oligocene/Miocene boundary in the northern South China Sea and its regional implications. Journal of Earth Science, 20(1): 49–56, doi: 10.1007/s12583-009-0005-4

Porębski S J, Steel R J. 2001. Delta types and sea level cycle. AAPG Annual Convention, 10: A160

Porębski S J, Steel R J. 2003. Shelf-margin deltas: their stratigraphic significance and relation to deepwater sands. Earth-Science Reviews, 62(3–4): 283–326

Prell W L. 1982. Oxygen and carbon isotope stratigraphy for the quaternary of Hole 502B: evidence for two modes of isotopic variability. In: Initial Reports of the Deep Sea Drilling Project. Washington: U.S. Government Printing Office, 68: 455–464

Prell W L, Kutzbach J E. 1987. Monsoon variability over the past 150, 000 years. Journal of Geophysical Research, 92(D7): 8411–8425, doi: 10.1029/JD092iD07p08411

Qin Guoquan. 1996. Application of micropaleontology to the sequence stratigraphic studies of late Cenozoic in the Zhujiang River Mouth Basin. Marine Geology & Quaternary Geology (in Chinese), 16(4): 1–18

Shackleton N J. 1987. Oxygen isotopes, ice volume and sea level. Quaternary Science Reviews, 6(3–4): 183–190

Sun Zhen, Zhong Zhihong, Zhou Di, et al. 2008. Dynamics analysis of the Baiyun Sag in the Pearl River Mouth Basin, North of the South China Sea. Acta Geologeca Sinica, 82(1): 73–83

Tang Song, Shao Lei, Zhao Quanhong. 2004. Characteristics of clay mineral in South China Sea since Oligocene and its significance. Acta Sedimentologica Sinica (in Chinese), 22(2): 337–342

Vail P R. 1987. Seismic stratigraphy interpretation using sequence stratigraphy, Part 1: seismic stratigraphy interpretation procedure. In: Bally A W, ed. Atlas of Seismic Stratigraphy. Tulsa, OK: AAPG Studies in Geology, 27: 1–10

Vail P R, Audemard F, Bowman S A, et al. 1991. The stratigraphic signatures of tectonics, eustasy and sedimentology-an overview. In: Einsele G, Ricken W, Seilacher A, eds. Cycles and Events in Stratigraphy. Berlin: Springer-Verlag, 617–659

Vail P R, Mitchum R M, Todd R G, et al. 1977a. Seismic stratigraphy and global changes in sea level. In Payton C E, ed. Seismic Stratigraphy-Applications to Hydrocarbon Exploration. Tulsa: American Association of Petroleum Geologists, 26: 49–212

Vail P R, Mitchum R M, Todd R G, et al. 1977b. Seismic stratigraphy and global changes of sea-level, Part 9. Seismic interpretation of elastic depositional fades. In: Payton C E, ed. Seismic Stratigraphy-Application to Hydrocarbon Exploration. Tulsa: American Association of Petroleum Geologists, 26: 83–97

Wang Pinxian, Jian Zhimin, Zhao Quanhong, et al. 2003. Evolution of the South China Sea and monsoon history revealed in deep-sea records. Chinese Science Bulletin, 48(23): 2549–2561, doi: 10.1360/03wd0156

Wang Pinxian, Li Qianyu. 2009. The South China Sea: Paleoceanography and Sedimentology. Netherlands: Springer, 1–50

Wang Pinxian, Li Qianyu, Tian Jun. 2014. Pleistocene paleoceanography of the South China Sea: Progress over the past 20 years. Marine Geology, 352: 381–396, doi: 10.1016/j.margeo.2014.03.003

Wang Guozhi, Wang Chenshan, Zeng Yunfu. 1999. Sedimentary Evidence of the Western Yunnan Plateau Uplift since Miocene. Bulletin of Mineralogy, Petrology and Geochemistry (in Chinese), 18(3): 167-170

Wu Shiguo, Liu Zhan, Wang Wanyin, et al. 2004. Late Cenozoic neotectonics in the Dongsha islands region and its responds to collision between Chinese continental margin and Luzon. Oceanologia et Limnologia Sinica (in Chinese), 35(6): 481–490

Wu Jinggu, Xu Qiang, Zhu Yanhe. 2010. Generation and dvolution of the shelf-ddge delta in Oligocene and Miocene of Baiyun Sag in the South China Sea. Earth Science (in Chinese), 35(4): 681–690

Xie Lihua, Lin Changsong, Dong Wei, et al. 2009. High-resolution sequence stratigraphy of Zhujiang Formation and Zhuhai formation in Panyu low uplift of the Zhujiang River mouth basin. Geology in China (in Chinese), 36(2): 366–377

Xie Hui, Zhou Di, Li Yuanping, et al. 2014. Cenozoic tectonic subsidence in deepwater sags in the Pearl River Mouth Basin, northern South China Sea. Tectonophysics, 615–616: 182–198

Zhang Yulan. 2008. Sporopollen and algae in Core C4 of northern South China Sea and its paleoenvironment. Journal of Tropical Oceanography (in Chinese), 27(6): 44–48

Zhang Xunhua, Li Yancheng, Qi Zhenhua, et al. 1997. An approach to the formation and evolution model of South China Sea Basin.

Marine Geology & Quaternary Geology (in Chinese), 17(2): 1–7

Zhang Peizhen, Molnar P, Downs W R. 2001. Increased sedimentation rates and grain sizes 2–4 Myr ago due to the influence of climate change on erosion rates. Nature, 410(6831): 891–897, doi: 10.1038/35073504

Zhao Quanhong, Jian Zhimin, Wang Jiliang, et al. 2001. Neogene oxygen isotopic stratigraphy, ODP Site 1148, northern South China Sea. Science in China Series D: Earth Sciences, 44(10): 934–942, doi: 10.1007/BF02907086

Zheng Hongbo, Powell C M, An Zhisheng, et al. 2000. Pliocene uplift of the northern Tibetan Plateau. Geology, 28(8): 715–718, doi: 10.1130/0091-7613(2000)28<715:PUOTNT>2.0.CO;2

Zhisheng A, Kutzbach J E, Prell W L, et al. 2001. Evolution of Asian monsoons and phased uplift of the Himalaya-Tibetan plateau since Late Miocene times. Nature, 411(6833): 62–66, doi: 10.1038/35075035

Zhou Wei, Wang Yingmin, Gao Xianzhi, et al. 2015. Architecture, evolution history and controlling factors of the Baiyun submarine canyon system from the middle Miocene to Quaternary in the Pearl River Mouth Basin, northern South China Sea. Marine and Petroleum Geology, 67: 389–407, doi: 10.1016/j.marpetgeo.2015.05.015

Zhu Yanhe, Zhu Weilin, Xu Qiang, et al. 2011. Sedimentary response to shelf-edge delta and slope deep-water fan in 13.8 Ma of Miocene epoch in Pearl River Mouth Basin. Journal of Central South University (Science and Technology) (in Chinese), 42(12): 3827–3834

Zhuo Haiteng, Wang Yingmin, Shi Hesheng, et al. 2015. Contrasting fluvial styles across the mid-Pleistocene climate transition in the northern shelf of the South China Sea: Evidence from 3D seismic data. Quaternary Science Reviews, 129: 128–146, doi: 10.1016/j.quascirev.2015.10.012

Acoustic backscattering measurement from sandy seafloor at 6–24 kHz in the South Yellow Sea

Guangming Kan[1, 2], Baohua Liu[2, 3*], Zhiguo Yang[2, 3], Shengqi Yu[2, 3], Lehua Qi[1, 4], Kaiben Yu[2, 3], Yanliang Pei[1, 2]

[1] Key Laboratory of Marine Sedimentology and Environmental Geology, First Institute of Oceanography, Ministry of Natural Resources, Qingdao 266061, China

[2] Laboratory for Marine Geology and Environment, Pilot National Laboratory for Marine Science and Technology (Qingdao), Qingdao 266237, China

[3] National Deep Sea Center, Ministry of Natural Resources, Qingdao 266237, China

[4] College of Marine Geosciences, Ocean University of China, Qingdao 266100, China

Abstract

The acoustic bottom backscattering strength was measured at the frequency range of 6–24 kHz on a typical sandy bottom in the South Yellow Sea by using omnidirectional sources and omnidirectional receiving hydrophones. In the experiment, by avoiding disturbances due to scattering off the sea surface and satisfying the far-field condition, we obtained values of acoustic bottom backscattering strength ranging from –41.1 to –24.4 dB within a grazing angle range of 18°–80°. In the effective range of grazing angles, the acoustic scattering strength generally increases with an increase in the grazing angles, but trends of the variation were distinct in different ranges of frequency, which reflect different scattering mechanisms. The frequency dependence of bottom backscattering strength is generally characterized by a positive correlation in the entire frequency range of 6–24 kHz at the grazing angles of 20°, 40° and 60° with the linear regression slopes of 0.222 9 dB/kHz, 0.513 0 dB/kHz and 0.174 6 dB/kHz, respectively. At the largest grazing angle of 80°, the acoustic backscattering strength exhibits no evident frequency dependence.

Key words: acoustic backscattering strength, sandy bottom, South Yellow Sea, gazing angle dependence, frequency dependence

1 Introduction

The ocean bottom is an important boundary for the underwater sound field and the acoustic properties of ocean bottom are important factors that influence the spatial structure of underwater sound field as well as the propagation of sound waves in the sea. The complexity of sound propagation in shallow water at sea is mainly due to the strong interaction between sound waves and the bottom. Without knowing the acoustic properties of the ocean bottom, it is difficult to fully understand the laws of acoustic propagation in oceans. Therefore, it is important for underwater acousticians to measure and study the acoustic properties of the ocean bottom, which is usually treated as a black box (Zou et al., 2014; Zhang et al., 2013; Wen et al., 2006).

When an acoustic wave is incident onto the ocean bottom, it is scattered by the rough interface of the seabed. The scattered waves deviate from the direction of specular reflection and decentralize the wave energy distribution in the seawater, complicating the structure of the underwater sound field. Moreover, reverberation caused by bottom scattering is an important source of ocean reverberation, which is a key factor affecting the performance of underwater sonar and the accuracy of underwater target detection (Peng et al., 2004; Jin et al., 1987; Hu, 2009; Dong et al., 2013). Therefore, studying the properties of acoustic bottom scattering has important applications to the prediction of ocean reverberation, object detection on the ocean bottom, and research on ocean acoustics in general (Gao, 2013; Li and Sun, 2008).

Researchers have conducted numerous measurements and research on acoustic bottom scattering at frequencies higher than 20 kHz (Jackson et al., 1986; Stanic et al., 1988a, b, 1989; Williams et al., 2002, 2009; Williams, 2009). The mid-to-low-frequency acoustic bottom scattering at frequencies lower than 20 kHz (especially lower than 10 kHz) is easily influenced by reflection and scattering from the sea surface, thus making it more challenging to measure and rendering its scattering mechanism more complicated, in comparison with high-frequency acoustic scattering. Researchers have thus begun attending to pay increasing attention to the measurement and research of mid- to low-frequency acoustic bottom scattering. Soukup and Gragg (2003) measured acoustic bottom backscattering at frequencies

of 2–3.5 kHz on a limestone bottom in the sea area near South Carolina, USA (Soukup and Gragg, 2003). Hines et al. (2005) measured acoustic bottom backscattering at frequencies of 4 and 8 kHz at two sandy bottom sites using parametric array sources with a grazing angle range of 3°–15° (Hines et al., 2005). La and Choi (2010) measured acoustic bottom scattering at a frequency of 8 kHz on a nearshore silty bottom in the southern part of South Korea with a grazing angle range of 6°–31° using omnidirectional sources and omnidirectional hydrophones (La and Choi, 2010). Yu et al. (2017) established a backscattering model for a stratified seafloor applying to low frequency from 0.1 to 10 kHz (Yu et al., 2017). The researches mentioned-above indicate that the acoustic bottom scattering strength is distinct at different frequency range. Beside the frequency dependence of acoustic bottom scattering strength, it also has obvious contrasts for different sediment types (McKinney and Anderson, 1964; Jackson et al., 1986; Stanic et al., 1988a, b, 1989; Jackson and Briggs, 1992; Pouliquen and Lyons, 2002; La and Choi, 2010; Hines et al., 2005). The result from McKinney and Anderson indicates that the acoustic backscattering strength from medium sandy bottom is about 5 dB higher than very fine sandy muddy bottom, but is about 7 dB lower than medium sandy clay bottom at the same grazing angles. The bottom scattering from medium sandy bottom measured by Hines et al. (2005) is about 9 dB higher than that from silty bottom measured by La and Choi (2010). In addition, the acoustic bottom scattering strength is related to the roughness of bottom and the volume heterogeneity in sediments (Jackson and Briggs, 1992; Jackson and Richardson, 2007). Therefore, it is necessary to systematically investigate the acoustic bottom scattering property in a specified area and at a wide frequency range.

At present, the measurement and research of the mid-frequency bottom scattering are only concentrated on several discrete frequency points, rather than continuous and systematic measurement in a wide frequency band. Moreover, current measurements were made in different types of seafloors, which makes difficult to compare the data at different frequencies. This paper reports the procedure and results of an experiment to measure acoustic bottom backscattering at a mid-frequency range of 6–24 kHz on a typical sandy bottom in the South Yellow Sea. Following the introduction, relationships between the characteristics of mid-frequency acoustic backscattering from the sandy bottom and the grazing angle, frequency, and features of bottom sediment are discussed.

2 Measurement of bottom backscattering and data processing

2.1 *Measurement of the environmental parameters at seafloor*

The study area is located in a sandy bottom region of the South Yellow Sea with the latitude ranging from 34.87°N to 35.37°N and the longitude ranging from 121.01°E to 121.62°E, approximately 70 nautical miles southeast of Qingdao City. At a depth of 36–41 m, the bottom of the study area is flat and the sediment is dominated by fine sand. Three measuring sites were arranged—S1, S2 and S3—in the study area, with depths of approximately 36 m at Sites S2 and S3, and that of approximately 41 m at Site S1. Results of measurement of the sound speed profile of seawater in the area revealed a thermocline approximately 20 m deep in September, with a difference of approximately 20 m/s in the sound speed above and below the thermocline (Fig. 1). Some sediment samples were collected using a box corer. However, as all zones near the three measuring sites had "very hard sand sheet" bottoms, only a small amount of sediment was obtained. Sediments approximately 10 cm thick were obtained at S1 and
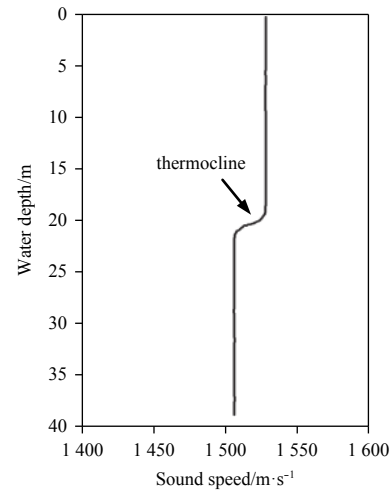

Fig. 1. Sound speed profile in seawater measured in September at Site S1.

S3. The upper 5 cm of the sediments consisted of relatively evenly distributed fine sand and the lower 5 cm had many shell fragments. Photographs of the bottom obtained using an underwater camera show that there are many shell fragment in the bottom at S1 and S3 (Fig. 2). The sampling depth at S2 was approximately 7 cm, where the sediment consists of evenly distributed fine sand without shell fragments (Fig. 2). Results of the measurement of physical properties of the sediment samples show that the content of fine sand in the samples collected at S1 is 79.9%, and the average grain size is in the range from 3.07Φ to 3.35Φ. The content of fine sand in the samples collected at S2 is 86.8%, and the average grain size is in the range from 2.75Φ to 3.04Φ (with an average value of 2.989Φ). The content of fine sand in the samples collected at S3 is 78.4%, and the average grain size is in the range from 2.82Φ to 4.31Φ.

2.2 *Method of bottom backscattering strength calculation*

The method to measure acoustic bottom backscattering strength by using a spherical omnidirectional source and an omnidirectional hydrophone is shown in Fig. 3. Sound waves transmitted by the acoustic source reach the bottom at Point A at time t (corresponding to a grazing angle of θ), and the backscattered waves from the bottom are received by the hydrophone fixed just below the acoustic source. As the hydrophone is close to the source, the bottom backscattering is regarded as having approximately a monostatic geometry in the experiment. For monostatic bottom backscattering, the ensonified zone at time t is an annulus, and its width is determined by the pulse length of the emitting signal. The slant range from the acoustic source to the inner and outer boundary of the scattering zone is denoted by r and and r', respectively, and is calculated by:

$$r = c_{\mathrm{w}}t/2, \tag{1}$$

and

$$r' - r = \tau/2c_{\mathrm{w.}} \tag{2}$$

If the height of the source and hydrophone above the seafloor is denoted by H, the following relationship is obtained according to the geometry in Fig. 3.
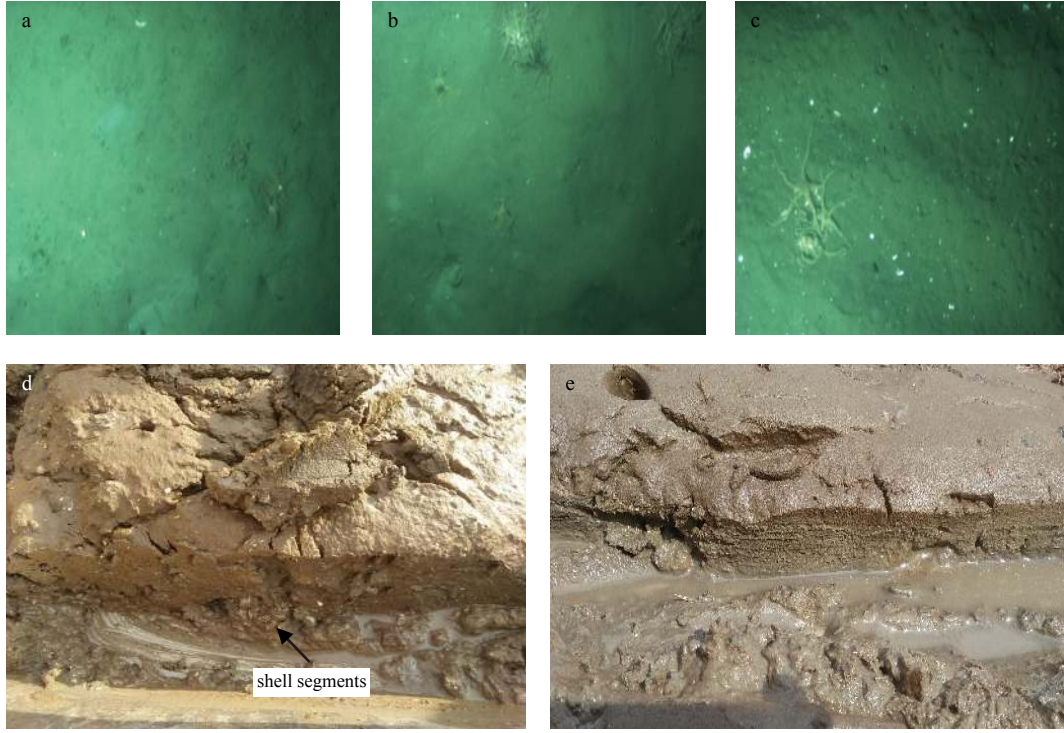
Fig. 2. Photos of bottom obtained using underwater camera and sediment collected using sampling boxer. a. Bottom photo at S1, b. bottom photo at S2, c. bottom photo at S3, d. sediment collected at S1, and e. sediment collected at S2.
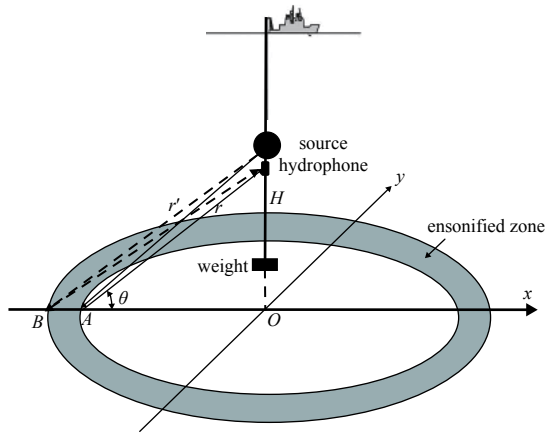

Fig. 3. Diagram of backscattering measurement using a omnidirectional source and a omnidirectional hydrophone.

$$r^2 = H^2 + R^2, \tag{3}$$

and

$$r'^2 = H^2 + R'^2, \tag{4}$$

where R and R' are the distance from Point O to Points A and B, respectively. The area of the ensonified zone on the bottom can then be calculated as

$$A = \pi \left(R'^2 - R^2 \right). \tag{5}$$

Combining Eqs (1) –(5), we get:

$$A = \pi \left(r + \frac{1}{4} c_w \tau \right) c_w \tau, \tag{6}$$

where τ is the length of the transmitted signal, c_w is the sound speed in seawater, and θ is the grazing angle.

For bottom backscattering using an omnidirectional source and an omnidirectional hydrophone in case both are (or approximately are) at the same position, the intensity of the scattered sound corresponding to grazing angle θ can be expressed as

$$\langle I_s(\theta) \rangle = \int \frac{I_0}{r^4} \sigma(\theta) \mathrm{d}A, \tag{7}$$

where $I_s(\theta)$ is the scattering intensity at grazing angle θ, and the angle bracket "$\langle \rangle$" denotes the average value of the random variable over the entire measurement set accounting for the randomness of the scattering intensity. In measurement in practice, random samples are typically obtained by transmitting the sound many times from a survey ship floating near the site. I_0 is the intensity of the incident sound one meter from the acoustic source, $\sigma(\theta)$ is the backscattering cross section, r is the slant range from the acoustic source to the inner boundary of the scattering zone corresponding to a grazing angle θ, and $\mathrm{d}A$ is the the differential element of the area of the ensonified zone on the bottom.

Equation (7) can be rewritten in terms of the real voltage output of the hydrophone as (under the condition that the change in r over Area A is small enough)

$$\langle v_r(t)^2 \rangle = \frac{s_t^2 s_r^2}{r^4} \int \sigma(\theta) \mathrm{d}A, \tag{8}$$

where $v_r(t)^2$ denotes the mean square value of the real voltage output of the hydrophone in volt before being amplified. Parameters s_t and s_r are related to the source level and the sensitivity

of the hydrophone, repectively, as

$$SL = 20\log_{10}(s_t/10^{-6}), \qquad (9)$$

$$RS = 20\log_{10}(s_r/10^{6}), \qquad (10)$$

where *SL* is the acoustic source level of the acoustic source in dB *re.* 1 μPa one meter from the source, and *RS* is the sensitivity of hydrophone in dB *re.* 1 V/μPa. *SL* and *RL* can be measured through the calibration of the source and the hydrophone, respectively, in the laboratory. If the change in grazing angle θ is small enough such that $\sigma(\theta)$ is approximately constant over the ensonified zone, the bottom backscattering strength can be calculated by the following sonar equation,

$$\begin{aligned} S_b(\theta) = 10\log_{10}\sigma(\theta) = 10\,\log_{10} < v_r(t)^2 > \, -SL - \\ RS + 2TL - 10\log_{10}(A), \end{aligned} \qquad (11)$$

where $S_b(\theta)$ is the backscattering strength at grazing angle θ in dB, $TL = 20\log_{10} r$ is the one-way transmission loss in dB, and *A* is the area of the ensonified zone shown in Fig. 3, $v_r(t)$ is the output of the effective voltage from the hydrophone and can be approximately expressed by the envelope $V_r(t)^2$ as

$$v_r(t)^2 = \frac{V_r(t)^2}{2}. \qquad (12)$$

In Eq. (11), *TL* and *A* are related to the slant range *r*, which is represented in terms of θ as

$$r = H/\sin\theta. \qquad (13)$$

According to different grazing angle θ, the slant range *r* can be calculated by Eq. (13). Then, *TL* and *A* can be obtained. Finally, the acoustic bottom backscattering strength $S_b(\theta)$ can be calculated by using Eqs (11) and (12).

2.3 *Description of the experiment and data processing*

In this experiment, three spherical omnidirectional source transducers with central frequencies of 8 kHz, 15 kHz and 20 kHz, respectively, and an omnidirectional broadband hydrophone were used to measure the acoustic bottom backscattering strength. The geometry of the experiment is shown in Fig. 4. A TL-30 hydrophone was located one meter below the spherical acoustic sources and was connected to a single-channel self-contained recorder that had an acoustic wave sampling rate of 96 kHz. The sound waves received by the TL-30 hydrophone were used to calculate the bottom backscattering strength. Moreover, an HTI hydrophone on one side of the source, connected to a real-time recorder in a deck laboratory, was used to monitor the acoustic waves emitted by the source. The spherical acoustic sources were generally 7–8 m from the bottom. Self-contained temperature and depth (short for STD) recorders were fixed near the acoustic source and the hydrophone to monitor the distances between each and the bottom. The acoustic source levels of the three spherical transducers at their central frequencies were 203 dB *re.* 1 μPa at 8 kHz, 201 dB *re.* 1 μPa at 15 kHz, and 205 dB *re.* 1 μPa at 20 kHz. The sensitivity of the TL-30 omnidirectional broadband hydrophone in an operating band of 2.5–60 kHz was –197 to –190 dB *re.* 1 V/μPa. During the experiment, the survey ship floated near the corresponding measure-
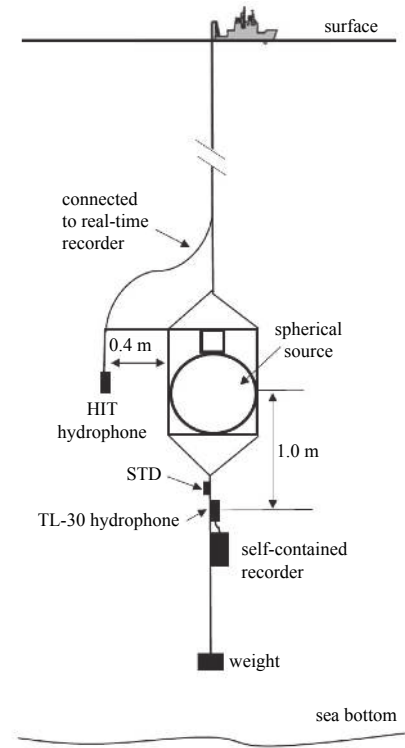

Fig. 4. The geometry of the bottom backscattering measurement.

ment site, transmitting a 1 ms sinusoidal pulse signal every time and repeating the signal 90 times at an interval of 2 s. In the range 6–24 kHz, the above operation was repeated at a frequency interval of 1 kHz so that the signal could cover all frequencies.

According to the maximum effective recording length and transmitting interval, the waveform of each ping at the target frequency was extracted from the entire data set. The received original signals with 90 waveforms superposed at frequencies of 8 kHz and 22 kHz are shown in Fig. 5. The first arrival waveform, the bottom reflected waveform, and the sea surface reflected waveform can be clearly identified in the figure. Because the hydrophone is very close to the acoustic source, the amplitude of the first arrival waveform is beyond the dynamic range of the acquisition unit, and resulted in signal truncation. The weak scattered signal after the first arrival wave (at 4–5 ms) is the acoustic scattering from the weight. By comparing Fig. 5a with Fig. 5b, it is evident that with an increase in frequency, acoustic scattering from the weight becomes more prominent. The zone after the bottom-reflected signal (~10 ms) is the acoustic bottom scattering zone. The signal after 39 ms can not be used to calculate bottom scattering due to the influence of reflection and scattering from the sea surface. The signal that can be used to calculate the acoustic bottom scattering strength is limited between the bottom-reflected signal and the sea surface-scattered signal, and determines the range of the grazing angle for the calculation of the bottom backscattering strength. In shallow sea, due to the influence of reflection and scattering from the sea surface, the scattering strength can not be calculated when the grazing angle is very small, which is a shortcoming of measuring bottom scattering using an omnidirectional source and a omnidirectional hydrophone. According to the characteristics of the signal shown in Fig. 5 and the corresponding measurement geometry, the calculated lower limit of the grazing angle to measure scattering strength is approximately 18°. In this experiment, distances from
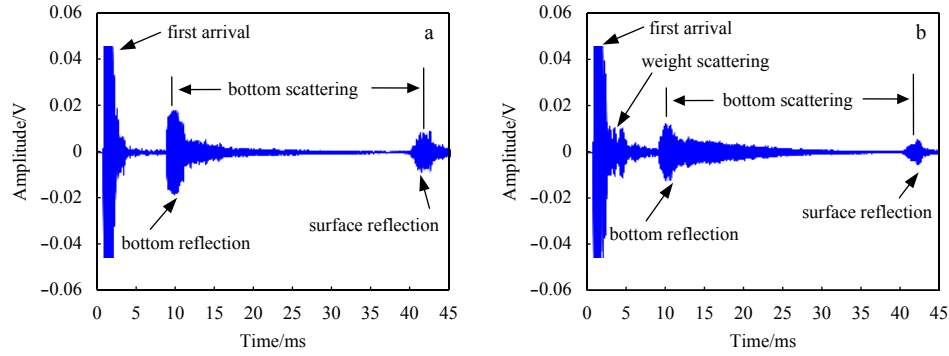
Fig. 5. Waveform received by TL-30 hydrophone at Site S1. a. 8 kHz, and b. 22 kHz.

both the acoustic source and the hydrophone to the bottom are greater than 5 m, thus satisfying the far-field conditions. Therefore, the upper limit of the grazing angle is mainly determined by the characteristics of the bottom reflected and scattered signals, and it was set to 80° in this experiment.

At first, the amplitude envelope of the temporal waveform of each ping, i.e., the voltage value output from the hydrophone $V(t)$, was obtained through a Hilbert transform of temporal series of the waveform at one target frequency. Generally, the mean value of amplitude envelope for different pings at the same target frequency was used to calculate the scattering strength in order to eliminate the random noise. Then, the amplitude envelops were calculated at all frequencies from 6 kHz to 24 kHz with 1 kHz step. As an example, the amplitude envelopes of 90 effective pings at two frequencies of 8 kHz and 22 kHz were superposed and drawn in Fig. 6 corresponding the waveform in Fig. 5. Their averaged envelopes of 90 effective pings were also shown in Fig. 6 with red curves. The procedure of scattering strength calculation was as follows. Firstly, at one target frequency, the grazing angle θ ranges from 18° to 80° with the step of 1°. According to Eq. (13) and Eq. (6), the slant range r and the area of the ensonified zone A corresponding to each grazing angle θ are calculated. Secondly, The effective voltage value $v_r(t)$ corresponding to each grazing angle θ and slant range r was calculated by using Eq. (12), where the $V(t)$ in Eq. (12) was averaged over 90 pings and t can be obtained by using $t = 2r/c_w$. The one-way transmission loss can be calculated according to the formula of $TL = 20 \log_{10} r$. Finally, By substituting the effective voltage value $v_r(t)$, the one-way transmission loss TL, the area of the ensonified zone A into Eq. (11), the acoustic bottom backscattering strength $S_b(\theta)$ at one target frequency can be obtained with the grazing angle ranging from

18°–80°, where SL and RS can be obtained through the calibration of source level of omni-directional source and receiving sensitivity of omni-directional hydrophone. The bottom backscattering strength at frequencies in the range of 6–24 kHz can be calculated by repeating the three processes for each target frequency when the frequency ranges from 6 kHz to 24 kHz with the step of 1 kHz. The calculation results show that the acoustic bottom scattering strength falls between –41.1 and –24.4 dB in the grazing angle range of 18°–80° and in the frequency range of 6–24 kHz.

3 Results and discussion

3.1 *Relationship between the backscattering strength and the grazing angle*

Figure 7 shows the relationship between the acoustic bottom scattering strength and the grazing angles at different frequencies in S1. It is clear that the range of the effective grazing angle is 18°–80° in this experiment, over which the acoustic bottom scattering strength was obtained effectively. Due to the influence of sea surface reflection, the scattering strength at smaller grazing angles could not be calculated correctly, which is a limitation in measuring acoustic scattering in shallow water using omnidirectional sources and receivers. Figure 7 shows that the acoustic bottom scattering strength at S1 generally increases with an increase in the grazing angle, but the trends of variation are different at different frequencies. In different frequency bands and at different grazing angles, the acoustic scattering strength exhibits different properties. In the frequency band 6–18 kHz, the scattering strength increases rapidly with the grazing angle for angles greater than 70°, which is the so-called backscattering enhance-
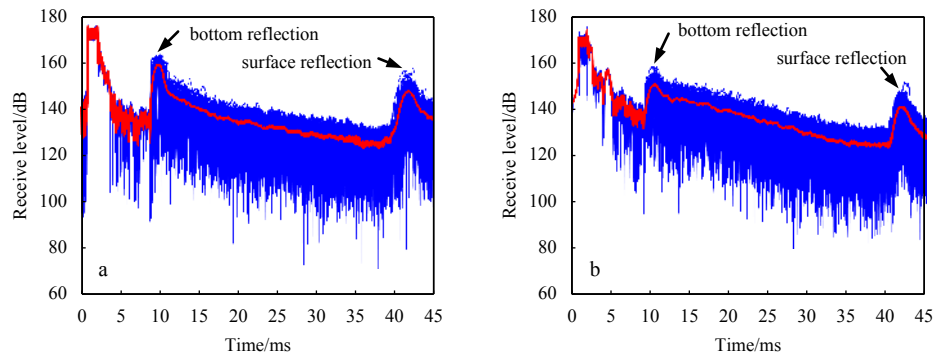
Fig. 6. Envelopes corresponding to the waveform in Fig. 5. Blue curves are envelopes for 90 realization and red curve is their averaged envelope. a. 8 kHz, and b. 22 kHz.

ment phenomenon. This indicates that acoustic scattering for grazing angles greater than 70° is not completely diffuse, but is significantly enhanced along the direction near to the specular reflection. In the frequency band 20–24 kHz, there is no signific-

ant enhancement in backscattering for grazing angles greater than 70°. With an increase in frequency, the trend of variation in scattering strength with grazing angle tends to be gentle at large grazing angles. In particular at 24 kHz, the scattering strength ex-

Fig. 7.

Fig. 7. Relationships between the backscattering strength and the grazing angles at different frequencies at Site S1. a. 6 kHz, b. 8 kHz, c. 10 kHz, d. 12 kHz, e. 14 kHz, f. 16 kHz, g. 18 kHz, h. 20 kHz, i. 22 kHz, and j. 24 kHz.

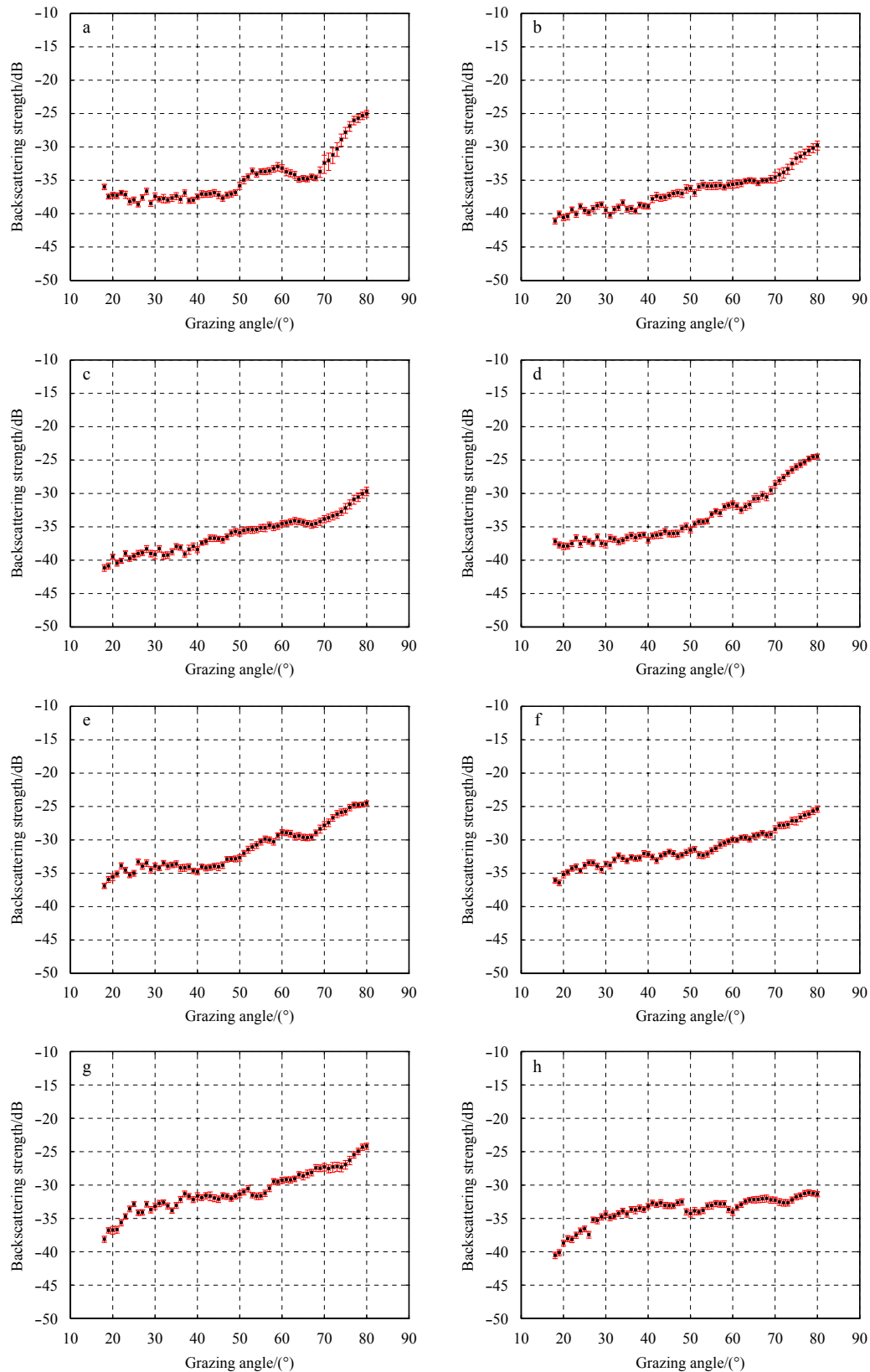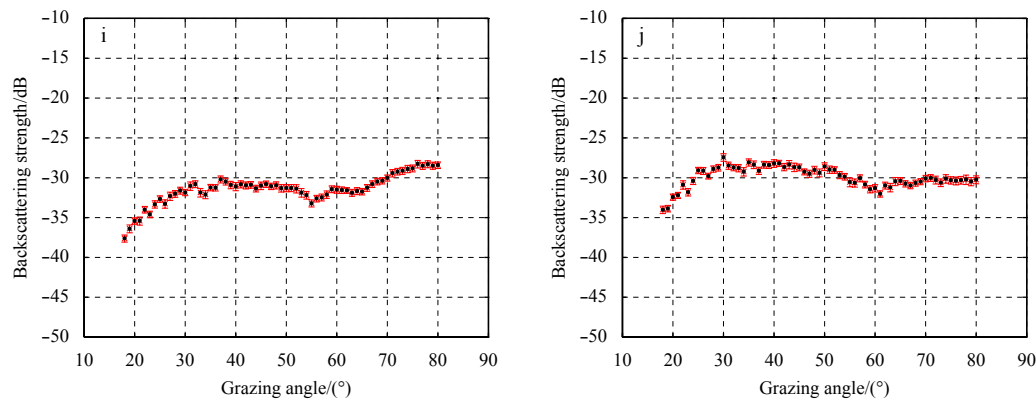hibit a decrease with an increase in the grazing angles greater than 50°, perhaps because of the low SNR (signal-to-noise ratio) at high frequency. The different trends of variation in scattering strength with grazing angle at different frequency bands reflect different acoustic scattering mechanisms, and this needs to be analyzed comprehensively combining with such bottom environmental parameters as bottom roughness and geoacoustic properties.

Hines et al. (2005) conducted measurements using parametric array sources at two well-sorted medium sandy bottom sites with the grain sizes ranging from 1.39Φ to 0.69Φ (0.25–0.50 mm) in the New Jersey continental shelf area and the Scotian continental shelf area, and obtained acoustic bottom backscattering strength values of –25.4 to –23.1 dB, and of –29.0 to –26.1 dB, repectively, at a grazing angle of 15° and a frequency of 8 kHz (Hines et al., 2005). Figure 7b shows that the backscattering strength varies from –41.1 to –40.6 dB at S1 at the grazing angles ranging from 18° to 20° and a frequency of 8 kHz, lower than the results measured by Hines et al. (2005). La and Choi (2010) conducted measurements on a nearshore silty bottom in South Korea to obtain bottom backscattering strength of approximately –33 dB within a grazing angle range of 18°–20° and at a frequency of 8 kHz, which is approximately 8 dB higher than the backscattering strength at Site S1 (La and Choi, 2010). Bottom backscattering strength measured by Jackson et al. (1986) at a site with very fine sand bottom and grain size of 0.12 mm is approximately –24 dB at a grazing angle of 20° at 20 kHz. This is approximately 16 dB higher than the results obtained in our experiment at the same grazing angle (20°) and frequency (20 kHz) (Jackson et al., 1986), where the grain sizes are very similar. Jackson et al. (1986) pointed out that scattering strength can differ by 10–15 dB for sediments with similar grain size. This difference indicates that the mechanism of acoustic bottom scattering is very complex and is dominated not only by grain size, but also by the roughness of the bottom, heterogeneity of the sediment and other factors.

3.2 *Frequency dependence of the backscattering strength*

For the dependence of the acoustic bottom backscattering strength on acoustic wave frequency, different researchers have calimed different relationships according to different bottom types and measurement frequencies. The data collected by Jackson et al. (1986) in Puget Sound exhibited a frequency dependence with a positive slope of 1.4 dB/octave at a frequency of 20–85 kHz and a grazing angle of 20° for a silty sand bottom and a frequency dependence with a positive slope of 0.8 dB/octave at a frequency of 20–80 kHz and a grazing angle of 20° for a very fine

sand bottom. However, another set of data obtained by Jackson at a North Sea site exhibited a frequency dependence with a negative slope of –0.2 dB/octave at a frequency of 20–75 kHz and a grazing angle of 20° for sandy silt bottom (Jackson et al., 1986). Based on the results measured on the nearshore shell-rich coarse sand bottom in Jacksonville, Florida, Stanic et al. (1989) found that acoustic bottom backscattering strength exhibited a negative correlation with frequency with a slope of –0.75 dB/octave in the frequency range of 20–180 kHz (Stanic et al., 1989). At present, few studies have addressed the frequency dependence of acoustic bottom backscattering in the mid-frequency band of 6–24 kHz. Figure 8 shows the curves of variation in backscattering strength with grazing angle at different frequency ranges based on the results in this experiment. It is evident from Fig. 8a that the frequency dependence of backscattering strength is very weak and there is no clear trend in the variation of the backscattering strength with frequency at 6–12 kHz. The scattering strength shows a relatively significant frequency dependence in the range from 12 kHz to 24 kHz, as shown in the Figs 8b and c, where the backscattering strength increases with an increase in frequency except at grazing angles greater than 65°. Four grazing angles (i.e., 20°, 40°, 60°, 80°) were chosen to draw the curves of backscattering strength versus frequency, as shown in Fig. 9. It shows that the frequency dependence of acoustic backscattering strength can be generally characterized by a positive correlation with frequency as a whole in the range of 6–24 kHz . As listed in Table 1, the slopes of linear regression between backscattering strength and the frequency in the range of 6–24 kHz at grazing angles of 20°, 40° and 60° are 0.222 9 dB/kHz, 0.513 0 dB/kHz and 0.174 6 dB/kHz, respectively. The result of measurements of the environmental parameters on the bottom indicates that the bottom at Site S1 is very flat, and has no significant local relief such as sand ripples on the bottom. Therefore, the bottom backscattering is mainly caused by the micro-roughness of the bottom and is more sensitive for higher frequency, which corresponds to the frequency dependence of backscattering strength whereby the latter increases with the former. The backscattering strength shows no evident frequency dependence at 80°, perhaps because of the inclusion of some coherent component in backscattering field and the poor quality data at the largest grazing angle of 80°.

3.3 *Relationship between the backscattering strength and the bottom sediment properties*

Figure 10 shows a comparison of backscattering strength among Sites S1, S2 and S3 at a frequency of 11 kHz. It is evident
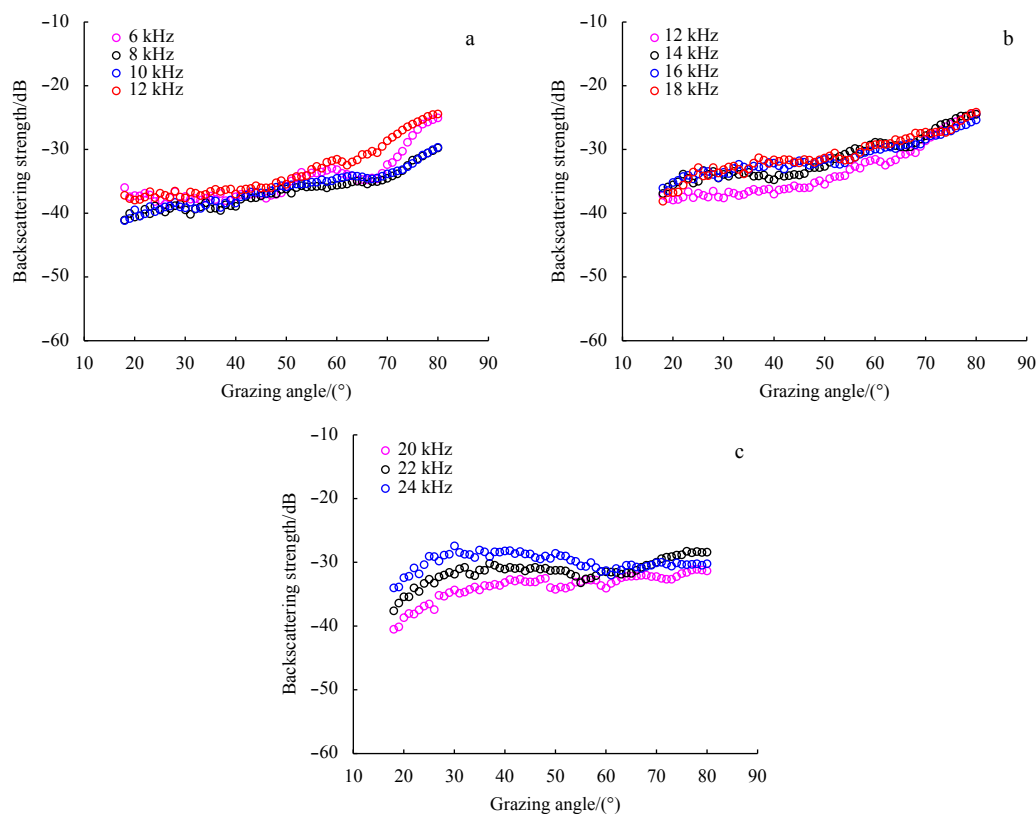
Fig. 8. Relationship between backscattering strength and frequency at different grazing angles at Site S1. a. 6–12 kHz, b. 12–18 kHz, c. 20–24 kHz.
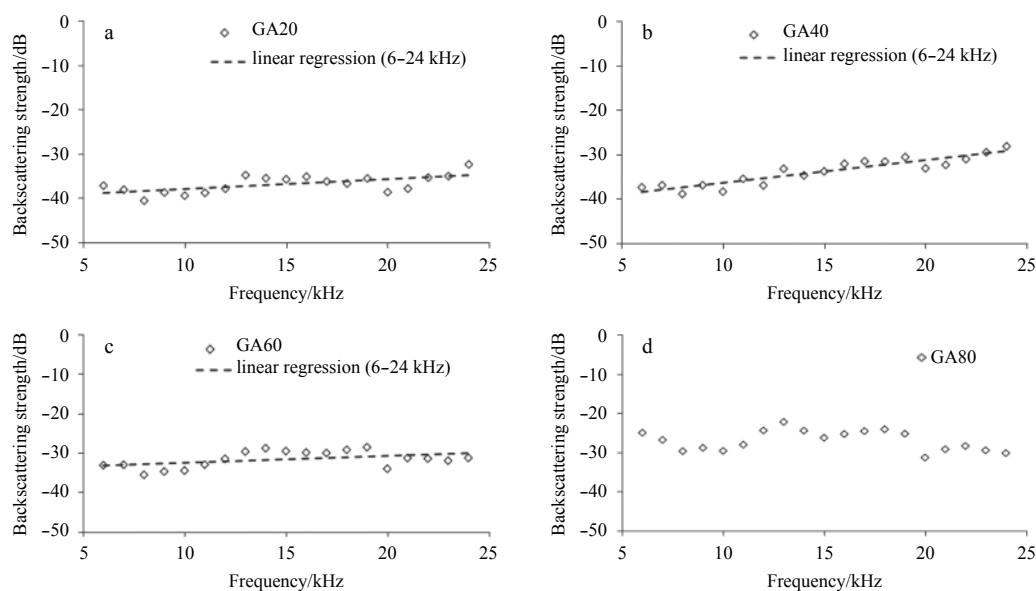

Fig. 9. Frequency dependence of backscattering strength at frequency ranges of 6–24 kHz at different grazing angles at Site S1. Grazing angle: a. 20°, b. 40°, c. 60°, and d. 80°.

that the backscattering strength at S2 is significantly higher than that at S1. The maximum and minimum offsets are 7.03 dB and 1.18 dB, respectively, and the average is 4.63 dB. The corresponding grazing angles for the maximum and minimum offsets are 78° and 25°, respectively. The backscattering strength at S2 is higher than that at S3 as a whole, excepting in the grazing angle from 67° to 73°. The the maximum offset is 7.8 dB at the grazing angle of

74°. The results of measurements of the physical properties of the bottom sediment show that the sediments at S2 have larger grain size and higher content of sandy grain than at S1 and and S3. The difference in grain size of bottom sediments among the three sites might be the main cause of the above difference in backscattering strength. In addition, as shown in Fig. 2, there are a large number of shell fragments in the sediment at Sites S1 and S3, but

Table 1. Parameters of linear regression between backscattering strength and frequency at 6–24 kHz at Site S1

Grazing angle/(°)	Equation of linear regression	Slope/dB·kHz⁻¹	Correlation coefficient
20	BBS=0.222 9×*f*–40.207	0.222 9	0.63
40	BBS=0.513 0×*f*–41.552	0.513 0	0.92
60	BBS=0.174 6×*f*–34.303	0.174 6	0.46
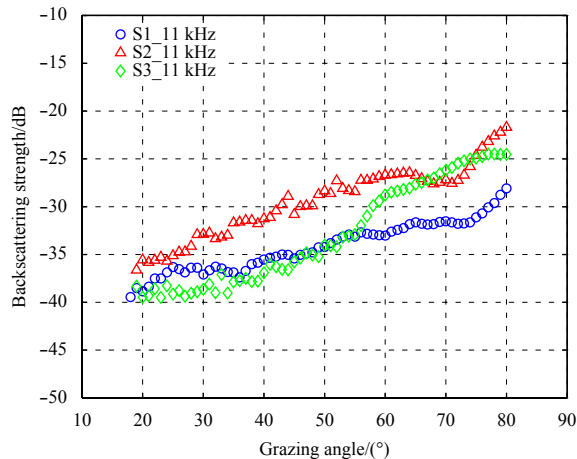
Fig. 10. Comparison of backscattering strength among Sites S1, S2 and S3.

no evident shell fragments in that at Site S2. The presence of shell fragment in the sediment might be another factor contributing to the difference of backscattering strength. Shell fragments in the sediment cause diffuse scattering of the sound waves along all directions, resulting in a reduction in along the direction of the backscattering.

4 Conclusions

(1) By avoiding disturbance from scattering off the sea surface and satisfying the far-field condition, we successfully measured the acoustic bottom backscattering strength, which ranges from –41.1 to –24.4 dB in a grazing angle range of 18°–80° and a frequency range of 6–24 kHz. Within the range of the effective grazing angle, the acoustic scattering strength generally increases with an increase in grazing angles, but the trends of the variation are different at different frequencies, which reflect different scattering mechanisms. Because of the very shallow water depth in the study area (only approximately 40 m in deep), the scattering strength at grazing angles lower than 18° can not be obtained in this experiment by using the omnidirectional source and receiver. In order to obtain bottom backscattering strength at lower grazing angle, more advanced instruments such as parametric array source with directional beam and vertical array with many receiving elements are needed.

(2) The frequency dependence of the bottom backscattering strength is generally characterized by a positive correlation in the entire frequency range of 6–24 kHz at the grazing angles of 20°, 40° and 60° with the linear regression slopes of 0.222 9 dB/kHz, 0.513 0 dB/kHz, and 0.174 6 dB/kHz, respectively. At a grazing angle of 80°, the acoustic backscattering strength exhibits no evident frequency dependence in the range of 6–24 kHz. The probable reasons lie in the inclusion of some coherent component in backscattering field and the poor quality data at the largest grazing angle.

(3) The acoustic scattering strength varies with the properties of the bottom sediment. The backscattering strength from the

bottom with larger grain size and shell-free sediment is approximately 1–8 dB higher than that from a bottom with smaller grain size and shell-rich sediment. The difference in grain size of bottom sediment and the presence of shell segments in it may be important factors that lead to this difference in the backscattering strength at S1, S2 and S3.

References

Dong Zhongchen, Li Yanan, Jin Yanfeng. 2013. Shallow seafloor reverberation modeling and simulation of torpedo. Torpedo Technology (in Chinese), 21(2): 100–104

Gao Bo. 2013. Modeling and characteristic of long-range bottom reverberation in shallow water (in Chinese) [dissertation]. Harbin: Harbin Engineering University

Hines P C, Osler J C, MacDougald D J. 2005. Acoustic backscatter measurements from littoral seabeds at shallow grazing angles at 4 and 8 kHz. The Journal of the Acoustical Society of America, 117(6): 3504–3516, doi: 10.1121/1.1898064

Hu Jianzhong. 2009. Measurement and model calculation of sea bottom three-dimensional scattering strength (in Chinese) [dissertation]. Harbin: Harbin Engineering University

Jackson D R, Baird A M, Crisp J J, et al. 1986. High-frequency bottom backscatter measurements in shallow water. The Journal of the Acoustical Society of America, 80(4): 1188–1199, doi: 10.1121/1.393809

Jackson D R, Briggs K B. 1992. High-frequency bottom backscattering: roughness versus sediment volume scattering. The Journal of the Acoustical Society of America, 92(2): 962–977, doi: 10.1121/1.403966

Jackson D R, Richardson M D. 2007. High-frequency seafloor acoustics. New York: Springer Science+Business Media, LLC

Jin Guoliang, Wu Chengyi, Zhang Guohua, et al. 1987. The measurement of two-dimensional bottom backscattering coefficients at shallow water. Acta Acustica (in Chinese), 12(3): 227–231

La H, Choi J W. 2010. 8-kHz bottom backscattering measurements at low grazing angles in shallow water. The Journal of the Acoustical Society of America, 127(4): EL160–EL165, doi: 10.1121/1.3338987

Li Songwen, Sun Liangyi. 2008. Subcritical detection of buried mine - a review on the theories, experiments and equipment. Ship Electronic Engineering (in Chinese), 28(2): 136–140

McKinney C M, Anderson C D. 1964. Measurements of backscattering of sound from the ocean bottom. The Journal of the Acoustical Society of America, 36(1): 158–163, doi: 10.1121/1.1918927

Peng Zhaohui, Zhou Jixun, Zhang Renhe. 2004. In-plane bistatic backward scattering from seabottom with randomly inhomogeneous sediment and rough interface. Science in China Series G: Physics, Mechanics and Astronomy, 47(6): 702–716, doi: 10.1007/BF02687341

Pouliquen E, Lyons A P. 2002. Backscattering from bioturbated sediments at very high frequency. IEEE Journal of Oceanic Engineering, 27(3): 388–402, doi: 10.1109/JOE.2002.1040926

Soukup R J, Gragg R F. 2003. Backscatter from a limestone seafloor at 2-3.5 kHz: measurements and modeling. The Journal of the Acoustical Society of America, 113(5): 2501–2514, doi: 10.1121/1.1558039

Stanic S, Briggs K B, Fleischer P, et al. 1988a. Shallow-water high-fre-
    quency bottom scattering off Panama City, Florida. The Journ-
    al of the Acoustical Society of America, 83(6): 2134–2144, doi:
    10.1121/1.396341

Stanic S, Briggs K B, Fleischer P, et al. 1989. High-frequency acoustic
    backscattering from a coarse shell ocean bottom. The Journal of
    the Acoustical Society of America, 85(1): 125–136, doi: 10.1121/
    1.397720

Stanic S, Eckstein B E, Williams R L, et al. 1988b. A high-frequency,
    shallow-water acoustic measurement system. IEEE Journal of
    Oceanic Engineering, 13(3): 155–162, doi: 10.1109/48.572

Wen Mingming, Xiao Bo, Cui Huayi. 2006. The method for measur-
    ing the acoustics characteristic of the ocean sediment. Ocean
    Technology (in Chinese), 25(1): 124–126

Williams K L. 2009. Forward scattering from a rippled sand/water in-
    terface: modeling, measurements, and determination of the
    plane wave, flat surface reflection coefficient. IEEE Journal of
    Oceanic Engineering, 34(4): 399–406, doi: 10.1109/JOE.
    2008.2002121

Williams K L, Jackson D R, Tang Dajun, et al. 2009. Acoustic backscat-
    tering from a sand and a sand/mud environment: experiments
    and data/model comparisons. IEEE Journal of Oceanic Engin-
    eering, 34(4): 388–398, doi: 10.1109/JOE.2009.2018335

Williams K L, Jackson D R, Thorsos E I, et al. 2002. Acoustic backscat-
    tering experiments in a well characterized sand sediment:
    data/model comparisons using sediment fluid and biot models.
    IEEE Journal of Oceanic Engineering, 27(3): 376–387, doi:
    10.1109/JOE.2002.1040925

Yu Shengqi, Liu Baohua, Yu Kaiben, et al. 2017. A backscattering
    model for a stratified seafloor. Acta Oceanologica Sinica, 36(7):
    56–65, doi: 10.1007/s13131-017-1084-1

Zhang Renhe, Li Zhenglin, Peng Zhaohui, et al. 2013. Overview of
    shallow water acoustics. Scientia Sinica Physica, Mechanica &
    Astronomica (in Chinese), 43(S1): S2–S15

Zou Dapeng, Kan Guangming, Long Jianjun. 2014. Methods of in-situ
    acoustic measurement of seafloor surface sediment. Haiyang
    Xuebao (in Chinese), 36(11): 111–119

Effects of igneous bodies on modification of modern slope morphology: Insights from the continental slope offshore Dongsha Islands, South China Sea

Chao Liang[1, 2], Xinong Xie[1, 2]*, Hua Wang[2, 3], Guangjian Zhong[4], Entao Liu[1, 2], Ming Sun[4], Hai Yi[4], Chunyu Qin[3], Haiyang Cao[5], Jie He[3], Yanpu Zhao[3]

[1] College of Marine Science and Technology, China University of Geosciences, Wuhan 430074, China

[2] Key Laboratory of Tectonics and Petroleum Resources of Ministry of Education, China University of Geosciences, Wuhan 430074, China

[3] Faculty of Earth Resources, China University of Geosciences, Wuhan 430074, China

[4] Guangzhou Marine Geological Survey, China Geological Survey, Guangzhou 510760, China

[5] Institute of Sedimentary Geology, Chengdu University of Technology, Chengdu 610059, China

Abstract

A statistical analysis for the morphological parameters extracted from numerous seismic profiles, and a high-resolution seismic study of the southeastern slope of the Dongsha Islands (South China Sea) with water depth between approximately 500 and 3 100 m, has revealed the variation of morphological features due to the intrusion of igneous bodies and associated sedimentary processes. Three types of the continental slope are distinguished: (1) a rough and steep slope with multiple igneous bodies (Type 1), (2) a relatively smooth and gentle slope with the single igneous body (Type 2), and (3) a smooth and gentle slope without igneous bodies (Type 3). These igneous bodies, formed in the post-seafloor spreading of the South China Sea, are often characterized by high positive seismic amplitudes, and chaotic reflections with complex shapes. The igneous bodies in Type 1 separated the slope into two or more upper sub-sags and a lower main-sag, in which the sub-sags and main-sag could be filled with sediments transported by alongslope bottom currents at the same time. Whereas, the igneous body in Type 2 just separated the slope into an upper sub-sag and a lower main-sag, in which the sediments could be transported into the lower main-sag only after the upper sub-sag has been filled up. Type 3 represents a normal slope with common clinoform progradation. The modern slope morphologies in the study area are the results of adjustments of the continental slope due to the intrusion of igneous bodies and associated sedimentary processes. The distinctions among three types of modern slope morphologies indicate different depositional conditions and adjustments of slope morphologies.

Key words: igneous bodies, modern slope morphology, Dongsha Islands, South China Sea

---

1 Introduction

Modern continental slope morphology is the product of variously complex geologic processes that might be constructional or destructional over millions of years (Brothers et al., 2013), whereas many present continental slope morphologies are mainly reflective of recent and ongoing geological processes (O'Grady et al., 2000). Moreover, a series of crucial factors have been proposed to explain the variation of modern continental slope morphology, such as sediment supply (Kenyon and Turcotte, 1985; Goff, 2001; O'Grady et al., 2000), sediment grain size (Adams et al., 1998), sedimentary texture (Schlager and Camber, 1986), sedimentary transport mechanisms (Cacchione et al., 2002), sediment over loading and tectonic deformation (Del Bianco et al., 2015), bottom currents (García et al., 2009; Sayago-Gil et al., 2010;

Chen et al., 2014), the presence of mobile substrates (Pratson and Haxby, 1996), and so forth. However, rare attention has been paid to the relationship between igneous bodies and modern slope morphology. In addition, the accurate effects of igneous bodies on modification of modern slope morphology also remains ambiguous.

An enormous body of evidence from seismic and drilling data document that a spot of small-scale late Oligocene–middle Miocene volcanism occurred sporadically on the northern South China Sea margin (Li and Rao, 1994), however, the Neogene magma activities along the lower slope of the northern South China Sea were fierce (Lüdmann and Wong, 1999; Song et al., 2017). Igneous bodies formed by magma emplacement could also be recognized on the seismic profiles in our study area,

where represents an unique opportunity to examine the relationship between igneous bodies and modern slope morphology.

In this paper, we describe and analyze modern slope morphology formed by igneous bodies and associated sedimentary processes, as well as document the effects of igneous bodies on modification of modern slope morphology in detail. Finally, conceptual models are presented and discussed.

2 Regional setting

The South China Sea (SCS), one of the biggest margin sea of the West Pacific, lies at the intersections of the Eurasian Plate, Philippine Sea Plate and Indo-Australian Plate (Zhang and Zhong, 1996; Cheng et al., 2012). As the result of Cenozoic continental margin rifting, the South China Sea has experienced a complete Wilson Cycle (Song et al., 2017), which drifted to its present position in the Middle Miocene, with a subsequent seafloor spreading in its central part (Taylor and Hayes, 1983). The northern margin of SCS is a portion of the South China Block, which is floored with continental crust (Yao et al., 2004). The Dongsha Islands are located in the central part of the northern margin of the SCS, and the study area (black rectangle in Fig. 1a) is situated on the southeast of Dongsha Islands between 18.37° and 20.92°N, and 116.52° and 118.23°E, with the water depth of approximately 500–3 100 m. The continental slope in the study area tilts from northwest to southeast (Fig. 1b).

Consistent with the tectonic evolution of the northern margin of the SCS, the research area was affected by multiple tectonic events during the Cenozoic (Taylor and Hayes, 1983), for instance, the rifting of the South China Sea Basin and tectonic escape of the Indochina Block (Zhang and Zhong, 1996), and so on. However, the most prominent tectonic event is the Dongsha Events occurring between approximately 10.5–5.5 Ma BP (Wu et al., 2014a). Consequences of the Dongsha Events were generalized uplift of the northern continental slope of the SCS, the fault of the upper crust, erosion and widespread magma activities (Li et al., 2016).

Additionally, water circulations of the SCS comprise SCS surface water, SCS intermediate water, and SCS deep water (Wang and Li, 2009). The range of the surface water is commonly above 350 m-depth, while the lower limit of the Intermediate Water is still debated, with water depth of 1 000 m (Zhao et al., 2009), or 1 200 m (Li et al., 2013), or exceeding 1 500 m (Xie et al., 2013), and so on. Pathways for the surface water circulation are cyclonic in winter and anti-cyclonic in summer (Xu et al., 2014), whereas the intermediate water in the northern South China Sea should be anti-cyclonic (Li et al., 2013) (Fig. 1a). Unlike the surface and intermediate water, the SCS deep water was proven to be cyclonic (Gong et al., 2012) (Fig. 1a). The continental slope in the study area is mainly sculpted by the SCS intermediated water and deep water.

3 Data and methods

This study was based on numerous 2D seismic profiles provided by the Guangzhou Marine Geological Survey. These seismic profiles almost covered the whole study area, with water depth of approximately 500–3 100 m. The seismic data consist of NW–SE and NE–SW seismic profiles with a trace interval of 6 m, the vertical scale of 3.0 cm/s, and the horizontal scale of 40.17 traces/cm. The two-way time of these profiles was converted to depth using the velocity of 1 500 m/s for water column. By applying the polynomial interpolation method to the depth data extracted from these seismic profiles, bathymetric grids were constructed at a grid resolution of 100 m×100 m. Then seafloor gradi-

ents were created, and each bathymetric grid has associated values of depth and slope magnitude. Gradient data were binned into 50 m depth intervals, and the average gradient of each interval was calculated. Types of the slope morphology were distinguished according to the slope structures, further evidenced by the results of Kruskal-Wallis One Way ANOVA Testing and Pairwise Comparison with no priori assumptions for the seafloor gradients of the slope. Based on the interpretations of the seismic data, igneous bodies and associated sedimentations were described and analyzed by typical seismic facies. Special attention was paid to the relationship between igneous bodies and modern slope morphology, therefore, the effects of igneous bodies on modification of the continental slope were documented.

4 Slope morphology features

Figure 1b presents the overall slope morphology in the study area, on the basis of which three types of the continental slope could be distinguished directly according to slope structures: (1) Type 1, a rough and steep slope with multiple igneous bodies; (2) Type 2, a relatively smooth and gentle slope with single igneous body; (3) Type 3, a smooth and gentle slope without igneous bodies. Subsequently, the differences of modern slope morphologies among three types of the slope were determined, using the Kruskal-Wallis One Way ANOVA Testing and Pairwise Comparison with no priori assumptions, and found to be significantly different (p=0.000<0.05, as shown in Table 1 and Table 2).

The slope morphology of Type 1 is primarily characterized by numerous morphology anomalies caused by igneous bodies, which could be easily recognized on the typical depth profile (Fig. 2a, Type 1). Like Fig. 2b, a pictured here, a wider shaded region occurred above approximately 2 100 m depth, representing ±1 standard deviation around the average gradient value of every given 50 m depth interval, indicates that the slope gradients exhibit considerable variability, with the maximum average gradient of these given 50 m depth bins reaching up to 7.13° in water depth between 1 200 and 1 250 m.

Although morphology anomalies could also be distinguished (Fig. 2a), the slope morphology of Type 2 varies from the rough and steep slope surface in type1, which is relatively smooth and gentle merely with a wider shaded region at approximately 2 400–2 850 m water depth. The maximum average gradient of these given 50 m intervals reached 5.21° in water depth of 2 750–2 800 m (Fig. 2b).

The slope morphology of Type 3 is mainly characterized by its pattern of consistently gentle seafloor gradients over its entire depth range (Figs 2a and b). Changes in slope with depth are very subtle on this slope, and the highest average slope value of these given 50 m intervals is 4.71°, in water depth of about 1 350–1 450 m, where is located in the slope break. The majority of the slope gradients are lower than 2.5°. What was less visible then, characterizing this slope morphology is a relatively narrow shaded region, representing ±1 standard deviation around the average gradient of every given 50 m depth interval.

5 Igneous bodies and associated sedimentary features

Based on the interpretations of the seismic data, igneous bodies and associated sedimentary features are recognized on the seismic profiles. Effects of igneous bodies on modification of modern slope morphology will be made in the discussion section.

5.1 *Contourite deposits between the igneous bodies*

Numerous igneous bodies could be recognized on the seismic profile apparently in Fig. 3, which show high amplitudes and
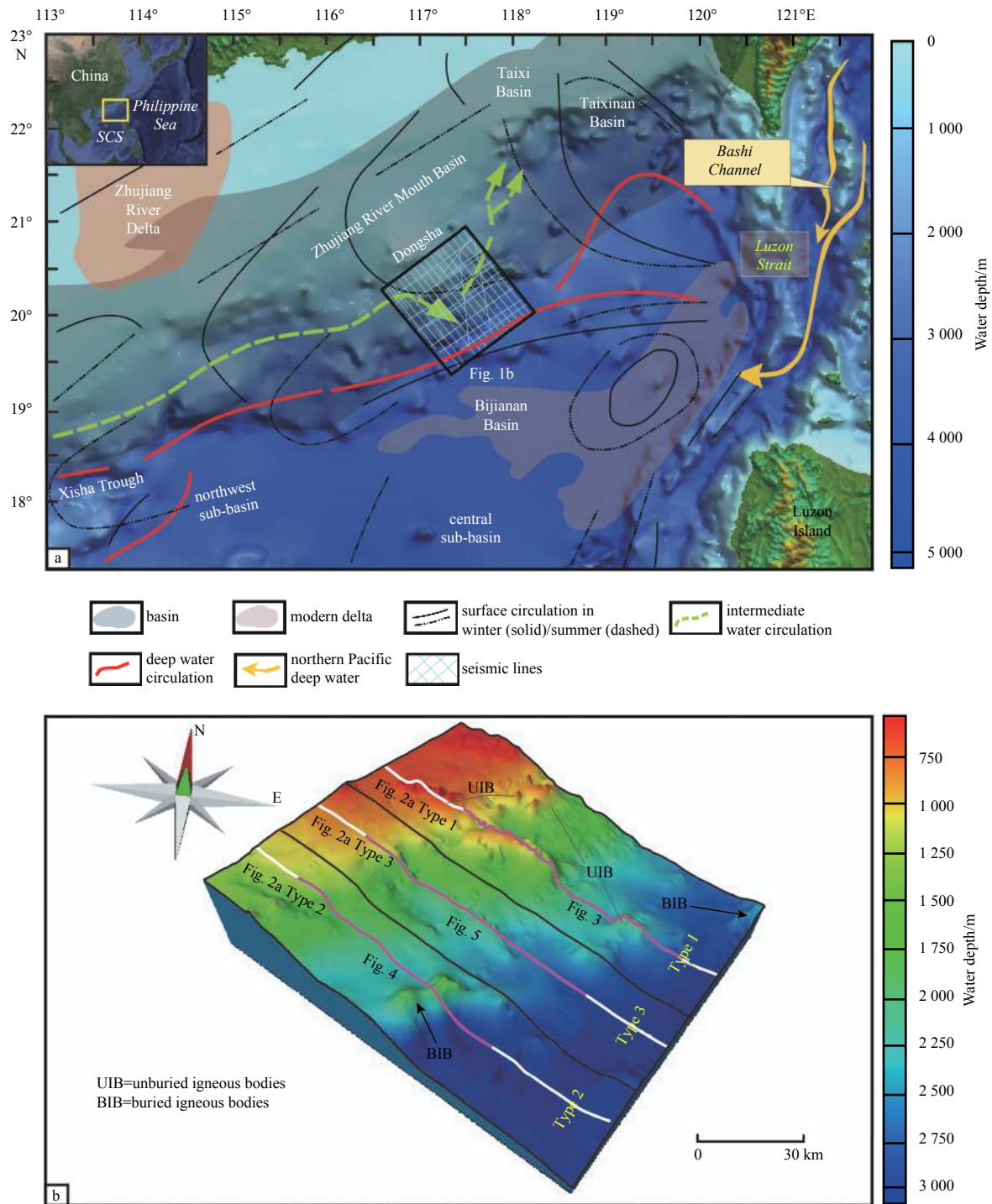
Fig. 1. Overview map of the mid-eastern part of the northern South China Sea and the study area. a. Global relief map of the mid-eastern part of the northern South China Sea, with the locations of the sedimentary basins, modern delta, and ocean current circulations (modified after Chen et al. (2014)); the yellow solid means that the northern Pacific deep water flows into the South China Sea via Bashi Channel and Luzon Strait (Gong et al., 2012); the red arrows are pathways for the circulation of the assumed deep water (modified after Chen et al. (2014)); the black dashed and solid arrows show the main surface circulation pathways in summer and winter, respectively (Wang and Li, 2009); boundary of the study area is shown in black rectangle; and the locations of seismic profiles are labeled by blue solid lines. b. Topographic map of the study area, presenting locations of the studied seismic lines in Figs 2–5, as well as different types of the continental slope in the study area.

chaotic reflections in the interior with a clear external outline, as well as numerous morphological highs on the seabed. However, these morphological highs may induce streamline distortions of oceanic currents, hence, affecting the sediment distribution around these morphological highs (Hernández-Molina et al., 2006; Faugères and Stow, 2008; Chen et al., 2014). Different shear

Table 1. Hypothesis test summary

Null hypothesis	Test	P	Decision
The distribution of gradient is the same across categories of Group	independent-samples Kruskal-Wallis Test	0	rejected the null hypothesis

Note: The significance level is 0.05.

Table 2. Pairwise comparison of three types of modern slope morphologies

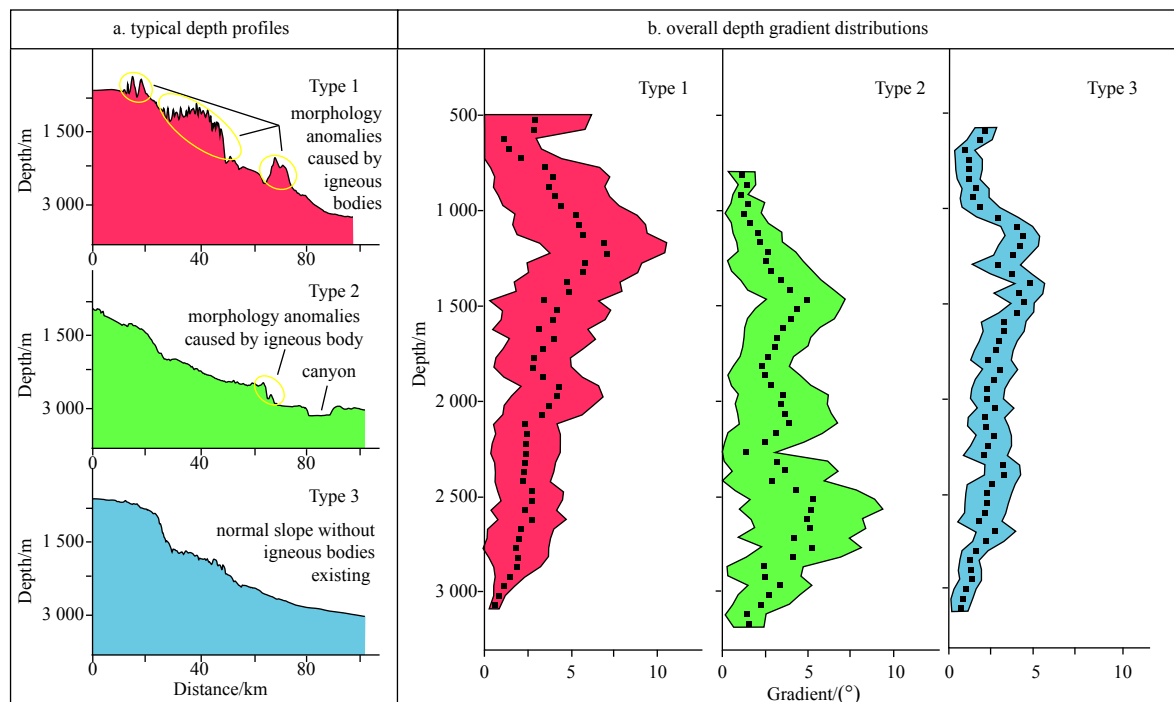| Sample 1–Sample 2	Test statistics	Std. error	Std. test statistics	P
Type 2–Type 1	32 575.806	761.293	42.790	0
Type 2–Type 3	–48 530.480	728.965	–66.574	0
Type 1–Type 2	–15 954.674	699.463	–22.810	0

Note: The significance level is 0.05.

Fig. 2. Morphological characteristics of the modern slope in the study area. a. Typical depth profiles showing morphology anomalies of three types of the slope. b. Depth-gradient distributions, black dots indicate the average gradient of given 50 m depth bins, and the shaded region around black dots indicating ±1 standard deviation. Both Figs 2a and b are colored according to the results of Kruskal-Wallis One Way ANOVA Testing and Pairwise Comparison.

velocities are generated for diverse frictions when the bottom currents are deflected and intensified by morphological highs, formed by igneous bodies, and the Coriolis Force could push the bottom currents into the right in the northern hemisphere, as well as the degree of morphological convex results in a curved framework, where the secondary circulation occur (Faugères et al., 1999; Wynn and Stow, 2002; Li et al., 2013; Rebesco et al., 2014). Such as Fig. 3, the morphological depressions near these igneous bodies will be interpreted as moats. Both sides of the mounded-confined drifts are restricted by igneous bodies, and the mounded-confined drifts have the distinct bottom boundary with a relatively flat and smooth top. The bottom currents between these igneous bodies were intensified and deflected, hence, two deep and narrow moats were formed on both sides of the mounded-confined drifts. Nevertheless, the bottom currents near the rightness of the right igneous body on the section (Fig. 3), was not restricted, forming a relatively shallow and wide morphology depression also named moat, as well as the elongated-

mounded drifts. The reflections of these drifts, in Fig. 3, show moderate to high amplitude and moderate to low continuity. The bottom currents away from the igneous bodies were not affected by the igneous bodies, which comprise the SCS intermediate and deep water, commonly formed sheeted drifts (Fig. 3).

5.2 Slope block formed by the igneous body

Equally, the single igneous body could also be determined by the seismic profile directly in Fig. 4, showing internal chaotic reflections with a clear external boundary. Near the abrupt morphology change on the left part of the section (Fig. 4), the slight depression will be interpreted as a moat. In Fig. 4, the rightness of the moat, a mounded topography could be observed, which could be interpreted as elongated-mounded drifts. This moat and drifts might be formed by the SCS deep water, which was deflected and intensified by the steeper slope morphology on the left side of the section (Fig. 4). Subsequently, destroyed by the gravity force, a downslope creep zone was formed on the basis of
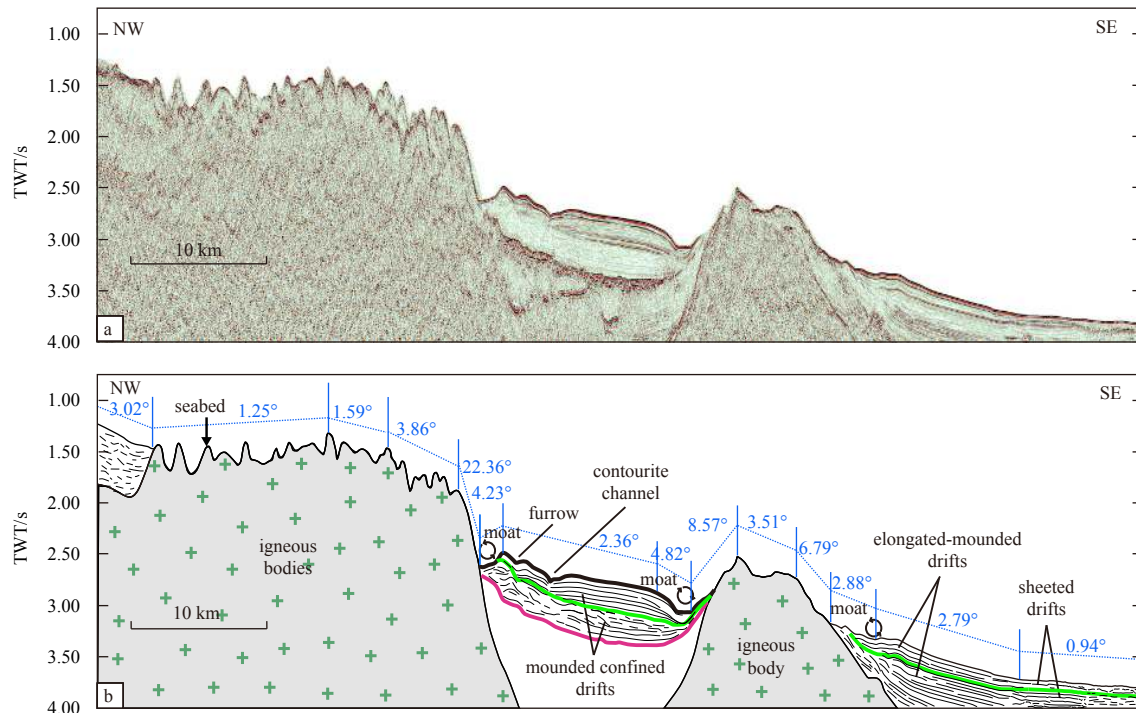
Fig. 3. NW-SE oriented profile (see the location in Fig. 1b). a. Original seismic profile. b. Interpreted profile showing the slope with multiple igneous bodies and its morphology changes; and the depressions formed by the igneous bodies could be filled with contourites (mounded confined drifts, elongated mounded drifts and sheeted drifts) at the meantime.

Fig. 4. NW-SE oriented profile (see the location in Fig. 1b). a. Original seismic profile. b. Interpreted profile displaying the slope with the single igneous body and its morphology changes; sediments were prevented by the igneous body from being transported downslope; and the inset showing sediment waves formed by the secondary circulation of bottom currents.

the elongated-mounded drifts, with the presence of ridges, troughs, local faults and the gradually decreased wavelength and wave height. The downslope morphology anomalies caused by the igneous body on the seafloor, are still preserved well, whereas the upslope morphology anomalies had been eliminated by sediments. On the right side of the seismic profile in Fig. 4, the

right-migrating sediment waves are presented. In fact, the migration directions of all deposits on the seismic profile trend parallel to the downslope direction. Moreover, it is clear that the igneous body, like a slope block, prevents the deposits from being transported into the abyssal plain. Above all, sediments could not be transported into the abyssal plain until the upslope morphology
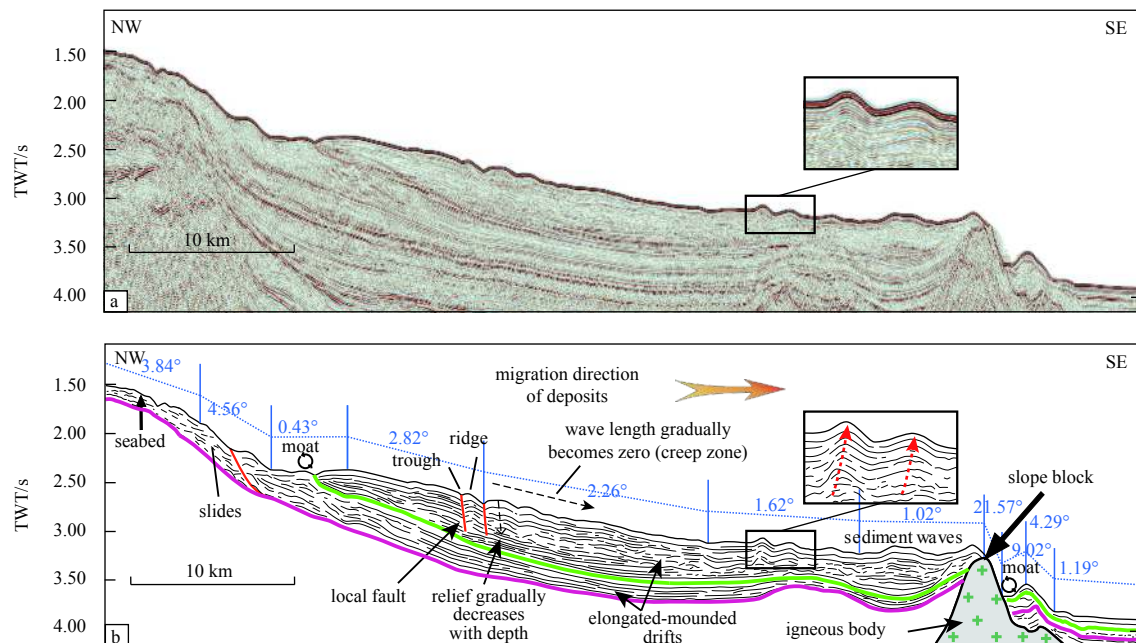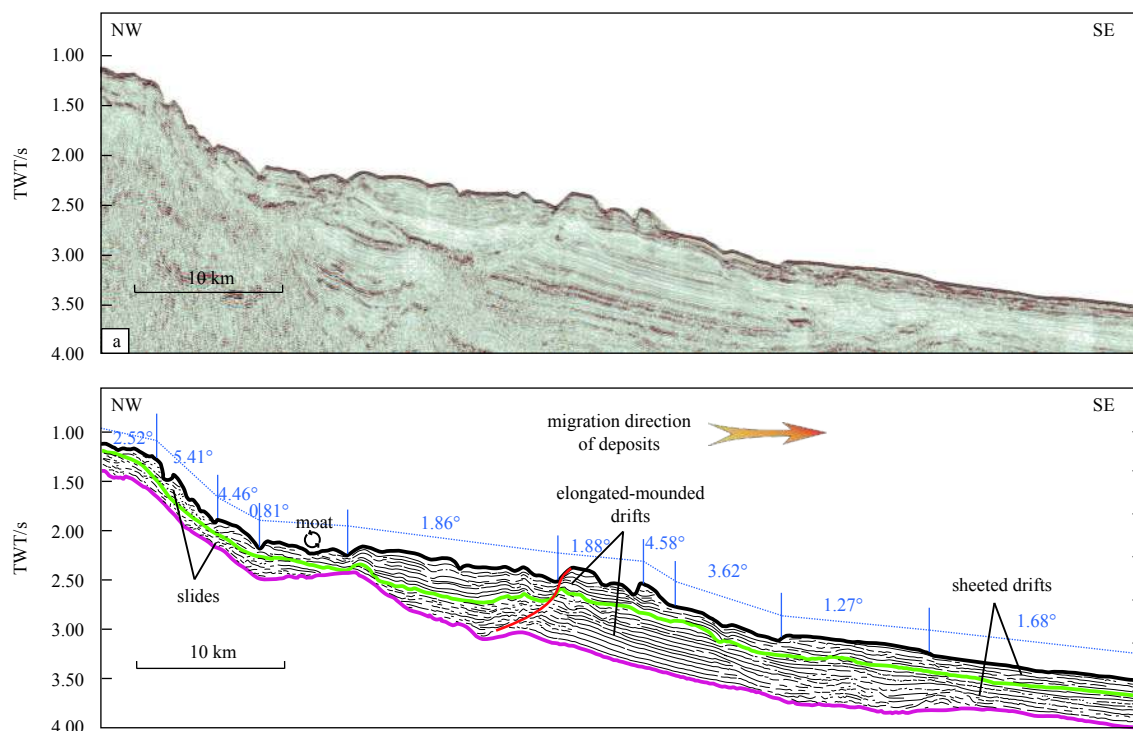
Fig. 5. NW-SE oriented profile (see the location in Fig. 1b). a. Original seismic profile. b. Interpreted profile exhibiting the slope without igneous body and its morphology changes; and sediments could be normally transported downslope by the secondary circulation of bottom currents.

anomalies caused by igneous body were eliminated by sediments.

6 Discussion

The continental slope in the study area has been subdivided into three types of the slope with different modern slope morphologies. The typical sedimentary features in Type 1 is represented by contourites related to igneous bodies and bottom currents (Fig. 3), while the sediments were prevented by the igneous body from being transported into the abyssal plain (Fig. 4) in Type 2. Unlike the sedimentary processes occurring in Types 1 and 2, sedimentary processes in Type 3 were not influenced by igneous bodies, just with normal clinoform progradation (Fig. 5). Previous studies attempting to study seismic patterns of most margins reveal that changes to the overall shape of a margin through time tend to be incremental, cumulative, and slow (Steckler et al., 1999; O'Grady et al., 2000). Equally, the distinctions among three types of modern slope morphologies will gradually decrease. Finally, they will be eliminated, therefore, the overall slope morphology becomes extremely smooth and gentle.

To better understand the effects of igneous bodies on modification of modern slope morphology in detail, conceptual models for three types of the slope explaining the effects of igneous bodies on controlling sedimentary processes, in the study area, were established and presented in Fig. 6.

On the slope with multiple igneous bodies (Fig. 6Aa), slope morphology anomalies were formed by the intercepts and complex shapes of igneous bodies firstly. Meanwhile, the presence of the igneous bodies separated the slope into two or more upper sub-sags and a lower main-sag, making streamline distortions of bottom currents to form contourites. These upper sub-sags and the lower main-sag could be filled simultaneously. First of all, the sedimentation unit 1 will be formed (Step 1), followed by the sedi-

mentation 2 (Step 2). At this point, slope morphology anomalies caused by multiple igneous bodies were eliminated completely. The sedimentation unit 3 (Step 3) represents normal sedimentation.

However, as shown in Fig. 6Ba, the single igneous body merely separated the slope into an upper sub-sag and a lower main-sag. On this slope, the migration direction of deposits is downslope, and the sediments could be transported by gravity flows or bottom currents. The sediments will be prevented by the igneous body from migrating into the main-sag until the sub-sag is filled up. Therefore, the sedimentation unit 1 will form at first, followed by the sedimentation unit 2, finally the sedimentation unit 3. In comparison, on the slope without igneous bodies, sedimentary processes were not affected by igneous bodies, with normal slope aggradations all the time (Fig. 6C).

In the study area, the slope with multiple igneous bodies (Type 1) is at the end of the Step 1 (Fig. 6Ab), while the slope with single igneous bodies (Type 2) is at the beginning of Step 2 (Fig. 6Bc), in which sediments start to be transported into the lower main-sag to form sedimentation unit 2. Although the modern slope morphologies of these slopes will constantly change over time due to the different Steps that they will be in, the morphology of the overall slope will tend to be smooth and gentle, therefore, the differences among three types of the modern slope morphologies will decrease constantly. Modern slope morphologies in the study area are the results of adjustments of the continental slope due to the intrusion of igneous bodies and associated sedimentary processes. The distinctions among three types of modern slope morphologies indicate different depositional conditions and adjustments of slope morphologies. Additionally, the distributions of foot lines of the continental slope may change over time, due to the adjustment of slope morphologies (e.g., Wu et
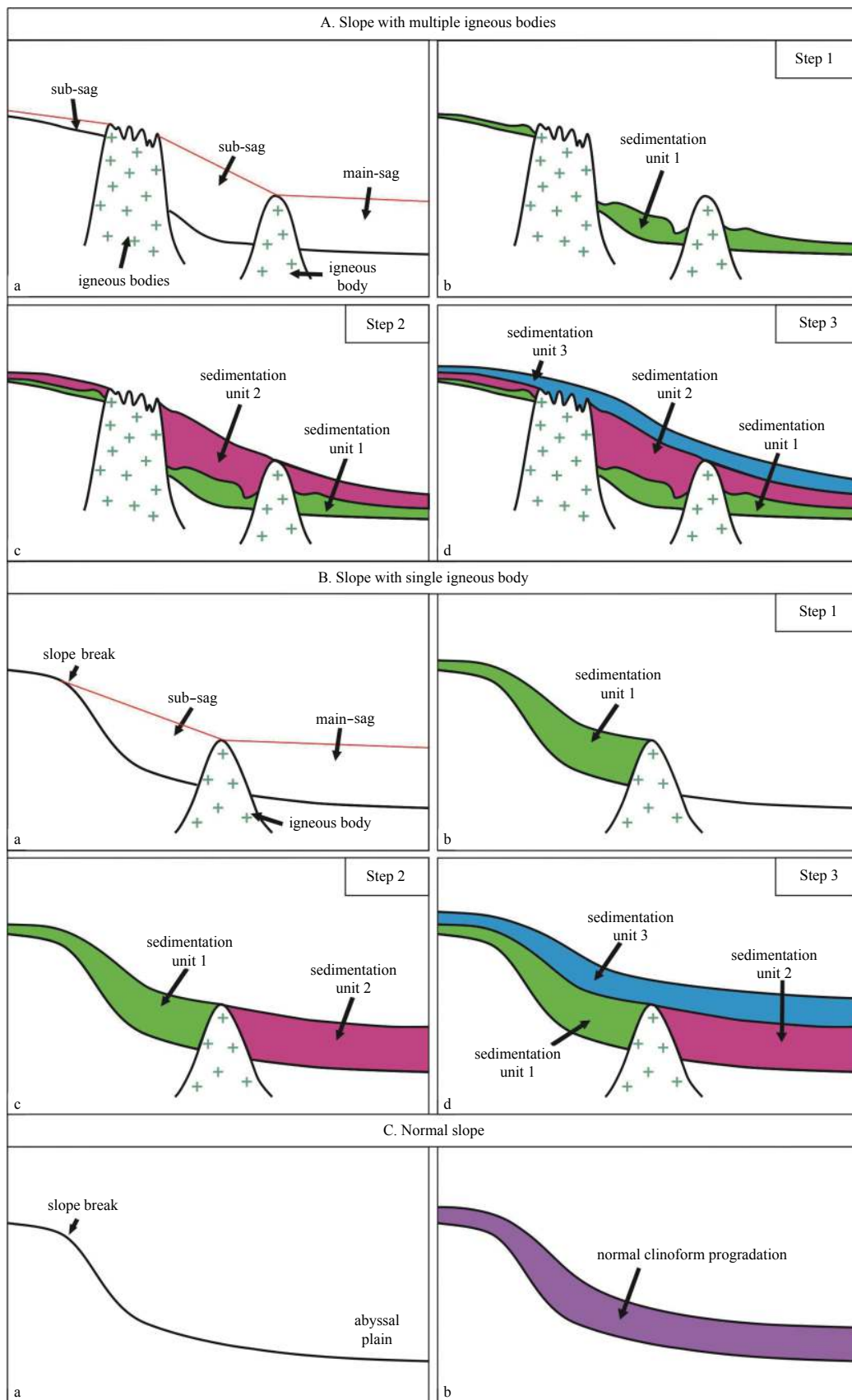
Fig. 6. Conceptual models for explaining the effects of igneous bodies on controlling sedimentary processes in the study area, which help us understand the different depositional conditions and different adjustments of slope morphologies mainly caused by igneous bodies.

al., 2014b, 2017).

7 Conclusions

This paper has investigated a 2D multi-channel reflection seismic data, explaining the effects of igneous bodies on modification of modern slope morphology, offshore Dongsha Islands, South China Sea. The main conclusions of this study are as follows.

(1) The continental slope, in the study area, could be subdivided into three types according to slope structures, i.e., the rough and steep slope with multiple igneous bodies (Type 1), the relatively smooth and gentle slope with single igneous body (Type 2), and the smooth and gentle slope without igneous bodies (Type 3). Moreover, modern slope morphologies of three types of the slope reveal significant differences, evidenced by the results of Kruskal-Wallis One Way ANOVA Testing and Pair- wise Comparison.

(2) The igneous bodies in Type 1 separated the slope into two or more upper sub-sags and a lower main-sag, in which these upper sub-sags and the lower main-sag could be filled with sediments transported by alongslope bottom currents simultaneously. However, the single igneous body in Type 2 just separated the slope into an upper sub-sag and a lower main-sag, in which the sediments could be transported into the lower main-sag only after the upper sub-sag has been filled up. Type 3 represents a normal slope with common clinoform progradation.

(3) Due to the different steps that these slopes will be in, modern slope morphologies will constantly change over time. The distinctions among three types of modern slope morphologies indicate different depositional conditions and adjustments of slope morphologies.

References

Adams E W, Schlager W, Wattel E. 1998. Submarine slopes with an exponential curvature. Sedimentary Geology, 117(3–4): 135–141, doi: 10.1016/S0037-0738(98)00044-X

Brothers D S, Brink U S T, Andrews B D, et al. 2013. Geomorphic characterization of the U. S. Atlantic continental margin. Marine Geology, 338: 46–63

Cacchione D A, Pratson L F, Ogston A S. 2002. The shaping of continental slopes by internal tides. Science, 296(5568): 724–727, doi: 10.1126/science.1069803

Chen Hui, Xie Xinong, Van Rooij D, et al. 2014. Depositional characteristics and processes of alongslope currents related to a seamount on the northwestern margin of the Northwest Sub-Basin, South China Sea. Marine Geology, 355: 36–53, doi: 10.1016/j.margeo.2014.05.008

Cheng Shixiu, Li Sanzhong, Suo Yanhui, et al. 2012. Cenozoic tectonics and dynamics of basin groups of the northern South China Sea. Marine Geology & Quaternary Geology (in Chinese), 32(6): 79–93

Del Bianco F, Gasperini L, Angeletti L, et al. 2015. Stratigraphic architecture of the Montenegro/N. Albania continental margin (Adriatic sea-central Mediterranean). Marine Geology, 359: 61–74

Faugères J C, Stow D A V, Imbert P, et al. 1999. Seismic features diagnostic of contourite drifts. Marine Geology, 162(1): 1–38, doi: 10.1016/S0025-3227(99)00068-7

Faugères J C, Stow D A V. 2008. Contourite drifts: nature, evolution and controls. Developments in Sedimentology, 60: 257–288, doi: 10.1016/S0070-4571(08)10014-0

García M, Hernández-Molina F J, Llave E, et al. 2009. Contourite erosive features caused by the Mediterranean outflow water in the gulf of Cadiz: quaternary tectonic and oceanographic implications. Marine Geology, 257(1–4): 24–40, doi: 10.1016/j.margeo.2008.10.009

Goff J A. 2001. Quantitative classification of canyon systems on continental slopes and a possible relationship to slope curvature. Geophysical Research Letters, 28(23): 4359–4362, doi: 10.1029/2001GL013300

Gong Chenglin, Wang Yingmin, Peng Xuechao, et al. 2012. Sediment waves on the South China Sea slope off southwestern Taiwan: implications for the intrusion of the northern pacific deep water into the South China Sea. Marine and Petroleum Geology, 32(1): 95–109, doi: 10.1016/j.marpetgeo.2011.12.005

Hernández-Molina F J, Larter R D, Rebesco M, et al. 2006. Miocene reversal of bottom water flow along the Pacific Margin of the Antarctic Peninsula: stratigraphic evidence from a contourite sedimentary tail. Marine Geology, 228(1–4): 93–116, doi: 10.1016/j.margeo.2005.12.010

Kenyon P M, Turcotte D L. 1985. Morphology of a delta prograding by bulk sediment transport. GSA Bulletin, 96(11): 1457–1465, doi: 10.1130/0016-7606(1985)96<1457:MOADPB>2.0.CO;2

Li Wei, Alves T M, Wu Shiguo, et al. 2016. A giant, submarine creep zone as a precursor of large-scale slope instability offshore the Dongsha Islands (South China Sea). Earth and Planetary Science Letters, 451: 272–284, doi: 10.1016/j.epsl.2016.07.007

Li Pinglu, Rao Chuntao. 1994. Tectonic characteristics and evolution history of the Pearl river mouth basin. Tectonophysics, 235(1–2): 13–25, doi: 10.1016/0040-1951(94)90014-0

Li Hua, Wang Yingmin, Zhu Weilin, et al. 2013. Seismic characteristics and processes of the Plio-Quaternary unidirectionally migrating channels and contourites in the northern slope of the South China Sea. Marine and Petroleum Geology, 43: 370–380, doi: 10.1016/j.marpetgeo.2012.12.010

Lüdmann T, Wong H K. 1999. Neotectonic regime on the passive continental margin of the northern South China Sea. Tectonophysics, 311(1–4): 113–138, doi: 10.1016/S0040-1951(99)00155-9

O'Grady D B, Syvitski J P M, Pratson L F, et al. 2000. Categorizing the morphologic variability of siliciclastic passive continental margins. Geology, 28(3): 207–210, doi: 10.1130/0091-7613(2000)28<207:CTMVOS>2.0.CO;2

Pratson L F, Haxby W F. 1996. What is the slope of the U. S. continental slope?. Geology, 24(1): 3–6, doi: 10.1130/0091-7613(1996)024<0003:WITSOT>2.3.CO;2

Rebesco M, Hernández-Molina F J, Van Rooij D, et al. 2014. Contourites and associated sediments controlled by deep-water circulation processes: state-of-the-art and future considerations. Marine Geology, 352: 111–154, doi: 10.1016/j.margeo.2014.03.011

Sayago-Gil M, Long D, Hitchen K, et al. 2010. Evidence for current-controlled morphology along the western slope of Hatton Bank (Rockall Plateau, NE Atlantic Ocean). Geo-Marine Letters, 30(2): 99–111, doi: 10.1007/s00367-009-0163-5

Schlager W, Camber O. 1986. Submarine slope angles, drowning unconformities, and self-erosion of limestone escarpments. Geology, 14(9): 762–765, doi: 10.1130/0091-7613(1986)14<762:SSADUA>2.0.CO;2

Song Xiaoxiao, Li Chunfeng, Yao Yongjian, et al. 2017. Magmatism in the evolution of the South China Sea: geophysical characterization. Marine Geology, 394: 4–15, doi: 10.1016/j.margeo.2017.07.021

Steckler M S, Mountain G S, Miller K G, et al. 1999. Reconstruction of Tertiary progradation and clinoform development on the New Jersey passive margin by 2-D backstripping. Marine Geology, 154(1–4): 399–420, doi: 10.1016/S0025-3227(98)00126-1

Taylor B, Hayes D E. 1983. Origin and history of the South China Sea basin. In: Hayes D E, ed. The Tectonic and Geologic Evolution of Southeast Asian Seas and Islands: Part 2. Washington, DC: AGU Geophysical Monograph, 23–56

Wang Pinxian, Li Qianyu. 2009. Oceanographical and geological background. In: Wang Pinxia, Li Qianyu, eds. The South China Sea: Paleoceanography and Sedimentology. Dordrecht: Springer

Wu Shiguo, Gao Jinwei, Zhao Shujuan, et al. 2014a. Post-rift uplift and focused fluid flow in the passive margin of northern South China Sea. Tectonophysics, 615–616: 27–39, doi: 10.1016/j.tecto.2013.12.013

Wu Ziyin, Li Jiabiao, Li Shoujun, et al. 2017. A new method to identify the foot of continental slope based on an integrated profile analysis. Marine Geophysical Research, 38(1–2): 199–207, doi: 10.1007/s11001-016-9273-4

Wu Ziyin, Li Jiabiao, Jin Xianglong, et al. 2014b. Distribution, features, and influence factors of the submarine topographic boundaries of the Okinawa trough. Science China Earth Sciences, 57(8): 1885–1896, doi: 10.1007/s11430-013-4810-3

Wynn R B, Stow D A V. 2002. Classification and characterisation of deep-water sediment waves. Marine Geology, 192(1–3): 7–22, doi: 10.1016/S0025-3227(02)00547-9

Xie Qiang, Xiao Jingen, Wang Dongxiao, et al. 2013. Analysis of deep-layer and bottom circulations in the South China Sea based on eight quasi-global ocean model outputs. Chinese Science Bulletin, 58(32): 4000–4011, doi: 10.1007/s11434-013-5791-5

Xu Weihai, Yan Wen, Chen Zhong, et al. 2014. Organic matters and lipid biomarkers in surface sediments from the northern South China Sea: origins and transport. Journal of Earth Science, 25(1): 189–196, doi: 10.1007/s12583-014-0412-z

Yao Bochu, Wan Ling, Wu Nengyou. 2004. Cenozoic plate tectonic activities in the Great South China Sea area. Geology in China (in Chinese), 31(2): 113–122

Zhang Liansheng, Zhong Dalai. 1996. The red river strike-slip shear zone and Cenozoic tectonics of east Asia continent. Scientia Geologica Sinica (in Chinese), 31(4): 327–341

Zhao Quanhong, Li Qianyu, Jian Zhimin. 2009. Deep waters and oceanic connection. In: Wang Pinxian, Li Qianyu, eds. The South China Sea. Dordrecht: Springer, 395–437

Patterns of gas hydrate accumulation in mass transport deposits related to canyon activity: Example from Shenhu drilling area in the South China Sea

Chao Fu[1], Shengli Li[1]*, Xinghe Yu[1], Jinqiang Liang[2], Zenggui Kuang[2], Yulin He[2], Lina Jin[1]

[1] School of Energy Resources, China University of Geosciences, Beijing 100083, China

[2] Guangzhou Marine Geological Survey, China Geological Survey, Guangzhou 510760, China

Abstract

Since 2017, a plenty of gas hydrates have been drilled in a new area of Shenhu, and good heterogeneity has been found throughout the spatial distribution of the reservoir. After distinguishing different sedimentary sequence types and matching their formation with slope deposition settings, this study proposes three mass transport deposit (MTD) patterns related to canyon activity that occurred contemporaneously or epigenetically with it: well preserved MTDs, MTDs eroded by canyon migration, and MTDs dislocated by contemporaneous faults. Based on seismic reflection characteristics, this study proposed methods of quantitatively analyzing sedimentary factors, such as measuring the turbidities flow rate in the canyon, and results are interpreted with respect to canyon activity. Combining the above parameters and their relationship with gas hydrate accumulation, fine-grained seals overlapping coarse MTDs reservoirs are found to be indispensable to gas hydrate accumulation, as they prevent the release of free gas. Based on grain size data of hydrate samples from drilling wells, multi-layered gas hydrate reservoirs capped by fine-grained sediments and overlapping mud show favorable hydrate-bearing prospects. The release of gas hydrates, however, is mostly caused by the lack of mud sealing in relation to canyon activity, such as turbidities flow erosion and contemporaneous fault breaking. Canyon migration with respect to MTDs may be the actual cause of erosion of overlapping syn-sedimentary layers, and high bottom flows may contribute to an increase in the release of free gas. It is believed that contemporaneous faults caused by unstable canyon walls may break the muddy over layers and decrease the accumulation pressure of gas hydrate bearing. Thus, according to the sedimentary characteristics of MTDs and the hydrate accumulation process, three responding accumulation or releasing patterns are proposed, which respond to the different types of MTDs distinguished above: a well-preserved MTD accumulation pattern; a canyon migration eroded MTD release pattern; and a micro-contemporaneous fault dislocated MTD release pattern.

Key words: South China Sea, gas hydrate, sedimentary characteristics, MTDs, hydrate responding pattern

1 Introduction

Natural gas hydrates are quasi-ice crystalline compounds composed of water and natural gas that are formed in a low temperature and high-pressure environment (Holbrook et al., 1996). Former studies have shown that mass transport deposits (MTDs) are favorable reservoirs for gas hydrate accumulation (Wu et al., 2011; Yu et al., 2014). Complex hydrodynamic settings in slope regions and canyon activity migration science the Miocene have led to the development of many MTD types, which makes investigations into MTD preservation and corresponding gas hydrate accumulation patterns challenging (Yu et al., 2014; Riedel et al., 2013b).

If pore types are effective and suitable accumulation conditions are provided, such as suitable temperatures and pressures, it is believed that MTDs could enable gas accumulation and serve as potential reservoirs (Wu et al., 2011; Yu et al., 2014). In addition, many different deposition processes intervene with MTDs, and successive reworking lead to valuable gas hydrate accumulation patterns therein. For example, Scholz et al. (2012) and Riedel

et al. (2013a) analyzed seismic data and core samples from the Ulleung Basin and found hydrate-bearing heterogeneity in different MTD reservoir types (Scholz et al., 2012; Riedel et al., 2013b). However, they also found extremely low gas hydrate saturation in a single MTD, but as it did not have a fine-grained seal bed they determined that gas hydrates mainly occur in multiple MTDs (multi-MTDs). Multi-MTDs create thick reservoirs and have good sealing conditions that are suitable for gas hydrate accumulation. Bangs et al. (2011) found variable bottom simulating reflections (BSR) between well-preserved MTDs where there was no later canyon activity reworking, and displaced one during study of the hydrate ridge in the Northwest Pacific in Western North America (Bangs et al., 2011). Nevertheless, the relationship between MTDs and hydrate accumulation has not been adequately defined and currently remains unclear.

The GMGS-3 drilling area (Fig. 1a) is located at the bottom of the northern slope of the South China Sea (SCS). Earlier research has studied the complex sedimentary setting and its depositional characteristics in the area (He et al., 2013, Chen et al., 2016). For

*Corresponding author, E-mail: slli@cugb.edu.cn
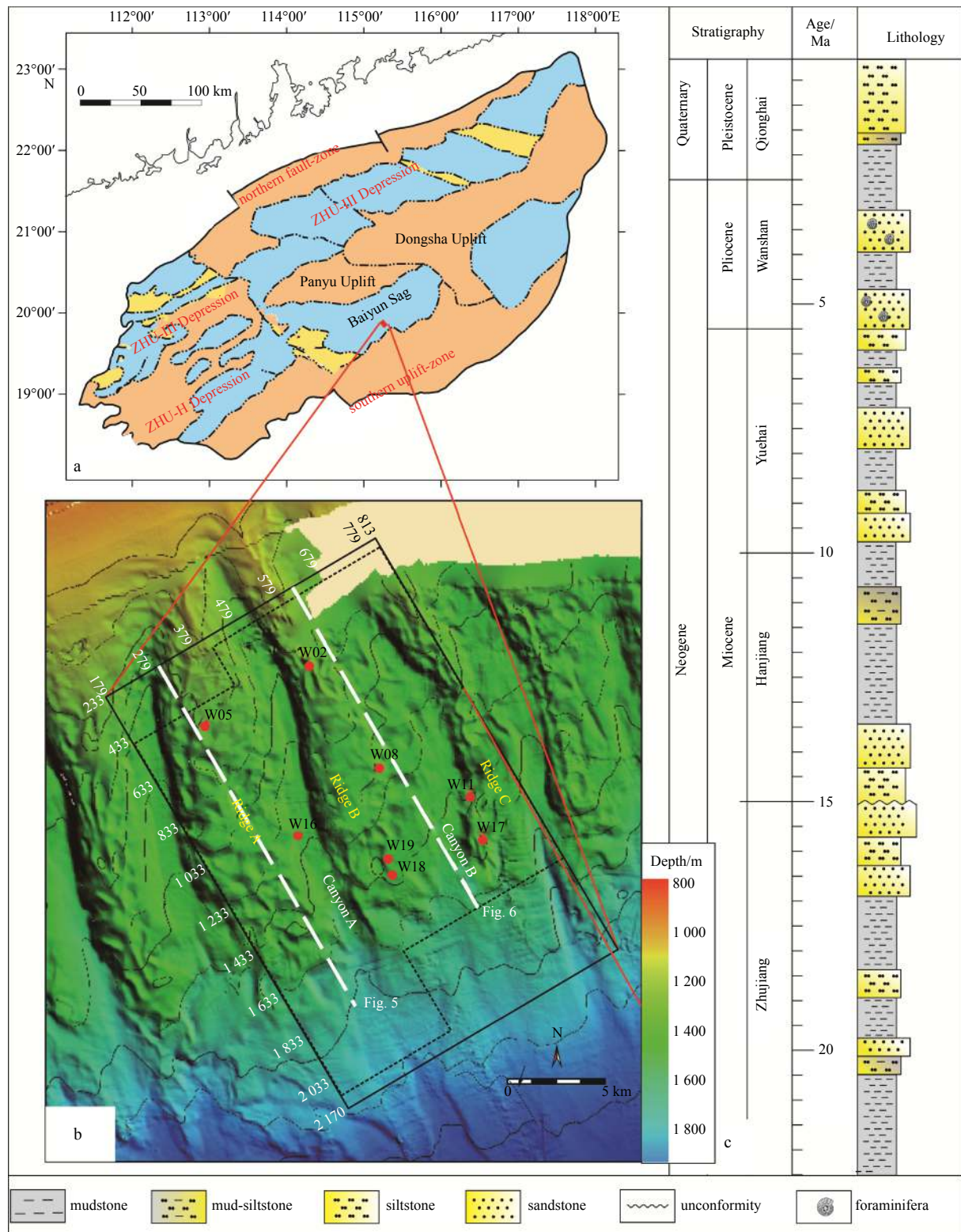
Fig. 1. Location of study area and integrated histogram. a. Tectonic units of Baiyun Sag and position of GMGS3; b. geomorphological map and well sites, water depth ranges from 800 m to 2 000 m, main topography includes ridges and valleys. Ridge areas are numbered from left to right: Ridge A, Ridge B, and Ridge C; and canyons are also numbered from left to right: Canyon A and Canyon B; and c. integrated histogram, from left to right: formation names of layers, chrono-stratigraphic age, main lithologies.

example, per studied sedimentary characteristics in the earlier drilling area of Shenhu (GMGS-1: location shown in Fig. 1) and found that MTDs could sever as an ideal gas hydrate reservoir

and that their classification can be based on topographical changes (Yu et al., 2014). From the perspective of bottom flow interaction and reworking, Gong et al. (2016) showed that the con-

tourites or bottom currents rebuild canyons lead to canyon migration, and that the intensity of the bottom flow may also act as an external mechanism for MTD formation. He classified MTDs into two types: normal MTDs and MTDs eroded by external turbidities flow. However, due to the lack of deep-water core samples from Shenhu, the characteristics of MTD reservoirs and their hydrate response patterns therein could not be clarified.

This study uses measurements of MTDs, such as thickness, distribution length, scale covered, sedimentary characteristics, and core-log-seismic integration analyses to categorize MTDs into three types in relation to canyon activity. Unidirectional canyon migration (UCM) and erosion of the canyon wall enabled the number of MTDs in the study area to be identified using 3D seismic data interpretation and attribute analyses. In addition, seismic facies were distinguished and their profiles interpreted, which enabled classification of MTDs into three types: (1) well-preserved MTDs, (2) MTDs eroded by canyon migration, and (3) MTDs dislocated by contemporaneous faults. An analysis of hydrate accumulation theory has led to the suggestion of three corresponding patterns, namely: (1) a well-preserved MTD accumulation pattern (such as the sandwich pattern, which has two layers of fine sediment beneath and above a coarse-grained reservoir and was introduced by Malinverno (2010) in the Cascadia margin); (2) a canyon-migration eroded MTD release pattern (such as the canyon pattern introduced by Boswell et al. (2012), in the Gulf of Mexico and Vadakkepuliyambatta et al. (2015), in the Barents Sea, in which the decrease in heat flow and increase in the erosion rate in the canyon area was defined); and (3) a micro- contemporaneous faults dislocated MTD release pattern (which is determined in this study). Turbidites flow may lead to canyon wall erosion, which then causes sediments to become unstable; therefore, the above patterns may also form micro-contemporaneous faults. In each of these three patterns, a fine reservoir seal is found to be indispensable to hydrate accumulation and release. It is considered that the response patterns presented in this paper will enhance understanding of the relationship between MTD development and hydrate accumulation, and enable improved hydrate prediction in the high dip, angular, slope of passive continental margins (an area that facilitates MTD development).

This paper is organized as follows: the geological settings, methodologies, and data preparation are firstly presented to provide a background to this study. The different types of MTDs are then identified through seismic-log-core integration analysis, and MTD hydrate-bearing patterns are constructed in relation to the hydrate distribution area. Finally, factors impacting accumulation patterns are discussed.

2 Geological setting

The new drilling area in Shenhu is located in the central section of the northern slope of the SCS and constitutes a deep-sea sedimentary area of the Baiyun Sag in the southern Zhujiang (Pearl) River Mouth Basin (ZRMB) (115°10′ to 115°20′E) (Fig. 1a). The ZRMB is a Cenozoic sedimentary basin that has experienced three tectonic stages since the Paleogene, namely a rift stage during the Paleocene to the early Oligocene, a transition in the late Oligocene, and a depression during the early Miocene to Quaternary (Han et al., 2016). During the late Oligocene to early Miocene, "Baiyun" movement (belonging to the latest tectonic stage) caused the Zhujiang (Pearl) River Estuary shelf slope to break and drift northwards, thereby becoming the depositional center of the Baiyun Sag; it then evolved into a deep-water slope environment (Clift et al., 2002; Han et al., 2016).

Han et al. (2016) proposed the following: sea levels in SCS have been rising continuously since the late Miocene, there has been an increase in the extent of SCS transgression, the seaward progress of the Zhujiang River Estuary shelf delta is limited, and there has been a simultaneous and significant northward migration of the sedimentation process. The Shenhu area lies in the southern deep-water area of the ZRMB (Fig. 1b), which is far from the provenance form the Zhujiang River; therefore, transported sediment is relatively small and fine-grained (Li et al., 2015).

The main well sites studied here are distributed in the canyon area (well sites shown in Fig. 1b). The canyon is located in the central part of the Baiyun Sag and lies mostly in a NNW direction (Fig. 1b). The drilled hydrate reservoirs are mainly composed of hemipelagic foraminifera, and fine silt and shale in the Yuehai and Wanshan Formations (Fig. 1c) (Wang et al., 2014; Sha et al., 2015). Based on multi-beam submarine topography data (Fig. 1b), the upper part of the slope is found to mainly have an asymmetric V-shaped or symmetric U-shaped structure, whereas the lower part of the slope is relatively flat. The study area is located at depths of 800–2 000 m, and there is a large gradient throughout the entire study area, with a maximum gradient of 3°.

The modern ocean circulation in the SCS is mainly controlled by semi-enclosed basin physiography and can be divided into seasonal surface-water circulation (<350 m), intermediate water circulation resulting from North Pacific intermediate water (NPIW; 350–1 350 m), and deep-water circulation associated with North Pacific deep water (>1 350 m). Along-slope bottom (contour) currents generally involve significant water masses at certain bathymetric depth ranges that persist for very long time intervals. It is therefore considered that the bottom currents associated with intermediate water circulation resulting from the NPIW (NPIW-BCs) are most likely to have had a profound influence on the development of the unidirectional migrating deep-water channels that are studied here, which are located primarily in water depths ranging from 500–1 300 m.

3 Data and methodology

Pseudo-three-dimensional (3D) survey data were acquired by GMGS between 2008 and 2009, using a frequency of 65 Hz and a sampling interval of 1 ms over an area measuring approximately 15 km by 25 km. To accurately describe the hydrate-bearing layers, time windows were set at 3 ms per slice. Log data were acquired by Fugro and processed by Schlumberger in 2015. Data acquired by the Guangzhou Marine Geological Survey (GMGS)-3 include the use of natural gamma-rays, gamma density, resistivity, and sonic velocity. *In situ* core samples in the target layers were taken using two kinds of pressure-core-barre tools (FPC, PCTB) and three non-pressure-core-barre tools (FHPC, FMCB, FXMCB). Due to the salt extraction effect of hydrate, the value of the resistivity log was abnormally high in the target layers (Riedel et al., 2013a). The grain size was measured using Mastersizer® 2000 with a laser particle size analyzer (SYE209) in Well11 (W11), Well17 (W17), Well18 (W18), and Well 19 (W19).

Studies of variable MTD development patterns are based on the integration of seismic data, log data, and core analyzes. Mitchum (1977) first proposed the seismic facies analysis methodology to study sedimentary characteristics; this is based on the morphology of seismic reflectors, reflection of the seismic boundary, and the contact relation between different seismic facies (see the seismic facies listed in Fig. 2).
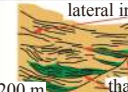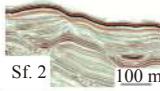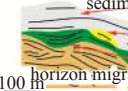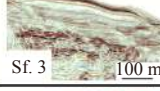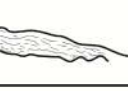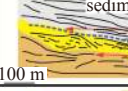
Fig. 2. Characteristics of seismic facies (Sf.) with respect to contact relationship with seismic events. Given the inner character of seismic packages its boundary, seismic facies are divided into two types, concave and chaotic facies. Seismic facies are then divided into four types, numbered from Sf. 1 to Sf. 4.

In this study, the turbidities flow rate in the canyon was calculated using the following four steps: (1) dividing the seismic data into three slices (Figs 3a–c: 1 500 ms, 2 000 ms and 2 500 ms); (2) decompacting the surface of each sequence using 2DMove software and reconstructing the paleo-geomorphology of each slice (Figs 3a–c); (3) calibrating the depositional rate of each well (W02, W05, W08, W16, W17, W18, W19) using the equation: $v_s=4.2\Phi-0.2$, where Φ is the corresponding grain size (see the Rose graph in Fig. 3); and (4) calibrating each well, subtracting the thickness of adjacent slices, then calculating the turbidities flow rate with well-integrated data.

The methodology used to distinguish hydrates is based on seismic reflection and corresponding log calibration. Using core samples from Wells W11, W17, W18 and W19 (Fig. 4) and their corresponding resistance curves (Rt) at depths of 40–100 m and >120 m (Fig. 4), the hydrate saturation of the bearing layers was calculated (Table 1) using Archie's formula (the empirical parameter is determined as 'a' = 1.0 and 'm' = 1.8 (unconsolidated), through *in situ* pore turbidities flow salinity data).

4 Seismic geomorphology and recognition of MTDs

4.1 *Seismic facies analysis*

With respect to studies of 3-D seismic volume work conduc-
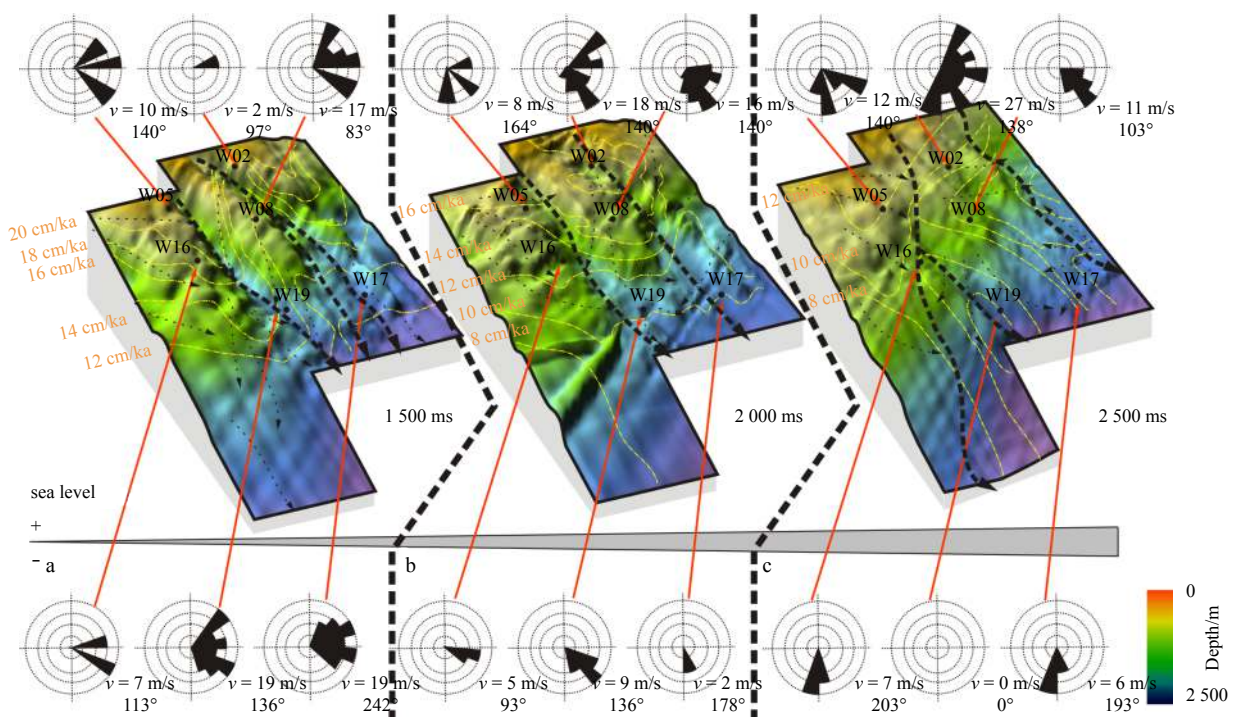
Fig. 3. Sedimentary and turbidities flow rates in study area. Paleo-geomorphology of different geological times since 11.8 Ma, from bottom to top: top of 1 000 ms (a), top of 1 250 ms (b), and top of 1 500 ms (c). Yellow dotted-line refers to changes in turbidities flow rate. Rose-diagram represents the flow rate and direction of turbidities flows in the channel.
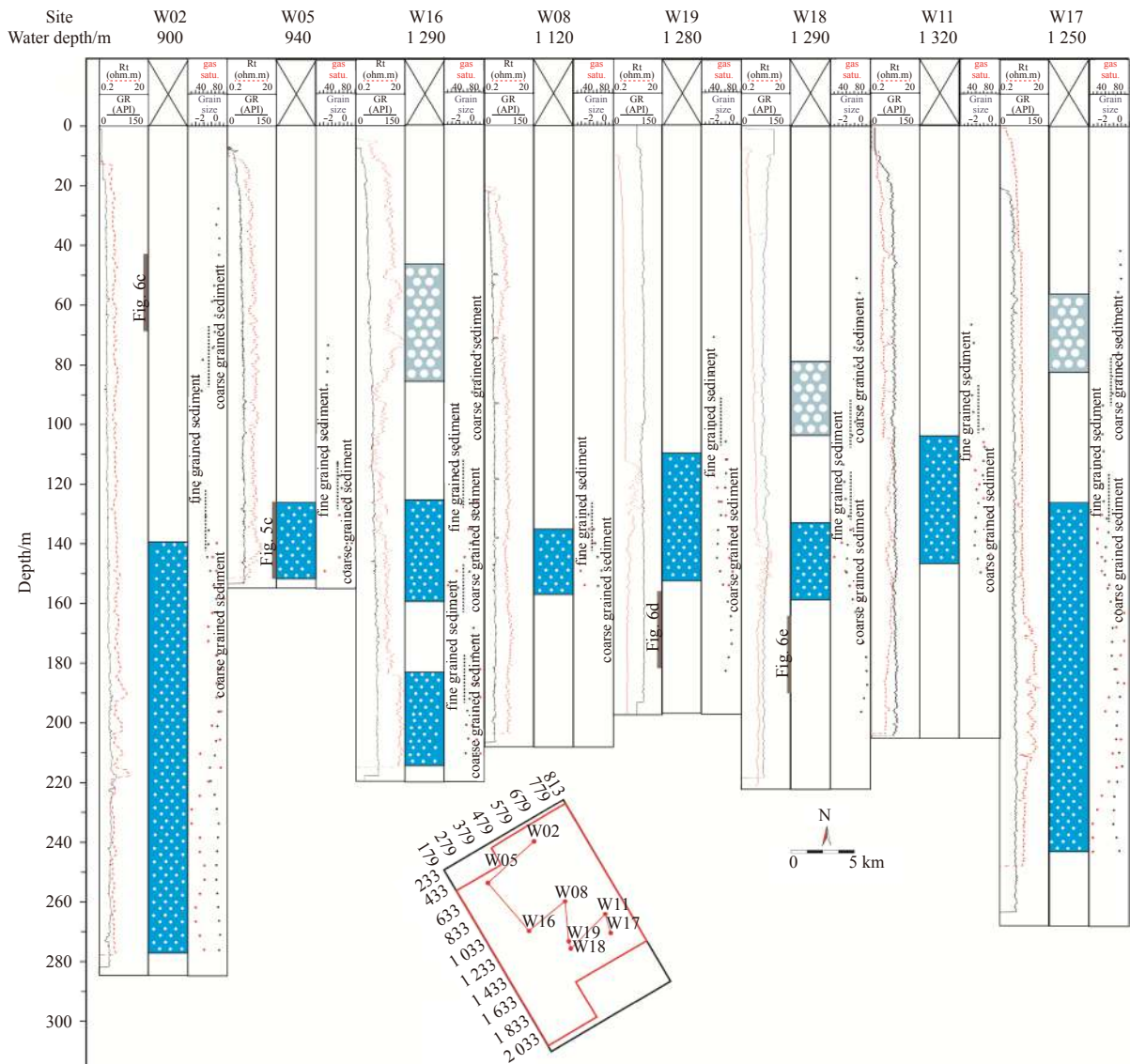
Fig. 4. Log data of GMGS-3 and corresponding saturation. Red dotted-line represents GR and black active line resistivity; hydrate layers interpreted in the middle are based on the Archie formula and core sample observation; gain size and hydrate saturation on the right are the result of calculations, which show that fine-grained layers exist above and beneath the coarse-grain layers.

Table 1. Saturation distribution of different wells

Well	Hydrate layers	Accumulation state	Crack width and developed density	Hydrate saturations
W11	14.94–19	fracture filling	development of subtle cracks, average width 2 mm	0.2–0.4
	27–33.98	fracture filling	development of subtle cracks, average width 2 mm	0.2–0.4
W17	104–122.3	fine grain filling	non-development of crack, soup structure	0.6–0.7
	54–65.49	fracture filling	development of subtle cracks, average width 3 mm	0.35–0.5
W18	155.44–203.75	fine grain filling	non-development of crack, soup structure	>0.8
	117.44–130	fine grain filling	development of subtle cracks, average width 2 mm	0.4–0.5
W19	130–163.5	fine grain filling	development of subtle cracks, average width 2 mm	0.4–0.5
	53.08–59.08	fracture filling	development of subtle cracks, average width 2 mm	<0.3

ted in the study area, and according to seismic reflection results and strengths and weaknesses, the seismic facies can be divided into two types: concave facies and chaotic facies (Fig. 2). Concave facies are characterized by down lap reflector packages (Fig. 2: concave) and chaotic facies are characterized by discontinuous and disorderly reflector packages (Fig. 2: radom); these are fur-

ther described as follows.

Concave facies: Based on the external geometric morphology of a seismic reflection, concave facies can be divided into lateral-concave facies (Sf. 1) and horizontal-concave facies (Sf. 2). Lateral-concave facies (Sf. 1) are characterized by discontinuous reflector packages, high-amplitude reflections, and unidirectional

migration of the truncated surface (reflector packages undergo upward migration following aggrading), which can be explained as being the directional migration of the canyon (Wang et al., 2014). Horizontal-concave facies (Sf. 2) have continuous reflector packages, low-amplitudes, and show horizontal migration of the truncated surface.

Chaotic facies: chaotic facies present as discontinuous internal seismic reflectors and can be divided into mound-chaotic (Sf. 3) and chimney-chaotic (Sf. 4) facies. Mound-chaotic facies (Sf. 3) have a chaotic internal reflector package with a high amplitude and a mound reflection boundary, representing MTDs; but chimney-chaotic facies (Sf. 4) also have a chaotic internal reflector package. The chimney-shaped reflection boundary is thought to be an abnormal reflection caused by the upward movement of free gas from the bottom.

4.2 *Seismic profile analysis*

This paper refers to two NNW-direction profiles through well sections (inline 300 and inline 500) that were selected to study the vertical MTD distribution of sedimentary facies. Positions of the profiles are shown in Fig. 1b, where the section indicates 20 km of inline direction and 15 km of crossline direction.

Profile A (Fig. 5: inline 300) is located in the western part of the study area (profile position is shown in Fig. 1b) and passes through Well W05. Use of 1 250–1 750 ms distinguishes mound-chaotic facies (Sf. 4), and two types can be identified in the profile: (1) mound-chaotic facies (Fig. 5c) have a continuous seismic

facies boundary, cluttered internal seismic event, and high attributes, while the seismic event of the upper overburden is not significantly broken; (2) mound-chaotic facies (Fig. 5d) have an indistinct facies boundary, and the seismic event of the upper overburden has an obvious dislocation.

Profile B (Fig. 6: inline 500) is located in the east of the study area (profile position is shown in Fig. 1), passes through wells W02, W08, W19, and W18, and mainly through Canyon A and Ridge B. Use of 1 250–1 500 ms enables identification of three types of mound-chaotic facies in the profile: (1) MTDs (Fig. 6c) are influenced by the effect of erosion and have a serious seismic erosion surface with a high amplitude; (2) chaotic facies (Fig. 6d) and (3) fault lines of mound-chaotic facies (Fig. 6e) are also development with a maximum length of more than 100 m and a small overall thickness.

5 Corresponding MTD classification and sedimentary characteristics

5.1 *Type I MTDs*

Well-preserved MTDs developed along the unstable slope setting, and most developed along slope-breaks, such as within the southern Cretan Sea, Peri-Adriatic Sea, and SCS (Strozyk et al., 2009; Di Celma, 2011; Zhou et al., 2015). Profile B, shown in Fig. 6, shows that multi-layer developed over the well-persevered MTDs, meaning the. Combined with the corresponding hydrate-bearing core sample in Fig. 4, W11, W17, W18 and W19
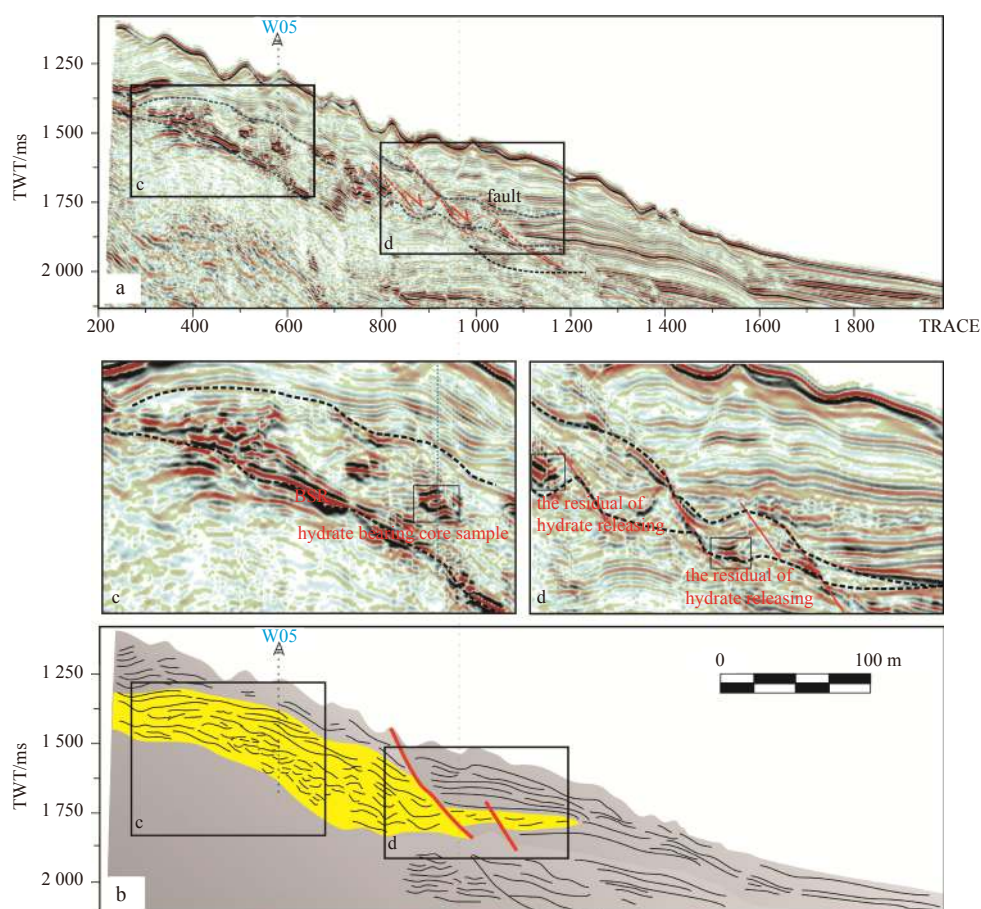
Fig. 5. Seismic Section A passing through W05 (select inline 300); the lower part is the sedimentary section used to analyze the internal structure of a seismic event. c and d show the enlarged MTD of the seismic profile; c shows a well-preserved MTD; and d shows an MTD broken by micro- contemporaneous faults, which have not dislocated the upper fine-grained layer.
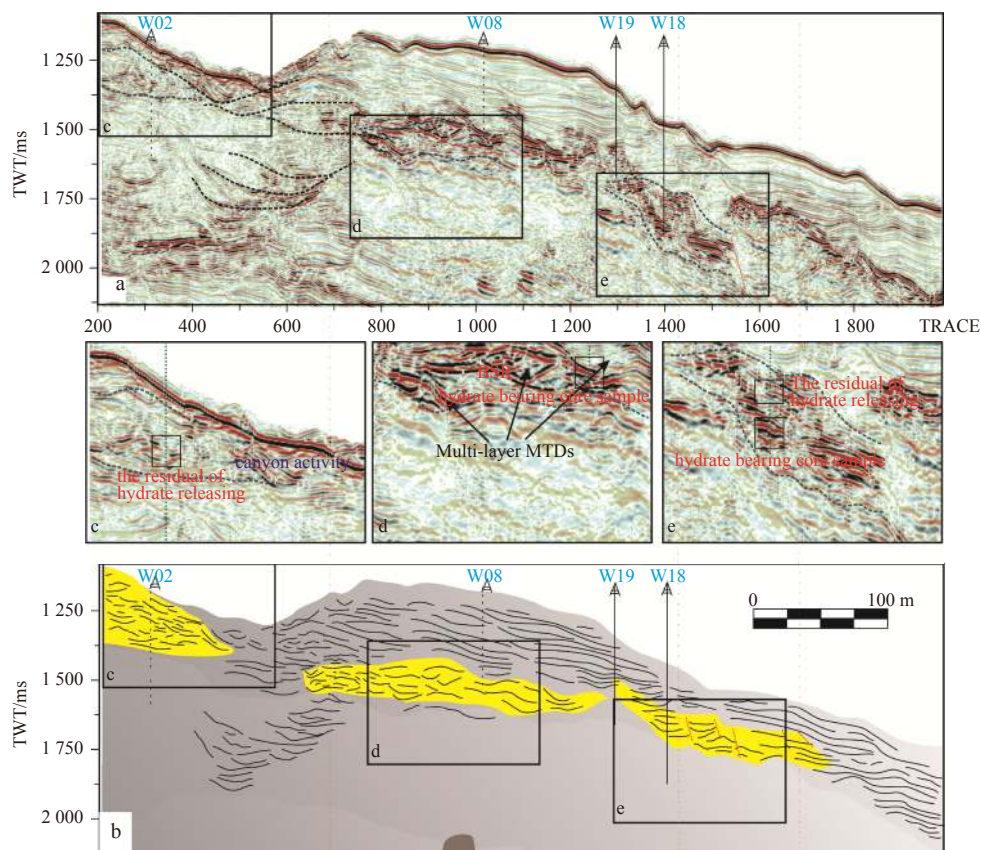
Fig. 6. Seismic Section B passing through W08, W18 and W19 (select inline 500); the lower part is the sedimentary section used to analyze the internal structure of a seismic event. c, d and e show the enlarged MTD of the seismic profile; c shows MTDs eroded by the lateral canyon; d shows multi- layers MTDs; and e shows an MTD broken by micro- contemporaneous faults.

show rhythmic variations in MTD grain sizes, which can be referred to as "sandwich layers".

5.2 *Type II MTDs*

Based on interpretation of the seismic profile shown in Fig. 6c above, it appears that most Type II MTDs developed upstream of Type I MTDs and therefore underwent more intensive and complex reworking by the flow. Alsop et al. (2016) showed that sedimentation and turbidities flow rates are important factors in MTD formation. Meanwhile, the fine-grained layers over Type II MTDs are mostly reworked during later turbidities flow erosion.

5.3 *Type III MTDs*

Based on the seismic profiles shown in Figs 5b, 6c and the interpretation above, Type III MTDs are developed over a larger region. However, most are developed in the downstream slope-bottom of Type I MTDs (Fig. 7a: Type III). Micro-contemporaneous faults may have developed in relation to the following factors: free gas flow and a decrease in cementation between particles, differential settlement, and tectonic movement. For example, due to tectonic movement, the feet of Ridges A and B are formed in areas that have undergone rapid geomorphic basement changes (the dip angle changes from 5° to 2°–4° per km). Contemporaneous faults are formed when the shear stress is larger than the shearing strength of the MTD; when the sheer force of MTDs increases, the slump in progress restarts. Thus, contemporaneous faults may dislocate the above fine-grained over-layers (as in profiles Figs 5d, 6e).

6 Corresponding MTD hydrate-bearing patterns

6.1 *Hydrate reflection characteristics*

Hydrate saturation in each well was determined by the pressure release in the core through in-situ observations of the four core wells (W11, W18, W17 and W19) (Table 1). However, due to the restricted number of wells in the GMGS-3 area and other parameters, and therefore the lack of data for the drilling area, it was necessary to study and evaluate the seismic reflection characteristics of the hydrate-bearing layers (Table 2) to determine the hydrate distribution. From a comparison between original sections and synthetic seismograms from high-resistivity regions (Wang et al., 2011), the bottom of the hydrate-bearing layer (BGHSZ) in GMGS-3 was found to be developed with an amplitude anomaly due to free gas, and this was found to decrease the P-velocity. Nevertheless, the BGHSZ shows a blank reflection band in the seismic profiles (Horozal et al., 2015), and the hydrate response in the BSR indicates skewed reflection characteristics and exhibits an amplitude anomaly.

6.2 *Response pattern of hydrate-bearing MTDs*

The progress of gas hydrate accumulation is controlled by many sediment-related factors, such as grain size, sand content, porosity, and turbidities flow rate (Wood et al., 2008; Behseresht and Bryant, 2012). The combination of a hydrate-bearing core sample and hydrate accumulation system, where the above MTDs types could be projected into three patterns, to respond to hydrate accumulation/ released (Wu et al., 2011; Sha et al., 2015;

Table 2. BSR reflection characteristics of hydrate-bearing layers in each well

Site	BSR reflection characteristics	Type	Time	Depth range/m	Lithology	C1/C2
W11	moderate amplitude, low continuity, appearance BGHSZ	W/S	late Miocene	94–399 (from core sample)	silt stone	200
W17	high amplitude, low continuity, appearance BGHSZ	S	late Miocene	94–399 (from core sample)	silt stone	180
W18	high amplitude, low continuity, appearance BGHSZ	S	late Miocene	160–345 (from core sample)	silt stone	200
W19	low amplitude, low continuity, appearance BGHSZ	S	late Miocene	160–345 (from core sample)	silt stone	250

Vadakkepuliyambatta et al., 2015) (AM.1, RM.2 and RM.2) (Fig. 8), and these are explained as follows.

6.2.1 *Well-preserved MTDs accumulation pattern*

Type I MTDs shown in seismic profiles (Figs 5a, 6b) are well-preserved MTDs that have developed with a complete sedimentary structure, namely crown cracks, basal shear surface, and toe thrust (Fig. 7a2). These kinds of MTDs develop with moderate thicknesses (40–80 m per MTDs) and have moderate spans (100–200 m² per MTDs). The continuous seismic events occurring above MTDs can be interpreted by the fine layer, serving as a seal and cap for free gas. Based on hydrate calculations and the volume of MTD development (as shown in Fig. 7a3) Type I MTDs

have good gas hydrate reflections.

The well-preserved MTD accumulation pattern can be simplified and referred to as a "sandwich accumulation pattern" (Fig. 8a3). As shown by the porosity curve in Fig. 8a3, hydrate-bearing sand and fine mud mutually overlaps in Type I MTDs. During gas hydrate resource appraisal, the following are considered: the thermal genetic gas supply, reaction time, effective migration, reservoir litho-facies, effective porosity, and gas hydrate stability zone. This type of sandwich pattern (AM.1) not only provides sufficient reaction time for the formation of clathrate hydrates but also provides sufficient porosity for hydrates. Therefore, AM.1 types serve as reservoirs for fine-grained filling hydrate under suitable temperatures and pressures.

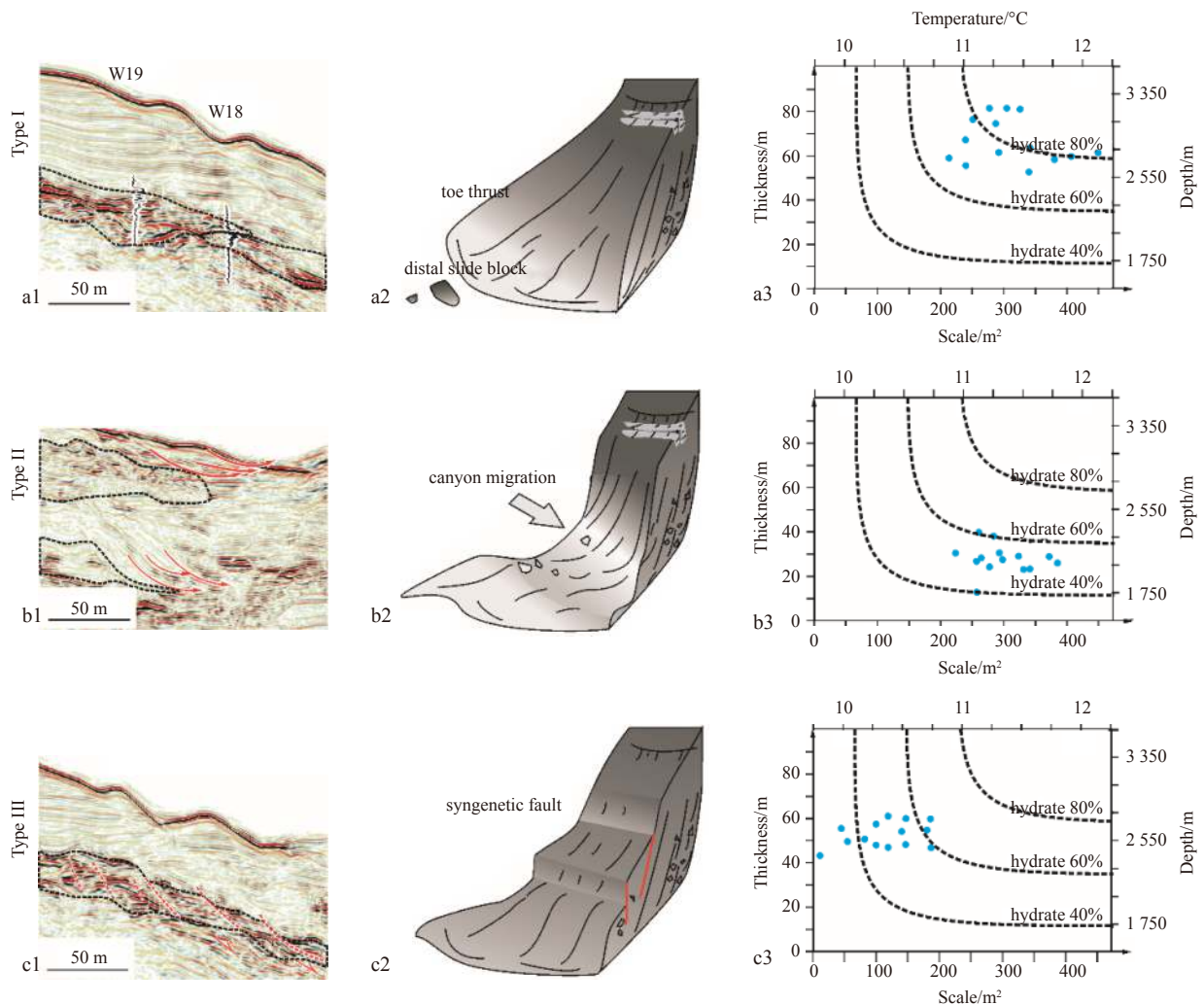**Fig. 7.** Different types of MTDs distinguished in the study relating to gas hydrate accmulation; a1, a2 and a3 are seismic profiles showing different types of MTD-bearing hydrates; b1, b2 and b3 are sedimentary patterns of the above MTDs; c1, c2 and c3 are thickness and scale of MTD statistics obtained from the seismic profile; and the blue scatter shows hydrate saturation bearing in variable types of MTDs.
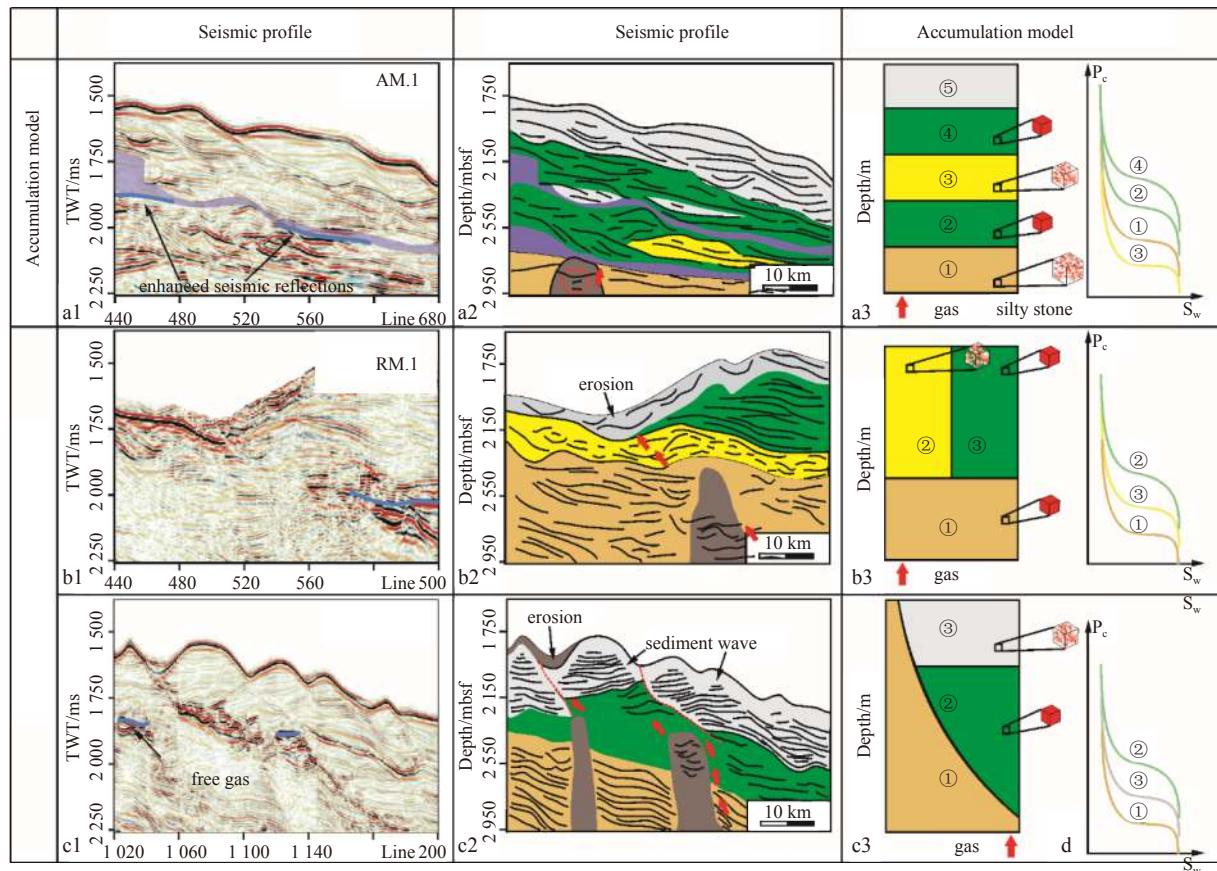
Fig. 8. Three response models for hydrate accumulation. a1, a2 and a3 seismic profiles selected in the study area, where the purple line is the BSR; b1, b2 and b3 sedimentary interpretations of seismic profile where the yellow area represents MTD development; c1, c2 and c3 response models with porosity curve on the right. The red cube represents grain sizes in different layers. mbsf represents meters below sea floor.

6.2.2 *Canyon migration eroded MTD release pattern*

In Type II MTDs (shown in the seismic profile of Fig. 6a), canyon migration eroded MTDs developed with an incomplete depositional structure (Fig. 7a2), small thicknesses (20–40 m per MTD) and on a moderate scale (100–200 m² per MTD). Despite not procuring a drilling sample, the type of BRS reflection and low amplitude (Profile B and Well 2 shown in Fig. 6) prove that these MTDs have low saturation levels (Fig. 7b3). When UCM erosion has occurred and the MTD structure has been broken, a release pattern (RM. 1) is likely to form. The fine layer overlapping the coarse hydrate-bearing siltstone is also eroded. In addition, with respect to the high turbidities flow rate caused by turbidities passing (the turbidities flow rate is shown in Fig. 3), the release of free gas leads to a decrease in gas saturation in these reservoirs. Thus, as shown by RM.2 in Fig. 8b3, free gas migrates from the gas chimney and is easily released into the sea water. In addition, there is insufficient reaction time, and excess turbidities flowing in the canyon may change the heat flux distribution and geochemistry, thereby influencing hydrate accumulation.

6.2.3 *Micro- contemporaneous faults dislocated MTD release pattern*

Type III MTDs shown in the seismic profile (Figs 5c and 6c) are related to micro-contemporaneous faults that have dislocated MTDs (Fig. 7c2). These kinds of MTDs develop with moderate thicknesses (20–40 m per MTD) and on a small scale (<100 m²

per MTD). The seismic amplitude is less intense than that of Type I, which implies that Type III MTDs have a lower hydrate saturation than Type I MTDs (Fig. 7c3).

A previous study showed that normal faults can not only break the primary structure but can also serve as a pathway for free gas migration (Lee et al., 2012; Jeong et al., 2014). Meanwhile, normal faults provide available space for hydrates and can also serve as reservoirs for fracture-filling hydrates.

Therefore, as shown in Figs 8a3 and c3, fault slip may be a key factor for gas accumulation. If the slip distance is less than half the thickness of the MTD, it is classified as AM.1, and if not it is classified as RM. 2.

The three different MTD types shown above have different hydrate responses, and all patterns can be summarized into litho-facies assemblages. If fine layers act as a seal for the hydrate reservoir, free gas is not easily released and hydrate accumulation progresses easily. Thus, in a fine canyon system, UCM and uneven subsidence of the canyon floor may be the main causes of broken MTD reservoirs in the Shenhu new drilling area.

7 Factors impacting gas hydrate bearing-MTDs

The hydrate accumulation pattern in Fig. 8 considers both porosity and the fine-grain seal above the MTD. In addition, according to the hydrate accumulation system, the temperature, pressure, and gas source also have an impact on accumulation.

7.1 *Effect of pressure-temperature*

Hydrate accumulation pressure is comprised of hydrostatic pressure and litho-static pressure. In the drilling area, the water depth ranges from 820 m to 1 445 m. On the northern slope of the SCS, values of heat flow range from 6 to 191 mW/m² with an average value of 76 mW/m² (Shi et al., 2003; Zhang et al., 2011).

However, differences between the preservation settings of MTDs may lead to considerable heterogeneity in the heat flow. According to the study of Vadakkepuliyambatta et al. (2015) in the Barents Sea, canyon migration cannot not only break the original MTD structure, but it can also impact the local heat distribution, which may lead to an increase in heat flow on the sides of the canyon walls. Therefore, due to the minimal impact from later canyon activity, the pressure-temperature balance of well-preserved MTDs fluctuate and has an impact on hydrate accumulation. However, when later canyon activity reworks MTDs, the original litho-static pressure and its corresponding heat flow distribution may be changed, and the gas hydrate is more easily decomposed and released.

7.2 *Effect of available water and gas resources*

Available water provides a clathrate molecule skeleton; therefore, an adequate amount of free water is required within pores to effectively form hydrates. However, excess available water in pores may occupy spaces between free gases and have a negative impact on hydrate accumulation. In addition, Handa (1990) found that a suitable matching relation between available water and the gas source is crucial for enabling a hydrate synthesis reaction. In pattern AM.1, abundant gas sources are provided from the bottom gas chimney, and the well-preserved MTDs provide a suitable storage space and available water. Furthermore, the fine-grain seal above the MTD acts as a seal that stops free gas diffusion, and thereby provides enough refection time between the methane gas and available water.

In patterns RM.1 and RM.2, the accumulation factors, such as gas sources, suitable storage space, and available water, are similar to those for AM.1. However, canyon-migration erosion and normal-fault dislocation are capable of breaking the original fine-grain layers above the MTD, thereby suggesting that it is difficult for gas hydrate refection over a longer time period.

7.3 *Effect of later canyon migration*

The three types of MTDs have relationships with canyon development and migration. Hence, the three corresponding pattern types have mutual transformations. For example, the flow action of later turbidities may lead to an unstable and unconsolidated ridge and the development of MTDs, and later geological movements may cause conversion between these three patterns. Later canyon migration leads to basement erosion and may increase the occurrence of normal MTD development. However, if the canyon migrates to a region where MTDs are developing, the AM.1 pattern may be converted into a RM.1 pattern. Furthermore, if canyon migration is limited and tractive current develops, fine sediment (sedimentary wave or levee) may cover the reservoir and serve as a seal for free gas, which may then lead to the conversion of RM. 1 and RM. 2 in to AM. 1.

8 Conclusions

Based on the analysis of the deep-water canyon system in GMGS-3, this paper describes three types of MTDs. Three patterns are summarized based on results of a core-log-seismic integration study and with respect to hydrate accumulation.

(1) Two hydrate-bearing layers are distinguished based on an analysis of electronic log and a core sample. The upper layer is fracture-filling hydrate and the lower layer is fine-grain-filling hydrate. A saturation count of the hydrate was conducted and reflective characteristics of 3D seismic data were evaluated. The regions overwhelmed by BSR distribution fit well with the MTDs along the ridge.

(2) Through seismic data interpretation, three kinds of MTDs are classified in the new drilling area at Shenhu: well preserved MTDs, MTDs eroded by canyon migration, and MTDs dislocated by contemporaneous faults.

(3) Three types of patterns are proposed based on a comparison of the three types of MTDs and their relationships with hydrate accumulation. Results show that a fine-grained seal is the key to gas accumulation. With respect to canyon migration and normal faults, the primary structure of the MTD often breaks and layers are sealed. Sand and fine mud mutually overlap in a sandwich pattern, which is the ideal type of MTD for accumulating hydrates on the northern slope of the SCS.

References

Alsop G I, Marco S, Weinberger R, et al. 2016. Sedimentary and structural controls on seismogenic slumping within mass transport deposits from the Dead Sea Basin. Sedimentary Geology, 344: 71–90, doi: 10.1016/j.sedgeo.2016.02.019

Bangs N L B, Hornbach M J, Berndt C. 2011. The mechanics of intermittent methane venting at South Hydrate Ridge inferred from 4D seismic surveying. Earth and Planetary Science Letters, 310(1–2): 105–112, doi: 10.1016/j.epsl.2011.06.022

Behseresht J, Bryant S L. 2012. Sedimentological control on saturation distribution in Arctic gas-hydrate-bearing sands. Earth and Planetary Science Letters, 341–344: 114–127, doi: 10.1016/j.epsl.2012.06.019

Boswell R, Frye M, Shelander D, et al. 2012. Architecture of gas-hydrate-bearing sands from Walker Ridge 313, Green Canyon 955, and Alaminos Canyon 21: Northern deepwater Gulf of Mexico. Marine and Petroleum Geology, 34(1): 134–149, doi: 10.1016/j.marpetgeo.2011.08.010

Chen Duanxin, Wang Xiujuan, Völker D, et al. 2016. Three dimensional seismic studies of deep-water hazard-related Features on the northern slope of South China Sea. Marine and Petroleum Geology, 77: 1125–1139, doi: 10.1016/j.marpetgeo.2016.08.012

Clift P, Lin Jian, Barckhausen U. 2002. Evidence of low flexural rigidity and low viscosity lower continental crust during continental break-up in the South China Sea. Marine and Petroleum Geology, 19(8): 951–970, doi: 10.1016/S0264-8172(02)00108-3

Di Celma C. 2011. Sedimentology, architecture, and depositional evolution of a coarse-grained submarine canyon fill from the Gelasian (early Pleistocene) of the Peri-Adriatic basin, Offida, central Italy. Sedimentary Geology, 238(3–4): 233–253, doi: 10.1016/j.sedgeo.2011.05.003

Gong Chenglin, Wang Yingmin, Zheng Rongcai, et al. 2016. Middle Miocene reworked turbidites in the Baiyun Sag of the Pearl River Mouth Basin, northern South China Sea margin: Processes, genesis, and implications. Journal of Asian Earth Sciences, 128: 116–129, doi: 10.1016/j.jseaes.2016.06.025

Han Jianhui, Xu Guoqiang, Li Yangyang, et al. 2016. Evolutionary history and controlling factors of the shelf breaks in the Pearl River Mouth Basin, northern South China Sea. Marine and Petroleum Geology, 77: 179–189, doi: 10.1016/j.marpetgeo.2016.06.009

Handa Y P. 1990. Effect of hydrostatic pressure and salinity on the stability of gas hydrates. The Journal of Physical Chemistry, 94(6): 2652–2657, doi: 10.1021/j100369a077

He Yunlong, Xie Xinong, Kneller B C, et al. 2013. Architecture and controlling factors of canyon fills on the shelf margin in the Qiongdongnan Basin, northern South China Sea. Marine and Petroleum Geology, 41: 264–276

Holbrook W S, Hoskins H, Wood W T, et al. 1996. Methane hydrate and free gas on the Blake ridge from vertical seismic profiling. Science, 273(5283): 1840–1843, doi: 10.1126/science.273.5283.1840

Horozal S, Kim G Y, Bahk J J, et al. 2015. Core and sediment physical property correlation of the second Ulleung Basin Gas Hydrate Drilling Expedition (UBGH2) results in the East Sea (Japan Sea). Marine and Petroleum Geology, 59: 535–562, doi: 10.1016/j.marpetgeo.2014.09.019

Jeong T, Byun J, Choi H, et al. 2014. Estimation of gas hydrate saturation in the Ulleung basin using seismic attributes and a neural network. Journal of Applied Geophysics, 106: 37–49, doi: 10.1016/j.jappgeo.2014.04.006

Lee M W, Collett T S, Lewis K A. 2012. Anisotropic models to account for large borehole washouts to estimate gas hydrate saturations in the Gulf of Mexico Gas Hydrate Joint Industry Project Leg II Alaminos Canyon 21 B well. Marine and Petroleum Geology, 34(1): 85–95, doi: 10.1016/j.marpetgeo.2011.06.010

Li Gang, Yan Wen, Zhong Lifeng, et al. 2015. Provenance of heavy mineral deposits on the northwestern shelf of the South China Sea, evidence from single-mineral chemistry. Marine Geology, 363: 112–124, doi: 10.1016/j.margeo.2015.01.015

Malinverno A. 2010. Marine gas hydrates in thin sand layers that soak up microbial methane. Earth and Planetary Science Letters, 292(3–4): 399–408, doi: 10.1016/j.epsl.2010.02.008

Mitchum R M Jr. 1977. Seismic stratigraphy and global changes of sea level, Part 11, Glossary of terms used in Seismic Stratigraphy. In: Payton C E, ed. Seismic Stratigraphy-Applications to Hydrocarbon Exploration. USA: AAPG Memoir, 205–212

Riedel M, Bahk J J, Kim H S, et al. 2013b. Seismic facies analyses as aid in regional gas hydrate assessments. Part-I: Classification analyses. Marine and Petroleum Geology, 47: 248–268

Riedel M, Collett T S, Kim H S, et al. 2013a. Large-scale depositional characteristics of the Ulleung Basin and its impact on electrical resistivity and Archie-parameters for gas hydrate saturation estimates. Marine and Petroleum Geology, 47: 222–235, doi: 10.1016/j.marpetgeo.2013.03.014

Scholz N A, Riedel M, Bahk J J, et al. 2012. Mass transport deposits and gas hydrate occurrences in the Ulleung Basin, East Sea-Part 1: Mapping sedimentation patterns using seismic coherency. Marine and Petroleum Geology, 35(1): 91–104, doi: 10.1016/j.marpetgeo.2012.03.004

Sha Zhibin, Liang Jinqiang, Zhang Guangxue, et al. 2015. A seepage gas hydrate system in northern South China Sea: Seismic and well log interpretations. Marine Geology, 366: 69–78, doi: 10.1016/j.margeo.2015.04.006

Shi Xiaobin, Qiu Xuelin, Xia Kanyuan, et al. 2003. Characteristics of surface heat flow in the South China Sea. Journal of Asian Earth Sciences, 22(3): 265–277, doi: 10.1016/S1367-9120(03)00059-2

Strozyk F, Huhn K, Strasser M, et al. 2009. New evidence for massive gravitational mass-transport deposits in the southern Cretan Sea, western Mediterranean. Marine Geology, 263(1–4): 97–107, doi: 10.1016/j.margeo.2009.04.002

Vadakkepuliyambatta S, Hornbach M J, Bünz S, et al. 2015. Controls on gas hydrate system evolution in a region of active fluid flow in the SW Barents Sea. Marine and Petroleum Geology, 66: 861–872, doi: 10.1016/j.marpetgeo.2015.07.023

Wang Xiujuan, Collett T S, Lee M W, et al. 2014. Geological controls on the occurrence of gas hydrate from core, downhole log, and seismic data in the Shenhu area, South China Sea. Marine Geology, 357: 272–292, doi: 10.1016/j.margeo.2014.09.040

Wang Xiujuan, Wu Shiguo, Lee W, et al. 2011. Gas hydrate saturation from acoustic impedance and resistivity logs in the Shenhu area, South China Sea. Marine and Petroleum Geology, 28(9): 1625–1633, doi: 10.1016/j.marpetgeo.2011.07.002

Wood W T, Hart P E, Hutchinson D R, et al. 2008. Gas and gas hydrate distribution around seafloor seeps in Mississippi Canyon, Northern Gulf of Mexico, using multi-resolution seismic imagery. Marine and Petroleum Geology, 25(9): 952–959, doi: 10.1016/j.marpetgeo.2008.01.015

Wu Nengyou, Zhang Haiqi, Yang Shengxiong, et al. 2011. Gas hydrate system of Shenhu Area, northern south China Sea: geochemical results. Journal of Geological Research, 2011: 370298

Yu Xinghe, Wang Jianzhong, Liang Jinqiang, et al. 2014. Depositional characteristics and accumulation model of gas hydrates in northern South China Sea. Marine and Petroleum Geology, 56: 74–86, doi: 10.1016/j.marpetgeo.2014.03.011

Zhang Yi, He Lijuan, Wang Jiyang, et al. 2011. Heat flow pattern, base of methane hydrates stability zones and BSRs in Shenhu Area, northern South China Sea. Acta Oceanologica Sinica, 30(1): 59–67, doi: 10.1007/s13131-011-0091-x

Zhou Wei, Wang Yingmin, Gao Xianzhi, et al. 2015. Architecture, evolution history and controlling factors of the Baiyun submarine canyon system from the middle Miocene to Quaternary in the Zhujiang River Mouth Basin, northern South China Sea. Marine and Petroleum Geology, 67: 389–407, doi: 10.1016/j.marpetgeo.2015.05.015

Multibeam water column data research in the Taixinan Basin: Implications for the potential occurrence of natural gas hydrate

Yilan Chen[1], Jisheng Ding[1]*, Haiquan Zhang[1], Qiuhua Tang[1], Xinghua Zhou[1], Xiaoyu Liu[1]

[1] First Institute of Oceanography, Ministry of Natural Resources, Qingdao 266061, China

Abstract

A multi beam sonar survey is carried out in the continental slope of the Taixinan Basin to obtain submarine topographic and water column data. The data are processed to obtain water column images. Anomalous water column images, displaying plume characteristics, are found in gas hydrate enriched areas in the Taixinan Basin. This indicates the presence of natural gas resources in the Taixinan Basin. The multibeam sonar system is shown to provide an accurate and effective approach for detecting sub-sea gas hydrate.

Key words: multibeam sonar, water column image, plume flow, Taixinan Basin, gas hydrate

---

1 Introduction

In recent decades, the multibeam sonar system has been widely used in underwater topographic surveys because of its full coverage, high resolution, high precision, and high efficiency. The multibeam survey has become a main investigation method for the underwater topography surveys. In addition to the development of underwater multibeam sonar systems, and the development of computer processing and storage, a large amount of marine acoustic information has been collected. This information is not only used in hydrographic surveying, but also in the fields of marine biology, physical oceanography, marine geology, and geophysics. Many researchers have done studies based on multibeam sonar data. The sonar data can be used to detect fish schools, plankton, internal waves, and hydrothermal vents, and to identify ocean habitats (Yang et al., 2013; Colbo et al., 2014; Melvin and Cochrane, 2015; Bayrakci et al., 2014). In recent years, multibeam water column data have been used to detect natural gas vents. For example, Elhegazy (2011) used water column images to detect and analyze undersea black smokers and natural gas vents. Nakamura et al. (2015) detected many undersea hydrothermal vents in the central area of the Okinawa Trough using multibeam water column images. These examples show that multibeam water column image investigations are an effective method for detecting the hydrothermal vents. Multibeam sonar images can be used to rapidly detect areas where hydrothermal fluids and cold seepages have developed, and provide new approaches for the detection of undersea resources. Geophysical methods have often been used to detect oil and gas resources (Luan et al., 2008; Xu et al., 2012), but the efficiency of these methods was low. Because the multibeam systems can acquire and process data more quickly and efficiently, the application of the multibeam water column data to hydrocarbon exploration will greatly improve the efficiency of oil and gas explora-

tion. In the multibeam sonar approach, possible target areas for oil and gas resources are quickly delineated. Then, the geological, geophysical and geochemical surveys of the target area are carried out. This approach can save on costs and improve the success rate of oil and gas detection. The present study the analyses water column data from the multibeam sonar for natural gas detection in the Taixinan Basin.

2 Brief introduction to the research area

The Taixinan Basin is also known as the Tainan Basin. It is located on the continental slope from the southern part of the Taiwan Strait to the northeastern South China Sea, and forms part of China's offshore basins. Its geographic range is 20°50′–23°30′N, 117°00′–120°40′E (Fig. 1). The basin is centered on 22°N and 119°E, and is orientated in a NE–SW orientation. The length of the basin is about 480 km, and the width is about 240 km (Du et al., 1991). The total area is 72 000 km². The Taixinan Basin belongs to the rift-type (opening mode), Meso-Cenozoic superimposed or residual basin. The basin has the Penghu-Kaohsiung uplift as its northern boundary, and connects to the South China Sea Basin in the south. The Tainan-Kaohsiung epicontinental area forms its eastern boundary and the basin connects to the Chaoshan sag and Zhujiang River Mouth Basin in the west. The Taixinan Basin is one of the Meso-Cenozoic superimposed basins in the northern epicontinental sedimentary basin chain of the South China Sea. It is located in a favorable tectonic area for natural-gas enrichment. The characteristics of hydrocarbon migration and accumulation in the Taixinan Basin are similar to those of the continental fault basins in eastern China (He et al., 2006). Many studies have shown that the Taixinan Basin has abundant conventional oil and gas resources, and a large exploration potential for gas hydrates. Du et al. (1994) identified the Taixinan Basin as being a favorable area for oil and gas explora-
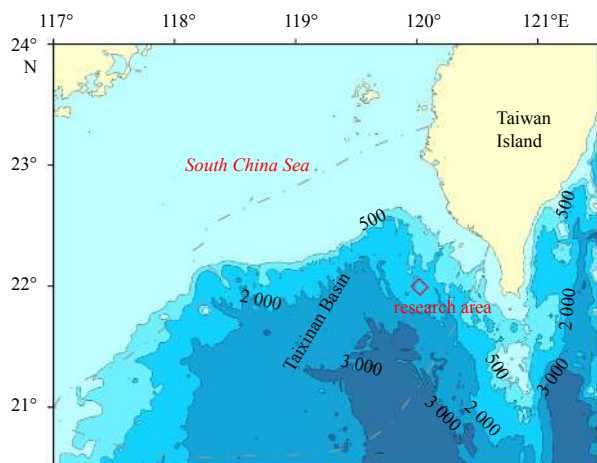
Fig. 1. Location of the research area (─ ─ basin boundary from Ma (2016)).

tion. Oung et al. (2006) analyzed seafloor sediment samples collected southwest of Taiwan and detected thermogenic gas. Using a deeply-towed, side-scan sonar, subbottom profiler, Chen et al. (2010) discovered gas seepages in the nearshore area of the Taixinan Basin. Zhang et al. (2014) studied the accumulation characteristics of gas hydrates of the Taixinan Basin using samples from drillings. A bottom simulating reflector (BSR) obtained from geophysical surveys also showed the existence of gas hydrates in the area, and indicated that there were large accumulations of gas hydrates (Zhang et al., 2014). However, there are no studies that document using the multibeam sonar and the water column images to search for oil and gas on the eastern continental slope of the Taixinan Basin (Fig. 1). The present study helps address this knowledge gap.

3 Data and methods

3.1 *Data acquisition*

In 2016, we carried out sonar data acquisition in the Taixinan Basin using a Kongsberg EM302 deep-water, multibeam system. Three lines were used and were surveyed in both directions to give a total of six survey lines (Fig. 2). Repeat surveys were done to ensure data validity (Fig. 2). The performance parameters of
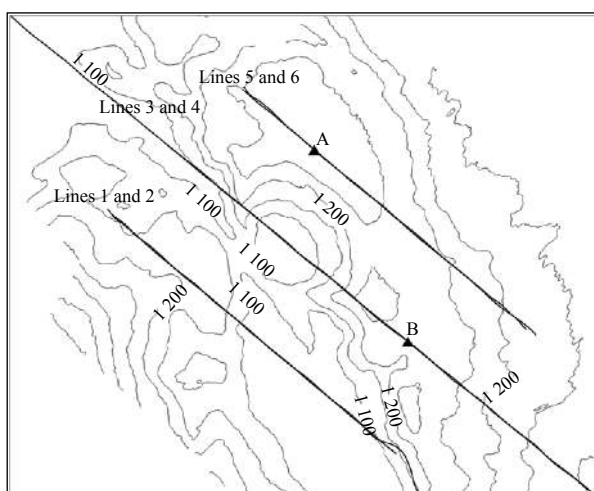
Fig. 2. Survey line setting.

the Kongsberg EM302 system are as follows: frequency 30 kHz, depth range 10–7 000 m, beam angle 1°×1°, maximum ping rate greater than 10 Hz, and beams in each ping 288. The multibeam system also acquires depth data and water column data, which are saved in the same data file to facilitate data processing.

3.2 *Data processing and display*

3.2.1 *Data processing*

Data processing included depth data processing and water column data processing. The depth data processing focused on signal filtering to remove erroneous data and display the authentic bottom topography. The filtering was performed by combining automatic filtering and manual filtering, and by setting the threshold values of, for example, beam and water depth. On the basis of the known water depth of the survey area the depth threshold was set at 800–1 600 m. Twenty edge beams were filtered out because edge beams are of poor quality. However, the automatic filtering cannot eliminate all outliers. The remaining outliers were manually removed. The water column data processing also focused on filtering to remove noise and retain the geographical features of the target. The water column data are time series observation values of the echo intensity for each beam footprint. The volume of water column data is ten to one hundred times that of the depth data (Liu, 2013). The echo intensity information is mainly used for the filtering of the sampling points of the water column data. The back scattering characteristics of acoustic signals for different materials are different. Normally, the echo intensity of noise and side lobe effects in water are low, and thus the echo intensity information can be used for the filtering of sampling points whose echo intensity signal is beyond the threshold. The echo intensity parameter was set between –60 and 0 dB.

3.2.2 *Displaying water column data*

The water column data can be displayed as a water column image to intuitively depict the water data and identify special targets in water. The water column data can be displayed in two ways: (1) as a cross-section perpendicular to the track direction, with the variation in a water intensity in each ping perpendicular to the track direction. The abscissa axis is a distance, and the ordinate axis is a water depth (Fig. 3); and (2) along the track section, with the variation in the central part of the water intensity along the track direction clearly visible (Liu, 2013; Zheng et al., 2016). The abscissa axis is time, and the ordinate axis is the water depth (Fig. 4). The colors of the images represent a back-scatter-
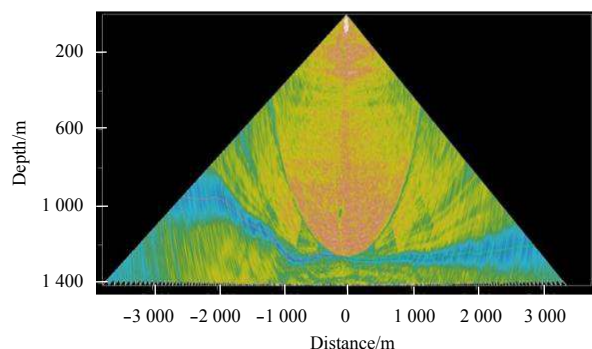
Fig. 3. Water image cross-section perpendicular to the track direction, where the abscissa axis is the distance to the center beam and the ordinate axis is the depth.
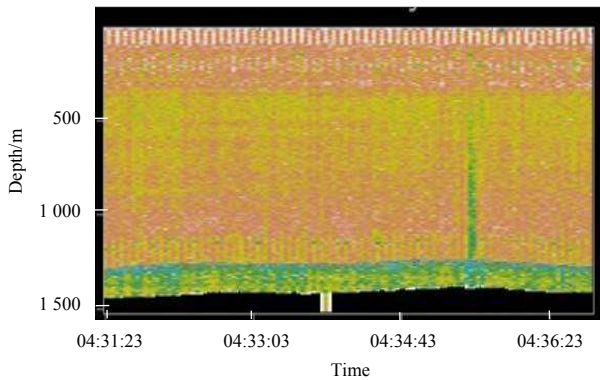
Fig. 4. Water image cross-section along the track direction, where the abscissa axis is time and the ordinate axis is the depth.

ing intensity.

4 Results and discussion

4.1 *Water image data results*

The multibeam water column images were obtained by processing and displaying the multibeam data. Lines 3 and 4 represent different measuring directions along the same line. Acoustic water column anomalies were found in the same region (Figs 5 and 6). Lines 5 and 6 are back and forth measurements along the same line. The acoustic water column anomalies were also found in the same region (Fig. 7). No obvious water column anomalies were found in Lines 1 and 2. The water columns in Fig. 7 are located at Position A in Fig. 2. The water columns in Figs 5 and 6 are located at Position B in Fig. 2. The image on the left of Fig. 5 shows the water column image at a specific time, while the im-

age on the right shows a stacked view of all the water column images at Position B. The two images in Fig. 6 represent the water column images at different times at Position A.

No beams were lost on Line 3, but many beams were lost on Line 4, and thus the quality of Line 3 is much higher than that of Line 4, even though the section tracks are the same. Similarly, although a significant beam loss occurred because of difficult sea conditions during the survey of Lines 5 and 6, the water column anomalies were still captured. Figure 5 shows that the water column anomalies take the form of one or more acoustic scattering plumes that rise from the seafloor (the max height is about 500 m). Some ascending plumes are continuous, while some are not continuous. Most plumes are changeable. The ascending height of the water column anomalies shown in Fig. 6 is nearly identical to that in Fig. 5, but most plumes are suspended. The ascending height of the water column anomalies (Fig. 7) is about 200 m, and is not continuous. The width of the plumes is 20–50 m. The plumes are slightly curved. The lower parts all display vertical movement, and there is only a slight inclination in the upper area.

4.2 *Discussion*

4.2.1 *Causes of the scattering anomalies*

The water column images show that there are many plume-like anomalies in the study region. A seafloor plume is a typical expression of gas seepage. A large volume of gas is generated, probably from the lower part of the natural gas hydrates, oil and gas reservoir, or organic matter-rich anaerobic sediments, and then mixes with the surrounding water and finally forms buoyant plumes (Yin et al., 2008). A large amount of gas entering the sea water from the seafloor will inevitably result in a plume. The bubble-rich plumes have a strong scattering effect because of the large density and acoustic speed contrasts between the plumes
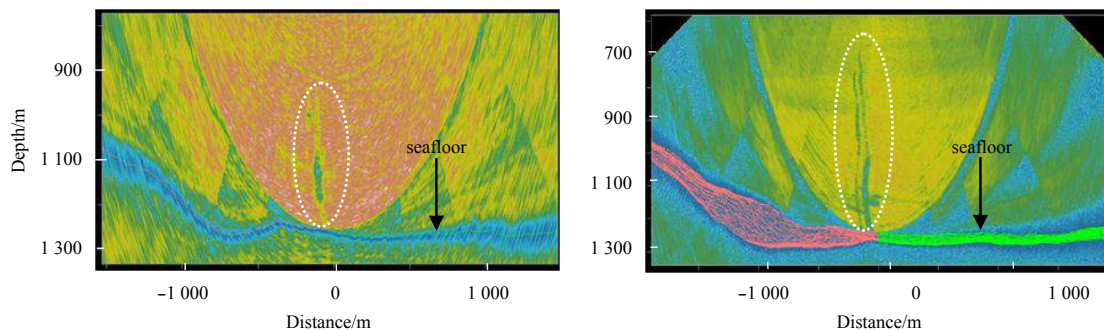
Fig. 5. Track cross-sections for Line 3.
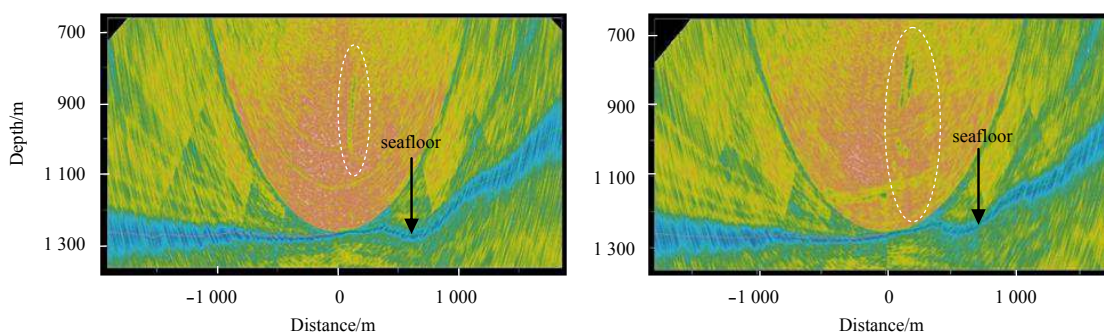
Fig. 6. Track cross-sections for Line 4.
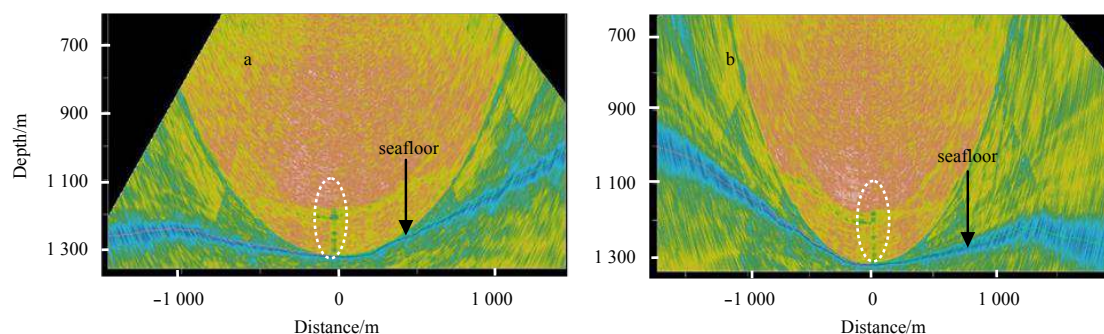
Fig. 7. Track cross-sections for Lines 5 (a) and 6 (b).

and ambient water (Kentaro et al., 2015). This allows gas seepages to be detected by an acoustic equipment.

There has been much integrated subsea floor geological exploration of the northern South China Sea, and this exploration has discovered many BSR and blanking zones as well as geochemical anomalies related to gas hydrates (Bi, 2010; He et al., 2006; Oung et al., 2006). All these discoveries illustrate the potential existence of natural gas hydrates in the research area. Yin et al. (2008) detected obvious methane density anomalies in the bottom water of the northern South China Sea. The anomalies resulted from methane seepage in the seafloor. The seepage may have originated from the decomposition of gas hydrates under the sediments. Bi (2010) analyzes the anomalous methane density in the bottom water of the southwest of Taiwan Island, and concludes that the anomalies are related to the seepage of methane generated from gas hydrate decomposition. The formation conditions for hydrates and the generation mechanism of the plumes indicate that there is not a one-to-one correspondence between hydrate and plume phenomena. However, seafloor sedimentary layers were often found in the development areas of plume, and plumes have been found in many sea areas where hydrates are found (Li et al., 2013, 2016). The results of our study indicate that there is a large amount of evidence for hydrate existence in the study area, and thus it can be inferred that the reason for the occurrence of the abnormal acoustic water column is most likely plume formation by gas leakage from natural gas hydrate. However, because of the lack of seismic data in the study area, it is difficult to further investigate the gas source of the plume. The abnormal acoustic water columns in the research area ascend for 200–500 m and then disappear. The authors believe the plume to be gas hydrate-coated methane bubbles. When the plume reaches a certain height from the seafloor, gas hydrate crusts become unstable and gradually dissolve as the surrounding pressure varies (Kentaro et al., 2015; Sauter et al., 2006). The anomalies then abruptly disappear. The ascending height of the plume may be related to the seepage volume of natural gas and the stability of hydrates. Some plumes in Line 4 appear to have no root, probably because the poor quality data from the line prevents the bottom of the plume from being detected. Another possible reason for some plumes having no apparent root is that the plumes were curved because of currents and only the top of the plumes was detected (Liu and Liu, 2017).

4.2.2 *Topographic analysis of the research area*

The seafloor topography of the research area is shown in Fig. 8. The depth is 1 000–1 420 m. The research area is located between two gorges on the continental slope of the South China Sea. The topography is complex. The terrain tilts from the central part to
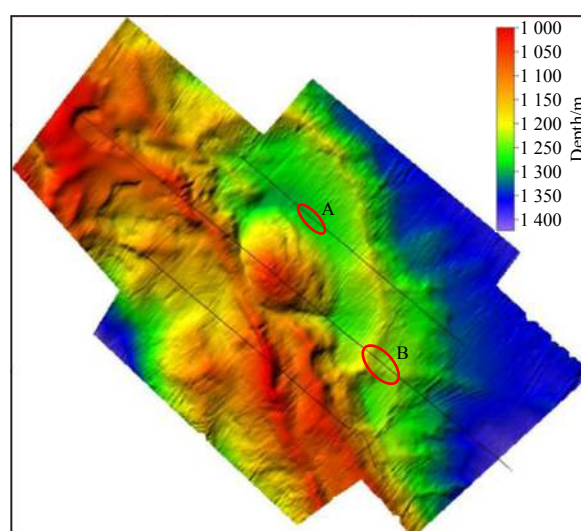
Fig. 8. Seafloor topography of the research area.

the east and to the west. The central part is shallow, but the eastern and western parts are deep. The depth of the eastern part is 1 300 m, and the seafloor is flat. The terrain in the central part is complex. Two sea ridges extend from north to south. One ridge has a height difference of 220 m and extends from northwest to south, with steep sides on both sides of the ridge. The other ridge extends from northeast to south. Its height difference is 50 m, and both sides of the ridge slope gently. The two ridges join the south to form one sea ridge. An elliptical-shaped knoll is located between the two sea ridges. The long axis of the seamount is 3 000 m, and the short axis is 2 000 m, and the height difference is 200 m. The western part of the knoll is closely connected to the sea ridge.

Obvious plumes are found in two positions in the research area (Fig. 8). Position A (Fig. 7) is located between two sea ridges. The water depth is 1 270–1 280 m. Position B (Figs 5 and 6) is located on a sea ridge, and the water depth is 1 210–1 230 m. The plume at Position B is the more obvious in the two of the water column images. This indicates a relatively high gas seepage speed at Position B.

Seafloor natural gas seepages can alter the seafloor terrain, and create unique micro-topography on the seafloor that includes such features as seabed pits, seabed mounds, and mud volcanoes (Liu, 2017; Shang et al., 2014; Sha et al., 2002; Chen et al., 2009). However, no obvious micro-topographic features were found in the plume areas in the present research. A possible reas-

on for this is that the speed and volume of gas seepage are low, and only result in small topographic alterations. These alterations are too small to be detected because of the resolution and accuracy of the shipborne multibeam system.

5 Conclusions

(1) Multibeam water column image anomalies were obtained for a new research area in the Taixinan Basin. The anomalies occur as single or multiple plumes, and ascend almost vertically from the seafloor to a height of 200–500 m.

(2) The plumes in the research area are possibly caused by methane seepage from the gas hydrate dissociation on the seafloor into the bottom water. The multibeam water column data reveal the possible existence of gas hydrates and provide a target for the future study of gas hydrate in this area.

(3) The successful detection of plumes in the Taixinan Basin using the multibeam sonar system has shown that the system can precisely locate in the position of plumes. Compared with the seismic detection technology, the multibeam sonar system has a fuller coverage, higher resolution, and higher efficiency. The multibeam sonar provides a systematic and reliable technology for the detection of subsea gas hydrate.

References

Bayrakci G, Scalabrin C, Dupré S, et al. 2014. Acoustic monitoring of gas emissions from the seafloor: Part II. A case study from the sea of Marmara. Marine Geophysical Research, 35(3): 211–229, doi: 10.1007/s11001-014-9227-7

Bi Haibo. 2010. Amount estimation and geochemical analysis of gas hydrate of Taixinan Basin (in Chinese) [dissertation]. Beijing, China: Graduate University of Chinese Academy of Sciences

Chen Shenhong, He Zhenhua, He Jiaxiong, et al. 2009. The characters of the mud volcanoes in the north-east marginal of the South China Sea and the relationship with the accumulation and migration of oil and gas. Natural Gas Geoscience (in Chinese), 20(6): 872–878

Chen S C, Hsu S K, Tsai C H, et al. 2010. Gas seepage, pockmarks and mud volcanoes in the near shore of SW Taiwan. Marine Geophysical Researches, 31(1–2): 133–147, doi: 10.1007/s11001-010-9097-6

Colbo K, Ross T, Brown C, et al. 2014. A review of oceanographic applications of water column data from multibeam echosounders. Estuaries, Coastal and Shelf Science, 145: 1–56, doi: 10.1016/j.ecss.2014.04.009

Du Deli. 1991. Characteristics of geologic structure and hydrocarbon potential of the southwest Taiwan Basin. Marine Geology & Quaternary Geology (in Chinese), 11(3): 21–33

Du Deli. 1994. Tectonic evolution and analysis of oil-gas accumulation in southwest Taiwan Basin. Marine Geology & Quaternary Geology (in Chinese), 14(3): 5–18

Elhegazy H. 2011. Gas plumes analysis using multibeam EM710 water column image in Saint John River. http://omg.unb.ca/omg/papers/Elhegazy_6922_Report.pdf [2011–10–11/2015–06–08]

He Jiaxiong, Xia Bin, Wang Zhixin, et al. 2006. Petroleum geologic characteristics and exploration base of Taixinan Bbasin in eastern area of continental shelf in north of the South China Sea. Natural Gas Geoscience (in Chinese), 17(3): 345–350

Kentaro Nakamura, Shinsuke kawagucc, Kazuya kitada, et al. 2015. Water column imaging with multibeam echo-sounding in the mid-Okinawa Trough: Implications for distribution of deep-sea hydrothermal vent sites and the cause of acoustic water column anomaly. Geochemical Journal, 49: 579–596, doi: 10.2343/geochemj.2.0387

Li Canping, Liu Xuewei, Zhao Luochen, et al. 2013. Progress on cold seeps and bubble plumes produced by gas hydrate. Progress in Geophysics (in Chinese), 28(2): 1048–1056

Li Canping, You Jiachun, Zhu Wenjuan. 2016. Identification of bubble plumes and analysis of its correlation with resource environment. Progress in Geophysics (in Chinese), 31(6): 2747–2755

Liu Zhibo. 2013. The least depth point detection of wreck using multibeam water column imaging (in Chinese)[dissertation]. Qingdao: Shandong University of Science and Technology

Liu Bin. 2017. Gas and gas hydrate distribution around seafloor mound in the Dongsha area, north slope of the South China Sea. Haiyang Xuebao (in Chinese), 39(3): 68–75

Liu Bin, Liu Shengxuan. 2017. Gas bubble plumes observed at north slope of South China Sea from multibeam water column data. Haiyang Xuebao (in Chinese), 39(9): 83–89

Luan Xiwu, Zhao Kebin, Sun Dongsheng, et al. 2008. Geophysical methods for marine gas hydrates exploration. Progress in Geophysics (in Chinese), 23(1): 210–219

Ma Yong. 2016. Sediment waves characteristics and their formation mechanism, the southwest Taiwan Basin, South China Sea (in Chinese) [dissertation]. Nanjing: Nanjing University

Melvin G D, Cochrane N A. 2015. Multibeam acoustic detection of fish and water column targets at high-flow sites. Estuaries and Coasts, 38(S1): S227–S240, doi: 10.1007/s12237-014-9828-z

Nakamura K, Kawagucc S, Kitada K, et al. 2015. Water column imaging with multibeam echo-sounding in the mid-Okinawa Trough: implications for distribution of deep-sea hydrothermal vent sites and the cause of acoustic water column anomaly. Geochemical Journal, 49(6): 579–596, doi: 10.2343/geochemj.2.0387

Oung J N, Lee C Y, Lee C S, et al. 2006. Geochemical study on hydrocarbon gases in seafloor sediments, southwestern offshore Taiwan-Implications in the potential occurrence of gas hydrates. Terrestrial, Atmospheric and Oceanic Sciences, 17(4): 921–931, doi: 10.3319/TAO.2006.17.4.921(GH)

Sauter E J, Muyakshin S I, Charlou J L, et al. 2006. Methane discharge from a deep-sea submarine mud volcano into the upper water column by gas hydrate-coated methane bubbles. Earth and Planetary Science Letters, 243(3–4): 354–365, doi: 10.1016/j.epsl.2006.01.041

Sha Zhibin, Yang Muzhuang, Liang Jin, et al. 2002. The characteristics of the abnormal physiognomys of seabed related to gas hydrate in North Slope, South China Sea. Geological research on the South China Sea (in Chinese), (1): 29–34

Shang Jiujing, Wu Lushan, Liang Jinqiang, et al. 2014. The microtopographic features and gas seep model on the slope in the northeastern South China Sea. Marine Geology & Quaternary Geology (in Chinese), 34(1): 129–136

Xu Huaning, Xing Tao, Wang Jiasheng, et al. 2012. Detecting seepage hydrate reservoir using multi-channel seismic reflecting data in Shenhu area. Earth Science-Journal of China University of Geosciences (in Chinese), 37(S1): 195–202

Yang Fanlin, Han Litao, Wang Ruifu, et al. 2013. Progress in object detection in middle and bottom-water based on multibeam water column image. Journal of Shandong University of Science and Technology: Natural Science (in Chinese), 32(6): 75–83

Yin Xijie, Zhou Huaiyang, Yang Qunhui, et al. 2008. The evidence for the existence of methane seepages in the northern South China Sea: abnormal high methane concentration in bottom waters. Haiyang Xuebao (in Chinese), 30(6): 69–75

Zhang Guangxue, Liang Jinqiang, Lu Jing'an, et al. 2014. Characteristics of natural gas hydrate reservoirs on the northeastern slope of the South China Sea. Natural Gas Industry (in Chinese), 34(11): 1–10

Zheng Shuangqiang, Liu Hongxia, Yang Fanlin, et al. 2016. Design and implementation of multibeam sonar water column image analysis toolkit. Hydrographic Surveying and Charting (in Chinese), 36(6): 46–49

A new automatic oceanic mesoscale eddy detection method using satellite altimeter data based on density clustering

Jitao Li[1], Yongquan Liang[1], Jie Zhang[2], Jungang Yang[2]*, Pingjian Song[2], Wei Cui[2, 3]

[1] College of Computer Science and Engineering, Shandong University of Science and Technology, Qingdao 266590, China

[2] First Institute of Oceanography, Ministry of Natural Resources, Qingdao 266061, China

[3] Physical Oceanography Lab, Qingdao Collaborative Innovation Center of Marine Science and Technology, Ocean University of China, Qingdao 266100, China

Abstract

The mesoscale eddy is a typical mesoscale oceanic phenomenon that transfers ocean energy. The detection and extraction of mesoscale eddies is an important aspect of physical oceanography, and automatic mesoscale eddy detection algorithms are the most fundamental tools for detecting and analyzing mesoscale eddies. The main data used in mesoscale eddy detection are sea level anomaly (SLA) data merged by multi-satellite altimeters' data. These data objectively describe the state of the sea surface height. The mesoscale eddy can be represented by a local equivalent region surrounded by an SLA closed contour, and the detection process requires the extraction of a stable closed contour structure from SLA maps. In consideration of the characteristics of mesoscale eddy detection based on SLA data, this paper proposes a new automatic mesoscale eddy detection algorithm based on clustering. The mesoscale eddy structure can be extracted by separating and filtering SLA data sets to separate a mesoscale eddy region and non-eddy region and then establishing relationships among eddy regions and mapping them on SLA maps. This paper overcomes the problem of the sensitivity of parameter setting that affects the traditional detection algorithm and does not require a sensitivity test. The proposed algorithm is thus more adaptable. An eddy discrimination mechanism is added to the algorithm to ensure the stability of the detected eddy structure and to improve the detection accuracy. On this basis, the paper selects the Northwest Pacific Ocean and the South China Sea to carry out a mesoscale eddy detection experiment. Experimental results show that the proposed algorithm is more efficient than the traditional algorithm and the results of the algorithm remain stable. The proposed algorithm detects not only stable single-core eddies but also stable multi-core eddy structures.

Key words: mesoscale eddy, density clustering, shape discrimination, outermost closed contour

1 Introduction

The mesoscale eddy is an important form of seawater transport having a long-term closed state and a spatial scale ranging from dozens to hundreds of kilometers and a time scale ranging from a few days to a few hundred days. The mesoscale eddy is responsible for sea power transfer and mass transfer and affects oceanic elements, such as oceanic temperature and salinity distributions. There are many factors of the formation of mesoscale eddies. In general, ocean flow is affected by many factors, such as wind, topography and ambient field flow, which forms mesoscale eddies. The study of mesoscale eddies is important to marine military activities and fisheries.

The study of mesoscale eddies in the ocean can be divided into the detection, observation and tracking of mesoscale eddies. Data of the global sea level can be obtained from satellite altimeter data, and sea level anomaly (SLA) results can then be used for the detection of mesoscale eddies. In the detection of mesoscale eddies, existing automatic detection methods based on an SLA map can be divided into four categories: methods using physical parameters, methods employing wavelet analysis, methods using streamline geometry features and methods using sea surface height anomaly characteristics.

The classic physical mesoscale eddy detection algorithm is the Okubo-Weiss (OW) algorithm (Okubo et al., 1970), which realizes the automatic detection of mesoscale eddies (Morrow et al., 2004). This method is widely used in the mesoscale eddy analysis of oceans, such as the Tasman Sea (Waugh et al., 2006), the Gulf of Alaska (Henson and Thomas, 2008) and the South China Sea (Nan et al., 2011). There are two deficiencies of the OW algorithm. Firstly, the parameter calculation may enlarge error in the SLA and results in a misjudgment. Secondly, for the boundary of mesoscale eddies, the algorithm cannot provide a precise

closed contour but a scope.

A mesoscale eddy detection method based on wavelet analysis is (Doglioli et al., 2007) regards vorticity as a semaphore radar signal. By processing this vorticity obtained from SLA data, the obtained signal curve is decomposed and mapped onto a vorticity space to extract mesoscale eddies. This method makes full use of the rapidity of the wavelet transform and the signal sensitivity and is able to handle massive data. However, the limit of the dimensions of data sets leads to the low identification accuracy of eddies and the detection ability is poor for mesoscale eddies with an irregular closed contour shape of the SLA value.

The winding angle (WA) method is a representative detection algorithm based on geometrical features (Ari Sadarjoen and Post, 2000) and has been improved and applied to the detection of mesoscale eddies (Chaigneau et al., 2008). The default structure of the WA algorithm is a single-core structure. The maximum range of the SLA closed contour is found as the boundary around an initial core point. This algorithm is simple and easy to understand and is the most popular algorithm for the detection of mesoscale eddies. However, the algorithm has deficiencies in that it is unable to find multi-core structures, has high algorithm complexity and requires a sensitivity test for the setting of parameters. Another method based on the geometric streamline feature is the vector geometry (VG) method (Nencioli et al., 2010), which uses the geometrical characteristics of the velocity vector to judge eddy cores. The velocity of the flow field is a minimum around an eddy core, and the tangential velocity of the flow field increases with the distance from the core. At the eddy border, the tangential velocity of the flow field begins to abate. The VG method uses the maximum peripheral speed at the boundary. However, the situation is complex when judging the mesoscale eddy boundary and eddy core, and two additional parameters are needed to limit the detection results while the parameter setting requires a sensitivity test.

The SSH-based method is an example of a method of automatic mesoscale eddy detection without a threshold value (Chelton et al., 2011) that aims to avoid the complicated problems caused by the threshold setting. The SLA extreme-value point is used as the eddy core, the opposite polarity eddy boundary is taken as the starting point, the closed contour line is searched for in steps of 1 cm from the outer boundary toward the eddy core, and the outermost SLA closed contour is found as the boundary of the mesoscale eddy. Compared with traditional algorithms, the SSH-based method can detect multi-core structures but does not judge the shape of the eddy, and there are many unstable multicore structures in the detection results. It is necessary to initialize the eddy area in the process of searching for the multicore structure. The sensitivity of the parameter setting is high and the adaptability is poor.

The hybrid detection (HD) algorithm is a hybrid algorithm combining traditional OW and SSH-based methods (Yi et al., 2014). The combined application of the OW algorithm and SSH-based method to initial cores reduces the effect of noise on the OW algorithm and avoids the sensitivity of threshold setting during initialization. This algorithm improves the accuracy of mesoscale eddy boundary detection by reducing the incremental step size and eliminating mesoscale eddies with irregular boundaries to guarantee the stability of the selected-scale eddies. The main problem that the HD algorithm solves is that it finds multicore structures that are more stable, but the parameter setting in the eddy selection process requires a sensitivity test and the algorithm steps are complicated. Another algorithm distinguishes color attributes of an SSH image to extract mesoscale eddies

(Zhang et al., 2014). The algorithm separates a region having a defined pixel density from a region of low pixel density to detect the boundaries of mesoscale eddies. The same method has been used in handling SST images (Zhang et al., 2015). In the case of an SSH-image-based method, the algorithm has too many initialization parameters and the parameter setting requires a sensitivity test, resulting in low adaptability of the algorithm. A parallel method has been added to the SSH-based algorithm to improve the operation efficiency of the algorithm (Liu et al., 2016). The computational efficiency is greatly improved by dividing the global data set into several sub-regions.

The traditional mesoscale eddy detection algorithm has deficiencies, such as the sensitivity of the parameter setting, the problem of defining the initial threshold value for the eddy core, and the stability problem of the mesoscale eddy result. To solve the above problems, the present paper proposes the density-based clustering mesoscale eddy detection algorithm (DC). Density clustering algorithms have been used for data analysis in machine learning, and stable mesoscale eddies can be filtered by establishing potential relations among the data. The advantages of the proposed algorithm are that it has fewer parameters, the parameters have higher stability, it is easier to set parameters, and parameters are initialized mostly according to the attributes of the data set. For the same attribute data sets, the parameters are the same and the method has good adaptability. The proposed algorithm does not use the core points of the mesoscale eddies as the initialization condition and thus avoids the sensitivity problem of the initialization threshold of the initial core points. For the stability problem of finding mesoscale eddies, the algorithm guarantees the stability of the results by shape discrimination, and irregular mesoscale eddy structures in the process of convergence are filtered out.

2 Data and method

2.1 *Altimetry data*

The satellite altimeter product used in this paper is fusion data of SLA recorded by multiple satellites and distributed by AVISO (http://www.aviso.oceanobs.com). The SLA data are merged altimeter data recorded by TOPEX/Poseidon, Jason-1, Jason-2, ERS-1, ERS-2 and Envisat satellites with spatial resolution of $0.25° × 0.25°$. Daily altimeter data are the integration of data from at least two satellites. As a result, the data of different satellites can be calibrated, and the precision and consistency of the fusion products can be ensured at the same time.

2.2 *Eddy detection methodology*

In general, a mesoscale eddy detection algorithm aims to find the potential internal relation within SLA data and to find the outermost closed contours through interpolation and thus identify eddies. In SLA data there are plentiful regional maximum and minimum values, which are regarded as the cores of eddies. There are several closed contours of SLA data, which may contain one or more extreme points with the same polarity. Such a closed region can be seen as a mesoscale eddy, and the data points contained in the closed region can be regarded as data points having the same attributes with potential relations.

In the field of machine learning, a clustering algorithm is used to discover potential relations within a data set. The present paper therefore includes a clustering algorithm in the detection process and transforms the algorithm into a process of discovering and recognizing a data set having the same attributes. The present paper uses a density-based clustering method for the

clustering process. The advantage of the density-based clustering method lies in the method's better adaptability to the irregularity of clustering patterns and better adaptability to the number of clustering classes. For the SLA-based data set used in the present paper, data characteristics and data density are fixed values. Disadvantages of the traditional density-based clustering method, such as the high sensitivity of the parameter setting, are overcome in this case. For different data sets with the same properties, the same *MinPts* (minimum points) and ε values are chosen, which shows the strong adaptability and intelligence of the algorithm and the reduction of human intervention.

The process of detection by the proposed mesoscale eddy algorithm is divided into five steps. (1) Data are segmented to separate the non-eddy region from the eddy region. (2) Clustering is conducted to recognize mesoscale eddies and establish intraregional relations. The preprocessed data set is divided into multiple sub-data sets and each sub-data set represents a potential mesoscale eddy. (3) Data are classified and filtered to obtain sub-data sets that meet preconditions; data that are too large or too small ought to be filtered out. (4) Shape discrimination is conducted to judge the shape of a mesoscale eddy and to ensure the stability of the selected mesoscale eddy. (5) The outermost contour is determined to find the closed outermost contours and the result is output. To avoid repeating operations in the subsequent iteration process, the data point is deleted from the original data set for the sub-data set obtained a closed contour.

The remaining data sets that are not empty enter the next iteration process, the filter value is increased according to a preset increment, and the above five steps are re-executed until the required data set is empty.

In each iteration, the quantity of data required to manage becomes smaller. The algorithm converges when the data set is empty. Results are integrated to obtain all the outermost closed contours. Results are then output and the detection process finishes. A flowchart of the algorithm is shown in Fig. 1. The whole algorithm goes through several iterations, with only the data segment value changing in the iteration and the other parameters remaining unchanged.

2.2.1 *Data segmentation: preprocessing*

To distinguish data sets by different attributes and to separate an eddy region from the surrounding environment, the data sets are divided into two classes according to the algorithm objective. In the algorithm, the data points contained in the anticyclonic eddy range are the data points whose SLA values are greater than zero while the data points contained in the cyclonic eddy range are the data points whose SLA values are smaller than zero in most cases. The algorithm initially divides all data points into two categories, those whose SLA values are greater than zero and those whose SLA values are smaller than zero. In the process of detecting cyclonic eddies, the present paper clusters the data sets with SLA values smaller than zero, then uses a data increment of –1 cm to partition the data sets and separates an eddy region from the non-eddy region. In the process of determining the anticyclonic eddies, the present paper considers the data points whose SLA values are greater than zero, and the steps are opposite those followed in the process of recognizing a cyclonic eddy.

2.2.2 *Cluster analysis: association management*

The present paper uses the density-based clustering method to analyze the partitioned data set. The advantage of the density-based clustering method is that it can identify the class characteristics of irregular shapes, and there is no need to specify the core
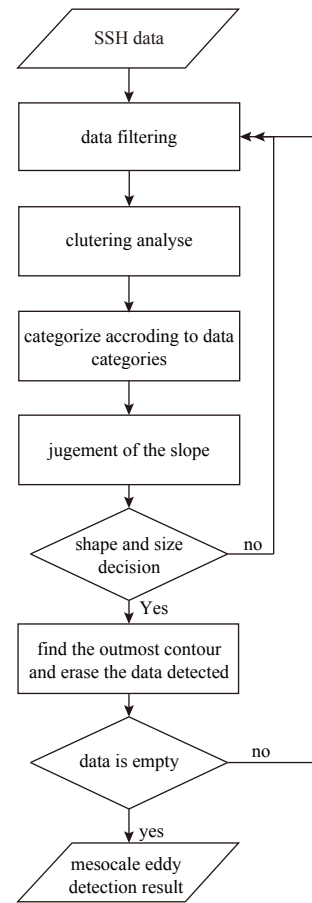
Fig. 1. Flowchart of the DC method.

points in advance. In addition, it can automatically filter out noisy points in the clustering process and thus avoid their effect on the data clustering result (He et al., 2014). The algorithm complexity of the density-based clustering method is based on the number of selected data sets (n) and the complexity of the algorithm $O(n^2)$. Clustering is the most complex part of the algorithm. The complexity of the algorithm can therefore be defined as $O(n^2)$, which is similar to that of the SSH-based algorithm (Chelton et al., 2011).

The notion of density-based clustering is defined as follows.

(1) The distance measure between points in the data set (DB) is defined as

$$\mathrm{Dist}(p,q) = \sqrt{(x_p - x_q)^2 + (y_p - y_q)^2}, \; p, q \in \mathrm{DB}. \qquad (1)$$

(2) For a point $p \in$ DB, if a given object p such that within the radius range of ε has at least *MinPts* samples, it is said that the point in the radius range belongs to the data set ε-nbhd (p).

(3) Given $p, q \in$ DB, if the distance between points q and p is smaller than the distance ε and belongs to data set ε-nbhd (p), then point q is directly density-reachable from point p.

(4) For points p and q, if the sample can be directly arrived at q from p by means of samples $x_1, x_2, ..., x_t$, it is called density-reachable. From the asymmetry of density reachability, it is concluded that density-reachability cannot satisfy symmetry.

(5) If both points p and q are density-reachable, then they can be called density-connected, which satisfies symmetry.

The density-based clustering method for a data set C is as fol-

lows. For any *p* and *q* with the same class label, *p* and *q* are density-connected. For any *p* belonging to class *C* and for *q* ∈ DB, if *p* and *q* are density-connected, then *q* can be added to class *C*. If there is a point that cannot be classified into any class, it is called a noisy point. In addition, if a point *p* has a class label and the point set does not satisfy *ε*-nbhd (*p*) from point *p*, then point *p* is classified as a border point. Therefore, after rounds of density clustering, several data sets can be obtained, and each point can be classified as a border point or noisy point.

The basic idea of the density-based clustering method is to classify high-density regions in different regions by separating the parts with high data density from those with low data density. The algorithm uses the phenomenon that the closer the mesoscale eddy data are to the eddy core, the higher the data density will be after data segmentation. In this way, a potential mesoscale eddy region with high density can be separated from its surrounding and adjacent mesoscale eddies. After density clustering, the data set can be divided into several different regions, each of which is one or several potential mesoscale eddies.

In the process of density-based clustering, the sensitivity of the parameters is tested according to the characteristics of the selected SLA data. When the search radius is 0.25 (*ε* = 0.25) and the minimum number of points within the radius is four (i.e., *MinPts* = 4), the separated mesoscale eddy sub-data sets can be obtained in the clustering process. When selecting different search border lengths and numbers of points, the sensitivity of parameter correlation may be too high, and the initialization definition can be complicated, which may lead to an undivided difference between different sub-data sets.

2.2.3 *Data classification and selection: data set filtering*

In clustering analysis, each data point can be assigned a class label or classified as noise, and the data set can be divided into several classes according to the class label. After eliminating data that have been identified as a noisy point, the results of each class label can be extracted separately to form a number of different sub-data sets. The algorithm regards each formed sub-data set as a mesoscale eddy containing all the data points, and the outermost contour should contain all the data points in this sub-data set.

Considering the observation error in the altimetry and resolution of the AVISO fusion product, the recognition conditions for sub-data sets and the standard for identifying mesoscale eddies in literature (Chelton et al., 2011), the specific identification con-

ditions are as follows. (1) SLA values of all grid points in the cyclonic eddy (anticyclonic eddy) are smaller (greater) than that of boundary SLA value. (2) The number of grid cells of the eddy is not less than 5 and not more than 400. (3) The amplitude of the mesoscale eddy is not less than 3 cm. (4) The distance to a nearby grid point in the mesoscale eddy is less than 600 km.

2.2.4 *Shape discrimination: stability criterion*

For the obtained sub-data set of the same class of data, the attributes in the data set are the longitude, latitude and corresponding SLA values. Using the longitudes and latitudes of the sub-data set, the position and shape of a data point in a certain mesoscale eddy can be obtained. To ensure the shape and high stability of the mesoscale eddy, this paper refers to the shape criterion provided in the literature (Liu et al., 2016). The area of deviation is the area of a graph surrounded by a closed contour. The area of the circle adopted as a decision graph is the minimum circular area that covers the closed contour (Fig. 2a). The ratio of the formed graph to the standard graph is obtained. Existing algorithms consider the shape of the eddy to be approximately regular and the structure of the eddy to be stable when the graph ratio is greater than 55%.

In the proposed algorithm, the sub-data set is determined to have a stable shape because the sub-data set can represent all the data points contained in the selected mesoscale eddy. Finding a minimum covering square is more convenient than finding a minimum covering circle. A square is also a regular graph and is more suitable for a data set that is discrete. The decision graph used in this paper is therefore a square rather than a traditional circle. The formulas for finding a square are:

$$length_{wide} = \max(lon_i) - \min(lon_i),$$
$$length_{hight} = \max(lat_i) - \min(lat_i),$$
$$length = \max(length_{wide}, length_{hight}),$$
$$Num_{square} = (length \times (1/resolution) + 1)^2,$$
$$Error_{shape} = Num_{deviation}/Num_{square}. \tag{2}$$

It is straightforward to find the minimum covering square using the maximum and minimum values of longitude and latitude in the sub-data set (Fig. 2b). In this paper, it is assumed that the diameter of the minimum covering circle is equal to the side length of the minimum covering square.

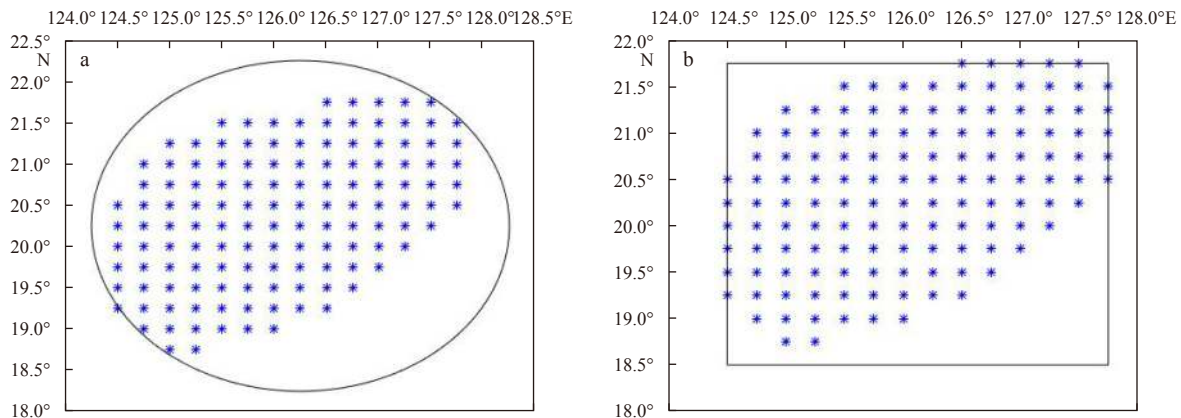It is assumed that the radius of the minimum covering circle

Fig. 2. Shape discrimination, with blue points representing positions of the data point set. a. A minimum covering circle, and b. a minimum covering square.

is 1, the area of the circle is 3.14, the area of the corresponding square is 4, and the coverage of the circular area is 55%, corresponding to coverage of the area of the square area of 43%. A ratio is taken of the number of data in the sub-data set belonging to the same category provided by the filtering process divided by the number of data points included in the minimum covering square. When the ratio is greater than 43%, it is believed that the enclosed graph is a regular graph. A sub-data set enters the next step when it is judged as a regular data set. Otherwise it skips the next step and waits for the next loop for graph judgment again.

A sensitivity test of the parameters shows that the results are more regular if the shape discriminant parameter set is large. However, the mesoscale eddy will be too small or it is not possible to detect some mesoscale eddies directly. At the same time, the computation time is long and there are many iterations of the algorithm. When the parameters are set small, there are many irregular eddy structures. These eddy structures should be divided into smaller mesoscale eddies. Additionally, some mesoscale eddies will be found twice because the selection range is too large in the search process, leading to the repeated identification of eddies.

2.2.5 *Outermost closed contour determination: output results*

After the shape judgment step, the algorithm moves to the step of searching for closed contours. As the closed contour detected should contain all points of the corresponding sub-data sets, it is necessary to extend the selected sub-data sets to find a closed contour over a larger range. A rectangle can be used to represent the position at which the sub data set is located (Fig. 3a). To extend the data set, this paper selects all the encircled longitudes and latitudes to add and subtract a resolution data point and obtain an extended data set. The resulting data set is a rectangular data set with a slightly larger range than the original data set; the border shown in Fig. 3a marks the expanded range of the data set. All contours can then be found using the extended data set (Fig. 3b).
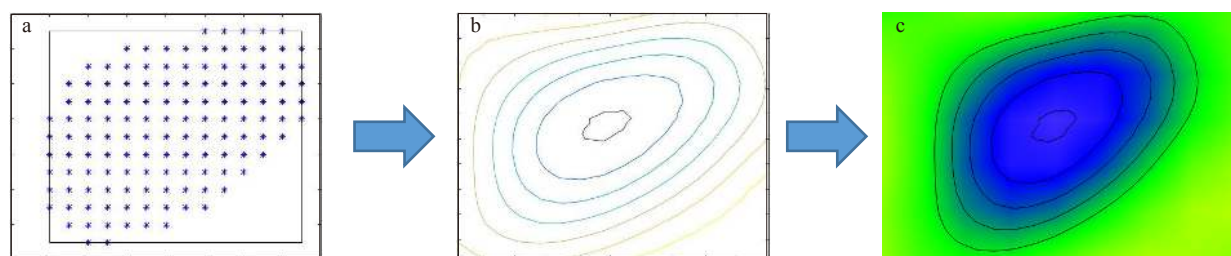
Fig. 3. Process of finding the outermost closed contour. a. Distribution of the clustering results, b. all contours obtained after the extension process, and c. all closed contours on the SLA map and the identification of eddy structure.

In this step, it is necessary to find the closed contour among all closed contours that are equal to the partition values in Section 2.2.1, and this closed contour certainly exists.

2.3 *Eddy detection*

Figure 4 shows the process of the regional segmentation and detection of an eddy. Figure 4a shows the SLA map before the detection process while Figs 4b–g shows the sub-data set after clustering analysis with a modified value of the data segmentation process. Different colors represent different clustering effects. Shape discrimination is carried out in accordance with the data classification and selection preconditions. In the case that the shape is judged to be regular, the outermost closed contour in this region is determined and the result is output; otherwise the process jumps to the next iteration.

Regions C and D are the two parts after the division of Region B (marked in Fig. 4e), while region E is a part after the division of Region D (marked in Fig. 4f), and suitable mesoscale eddies are found in Regions A, C and E. Figure 4h shows three mesoscale eddy structures as the final result.

3 Experiment on mesoscale eddy detection

Employing the proposed algorithm, we detected mesoscale eddies in the Northwest Pacific and South China Sea (0°–50°N, 100°–160°E). In this region, there are many mesoscale eddies, the numbers of cyclonic and anticyclonic eddies are relatively balanced, and there are various eddy forms. The region is thus well suited to testing the performance of the proposed algorithm.

3.1 *Comparison with the SSH-based method*

Mesoscale eddy detection algorithms have been well re-
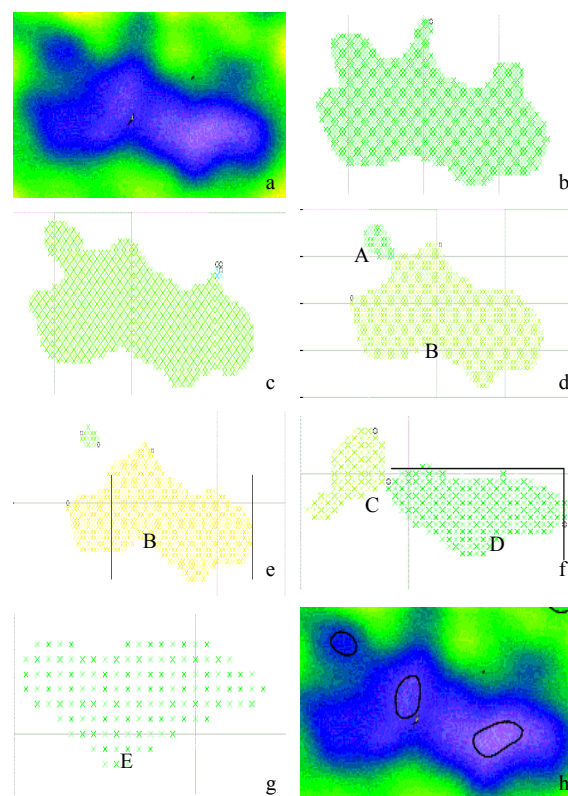
Fig. 4. Process of regional segmentation and detection.

searched in the literature. Classic algorithms include WA and SSH-based methods. The SSH-based method is a widely used eddy detection algorithm that is able to find multi-core structures. This paper compares the SSH-based method with the DC algorithm in the mesoscale region (30°–45°N, 140°–155°E) of the Northwest Pacific.

To ensure large differences in the eddy morphology between two time nodes, we picked nodes more than 40 days apart for the comparison experiments. With three time nodes, we can better test the adaptability of the two algorithms to different data sets and thus better compare the performances of the two algorithms (Fig. 5). In general, both the DC method and traditional SSH-based algorithm detect the main scopes of mesoscale eddies. However, the SSH-based algorithm faces the problems of threshold sensitivity and results instability.

Table 1 shows that the DC algorithm in most cases detects more eddies than the SSH-based algorithm and with better accuracy, as the DC algorithm avoids the threshold sensitivity problem. Meanwhile, avoiding error due to an excessive scope of the closed contour, detection results obtained with the DC algorithm and SSH-based algorithm are compared in Fig. 6. As the traditional SSH-based method simply aims to obtain closed contours and the result would thus have irregular eddy shapes, results obtained by the DC algorithm are filtered with the shape maximum approximating a circle to guarantee the stability of the eddies detected. In comparison with the traditional SSH-based method, the SSH-based method used here regards the area between the

multiple eddies also as an eddy structure while the proposed algorithm regards this region as a non-eddy area without processing. This type of eddy structure is relatively small (Fig. 7).

3.2 *Mesoscale eddy detection results*

Figure 8 shows the results of mesoscale eddy detection in the Northwest Pacific and the South China Sea obtained using the algorithm proposed in this paper and the traditional SSH-based method. There are many single-core structures and several multi-core structures in this region. The present paper focuses on solving the problem of how to select and maintain a stable multi-core structure or how to divide an unstable multi-core structure into several stable single-core structures.

A multi-core structure is a mesoscale eddy with two or more eddy cores having the same polarity within the boundary. A mesoscale eddy will sometimes undergo division, merging or other processes in the course of its life. There are many multi-core structures in the Northwest Pacific region, and the question of whether to maintain or to break them down has seldom been

Table 1. Comparison of the number of eddies obtained with the DC algorithm and SSH-based algorithm, where CE refers to a cyclonic eddy and AE to an anticyclonic eddy

Date	DC method		SSH-bd method	
	CE	AE	CE	AE
20080201	20	16	14	13
20080320	19	14	16	13
20080501	19	13	19	15
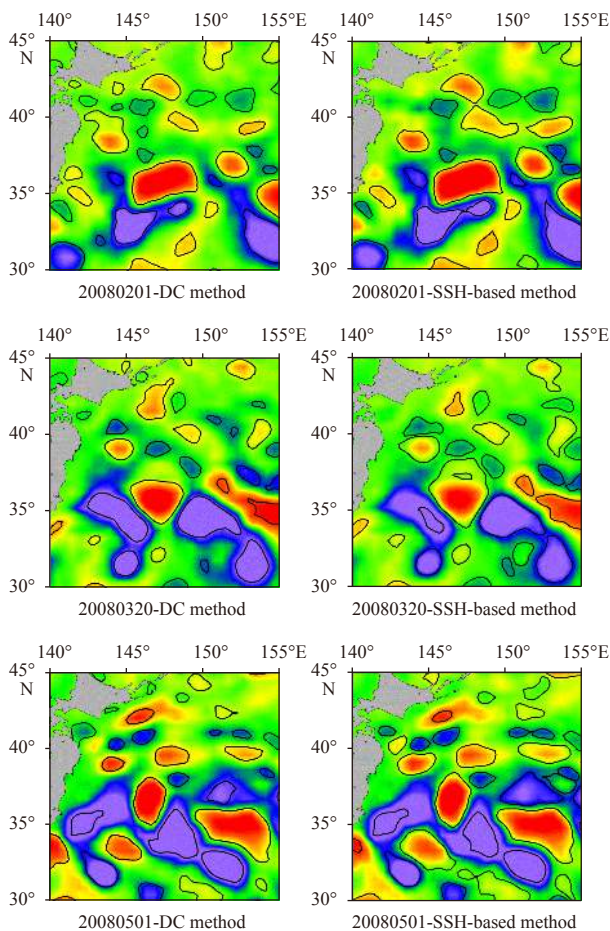
Fig. 5. Comparison of detection results obtained with the DC algorithm and SSH-based algorithm for a 2008 SLA map.
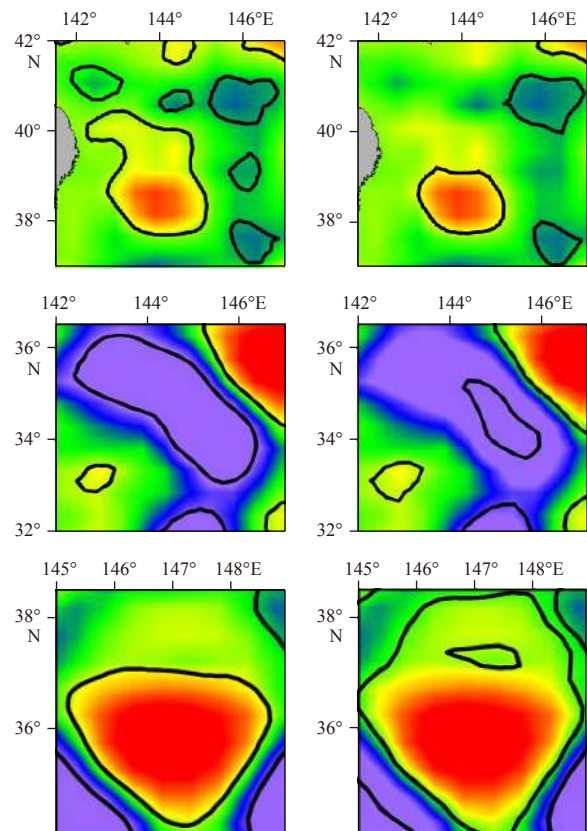
Fig. 6. Detailed comparison of detection results obtained with the DC algorithm and SSH-based algorithm. The left column presents results of the DC algorithm and the right column results of the SSH-based algorithm.
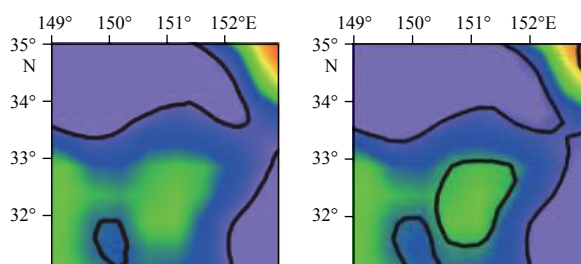
Fig. 7. Initialization difference between the DC algorithm and SSH-based algorithm. a. DC algorithm, and b. SSH-based algorithm.
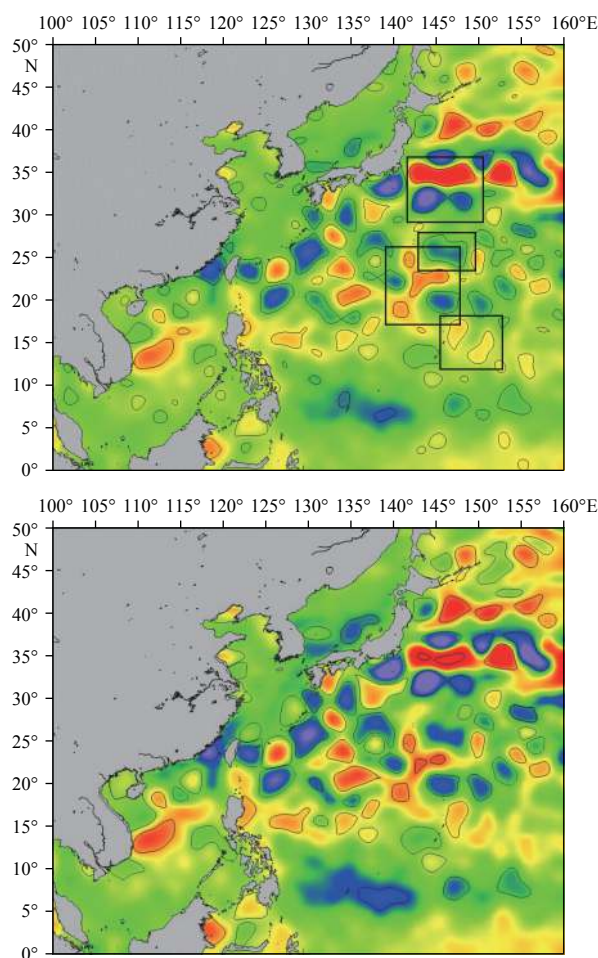
Fig. 8. Results of eddy detection for the region of the Northwest Pacific and South China Sea on May 9, 2016. Contours fill warm color indicate anticyclonic eddies while those filled with a cool color indicate cyclonic eddies. a. Results of DC algorithm, and b. results of traditional SSH-based algorithm.

mentioned in previous work. The first time that this problem was addressed was the proposal of the SSH-based method for the detection of a multi-core structure (Chelton et al., 2011), but owing to the instability of the multi-core structure, the form is more complex. In many cases, although the SSH-based algorithm can detect a closed contour, it is unable to track the movement in the process. The SSH-based method as a kind of detection algorithm of a multi-core structure. It lacks a judgment of the eddy shape. Although it overcomes the particular problem of traditional al-

gorithms that each eddy can have only one core, it cannot automatically identify an irregular eddy structure and decompose it to a more stable structure.

The DC algorithm proposed in this paper increases the stability of found multi-core structures through the shape judgment.

Figure 9 shows the results of multi-core structure detection. Figure 9a shows a segmentation of a larger scale eddy of irregular shape, which contains more than one local maximum or minimum point on a larger scale. Using the proposed algorithm, we get two stable single-core structures and one multi-core structure having two extremum cores. Figures 9b–d shows that multi-core structures are found and preserved. These multi-core structures have relatively regular shapes with little fluctuation of the SLA value within the contour.
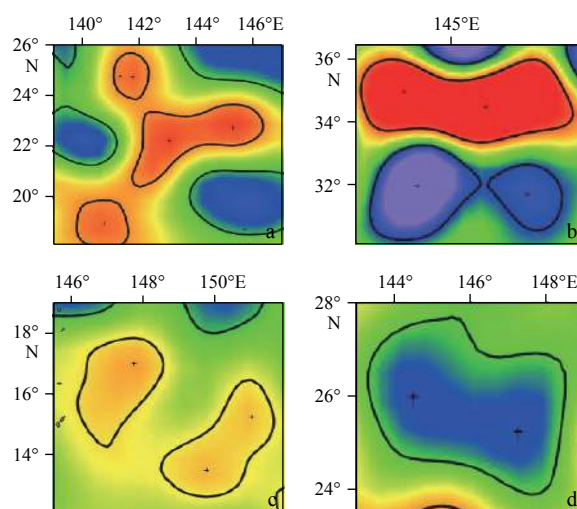
Fig. 9. Examples of eddy structure detection. "+" indicates the extremum core.

4 Conclusions

To solve the problem of automatically detecting mesoscale eddies from an SLA map, this paper proposed a combination of the density clustering algorithm used in the field of machine learning with a mesoscale eddy detection algorithm: the density-based clustering mesoscale eddy detection algorithm.

The basic theory of this algorithm and traditional methods, such as the WA and SSH-based algorithms, is the same in that we search for the outermost closed contour with which to locate mesoscale eddies. However, the proposed algorithm does not require an initialization process that searches for a local extremum to define the cores of eddies and extracts a closed contour, and rather extracts data features to detect regular mesoscale eddies step by step.

The proposed algorithm takes advantage of the strong adaptability of the density clustering algorithm to an unsupervised data set and identifies potential relations by means of density clustering for regions in which mesoscale eddies can be separated. By including eddy shape discrimination in the detection process, the boundary of potential eddies is fitted within a minimum coverage square, and the coverage ratio is determined to approximately judge whether the eddy shape is regular. The method ensures the stability of the selected eddy structure, and regular mesoscale eddy patterns are maintained to the maximum extent.

In comparison with the traditional SSH-based algorithm, the

proposed algorithm requires less parameter setting, and as an automatic algorithm that eliminates manual intervention, it avoids the sensitivity of the threshold setting. The detection results of eddy structures are more stable, and the eddy shapes are more similar to regular patterns. The discovered mesoscale eddies can also be used for subsequent research work and prediction.

References

Ari Sadarjoen I, Post F H. 2000. Detection, quantification, and tracking of vortices using streamline geometry. Computers & Graphics, 24(3): 333–341, doi: 10.1016/S0097-8493(00)00029-7

Chaigneau A, Gizolme A, Grados C. 2008. Mesoscale eddies off Peru in altimeter records: identification algorithms and eddy spatio-temporal patterns. Progress in Oceanography, 79(2–4): 106–119, doi: 10.1016/j.pocean.2008.10.013

Chelton D B, Schlax M G, Samelson R M. 2011. Global observations of nonlinear mesoscale eddies. Progress in Oceanography, 91(2): 167–216, doi: 10.1016/j.pocean.2011.01.002

Doglioli A M, Blanke B, Speich S, et al. 2007. Tracking coherent structures in a regional ocean model with wavelet analysis: application to Cape Basin eddies. Journal of Geophysical Research: Oceans, 112(C5): C05043

He Yaobin, Tan Haoyu, Luo Wuman, et al. 2014. MR-DBSCAN: a scalable MapReduce-based DBSCAN algorithm for heavily skewed data. Frontiers of Computer Science, 8(1): 83–99, doi: 10.1007/s11704-013-3158-3

Henson S A, Thomas A C. 2008. A census of oceanic anticyclonic eddies in the Gulf of Alaska. Deep Sea Research Part I: Oceanographic Research Papers, 55(2): 163–176, doi: 10.1016/j.dsr.2007.11.005

Liu Yingjie, Chen Ge, Sun Miao, et al. 2016. A parallel SLA-based algorithm for global mesoscale eddy identification. Journal of Atmospheric and Oceanic Technology, 33(12): 2743–2754, doi:

10.1175/JTECH-D-16-0033.1

Morrow R, Birol F, Griffin D, et al. 2004. Divergent pathways of cyclonic and anti-cyclonic ocean eddies. Geophysical Research Letters, 31(24): L24311, doi: 10.1029/2004GL020974

Nan Feng, He Zhigang, Zhou Hui, et al. 2011. Three long-lived anti-cyclonic eddies in the northern South China Sea. Journal of Geophysical Research: Oceans, 116(C5): C05002

Nencioli F, Dong Changming, Dickey T, et al. 2010. A vector geometry-based eddy detection algorithm and its application to a high-resolution numerical model product and high-frequency radar surface velocities in the southern California bight. Journal of Atmospheric and Oceanic Technology, 27(3): 564–579, doi: 10.1175/2009JTECHO725.1

Okubo A. 1970. Horizontal dispersion of floatable particles in the vicinity of velocity singularities such as convergences. Deep Sea Research and Oceanographic Abstracts, 17(3): 445–454, doi: 10.1016/0011-7471(70)90059-8

Waugh D W, Abraham E R, Bowen M M. 2006. Spatial variations of stirring in the surface ocean: a case study of the Tasman Sea. Journal of Physical Oceanography, 36(3): 526–542, doi: 10.1175/JPO2865.1

Yi J, Du Y, He Z, et al. 2014. Enhancing the accuracy of automatic eddy detection and the capability of recognizing the multi-core structures from maps of sea level anomaly. Ocean Science, 10(1): 39–48, doi: 10.5194/os-10-39-2014

Zhang Chunhua, Li Honglin, Liu Songtao, et al. 2015. Automatic detection of oceanic eddies in reanalyzed SST images and its application in the East China Sea. Science China Earth Sciences, 58(12): 2249–2259, doi: 10.1007/s11430-015-5101-y

Zhang Chunhua, Xi Xiaoliang, Liu Songtao, et al. 2014. A mesoscale eddy detection method of specific intensity and scale from SSH image in the South China Sea and the Northwest Pacific. Science China Earth Sciences, 57(8): 1897–1906, doi: 10.1007/s11430-014-4839-y

Deep learning classification of coastal wetland hyperspectral image combined spectra and texture features: A case study of Huanghe (Yellow) River Estuary wetland

Yabin Hu[1, 2], Jie Zhang[2], Yi Ma[2]*, Xiaomin Li[2], Qinpei Sun[3], Jubai An[1]

[1] Information Science and Technology College, Dalian Maritime University, Dalian 116026, China

[2] First Institute of Oceanography, Ministry of Natural Resources, Qingdao 266061, China

[3] College of Surveying Science and Engineering, Shandong University of Science and Technology, Qingdao 266590, China

Abstract

This paper develops a deep learning classification method with fully-connected 8-layers characteristics to classification of coastal wetland based on CHRIS hyperspectral image. The method combined spectral feature and multi-spatial texture feature information has been applied in the Huanghe (Yellow) River Estuary coastal wetland. The results show that: (1) Based on testing samples, the DCNN model combined spectral feature and texture feature after K-L transformation appear high classification accuracy, which is up to 99%. (2) The accuracy by using spectral feature with all the texture feature is lower than that using spectral only and combing spectral and texture feature after K-L transformation. The DCNN classification accuracy using spectral feature and texture feature after K-L transformation was up to 99.38%, and the outperformed that of all the texture feature by 4.15%. (3) The classification accuracy of the DCNN method achieves better performance than other methods based on the whole validation image, with an overall accuracy of 84.64% and the Kappa coefficient of 0.80. (4) The developed DCNN model classification algorithm ensured the accuracy of all types is more balanced, and it also greatly improved the accuracy of tidal flat and farmland, while kept the classification accuracy of main types almost invariant compared to the shallow algorithms. The classification accuracy of tidal flat and farmland is up to 79.26% and 56.72% respectively based on the DCNN model. And it improves by about 2.51% and 10.6% compared with that of the other shallow classification methods.

Key words: coastal wetland, hyperspectral image, deep learning, classification

1 Introduction

Coastal wetland locates in a transitional belt between land and marine system. It has the ability to reserve resources, regulate climate, protect environment and purify air, while can provide good habitat for wild animals and plants. Coastal wetland is connected with human life closely.in recent years, its area has declined dramatically due to human activities and natural factors, which disturbed the balance of land-sea resources exchange and affected human being directly. Therefore, it is significant to carry out distribution and change monitoring of the coastal wetland, which is beneficial to the effective utilization and sustainable development of wetland resources and environment.

Remote sensing technology has the advantage of large area synchronous observation and high time resolution, which solves the problem that people are hard to enter the costal wetland. It is a challenge to monitor the distribution and variation of the wetland types accurately. In recent years, many scholars have employed different methods to carry out remote sensing classification research based on multi-spectral and multi-temporal satellite remote sensing images, including support vector machine (SVM) (Melgani and Bruzzone, 2004), decision tree (DT) (Licciardi et al., 2009), decision fusion (Li et al., 2015; He et al., 2010), random forest (RF) and fuzzy mathematics etc (Xu et al., 2006; Freund, 1995; Chubey et al., 2006; Sun et al., 2013; Cao et al., 2016). However, it is difficult to obtain satisfied results in real scene. In fact, the above-mentioned coastal wetland remote sensing classification methods are mainly applied with multi-spectral remote sensing images of medium and low resolution. These application methods are confined to the level of shallow learning, and it is difficult to meet the requirement of fine classification for coastal wetland. The deep learning is a new research direction in the field of machine learning, whose basic process is to obtain a deep network structure with multiple layers through a certain training model (Hinton et al., 2014), and it solves the strong nonlinear problem that shallow methods are out of operation. At present, deep learning has obtained great achievements in the fields of image processing (Krizhevsky et al., 2012; Farabet

et al., 2013), natural language recognition (Waibel et al., 1989; Hinton et al., 2012) and target detection (Xu et al., 2016; Teoh et al., 2012; Tian et al., 2016). It has become a hotspot in the hyperspectral remote sensing images classification (Li et al., 2012; Mei et al., 2016; Yang et al., 2016; Chen et al., 2017; Lee and Kwon, 2016; Slavkovikj et al., 2015; Tarabalka et al., 2009). Convolution Neural Network (CNN) (Hinton and Salakhutdinov, 2006), a deep learning method, has the characteristics of image displacement and rotation invariance. Yue et al. (2015) proposed a CNNs-LR model based on spectral-spatial feature, then applied the model in the Pavia data set. The results showed that the overall accuracy of classification was 95.18%, and the Kappa coefficient was 93.64% (Yue et al., 2015). Hu et al. (2015) used 5-layer CNNs model with hyperspectral image spectral features to carry out classification, the results indicated that the method was superior to the traditional SVM method (Hu et al., 2015). In summary, many scholars used CNNs algorithm in hyperspectral image remote sensing classification, but the research stayed in the verification stage of model algorithm generally. The accuracies of these methods were based on testing samples only, lacking global region verification. On the other hand, the DCNN model has not been applied in the coastal wetland remote sensing image classification. In fact, it is necessary to obtain the high accuracy coastal wetland classification results by using the DCNN model.

According to the needs of coastal wetland monitoring, the paper put forward a deep learning method with fully-connected 8-layers characteristics to carry out coastal wetland classification based on CHRIS hyperspectral remote sensing image, and we applied it in Huanghe (Yellow) River Estuary coastal wetland. Simultaneously, we compared the remote sensing classification accuracy between the DCNN method and several shallow learning methods.

2 Data and methods

2.1 *Data*

2.1.1 *Hyperspectral remote sensing data*

The hyperspectral image was used in this paper acquired from PROBA satellites launched by ESA on October 22, 2001. The satellite was equipped with CHRIS (Compact High Resolution Imaging Spectrometer), and the revisit period was 18 d. CHRIS Hyperspectral images with 18 bands can be obtained from five imaging modes and five angle observations. There were 18 bands in each image, whose spectral range covered from visible spectrum to near infrared spectrum. Their wavelength of spectral bands was ranging from 406 to 1 036 nm. The width of each image width was 13 km×13 km, and the spectral resolution was ranging from 5.8 to 44.1 nm, while spatial resolution was 17 m. The detail information of band parameter setting (An et al., 2016) was shown in Table 1. The CHRIS hyperspectral images of coastal wetland was used in this paper that were obtained in June 2012 and September 2009, whose operating mode stays at State 2 and image angle is 0°. The preprocessing of CHRIS coastal wetland image includes geometric correction, missing pixel filling and noise elimination.

In this paper, the Huanghe River Estuary coastal wetland, the study area, is a national nature reserve surrounded by the Bohai Bay and Laizhou Bay, locates in Dongying City, Shandong Province. It is the habitat for many rare and endangered species. The geographical coordinates of the study area are between 37°44′–37°51′N and 119°04′–119°14′E, which belongs to the warm temperate continental monsoon climate, and the annual average temperature and precipitation is about 12.8°C and 555 mm, respectively. The location of the study area is shown in Fig. 1.

2.1.2 *Field data*

The study area was covering the intersection of the old and

Table 1. The band parameter setting of CHRIS hyperspectral image

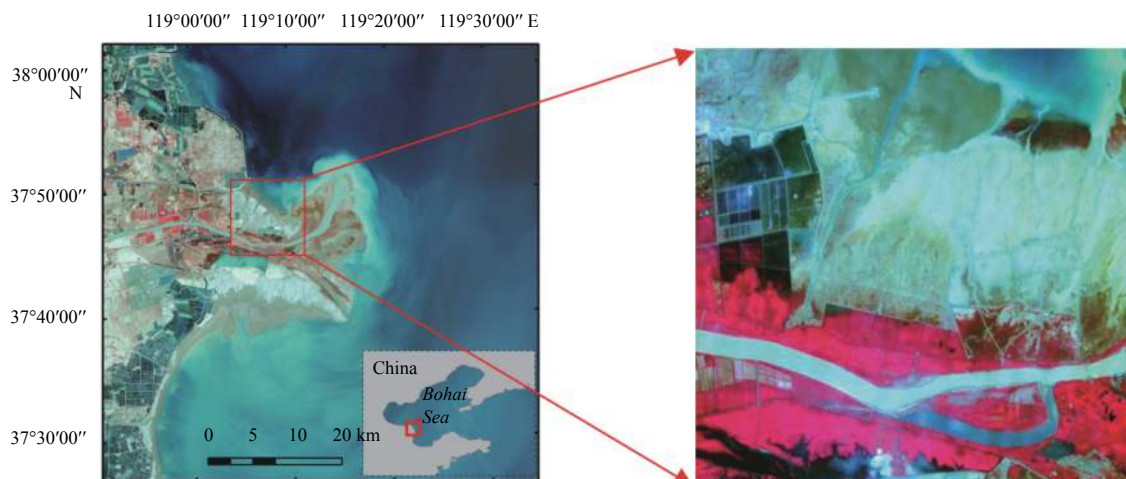| Band parameter	Band 1	Band 2	Band 3	Band 4	Band 5	Band 6	Band 7	Band 8	Band 9
Band center/nm	411.3	443.6	491.8	511.5	532.0	563.6	576.1	593.2	625.3
Band width/nm	10.9	10.6	11.7	12.9	11.6	13.8	11.0	16.0	13.7
Band parameter	Band 10	Band 11	Band 12	Band 13	Band 14	Band 15	Band 16	Band 17	Band 18
Band center/nm	654.3	672.9	684.1	692.7	710.7	760.4	786.1	878.6	1 026.7
Band width/nm	15.4	10.9	11.4	5.8	18.5	14.2	22.8	27.6	44.1

Fig. 1. The location of the Huanghe River Estuary coastal wetland.

new rivers in the Huanghe River Estuary, which was situated at the intersection of the two branches of Qingbacha River and Qingshuigou River. The study area included natural wetlands (reed, Tamarix, spruce and seawater) and artificial wetlands (farmland, aquaculture and ponds). In order to evaluate the classification accuracy of CHRIS image accurately, our group went to the study area to carry out field survey by using a typical sample and route record method in June 2008 and September 2012.

We obtained hundreds of hyperspectral data and more than 400 photos of typical types. Based on field data and high-resolution remote sensing images in the same period, we acquired the interpretation map of typical types by using human-computer interaction method, and we took it as a whole validation image (Fig. 2). At the same time, we verified the accuracy of the interpretation map through RTK instruments in May 2016 (Fig. 3).

Convolution Neural Network (CNN) is a kind of deep learning method, which is specially designed for image classification and recognition based on multi-layer neural network. A typical CNN model includes input layer, convolution layer, drop sampling layer, fully-connected layer and output layer.
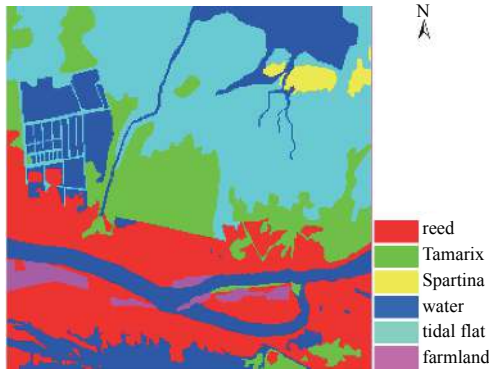
Fig. 2. The interpretation map of the Huanghe River Estuary coastal wetland.

Fig. 3. The photo of field survey.

2.1.3 *DCNN structure*

Although the hyperspectral remote sensing is characterized by high spectral resolution, the hyperspectral image sometimes indicates the phenomenon that different types with same spectrum and the same types with different spectrum due to the complicated atmospheric, light and sensor conditions. It will affect the image classification accuracy seriously if we just adopt the spectral characteristics. Therefore, we introduced the spatial fea-

ture information of the similarity of adjacent pixels into the classification algorithm. The developed classification algorithm was combined with spatial features and spectral features, which took the direction and neighborhood information into account, and it might effectively improve the classification accuracy of object types. Although many scholars used spectral features and spatial features to identify types based on hyperspectral images, the coastal wetland DCNN model classification based on hyperspectral remote sensing image is relatively poor. Therefore, this paper proposed an 8-layers DCNN model that took spatial features and spectral features into account, which consisted of an input layer, two convolution layers, two drop sampling layers, two fully-connected layers and one output layer. The proposed DCNN model structure was shown in Fig. 4.

2.1.4 *Input layer*

The input layer of the proposed DCNN model consists of a feature vector which contains the spectral and texture features information. The input vector z_i can be expressed by Eq. (1):

$$z_i = [X_i^1, X_i^2, ..., X_i^d, X_i^1, y_i^1, y_i^2, ..., y_i^d] \quad i \in (1, 2, ..., N), \quad (1)$$

where z_i denotes the feature value of image pixels, N is the number of samples, d is the number of bands, and X_i^1 indicates the spectral value of the i sample in Band d.

The input vector g^{l+1} of convolution layer is the result of the conversion of input layer by Eq. (2):

$$g^{l+1} = f^l \left(W^{lT} g^l + b^l \right), \quad (2)$$

where g^l denotes the input value of lth layer and the output value of $(l-1)$th layer, W^T is a weight matrix of the lth layer acting on the input feature data, b^l is an additive bias vector for the lth layer, and $f^l (\bullet)$ represents the activate function of the lth layer.

2.1.5 *Convolution layer*

Convolution layer is a process to obtain a new feature map that a result of the input feature map can obtain through convolution operation with the learning of the convolution kernel and an activation function. A DCNN model can include multiple convolution layers. According to different purposes, different convolution can be used to convolve the input feature map in the convolution layer, so different convolution kernels will obtain different feature map by convolution operation. An output feature map can be obtained by multiple convolution processes. Multi-convolution kernel is a sampling process in time domain or space domain, which can reduce the complexity of the network and the resolution of the feature map effectively, and reduce the sensitivity to displacement, rotation and scaling. The convolution layer is calculated by Eq. (3):

$$V_m^l = f_l \left(\sum_{n \in G} V_n^{l-1} \otimes H_{mn}^l + b_m^l \right), \quad (3)$$

where V_m^l is the activate value of the output feature map in the lth layer, G represents the feature map in l th feature layer, H_{mn}^l represents the convolution kernel that links the input feature map n in lth feature layer and the output feature map m in $(l-1)$th feature layer, b_m^l is the bias coefficient for the lth feature layer, $\otimes$ denotes convolution operation, $f_l (\bullet)$ represents the
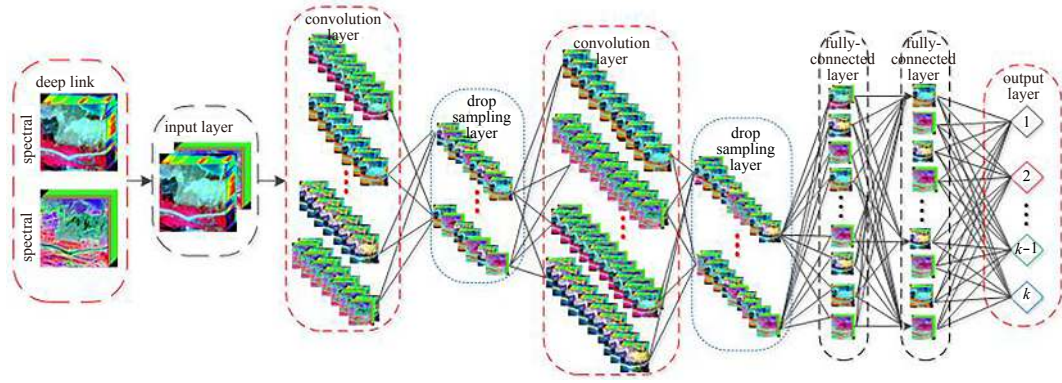
Fig. 4. The structure of the proposed DCNN model.

softmax activate function. The softmax regression models is defined as Eq. (4):

$$f(x) = \frac{1}{1 + e^{-ax}}, \tag{4}$$

where a is the tilt coefficient.

2.1.6 Drop sampling layer

The main purpose of drop sampling layer is to reduce the number of output parameters of feature map through the convolution layer, and to feature that can make the feature representation keep the invariance of rotation, translation and stretching. If the number of feature maps is too large in the DCNN model, it will lead to overfitting. The sampling layer is calculated by Eq. (5):

$$V_m^l = f^l \left(\alpha_m^l \times \text{down} \left(V_m^{l-1} \right) + b_m^l \right), \tag{5}$$

where α_m^l and b_m^l represent the multiplicative bias coefficient and the additive bias coefficient of feature map m for the lth feature layer, respectively; and down $(\bullet)$ is a down-sampling function acting on the lth feature layer.

Drop sampling methods include max-pooling and mean pooling. The max-pooling method is adopted in the proposed DCNN model, which is to reduce the estimated mean shift caused by convolutional parameters error to preserve image texture information, and the result of error is obtained by the statistical calculation of the features of different positions. The down-sampling value is given by Eq. (6):

$$U_m = \max \left(U_m^1, U_m^2, \cdots, U_m^q \right), \tag{6}$$

where U_m^q represents the value of element q in feature map m; and q is the number of feature map m, which depends on the size of the down-sampling window.

2.1.7 Fully-connected layer

The fully-connected layer is a reorganization process of the feature map in the model, which can improve the effect of model training. Compared with the sparse connection, the full connection takes the nature of all feature maps in upper layer network into account, and obtains the combined coefficient of the feature maps by learning method, which further improves the expression ability and adaptability of model. The value of the feature map V_n^l through fully-connected layer can be expressed by the

Eq. (7):

$$V_n^l = f \left(\sum_{m=1}^{Z} \partial_{mn}{}^* V_m^{l-1} + b_j^l \right), \tag{7}$$

where Z is the total number of feature maps in the input $(l-1)$th feature layer, ∂_{mn} represents the weight value that link the feature map n in lth feature layer and the input feature map m in $(l-1)$th feature layer, b_m^l represents the additive bias coefficient of feature map m for the lth feature layer, the weight ∂_{mn} can be enhanced by the soft-max function of a set of unconstrained implicit weight c_{mn}, and ∂_{mn} is defined as Eq. (8):

$$\partial_{mn}\Theta \begin{cases} 0 \leqslant \partial_{mn} \leqslant 1, \\ \partial_{mn} = \dfrac{\exp \left(c_{mn} \right)}{\sum_k \exp \left(c_{kn} \right)}, \\ \sum_m^Z \partial_{mn} = 1, \end{cases} \tag{8}$$

where Θ denotes constraint condition.

2.1.8 Output layer

The output layer of the proposed DCNN model needs to predict the maximum likelihood of input neurons, and a neuron in output layer reflects a class of object. The softmax regression activation function was used to enhance the binding between neurons in the output layer, and to reduce the confusion of the categories of neurons. The class estimation function can be defined by the softmax regression activation function P as Eq. (9):

$$P = \begin{bmatrix} P\left(Y = 1 \,|\, V, W, b \right) \\ P\left(Y = 2 \,|\, V, W, b \right) \\ \dots \\ P\left(Y = k \,|\, V, W, b \right) \end{bmatrix}$$

$$= \frac{1}{\sum_{i=1}^{k} e^{W_{nk}^{\mathrm{T}} V_n + b_k}} \begin{bmatrix} W_{n1}^{\mathrm{T}} V_n + b_1 \\ W_{n2}^{\mathrm{T}} V_n + b_2 \\ \dots \\ W_{nk}^{\mathrm{T}} V_n + b_k \end{bmatrix}, \tag{9}$$

where W and b represents the multiplicative weight and the additive bias coefficient; W_{nk} and b_k represent the weight and bias

coefficient of the input neuron n which is classified as class k of object type; Y represents the classification result of the input neuron, which corresponds to the label of training samples; and $P (\bullet)$ represents the potential probability of input pixel g is attributable to object type k. The probability of sample classification i in the softmax function is given by Eq. (10):

$$P = (Y = i \,|\, V, W, b) = \frac{\mathrm{e}^{W_{nk}^{\mathrm{T}} V_n + b_k}}{\displaystyle\sum_{i=1}^{k} \mathrm{e}^{W_{nk}^{\mathrm{T}} V_n + b_k}} \,. \tag{10}$$

2.2 *Feature extraction*

2.2.1 *Spectral feature*

The spectral curve reflects the characteristics of absorption and reflection of objects. Different objects indicate different spectral waveform. Spectral features can be extracted from spectral curve, such as absorption wavelength position, reflection value, depth, width, slope, symmetry, area and so on. Based on the spectral feature of parameters, the purposes of rapid identification and accurate classification of different object types can be achieved.

The types of the Huanghe River Estuary coastal wetland are diverse. According to the features of CHRIS hyperspectral image and field survey data, the types of Huanghe River Estuary coastal wetland are defined as six categories: reed, Tamarix, Spartina, water, tidal flat and farmland.

2.2.2 *Texture feature*

Texture is an inherent important feature in an image, which is formed by the gray distribution of different objects in the spatial position, so there will be a certain degree of gray relationship among the adjacent pixels in image space. Of course, different object types indicate different texture features in the image. Texture Gray Level Co-occurrence Matrix (GLCM) is an algorithm that describes the properties of gray spatial correlation to reflect texture features, which reflects information of image gray level, neighborhood pixel spacing, direction and amplitude of change. The GLCM will be different due to the diversity of texture scale, so we use the texture gray level covariance matrix algorithm to extract eight texture features in the CHRIS hyperspectral images of coastal wetland. These texture features consist of mean, variance, homogeneity, contrast, dissimilarity, entropy, angular second moment and correlation.

The eight types of texture features based on the GLCM algorithm contain different direction information and neighborhood information, but not all the texture features are beneficial to the classification accuracy, some texture features may reduce the image classification accuracy. Therefore, it is necessary to carry out an information comprehensive selection from the 8 texture features, which can preserve the texture information and improve the efficiency and the classification accuracy at the same time. In this paper, K-L transform (Karhunen-Loeve transform) is used to extract the information of 8 types of texture features, which is a best transformation with strong correlation and mean square error based on the statistical properties. The first component after K-L transformation has the most of texture information, and the texture information of the other components decreases in turn. The amount of texture information contained in the first three components is up to 95%, so we retain them as the texture feature information.

2.3 *Model training*

2.3.1 *CNN parameter setting*

The input of the proposed DCNN model included spectral features and texture features. The fusion result contained 21-dimensional information, because we obtained the first three components of texture features with 8 texture parameters after K-L transform. In order to facilitate the operation of DCNN model, we expanded the 21-dimensional information twice, namely, the input layer contains 42-dimensional information. In this paper, the parameters of the DCNN model were set as follows: the number of feature maps was 4 and 8, respectively, the convolution kernel size was 3×3, and the number of iterations was 10.

2.3.2 *The label of training samples and testing samples*

In order to achieve the fine classification of object types of coastal wetland, we need to train and test the DCNN model to find the best matching parameters. The selection of training samples and test samples affected the accuracy of classification greatly. Because the characteristic of non-singularity about training sample pixels would change the construction of nonlinear functions in DCNN model, and then confuse the attribution of pixels. Therefore, the selection of typical training samples and test samples must ensure the purity of pixels. The selection of test samples was used to evaluate the accuracy of the DCNN model established by the training samples. In this paper, we selected 6 classes of typical object types as training samples and test samples based on field data and pictures in the Huanghe River Estuary, which were reed, Tamarix, Spartina, water, tidal flat and farmland. At last we selected 7 092 training samples and 1 396 test samples, respectively. The sample distribution was shown in Fig. 5 and Table 2.

We performed 10 Monte Carlo runs, where each run we selected a training set and a testing set of the labeled samples according to Table 2 to train our model. We reported the average and standard error of the 10 Monte Carlo runs in terms of the overall
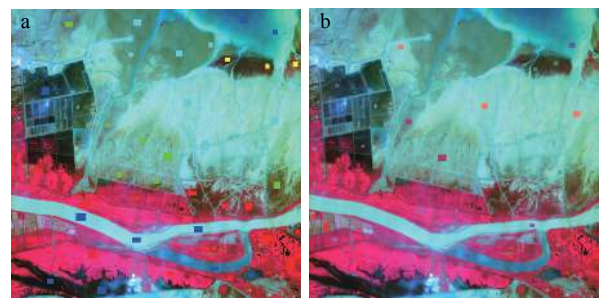

Fig. 5. The sample distribution map. a. Testing samples and b. training samples.

Table 2. The information of training samples and testing samples

Type	Training samples	Testing samples
Reed	2 428	251
Tamarix	1 000	322
Spartina	250	140
Water	1 828	242
Tidal flat	1 349	284
Farmland	237	157
Sum	7 092	1 396

classification accuracy (OCA).

3 Results and discussion

3.1 *Classification accuracy evaluation of DCNN model based on testing samples*

Based on the six typical types of training samples and testing samples selected from the coastal wetland in the Huanghe River Estuary, we carried out the classification experiments by the developed DCNN model in the case of using the spectral feature information only, combining the spectral feature information with all the texture feature information, and combining the spectral feature information with the texture feature after K-L transformation. At the same time, this paper introduced support vector machine (SVM) to compare with the proposed DCNN model. SVM is a machine learning method that can solve the existing problems such as small sample, nonlinearity, high dimension and local minimum point. The core of SVM is to find an optimal separable hyperplane, which distinguishes two types of samples from the training sample. This paper uses the SVM algorithm based on 4 types of kernel function called linear, polynomial, radial basis function and sigmoid kernel function. we carried out the classification experiments of CHRIS hyperspectral image in the case of using spectral feature information only and combining the spectral feature information with the texture feature after K-L transformation by the same training samples. Then we evaluated the classification accuracy by the same testing samples. The test results based on different classification methods are shown in Table 3.

It can be seen from Table 3, the classification accuracy of reed in all kinds of methods is up to 100%. The classification accuracy of Tamarix by SVM method based on linear and polynomial kernel was up to 100%. The classification accuracy of water by SVM method based on the polynomial and RBF kernel, and the DCNN model by using the spectral feature information combined with the K-L transformed texture feature information reaches 100%. While the classification accuracy of tidal flat reaches up to 99%, only in the case of combing spectral feature with all the texture feature classified by the DCNN model. In the form of different classification methods, the DCNN model combing spectral feature with texture K-L transformation feature had the highest classification accuracy of farmland, reaching 98.41%, and the accuracy of SVM algorithm based on sigmoid kernel is the lowest. Among all the classification methods, the overall accuracy of testing sample was up to 99% based on the DCNN model combined spectral feature and texture feature after K-L transformation only.

At the same time, it can be found in Table 3 that in a classification method, the accuracy by using spectral feature with all the texture feature was lower than that using spectral only and spectral combing texture feature after K-L transformation, and the accuracy by using spectral feature only was lower than that combing spectral feature and texture feature after K-L transformation. In each classification method, compared with the two cases that based on spectral feature and combined spectral feature and all the texture feature, the classification accuracy of combined spectral feature and texture feature after K-L transformation improves by about 2% and 3%. In the three different cases by DCNN model, we could see that the classification accuracy by using all texture feature was the lowest, only 95.23%, and the classification accuracy by using spectral feature and texture feature after K-L transformation was up to 99.38%, and it improved by 4.15% compared with using all the texture feature. The method used all the texture features will affect the accuracy of image classification, and the method used texture feature after K-L transformation. It can also be explained that not all texture features are beneficial to the classification results, some of them will affect the accuracy of image classification.

3.2 *Classification accuracy evaluation of DCNN model based on whole validation image*

In this study, we selected five classification methods whose classification accuracy was over 98% by being applied to the CHRIS high resolution image about the Huanghe River Estuary. The total pixel number of CHRIS hyperspectral data is 262 144. The results of the five classification methods were shown in Fig. 6. In order to verify the accuracy of five classification methods for coastal wetland, we used the remote sensing interpretation of the Huanghe River Estuary as the whole validation image to verify the overall accuracy and typical classification accuracy from global region. The accuracy information of the classification results was shown in Table 4. It could be seen from Table 4 that the accuracy of the SVM method based on linear, polynomial and RBF kernels, and the DCNN model combing the spectral feature and texture feature after K-L transformation were both higher than that of the DCNN model using the spectral feature only. Among all the methods that combined spectral feature with texture feature after K-L transformation, the classification accuracy of the DCNN model was the highest, the accuracy was 84.64%, and the Kappa coefficient was 0.80.

Among all the classification results of typical types, the developed DCNN model classification algorithm ensured the accuracy of all types more balanced, and it greatly improves the accuracy of tidal flat and farmland, while kept the classification accuracy of main types almost invariant compared to the shallow algorithms. The SVM-polynomial method that used in water had the highest recognition accuracy was 89.42% in the case of confined spectral feature and texture feature information after K-L

Table 3. The classification results (%) of testing samples

Type	Classification method														
	SVM-linear			SVM-polynomial			SVM-RBF			SVM-sigmoid			DCNN		
	SO	ST	STKL	SO	ST	STKL	SO	ST	STKL	SO	ST	STKL	SO	ST	STKL
Reed	100	100	100	100	100	100	100	100	100	100	100	100	100	100	100
Tamarix	99.07	98.76	99.84	100	98.76	100	98.76	98.45	98.76	18.01	18.94	21.12	99.38	97.67	97.52
Spartina	95.71	95	99.64	93.57	94.29	97.8	92.85	94.29	97.5	21.07	20.71	51.78	98.93	95.35	96.79
Water	93.59	90.08	96.28	100	93.39	100	100	96.28	100	92.56	91.32	94.62	97.93	95.04	100
Tidal flat	95.95	94.72	98.41	96.48	94.01	98.24	98.24	95.42	98.77	84.51	91.55	90.14	98.42	96.94	98.59
Farmland	92.99	92.36	98.09	91.08	91.72	95.86	92.99	91.72	97.13	70.16	48.6	62.74	97.77	95.69	98.41
OCA	96.63	95.56	98.75	97.63	95.85	98.96	97.85	96.56	98.89	65.37	64.33	69.84	98.82	95.23	99.38

Note: SO represents spectral only, ST spectral + all texture, and STKL spectral + texture after K-L transform.
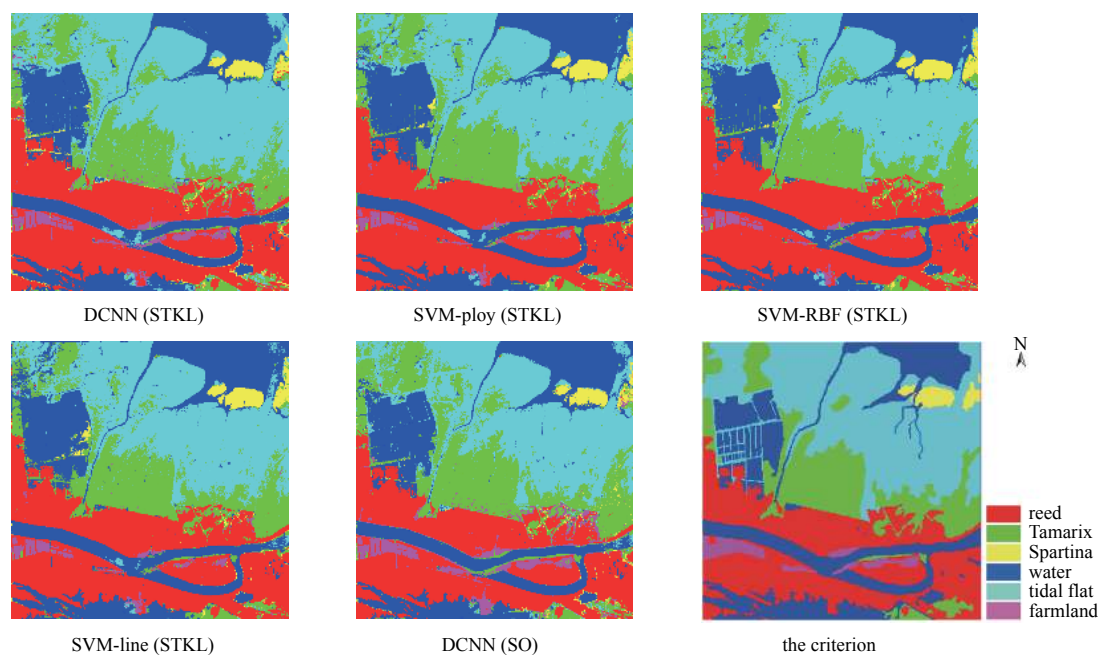
Fig. 6. The results of each classification method and the criterion.

Table 4. The classification results based on the whole validation image (%)

Type	Classification method														
	SVM-linear			SVM-polynomial			SVM-RBF			SVM-sigmoid			DCNN		
	SO	ST	STKL	SO	ST	STKL	SO	ST	STKL	SO	ST	STKL	SO	ST	STKL
Reed	94.2	96.61	95.35	92.75	96.78	94.94	96.06	96.99	94.63	88.89	89.36	91.4	92.57	92.99	94.01
Tamarix	77.71	76.52	79.91	80.17	78.07	83.62	78.99	78.76	82.46	19.2	19.88	27.66	78.33	78.54	79.24
Spartina	79.91	78.69	85.51	87.92	79.69	87.02	82.6	78.62	87.27	15.47	15.41	31.96	76.14	75.32	79.81
Water	83.32	78.11	88.67	86.5	78.59	89.42	83.63	80.64	89.39	69.75	68.39	73.01	85.31	85.23	86.36
Tidal flat	73.64	71.43	76.75	72.52	71.44	76.15	74.09	70.75	75.75	90.52	91.65	89.16	77.96	75.84	79.26
Farmland	43.99	45.91	38.78	45.34	45.42	43.81	42.1	45.34	45.18	46.12	31.13	35.15	51.85	52.37	56.72
OCA	81.04± 2.26	79.70± 0.88	83.80± 0.12	81.75± 1.01	80.11± 0.13	84.43± 0.04	81.95± 1.60	80.48± 0.65	84.06± 0.07	71.57± 1.06	71.46± 0.95	73.84± 0.41	82.68± 0.15	82.14± 0.39	84.64± 0.20
Kappa	0.75	0.73	0.78	0.76	0.74	0.79	0.76	0.74	0.71	0.61	0.61	0.64	0.77	0.77	0.8

transformation. Tidal flat is the most widely covered area in the coastal wetland of Huanghe River Estuary. The most two difficult types to classify in the coastal wetland are tidal flat and farmland. Compared with other classification methods, the developed DCNN model can effectively extract them, and the extraction accuracy can be up to 79.26% and 56.72%, respectively. While the accuracy of them by the SVM methods with linear, polynomial and RBF kernel was less than 76.75% and 46.12%, and the accuracy improving about 2.51% and 10.6%.

In each classification method, the classification accuracy of combined spectral feature and all the texture feature was lower than the accuracy based on spectral feature and combined spectral feature and texture feature after K-L transformation. In the SVM methods, the classification accuracy of combined spectral feature and texture feature after K-L transformation improved by about 1% and 4%. In the three different cases by DCNN model, we can see that the classification accuracy was over 82%, and the classification accuracy by using all texture feature is the lowest, it was 82.14%, the classification accuracy by using spectral feature and texture feature after K-L transformation was up to 84.64%, and it improved by 2.5% compared with using all the texture feature.

3.3 *The DCNN model application*

Considering the applicable area of the proposed model and the accuracy of training samples and testing samples, the CHRIS hyperspectral image of the Huanghe River Estuary coastal wetland was obtained in September 2009, whose operating mode stays at State 2 and image angle is 0°. The image scene has 210× 262 pixels and 18 spectral bands. There are 4 classes in this data. We randomly chose 730 training samples and 370 testing samples. Based on the selected samples, we adapted the developed DCNN model and SVM method to classify the hyperspectral image.

The classification results based on different methods are shown in Fig. 7. The results showed that the classification accuracy of the DCNN model combined spectral feature and texture feature after K-L transformation was the highest, the accuracy was 90.05%. In the three different cases by DCNN model, we could see that the classification accuracy by using all texture feature was the lowest, it was 72.23%, and it reduced by 17.72% and 14.25% compared with using spectral only and combined spectral feature and texture feature after K-L transformation. The developed DCNN model can be applied to the coastal wetland hyperspectral images classification.
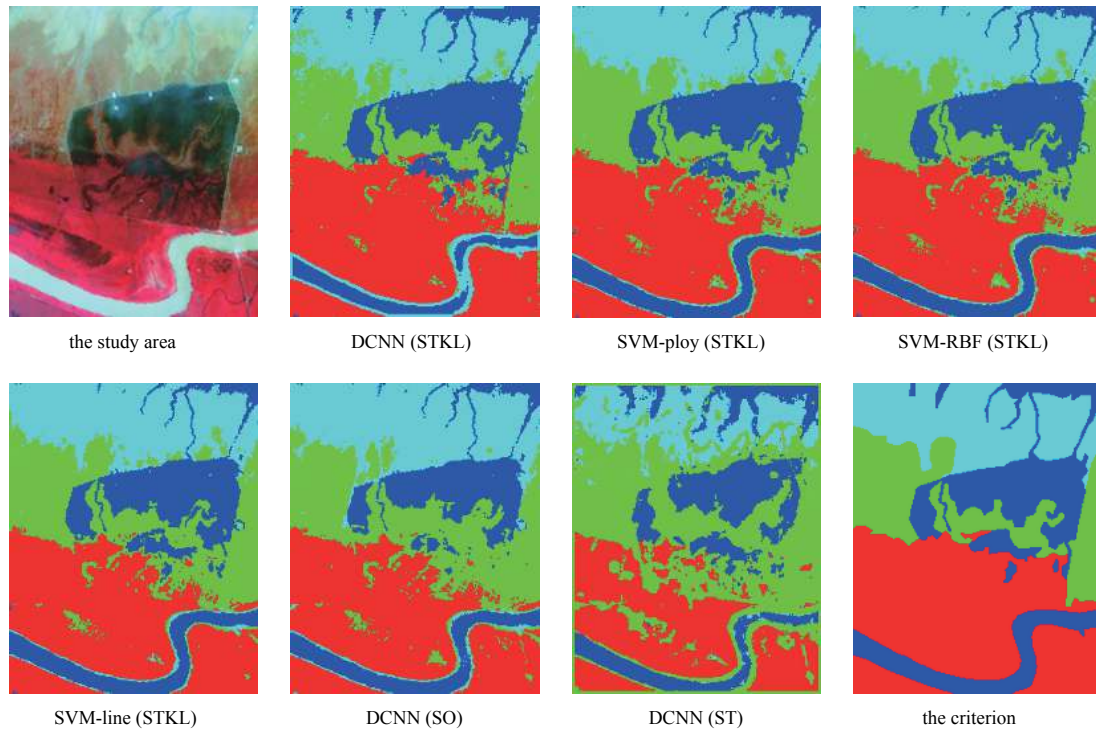
Fig. 7. The study area, the classification results and the criterion.

4 Conclusions

Coastal wetland locates in a transitional belt between land and marine system that carry out mutual material flow and energy transfer. It has important ecological and economic value. It is great significance to study the distribution and evolution of coastal wetland types. This paper developed a deep convolution neural network classification algorithm with fully-connected 8-layers based on CHRIS hyperspectral images, which combined spectral feature and multi-spatial texture feature information. We compared it with the SVM classification algorithm using the kernel of linear, polynomial, radial basis function and sigmoid function. At the same time, we evaluated the hyperspectral images classification accuracy with different input information. In the end, we validated the accuracy of the developed DCNN model for coastal wetland classification based on remote sensing interpretation map of coastal wetland of the Huanghe River Estuary. The results are shown as follows.

(1) Based on CHRIS hyperspectral remote sensing image of the coastal wetland, this paper constructed a classification system for typical object types of coastal wetland, and developed a fully-connected DCNN remote sensing classification model with 8-layer structure for coastal wetland, which combines spectral feature and multi-spatial texture information.

(2) From the verification of training sample, the developed DCNN classification algorithm model had high classification accuracy for tidal flat, and the classification accuracy reached up to 99%. The SVM classification algorithm based on sigmoid kernel had the lowest accuracy and the overall classification accuracy was less than 70%. The overall accuracy of testing sample was up to 99% based on the DCNN model combined spectral feature and texture feature after K-L transformation only. In each classification method, compared with the two cases that based on spectral feature and combined spectral feature and all the texture feature, the classification accuracy of combined spectral feature and tex-

ture feature after K-L transformation improves by about 2% and 3%. In the three different cases by DCNN model, we could see that the classification accuracy by using spectral feature and texture feature after K-L transformation was up to 99.38%, and it improved by 4.15% compared with using all the texture feature. Partial texture features would directly affect the classification accuracy.

(3) From the verification of whole image, the developed DCNN model classification method had the highest classification accuracy for coastal wetland of Huanghe River Estuary, which was 84.64%, and the Kappa coefficient was 0.80. Compared with other classification methods, the developed DCNN model can effectively extract them, with the accuracy of up to 79.26% and 56.72%, respectively. While the accuracy of them by the SVM methods with linear, polynomial and RBF kernel was less than 76.75% and 46.12%, improving about 2.51% and 10.6%. In the three different cases using DCNN model, we could see that the classification accuracy was over 82%, and the classification accuracy by using all texture feature is the lowest, it was 82.14%, the classification accuracy by using spectral feature and texture feature after K-L transformation was up to 84.64%, and it improved by 2.5% compared with that using all the texture feature.

(4) The developed DCNN model classification algorithm ensured the accuracy of all types more balanced. It also greatly improved the accuracy of tidal flat and farmland, while kept the classification accuracy of main types almost invariant compared to the shallow algorithms. Compared with other classification methods, the developed DCNN model performed better. The extraction accuracy can be up to 79.26% and 56.72%, respectively, and the accuracy improved about 2.51% and 10.6% compared with those by SVM methods with linear, polynomial and RBF kernel.

The coastal wetland classification algorithm based on the developed deep learning DCNN model was applied in the CHRIS

hyperspectral image of the Huanghe River Estuary, but whether it was suitable for other satellite imagery and other areas of coastal wetland classification was still to be further studied. On the other hand, there were some insufficiencies in the selection of the number of samples. The less selection samples of object types would affect the classification accuracy. Our future work will focus on solving the problem of sample selection.

References

An Ni, Ma Yi, Bao Yuhai. 2016. Spectral fidelity analysis of scaling transformation of hyperspectral remote sensing image based on empirical mode decomposition. Remote Sensing Technology and Application (in Chinese), 31(2): 230–238

Cao Linlin, Li Haitao, Han Yanshun, et al. 2016. Application of convolutional neural networks in classification of high resolution remote sensing imagery. Science of Surveying and Mapping (in Chinese), 41(9): 170–175

Chen Yushi, Lin Zhouhan, Zhao Xing, et al. 2017. Deep learning-based classification of hyperspectral data. IEEE Journal of Selected Topics in Applied Earth Observations and Remote Sensing, 7(6): 2094–2107

Chubey M S, Franklin S E, Wulder M A. 2006. Object-based analysis of ikonos-2 imagery for extraction of forest inventory parameters. Photogrammetric Engineering & Remote Sensing, 72(4): 383–394

Farabet C, Couprie C, Najman L, et al. 2013. Learning hierarchical features for scene labeling. IEEE Transactions on Pattern Analysis and Machine Intelligence, 35(8): 1915–1929, doi: 10.1109/TPAMI.2012.231

Freund Y. 1995. Boosting a weak learning algorithm by majority. Information and Computation, 121(2): 256–285, doi: 10.1006/inco.1995.1136

He Y, Qian D, Ben M. 2010. Decision fusion on supervised and unsupervised classifiers for hyperspectral imagery. IEEE Transactions on Geoscience and Remote Sensing Letters, 7(4): 875–879

Hinton G, Deng Li, Yu Dong, et al. 2012. Deep neural networks for acoustic modeling in speech recognition: the shared views of four research groups. IEEE Signal Processing Magazine, 29(6): 82–97, doi: 10.1109/MSP.2012.2205597

Hinton G E, Osindero S, Teh Y W. 2014. A fast learning algorithm for deep belief nets. Neural Computation, 18(7): 1527–1554

Hinton G E, Salakhutdinov R R. 2006. Reducing the dimensionality of data with neural networks. Science, 313(5786): 504–507, doi: 10.1126/science.1127647

Hu Wei, Huang Yangyu, Wei Li, et al. 2015. Deep convolutional neural networks for hyperspectral image classification. Journal of Sensors, 2015: 258619

Krizhevsky A, Sutskever I, Hinton G E. 2012. ImageNet classification with deep convolutional neural networks. In: Proceedings of the 25th International Conference on Neural Information Processing Systems. Lake Tahoe, Nevada: Curran Associates Inc, 1097–1105

Lee H, Kwon H. 2016. Contextual deep CNN based hyperspectral classification. In: Proceedings of 2016 IEEE International Geoscience and Remote Sensing Symposium. Beijing, China: IEEE

Li Wei, Prasad S, Fowler J E, et al. 2012. Locality-preserving dimensionality reduction and classification for hyperspectral image

analysis. IEEE Transactions on Geoscience and Remote Sensing, 50(4): 1185–1198, doi: 10.1109/TGRS.2011.2165957

Li Xiaomin, Zhang Jie, Ma Yi, et al. 2015. Research on the classification method of the hyper-spectral image based on principal component analysis and decision level fusion. Marine Sciences, 39(2): 25–34

Licciardi G, Pacifici F, Tuia D, et al. 2009. Decision fusion for the classification of hyperspectral data: outcome of the 2008 GRS-S data fusion contest. IEEE Transactions on Geoscience and Remote Sensing, 47(11): 3857–3865, doi: 10.1109/TGRS.2009.2029340

Mei Shaohui, Ji Jingyu, Bi Qianqian, et al. 2016. Integrating spectral and spatial information into deep convolutional Neural Networks for hyperspectral classification. In: Proceedings of 2016 International Geoscience and Remote Sensing Symposium. Beijing, China: IEEE, 5067–5070

Melgani F, Bruzzone L. 2004. Classification of hyperspectral remote sensing images with support vector machines. IEEE Transactions on Geoscience and Remote Sensing, 42(8): 1778–1790, doi: 10.1109/TGRS.2004.831865

Slavkovikj V, Verstockt S, De Neve W, et al. 2015. Hyperspectral image classification with convolutional neural networks. In: Proceedings of the 23rd ACM International Conference on Multimedia. Brisbane, Australia: ACM, 1159–1162

Sun Junjie, Ma Daxi, Ren Chunying, et al. 2013. Method of extraction of wetlands' information in nanweng river basin based on multi-temporal environment satellite images. Wetland Science (in Chinese), 11(1): 60–67

Tarabalka Y, Benediktsson J A, Chanussot J. 2009. Spectral-spatial classification of hyperspectral imagery based on partitional clustering techniques. IEEE Transactions on Geoscience and Remote Sensing, 47(8): 2973–2987, doi: 10.1109/TGRS.2009.2016214

Teoh S S, Bräunl T. 2012. Symmetry-based monocular vehicle detection system. Machine Vision and Applications, 23(5): 831–842, doi: 10.1007/s00138-011-0355-7

Tian Zhuangzhuang, Zhan Ronghui, Hu Jiemin, et al. 2016. SAR ATR based on convolutional neural network. Journal of Radars (in Chinese), 5(3): 320–325

Waibel A, Hanazawa T, Hinton G E, et al. 1989. Phoneme recognition using time-delay neural networks. IEEE Transactions on Acoustics, Speech, and Signal Processing, 37(3): 328–339, doi: 10.1109/29.21701

Xu Yingxue, Shao Jingli, Yang Wenfeng, et al. 2006. Research on classification and change of seaside wetland around Yalujiang river estuary based on RS and GIS. Geoscience (in Chinese), 20(3): 500–504

Xu Zhenlei, Yang Rui, Wang Xinchun, et al. 2016. Based on leaves convolutional neural network recognition algorithm. Computer Knowledge and Technology (in Chinese), 12(10): 194–196

Yang Jingxiang, Zhao Yongqiang, Chan J C W, et al. 2016. Hyperspectral image classification using two-channel deep convolutional neural network. In: Proceedings of 2016 International Geoscience and Remote Sensing Symposium. Beijing, China: IEEE, 5079–5082

Yue Jun, Zhao Wenzhi, Mao Shanjun, et al. 2015. Spectral-spatial classification of hyperspectral images using deep convolutional neural networks. Remote Sensing Letters, 6(6): 468–477, doi: 10.1080/2150704X.2015.1047045

An interpretation of wave refraction and its influence on foreshore sediment distribution

Vincent Jayaraj Joevivek[1, 2*], Nainarpandian Chandrasekar[2, 4], Ramakrishnan Jayangondaperumal[3], Vikram Chandra Thakur[3], Krishnan Shree Purniema[1]

[1] Akshaya College of Engineering and Technology, Coimbatore 642109, India

[2] Centre for GeoTechnology, Manonmaniam Sundaranar University, Tirunelveli 627012, India

[3] Structure and Tectonics Group, Wadia Institute of Himalayan Geology, Dehradun 248001, India

[4] Francis Xavier Engineering College, Tirunelveli 627003, India

Abstract

To analyze the grain size and depositional environment of the foreshore sediments, a study was undertaken on wave refraction along the wide sandy beaches of central Tamil Nadu coast. The nearshore waves approach the coast at 45° during the northeast (NE) monsoon, at 135° during the southwest (SW) monsoon and at 90° during the non-monsoon or fair-weather period with a predominant wave period of 8 and 10 s. A computer based wave refraction pattern is constructed to evaluate the trajectories of shoreward propagating waves along the coast in different seasons. The convergent wave rays during NE monsoon, leads to high energy wave condition which conveys a continuous erosion at foreshore region while divergent and inept condition of rays during the SW and non-monsoon, leads to moderate and less energy waves that clearly demarcates the rebuilt beach sediments through littoral sediment transport. The role of wave refraction in foreshore deposits was understood by grain size and depositional environment analysis. The presence of fine grains with the mixed population, during the NE monsoon reveals that the high energy wave condition and sediments were derived from beach and river environment. Conversely, the presence of medium grains with uniform population, during SW and non-monsoon attested less turbulence and sediments were derived from prolong propagation of onshore-offshore wave process. These upshots are apparently correlated with the *in situ* beach condition. On the whole, from this study it is understood that beaches underwent erosion during the NE monsoon and restored its original condition during the SW and non-monsoon seasons that exposed the stability of the beach and nearshore condition.

Key words: foreshore, grain size, wave refraction, sediment transport, beach, India

1 Introduction

The waves and wave induced currents are the primary sea undulations that lead to the sediment transportation in the nearshore region. The direction of wave propagation depends on the seabed topography. The uneven nearshore topography influences wave celerity, breaking wave height and direction and thus the direction of the wave approaching the coast is altered. Therefore, the waves undergo refraction and tend to become normal to the shoreline. This phenomenon is called wave refraction (Kirby and Dalrymple, 1994; López-Ruiz et al., 2015). Munk and Traylor (1947) provided a detailed mathematical structure for constructing wave refraction and discussed the wave refraction impact on nearshore process. Followed by this, many researchers used computer based wave refraction models to examine the physical process of different types of coasts (Shepard and Inman, 1950; Harrison and Wilson, 1964; Orr, 1969; Skovgaard et al., 1975; Jing and Massel, 1994; Mathiesen, 1987; Kirby and Dalrymple, 1994; López-Ruiz et al., 2015; Joevivek and Chandrasekar, 2016). From these studies, it is understood that four oceanographic parameters namely seabed topography, wave period, direction of wave approach the coast and deep-water wave height are the key para-

meters for constructing wave refraction diagram. In general, wave refraction helps to understand the wave process and the depositional environment at a particular region. Even though, quite a lot of papers had provided the spatial relationship between wave refraction and sediment distribution (Angusamy et al., 1998; Bird, 2000; Kunte et al., 2001; Short, 2006; Amrouni-Bouaziz et al., 2007; Soomere et al., 2008; Yates et al., 2011; Joevivek and Chandrasekar, 2014, 2017; Segtnan, 2014; Saravanan and Chandrasekar, 2015), this particular study provides a comprehensive view of the physical impact of wave refraction on grain size and depositional environment in accordance to the varying monsoonal condition.

In this research, about ten beaches were chosen between Thirukadaiyur and Velankanni along the central Tamil Nadu coast, India (Fig. 1). This area is mainly composed of the coastal plain, fringing the Eastern Ghats with varying altitude of 75 to 105 m. As majority of these coastal plain forms a part of the Cauvery delta, a thick cover of alluvium is commonly observed (Joevivek and Chandrasekar, 2014, 2017). Beaches are found to be in semi-diurnal tidal condition with mean high tide of 0.68 m and mean low tide of 0.28 m (Chart No. 3007, scale 1: 35 000, Year 2010,

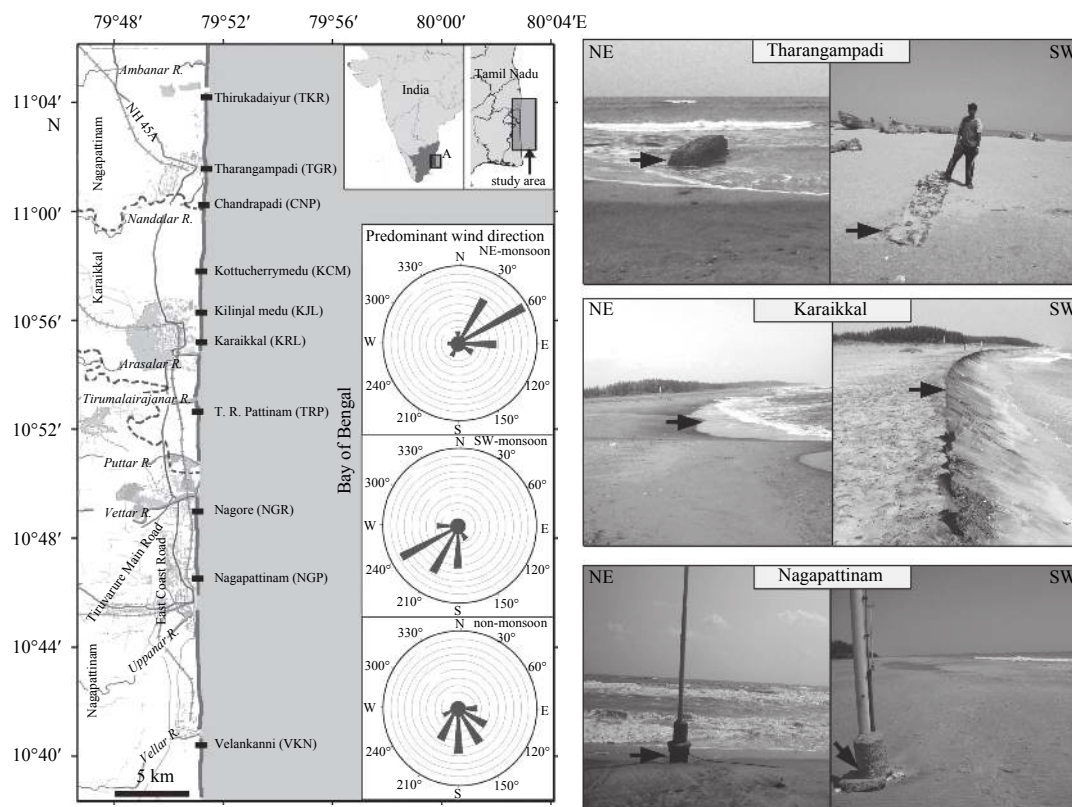*Corresponding author, E-mail: vjoevivek@gmail.com

Fig. 1. Location map of the study area. The wind rose diagram depicts predominant wind direction prevailed in the coast. The field photographs illustrate beach morphodynamic condition with respect to the NE and SW monsoon condition.

published by NHO, Dehradun). Wind speed is normally ranging between 11 to 26 km/h and the speed is observed to exceed 50–75 km/h during the storm/tropical cyclone condition. The corresponding study area encloses some of the major rivers namely Ambanar and Nandalar in the north, Arasalar, Tirumalairajanar, Puttar and Vettar in the central part and Uppanar and Vellar in the south. Majority of the subsurface water is consumed by the industries along the coastal regions, which is found to be a developing threat, apart from other threat caused by the industries. In addition to this, lowering of water levels below mean sea level is observed throughout the year due to the influence of natural and man-made activities. According to the Central Ground Water Board, Chennai–2011, the quality of the ground water in eastern and southeastern parts is insufficient. The cultivation of Paddy these regions has resulted in the extraction of the water from the aquifer and the fertilizers used for this purpose has also affected the medium. Mangroves are found to appear on the high tidal mudflats near the Karaikkal coast. The coastal stretch includes backwaters, salt pans, several distributaries channels, two fishing harbors and one port.

The northeast (NE) monsoon (October to January), southwest (SW) monsoon (June to September) and non-monsoon (February to May) are the three seasons, that is experienced by the study area, in a year. Though there were no official bounds, the formation of cyclones typically formed between May and December, with the peak from October to December along the east coast of Tamil Nadu. An analysis of the frequency of cyclones on the East coast of India between 1891 and 1995 shows 449 cyclones and 189 severe cyclonic storms occurred in and around east coast stretch which indicates that a moderate to severe cyclone hits the Tamil Nadu coast every two years during the NE monsoon. Re-

cently, tropical cyclones such as Thane (2011), Nilam (2012), Kyant (2016), Nada (2016), Vardah (2016) and Ockhi (2017) creates severe damage along the central Tamil Nadu coast. However, there is no significant storm effect found in the SW and non-monsoon seasons. It shows that formations of cyclones in these regions are strongly related to the seasonal migration of Inter Tropical Convergence Zone (ITCZ) (Dube et al., 1997).

2 Data and methods

The major parameters needed for the construction of wave refraction diagram is wave direction (angle in (°)), wave period (s), deep-water wave height (m) and bathymetry data. The wave period and the direction of wave approach the coast are obtained from the field observation. The field data is collected from 2011 till 2013 on a monthly and seasonal basis. From the field data, we observed that wave condition and grain size variations are stable for three years. Hence, we used the seasonal data of one year, instead of entire dataset (20 January 2011 (NE monsoon), 17 May 2011 (non-monsoon) and 12 September 2011 (SW monsoon)). The wave period is obtained by observing the time taken by waves for passing two successive crests at a fixed point. Thus the predominant high and low wave period is estimated from the observation of 300 successive waves. The direction of wave approach, along the coast is measured by observing the average direction of a floating buoyant plate at breaker zone within 30 minutes time period. The deep-water wave height is obtained from the wave atlas of the Indian coast (Chandramohan et al., 1990). The bathymetry of the present study region is extracted from Global 30 Arc-Second Elevation Data Set (GTOPO30).The wind and tide data were obtained from the online resource (https://www.windfinder.com/).

The wave refraction diagram for different monsoon seasons is created with the help of the computer program, the OceaN WavE Tool (ONWET). This software is exclusively designed for the beach morphology and wave analysis. This tool is mainly deployed in order to perform the special temporal analysis of beach profile, empirical orthogonal function (EOF) analysis, wave refraction analysis and quantifying sediment transport rate. This software is a window based application which is compiled under the Matlab environment. The outcome of the ONWET is reliable with the widely accepted wave refraction tools (Joevivek and Chandrasekar, 2016).

The beach and wave classification has been carried out by using breaking wave type and beach morphodynamic state model. Galvin (1968) proposed a semi empirical formula to estimate breaking wave type:

$$\zeta = \frac{\tan\beta}{(H_b/L_0)^{0.5}}\,, \tag{1}$$

where H_b is breaking wave height, L_0 is deep water wavelength, and β is foreshore slope (°). The data of breaking wave height and foreshore slope for the entire study area is shown in Table 1.

Similarly, morphodynamic state of beach system can be calculated based on Wright and Short's morphodynamic state model (Wright and Short, 1984):

$$\Omega = \frac{H_b}{w_s T}\,, \tag{2}$$

where w_s is the particle settling velocity and T is the wave period.

The results of breaking waves and morphodynamic state are classified into three domains (Short, 2006). The breaking wave type is classified as surging breakers, plunging breakers and spilling breakers. If $\zeta>2$, it is a surging breakers. If ζ is between 0.4 and 2, it is a plunging breakers, and if $\zeta<0.4$, it is a spilling breakers. Similarly, beach morphodynamic state can be categorized as reflective, intermediate and dissipative. If $\Omega<1$, it is a reflective beach. If Ω is between 1 and 6, it is an intermediate beach and if the value of $\Omega>6$, it is a dissipative beach.

The foreshore (swash zone) is the zone of land-water interaction and hence it is considered to be a major dynamic region. Therefore, sediment samples were collected from the foreshore region during the spring low tide. The precise region, from which the sample is obtained, is shown in Table 1. Aluminum grabber was used to collect surface sediments; it is properly labeled and taken to laboratory for grain size analysis. About 100 g were collected from each sample with the help of the coning and quartering method. These collected samples were further pre-treated through the following chemical processes. Initially, the clay fractions were removed by shuffling in the fresh water. Further, organic, inorganic contents and fine broken shells were removed by the addition of 6% H_2O_2, followed by the addition of 10% of HCl. The size of the pre-treated sediments was categorized based on the report of Wentworth (1922). A mechanical sieve shaker with quarter Φ interval from +40 to +230 ASTM units was used for sieving the pre-treated samples. The logarithmic method of moments was used to evaluate the statistical measure of sieve fractions as it produces a better reliable outcome, compared to that of the arithmetic, geometric and graphical measures (Blott and Pye, 2001). Further, depositional environment of the beach sediments were examined by traditional methods namely, bi-variant plot (Friedman, 1967; Moiola and Weiser, 1968), Visher plot or log–normal distribution curve (Visher, 1969) and CM diagram (C is the coarsest one percentile and M is the median grain size) (Passega, 1964).

3 Results and discussion

3.1 *Wave refraction*

The physical behavior of the waves is exhibited by wave refraction pattern, when these waves propagate from deep to shallow region. When waves enter the breaker zone, undertow current is interrupted by the sea bed. Hence wave speed and wavelength decreases while wave period remains constant (Davidson-Arnott and Greenwood, 2009; Masselink and Puleo, 2006). The direction of waves at breaker zone tends to become parallel to the shoreline, which creates refraction depending upon the bottom topography. Figure 2 illustrates elevation profile of seabed topography at 5 m interval contours. This figure shows the existence of a uniform and even seafloor in the northern part and a non-uniform and uneven seafloor in the central and southern part. The arrows represent the actual direction of wave approach, in the coast during different seasonal conditions. According to the traces of bottom topography the deep water waves are observed to approach the coast 45° (from NE to SW) during the NE monsoon. The contour traces along this direction reveals that the sea bed is relatively steady from the deeper to the shallow water region. On the other hand, deep water waves approach the coast at 135° from SE to NW direction and the contour traces along this direction reveals an uneven sea bed condition. During the non–monsoon period, the waves were observed to attain a calm condition and the direction of wave approach on the coast was observed to be at 90° (from E to W), almost normal to the shoreline.

The refraction patterns of wave approach at 45° in the wave period (T) of 8 and 10 s reveals a series of convergence zone at breaking point (Fig. 3). This convergence leads an increase in the wave height or energy that causes foreshore erosion (Fig. 1). During this period, the sediments are eroded by uprush and it is carried by back wash, towards surf zone (Joevivek and Chandrasekar, 2014, 2017). Due to collision between backwash and shoreward successive spilling breakers, the eroded sediments are formed as the sandbars in the surf zone (Table 1). In addition to that, almost all the river mouths in the study area reveal a convergence towards the shoreline, due to the presence of a shoal at the adjacent shoreface. The refraction patterns for 135° in a wave period of 8 and 10 s have shown a slight divergence pattern in the shoaling zone (Fig. 3). The presence of the sea bed topography at this position is uneven, as the wave rays diverge during the SW monsoon. Divergence reduces wave heights or energy that results in accretion or deposition. Therefore, the waves approaching the coast appeared to be surging breakers with calm condition at a constant wave period and with small amplitude (Table 1). In this process, sediments get deposited in the foreshore region; the heavies get settled at the beginning of the divergence zone and the lighter minerals get settled in the forth-coming stages (Fig. 1). The refraction patterns at 90° and T=8 and 10 s are almost similar and orthogonal to the shoreline (Fig. 3). During the process, the sandbars are destroyed by the plunging and collapsing breakers and it is further transported by onshore–offshore sediment transport (Joevivek and Chandrasekar, 2014, 2017).

3.1.1 *Impact on grain size distribution*

The textural results reveals that the foreshore sediments are mostly composed of medium to fine sand (1.71Φ–2.09Φ), moder-

Table 1. Grain size, beach and wave morphology along the entire study area during the different monsoonal condition

Grain size and wave morphology	TKR 11.073°N, 79.857°E	TGP 11.024°N, 76.856°E	CNP 11.002°N, 79.855°E	KCM 10.964°N, 79.854°E	KJL 10.940°N, 79.853°E	KRL 10.918°N, 79.853°E	TRP 10.883°N, 79.852°E	NGR 10.813°N, 79.851°E	NGP 10.787°N, 79.851°E	VKN 10.676°N, 79.854°E
NE monsoon										
Grain size parameters										
Mean (Φ)	2.06	2.07	2.06	2.06	2.07	2.08	2.07	2.09	2.09	2.11
Sorting (Φ)	0.57	0.58	0.53	0.55	0.58	0.58	0.57	0.58	0.58	0.67
Skewness (Φ)	1.13	1.11	1.12	1.12	1.09	1.06	1.08	1.00	1.00	0.94
Kurtosis (Φ)	2.92	2.89	2.90	2.93	2.86	2.79	2.89	2.69	2.71	2.59
Beach & wave parameters										
Breaking wave height/m	0.88	0.82	0.74	0.94	0.88	0.83	0.92	0.92	0.98	0.70
Foreshore slope/(°)	1.80	1.60	1.50	1.40	1.60	1.70	1.60	1.90	1.90	2.0
Beach morphodynamic state	dissipative	dissipative	dissipative	dissipative	dissipative	dissipative	dissipative	dissipative	dissipative	dissipative
Breaking wave type	spilling	spilling	spilling	spilling	spilling	spilling	spilling	spilling	spilling	spilling
Mean wave direction/(°)	45	45	45	45	45	45	45	45	45	45
Tide (high/low)/m	0.72/0.06	0.69/0.09	0.73/0.08	0.71/0.07	0.73/0.05	0.75/0.08	0.72/0.09	0.77/0.08	0.73/0.08	0.71/0.09
SW monsoon										
Grain size parameters										
Mean (Φ)	1.79	1.8	1.79	1.80	1.79	1.81	1.85	1.86	1.86	1.85
Sorting (Φ)	0.35	0.36	0.32	0.35	0.37	0.36	0.39	0.34	0.35	0.37
Skewness (Φ)	2.47	2.39	2.40	2.37	2.39	2.23	1.95	1.85	1.85	1.89
Kurtosis (Φ)	8.75	8.30	8.41	8.31	8.46	7.55	6.10	5.63	5.71	5.91
Beach & wave parameters										
Breaking wave height/m	0.48	0.67	0.49	0.46	0.42	0.68	0.38	0.41	0.53	0.46
Foreshore slope/(°)	9.78	10.49	10.44	9.45	9.31	10.51	11.51	10.82	10.79	9.64
Beach morphodynamic state	reflective	reflective	reflective	reflective	reflective	reflective	reflective	reflective	reflective	reflective
Breaking wave type	surging	surging	surging	surging	surging	surging	surging	surging	surging	surging
Mean wave direction/(°)	135	135	135	135	135	135	135	135	135	135
Tide (high/low)/m	0.94/−0.08	0.92/−0.09	0.91/−0.12	0.88/−0.13	0.92/−0.09	0.94/−0.08	0.92/−0.13	0.87/−0.14	0.89/−0.17	0.91/−0.15
Non-monsoon										
Grain size parameters										
Mean (Φ)	1.91	1.92	1.92	1.92	1.93	1.94	1.93	1.95	1.95	1.98
Sorting (Φ)	0.47	0.46	0.47	0.48	0.49	0.47	0.42	0.44	0.45	0.49
Skewness (Φ)	1.69	1.65	1.67	1.64	1.61	1.55	1.55	1.45	1.44	1.36
Kurtosis (Φ)	4.71	4.58	4.66	4.57	4.50	4.30	4.33	4.00	4.00	3.72
Wave parameters										
Breaking wave height/m	0.68	0.72	0.70	0.74	0.78	0.68	0.75	0.74	0.86	0.67
Foreshore slope/(°)	4.62	3.35	4.51	3.40	3.08	4.24	3.12	4.18	3.24	4.42
Beach morphodynamic state	intermediate	intermediate	intermediate	intermediate	intermediate	intermediate	intermediate	intermediate	intermediate	intermediate
Breaking wave type	plunging	collapsing	collapsing	plunging	plunging	plunging	collapsing	collapsing	plunging	collapsing
Mean wave direction/(°)	90	90	90	90	90	90	90	90	90	90
Tide (high/low)/m	0.82/0.15	0.89/0.16	0.83/0.19	0.81/0.17	0.84/0.21	0.82/0.18	0.85/0.19	0.87/0.16	0.83/0.18	0.81/0.19

Sampling site and geo-coordinate (stations from north to south, see Fig. 1)

Note: TKR represents Thirukadaiyur, TGP Tharangampadi, CNP Chandrapadi, KCM Kottucherrymedu, KJL Kilinjal medu, KRL Karaikkal, TRP T. R. Pattinam, NGR Nagore, NGP Nagapattinam, and VKN Velankanni.
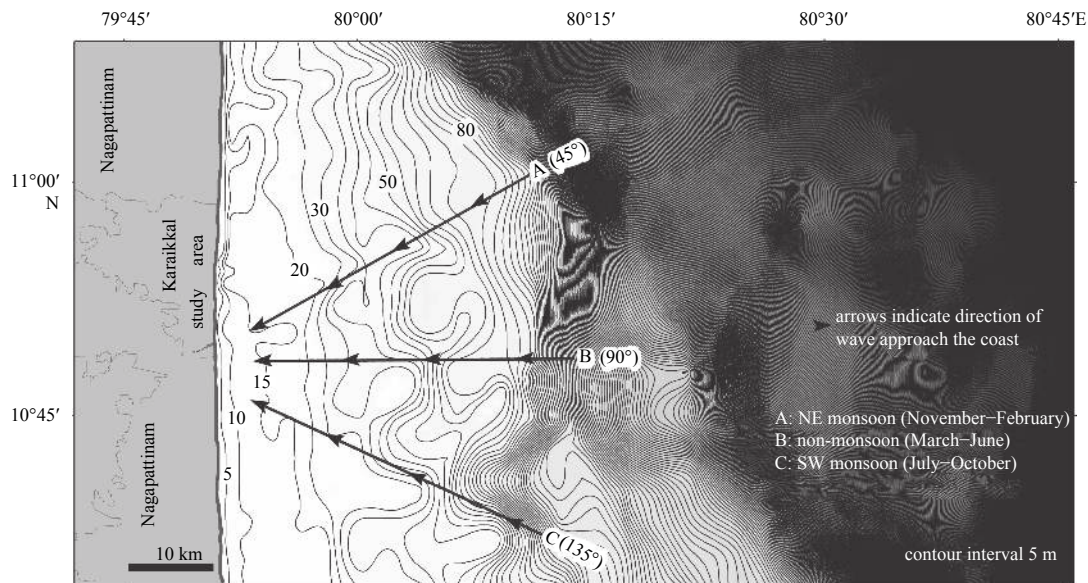
Fig. 2. Sea bed bottom topography of the study area is represented by the contour lines with 5 m interval. The arrow indicates direction of the wave approach the coast.

ately to very well sorted (0.67Φ–0.44Φ), fine skewed to very fine skewed (1.0Φ–2.47Φ) and mesokurtic to very leptokurtic (2.71Φ–8.75Φ) (Table 1). The mean value reflects the average size distribution that was influenced by the source of supply or environment of deposition. Figure 4 shows the grain size distribution and cumulative distribution of the sediment samples. The frequency curve plot shows the presence of bi-model grain size distribution in the coast. The first population peaked at 2Φ and the second population peaked at 3Φ. The first population increase from NE to SW monsoon clearly reflects the seasonal wave condition. During the SW and non-monsoon season, the medium size fraction tends to be highly populated as the sediment supplied by the swash zone posses low wave energy. Conversely, during the NE monsoon the second population reveals comparatively higher peak of the fine population which is probably due to the fluvial action along with active erosion of beach terrace. The cumulative plot shows the existence of similar grain size population in the entire study area. As observed, the NE monsoon displays a cumulative distribution blend of medium and fine sands. This is due to the sediments that were derived from mixture of wave and fluvial processes. However, in SW and non-monsoon season, medium sand is dominated as compared to fine sand. This is due to the sedimentation process that takes place by suspension process in calm wave condition.

During the NE monsoon, the majority of the sediments are fine grained with mixed population due to the influx of sediments by river discharge. In contrast, during the SW and non-monsoon seasons, sediments are medium grained with uniform population due to the continuous process of longshore sediment drift (Joevivek et al., 2018a). The variations observed in sediment sorting shows the nature of the wave energy and sediment transport, prevailed in the coast. Lesser sorting values denotes that sediments are better sorting by prolong transportation processes (Briggs, 1977; Dyer, 1986; Folk and Robles, 1964). During the SW monsoon, the study area accomplished less sorting values which indicates deposition caused by the onshore–offshore sediment transport. During the NE monsoon, coast experienced moderate sorting values that indicate moderately well sorted condition. The confluence of river mouth brought unconsolidated sedi-

ments, during the rainy season and therefore river sediments gets mixed with the offshore sediments which tends to reduce sorting nature.

From an entire study period, sediments reveals positive skewness which indicates that foreshore region had influenced fine skewed to very fine skewed conditions. The positive or negative sign of skewness indicate high or less wave energy conditions (Martins, 1965; Friedman, 1961; Duane, 1964). During the SW monsoon, sediments reveal a positive with very fine skewness that indicates continuous process of sediment deposition over a low energy wave condition. During the NE monsoon, the sediments became fine skewed (that is nearly symmetrical distribution), indicates the mixture of fluvial and beach sediments. The Kurtosis analysis shows that sediments are observed to be in mesokurtic to very leptokurtic nature. Higher kurtosis value revealed better sorting process while lower kurtosis value revealed poor sorting nature (Boggs, 2009). In this study, higher kurtosis value (leptokurtic to very leptokurtic) is noticed during the SW monsoon. It is due to the fact that, divergence waves produce better sorting by low energy wave propagation. During the NE monsoon, sediments attained lesser kurtosis value (mesokurtic) which indicates that, high energy waves leads to transport of river and beach sediments.

3.1.2 *Impact on sediment depositional environment*

The bivariant plot shows distinction within the group of samples of the entire coast with respect to the seasonal variation (Fig. 5a). The standard deviation against inclusive skewness indicates that moderately well sorted with fine skewed sediments are mostly of river and beach environments and well sorted with very fine skewed sediments are mostly of beach environment (Friedman, 1961). During the NE monsoon, convergence of waves influence suspended sediment transport of sediments present in the nearshore bed and adjacent to the river mouth. This causes mixture of sediment distribution and hence the source of deposition is mostly of river and beach. In contrast, during the SW and non-monsoon, divergence and calm waves produce the well sorted reworking of sediments by wave processes and therefore source of deposition belongs to the beach
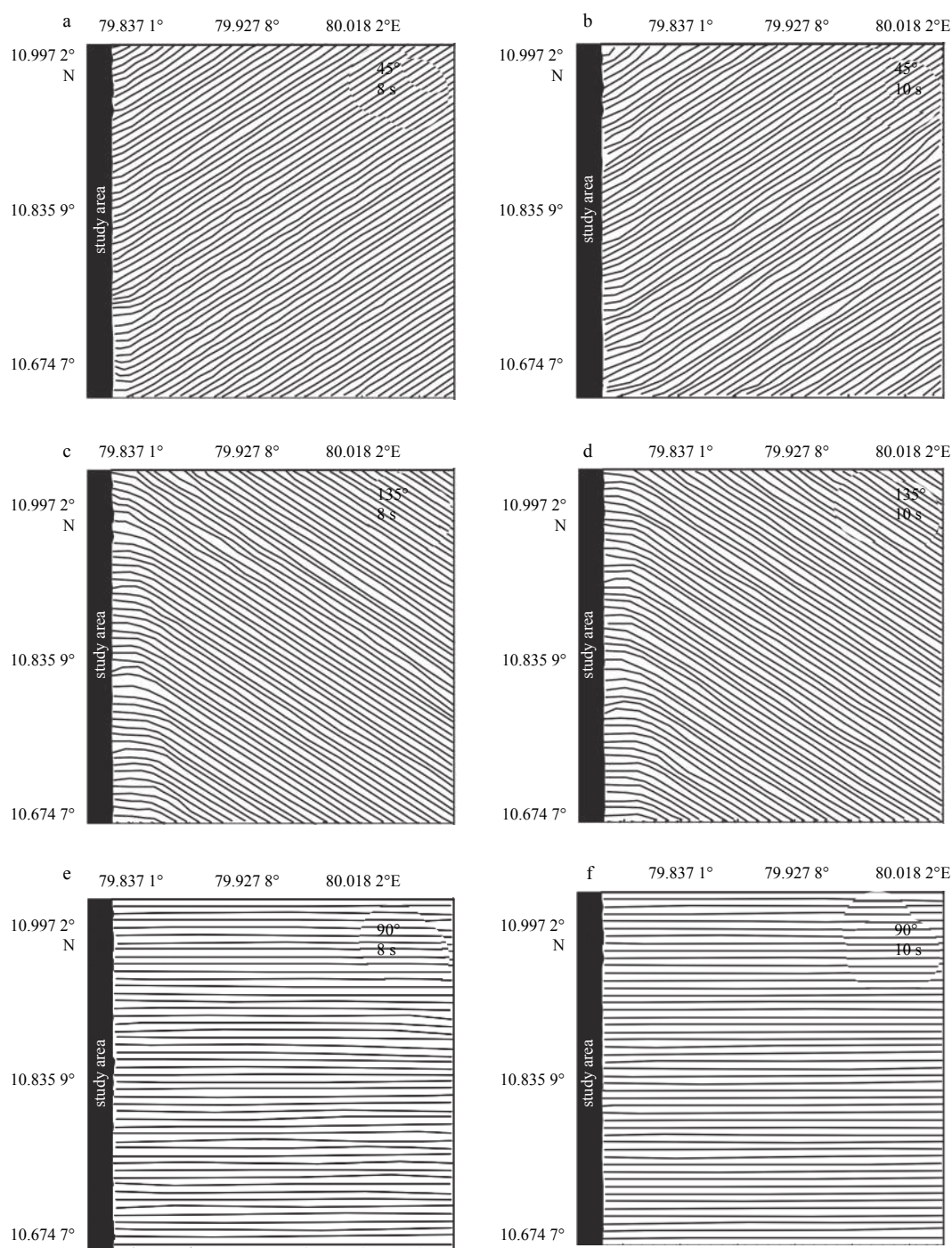
Fig. 3. Wave refraction diagram for the different seasonal condition. a and b. Refraction patterns of wave approach the direction of 45° and wave period (*T*) of 8 and 10 s, c and d. Refraction patterns of wave approach the direction of 135° and wave period (*T*) of 8 and 10 s, and e and f. refraction patterns of wave approach the direction of 90° and wave period (*T*) of 8 and 10 s.

environment.

As seen in the Visher plot (Fig. 5b), a well-developed suspension population noticed during the NE monsoon, while less suspension noticed during the SW monsoon. The presence of a suspension population and the truncation of the coarse population account for the positive skewness characteristic of foreshore deposits (Visher, 1969). The high suspension population during NE monsoon indicates high energy conditions, thereby depositing finer particles and the discharge of sediments by river and beach.

The grain size ranging from 1.25Φ to 2.25Φ falls under the traction population. The truncation between saltation and suspension within the range of 2.25Φ to 3.25Φ. The slope of saltation population is high during NE monsoon as compared to the SW monsoon. It reveals moderately well sorted saltation population and poorly sorted suspension population and implies that sediments are fluvial type (Angusamy and Rajamanickam, 2006). The gentle slope of saltation during SW monsoon, accomplished the deposition of suspended sediments and sand movement due to
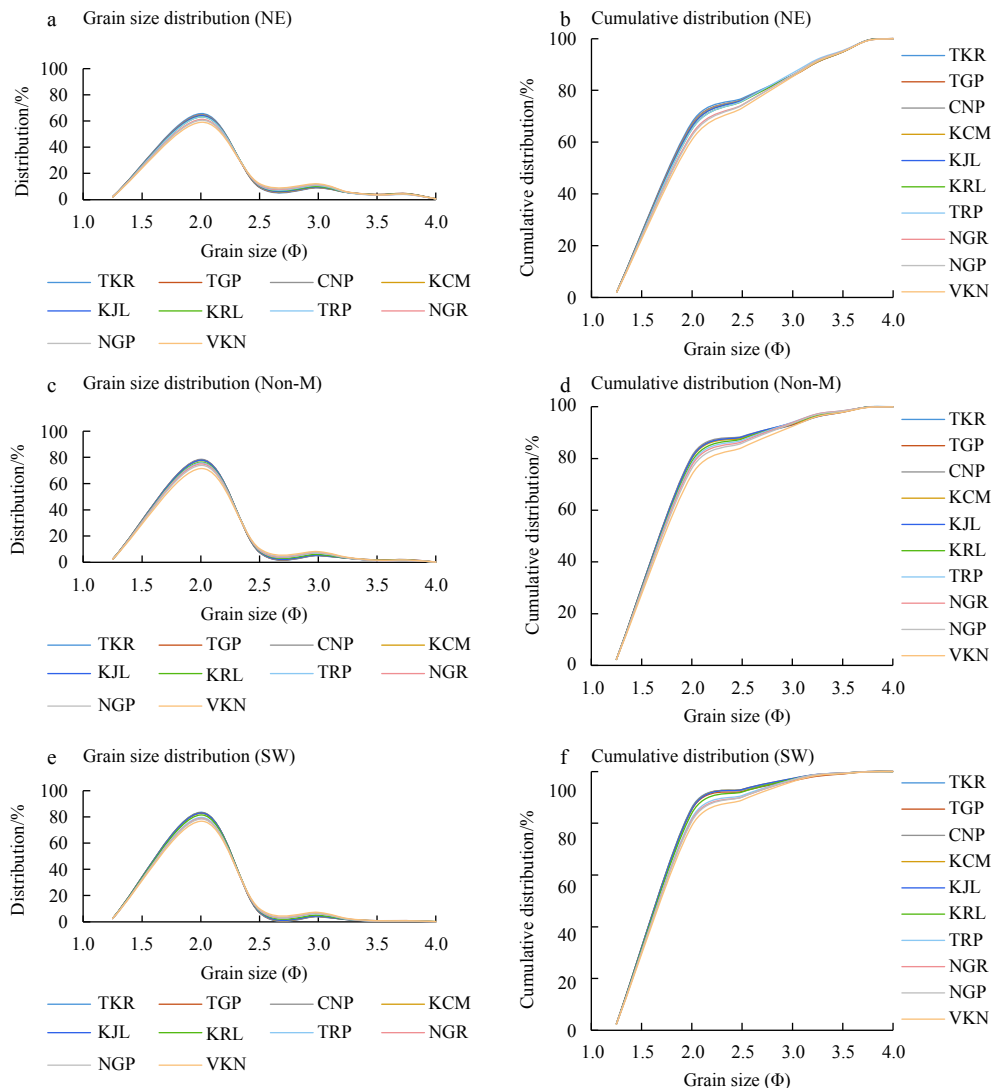
Fig. 4. Grain size and cumulative distribution in different seasons. a and b. Northeast (NE) monsoon (January 2013), c and d. non-monsoon (Non-M) season, and e and f. southwest (SW) monsoon. Stations: TKR represents Tirukadaiyur, TGP Tharangampadi, CNP Chandrapadi, KCM Kottucherrymedu, KJL Kilinjal medu, KRL Karaikkal, TRP T.R. Pattinam, NGR Nagore, NGP Nagapattinam, and VKN Velankanni.

littoral drift. As shown in the CM plot (Fig. 5c), the foreshore sediments falls under the uniform and graded suspension condition. During the NE monsoon, the predominant concentration of sediments is found to have segregated in PQ segment which has attested that the sediment samples of fluvial–marine process are influenced by the river discharge (Kulkarni et al., 2015). The convergent rays create maximum turbulence that leads to fluctuating size of the coarsest particles in the graded suspension (Rajaganapathi et al., 2013). Conversely, the sediments fall on overlying or uniform graded suspension (RS segment) during the SW monsoon. The divergence of waves decreases the turbulence, allowing the graded suspension to settle on the foreshore region. Hence, foreshore sediments appear as uniform suspension with well sorting nature during the SW monsoon.

3.2 *Present results compared with in situ beach condition*

The result of wave refraction and its impact on grain size and depositional environment is apparently correlated with the physical behavior of *in situ* beach and wave condition. During the NE

monsoon, waves break in the nearshore and cause significant widening of the surf zone and set a large amount of sediment in motion. Moreover, the beaches have attained flat terrace at low tide region by continuous erosion. This is due to the convergence of waves that leads to an increase the wave energy during the both uprush and backwash process. The energetic backwash lifts the foreshore sediments to form a serious of sandbars at the surf zone (Joevivek et al., 2018a). From field observation, it could be noted that the foreshore sediments are mostly of fine grained heavy minerals (Joevivek et al., 2018b). Since, the less density of light mineral sand is washed by onshore–offshore wave processes; hence foreshore region enriched of fine-grained heavies (Fig. 1). During the SW monsoon, foreshore region attained continuous deposition. The divergence of waves leads to decrease the wave energy so that it leads to the littoral drift, produces sediment deposition. Hence, the uprush waves continuously supplied sediments to the foreshore and lift negligible amount of sediments while backrush (Fig. 1).

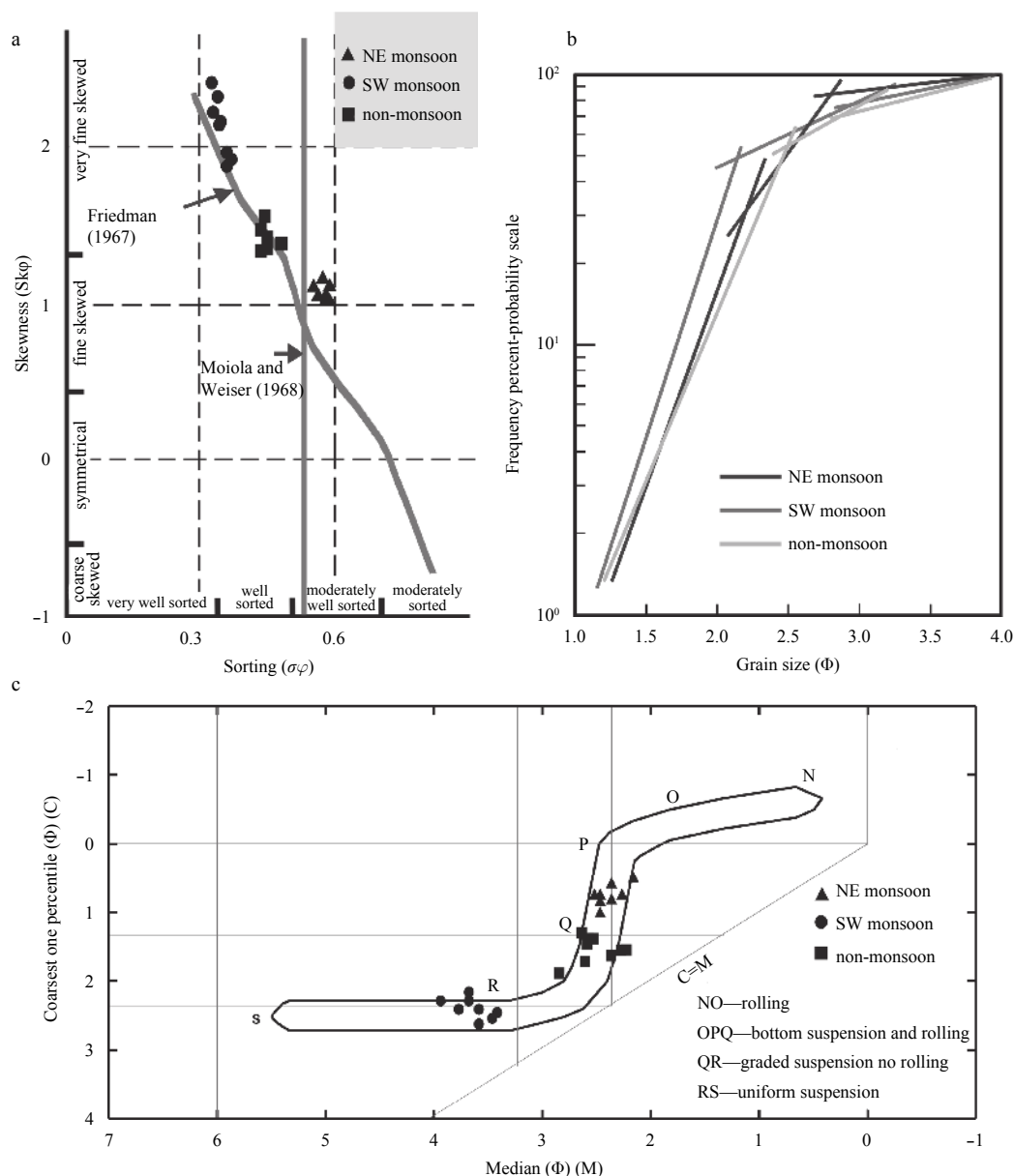During the study period, the key parameter that is often con-

Fig. 5. Sediment depositional environment derived from the grain size distribution. a. Bi-variant plot classifies the sediment depositional environment, b. Visher plot demarcates the traction, saltation and suspension characteristics of the grain size, c. CM diagram shows the source of sediment population and depositional environment.

sidered for understanding the sediment distribution is the tidal fluctuation. Generally, the erosion process happens during the rising tide whereas the accretion process happens during the falling tide diurnally (Darsan, 2013). In the case of the micro-tidal beach systems, these short-term variations are considered to be insignificant and in case of assessing the long-term beach morphodynamics, tides are considered to be insignificant (Short, 1996). Nevertheless, the fluctuation in the tidal range is found to influence the shape, nature of the beach and the surf zone morphodynamics (Davis and Hayes, 1984; Short, 1991). From the above mentioned, it can be observed that the study area reveals the following conditions. During the southwest monsoon, it is found to be reflective beach state and mean spring tide range is relatively high (>1.0 m) (Table 1). The beach face appeared as steep slope, and a pronounced coarse step is usually found at the base of the swash zone fronted by a lower gradient. Whereas,

during the northeast monsoon, dissipative beach with low spring tide range (<0.7 m) showing spilling breakers and the low gradient beach face (see field photograph of Karaikkal in Fig. 1). Similarly, non-monsoon season shows spring tide range of <0.6 m which reflects the plunging and collapsing breakers and the transverse bar and rip beach system (Short, 1996). This physical phenomenon is consistent with the results obtained from the wave refraction, grain size and depositional environment. Overall, the NE monsoon waves erode the beach material and the SW and non-monsoon season waves rebuild it which results in stability of beach and nearshore condition over an annual cycle.

for their help in developing the manuscript.

References

Amrouni-Bouaziz O, Souissi R, Barusseau J P, et al. 2007. Grain-size and morphodynamical state of the bay-of-Mahdia shoreface (Tunisia). Contribution to the assessment of coastal sensitivity. Geo-Eco-Marina, No 13/2007, 5–19. http://doi.org/10.5281/zenodo.57333

Angusamy N, Rajamanickam G V. 2006. Depositional environment of sediments along the southern coast of Tamil Nadu, India. Oceanologia, 48(1): 87–102

Angusamy N, Udayaganesan P, Rajamanickam G V. 1998. Wave refraction pattern and its role in the redistribution of sediment along southern coast of Tamilnadu, India. Indian Journal of Geo-Marine Sciences, 27(2): 173–178

Bird E C F. 2000. Coastal Geomorphology: An Introduction. New York: John Wiley & Sons, 322

Blott S J, Pye K. 2001. GRADISTAT: A grain size distribution and statistics package for the analysis of unconsolidated sediments. Earth Surface Processes and Landforms, 26(11): 1237–1248, doi: 10.1002/esp.v26:11

Boggs S Jr. 2009. Petrology of Sedimentary Rocks. 2nd ed. Cambridge: Cambridge University Press, 600

Briggs D J. 1977. Sources and Methods in Geography: Sediments. London: Butterworth and Co (Publ) Ltd, 55–86

Chandramohan P, Nayak B U, Raju N S N. 1990. Wave tables for the Indian coast based on ship observations (1968–1986). National Institute of Oceanography, GOA, 312

Darsan J. 2013. Beach morphological dynamics at Cocos Bay (Manzanilla), Trinidad. Atlantic Geology, 49: 151–168, doi: 10.4138/atlgeol.2013.008

Davidson-Arnott R G D, Greenwood B. 2009. Waves and sediment transport in the nearshore Zone. In: Islaay F I, ed. Coastal Zones and Estuaries (Volume I). Encyclopedia of Life Support Systems (EOLSS). Paris, France: UNESCO, Eolss Publishers, 43–60

Davis R A, Hayes M O. 1984. What is a wave-dominated coast?. Marine Geology, 60(1–4): 313–329, doi: 10.1016/0025-3227(84)90155-5

Duane D B. 1964. Significance of skewness in recent sediments, Western Pamlico Sound, North Carolina. Journal of Sedimentary Research, 34(4): 864–874

Dube S K, Rao A D, Sinha P C, et al. 1997. Storm surge in the Bay of Bengal and Arabian Sea: The problem and its prediction. Mausam, 48(2): 283–304

Dyer K R. 1986. Coastal and Estuarine Sediment Dynamics. New York: John Wiley and Sons Ltd, 342

Folk R L, Robles R. 1964. Carbonate sands of Isla Perez, alacran reef complex, Yucatán. The Journal of Geology, 72(3): 255–292, doi: 10.1086/626986

Friedman G M. 1961. Distinction between dune, beach, and river sands from their textural characteristics. Journal of Sedimentary Research, 31(4): 514–529

Friedman G M. 1967. Dynamic processes and statistical parameters compared for size frequency distribution of beach and river sands. Journal of Sedimentary Research, 37(2): 327–354

Galvin C J. 1968. Breaker type classification on three laboratory beaches. Journal of Geophysical Research, 73(12): 3651–3659, doi: 10.1029/JB073i012p03651

Harrison W, Wilson W S. 1964. Development of A Method for Numerical Calculation of Wave Refraction. Washington: Coastal Engineering Research Centre

Jing Lou, Massel S R. 1994. A combined refraction-diffraction-dissipation model of wave propagation. Chinese Journal of Oceanology and Limnology, 12(4): 361–371, doi: 10.1007/BF02850497

Joevivek V, Chandrasekar N. 2014. Seasonal impact on beach morphology and the status of heavy mineral deposition-central Tamil Nadu coast, India. Journal of Earth System Science, 123(1): 135–149, doi: 10.1007/s12040-013-0388-6

Joevivek V, Chandrasekar N. 2016. ONWET: A simple integrated tool for beach morphology and wave dynamics analysis. Marine

Georesources & Geotechnology, 34(6): 581–593, doi: 10.1080/1064119x.2015.1040904

Joevivek V, Chandrasekar N. 2017. Data on nearshore wave process and surficial beach deposits, central Tamil Nadu coast, India. Data in Brief, 13: 306–311, doi: 10.1016/j.dib.2017.05.052

Joevivek V, Chandrasekar N, Saravanan S, et al. 2018a. Spatial and temporal correlation between beach and wave processes: Implications for bar-berm sediment transition. Frontiers of Earth Sciences, 12(2): 349–360, doi: 10.1007/s11707-017-0655-y

Joevivek V, Chandrasekar N, Shree P K. 2018b. Influence of porosity in quantitative analysis of heavy mineral placer deposits. Oceanography & Fisheries Open Access Journal, 6(3): 555689, doi: 10.19080/OFOAJ.2018.06.555689

Kirby J T, Dalrymple R A. 1994. Combined Refraction/Diffraction Model REFDIF-1, Version 2.5. Technical Report No. CACR-94-22. Newark, DE: Center for Applied Coastal Research, Department of Civil Engineering, University of Delaware, 122

Kulkarni S J, Deshbhandari P G, Jayappa K S. 2015. Seasonal variation in textural characteristics and sedimentary environments of beach sediments, Karnataka Coast, India. Aquatic Procedia, 4: 117–124, doi: 10.1016/j.aqpro.2015.02.017

Kunte P D, Wagle B G, Sugimori Y. 2001. Littoral transport studies along west coast of India—A review. Indian Journal of Marine Sciences, 30(2): 57–64

López-Ruiz A, Solari S, Ortega-Sánchez M, et al. 2015. A simple approximation for wave refraction—Application to the assessment of the nearshore wave directionality. Ocean Modelling, 96: 324–333, doi: 10.1016/j.ocemod.2015.09.007

Martins L R. 1965. Significance of skewness and kurtosis in environmental interpretation. Journal of Sedimentary Research, 35(3): 768–770, doi: 10.1306/74D7135C-2B21-11D7-8648000102C1865D

Masselink G, Puleo J A. 2006. Swash-zone morphodynamics. Continental Shelf Research, 26(5): 661–680, doi: 10.1016/j.csr.2006.01.015

Mathiesen M. 1987. Wave refraction by a current whirl. Journal of Geophysical Research, 92(C4): 3905–3912, doi: 10.1029/JC092iC04p03905

Moiola R J, Weiser D. 1968. Textural parameters: An evaluation. Journal of Sedimentary Research, 38(1): 45–53

Munk W H, Traylor M A. 1947. Refraction of ocean waves; A process linking underwater topography to beach erosion. The Journal of Geology, 55(1): 1-26

Orr T E. 1969. Numerical calculation of wave refraction by digital computer. Texas: Texas A&M University

Passega R. 1964. Grain size representation by CM patterns as a geologic tool. Journal of Sedimentary Research, 34(4): 830–847, doi: 10.1306/74D711A4-2B21-11D7-8648000102C1865D

Rajaganapathi V C, Jitheskumar N, Sundararajan M, et al. 2013. Grain size analysis and characterization of sedimentary environment along Thiruchendur coast, Tamilnadu, India. Arabian Journal of Geosciences, 6(12): 4717–4728, doi: 10.1007/s12517-012-0709-0

Saravanan S, Chandrasekar N. 2015. Wave Refraction Pattern and Littoral Sediment Transport along the SE Tamilnadu Coast, India. Journal of Coastal Research, 31(2): 291–298

Segtnan O H. 2014. Wave refraction analyses at the coast of norway for offshore applications. Energy Procedia, 53: 193–201, doi: 10.1016/j.egypro.2014.07.228

Shepard F P, Inman D L. 1950. Nearshore water circulation related to bottom topography and wave refraction. Eos, Transactions American Geophysical Union, 31(2): 196–212, doi: 10.1029/TR031i002p00196

Short A D. 1991. Macro-meso tidal beach morphodynamics: An overview. Journal of Coastal Research, 7(2): 417–436

Short A D. 1996. The role of wave height, period, slope, tide range and embaymentisation in beach classifications: a review. Revista Chilena de Historia Natural, 69(4): 589–604

Short A D. 2006. Australian beach systems-nature and distribution. Journal of Coastal Research, 22(1): 11–27

Skovgaard O, Bertelsen J A, Jonsson I G. 1975. Computation of wave heights due to refraction and friction. Journal of the Waterways,

Harbors and Coastal Engineering Division, 101(1): 15–32

Soomere T, Kask A, Kask J, et al. 2008. Modelling of wave climate and sediment transport patterns at a tideless embayed beach, Pirita Beach, Estonia. Journal of Marine Systems, 74: S133–S146, doi: 10.1016/j.jmarsys.2008.03.024

Visher G S. 1969. Grain-size distributions and depositional processes. Journal of Sedimentary Petrology, 39(3): 1074–1106

Wentworth C K. 1922. A scale of grade and class terms for clastic sedi-

ments. The Journal of Geology, 30(5): 377–392, doi: 10.1086/622910

Wright L D, Short A D. 1984. Morphodynamic variability of surf zones and beaches: A synthesis. Marine Geology, 56(1–4): 93–118, doi: 10.1016/0025-3227(84)90008-2

Yates M L, Guza R T, O'Reilly W C, et al. 2011. Equilibrium shoreline response of a high wave energy beach. Journal of Geophysical Research, 116(C4): C04014

Perspective

Invasion of the biosphere by synthetic polymers: What our current knowledge may mean for our future

Charles J. Moore[1]*

[1] Algalita Marine Research and Education, Long Beach CA 90803, USA

In 1974, a member of the Council of the British Plastics Federation and a fellow of the Plastics Institute, stated that "Plastics litter is a very small proportion of all litter and causes no harm to the environment except as an eyesore"(Derraik, 2002). It has taken less than fifty years for that opinion to be completely discredited, indeed, that opinion was already in doubt the moment it was stated. Nevertheless, it was the strong denial by the plastic industry that plastics could cause harm that delayed the study of plastic's environmental effects for decades. Not until Moore et al. (2001) found six times as much plastic as zooplankton by weight in the surface waters of the North Pacific Subtropical Gyre (NPSG), did plastic environmental pollution begin to receive increasing attention by scientists, policy makers, regulators, and the media, who began referring to the area as "The Great Pacific Garbage Patch", a term coined by an oceanographer, Curtis Ebbesmeyer (Ebbesmeyer and Scigliano, 2009). Today it is widely acknowledged that vagrant plastic waste is polluting oceans, rivers, soil, food, the water we consume, and even the air we breathe. The invasion of this synthetic waste into organisms is facilitated by the fact that with surface ablation and disintegration mechanisms over time, micro- and nano-sized synthetic polymers are created that can be readily assimilated into living organisms. Recent studies reveal that these micro- and nano- scale polymers, which sorb and desorb pollutants, can pass through the intestinal wall and from the lungs to the circulatory system and in contact with human cells produce reactive oxygen species (ROS), which are implicated in many pathologies (Schirinzi et al., 2017). As primarily a marine scientist, I focus on the threats to marine ecosystems, but the topic of plastic pollution has grown to global proportions affecting not only the biosphere, but geological formations as well. Here I present a summary of the work done to date to understand our situation and discuss briefly the future of plastic pollution.

Use of plastic in construction of natural structures:

(1) As early as 1973, Kartar et al. (1973) reported polychaetes in the Severn estuary incorporating plastic pellets into their dwelling tubes.

(2) I have observed nests of birds and rodents with plastic as a nest building material.

(3) MacIvor and Moore (2013) found bees constructing brood cells with bits of plastic bags and polyurethane sealant.

(4) Reichert et al. (2018) found that reef building corals built their bodies around adhering plastic particles.

(5) Corcoran et al. (2014) identified in Hawaii "...the appearance of a new 'stone' formed through intermingling of melted plastic, beach sediment, basaltic lava fragments, and organic debris...which could be preserved by burying in marine sediments and signals...the occurrence of the informal Anthropocene epoch".

(6) Beach sands are increasing the percentage of microplastics incorporated and the speculation by Gregory (1977) that mankind will sunbathe on plastic sand beaches is becoming a reality.

Use of plastic as an aid in reproduction and range extension for organisms:

(1) Gregory (2009) called out "alien invasions" on plastic: "Dispersal of aggressive alien and invasive species...could endanger sensitive, or at-risk coastal environments (both marine and terrestrial) far from their native habitats."

(2) Zettler et al. (2013) found that these invaders were composed of unique communities that: "...are distinct from surrounding surface water, implying that plastic serves as a novel ecological habitat in the open ocean".

(3) Goldstein et al. (2012) found that floating plastic in the NPSG... "released the pelagic insect *Halobates sericeus* from substrate limitation for oviposition. High concentrations of microplastic in the NPSG resulted in a positive correlation between *H. sericeus* and microplastic, and an overall increase in *H. sericeus* egg densities."

(4) In a survey of benthic plastic, Gündoğdu et al. (2017) stated: "plastic debris as a substrate can contain a very high diversity of life just like natural substrates". And for organisms on surface plastics, Goldstein et al. (2014) observed that: "diversity patterns on plastic debris are compatible with the concept of island biogeography".

Given these findings, it seems logical to conclude that an increase in plastic "islands" would correspond to an increase in associated populations of organisms adapted to the introduced plastic habitat, and if in an area of limited food resources, that there would be a decrease of certain members of the indigenous population. As in any major ecosystem disruption, there will be winners and losers. In the marine environment of the depauperate gyres, where floating plastics accumulate, winners are likely to be epibionts and losers true pelagics. In the area where I work, the NPSG, I have noticed fewer salps as the number of barnacles on marine debris increases.

---

*Corresponding author, E-mail: cmoore@algalita.org

Ingestion of plastic by organisms:

(1) Plastic ingestion by marine megafauna (Germanov et al., 2018), fishes (Boerger et al., 2010; Lusher et al., 2013; Rochman et al., 2015), birds (Robards, 1993; Moser and Lee, 1992; van Franeker et al., 2011), jellyfish (Macali et al., 2018), marine worms (Browne et al., 2013), bivalves, corals (that have been said to find the plastic "tasty"), and zooplankton, point to the ability of synthetic polymers to mimic natural food throughout the entire food web, even in terrestrial soils, where Zhu et al. (2018) found that a common soil arthropod consumed plastic, which perturbed their gut microbiota. Plastic "food" does not provide nutrients, or decompose in the digestive tract. Rather it blocks passages, delivers pollutants and damages the epithelial lining.

(2) Plastic in its most insidious form is micro and nano sized; whether formed purposely for commerce or through the wearing and weathering of larger objects. At these size classes it has been shown to enter the brain of fishes and the physical features of the particles themselves cause more damage than the associated pollutants (Mattsson et al., 2017). The authors noted physiological and behavioral changes in the fish: less water than normal in the brain, less time feeding and less distance covered looking for food.

(3) Small plastic fibers and fragments are being ingested by humans in salt from different countries (Karami et al., 2017), in all types of water tested (Schymanski et al., 2018), and through respiration by humans, causing an inflammatory response and lesions in human cells (Prata, 2018). Catarino et al. (2018) stated that: "Our predictions of microplastics ingestion by humans via consumption of mussels is 123 particles every year for each person in the UK and can go up to 4 620 particles every year for each person in countries with a higher shellfish consumption. By comparison, the risk of plastic ingestion via mussel consumption is minimal when compared to fibre exposure during a meal via dust fallout in a household (13 731–68 415 particles every year for each person)."

Physiologists are beginning to assess the health impacts to humans and other animals caused by ingestion of micro- and nano-plastics, their two major lines of inquiry may be categorized as:

(1) Kinetics—how does the plastic get into organisms and where will it go?

(2) Effects—what will the plastic and associated toxicants do once assimilated into an organism?

These criteria are used in a request for proposals by the Dutch government, which has put up a million Euros to study human health impacts of plastics.

In Greek mythology, Zeus, king of the gods, created the first woman on earth, Pandora, in order to deliver a punishment to the first men for having obtained fire stolen from the gods. Pandora was made to be beautiful so that her delivery of the god's punishment to mankind in a sealed earthen jar would not raise an alarm. Pandora did not know there was anything dangerous in the jar, and though she had been warned to never open it, her curiosity overcame her, and when all around her were asleep, she opened it. Out flew "the thousand natural shocks that flesh is heir to" (Hamlet, Act III, Scene 1). When she saw what she had done and felt the stings of bugs she released, she attempted to put the troubles back in the jar without success. Plastics, like fire, confer innumerable opportunities for mankind, but mankind has not kept shut the jar containing plastic waste, and it is now impossible to retrieve it. The set of troubles caused by plastic waste is of a magnitude to affect essential planetary systems such as water, air and soil.

Dust and marine sediments were formerly of mineral origin and settled out of air and water or were removed through the action of natural barriers and other mechanisms. Plastic has characteristics that vary widely depending on type of polymer, but many plastics become neutrally buoyant, yet sediment-like and proliferate at different levels in the water column in complex ways, and their similarity to natural fibers allows them to occupy environmental niches formerly occupied by natural, biodegradable materials. The dictum that "in ecosystems, nothing is wasted" is challenged by synthetic polymers. Plastic waste accumulates and becomes more than ecosystems can process. This situation has been conceived of as the crossing of a "planetary boundary". Three criteria are used to determine if plastic pollution is a planetary boundary threat: Is it poorly reversible? Are there effects only visible at a planetary scale? Is there a disruptive effect on Earth-system processes?

Criteria 1 has clearly been met. It will be impossible to remove plastic waste from most niches of the environment.

Criteria 2: Villarrubia-Gómez et al. (2017) state: "...despite the fragmented state of current evidence, the mismanagement of discarded plastic is already implicated in globally systemic alteration to food webs, habitats, and biogeochemical flows". If it is not clear that criteria 2 has already been met, it shortly will be. In my own research, I have identified large areas of the ocean where surface plastics outweigh and in some cases outnumber the associated zooplankton (Moore et al., 2001).

Criteria 3: While most investigators believe that this question remains to be answered, and their focus is mainly on how ocean plastics retard carbon sequestration (Villarrubia-Gómez et al., 2017), I believe there is enough evidence from widely diverse sources to make the claim that the fitness of earth's biology as a whole is negatively affected by plastics and their associated chemicals. I believe that there are only negative consequences of plastic ingestion, that it is occurring on a planetary scale, and that it is rapidly increasing. Curtis Ebbesmeyer has termed ocean plastic pollution, "the greatest infection of the sea", and plastic pollution of air and fresh water threatens the circular loop of the water cycle as a clean source for drinking.

Over a decade ago, it was recognized at a conference where I presented, held by the World Federation of Scientists in Erice, Sicily, that the pollution of water by plastic was a planetary emergency. During that conference, I was able to enlist an editor of the Philosophical Transactions of the Royal Society to devote an issue to the problem. I was one of the editors of "Our Plastic Age", along with Richard Thompson, Fred vom Saal and Shanna Swan (Thompson et al., 2009). We were able to publish the first connection between chemicals sorbed to plastics and their transmission to wildlife (Teuten et al., 2009). Vagrant plastics may not be the main link in the transfer of manmade toxicants to biological systems, but their role is ever increasing.

The timid response to this planetary emergency caused by misuse of what I term "the solid phase of petroleum" is in part due to the adoption of petroleum industry tactics by the plastics industry. In papers quantifying plastic entering the environment, "leakage" is a term often used. Although plastic is a solid, it can spill (Webster definition: to cause or allow accidentally or unintentionally to fall, flow, or run out so as to be lost or wasted). Industries' modus operandi is to *spill*, *study and stall*. Compared to the petroleum industry,

the plastic industry has done little to study the problem of plastic waste, preferring to put the blame on consumers for irresponsible disposal, and the cost of research and cleanup is borne by both governmental and non-governmental institutions and society at large. Industry lobbyists have spent millions of dollars to stall proposed remedies such as carrier bag bans. Industry has not, however, resisted the regulating of plastic pellet loss from factories in the State of California, acknowledging the loss of virgin polymer feedstock as their "personal responsibility problem". Thus, based on my research funded by the California Water Resources Control Board to find how much of this plastic industry feedstock was lost to the aquatic environment; we were able to pass legislation to make their discharge illegal in California. As with most regulations, enforcement lags behind legislation.

Natural disasters such as floods, hurricanes and tsunamis also release millions of tons of plastic into the environment. If plastic were liquid petroleum, technologies would be deployed to retrieve the material after a disaster, but no laws or regulations mandate such a response for plastic, even though plastic will persist far longer in the environment than petroleum, and potentially cause more harm over time.

Part of the problem with our response to the plastic pollution crisis is the unrealistic assessment of possibilities by researchers themselves. In a paper titled "Global research priorities to mitigate plastic pollution impacts on marine wildlife", Vegter et al. (2014) concludes by saying: "Although there are still many questions surrounding the issue, the numerous negative impacts of plastic pollution make it clear that we must strive to reduce the amount of plastics reaching our oceans. If the methods for doing so are attainable (e.g., reducing plastic use, improvements in waste management, better access to recycling) and the costs are non-prohibitive, it would be feasible to deal with what is ultimately an entirely avoidable problem." It seems that at just this point, the scientists stop being objective and revert to fantasy. On a global scale, there is no evidence that the methods enumerated for reducing the amount of plastics entering the ocean are attainable. Plastic use will surge with 3-D printing of everything imaginable, recycling costs are prohibitive and the fraction of plastic waste recycled globally remains under 10%. Waste management is focused globally on incineration and landfilling, both of which create greenhouse gasses and waste the billions of dollars spent on the fabrication of valuable commodities from plastic feedstocks. Given the difficulty of capturing ubiquitous plastic of all types and sizes from earth orbit to the ocean depths, I ask: In what fantasy universe is plastic pollution "an entirely avoidable problem"?

In the Greek myth, Pandora, after releasing the world's torments, tried to put the lid back on the jar where they were once contained, but she failed. As she sat crying, one last creature flew out. Zeus had sent *Hope* to compensate mankind for its perpetual struggle. While there may be no hope of cleaning plastic from the environment in the foreseeable future, there is hope that mankind can respect and fear plastic enough to treat it with great care, by designing products and creating take-back infrastructure that makes plastic benign. It is difficult to imagine this, however, in a world where plastic is the omnipresent facilitator of global trade by packaging commodities in a vapor and moisture barrier, preserving "newness". But when the wrapper is ripped off, it becomes useless, and for many of the products it contains, the newness quickly fades, and they are replaced sooner rather than later. Hope seems a weak ally in the fight against the plastic plague overtaking our precious ocean, our land, our air, our water, and even the space around us with millions of waste plastics in earth orbit. The only ally powerful enough to push back against the "Plastic Attack", is us, all of us, and it will require that we fear plastic sufficiently to demand reduction in its use drastically. That fear will only come when plastic's dangers are widely exposed. Scientists are helping in this effort, as nature herself begins to spew plastic vomit worldwide. A world economy dependent on making and reproducing persistent, destructive and unrecoverable waste en masse is in no sense, sustainable.

References

Boerger C M, Lattin G L, Moore S L, et al. 2010. Plastic ingestion by planktivorous fishes in the North Pacific Central Gyre. Marine Pollution Bulletin, 60(12): 2275–2278

Browne M A, Niven S J, Galloway T S, et al. 2013. Microplastic moves pollutants and additives to worms, reducing functions linked to health and biodiversity. Current Biology, 23(23): 2388–2392, doi: 10.1016/j.cub.2013.10.012

Catarino A I, Macchia V, Sanderson W G, et al. 2018. Low levels of microplastics (MP) in wild mussels indicate that MP ingestion by humans is minimal compared to exposure via household fibres fallout during a meal. Environmental Pollution, 237: 675–684, doi: 10.1016/j.envpol.2018.02.069

Corcoran P L, Moore C J, Jazvac K. 2014. An anthropogenic marker horizon in the future rock record. GSA Today, 24(6): 4–8, doi: 10.1130/GSAT-G198A.1

Derraik J G B. 2002. The pollution of the marine environment by plastic debris: a review. Marine Pollution Bulletin, 44(9): 842–852, doi: 10.1016/S0025-326X(02)00220-5

Ebbesmeyer C, Scigliano E. 2009. Flotsametrics and the Floating World: How One Man's Obsession with Runaway Sneakers and Rubber Ducks Revolutionized Ocean Science. New York: Harper Collins, 167

Germanov E S, Marshall A D, Bejder L, et al. 2018. Microplastics: no small problem for filter-feeding megafauna. Trends in Ecology & Evolution, 33(4): 227–232

Goldstein M C, Carson H S, Eriksen M. 2014. Relationship of diversity and habitat area in North Pacific plastic-associated rafting communities. Marine Biology, 161(6): 1441–1453, doi: 10.1007/s00227-014-2432-8

Goldstein M C, Rosenberg M, Cheng Lanna. 2012. Increased oceanic microplastic debris enhances oviposition in an endemic pelagic insect. Biology Letters, 8(5): 817–820, doi: 10.1098/rsbl.2012.0298

Gregory M R. 1977. Plastic pellets on New Zealand beaches. Marine Pollution Bulletin, 8(4): 82–84, doi: 10.1016/0025-326X(77)90193-X

Gregory M R. 2009. Environmental implications of plastic debris in marine settings—entanglement, ingestion, smothering, hangers-on, hitch-hiking and alien invasions. Philosophical Transactions of the Royal Society B: Biological Sciences, 364(1526): 2013–2025, doi: 10.1098/rstb.2008.0265

Gündoğdu S, Çevik C, Karaca S. 2017. Fouling assemblage of benthic plastic debris collected from Mersin Bay, NE Levantine coast of Turkey. Marine Pollution Bulletin, 214(1): 147–154

Karami A, Golieskardi A, Choo C K, et al. 2017. The presence of microplastics in commercial salts from different countries. Scientific Reports, 7: 46173, doi: 10.1038/srep46173

Kartar S, Milne R A, Sainsbury M. 1973. Polystyrene waste in the Severn Estuary. Marine Pollution Bulletin, 4(9): 144

Lusher A L, McHugh M, Thompson R C. 2013. Occurrence of microplastics in the gastrointestinal tract of pelagic and demersal fish from the English Channel. Marine Pollution Bulletin, 67(1–2): 94–99

Macali A, Semenov A, Venuti V, et al. 2018. Episodic records of jellyfish ingestion of plastic items reveal a novel pathway for trophic transference of marine litter. Scientific Reports, 8(1): 6105, doi: 10.1038/s41598-018-24427-7

MacIvor J S, Moore A E. 2013. Bees collect polyurethane and polyethylene plastics as novel nest materials. Ecosphere, 4(12): Article 155, doi: 10.1890/ES13-00308.1

Mattsson K, Johnson E V, Malmendal A, et al. 2017. Brain damage and behavioural disorders in fish induced by plastic nanoparticles delivered through the food chain. Scientific Reports, 7(1): 11452, doi: 10.1038/s41598-017-10813-0

Moore C J, Moore S L, Leecaster M K, et al. 2001. A comparison of plastic and plankton in the north pacific central gyre. Marine Pollution Bulletin, 42(12): 1297–1300, doi: 10.1016/S0025-326X(01)00114-X

Moser M L, Lee D S. 1992. A fourteen-year survey of plastic ingestion by Western North Atlantic Seabirds. Colonial Waterbirds, 15(1): 83–94

Prata J C. 2018. Microplastics in wastewater: state of the knowledge on sources, fate and solutions. Marine Pollution Bulletin, 129(1): 262–265, doi: 10.1016/j.marpolbul.2018.02.046

Reichert J, Schellenberg J, Schubert P, et al. 2018. Responses of reef building corals to microplastic exposure. Environmental Pollution, 237: 955–960, doi: 10.1016/j.envpol.2017.11.006

Robards M D. 1993. NOAA-43ABNF203014, Plastic ingestion by North Pacific seabirds. Washington D C: US Department of Commerce

Rochman C M, Tahir A, Williams S L, et al. 2015. Anthropogenic debris in seafood: Plastic debris and fibers from textiles in fish and bivalves sold for human consumption. Scientific Reports, 5: 14340, doi: doi: 10.1038/srep14340

Schirinzi G F, Pérez-Pomeda I, Sanchís J, et al. 2017. Cytotoxic effects of commonly used nanomaterials and microplastics on cerebral and epithelial human cells. Environmental Research, 159: 579–587, doi: 10.1016/j.envres.2017.08.043

Schymanski D, Goldbeck C, Humpf H U, et al. 2018. Analysis of microplastics in water by micro-Raman spectroscopy: Release of plastic particles from different packaging into mineral water. Water Research, 129: 154–162, doi: 10.1016/j.watres.2017.11.011

Teuten E L, Saquing J M, Knappe D R U, et al. 2009. Transport and release of chemicals from plastics to the environment and to wildlife. Philosophical Transactions of the Royal Society B: Biological Sciences, 364(1526): 2027–2045, doi: 10.1098/rstb.2009.0054

Thompson R C, Swan S H, Moore C J, et al. 2009. Our plastic age. Philosophical Transactions of the Royal Society B: Biological Sciences, 364(1526): 1973–1976, doi: 10.1098/rstb.2009.0054

van Franeker J A, Blaize C, Danielsen J, et al. 2011. Monitoring plastic ingestion by the northern fulmar Fulmarus glacialis in the North Sea. Environmental Pollution, 159(10): 2609–2615

Vegter A C, Barletta M, Beck C, et al. 2014. Global Research Priorities to mitigate plastic pollution impacts on marine wildlife. Endangered Species Research, 25(3): 225–247, doi: 10.3354/esr00623

Villarrubia-Gómez P, Cornell S E, Fabres J. 2017. Marine plastic pollution as a planetary boundary threat: the drifting piece in the sustainability puzzle. Marine Policy, 96: 213–220, doi: 10.1016/j.marpol.2017.11.035

Zettler E R, Mincer T J, Amaral-Zettler L A. 2013. Life in the "plastisphere": microbial communities on plastic marine debris. Environmental Science and Technology, 47(13): 7137–7146, doi: 10.1021/es401288x

Zhu Dong, Chen Qinglin, An Xinli, et al. 2018. Exposure of soil collembolans to microplastics perturbs their gut microbiota and alters their isotopic composition. Soil Biology and Biochemistry, 116: 302–310, doi: 10.1016/j.soilbio.2017.10.027